HAL open science

Modelling of Transport in Homogeneous Turbulence

Antoine Briard

To cite this version:

Antoine Briard. Modelling of Transport in Homogeneous Turbulence. Fluids mechanics [physics.class-ph]. UPMC - Université Paris 6 Pierre et Marie Curie; Institut Jean le Rond d'Alembert, 2017. English. NNT : . tel-01621386

HAL Id: tel-01621386

https://theses.hal.science/tel-01621386

Submitted on 23 Oct 2017

HAL is a multi-disciplinary open access archive for the deposit and dissemination of scientific research documents, whether they are published or not. The documents may come from teaching and research institutions in France or abroad, or from public or private research centers.

L'archive ouverte pluridisciplinaire **HAL**, est destinée au dépôt et à la diffusion de documents scientifiques de niveau recherche, publiés ou non, émanant des établissements d'enseignement et de recherche français ou étrangers, des laboratoires publics ou privés.

THÈSE DE DOCTORAT DE L'UNIVERSITÉ PIERRE ET MARIE CURIE

Spécialité : Mécanique des Fluides

École Doctorale SMAER (ED 391)
Sciences Mécaniques, Acoustique, Electronique et Robotique de Paris

Présentée par :

Antoine Briard

Pour obtenir le grade de
DOCTEUR DE L'UNIVERSITÉ PIERRE ET MARIE CURIE

Modélisation du Transport en Turbulence Homogène

Dirigée par Thomas GOMEZ
à l'Institut Jean le Rond ∂'Alembert

Thèse soutenue à l'UPMC le 11 Octobre 2017 devant le jury composé de

Jean-Pierre BERTOGLIO	Directeur de Recherche, Ecole Centrale de Lyon	Rapporteur
Claude CAMBON	Directeur de Recherche, Ecole Centrale de Lyon	Examinateur
Luminita DANAILA	Professeur, CORIA, St-Étienne-du-Rouvray	Rapporteur
Thomas GOMEZ	Professeur, LML, Villeneuve d'Ascq	Directeur de thèse
Benoît-Joseph GRÉA	Ingénieur de Recherche CEA, CEA DAM Arpajon	Examinateur
Régis MARCHIANO	Professeur, UPMC ∂'Alembert, Paris	Examinateur
Annick POUQUET	Directrice de Recherche, NCAR, Boulder, USA	Examinateur
Pierre SAGAUT	Professeur, M2P2, Marseille	Examinateur

Abstract - Modelling of Transport in Homogeneous Turbulence

Modelling is essential to understand and reproduce the dominant physical mechanisms occurring in natural turbulent flows such as atmospheric and oceanic ones. Indeed, the dynamics of geophysical flows results of multiple complex processes interacting with each others, at various scales, intensities, and on different characteristic times. The fine description of such flows is currently out of reach of direct numerical simulations, notably because of Reynolds numbers limitations.

Consequently, we address in this thesis the modelling of homogeneous turbulence, using the spectral formalism of the eddy-damped quasi-normal Markovian (EDQNM) approximation. This first allows us to obtain results rapidly in terms of computational resources at very large Reynolds numbers, and thus to investigate separately some of the fundamental mechanisms at stake in natural turbulent flows, namely shear, mean temperature gradient, stratification, helicity, and combinations of these processes. In this framework, a two-step approach is considered: first, EDQNM is used to close the non-linear terms in the second-order moments equations, and anisotropy is then modelled through spherically-averaged tensors. This methodology is applied to the various configurations mentioned above, permits to propose new theoretical results, and to assess them numerically at large Reynolds numbers. Among the most important findings, we focused on (i) the prediction of the decay and growth laws of crucial one-point statistics such as the kinetic energy, the scalar variance, and helicity; (ii) the determination of spectral scalings; and (iii) the scale by scale distribution of anisotropy.

Key words: Spectral Modelling, EDQNM, Transport and Mixing, Homogeneous Turbulence

Résumé - Modélisation du Transport en Turbulence Homogène

La modélisation est essentielle pour comprendre et reproduire les phénomènes physiques dominants ayant lieu dans des écoulements turbulents naturels (atmosphériques, océaniques). En effet, la dynamique des écoulements géophysiques résulte d'interactions complexes à des échelles et intensités variées, et sur des temps différents. La description précise de tels écoulements est pour le moment hors de portée des simulations numériques directes, surtout à cause des limitations en nombre de Reynolds.

C'est pourquoi dans cette thèse on s'attaque à la modélisation de la turbulence homogène avec le formalisme spectral de l'approximation EDQNM. Ceci nous permet d'obtenir des résultats rapidement en termes de ressources numériques à très grands nombres de Reynolds, et ainsi d'étudier séparément la plupart des mécanismes en jeu dans les écoulements turbulents naturels, à savoir le cisaillement, le gradient de température, la stratification, l'hélicité, et des combinaisons de ces éléments. On procède en deux étapes: tout d'abord, l'EDQNM permet de fermer les équations des moments d'ordre 2, et ensuite l'anisotropie est modélisée grâce à des tenseurs moyennés sphériquement. Cette méthode est appliquée aux différentes configurations mentionnées ci-dessus, nous permet de proposer de nouveaux résultats et de les valider numériquement à grands nombres de Reynolds. Parmi les points les plus importants, nous nous sommes concentrés sur (i) la prédiction des lois de croissance et décroissance de quantités telles que l'énergie cinétique, la variance scalaire et l'hélicité; (ii) la détermination des comportements spectraux; et (iii) la distribution d'anisotropie échelle par échelle.

Remerciements

Tout d'abord, je souhaite remercier mon directeur, Thomas, qui m'a accompagné pendant toute cette longue et passionnante aventure depuis mon stage de M2. Malgré la distance et quand le téléphone était insuffisant, ce fut toujours avec plaisir que nous avons pu nous retrouver autour d'un café pour discuter turbulence, de mes derniers travaux, et de la rédaction des articles que nous avions sur le feu. J'imagine qu'il a pu être difficile d'encadrer cette thèse depuis Lille à partir de la deuxième année, car il faut savoir que j'ai besoin de discuter, d'échanger, et que j'envoie au moins trois mails par jour (dans une petite journée). J'ai cependant la conviction qu'en dépit de la distance qui nous a séparés, nous avons accompli un travail sérieux et complet: Thomas m'a laissé de l'autonomie dans le choix des thématiques que je souhaitais aborder, et m'a toujours suivi et encouragé malgré les changements parfois radicaux de mes intérêts, et je l'en remercie chaleureusement.

Je remercie grandement Luminita Danaila et Jean-Pierre Bertoglio qui ont accepté d'être rapporteurs de cette thèse, et je n'ose imaginer la quantité de travail que cela demande de lire avec attention les près de 300 pages qui vont suivre. Je souhaite adresser un remerciement très particulier aux autres membres de mon jury: en premier lieu, Pierre Sagaut, grâce à qui, avec son cours d'initiation à la turbulence en M2, je me suis découvert une passion pour cette discipline, et avec qui j'ai eu le privilège de collaborer sur certains travaux par la suite. Ensuite, j'aimerais remercier Claude Cambon, que je considère comme l'expert EDQNM anisotrope, pour toutes les discussions fructueuses que nous avons pu avoir lors de ses passages à Paris, au téléphone, ou encore en conférences. C'est grâce en partie à son "erreur de jeunesse" comme il l'appelle, que ce sujet de thèse est né, et pour cela, je lui en suis extrêmement reconnaissant. Je voudrais aussi remercier Annick Pouquet pour avoir accepté d'être membre de mon jury: c'est un immense honneur pour moi de rencontrer une des pionnières, entre autres, de l'EDQNM. J'adresse également de sincères remerciements à Benoît-Joseph Gréa pour toutes les discussions que nous avons pu avoir à de multiples occasions, et pour avoir partagé avec moi son expertise de l'USHT, ce qui m'a été d'une aide très précieuse : c'est avec lui que je continuerai ma formation en post-doc, et je lui en suis très reconnaissant. Enfin, je remercie Régis Marchiano d'être membre de mon jury, d'avoir participé activement à l'évaluation de ma thèse dès la deuxième année, même si mon travail n'est pas exactement dans sa thématique de recherche. Je remercie très chaleureusement l'ensemble du jury pour les discussions très intéressantes que nous avons eues après la soutenance.

Je tiens à remercier sincèrement les doctorants, post-doctorants et "permanents" du laboratoire avec qui j'ai pu discuter de tout et n'importe quoi au cours de ces trois années: faire une liste exhaustive serait fastidieux, aussi je vous prie de m'excuser si j'en oublie, mais les concernés se reconnaîtront: Anca, Aurélie, Claire, Clara, Maya, Alessio, Arthur, Augustin, Barend, Bruno, Charles, Christian, Gounseti, Hervé, Hugo, Julien, Jan, Jean-Camille, Jean-François, Philippe, Raphaël, Thomas, Valentin, ... Je remercie également Manasa, dont j'ai encadré le stage de M1, pour ces quelques mois très intéressants à travailler ensemble sur la turbulence stratifiée instable: je te souhaite bonne chance dans la recherche de ton sujet de thèse! Je voudrais adresser un merci très particulier à deux personnes: Sophie et Vincent, avec qui j'ai passé la majorité de mes pauses café et déjeuners, où les discussions à propos de Star Wars se sont enchaînées aux conversations scientifiques, entre des considérations politiques et des réflexions sur les super-héros et les séries du moment. Et à Vincent, notamment, un immense merci de m'avoir aidé au début de ma thèse dans ma lutte contre les développements EDQNM anisotropes: tu m'as passé le relais, et sans ton temps et ta bienveillance, j'aurais probablement mis beaucoup plus de temps à démarrer. Enfin, je remercie Olivier Joachim, mon professeur de physique de maths spé : si quelqu'un m'a donné envie de continuer les sciences et en particulier la *physique* (lire *mécanique* pour les âmes sensibles), c'est bien lui, et je n'aurais probablement pas songé à faire

une thèse sans ce qu'il m'a transmis, et c'est avec plaisir que nous nous retrouvons régulièrement autour d'un café : merci d'avoir assisté à la thèse.

Si ma thèse s'est bien déroulée au laboratoire, c'est aussi grâce aux équipes administratives et informatiques: j'aimerais remercier en particulier Simona Otarasanu, Olivier Labbey et Anne Marchal pour leur aide continue, les informaticiens de m'avoir dépanné plus d'une fois, et enfin les membres de l'école doctorale SMAER. J'insiste particulièrement sur l'aide de Simona, qui a débloqué certains verrous à des moments clés de ma thèse, et je lui en suis extrêmement reconnaissant.

Je souhaite également remercier les élèves de L1 et de L2 que j'ai encadrés lors des TD de Thermodynamique, Mathématiques, Thermique et Mécanique pendant ces trois années à l'UPMC: cela a été une expérience formidable et très formatrice pour moi, et je remercie tout particulièrement les encadrants, Catherine, Diana , Sophie, et Jean-Loïc.

Enfin, il me reste à remercier ma famille "étendue" pour son soutien sans faille. Se lancer dans l'aventure qu'est l'écriture d'une thèse, c'est un défi, et il y peut y avoir des périodes plus difficiles que d'autres, où plus rien ne fonctionne et où on ne comprend plus rien. Celle qui a été en première ligne et que je ne remercierai jamais assez, c'est Mathilde, qui est devenue Mme Briard le 10 septembre 2016. Désolé de t'avoir abandonnée par moments le soir pour répondre à mes élèves en panique la veille d'un examen, et de t'avoir agacée avec mon stress lorsque la review d'un article se faisait attendre. Mais au moins, grâce à moi, tu sais ce que veut dire EDQNM maintenant. Mes remerciements s'adressent à mon père et mes frères, à tous mes proches que j'ai côtoyés durant ces trois ans, à tous ceux qui pensaient (ou pensent encore!) que la thèse est un stage et que je n'avais pas un "vrai" travail, à ceux qui ont su me changer les idées quand il le fallait, et à ceux avec qui j'ai tout simplement passé du bon temps. Mes pensées émues se dirigent vers ma mère qui m'a toujours soutenu et qui n'a malheureusement pas pu savoir que j'avais réussi à décrocher ma bourse de thèse, mais je suis sûr qu'elle n'en a jamais douté.

Publications & Conférences

- Jenny, Plaut, & Briard, *Numerical study of subcritical Rayleigh-Bénard convection rolls in strongly shear-thinning Carreau fluids*, J. Non-Newtonian Fluid Mech., **219**, 19-34 (2015)
- Briard, & Gomez, *Passive scalar convective-diffusive subrange for low Prandtl numbers in isotropic turbulence*, Phys. Rev. E, **91**, 011001(R) (2015)
- Briard, Gomez, Sagaut, & Memari, *Passive scalar decay laws in isotropic turbulence: Prandtl number effects*, J. Fluid Mech., **784**, 274-303 (2015)
- Briard, Gomez, & Cambon, *Spectral modelling for passive scalar dynamics in homogeneous anisotropic turbulence*, J. Fluid Mech., **799**, 159-199 (2016)
- Briard, Gomez, Mons, & Sagaut, *Decay and growth laws in homogeneous shear turbulence*, J. Turbul., **17** (7), 699-726 (2016)
- Briard, & Gomez, *Mixed-derivative skewness for high Prandtl and Reynolds numbers in homogeneous isotropic turbulence*, Phys. Fluids, **28** (8), 081703 (2016)
- Briard, & Gomez, *Prandtl number effects on the cospectrum decay in homogeneous isotropic turbulence with a mean scalar gradient*, J. Turbul., **18** (5), 418-442 (2017)
- Briard, Iyer, & Gomez, *Spectral modelling for active scalar dynamics in homogeneous unstably stratified turbulence at large Reynolds numbers*, Phys. Rev. Fluids, **2** (4), 044604 (2017)
- Briard, & Gomez, *Dynamics of helicity in homogeneous skew-isotropic turbulence*, J. Fluid Mech., **821**, 539-581 (2017)

- Briard, Gomez, & Sagaut, *Passive scalar decay in homogeneous turbulence*, ERCOFTAC, Henri Bénard, ∂'Alembert, Paris (Mai 2015)
- Briard, Gomez, & Cambon, *Passive Scalar and Scalar Flux in Homogeneous Turbulence*, GDR Turbulence, LEGI, Grenoble (Juin 2015)
- Briard, Gomez, & Cambon, *Passive Scalar and Scalar Flux in Homogeneous Turbulence*, CFM, Lyon (Août 2015)
- Briard, Gomez, Mons, & Sagaut, *Return to isotropy of homogeneous sheared turbulence*, Turbulence cascades, EUROMECH, Lille (Décembre 2015)
- Briard, Gomez, Mons, & Sagaut, *EDQNM applied to sustained shear flows*, ERCOFTAC, Henri Bénard, ∂'Alembert, Paris (Mai 2016)
- Briard, & Gomez, *Decay of helicity in homogeneous isotropic turbulence*, GDR Turbulence, PMMH, Paris (Juin 2016)
- Briard, & Gomez, *Anisotropic spectral modelling for homogeneous turbulence: shear, stratification, and helicity*, LPS-ENS, Séminaire de groupe, Paris (Janvier 2017)
- Briard, Gomez, Iyer, & Gréa, *Anisotropic EDQNM modelling for unstably stratified homogeneous turbulence*, ERCOFTAC, Henri Bénard, M2P2, Marseille (Mai 2017)
- Briard, & Gomez, *Statistics of helicity in homogeneous skew-isotropic turbulence* , GDR Turbulence, IMFT, Toulouse (Juin 2017)
- Briard, Iyer, Gréa, & Gomez, *Anisotropic modelling for unstably stratified turbulence at large Reynolds and Schmidt numbers*, ETC, Stockholm (Août 2017)

Contents

Abstract i

Acknowledgement ii

Publications and conferences iv

Contents v

Abbreviations x

Symbols xi

Introduction 1

I Passive Scalar in Isotropic Turbulence & Velocity Field in Anisotropic Turbulence 8

1 Passive Scalar Mixing in Homogeneous Isotropic Turbulence 9
- 1.1 The equations of homogeneous isotropic turbulence . . . 9
- 1.2 The inertial scaling of E_T for $Pr \ll 1$ . . . 12
- 1.3 Mixed-derivative skewness S_T for $Pr \gg 1$ . . . 15
- 1.4 Time evolution of scalar integrated quantities . . . 21
  - 1.4.1 The basics of the CBC dimensional analysis . . . 23
  - 1.4.2 Validation at large Reynolds numbers for $Pr \neq 1$ . . . 25
  - 1.4.3 Transition to low Reynolds and Péclet numbers . . . 26
  - 1.4.4 Transition for $Pr \neq 1$ . . . 27
  - 1.4.5 Study of the integral scales L and L_T . . . 29
- 1.5 Conclusions for a passive scalar field in HIT . . . 31

2 Spectral Modelling of the Velocity Field in Homogeneous Turbulence 33
- 2.1 Equations in physical space . . . 33
- 2.2 Spectral equations and transfers . . . 35
  - 2.2.1 Craya equation for $\hat{R}_{ij}$ . . . 35
  - 2.2.2 Craya-Herring frame - $\mathcal{E} - Z$ decomposition . . . 36
  - 2.2.3 Generalized Lin equations . . . 37
- 2.3 The closure problem . . . 38
  - 2.3.1 The EDQNM approximation . . . 38
  - 2.3.2 Directional and Polarization transfers $T_{\mathcal{E}}$ and T_Z . . . 40

2.4 Spherically-averaged equations . . . 41
2.4.1 Spherically-averaged descriptors . . . 41
2.4.2 Spherically-averaged final Lin equations . . . 43
2.4.3 Return to isotropy - Spectral tensor . . . 44

3 Dynamics of the Velocity Field in Shear-driven Turbulence 46
3.1 Homogeneous Shear-Released Turbulence (HSRT) . . . 48
3.1.1 Validation of HSRT with Rapid Distortion Theory . . . 49
3.1.2 Kinetic energy spectrum $E(k,t)$ and spectral tensor $\phi_{ij}(k,t)$ . . . 49
3.1.3 Anisotropy descriptors $b_{ij}(t)$ and $H_{ij}^{()}(k,t)$ . . . 50
3.1.4 Modelling of the pressure-strain tensor $\Pi_{ij}^{(s)}$ . . . 51
3.1.5 Additional remarks on HSRT . . . 54
3.2 Decay of $K(t)$ and $R_{13}(t)$ in Saffman and Batchelor HSRT . . . 55
3.3 Homogeneous Shear Turbulence . . . 58
3.3.1 Exponential growth of the kinetic energy $K(t)$ . . . 58
3.3.2 Non-linear transfers and the shear wavenumber . . . 61
3.3.3 Discussion on the scattering of integrated quantities in HST . . . 62
3.4 Conclusion and perspectives . . . 65
3.4.1 Conclusions on HST and HSRT . . . 65
3.4.2 Exponential growth rate γ . . . 66
3.4.3 Perspectives . . . 67

II Transport and Mixing in Homogeneous Anisotropic Turbulence 75

4 Spectral Modelling of a Passive Scalar in Homogeneous Turbulence 76
4.1 Scalar and scalar flux generalized Lin equations . . . 77
4.2 EDQNM closure for $\mathcal{E}^T$ and F_i . . . 78
4.3 Final spherically-averaged scalar Lin equations . . . 80
4.3.1 Modelling of $\mathcal{E}^T$ and F_i . . . 80
4.3.2 Spherical average of the passive scalar and scalar flux . . . 81
4.4 Cospectrum for an uniform mean scalar gradient . . . 84

5 Dynamics of a Passive Scalar in Homogeneous Turbulence 86
5.1 Homogeneous shear-driven turbulence . . . 88
5.1.1 Scalar spectrum $E_T(k,t)$ and non-linear transfers . . . 88
5.1.2 Scalar decay laws and RTI in HSRT . . . 89
5.1.3 Sustained shear (HST) . . . 91
5.1.4 Decay and growth laws for the passive scalar in HSRT and HST . . . 92
5.2 Isotropic Turbulence with a mean Scalar Gradient . . . 92
5.2.1 Spectra and transfers . . . 93
5.2.2 Comparisons with experimental and numerical results . . . 94
5.2.3 Decay and growth laws for the cospectrum and passive scalar . . . 96
5.2.4 Return to isotropy in HITSG . . . 101
5.3 Homogeneous Shear Turbulence with Scalar Gradient . . . 102
5.3.1 Definitions and transfers . . . 102
5.3.2 Comparisons with experimental and numerical results . . . 103
5.3.3 Growth of K, K_T, $K_{\mathcal{F}}$ and $K_{\mathcal{F}}^S$ . . . 107
5.3.4 Streamwise flux spectrum $\mathcal{F}_S(k,t)$ . . . 109

5.3.5 Return to isotropy in HSTSG . . . 110
5.4 Conclusions for the passive scalar at $Pr = 1$ . . . 110

6 Prandtl Number Effects on Passive Scalar Dynamics 113
6.1 Prandtl number effects in HITSG . . . 114
6.1.1 Inertial scalings for $E_T(k,t)$ and $\mathcal{F}(k,t)$ - Comparisons . . . 114
6.1.1.1 Highly diffusive passive scalar $Pr \ll 1$ . . . 115
6.1.1.2 Weakly diffusive passive scalar $Pr \gg 1$ . . . 117
6.1.1.3 Spectral transfers and conclusions for the inertial scalings . . . 118
6.1.2 Numerical results - Time evolution and anisotropy . . . 119
6.1.2.1 Prandtl effects on the decay and growth of $< u_3\theta >$ and $< \theta^2 >$ 119
6.1.2.2 Cospectrum correlation $\rho_{w\theta}$, pressure-scalar correlation $\Pi_{\mathcal{F}}$, and Nusselt number Nu . . . 121
6.1.2.3 Return to isotropy of small scales . . . 123
6.1.3 Conclusions for $Pr \neq 1$ in HITSG . . . 124
6.2 Prandtl number effects in shear-driven turbulence . . . 125
6.2.1 Homogeneous shear-released turbulence . . . 126
6.2.2 Sustained shear flow . . . 126
6.2.3 Homogeneous Shear Turbulence with a mean Scalar Gradient . . . 129
6.2.4 Conclusions about shear-driven turbulence for $Pr \neq 1$ . . . 130

7 Spectral Modelling for Unstably Stratified Homogeneous Turbulence 131
7.1 Evolution equations in USHT . . . 132
7.1.1 Additional coupling terms . . . 132
7.1.2 Spherically-averaged Lin equations for USHT . . . 133
7.2 Spectral scaling and infrared dynamics . . . 134
7.2.1 Spectral scaling of E, E_T and $\mathcal{F}$ . . . 135
7.2.2 Infrared dynamics . . . 137
7.3 One-point statistics . . . 138
7.3.1 The Froude number Fr . . . 138
7.3.2 The mixing intensity Λ . . . 139
7.3.3 Growth of the kinetic energy $K(t)$ . . . 140
7.3.4 Global anisotropy . . . 142
7.3.5 Comparison with Burlot *et al.* (2015*b*) . . . 143
7.3.6 Conclusions on one-point statistics . . . 144
7.3.7 Eddy-damping constants . . . 145
7.4 Scale by scale anisotropy and structure of the flow . . . 146
7.5 Pressure spectra and high Schmidt numbers . . . 148
7.5.1 Pressure spectra . . . 149
7.5.2 Cospectrum at high Schmidt numbers . . . 150
7.6 Conclusion on USHT . . . 153
7.7 Perspective - Variable stratification $N(t)$ . . . 154
7.7.1 Evolution equations with variable stratification . . . 154
7.7.2 Prediction of the growth rate α^{RT} . . . 156
7.7.3 Numerical results . . . 157

8 Dynamics of Helicity in Skew-Isotropic Turbulence 160
8.1 Spectral modelling of helicity . . . 162
8.1.1 The $\mathcal{E}$-$\mathcal{H}$ decomposition . . . 162

8.1.2 Spherically-averaged helical Lin equations for $E(k,t)$ and $H(k,t)$ 164
8.2 Numerical results on the helical and kinetic fields 165
8.2.1 The importance of initial conditions $H(k,t=0)$ 165
8.2.2 Helical spectrum $H(k,t)$ and non-linear transfers 166
8.2.3 Infrared dynamics and non-local transfers 168
8.2.4 Decay laws in helical flows 171
8.2.5 Robustness of the decay exponents - Altered infrared dynamics 174
8.3 Structure functions in helical turbulence 175
8.3.1 Inertial scaling for $S(r)$ and $D^{(uu\omega)}(r)$ 176
8.3.2 Evolution equation of ϵ_H 178
8.4 Effect of helicity on the scalar flux 182
8.4.1 Modelling of the quadrature spectrum 183
8.4.2 Decay of $< \omega_3\theta >$ and inertial scaling of $Q(k,t)$ 184
8.5 Conclusion on homogeneous skew-isotropic turbulence 187

9 General Conclusions and Perspectives 189

A Statistics and Structure Functions 192
A.1 Evolution equations and definitions 192
A.2 Tensorial relations for homogeneous turbulence 193
A.2.1 Dissipation ϵ and enstrophy $< \omega^2 >$ 193
A.2.2 Identities for the velocity field 193
A.2.3 Evolution equations of $\mathcal{W}_{ij}$ and $< \omega^2 >$ 195
A.2.4 Evolution equation of ϵ_{ij} 195
A.2.5 Evolution equations of $< \xi_i\xi_j >$ and $< \xi^2 >$ 197
A.2.6 Cospectrum in isotropic turbulence with mean scalar gradient 197
A.3 Homogeneous isotropic turbulence 198
A.3.1 Spectral formalism 198
A.3.2 Second and third-order statistics 199
A.3.3 Results for the velocity field 201
A.3.4 Results for the passive scalar field 202
A.4 Structure functions and auto-correlations 203
A.4.1 Second-order longitudinal correlation and structure function 203
A.4.2 Third-order longitudinal correlation and structure function 205
A.4.3 Towards the Kármán-Howarth equation 206
A.4.4 Yaglom and Corrsin equations 209

B Non-local Expansions of the Non-Linear Transfers 212
B.1 Non-local fluxes 213
B.2 Expansions for $q \ll k \sim p$ 214
B.3 Expansions for $k \ll p \sim q$ 217
B.4 Applications of the isotropic non-local transfers 218

C Details on the Spherically-Averaged Lin Equations 220
C.1 Spectral evolution equations 220
C.1.1 Craya equation 220
C.1.2 Generalized Lin equations for $\mathcal{E}$ and Z 221

C.1.3 Evolution equation of $S_{ijk}(\boldsymbol{k}, \boldsymbol{p}, t)$ . . . 222
C.2 Calculations of $T_{\mathcal{E}}$ and T_Z . . . 223
C.2.1 Relations between frameworks . . . 223
C.2.2 Computation of $\mathfrak{T}_{ijn}^{\mathrm{QN}}$ . . . 224
C.3 Spherically-averaged non-linear transfers . . . 227
C.3.1 λ-integration . . . 227
C.3.2 Spherical integration . . . 227
C.4 Spherically-averaged linear transfers . . . 228
C.4.1 Spherical integration . . . 228
C.4.2 Computation of T_{ij}^{L} . . . 228
C.4.3 Return to isotropy . . . 230
C.4.4 Rotation . . . 230
C.5 Kinetic quadratic anisotropic contributions . . . 231
C.6 Fourth-order expansion for $\mathcal{E}$ and Z . . . 238
C.6.1 Fourth order linear transfers . . . 238
C.6.2 Fourth order non-linear transfers . . . 241
C.6.3 Fourth-order final spherically-averaged equations . . . 242

D Additional Results for the Velocity Field in Homogeneous Turbulence 243
D.1 Rapid Distortion Theory . . . 243
D.2 Homogeneous Axisymmetric Turbulence . . . 244
D.3 Homogeneous Plane Distortion . . . 246
D.4 Pressure fluctuations in HAT . . . 248
D.4.1 Evolution equation of the pressure correlation $\mathcal{E}_P$ . . . 248
D.4.2 Spectrum and pressure variance . . . 249
D.5 Details on helical turbulence . . . 250
D.5.1 Non-linear helical transfer T_H . . . 251
D.5.2 Non-linear purely helical transfer . . . 251
D.5.3 Details on the evolution equation of ϵ_H . . . 252
D.5.4 Re-interpretation of the helical viscous cutoff k_η^H . . . 255

E Details on Spherically-Averaged Scalar Lin Equations 257
E.1 Scalar-scalar correlation . . . 257
E.1.1 Scalar Craya equation . . . 257
E.1.2 EDQNM closure for $\mathcal{E}^T$ . . . 258
E.1.3 Spherically-averaged scalar Lin equations . . . 259
E.1.4 Scalar quadratic anisotropic contributions . . . 260
E.2 Scalar-velocity correlation $\boldsymbol{F}$ . . . 260
E.2.1 Craya equation for the cospectrum flux . . . 261
E.2.2 Quasi-normal approximation for F_i . . . 261
E.2.3 Computation of the non-linear transfers of F_i . . . 262
E.2.4 Spherically-averaged cospectrum Lin equations . . . 263
E.2.5 Alternative modelling for $\boldsymbol{F}$ . . . 263
E.2.6 Scalar flux quadratic anisotropic contributions . . . 266
E.2.7 Scalar flux in HHTSG . . . 267

Bibliography 270

Abbreviations

CBC	**C**omte-**B**ellot and **C**orrsin
DIA	**D**irect-**I**nteraction **A**pproximation
EDQNM	**E**ddy-**D**amped **Q**uasi-**N**ormal **M**arkovian
HAT	**H**omogeneous **A**nisotropic **T**urbulence
HAxT	**H**omogeneous **A**xisymmetric **T**urbulence
HHT	**H**omogeneous **H**elical **T**urbulence
HHTSG	**H**omogeneous **H**elical **T**urbulence with **S**calar **G**radient
HIT	**H**omogeneous **I**sotropic **T**urbulence
HITSG	**H**omogeneous **I**sotropic **T**urbulence with **S**calar **G**radient
HDRT	**H**omogeneous **D**istortion-**R**eleased **T**urbulence
HDT	**H**omogeneous **D**istortion **T**urbulence
HSRT	**H**omogeneous **S**hear-**R**eleased **T**urbulence
HST	**H**omogeneous **S**hear **T**urbulence
HSTSG	**H**omogeneous **S**hear **T**urbulence with **S**calar **G**radient
IBR	**I**nertial-**B**alanced **R**ange
ICR	**I**nertial-**C**onvective **R**ange
IDR	**I**nertial-**D**iffusive **R**ange
LES	**L**arge **E**ddy **S**imulation
LHDIA	**L**agrangian **H**istory **DIA**
MHD	**M**agneto**H**ydro**D**ynamics
PLE	**P**ermanence of **L**arge **E**ddies
RANS	**R**eynolds **A**veraged **N**avier-**S**tokes
RDT	**R**apid **D**istortion **T**heory
RTI	**R**eturn **T**o **I**sotropy
USHT	**U**nstably **S**tratified **H**omogeneous **T**urbulence
TFM	**T**est **F**ield **M**odel
VCR	**V**iscous **C**onvective **R**ange

Symbols

a	Thermal diffusivity, non-local parameter
A_{ij}	Mean velocity gradient matrix
A_1, A_2, A_3	Eddy-damping constants
$\mathcal{A}$	Atwood number
b_{ij}, b_{ij}^T	Kinetic and Scalar Anisotropy tensors
c	Active scalar: buoyant field scaled as a velocity
D_{LL}, D_{NN}, D_{LLL}	Second and third order structure functions for velocity
D_{TT}, D_{LTT}	Second and third order structure functions for scalar
$\mathcal{E}$, $\mathcal{E}^T$	Directional anisotropy and scalar correlation
E, E_T	Kinetic energy and scalar variance spectra
$f(r)$	Longitudinal velocity second-order correlation
Fr	Froude number
$\mathcal{F}$, $\mathcal{F}^S$	Cospectrum and streamwise flux
F_i	Scalar flux
$g(r)$	Transverse velocity second-order correlation
$G(t)$, $G_T(t)$	Normalized kinetic and scalar palinstrophy
$h(r)$	Second-order correlation in HHT
$H_{ij}^{(\mathrm{dir})}$, $H_{ij}^{(\mathrm{pol})}$, $H_{ij}^{(T)}$	Directional, polarization and scalar anisotropy descriptors
$H_{ijpq}^{(\mathrm{dir})}$, $H_{ijpq}^{(\mathrm{pol})}$	Anisotropy descriptors at the fourth order
$H_i^{(F)}$	Scalar flux anisotropy descriptor
H, $\mathcal{H}$	Helicity spectrum and density of helicity
$k(r)$	Longitudinal velocity third-order correlation
k_i, p_i, q_i, k, p, q	Wave vectors and wave numbers of the triad
k_L, k_T, k_H	Kinetic, scalar and helical integral wavenumbers
k_η, k_{B}, k_{CO}	Kolmogorov, Batchelor and Corrsin-Obukhov wavenumbers
k_η^H	Helical dissipative wavenumber
K, K_T, K_H	Kinetic energy, scalar variance, and helicity
$K_{\mathcal{F}}$, $K_{\mathcal{F}}^S$	Cospectrum and streamwise flux energies
K_0, K_{CO}, K_{CD}, C_H	Spectral constants
L, L_T, L_H	Kinetic, scalar and helical integral scales

N, L	Stratification frequency and mixing length for USHT
N_i, N_{ijkl}	Helical mode and generalized helical mode
Nu	Nusselt number
p, p_{S}, p_T, $p_{\mathcal{F}}$, p_E, p_H	Backscatter parameters
P_{ij}, P_{ijl}, P_{ijkl}	Projector, Kraichnan operator, and generalized projector
Pe, Pe_λ	Péclet numbers
Pr, Pr_T	Prandtl and turbulent Prandtl numbers
r_i	Separation vector
R_{ij}, R^T, R^H_{ii}	Velocity, scalar-scalar, helicity second-order correlations
Re_L, Re_λ	Reynolds numbers based on integral and Taylor scales
R_T	Ratio of kinetic and scalar characteristic times
$S(r)$	Third-order correlation in HHT
S	Mean velocity gradient
$S(t)$, $S_T(t)$	Normalized velocity and mixed derivative skewnesses in HIT
$\mathcal{S}$, $\mathcal{S}_\theta$	Dimensionless mean velocity and scalar gradients
Sc	Schmidt number
S_R, S_R^T, $S_R^{\mathcal{F}}$, $S_R^{\mathcal{F},S}$	Shear rapidity
$S^{\mathrm{NL(iso)}}$, $S_{ij}^{\mathrm{NL(dir)}}$, $S_{ij}^{\mathrm{NL(pol)}}$	Non-linear kinetic transfers
$S_{ij}^{(\mathrm{RTI})}$	Return to isotropy kinetic transfer
$S^{\mathrm{T,NL(iso)}}$, $S_{ij}^{\mathrm{T,NL(dir)}}$	Non-linear scalar transfers
$S^{\mathrm{NL(hel)}}$, S_{H2}^{NL}, S_{H1}^{NL}	Non-linear helical transfers
$S_{ijpq}^{\mathrm{NL(dir)}}$, $S_{ijpq}^{\mathrm{NL(pol)}}$	Non-linear kinetic transfers at the fourth order
$S^{\mathrm{L(iso)}}$, $S_{ij}^{\mathrm{L(dir)}}$, $S_{ij}^{\mathrm{L(pol)}}$	Linear kinetic transfers
$S_{ijpq}^{\mathrm{L(dir)}}$, $S_{ijpq}^{\mathrm{L(pol)}}$	Linear kinetic transfers at the fourth order
$\tilde{S}_{ij}^{\mathrm{L(pol)}}$	Additional linear transfer for rotation
$S_{()}^{\mathrm{L,USHT(...)}}$	Linear transfers for USHT
$S^{\mathrm{T,L(iso)}}$, $S_{ij}^{\mathrm{T,L(dir)}}$	Non-linear scalar transfers
$S_i^{\mathrm{F,NL}}$, $S_i^{\mathrm{F,L}}$, $S_i^{\mathrm{F,NL(hel)}}$	Non-linear and linear scalar flux transfers
$S_i^{\mathrm{Q,NL}}$	Non-linear quadrature transfer
$S_i^{\mathrm{F,(RTI)}}$	Scalar flux return to isotropy transfer
$T = \theta + \Theta$	Total scalar field
T_{ij}^{NL}, T_ε, T_Z	Total, directional and polarization kinetic non-linear transfers
$T_i^{\mathrm{F,NL}}$, $T^{\mathrm{T,NL}}$	Total non-linear scalar flux and scalar transfers
$\mathfrak{T}_{ijn}$, $\mathfrak{T}_{ij}^F$, $\mathfrak{T}_i^T$	Kinetic, scalar flux and scalar fourth order transfers
T^+, T^-, T_T^+, T_T^-	Non-local isotropic transfers
$v_i = u_i + U_i$	Total velocity field
$\mathfrak{v}_i$	Buoyant field scaled as a velocity for USHT
W_{ij}, W_i^F	Kinetic and scalar flux non-linear RTI transfers
x_i	Position

Z	Polarization anisotropy
$\alpha_i = k_i/k$	Unit vector along k
α, α_T, α_T^{Λ}, $\alpha_{\mathcal{F}}$	Kinetic, scalar and cospectrum CBC exponents
α^{RT}	Growth rate of the Rayleigh-Taylor mixing zone
β	Exponential growth rate in USHT
γ, γ_T, $\gamma_{\mathcal{F}}^{(S)}$	Kinetic, scalar and scalar flux exponential rates
δ_{ij}	Kronecker symbol
δ	Increment for structure functions
ϵ, ϵ_T, ϵ_H	Kinetic, scalar and helical dissipation rates
$\epsilon_{\mathcal{F}}$, $\epsilon_{\mathcal{F}}^S$	Cospectrum and streamwise flux dissipation rates
η	Kolmogorov scale
θ_{kpq}, θ_{kpq}^T, θ_{kpq}^F	Triple correlations characteristic times
λ_i, Λ	Mean scalar gradient vector and intensity (HITSG)
Λ	Mixing parameter (USHT)
μ_1, μ_2, μ_3	Eddy-damping terms
ν	Kinematic viscosity
Π_{ij}, $\Pi_{\mathcal{F}}$	Pressure-strain tensor and cospectrum destruction
$\Pi^{\pm}$, $\Pi_T^{\pm}$	Non-local isotropic fluxes
ρ	Density
$\rho_{u\theta}$, $\rho_{v\theta}$, $\rho_{w\theta}$	Scalar flux correlations
σ, σ_T	Kinetic and scalar infrared slopes
τ_0	Eddy turn-over time
$\boldsymbol{\phi}$, $\boldsymbol{\phi}^T$	Kinetic and scalar spectral tensors
ζ	Non-local expansion parameter
Ω_i	Mean rotation
$(\boldsymbol{e^{(1)}}, \boldsymbol{e^{(2)}}, \boldsymbol{\alpha})$	Vector of Craya-Herring Frame
$(\boldsymbol{\beta}, \boldsymbol{\gamma}, \boldsymbol{\alpha})$	Frame linked to the triad

Cette thèse est dédiée à ma mère, qui, même si elle ne comprenait pas toujours ce sur quoi je travaillais, m'a toujours soutenu pour cette aventure.

Que la Force soit avec toi.

Introduction

"When you have eliminated the impossible, whatever remains, however improbable, must be the truth."

– Conan Doyle, *Sherlock Holmes*

The understanding of turbulence is a complex task of crucial importance since turbulent flows can be found in many natural flows, such as atmospheric or oceanic ones, and in various industrial applications as well. The complexity of turbulence arises from the fact that it gathers multiple scales, from the largest which contain the energetic eddies and the signature of production mechanisms, to the smallest dissipative scales. These different scales notably interact with each other in an intricate way because of the non-linearity of the Navier-Stokes equation. This non-linearity constitutes both the richness and the challenge of turbulence since it makes it at the same time incredibly varied and complicated to predict. Though the **prediction** of turbulence is still extremely difficult, it is of practical interest for various applications, with meteorology among them. It is worth noting that proving the existence and uniqueness of a general solution to the three-dimensional Navier-Stokes equations remains one of the six problems of the millennium.

Even by assuming that the turbulence is **homogeneous**, the objective to fully master the distinct features of natural turbulent flows is rather ambitious. Indeed, the understanding of the impact of large scales anisotropic production mechanisms on the global dynamics is made difficult by the numerous interactions and energy transfers between scales that exist in developed turbulence. Moreover, turbulence is also known to considerably improve mixing properties, so that the **transport of a scalar field**, such as concentration or temperature fluctuations, is a relevant feature to address and comprehend, for both theoretical and practical purposes. If one considers for instance an unbounded **atmospheric flow**, it may be subjected to rotation and shear, while the advected scalar field can additionally experience stratification through a mean temperature or concentration gradient. Even with the homogeneity assumption, the task of disentangling the dominant mechanisms remains complex since they all contribute diversely in the dynamics, at various scales and during characteristic times which may be distinct for the velocity and scalar fields.

Thus, a relevant method would be to investigate separately some of these mechanisms, to accurately determine their dominant properties. In this spirit, some authors have brought insightful answers with pioneering experiments and Direct Numerical Simulations (DNS): Warhaft & Lumley (1978) studied the decay of a passive scalar field in grid turbulence, without any production

mechanisms, showing that the algebraic decay rate of the scalar variance $< \theta^2 >$ strongly depends on the initial conditions. Later on, Warhaft (1980) proved experimentally as well that the presence of a mean strain caused by an axisymmetric contraction was accelerating the decay of the scalar field. On the contrary, Sirivat & Warhaft (1983) added a mean temperature gradient by several means - heated grid, a mandoline (screen of heated wires), a toaster - to analyze the dynamics of a passive scalar when the fluctuations are sustained. In their famous experiment, Tavoularis & Corrsin (1981) (TC81) combined both shear and a mean temperature gradient and studied mixed velocity-scalar statistics, along with some crucial one-point quantities for modelling, such the turbulent Prandtl number and diffusivity tensor. Regarding early DNS, Rogers & Moin (1987) analyzed the properties of a shear flow and the resulting global anisotropy between the streamwise and transverse directions, and later Rogers *et al.* (1989) added a mean scalar gradient, which is the same configuration as TC81, that nevertheless exhibited some significant quantitative discrepancies.

An exhaustive list of the first DNS and experiments which greatly participated into our general understanding of homogeneous turbulence would be tedious, nevertheless the previous references illustrate that the idea of addressing separately the various fundamental mechanisms at stake in natural turbulent flows is not new. The review of such works reveals that there is a large discrepancy between quantities of primary importance, which goes against the "universal principles" postulated in Kolmogorov (1941*b*,*a*), which could be briefly reformulated as follows: at asymptotically large Reynolds numbers, small scales of a turbulent flow should be **locally isotropic** whatever the large scales anisotropic forcing mechanisms are. These small scales are uniquely determined by the kinematic viscosity ν and the kinetic energy dissipation rate ϵ. And finally, at any scale l larger than the dissipative scales, but smaller than anisotropic ones, the statistics of the velocity field are only given by l and ϵ.

To illustrate the breakdown of these universality assumptions, one can mention for instance the values of the velocity derivative skewness S, recently reported in Antonia *et al.* (2015), which are quite dispersed for various turbulent flows. The reasons for this scattering are very likely multiple and complex, but some of them are obvious: first of all, if the Reynolds number based on the Taylor scale Re_λ is not large enough, the small scales do not "forget" the large scales forcing mechanisms. Thus, one has **persistent small scales anisotropy**, which consequently renders the results flow-dependent. Other reasons can be proposed, such as the strong variations from one experimental apparatus to another, or low resolution of small scales in DNS. This suggests an essential requirement for the "mechanism by mechanism" investigation mentioned above: one should use the same consistent approach to accurately compare the results and draw relevant conclusions. We will come back to this later, and now return to the idea of anisotropic small scales, which is one of the reasons why some authors in the turbulence community question the local isotropy hypothesis of Kolmogorov. This makes the **return to isotropy** (RTI) of small scales a crucial point of interest, and it is required to first distinguish the turbulent velocity and scalar fields.

Indeed, it seems that the persistence of anisotropy at small scales for the scalar field is even more complicated than for the velocity field, as reviewed by Warhaft (2000). For the velocity field, it is more or less admitted that the small scales of the second-order moments return to isotropy, whereas higher order moments do not systematically, as observed in Pumir (1996). Of particular interest is the (third-order moment) velocity derivative skewness in shear flows, which should be zero if small scales were completely isotropic. The review by Antonia *et al.* (2015)

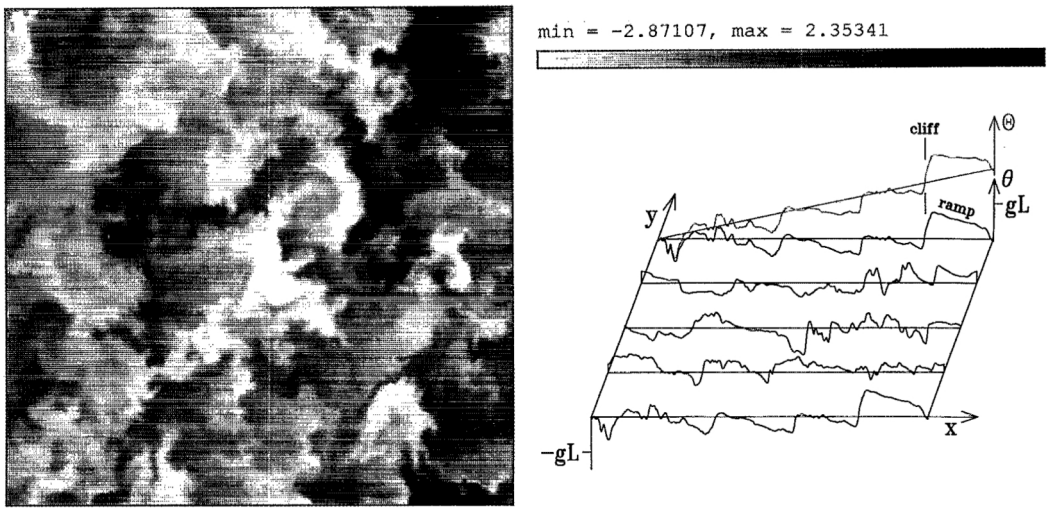

Figure 1: The ramp-cliff structures of a turbulent advected scalar field θ or mean field Θ forced by a mean scalar gradient $\boldsymbol{g}$ (from Holzer & Siggia (1994)). The velocity field of integral scale L is sustained by a Gaussian forcing. The curves at right represent horizontal slices of the plane at left.

clearly illustrates that it is not the case for various kinds of turbulent flows, not necessarily homogeneous. Nevertheless, S is generally found to decrease with increasing Re_λ in shear flows, even if the exponent is an open question: in the DNS of Schumacher *et al.* (2003*a*), $S \sim Re_\lambda^{-1}$ is reported, whereas $S \sim Re_\lambda^{-0.6}$ in the experiment by Garg & Warhaft (1998), and $S \sim Re_\lambda^{-0.5}$ in Shen & Warhaft (2000). In the latter reference, higher-order moments are either independent of Re_λ or increase with it. The issue is even more sensitive regarding the small-scales of a passive scalar field: indeed, in a presence of a mean scalar gradient only, both second and third-order moments were found to have persistent anisotropic small scales by Tong & Warhaft (1994): therein, the scalar derivative skewness S_θ, in the direction of the mean scalar gradient, is larger than unity instead of zero, and does not reduce with larger Re_λ: comparable observations are made for the second-order moments, very likely due to "ramp-cliff" structures, displayed in Fig. 1. Similar conclusions are drawn for higher-order moments of the scalar field in Pumir (1994). In addition, Sreenivasan & Tavoularis (1980) measured non-zero values for S_θ in shear flows, with no decreasing tendency with larger Reynolds numbers. On the contrary, local isotropy features were reported in Danaila *et al.* (1999*b*) where shear and mean temperature gradient are created by two-counter rotating cold and hot disks.

These different observations may be summarized by the conclusions of Sreenivasan (1991), who states that scalar small scales are very likely not universal, and that a necessary condition, but not sufficient, for local isotropy at the scalar level is that the small scales of the velocity field are isotropic. It is also reported that in more than a few works, some findings are misrepresented by the lack of data or convergence, with for instance inertial slopes of spectra far from the theoretical expectations with no justifications. Hence, persistent small scales anisotropy, among other issues, is responsible for the non-universality of some complex turbulent flows, and the Reynolds number has a critical role in it. *Would these conclusions be different if one had the possibility of running DNS at very large Reynolds numbers and designing experiments with extremely long wind tunnels?* This is an open question of great theoretical interest which is

the primary motivation of the thesis: indeed, it appears to be crucial to determine clearly the asymptotic behaviours of turbulence, in the Kolmogorov's paradigm of large Reynolds numbers.

Even though this if out of reach of DNS for now [1], the idea is not absurd if one thinks of **modelling**. The developments of multiple models in the past decades was not only an alternative to DNS great need of computational resources, but also a way to identify and deeply understand the dominant mechanisms of turbulence. As sketched in Fig. 2, there are roughly three methods available to address complex anisotropic flows: **Reynolds-Averaged Navier-Stokes** (RANS) models, which require the tuning of multiple constants and do not contain much information about small scales and details of the flow. **Large-Eddy Simulations** (LES), which necessitate the calibration of a turbulent viscosity and subgrid models to reflect the effects of the filtered small scales, very likely different depending of the flow considered. And finally DNS, which have all the information possible, as illustrated by the schematic signal, but which is the most limited in terms of Reynolds numbers.

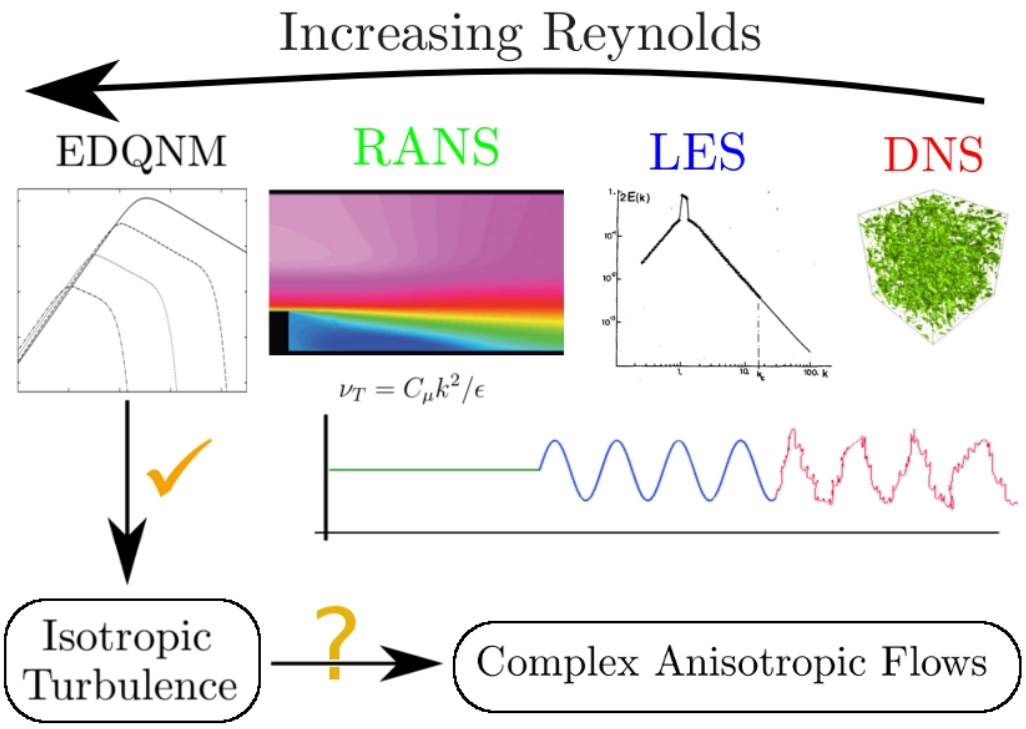

Figure 2: Schematic view of the different methods available to study turbulence. The Reynolds numbers reachable by simulations roughly increases from DNS to LES, RANS and EDQNM. The complexity of a three-part signal, corresponding to RANS, LES and DNS, is also presented for illustration purposes. Illustrations for RANS and DNS were taken online, whereas the one for LES if from Chollet & Lesieur (1981).

This figure also shows that there exists an alternative to these three approaches, namely the **Eddy-Damped Quasi-Normal Markovian** (EDQNM) closure, which is a one-time two-point model. Other spectral models were developed more or less in the same period as EDQNM: we do not wish to establish here an exhaustive list, but rather to point out some of them

[1] It is worth noting at this point the recent DNS by Ishihara *et al.* (2016) where $Re_\lambda \simeq 2300$ is reached with resolution 12288^3.

for informative purposes, and state why EDQNM is chosen among the collection of existing models. First, one can start with Kraichnan (1959), who developed the **Direct Interaction Approximation** (DIA). The DIA is a two-point two-time model, with rather complex analytical expressions due to the presence of equations for response-functions. Unfortunately, the DIA does not respect the Galilean Invariance and does not recover the $k^{-5/3}$ inertial scaling of the kinetic energy spectrum derived from the Kolmogorov (1941*b*) phenomenology. These defects were further corrected in the Lagrangian version of the DIA, namely the **Lagrangian History DIA** (LHDIA) (Kraichnan, 1965): in the LHDIA framework, Lagrangian correlation times are notably used to restore the build-up of triple correlations. However, the analytical complexity is increased by the additional presence of Lagrangian equations. Finally, let's mention the **Test-Field Model** (Kraichnan, 1971) which is perhaps the closest to EDQNM: basically, an additional transport equation of a compressible test-field is used to determine the characteristic time of the triple correlations, instead of prescribing it in EDQNM. Of course, other models exist, and variations of the previous ones as well, but for the sake of clarity, we choose to not go further in this description.

As illustrated in Fig. 2, EDQNM permits to reach large Reynolds numbers, but is mainly limited to HIT. It will be explained throughout the manuscript that even though EDQNM does not contain as much information as DNS, it nevertheless permits to have a statistical description of all scales for physical quantities of importance, unlike RANS and LES. For this reason, we choose the EDQNM as a good candidate to investigate and model homogeneous anisotropic turbulence, rather than LHDIA and TFM, which are most costly in terms of computational resources, and regarding the former, much more complex analytically even in HIT.

The complete EDQNM approximation was first developed for hydrodynamics homogeneous isotropic turbulence, notably by Orszag (1970); Leith (1971); Orszag (1977) (see also Lesieur (2008) and references therein for a more precise overview). Basically, it consists of three ingredients: a **quasi-normal** procedure to close the non-linear term in the evolution equation of the one-time two-point second-order spectral velocity-velocity correlation; an **eddy-damping** term which reflects the departure of statistics from normal laws; and finally a **Markovianization** step to ensure the realizability of the kinetic energy spectrum $E(k,t)$, which further strongly simplifies the time-integration. The EDQNM approximation has proven many times since its creation to be relevant and accurate in HIT (Lesieur & Schertzer, 1978; Métais & Lesieur, 1986; Lesieur & Ossia, 2000; Meldi & Sagaut, 2012). The EDQNM framework was also extended to the transport of passive scalar, which is relevant with regard to our problematic, by Herring *et al.* (1982), and then further applied to investigate the decay of the scalar variance in Lesieur *et al.* (1987). In addition, the EDQNM results were used to develop and improve subgrid-models for LES, for instance in Chollet & Lesieur (1981).

Furthermore, it is appealing to remember that EDQNM was also extended to more complex cases than HIT to explore configurations unreachable by DNS at this time: after the discovery that helicity, the scalar product between velocity and vorticity $< u_i\omega_i >$, is an inviscid invariant of the three-dimensional Navier-Stokes equations by Moffatt (1969), EDQNM was successfully used by André & Lesieur (1977) to show that the helical spectrum $H(k,t)$ scales in $k^{-5/3}$ in the inertial range, similarly to the kinetic energy spectrum. More or less at the same time, Pouquet *et al.* (1976) broadened the reach of EDQNM to **magnetohydrodynamics** (MHD) turbulence by additionally considering the magnetic energy and magnetic helicity spectra. For both helical and MHD turbulence, EDQNM was exploited for subgrid modelling (Baerenzung *et al.*, 2008*b*,*a*)

as well. In a different framework, more sophisticated methods involving EDQNM were also used to significantly improve RANS mixing models in stratified turbulence (Gréa *et al.*, 2016*b*). Moreover, it is important to stress that at some points, the EDQNM approximation inherited from particular DIA techniques. Three examples can be emphasized: first, in the framework of weakly compressible turbulence, Bertoglio *et al.* (2001) greatly enhanced the Markovianisation step of the EDQNM approximation by using the DIA equations of the response functions, in order to better take into account the time-history of the compressible part of the velocity field. Secondly, Bos & Bertoglio (2006) proposed an elegant way to get ride of the adjustable constant in the eddy-damping part of the EDQNM approximation, by using an additional field, namely the velocity-displacement correlation, which recalls the idea of the TFM. Thirdly, some information can be learnt thanks to the TFM regarding the characteristic time θ_{kpq} of the triple correlations in EDQNM (Herring *et al.*, 1982).

What about shear-driven flows? The first attempt to extend EDQNM to strongly anisotropic turbulence dates back to the pioneering work of Cambon *et al.* (1981): the concept relies on a two-step approach. The classical EDQNM is applied to close the non-linear transfer terms as in HIT, but the general tensorial equation of the spectral two-point velocity-velocity correlation is kept. The resulting expressions are then combined with an appropriate modelling for anisotropy. In 1981, this second step involved the choice of an arbitrary constant, an issue which was solved recently in Mons *et al.* (2016) (MCS). In the latter reference, the modelling of anisotropy is done through a truncated expansion into spherical harmonics of the spectral second-order moments, where part of the anisotropic angular information is restored thanks to deviatoric spherically-averaged tensors. As such, MCS is the starting point of this thesis, from which we aim at extending the **anisotropic EDQNM modelling** to the transport of a passive scalar field in shear-driven turbulence, to active scalar dynamics as well with stratification, and also to helical turbulence.

Upstream to practical considerations such as the development of subgrid-models for shear flows (Germano *et al.*, 1991), the principal objective of this thesis is to tackle various configurations partially representative of atmospheric turbulence with the same consistent approach: by this, we mean that the anisotropic EDQNM model aims at being valid in multiple cases, without changing any constants. The only constant is the eddy-damping one, which will be set once and for all on the well-known and accepted isotropic value. This is fundamentally different from RANS and LES models which require to tune some adjustable constants depending on the flow, or from earlier spectral models as well (Clark & Zemach, 1995; Bos & Bertoglio, 2007). In order to get ride of one significant issue mentioned above, the study will be performed in the framework of large Reynolds numbers. Addressing with the same method shear flows, passive scalar transport with a mean temperature gradient, and unstable stratification, is an important contribution in terms of modelling. The idea is the following one: if our model is reliable and accurate enough by comparisons with DNS and experiments at moderate Reynolds numbers, we can have confidence in the predictions we will make at larger Reynolds numbers while combining various mechanisms such as shear and mean scalar gradient. This is inherently distinct from what is usually done in DNS, LES and RANS models for instance, where different codes and settings are used depending on the flow considered.

Among the numerous features listed above, our purposes are rather fundamental, and the different aspects and method of the thesis could be listed as follows:

- **Development** of the model with **analytical** calculations and algebra specific to the spectral formalism.
- **Assessment** of the model by **comparisons** of the numerical results with DNS and experiments, implying a link between spectral and physical quantities.
- Establishment of **theoretical predictions** based on physical arguments, such as inertial scaling of spectra and time evolution of one-point statistics.
- **Numerical simulations** to test the predictions, and to investigate complex interactions, such as the scale by scale distribution of anisotropy resulting from non-linear exchanges and production at large scales.
- **Deduction** of the most important and relevant mechanisms for a given configuration, and **propose explanations** for some specific issues, such as the impact of moderate Reynolds numbers effects.

By going through all these points, we wish to constitute a "database" of both high Reynolds numbers simulations for homogeneous anisotropic turbulence, and a detailed form gathering the main analytical calculations in the spectral formalism which might be used for other purposes than EDQNM as well.

The manuscript is organized in three parts, as follows. In Part 1, we expose the two essential components of the thesis, namely the transport of a passive scalar field in HIT, and the spectral anisotropic model for the velocity field. More precisely, in Chapter 1, the transport of a passive scalar field in decaying HIT is addressed, along with effects of strong and weak diffusivity. Secondly, in Chapter 2, the anisotropic EDQNM modelling for the velocity field in homogeneous turbulence is presented, along with the main evolution equations and the spectral formalism. Various applications of this model are gathered in Chapter 3, where both sustained shear flows and freely decaying turbulence initially submitted to shear are tackled.

In Part 2, the anisotropic model is extended to deal with the transport of a scalar field. In particular, in Chapter 4, the modelling is consistently broadened to include passive scalar dynamics. Applications such as shear flows with a mean temperature gradient are gathered in Chapter 5, along with multiple successful comparisons with experimental and numerical studies. These different configurations are revisited in Chapter 6 for weakly and highly diffusive scalar, with the emphasis put on isotropic turbulence with a mean scalar gradient. Afterwards, the spectral modelling is further extended to the case of active scalar dynamics to deal with unstably stratified turbulence in Chapter 7. Homogeneous isotropic turbulence with helicity is the subject of Chapter 8, with some considerations about the additional presence of a mean scalar gradient.

Finally, all the appendices mainly contain details about the lengthy calculations necessary to develop the model, along with some additional theoretical considerations.

Part I

Passive Scalar in Isotropic Turbulence & Velocity Field in Anisotropic Turbulence

Chapter 1

Passive Scalar Mixing in Homogeneous Isotropic Turbulence

"Anyone who has never made a mistake has never tried anything new."

– Albert Einstein (or Theodore Roosevelt)

In this chapter, we begin the study of mixing and transport in homogeneous turbulence with the classical case where a passive scalar field is advected by a turbulent **isotropic** field, meaning that statistics are invariant under any translations, rotations and mirror symmetries. Since the objective of the thesis is to investigate and model the transport of a scalar field in homogeneous anisotropic turbulence (HAT), it makes sense to start with Homogeneous Isotropic Turbulence (HIT). The results of this chapter will serve as a point of comparison throughout the manuscript.

1.1 The equations of homogeneous isotropic turbulence

In homogeneous decaying isotropic turbulence, the kinetic energy $K =< u_i u_i > /2$ and scalar variance $K_T =< \theta^2 >$ of the fluctuating velocity and scalar fields u_i and θ respectively, where $< \cdot >$ is an ensemble average, evolve according to

$$\frac{\mathrm{d}K}{\mathrm{d}t} = -\epsilon(t), \qquad \frac{\mathrm{d}K_T}{\mathrm{d}t} = -\epsilon_T(t), \tag{1.1}$$

where ϵ and ϵ_T are the kinetic energy and scalar variance dissipation rates. These two equations come from the Navier-Stokes and scalar transport equations (2.1) and (4.2) for fluctuations, which will be detailed in the next chapters. These four quantities, K, K_T, ϵ and ϵ_T are obtained by integrating the kinetic energy and scalar variance spectra over the whole wavenumber space

$$K_{(T)}(t) = \int_0^\infty E_{(T)}(k,t)\mathrm{d}k, \quad \epsilon(t) = 2\nu \int_0^\infty k^2 E(k,t)\mathrm{d}k, \quad \epsilon_T(t) = 2a \int_0^\infty k^2 E_T(k,t)\mathrm{d}k, \tag{1.2}$$

where ν is the kinematic viscosity and a the scalar diffusivity. Since Kolmogorov (1941*b*), the inertial scaling of the kinetic energy spectrum is known, and more recent studies have

investigated the large scales scaling, so that

$$E(k,t) = \begin{cases} A(t)\,k^{\sigma} & \text{for} \quad k < k_L, \\ K_0\,\epsilon^{2/3}\,k^{-5/3} & \text{for} \quad k_L < k < k_\eta, \end{cases} \tag{1.3}$$

where the Kolmogorov constant is found to be $K_0 \simeq 1.3$ with the EDQNM simulations, and where

$$k_\eta = \left(\frac{\epsilon}{\nu^3}\right)^{1/4} \tag{1.4}$$

is the Kolmogorov wavenumber beyond which dissipation effects are dominant with regard to inertial ones, and k_L is the integral wavenumber, corresponding to the scale that contains most of the energy in decaying turbulence. The shape at large scales ($k < k_L$) is referred to as the **infrared range**, and is not part of Kolmogorov pioneering work. The scaling $E \sim k^{\sigma}$ is given by theoretical arguments which relate spectra and correlation functions in physical space (George, 1992*a*). Some important features should be mentioned about the infrared scaling: initial conditions with an infrared slope $\sigma > 5$, such as a sharply peaked energy spectrum around k_L, result in k^4, the so-called Batchelor turbulence, because of non-local interactions (Lesieur & Schertzer, 1978; Lesieur & Ossia, 2000). A k^2 infrared scaling is predicted by Lumley (1970) with energy equipartition arguments. These two configurations have physical meanings since they refer to the conservation of linear and angular momentum respectively. According to Llor & Soulard (2013), all real positive values of $\sigma \leq 4$ are possible, and $\sigma = 2$ might be the most probable value for experiments. Furthermore, only the slope near the peak of energy k_L (and not for $k \to 0$) is important and leads the decay (Meldi & Sagaut, 2012; Mons *et al.*, 2014*a*).

When Batchelor turbulence is mentioned, it is important to clearly define the **Permanence of Large Eddies** (PLE) (Eyink & Thomson, 2000; Meldi & Sagaut, 2012): the infrared range of the kinetic energy spectrum is given by $E(k < k_L, t) = Ak^{\sigma}$. The PLE is said to hold in *decaying turbulence* if both A and σ remain constant throughout the decay. Consequently, in HIT, PLE holds for Saffman turbulence, whereas it is broken for Batchelor turbulence, because of strong non-linear transfers from small to large scales.

The crucial assumption behind the scaling of the kinetic spectrum in the inertial range ($k \in [k_L; k_\eta]$) is the **local isotropy** of small scales, even if large scales are made anisotropic by various production mechanisms. This is discussed for instance in Sreenivasan *et al.* (1979); Sreenivasan (1991); Warhaft (2000) and will be investigated in this thesis, at the level of second-order moments, in the next chapters. A large inertial zone, and thus a clear separation of scales, requires a high Reynolds number. The integral Reynolds number is defined as

$$Re_L = \frac{K^2}{\nu\epsilon}, \tag{1.5}$$

which is linked to the integral and Kolmogorov wavenumbers through

$$k_\eta = Re_L^{3/4}\,k_L. \tag{1.6}$$

Kind of anisotropy	$Re_\lambda(t=0)$	Pr	$k_{\min}/k_L(t=0)$	$k_{\max}$
HSRT (High Pr)	5.10^3	1 ($\gg 1$)	10^{-7}	$10k_\eta$ ($10k_{\mathrm{B}}$)
HSRT Low Pr	5.10^4	$\ll 1$	10^{-7}	$10k_\eta$
HST (Low Pr)	5 (100)	1 and $\gg 1$ ($\ll 1$)	10^{-10}	$10^5 k_\eta$
HITSG (High Pr)	5.10^3	1 ($\gg 1$)	10^{-7}	$10k_\eta$ ($10k_{\mathrm{B}}$)
HITSG Low Pr	5.10^4	$\ll 1$	10^{-7}	$10k_\eta$
HSTSG	5	$\ll 1$, 1 and $\gg 1$	10^{-10}	$10^5 k_\eta$
HHT and HHTSG	5.10^4	1	10^{-7}	$10k_\eta$
USHT	5	1	10^{-10}	$10^5 k_\eta$

Table 1.1: Main numerical parameters used for the simulations: when low Reynolds numbers are reached in decaying turbulence, $k = 10^{-16}k_L(0)$. Some simulations, especially for comparisons, have different initial parameters. The meaning of the labels for the different kinds of anisotropy can be found in the Abbreviations list in page x: the conditions for HSRT and HIT are the same.

An additional Reynolds number is defined, based on the Taylor microscale

$$Re_\lambda = \sqrt{\frac{20}{3} Re_L}. \tag{1.7}$$

Finally, the evolution equations of the kinetic energy and scalar variance spectra, known as the kinetic and scalar **Lin equations**, read

$$\left(\frac{\partial}{\partial t} + 2\nu k^2\right) E(k,t) = S^{\mathrm{NL(iso)}}(k,t), \qquad \left(\frac{\partial}{\partial t} + 2ak^2\right) E_T(k,t) = S^{\mathrm{T,NL(iso)}}(k,t), \tag{1.8}$$

where $S^{\mathrm{NL(iso)}}$ and $S^{\mathrm{T,NL(iso)}}$ are conservative spherically-averaged isotropic non-linear transfers. For the sake of brevity and generality, the EDQNM procedure to obtain the explicit analytical expressions of these terms is detailed in Chapter 2 in the more general framework of HAT.

When it comes to the inertial scaling of the scalar variance spectrum $E_T(k,t)$, this is more complicated than for $E(k,t)$: indeed, depending on the value of the Prandtl number $Pr = \nu/a$, different scalings can be observed. For a unit Prandtl number, $E_T(k,t)$ scales in $k^{-5/3}$ in the **inertial-convective range** (ICR) between the scalar integral wavenumber k_T and the Kolmogorov wavenumber k_η, similarly to the kinetic energy spectrum (Obukhov, 1949; Corrsin, 1951*a*,*b*), so that

$$E_T(k,t) = K_{\mathrm{CO}}\, \epsilon_T\, \epsilon^{-1/3}\, k^{-5/3}, \tag{1.9}$$

where the Corrsin-Obukhov constant is found to be, with EDQNM simulations, $K_{\mathrm{CO}} \simeq 0.74$. Within the EDQNM framework, it is possible to obtain other values for K_0 and K_{CO} by changing the eddy-damping constants presented later in Chapters 2 and 4.

In what follows, the transport of a passive scalar field in HIT for $Pr \ll 1$ is firstly addressed. Then, the framework of $Pr \gg 1$ is considered and some new fundamental features are exposed regarding third-order statistics. Finally, the Pr impact on the time evolution of scalar integrated quantities is investigated, with in particular the transition from large to low Reynolds numbers.

Numerical set-up

At this point, we briefly present the numerical set-up of the simulations. Since the conditions are always more or less the same in the different configurations that will be addressed, the main elements are gathered here and in Table 1.1.
A third order Runge-Kutta scheme with implicit viscous term is used. The wavenumber space is discretized using a logarithmic mesh $k_{i+1} = rk_i$ for $i = 1, \ldots, n$ where n is the number of modes in the discretization. Typically, $r = 10^{1/f}$ where f is the number of discrete points per decade. Simulations have shown that in most of the cases, statistics are not modified within more than 1% from $f = 15$: for security, we nevertheless choose $f = 17$. This mesh extends from $k_{\min}$ to $k_{\max} = 10k_{\eta_T}$ with $k_{\eta_T} = \sqrt{Pr}k_\eta$ if $Pr \geq 1$ or $k_{\eta_T} = k_\eta$ if $Pr \leq 1$. The time step Δt is controlled by defining a constant CFL number. Moreover, the time step is obtained by considering the characteristic time scales of scalar and kinetic dynamics at large and small scales. In the presence of a mean-velocity or scalar gradient, the intensity of the mean-field is also taken into account. The values of the physical and numerical parameters for simulations at large and small Reynolds numbers are gathered in Table 1.1.
If not mentioned otherwise, the initial kinetic energy and scalar variance spectra $E(k,t)$ and $E_T(k,t)$ are isotropic and the expression is borrowed from Pope (2000); Meyers & Meneveau (2008)

$$E(k, t = 0) = K_0\, k^{-5/3}\, \epsilon^{2/3} f_L(kL)\, f_\eta(k\eta) \tag{1.10}$$

where f_L and f_η are shape functions for large and small scales respectively

$$f_L(x) = \left(\frac{x}{(x^{1.5} + 1.5 - \sigma/4)^{2/3}}\right)^{\frac{5}{3}+\sigma}, f_\eta(x) = \exp\Big(-5.3((x^4 + 0.4^4)^{\frac{1}{4}} - 0.4)\Big). \tag{1.11}$$

This corresponds to an initial energy spectrum with energy already at all scales.

1.2 The inertial scaling of E_T for $Pr \ll 1$

In this part, the emphasis is put on the scaling of E_T in the case of a highly diffusive passive scalar $Pr \ll 1$.

The contents of this section were published in:
Briard & Gomez, "Passive scalar convective-diffusive subrange for low Prandtl numbers in isotropic turbulence", *Physical Review E*, **91**, 011001(R) (2015)

The dynamics of a highly diffusive passive scalar is a very controversial topic. There are four different theories regarding the scaling of the **inertial-diffusive range** (IDR) of the scalar variance spectrum E_T. Batchelor (1959) proposed that in the IDR, for $k > k_{\mathrm{CO}}$ where the Corrsin-Obukhov wavenumber reads $k_{\mathrm{CO}} = Pr^{3/4}k_\eta$, one has

$$E_T(k,t) = \frac{K_0}{3}\, \epsilon_T\, a^{-3}\, \epsilon^{2/3}\, k^{-17/3}. \tag{1.12}$$

Whereas Chasnov *et al.* (1989) found $E_T \sim k^{-11/3}$ for a very rapidly stirred fluid. Moreover, Gibson (1968) derived a $E_T \sim k^{-3}$ scaling by considering convection effects when scalar gradients are very weak at small scales. Finally, Granatstein & Buchsbaum (1966) established a $E_T \sim k^{-13/3}$ range based on experimental data in a plasma. Thanks to EDQNM simulations, a large range of Prandtl numbers can be explored at high Reynolds numbers. First, it allows to explain directly how the $k^{-13/3}$ could have been obtained experimentally before: this subrange was observed for fluids with $0.01 \leq Pr \leq 0.1$ and $Re_\lambda \sim 160$. However, there is no IDR for $Pr = 0.1$ as revealed in Fig. 1.1a. And for $Pr = 10^{-2}$, the IDR is not completely established: this is probably the reason why $k^{-17/3}$ is not observed in Granatstein & Buchsbaum (1966).

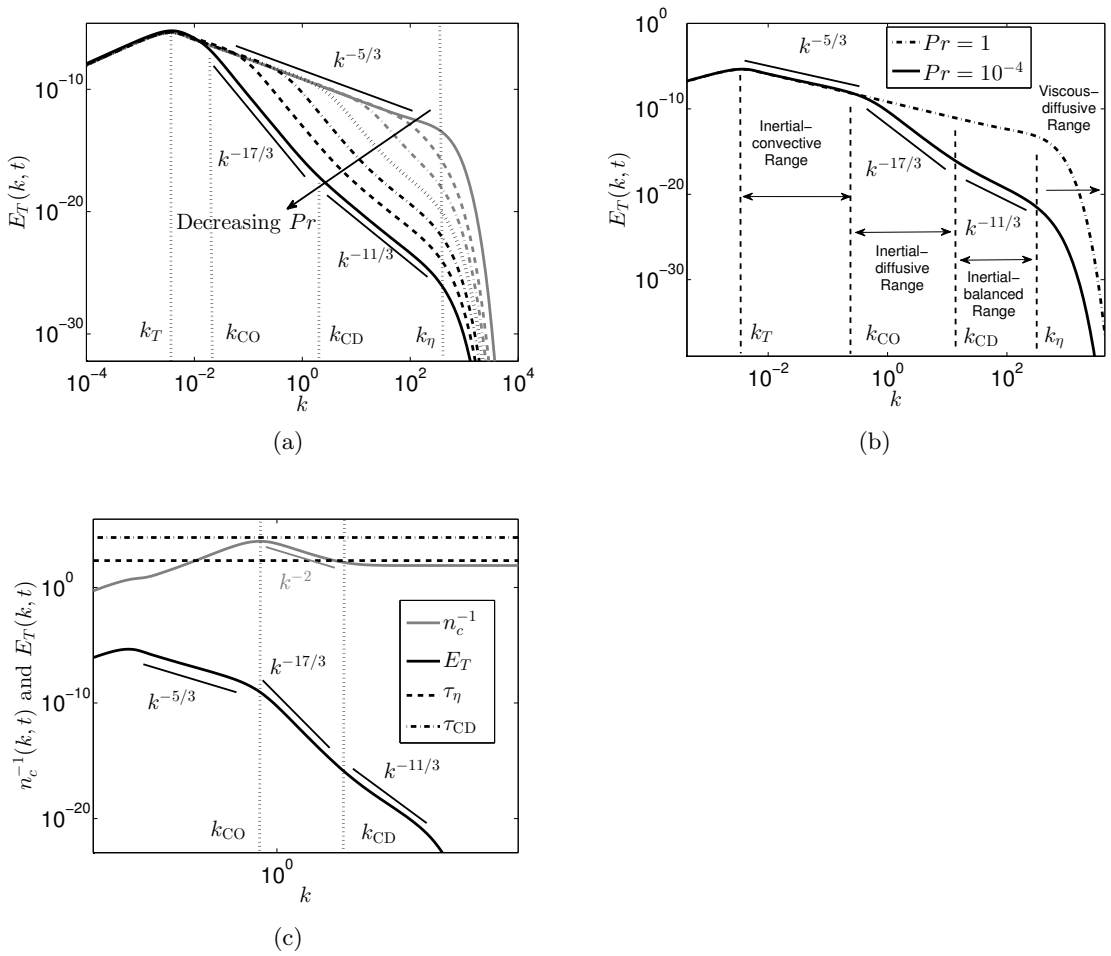

Figure 1.1: Scalar variance spectrum $E_T(k,t)$ for small Prandtl numbers in Saffman turbulence ($\sigma = 2$), along with the scalar integral, Corrsin-Obukhov, Convective-Diffusive, and Kolmogorov wavenumbers k_T, k_{CO}, k_{CD}, and k_η. The wavenumber k_{CD} is defined in (1.13). (a) $Pr = 10^{-n}$, $n = [0, \ldots, 6]$; (b) $Pr = 1$ and $Pr = 10^{-4}$ with the different ranges; (c) Characteristic time n_c^{-1} of the IBR, defined in (1.18), for $Pr = 10^{-4}$.

The first thing to remark in Fig. 1.1a is that the $k^{-17/3}$ IDR only clearly appears for $Pr \leq 10^{-3}$. Then, for $Pr = 10^{-6}$, the ICR has almost disappeared, which is expected from a physical point of view since the Péclet number $Pe_\lambda = Re_\lambda \sqrt{Pr}$ is rather small. Furthermore, there is clearly a third subrange, located between the IDR and k_η, where E_T decreases much slower. This effect can be understood as a transfer lack toward small scales while approaching the Kolmogorov wavenumber k_η. Indeed, in the IDR, the diffusive effects are stronger than the dissipative ones.

On the contrary, the new range is generated by small-scales convection, that was neglected in Batchelor (1959), as mentioned by Gibson (1968). From this point, we defined k_{CD}^{-1} as the characteristic length scale at which this new range starts, where CD stands for convective-diffusive.

In Fig. 1.1b, one can observe three distinct ranges between k_L and k_η for $Pr \ll 1$: (i) for $k \in [k_L, k_{\mathrm{CO}}]$, the $k^{-5/3}$ ICR, dominated by large scales convection: the designation "inertial" comes from the cascade of kinetic energy. Then, (ii) for $k \in [k_{\mathrm{CO}}, k_{\mathrm{CD}}]$, the $k^{-17/3}$ IDR, where diffusive effects drive the dynamics, and convection by large scales is negligible. Finally, for $k \in [k_{\mathrm{CD}}, k_\eta]$, convection from small scales, and more precisely from the Kolmogorov wavenumber k_η, dominates. There, the kinetic field creates small scalar fluctuations that balance diffusion of the IDR. Consequently, this new range is called the **inertial-balanced range** (IBR), where "balanced" stands for an equilibrium between diffusion and convection by small scales.

From Fig.1.1a, it is clear that the IBR grows in size with the IDR. Numerically, a good agreement with a $k^{-11/3}$ range for $Pr \leq 10^{-4}$ is obtained by a least square fit. In Fig.1.1b, the convective-diffusive wavenumber k_{CD} is consistently located between k_{CO} and k_η, and clearly separates the $k^{-17/3}$ scaling from the $k^{-11/3}$ one. Let us take a closer look at k_{CD}. Since we have a competition between diffusion and convection mechanisms in the IBR, a length scale taking into account these two effects is built. To this end, the characteristic diffusion time $t^* = k_{\mathrm{CO}}^{-2}/a$ is considered, based on Corrsin-Obukhov wavenumber and the diffusivity. Then, the convective length scale is obtained using Kolmogorov characteristic velocity $u_\eta = (\nu\,\epsilon)^{1/4}$ and t^*. This eventually yields

$$\boxed{k_{\mathrm{CD}} = (t^*\,u_\eta)^{-1} = a^{-1/2}\left(\frac{\nu}{\epsilon}\right)^{-1/4} = \sqrt{Pr}\,k_\eta.} \tag{1.13}$$

The latter relation is similar to the one for the Batchelor wavenumber k_{B} with $Pr \gg 1$ (see next section). This clearly underlines that convection effects are at the origin of the $k^{-11/3}$ IBR.

The new $k^{-11/3}$ IBR can be seen as the reconciliation of Batchelor and Chasnov theories. While Batchelor claims that for a strongly diffusive passive scalar, $E_T \sim k^{-17/3}$, Chasnov predicts a $k^{-11/3}$ scaling in particular conditions where the fluid is rapidly stirred. What we observe here is that the two ranges coexist when the Reynolds and Prandtl numbers are respectively large and small enough, and that we can find physical and theoretical arguments to explain it. Firstly, let's introduce an eddy conductivity a_t (Chasnov *et al.*, 1989; Batchelor, 1959)

$$a_t(t) = \int_k^\infty \frac{2E(k,t)}{3n_c(k,t)}\mathrm{d}k \tag{1.14}$$

where n_c^{-1} is a local characteristic time which depends on k. Using the eddy conductivity a_t, the scalar dissipation rate ϵ_T reads

$$\epsilon_T(t) = 2(a + a_t(t))\int_0^k k^2 E_T(k,t)\mathrm{d}k. \tag{1.15}$$

The integral from 0 to k takes into account the main contribution of dissipation since $k \gg 1$. The influence of small scales dynamics on ϵ_T is modelled through the eddy conductivity a_t. Consequently, one can assume that $\mathrm{d}\epsilon_T/\mathrm{d}k = 0$ (Chasnov *et al.*, 1989). If we derive (1.15) with

respect to k and consider that $E(k \to \infty) = 0$, one gets

$$E_T(k,t) = \frac{K_0}{3}\,\epsilon_T\,\epsilon^{2/3}k^{-11/3}(a+a_t)^{-2}n_c^{-1}. \tag{1.16}$$

In Batchelor (1959), a_t is introduced differently and the characteristic time n_c^{-1} is the diffusion time $(ak^2)^{-1}$. This makes sense when diffusion dominates in the $k^{-17/3}$ IDR. With (1.16), it is obvious that if n_c does not depend on k, then $E_T \sim k^{-11/3}$. In Chasnov *et al.* (1989), it is justified that for a rapidly stirred fluid (fluctuations at all scales) n_c is constant. A physical and general interpretation of a constant n_c could be the following one: in the IDR, the characteristic time $(ak^2)^{-1}$ decreases at small scales because the fluctuations produced by the kinetic field become weaker while approaching k_η. At a certain point, when $k \geq k_{\mathrm{CD}}$, small-scales convection plays a non-negligible role and thus balances small-scales convection and diffusion, so that n_c^{-1} becomes constant. We have two candidates to determine the characteristic time n_c^{-1}: the Kolmogorov time scale $\tau_\eta = \sqrt{\nu/\epsilon}$ and the characteristic time based on u_η and k_{CD}, namely

$$\tau_{\mathrm{CD}} = (u_\eta\,k_{\mathrm{CD}})^{-1} = \sqrt{\frac{a}{\epsilon}} = \tau_\eta Pr^{-1/2}. \tag{1.17}$$

If we use the common assumption verified numerically that $a \gg a_T$, one can write (1.16) differently

$$n_c^{-1}(k,t) = \frac{E_T(k,t)}{E(k,t)}\,\frac{3}{\epsilon_T(t)}\,k^2a^2. \tag{1.18}$$

In Fig.1.1c, it is clear that in the IBR, for $k \geq k_{\mathrm{CD}}$, one has n_c^{-1} constant. In other words, the prediction of Chasnov *et al.* (1989) is recovered. The other point of interest is that the constant reached by n_c^{-1} is really close to the Kolmogorov time scale τ_η. This result is consistent with the characteristic time of the convection being given by τ_η close to k_η. Moreover, one can observe that in the IDR, n_c^{-1} is proportional to k^{-2}, in agreement with Batchelor (1959). Finally, the scalar variance spectrum in the inertial-balanced range scales like

$$\boxed{E_T(k,t) = \frac{K_0}{3}\epsilon_T\,\epsilon^{1/6}\,\sqrt{Pr}\,a^{-3/2}\,k^{-11/3}.} \tag{1.19}$$

1.3 Mixed-derivative skewness S_T for $Pr \gg 1$

In this part, the case of a weakly diffusive passive scalar $Pr \gg 1$ is addressed, and we focus on scalar third-order statistics with the mixed-derivative skewness.

> The contents of this section were published in:
> Briard & Gomez, "Mixed-derivative skewness for high Prandtl and Reynolds numbers in homogeneous isotropic turbulence", *Physics of Fluids*, **28** (8), 081703 (2016)

The case $Pr \gg 1$ is of particular interest for various reasons. It specifically corresponds to the framework of biological fluids (Scalo *et al.*, 2012) (low temperature dissolved oxygen where $Sc \simeq 1000$, crucial for marine ecosystems), of chemical reactions (reduction of ferricyanide for instance, where Sc can exceed 10^4) and of experiments with tracers (such as disodium fluorescein where $Sc \simeq 2000$, or sulforhodamine 101 where $Sc \simeq 5000$). Beyond these practical

considerations, the case of weakly diffusive passive scalars is challenging as it presents some difficulties in DNS when it comes to solve the very small scales of the scalar field beyond the Kolmogorov wavenumber k_η. These small scales experience friction by the Kolmogorov scale velocity field, up to the Batchelor wavenumber $k_\mathrm{B} = \sqrt{Pr}k_\eta$. This continuous friction creates the **viscous-convective range** (VCR) where the scalar variance spectrum $E_T(k,t)$ scales as

$$E_T(k,t) = \frac{K_0}{3}\epsilon_T\sqrt{\frac{\nu}{\epsilon}}k^{-1}, \qquad k_\eta < k < k_\mathrm{B}. \tag{1.20}$$

The framework of HIT (with or without a mean scalar gradient) with $Pr \gg 1$ has already received some attention, especially numerically (Yeung *et al.*, 2002; Schumacher *et al.*, 2003*b*; Yeung *et al.*, 2004; Borgas *et al.*, 2004), and the k^{-1} viscous-convective range has been assessed numerous times. However in DNS, with an increasing Pr comes a diminishing Re_λ. Furthermore, at moderate Reynolds numbers, the spatial resolution beyond the Kolmogorov wavenumber can be questioned. Notably, it has been pointed out in a recent work of forced isotropic turbulence (Donzis & Yeung, 2010) that both the Reynolds number and the resolution are of great importance: especially, at a given Reynolds number, a better spatial resolution, of order k_B^{-1}, improves local isotropy. The same conclusion is made at constant resolution for an increasing Re_λ. A scalar field with a low diffusivity has also been studied experimentally (Buch & Dahm, 1996; Miller & Dimotakis, 1996; Lavertu *et al.*, 2008), often with dye where $Sc \sim 10^3$, at higher Reynolds numbers, but the framework is hardly homogeneous and isotropic (jets, shear flows, ...). Therefore, the present study is performed in HIT with EDQNM, which has been used recently (Bos *et al.*, 2012; Meldi & Sagaut, 2013*a*) to study third-order moments of the velocity field, especially the velocity derivative skewness S. Here, the emphasis is put on the mixed-derivative skewness S_T, which is of great theoretical interest since it directly appears in the equation of the scalar variance dissipation rate (Ristorcelli, 2006).

The evolution equations of the kinetic and scalar dissipation rates can be obtained by multiplying (1.8) by $2\nu k^2$ and $2ak^2$ respectively, and then integrating over k

$$\frac{\partial\epsilon}{\partial t} = 2\nu\int_0^\infty k^2 S^{\mathrm{NL(iso)}}(k,t)\mathrm{d}k - 4\nu^2\int_0^\infty k^4 E(k,t)\mathrm{d}k, \tag{1.21}$$

$$\frac{\partial\epsilon_T}{\partial t} = 2a\int_0^\infty k^2 S^{\mathrm{T,NL(iso)}}(k,t)\mathrm{d}k - 4a^2\int_0^\infty k^4 E_T(k,t)\mathrm{d}k. \tag{1.22}$$

Using classical algebra, which can be found in Kerr (1985); Ristorcelli (2006) and which is detailed in Appendix A, yields

$$\frac{\partial\epsilon}{\partial t} = -\left(\frac{7}{3\sqrt{15}}S(t)\sqrt{Re_L} + \frac{7}{15}G(t)\right)\frac{\epsilon^2}{K} = -\frac{7}{15}\left(\frac{1}{2}S(t)Re_\lambda + G(t)\right)\frac{\epsilon^2}{K}, \tag{1.23}$$

where $S(t)$ and $G(t)$ are the velocity derivative skewness and palinstrophy respectively

$$S(t) = \frac{<(\partial u/\partial x)^3>}{<(\partial u/\partial x)^2>^{3/2}} = -\frac{3\sqrt{30}}{14}\frac{\int_0^\infty k^2 S^{\mathrm{NL(iso)}}(k,t)\mathrm{d}k}{\left(\int_0^\infty k^2 E(k,t)\mathrm{d}k\right)^{3/2}}, \tag{1.24}$$

$$G(t) = <u^2>\frac{<(\partial^2 u/\partial x^2)^2>}{<(\partial u/\partial x)^2>^2} = \frac{30\nu}{7}\frac{K}{\epsilon}\frac{\int_0^\infty k^4 E(k,t)\mathrm{d}k}{\int_0^\infty k^2 E(k,t)\mathrm{d}k}. \tag{1.25}$$

Similarly, for the passive scalar field, one gets

$$\frac{\partial \epsilon_T}{\partial t} = -\left(\sqrt{\frac{5}{3}} S_T(t)\sqrt{Re_L} + r\frac{5}{9}G_T(t)\right)\frac{\epsilon\epsilon_T}{K} = -\left(\frac{1}{2}S_T(t)Re_\lambda + r\frac{5}{9}G_T(t)\right)\frac{\epsilon\epsilon_T}{K}, \tag{1.26}$$

where r is the kinetic to scalar time scales ratio $r = (K\,\epsilon_T)/(K_T\,\epsilon)$. These evolution equations (1.23) and (1.26) have already been obtained in previous works (Zhou *et al.*, 2000; Ristorcelli, 2006; Meldi & Sagaut, 2013*a*) in a similar manner. This numerical study focuses on the mixed-derivative skewness

$$S_T(t) = \frac{<(\partial u/\partial x)(\partial\theta/\partial x)^2>}{\sqrt{<(\partial u/\partial x)^2><(\partial\theta/\partial x)^2>}} = -\sqrt{\frac{3}{10}}\frac{\int_0^\infty k^2 S^{\mathrm{T,NL(iso)}}(k,t)\mathrm{d}k}{\sqrt{\int_0^\infty k^2 E(k,t)\mathrm{d}k}\left(\int_0^\infty k^2 E_T(k,t)\mathrm{d}k\right)}, \tag{1.27}$$

which directly appears in (1.26). Note that we obtain a factor $\sqrt{3/10}$, instead of $2/\sqrt{15}$ proposed by Antonia & Orlandi (2004). The scalar palinstrophy reads

$$G_T(t) =<\theta^2>\frac{<(\partial^2\theta/\partial x^2)^2>}{<(\partial\theta/\partial x)^2>^2} = \frac{18a}{5}\frac{K_T}{\epsilon_T}\frac{\int_0^\infty k^4 E_T(k,t)\mathrm{d}k}{\int_0^\infty k^2 E_T(k,t)\mathrm{d}k}. \tag{1.28}$$

The kinetic and scalar palinstrophy G and G_T can be interpreted as the dissipation of the gradients of the velocity and scalar fields respectively (Kerr, 1985), and more specifically, G represents the dissipation of enstrophy $<\omega^2>= \epsilon/\nu$.

Now that the theoretical aspects have been recalled, numerical results are presented at various Prandtl and Reynolds numbers. The use of EDQNM to study third-order statistics is validated by comparisons with a moderate Re_λ experiment (Zhou *et al.*, 2000) in Fig. 1.2a and with a DNS of forced HIT (Gotoh *et al.*, 2002) at higher Re_λ in Fig. 1.4b. In the experiment, $Re_\lambda \sim 50$ and the decay exponents $K \sim t^\alpha$ and $K_T \sim t^{\alpha_T}$ are $\alpha \simeq \alpha_T \simeq -1.33$. As a first approximation, this corresponds to infrared exponents $\sigma = \sigma_T = 3$ (see next section for more details). The comparison between experiment and EDQNM is presented in Fig. 1.2a where the velocity derivative and mixed-derivative skewnesses S and S_T are displayed. The agreement is better for S_T than for S, whose values obtained experimentally are more dispersed. At higher Reynolds numbers ($38 \leq Re_\lambda \leq 460$), the agreement for S between EDQNM and the DNS of Gotoh *et al.* (2002) of forced HIT is rather good, as revealed in Fig. 1.4b: the velocity derivative skewness is quantitatively recovered within 5% on a broad range of Re_λ. Finally, Fig. 1.2b gathers various values of S_T obtained in DNS and experiments for $Pr \geq 1$, and illustrates the noteworthy dispersion, probably due to the different kinds of forcing, whose consequences are amplified at moderate Reynolds numbers: furthermore, the DNS of Kerr (1985) suffers from a very low resolution. EDQNM results that will be discussed later are also displayed.

Now, the impact of a high Prandtl number on the mixed-derivative skewness S_T is investigated. Such a framework has been studied, notably in DNS. However, this has been done only at moderate (or low) Reynolds numbers. Indeed, the more Pr increases, the more additional points are necessary to describe the very small scales of the scalar spectrum which behave as k^{-1} beyond k_η and up to k_B. Thanks to EDQNM, it is possible to reach high Reynolds and Prandtl numbers, as illustrated in Fig. 1.3a, where the viscous-convective range predicted by Batchelor (1959) grows in size with increasing Pr and spans on two decades for $Pr = 10^5$. Nevertheless, because of the logarithmic discretization, elongated triads are not taken into

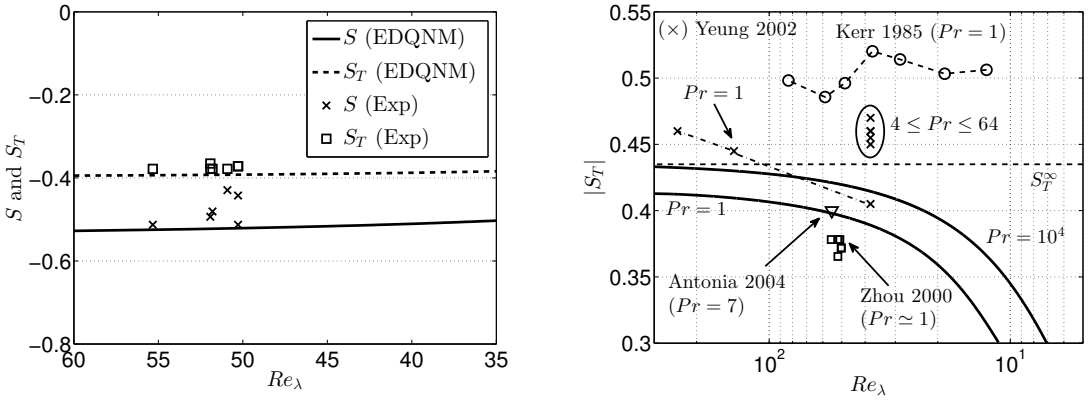

(a) (b)

Figure 1.2: (a) Comparison of S and S_T between EDQNM (lines) and experiment of Zhou *et al.* (2000) (symbols) at $Re_\lambda \simeq 50$ and $Pr = 0.7$. (b) Review of different values for $|S_T|$ obtained in DNS (Kerr, 1985; Yeung *et al.*, 2002; Antonia & Orlandi, 2004) and experiments (Zhou *et al.*, 2000): thick lines for EDQNM at $Pr = 1$ and $Pr = 10^4$. $(--)$ indicates the asymptotic Pr-state S_T^∞ at very large Re_λ and Pr. For Yeung *et al.* (2002) $(\times)$: the values of S_T presented are in the plane perpendicular to the mean scalar gradient, the Prandtl number is $1 \leq Pr \leq 64$, and the $Pr = 1$ results are linked by a dash-dot $(-\cdot)$ line.

account. Consequently, it is necessary to add non-local contributions to the scalar non-linear transfers of (1.8). For the sake of clarity, non-local considerations are gathered and detailed in Appendix B.

The Pr-dependence of the mixed-derivative skewness S_T is investigated in Fig. 1.3b in the high Reynolds numbers regime to avoid transitional effects towards low Reynolds numbers. It is revealed that $|S_T|$ increases from $Pr = 1$ to a critical Prandtl number $Pr_c = 10$ and then slightly decreases up to $Pr = 10^3$. Such variations of $|S_T|$ for $1 \leq Pr \leq 10^3$ have already been observed in DNS (Yeung *et al.*, 2002, 2004). The latter works, at moderate Reynolds numbers, indicate that the decrease of $|S_T|$ happens from $Pr_c \simeq 1$, which is smaller than in our high Reynolds numbers simulations where the decrease starts around $Pr_c \simeq 10$. Consequently, these observations suggest that the decay threshold for $|S_T|$ is Reynolds dependent, with $Pr_c \in [1, 10]$.

The remarkable feature is that for $Pr \geq 10^3$ at high Reynolds numbers, the mixed-derivative skewness saturates to a constant value $|S_T^\infty| \simeq 0.435$, which does not depend on the Prandtl number anymore. The ∞ symbol refers to the *saturated Pr-state* $Pr \geq 10^3$. DNS performed at higher values of Pr would be useful to confirm (or not) the saturation of S_T from $Pr \sim 10^3$. It is worth noting that in HIT, when the scalar field is forced with a mean scalar gradient, values of $S_T^\perp$ (in the direction perpendicular to the gradient) are close to the present $S_T^\infty = -0.435$: values of Yeung *et al.* (2002) are gathered in Fig. 1.2b, and one can note that at $Pr = 1$, $S_T^\perp$ increases with Re_λ $(- \cdot \times$ line) similarly to the present EDQNM results.

Physically, this saturation of the mixed-derivative skewness means that the statistical mixing properties of the flow do not evolve anymore at a sufficiently high Prandtl number, for high Reynolds numbers. This can be interpreted in terms of small scales equilibrium ($k > k_\eta$), if one considers the spectral definition (1.27) of the mixed-derivative skewness S_T. Indeed, considering

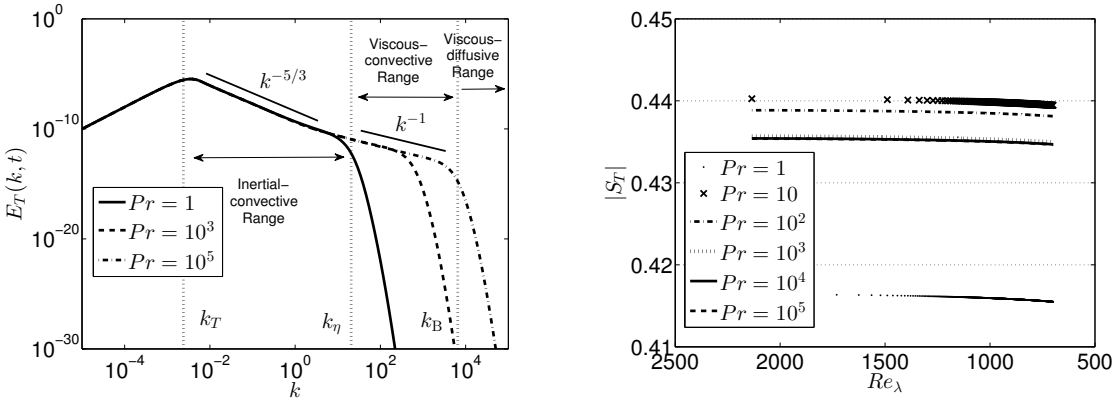

(a) (b)

Figure 1.3: (a) Scalar spectrum $E_T(k,t)$ for various Prandtl numbers $Pr = 1$, 10^3 and 10^5, at $Re_\lambda = 10^3$ in Saffman turbulence. The inertial convective $k^{-5/3}$ and viscous-convective k^{-1} ranges are displayed as well, along with the integral, Kolmogorov and Batchelor wavenumbers k_T, k_η and k_B for $Pr = 10^5$. (b) Absolute value of the mixed-derivative skewness S_T for various Prandtl numbers from 1 to 10^5 in Saffman turbulence. Because of the high-Pr saturation, the $Pr = 10^4$ and $Pr = 10^5$ curves are hardly distinguishable.

a given Reynolds number, or equivalently a given dissipation rate ϵ of kinetic energy, increasing Pr leads to an indefinite extension of the VCR of E_T toward small scales, whereas its ICR remains unchanged. Therefore, the variations of S_T when Pr increases are mainly due to the variations of the two functions appearing in the scalar integrated terms of S_T, namely $k^2 S^{\mathrm{T,NL(iso)}}$ and $k^2 E_T$ for $k \in [k_\eta; k_\mathrm{B}]$. These quantities represent respectively the production rate of mean-square temperature gradients and scalar dissipation at wavenumber k. Moreover, Fig. B.2 shows that the production is mainly a non-local mechanism unlike the scalar dissipation. For a sufficiently high Prandtl number, $Pr \geq 10^3$, these two integrals evolve similarly so that they balance each other. Therefore, for high Reynolds numbers, the convergence of S_T to a constant value S_T^∞ for increasing Prandtl numbers reflects an equilibrium, occurring in the viscous-convective range, between non-local production of mean-square temperature gradients and scalar dissipation by diffusion.

A similar independence with regard to Pr can be found for the scalar palinstrophy G_T: injecting classical scaling for E_T in the spectral definition (1.28) of G_T, and assuming that $Re_\lambda \gg 1$ and $Pr \gg 1$, yields $rG_T \sim Re_\lambda$. Such a result was also found in Ristorcelli (2006). Numerical simulations and experiments have shown that $r \sim \alpha_T/\alpha$ is a relevant approximation for the time scale ratio when the turbulence decay is algebraic. Therefore, one has $r \simeq 1$ when the kinetic energy and scalar variance decay similarly, *i.e.* when $\sigma = \sigma_T$ for the initial spectra considered here: this is relevant since it will be shown in the next section that Pr does not affect the asymptotic decay of scalar integrated quantities. Qualitatively, the independence of G_T with regard to Pr provides the same physical information as our numerical results on S_T: there is an asymptotic convergence of the mixing properties of the passive scalar field only for a sufficiently high Pr. As said before, a dependance on Pr for moderate Prandtl numbers, say $1 \leq Pr \leq 10^3$, is in agreement with DNS (Yeung *et al.*, 2002, 2004).

Finally, the decay of the derivative skewness $S(t)$ and mixed-derivative skewness $S_T(t)$ from

high to low Reynolds numbers is investigated in Fig. 1.4a for Saffman ($\sigma = \sigma_T = 2$) and Batchelor ($\sigma = \sigma_T = 4$) turbulence. The main results are the following ones: (i) Both S and S_T are constant for high Reynolds and Prandtl numbers, and independent of large scales initial conditions: indeed, the curves are identical for Saffman and Batchelor turbulence, except in the transition zone between the high and low Reynolds numbers regimes where a slight difference is observed. (ii) The transition toward the low Reynolds numbers regime for the scalar field starts after the one for the velocity field, which is expected since the Péclet number $Pe_\lambda = \sqrt{Pr}Re_\lambda$ is much larger than Re_λ in the case $Pr \gg 1$. (iii) For very low Reynolds numbers, both derivative skewnesses S and S_T are zero, consistently with the fact that for $Re_\lambda < 1$, the flow is not turbulent anymore and thus there is no turbulent mixing at all.

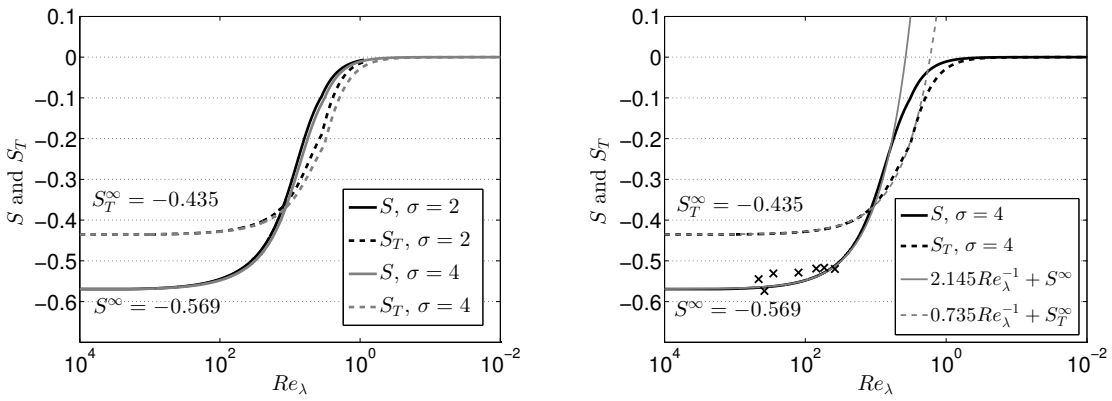

(a) (b)

Figure 1.4: Velocity derivative and mixed-derivative skewnesses S and S_T from high to low Reynolds numbers in the saturated Pr-state at $Pr = 10^4$. (a) In black for Saffman turbulence $\sigma = \sigma_T = 2$, and in grey for Batchelor turbulence $\sigma = \sigma_T = 4$. (b) Batchelor turbulence, along with correlations in grey that capture well the high Reynolds numbers regime and the beginning of the transition zone. $\times$: values of S from forced turbulence DNS of Gotoh *et al.* (2002).

One also has to point out that both S and S_T increase during the decay, *i.e.* when the Reynolds number decreases, in agreement with George (1992*a*). Moreover, it is stated in the latter work that at some point during the decay, S should behave as Re_λ^{-1} according to dimensional considerations. Assuming that the Taylor micro-scale λ is the relevant similarity length scale, and using self-preserving functions $E(k,t) = E^s(t)f(\eta)$, $S^{\mathrm{NL(iso)}}(k,t) = S^s(t)g(\eta)$, and $\eta = k\lambda$, one obtains

$$S(t) \sim \frac{\lambda^{-4}\nu u^2}{(\lambda^{-2}u^2)^{3/2}} \frac{\int \eta^2 g(\eta)\mathrm{d}\eta}{\left(\int \eta^2 f(\eta)\mathrm{d}\eta\right)^{3/2}} \sim Re_\lambda^{-1}. \tag{1.29}$$

But this scaling is not always clearly observed. We believe this might be the consequence of too low Reynolds numbers in DNS. A low Reynolds defect is in agreement with Schumacher *et al.* (2003*a*), where Figure 1 herein clearly shows that the Re_λ^{-1} scaling is achieved for high Reynolds numbers only ($10^2 \leq Re_\lambda \leq 10^3$).

In Fig. 1.4b, relevant correlations are presented (with constants determined by least square fit, set to match with the beginning of the transition) with a clear Re_λ^{-1} dependency for both the velocity derivative and mixed-derivative skewnesses. These correlations $S(t) = S^\infty + 2.145Re_\lambda^{-1}$

and $S_T(t) = S_T^\infty + 0.735 Re_\lambda^{-1}$, where $S^\infty = -0.569$ and $S_T^\infty = -0.435$, capture well the beginning of the transition zone. Hence, the scaling $S \sim Re_\lambda^{-1}$ seems relevant mainly for high Reynolds numbers. Moreover, an interesting result, never confirmed previously to our knowledge, is that the mixed-derivative skewness S_T scales in Re_λ^{-1} as well. This scaling is in agreement with George (1992*b*) where similarity assumptions were used for temperature fluctuations: $E_T(k,t) = E_T^s(t) f_T(\eta)$, $S^{\mathrm{T,NL(iso)}}(k,t) = S_T^s(t) g_T(\eta)$, and $\eta_T = k\lambda_T$. Using a classical result (George, 1992*b*; Zhou *et al.*, 2000) linking the ratio of the kinetic and scalar Taylor lengths λ and $\lambda_T = \sqrt{6aK_T/\epsilon_T}$ yields

$$\left(\frac{\lambda}{\lambda_T}\right)^2 = \frac{5}{6} r Pr, \qquad S_T(t) \sim \frac{a\lambda}{\lambda_T^2 u} \frac{\int \eta_T^2 g_T(\eta_T) \mathrm{d}\eta_T}{\sqrt{\int \eta^2 f(\eta) \mathrm{d}\eta} \int \eta_T^2 f_T(\eta_T) \mathrm{d}\eta_T} \sim r Re_\lambda^{-1}. \tag{1.30}$$

1.4 Time evolution of scalar integrated quantities

In this final part, the effects of a Prandtl number different from unity on the time evolution of scalar integrated quantities such as K_T, ϵ_T and L_T, is addressed.

The contents of this section were published in:
Briard, Gomez, Sagaut, & Memari, "Passive scalar decay laws in isotropic turbulence: Prandtl number effects", *Journal of Fluid Mechanics*, **784**, 274-303 (2015)

A crucial step toward the understanding of the passive scalar dynamics is the study of decay laws at very high or very small Prandtl numbers. Firstly, the decay permits to get ride of the forcing parameter, and secondly, dimensional analysis can provide theoretical results and boundaries regarding time exponents of one-point statistics. Thus, for the passive scalar field, the comparison between the experimental and numerical decay exponents of integrated quantities - such as the scalar variance $K_T(t)$, integral scale $L_T(t)$, and dissipation rate $\epsilon_T(t)$ - and the Comte-Bellot and Corrsin (CBC) theory could give interesting information on what are the main phenomena which drive the scalar decay.

Multiple experimental works and DNS (Lin & Lin, 1973; Warhaft & Lumley, 1978; Sreenivasan & Tavoularis, 1980; Danaila *et al.*, 2000; Zhou *et al.*, 2000, 2002; Antonia & Orlandi, 2004; Lee *et al.*, 2012; Antonia *et al.*, 2013) have focused on scalar decay exponents. However, these scalar decay exponents exhibit a significant dispersion, as shown in Fig. 1.5, whereas the experimental setups are designed to produce a very similar turbulent dynamics. There is up to 20% of discrepancy for similar Reynolds numbers and a fixed Prandtl number ($Pr \sim 0.7$). This scattering between the measured scalar decay exponents may be due to transitional effects towards low Reynolds numbers, as studied in the kinetic case in Meldi & Sagaut (2013*a*), and also probably to the experimental production mechanisms which do not permit to obtain a universal decay. A supplementary potential explanation for the scattering might be that the flow is not fully isotropic.

It is worth noting that the decay of the passive scalar has only been studied in experimental works and DNS in a small region of the (Re,Pr) map given in Fig. 1.5. In this region (the small grey zone), the Prandtl number is close to unity (0.7 for air which is the most used fluid) and

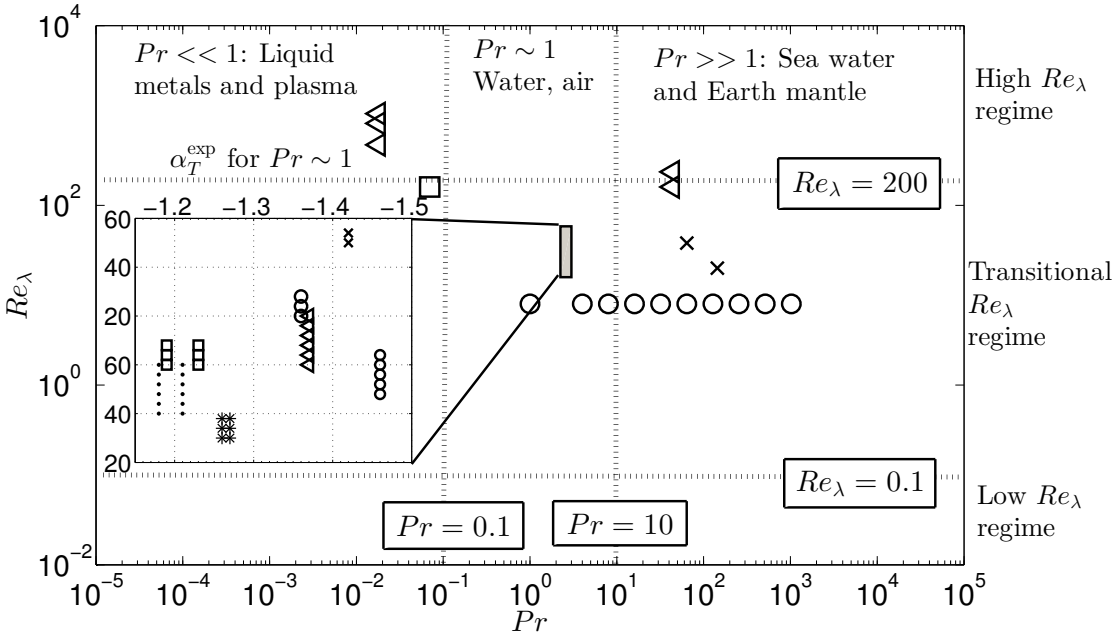

Figure 1.5: Schematic view of the (Re_λ, Pr) combinations used for the passive scalar decay analysis. On the main figure, triangles, squares, crosses and circles respectively refer to works of Rust & Sesonske (1966); Granatstein & Buchsbaum (1966); Yeung *et al.* (2002, 2004). On the zoom of the small grey region at $Pr \sim 1$, experimental scalar decay exponents of Fig. 1.7 are reported: dots, squares, stars, circles, triangles and crosses represent respectively works of Antonia *et al.* (2013); Lee *et al.* (2012); Antonia *et al.* (2013); Zhou *et al.* (2000); Antonia & Orlandi (2004); Danaila *et al.* (2000).

the Reynolds number based on Taylor scale is $Re_\lambda \leq 70$. The values of the decay exponents obtained in these works will be reported later on along with our numerical simulations. Other experiments and DNS performed for Prandtl numbers different from one, spanning from 10^{-2} to 10^2 in Fig. 1.5 (Rust & Sesonske, 1966; Granatstein & Buchsbaum, 1966; Watanabe & Gotoh, 2004; Yeung *et al.*, 2004) mainly focus on the inertial scaling of the scalar spectrum $E_T(k,t)$ and not on the decay of the passive scalar itself. Therefore, they cannot be exploited for comparison purpose in the present study.

When the Prandtl number departs from unity, as described in Tennekes & Lumley (1972), various theoretical arguments show that at large or small Pr, the shape of the scalar spectrum $E_T(k,t)$ is significantly modified at small scales. Nevertheless, as illustrated in Fig. 1.5, the regions where $Pr \ll 1$ and $Pr \gg 1$ have not been much explored for the passive scalar decay issue. Hence, an interesting question could be: does the Prandtl number, in addition to the Reynolds number and initial conditions, modify the decay laws of scalar integrated quantities such as $K_T(t)$ and $\epsilon_T(t)$? This study aims at answering this question of interest for the understanding of the passive scalar dynamics, and at providing an explanation to the scattering of experimental scalar decay exponents.

To this end, this part focuses on two main approaches. The first one is based on the CBC dimensional analysis that is extended to the more general case of passive scalar transport, following the work of Meldi & Sagaut (2012) in the kinetic case. The second approach relies on the EDQNM closure to perform numerical simulations of the turbulent mixing. The main

Reynolds	Cases	α, α_T	n_ϵ, n_{ϵ_T}	n_L, n_{L_T}	n_{Re_L}	n_{Re_λ}
High	Kinetic	$-2\frac{\sigma-p+1}{\sigma-p+3}$	$-3\frac{\sigma-p+5/3}{\sigma-p+3}$	$\frac{2}{\sigma-p+3}$	$-\frac{\sigma-p-1}{\sigma-p+3}$	$-\frac{1}{2}\frac{\sigma-p-1}{\sigma-p+3}$
	Scalar	$-2\frac{\sigma_T-p_T+1}{\sigma-p+3}$	$-\frac{\sigma-p+5+2\sigma_T-2p_T}{\sigma-p+3}$	$\frac{2}{\sigma-p+3}$		
Low	Kinetic	$-\frac{\sigma+1}{2}$	$-\frac{\sigma+3}{2}$	$\frac{1}{2}$	$-\frac{\sigma-1}{4}$	$-\frac{\sigma-1}{8}$
	Scalar	$-\frac{\sigma_T+1}{2}$	$-\frac{\sigma+3}{2}$	$\frac{1}{2}$		

Table 1.2: Kinetic and scalar exponents for the extended CBC analysis. K and K_T are the kinetic energy and scalar variance, ϵ and ϵ_T the kinetic and scalar dissipation rates, and L and L_T the kinetic and scalar integral scales. σ and σ_T are the kinetic and scalar infrared slopes, and p and p_T the kinetic and scalar backscatter parameters.

advantage of this method is its accuracy and low cost in investigating the turbulent dynamics for a broad range of Reynolds and Prandtl numbers. EDQNM simulations have already been used to study kinetic decay exponents (Lesieur & Ossia, 2000; Meldi & Sagaut, 2012, 2013*a*) and passive scalar dynamics (Lesieur *et al.*, 1987). Moreover, this method also allows to recover theoretical results regarding the scalar spectrum scaling when $Pr \leq 1$ and $Pr \geq 1$ that have been obtained experimentally and numerically (see the two previous sections). Hereafter, new theoretical and numerical arguments are proposed to understand how the decay of a passive scalar field is affected by a Prandtl number strongly different from unity.

1.4.1 The basics of the CBC dimensional analysis

In the CBC theory, the kinetic energy spectrum is given by (1.3). The original method of CBC is based on the concept of invariance of very large scale eddies (PLE) corresponding to $k < k_L$ which is notably valid for infrared slopes $\sigma = 1$, 2 and 3. In fact in the kinetic case, the value of the infrared spectral slope σ is time-independent and remains constant for $\sigma = 1$, 2 (Saffman), 3 and 4 (Batchelor). As for the coefficient $A(t)$ of the infrared spectrum, it remains constant for values of $\sigma \in [1, 2, 3]$, and evolves in time as $A(t) \sim L(t)^p$ in the case $\sigma = 4$, where p is the **backscatter parameter**. In the case of high Reynolds numbers, when there is an inertial zone, one obtains

$$\alpha(\sigma, p) = -2\frac{(\sigma + 1 - p)}{(\sigma + 3 - p)}, \qquad K(t) \sim t^\alpha \tag{1.31}$$

in which $p = 0$ if $\sigma \leq 3$ and $p \sim 0.55$ if $\sigma = 4$ as computed in Lesieur *et al.* (1987); Eyink & Thomson (2000); Meldi & Sagaut (2012). Other kinetic exponents such as n_ϵ and n_L can also be determined using (1.31) and are gathered in Table 1.2.

The relevant parameter to study the dynamics of the passive scalar is not only the Reynolds number, but also the (Taylor) Péclet number $Pe_\lambda = Re_\lambda\sqrt{Pr}$. In this section, the emphasis is put on the case $\sigma_T = 4$. Numerical simulations show that the scalar variance also decreases with time following a power law $K_T \sim t^{\alpha_T}$. Furthermore, after a transient relaxation phase, the kinetic and scalar integral scales L and L_T exhibit the same behaviour and their decay exponents n_L and n_{L_T} converge toward the same value. Consequently, we consider that $n_L = n_{L_T}$.

The scalar variance spectrum $E_T(k, t)$ scales similarly to $E(k, t)$ in the infrared range, namely

$$E_T(k < k_T, t) = A_T(t)k^{\sigma_T}, \qquad \sigma_T \in [1, 4]\,, \tag{1.32}$$

Infrared slope σ	$Pr = 10^{-4}$	$Pr = 10^{-2}$	$Pr = 1$	$Pr = 10$	$Pr = 10^2$	$Pr = 10^5$
1		0.5746	0.5745	0.5745		
2		0.4285	0.4254	0.4269		
3		0.2961	0.2842	0.2904		
4	0.3275	0.2814	0.2652	0.2754	0.3125	0.3495

Table 1.3: Some values of p_T for various Pr and σ with $\sigma_T = 4$.

where $k_T \simeq 1/L_T$ is the peak of E_T. Proceeding similarly to the kinetic case, the coefficient $A_T(t)$ is assumed to vary as $L_T^{p_T}$, where p_T is the **scalar backscatter parameter**. By writing the continuity of the scalar spectrum in $k = k_T$, one can use the expressions given in Table 1.2 of n_L and n_ϵ to conclude that

$$\epsilon_T \sim t^{n_{\epsilon_T}}, \qquad n_{\epsilon_T}(\sigma, \sigma_T, p, p_T) = -\frac{\sigma - p + 5 + 2(\sigma_T - p_T)}{\sigma - p + 3}. \tag{1.33}$$

Moreover, since ϵ_T is the time derivative of K_T, the exponent of the scalar variance reads

$$\alpha_T(\sigma, \sigma_T, p, p_T) = -2\frac{\sigma_T - p_T + 1}{\sigma - p + 3}. \tag{1.34}$$

From the theoretical decay exponents α and α_T, it seems that a decay in $K_{(T)} \sim t^{-1}$ (Ristorcelli, 2006) occurs only for $\sigma = \sigma_T = 1$ and corresponds to a constant Reynolds number.

All extended exponents (with p and p_T) for both the kinetic and scalar fields are gathered in Table 1.2. It will be shown later in Chapters 3 and 5 that these exponents are still valid when the turbulence is initially submitted to a mean-velocity gradient, and then freely decaying, as summarized in Table 5.1. However, when a mean scalar gradient is added, the continuous production of scalar fluctuations significantly modifies α_T.

Furthermore, simulations indicate that $A_T(t)$ varies with time when $\sigma_T = 4$. More precisely, p_T decreases when σ increases at a fixed Pr, and increases when Pr departs from unity: values are gathered in Table 1.3.

Finally, the emphasis is put on the dynamics at small Reynolds numbers. In this case, the inertial effects are rather small, and so inertial zone contributions to the kinetic and scalar spectra become negligible. Thus, the kinetic energy behaviour is assumed to be mainly determined by the contribution of the spectrum at large scales. By dimensional analysis $L(t) \sim \sqrt{\nu t}$ and so $n_L = 1/2$. This leads to

$$K(t) = \int_0^\infty E(k,t)\mathrm{d}k \simeq \int_0^{k_L} Ak^\sigma \mathrm{d}k = \frac{A}{\sigma+1}\nu^{-(\sigma+1)/2}t^{-(\sigma+1)/2}. \tag{1.35}$$

From the kinetic energy K, the other important kinetic decay exponents can be deduced, all gathered in Table 1.2. One obtains the exponent of the scalar variance using the relation $L_T(t) \sim \sqrt{at}$. Then, proceeding similarly, one gets

$$K_T(t) \simeq \int_0^{k_T} A_T k^{\sigma_T}\mathrm{d}k = \frac{A_T}{\sigma_T+1}a^{-(\sigma_T+1)/2}t^{-(\sigma_T+1)/2}. \tag{1.36}$$

The other scalar decay exponents derived from α_T are also presented in Table 1.2. For instance, n_{ϵ_T} is simply computed using $\mathrm{d}K_T/\mathrm{d}t = -\epsilon_T$. In what follows, all exponents are calculated using the EDQNM simulations for both σ and σ_T in the set $[1, 2, 3, 4]$. For the kinetic and scalar cases, there is an excellent agreement between the EDQNM results and the predictions of the extended CBC analysis.

1.4.2 Validation at large Reynolds numbers for $Pr \neq 1$

The emphasis is now put on the case where the initial Reynolds number is sufficiently large to allow the kinetic and scalar spectra E and E_T to decrease according to the extended CBC exponents given on the two first lines of Table 1.2. For the sake of brevity, only the case $Pr \ll 1$ is presented here since the results for $Pr \gg 1$ are very similar (for more details, see the complete paper). The initial Reynolds number is $Re_\lambda(0) \simeq 2.10^4$, high enough to ensure a large Péclet number, so that there is a clear separation of scales. Since $E_T(k,t)$ is located "under" $E(k,t)$, local energy transfers dominate, unlike the case $Pr \gg 1$ where the viscous-convective range is "outside" the kinetic energy spectrum. Time exponents of ϵ_T, L_T and K_T are investigated in Fig. 1.6 for $\sigma = \sigma_T = 2$ and $\sigma = \sigma_T = 4$. The scalar decay exponents clearly follow the extended CBC theory. The result is the same for any $Pr \leq 1$ as soon as the Péclet number is large enough. Hence, the extended scalar CBC exponents are valid at large Reynolds numbers for both $Pr \ll 1$ and $Pr \gg 1$.

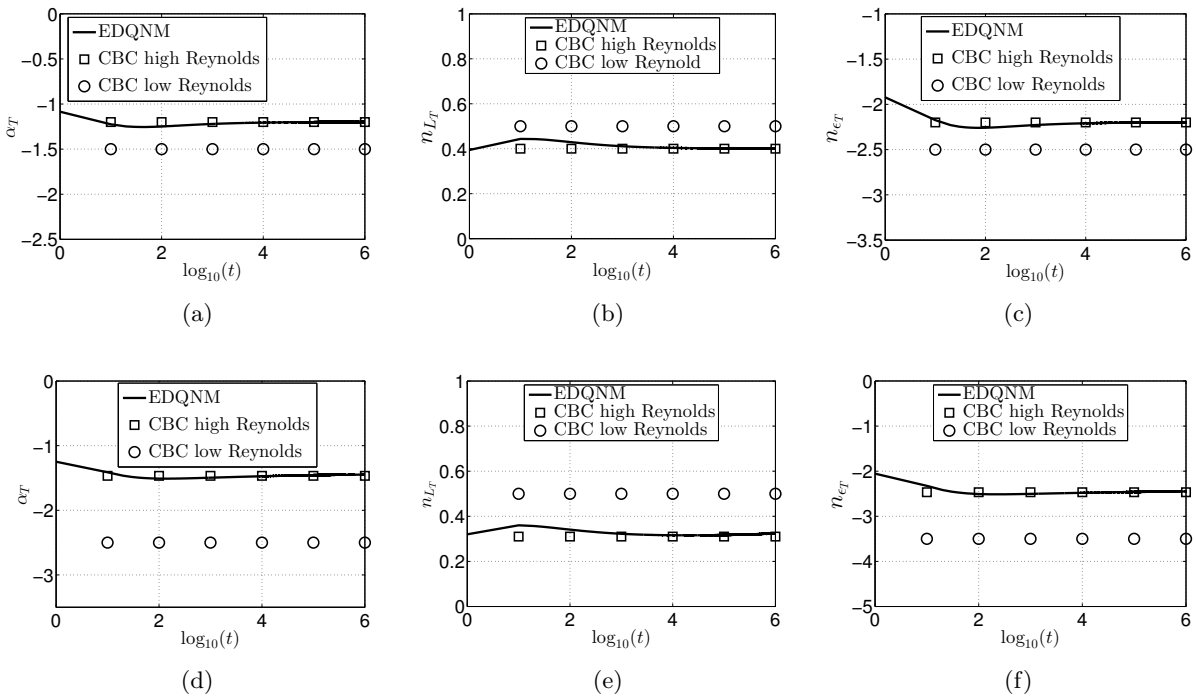

Figure 1.6: Exponents α_T (a)-(c), n_{ϵ_T} (b)-(d) and n_{L_T} (c)-(f) for $Pr = 10^{-4}$. Top line, $\sigma = \sigma_T = 2$; Bottom line $\sigma = \sigma_T = 4$. Symbols for the CBC predictions: □ high Reynolds numbers; ○: low Reynolds numbers.

1.4.3 Transition to low Reynolds and Péclet numbers

In this section, the transition from high to low Reynolds numbers with various Prandtl numbers is investigated. A detailed comparison with experimental results is performed to provide some explanations about the scattering between existing measured scalar decay exponents.

Validation of decay exponents for $Pr = 1$: The numerical method based on EDQNM analysis allows to illustrate the transition from high to low Reynolds numbers. Several simulations are made until very low Reynolds numbers $Re_\lambda \sim 10^{-1}$, starting from $Re_\lambda(t = 0) = 240$. This Reynolds number is high enough to capture the beginning of the transition and all the previous decay exponents are accurately recovered. According to the theory for the case $\sigma = 1$, the same exponents for both large and small Reynolds numbers are found. It is only from the shape of the spectrum that these two cases can be distinguished. For infrared exponents $\sigma \geq 2$ and $\sigma_T \geq 2$, the Reynolds number decreases over time and inertial ranges of both spectra disappear. This is the low Reynolds numbers regime and the decay exponents α and α_T converge to the values expected by the extended CBC analysis given in Table 1.2. This transition grows more rapidly for higher values of the infrared spectral slopes.

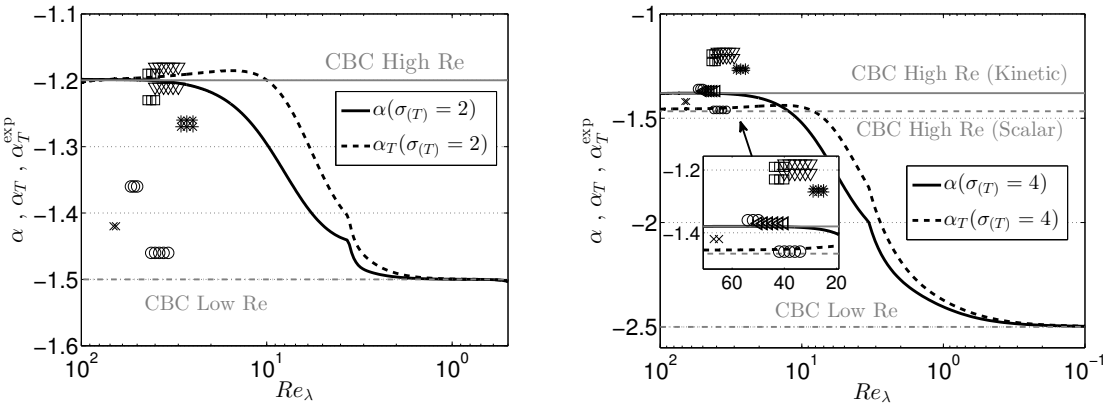

(a) (b)

Figure 1.7: Experimental scalar decay exponents at $Pr \sim 1$ in comparison with high Reynolds CBC theory and EDQNM simulations at $Pr = 1$. List of symbols: ∘ Zhou *et al.* (2000, 2002) ; ◁ Antonia & Orlandi (2004); □ Lee *et al.* (2012) Sq35; × Danaila *et al.* (2000); ▽ Antonia *et al.* (2013) Sq35 and Rd44w; ∗ Lee *et al.* (2012); Antonia *et al.* (2013) Rd35. (a) $\sigma = \sigma_T = 2$; (b) $\sigma = \sigma_T = 4$.

Transitions are shown for Saffman and Batchelor turbulence in Fig. 1.7 along with experimental results. The case $\sigma = \sigma_T = 3$, similar to $\sigma = \sigma_T = 2$, is not presented. The small peak that appears around $Re_\lambda = 5$ is due to the disappearance of the inertial range in both E and E_T. This corresponds to a transition between a regime dominated by inertial effects to a regime dominated by viscous ones. The horizontal lines correspond to theoretical predictions coming from the CBC theory. If one chooses a different initial Reynolds number, higher or lower, the resulting curve would collapse with the present one after a few turn-over times $\tau_0 \simeq K(0)/\epsilon(0)$. Similarly, if different initial spectra E and E_T are prescribed, there is only a slight change during the transition. Hence, the present curves for α and α_T in the transition zone seem quite robust. Nevertheless, there is no clear power law for the decay exponent in the transition. Two critical Reynolds numbers, at which the transition to the low Reynolds regime begins, are

observed for different kinetic and scalar cases, with infrared slope $\sigma = \sigma_T \in [2, 3, 4]$. The critical Reynolds number for the kinetic case Re_λ^c decreases when σ increases. Transitions happen at $Re_\lambda^c(\sigma = 2) \approx 38$, $Re_\lambda^c(\sigma = 3) \approx 20$, and $Re_\lambda^c(\sigma = 4) \approx 17$. Whereas the transition for the scalar field happens always around $Re_{\lambda_T}^c \approx 12$. Other scalar exponents such as n_{ϵ_T} and n_{L_T} also follow the CBC theory for low Reynolds and Péclet regimes.

Review of experimental results: In experiments for the passive scalar, the fluid is often air with $Pr \simeq 0.7$. In Fig. 1.7, several experimental results regarding the scalar decay exponent α_T^{exp} are gathered in order to compare them to experiments (Danaila *et al.*, 2000; Zhou *et al.*, 2000, 2002; Lee *et al.*, 2012; Antonia *et al.*, 2013), and DNS Antonia & Orlandi (2004). Firstly, it is important here to stress that in these experiments, the Reynolds number is rather low $Re_\lambda \leq 70$. EDQNM simulations show that such Reynolds numbers correspond to the beginning of the transition zone, between high and low Reynolds regimes. This could explain the large scattering of scalar decay exponents that have been measured in the past years. The Re_λ is not high enough to completely match with the high Reynolds and Péclet regimes, and thus the α_T^{exp} measured could be misrepresented by the transitional Re_λ-state. Even with DNS, Antonia & Orlandi (2004) found a α_T which is not the one predicted by the CBC theory. Once again, this might be because of the moderate Re_λ and a too low resolution of large scales, which are determinant for the decay exponents. In addition to this, the infrared initial slopes σ and σ_T cannot be fixed in grid turbulence: hence, it is impossible to compare rigorously α_T^{exp} with the CBC theory.

Nevertheless, interesting results have been obtained experimentally that deserve to be emphasized. First, the scattering of the measured scalar decay exponents α_T is more important than for the kinetic ones α (Lavoie *et al.*, 2007; Antonia *et al.*, 2013). In addition to the two facts mentioned earlier (low Re_λ and undefined infrared slopes), α_T^{exp} varies a lot depending on how the temperature fluctuations are generated. It has been shown (Warhaft & Lumley, 1978; Sreenivasan & Tavoularis, 1980; Zhou *et al.*, 2000) that the measured value of α_T^{exp} varies significantly depending on the experimental apparatus: the power used to create the temperature fluctuations or the influence of the measurements origin (for example the grid, corresponding to the kinetic integral scale L, or the heated screen, corresponding to the scalar one L_T). Recent experimental works (Zhou *et al.*, 2000, 2002; Lee *et al.*, 2012; Antonia *et al.*, 2013) have been performed on the scalar decay using similar parameters, which allows to make useful comparisons. Most of these experiments were done with a mesh size $M = 24.76$mm, an input speed $U \simeq 6\text{m.s}^{-1}$, a *mandoline* (screen of heated wires) located at $x_T = 1.5M$ and heated with 2kW that generates temperature fluctuations $T \in [2\text{K}, 3\text{K}]$. Scalar quantities are measured with the cold wires technique and the Reynolds number is such that $Re_\lambda \in [30, 70]$. However, as soon as Re_λ remains low, there is an uncertainty due to the transient phase from large to low Reynolds numbers. Finally, since the temperature is a passive scalar, it is still submitted to the variations of the kinetic field induced by the kind of grid chosen for experiments (square, round, solidity, active, passive, ...). Therefore, in addition to the moderate Re_λ effect, the various techniques used to create the turbulent kinetic and scalar fluctuations may be responsible for the scattering.

1.4.4 Transition for $Pr \neq 1$

In the previous high Reynolds and Péclet numbers cases, it has been shown numerically that the Prandtl number does not affect the scalar decay exponents predicted by the CBC theory. The

relevant question is now to determine if this is still valid for low Reynolds and Péclet numbers. It is worth noting that if the Reynolds number is low, it implies a low Péclet regime. In other words, the case of a kinetic field in low Reynolds regime with a scalar field in large Péclet regime does not exist, in terms of the CBC theory.

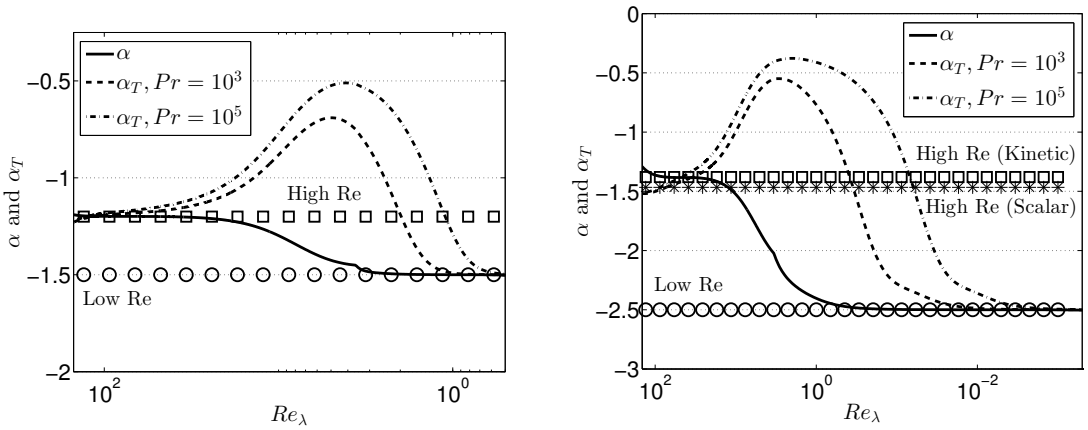

(a) (b)

Figure 1.8: Evolution of the kinetic and scalar decay exponents for $Re_\lambda(t = 0) = 240$ at $Pr = 10^3$ and $Pr = 10^5$. (a) $\sigma = \sigma_T = 2$; (b) $\sigma = \sigma_T = 4$.

Case $Pr \gg 1$: The transition towards low Reynolds numbers begins when the inertial $k^{-5/3}$ range of $E(k, t)$ tends to disappear. From this point, the scalar spectrum E_T still contains a k^{-1} VCR where the scalar destruction is fairly weak. At the beginning of the transition, with the disappearance of the inertial range, the production of small vortices stops but the friction between small scales creates some temperature fluctuations. Because of this production of scalar variance, the scalar decay slows down and α_T increases. Then with the disappearance of the viscous-convective zone, the destruction of scalar variance accelerates under the accumulated effects of diffusive and dissipative processes. Hence, K_T decreases more rapidly. Such a behaviour is recovered in Fig. 1.8 where α_T is investigated for Saffman and Batchelor turbulence at $Pr = 10^3$ and $Pr = 10^5$. Moreover, two critical Reynolds numbers are observed for the scalar field: a first one from which α_T increases, and a second one from which it decreases, corresponding respectively to the disappearance of the ICR and VCR. The second one is smaller than the one found in the case $Pr = 1$ which was $Re^c_{\lambda_T} \simeq 12$ in Fig. 1.7. Indeed, reaching a low Péclet regime with a large Prandtl number is longer than with $Pr = 1$, because Re_λ has to decrease more.

Case $Pr \ll 1$: In Fig. 1.9, scalar decay exponents follow, once again, the extended CBC theory. There is no particular behaviour of α_T during the decay: indeed, all scales of the scalar spectrum E_T are fully controlled by the kinetic one. In the case $Pr \ll 1$, the main difference with regard to the case $Pr = 1$ in Fig. 1.7 is that the transition happens earlier: the scalar critical Reynolds number $Re^c_{\lambda_T}(Pr \ll 1)$ is higher than $Re^c_{\lambda_T}(Pr = 1)$. Since the Prandtl number is very small, the Péclet number $Pe_\lambda = Re_\lambda \sqrt{Pr}$ tends faster to the low Péclet regime, and so the critical Reynolds number $Re^c_{\lambda_T}$ is larger than with $Pr \gg 1$.

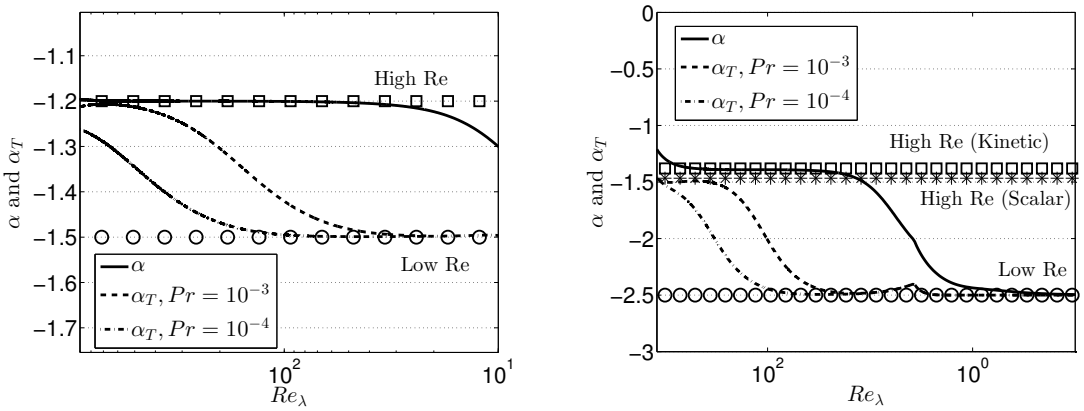

(a) (b)

Figure 1.9: Evolution of the kinetic and scalar decay exponents for $Re_\lambda(t=0) = 1620$ at $Pr = 10^{-3}$ and $Pr = 10^{-4}$. (a) $\sigma = \sigma_T = 2$; (b) $\sigma = \sigma_T = 4$.

The conclusion is that the scalar time exponents provided by the extended CBC theory are still valid in the cases $Pr \ll 1$ and $Pr \gg 1$ for small Reynolds numbers and all values of σ and σ_T. Only α_T, before reaching its asymptotic limit, is temporarily modified when $Pr \gg 1$.

1.4.5 Study of the integral scales L and L_T

The emphasis is now put on the kinetic and scalar integral scales L and L_T, defined as

$$L(t) = \frac{3\pi}{4K(t)} \int_0^\infty k^{-1} E(k,t) \mathrm{d}k, \qquad L_T(t) = \frac{\pi}{2K_T(t)} \int_0^\infty k^{-1} E_T(k,t) \mathrm{d}k. \tag{1.37}$$

Evolution of L_T: The aim of this part is to show that whatever the Prandtl number is, the relative initial position of the kinetic and scalar integral scales $L(t=0)$ and $L_T(t=0)$ does not change the asymptotic dynamics of the decay. The law provided by Lesieur *et al.* (1987) gives the temporal evolution of the scalar integral scale

$$L_T(t) = \left(\frac{\alpha}{\alpha_T}\right)^{3/2} L(t)\,(1 + B\,t^{\frac{\alpha-2}{3}})^{3/2}, \tag{1.38}$$

where B is a constant close to -1 evaluated thanks to initial conditions. At first approximation, at large times, one has $L_T/L = (\alpha/\alpha_T)^{3/2}$. Such an equation is obtained by dimensional analysis, assuming that in the inertial ranges, ϵ and ϵ_T scale like $\epsilon = 2K\,\epsilon^{1/3} L^{-2/3}$ and $\epsilon_T = 2K_T\,\epsilon^{1/3}\,L_T^{-2/3}$. However, in the low Reynolds and Péclet regimes, there are no longer inertial and inertial-convective ranges. Therefore (1.38) is only valid when $Re \gg 1$ and $Pe \gg 1$. In Lesieur *et al.* (1987), it is claimed that (1.38) is only valid in the case $L_T(t=0) < L(t=0)$, meaning that the scalar variance is injected at smaller scales than kinetic energy. Hereafter, it is shown that all the three different cases $L_T(t=0) = L(t=0)$, $L_T(t=0) > L(t=0)$ and $L_T(t=0) < L(t=0)$ collapse into the same evolution after a transient phase. The cases where $L_T(t=0) = 10^2$ and 10^{-2}, for $Pr = 10^{-2}$ and $Pr = 10^2$ with $L(t=0) = 1$ are investigated in Fig 1.10. Despite the large final turn-over time ($t \sim 10^{11}\tau_0$), the Reynolds number is still high

enough to make sure that there is a clear inertial range ($Re_\lambda \geq 300$). Results before $t = 10\tau_0$ are not shown for the sake of clarity as L/L_T is too high. The first conclusion is that Pr does not affect the asymptotic time evolution of L_T, as predicted by Lesieur *et al.* (1987).

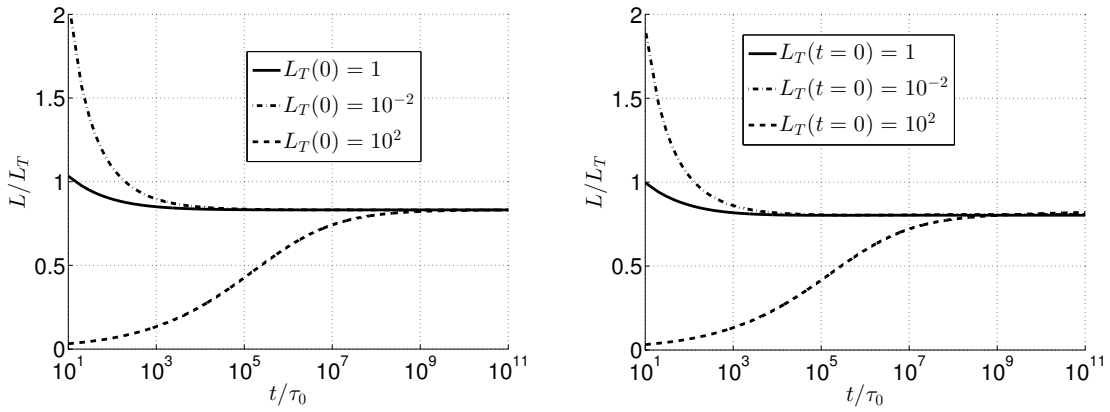

(a) (b)

Figure 1.10: Evolution of L/L_T for the three different cases $L_T(t = 0) = L(t = 0)$, $L_T(t = 0) > L(t = 0)$ and $L_T(t = 0) < L(t = 0)$. (a) $Pr = 10^{-2}$; (b) $Pr = 10^2$.

This is an asymptotic result since L and L_T collapse for very large turn-over times only. Such large turn-over times are never reached in practice in experiments. Nevertheless, the three cases $L(0) > L_T(0)$, $L(0) < L_T(0)$ and $L(0) = L_T(0)$ are physically meaningful: the first case correspond to the apparatus where the velocity fluctuations are heated after the grid by a *mandoline* for instance. The second case correspond to a *toaster*: the laminar field before the grid is heated. The comparison of these two settings has been done by Sirivat & Warhaft (1983). The latter case correspond to the heated grid (Warhaft & Lumley, 1978).

Prediction of k_L and k_T: Here, a law able to predict the relative position of the peaks of both kinetic and scalar spectra, respectively k_L and k_T, is derived. This law is valid in high Reynolds and Péclet regimes, as soon as kinetic and scalar integrated quantities decay according to the CBC theory. We define the ratio $\beta_L = k_T/k_L$. Even though the assumption $\beta_L = 1$ is commonly made, simulations reveal that it is not exactly verified. Moreover, the fact that $k_T \neq k_L$ has already been observed in experiments: Warhaft & Lumley (1978); Sreenivasan & Tavoularis (1980) noted that there was a link between the scalar decay exponent α_T and the ratio β_L. Furthermore, Zhou *et al.* (2000) also made the observation and proposed a correlation. Nevertheless, since the infrared exponents are unknown in experiments, it is impossible to make relevant comparisons. This is the reason why an analytical law linking β_L and α_T in the high Reynolds and Péclet regimes is proposed here. Piecewise spectra are used

$$E = \begin{cases} A(t)k^{\sigma}, & k < k_L, \\ K_0\, k^{-5/3}\epsilon^{2/3}, & k_L < k < k_\eta, \end{cases} \quad E_T = \begin{cases} A_T(t)k^{\sigma_T}, & k < k_T \\ K_{\mathrm{CO}}\epsilon_T\epsilon^{-1/3}k^{-5/3}, & k_T < k < k_{\mathrm{T,max}} \\ K_{\mathrm{B}}\epsilon_T\sqrt{\frac{\nu}{\epsilon}}k^{-1}, & k_\eta < k < k_{\mathrm{B}}, \\ K_0/3\,\epsilon_T\, a^{-3}\,\epsilon^{2/3}\,k^{-17/3} & k_{\mathrm{CO}} < k < k_\eta, \end{cases} \tag{1.39}$$

where $k_{\mathrm{T,max}}$ is either k_{CO} for $Pr \leq 1$ or k_η for $Pr \geq 1$. The computation of the ratio L/L_T yields $L/L_T = (3\beta_L\, C'\, C_T)/(2C\, C'_T)$, where $C = 1/(1+\sigma-p)+3/2$, $C_T = 1/(1+\sigma_T-p_T)+3/2$,

Cases	β_{th}	β_{num}	Error (%)	Cases	β_{th}	β_{num}	Error (%)
$\sigma = \sigma_T = 1$	2/3	0.6684	0.26	$\sigma = 2,\ \sigma_T = 3$	0.9104	0.8744	3.95
$\sigma = \sigma_T = 2$	2/3	0.6684	0.26	$\sigma = 2,\ \sigma_T = 4$	1.07	1	6.64
$\sigma = \sigma_T = 3$	2/3	0.6684	0.26	$\sigma = 3,\ \sigma_T = 2$	0.4882	0.5110	4.46
$\sigma = \sigma_T = 4$	0.7165	0.7645	6.2	$\sigma = 4,\ \sigma_T = 1$	0.31	0.299	3.5
$\sigma = 1,\ \sigma_T = 4$	1.418	1.496	5.21	$\sigma = 4,\ \sigma_T = 2$	0.430	0.4468	3.76

Table 1.4: Values of the ratio $\beta_L = k_T/k_L$ and relative errors given for several simulations with $\sigma = \sigma_T$ and $\sigma \neq \sigma_T$: the values are almost the same for all Pr in $[10^{-5}; 10^5]$.

$C' = 1/(\sigma - p) + 3/5$, and $C' = 1/(\sigma_T - p_T) + 3/5$. Then, using $L/L_T = (\alpha_T/\alpha)^{3/2}$, an explicit law for β_L is obtained

$$\boxed{\beta_L = \frac{2}{3}\left(\frac{\sigma - p}{\sigma_T - p_T}\right)\left(\frac{1 + \sigma_T - p_T}{1 + \sigma - p}\right)\left(\frac{\alpha_T}{\alpha}\right)^{3/2}.} \tag{1.40}$$

The law (1.40) is valid as soon as there are inertial and inertial-convective ranges for E and E_T. In order to show the relevance of this formula, β_L is computed in several cases with $\sigma = \sigma_T$ and with $\sigma \neq \sigma_T$. All results are gathered in Table 1.4 where β_{num} refers to the numerical results and β_{th} to the theoretical ones coming from (1.40). This formula provides less than 1% error when $\sigma = \sigma_T \leq 3$ and a maximum of 6.64% when $\sigma_T = 4$. Finally, (1.40) does not depend on Pr: all cases in Table 1.4 give similar values for various Pr, consistently with the fact that Pr does not affect large scales.

Th β_L-law (1.40) completes the work of Ristorcelli (2006) regarding the time scale ratio r: indeed in the latter reference, the ratio k_T/k_L is introduced in the analytical computation of r, but no explicit formula is provided.

1.5 Conclusions for a passive scalar field in HIT

In this first chapter dedicated to the transport of a passive scalar field in homogeneous isotropic turbulence, several results regarding the impact of a Prandtl number different from unity were proposed. There are summarized hereafter. It is recalled at this point that the next step is to extend the EDQNM approach to HAT in Chapter 2, in order to further combine anisotropic mechanisms and scalar transport from Chapter 4.

First, it has been shown that both theories of Chasnov *et al.* (1989) and Batchelor (1959) can be merged into a single one: for a highly diffusive scalar, a new $k^{-11/3}$ inertial-balanced range appears for $k \in [k_{\text{CD}}, k_\eta]$, where $k_{\text{CD}} = \sqrt{Pr}\, k_\eta$ is the characteristic wavenumber based on diffusion and small-scales convection. This new range appears thanks to small-scales convection that balances diffusion from the $k^{-17/3}$ inertial-diffusive range. This small-scales convection predicted by Gibson (1968) comes from small scales eddies of order k_η^{-1}. This new range appears conjointly with the $k^{-17/3}$ scaling when both the Reynolds and the Prandtl numbers are respectively high enough ($Re_\lambda \geq 2.10^4$) and small enough ($Pr \leq 10^{-3}$). Finally, both the k and Pr dependence of the scaling $E_T \sim \sqrt{Pr}\, k^{-11/3}$ were assessed numerically.

Secondly, the mixed-derivative skewness S_T has been investigated. The main results of this study are twofold. (i) At high Reynolds numbers and for $Pr \geq 10^3$, S_T saturates to a constant value $S_T^\infty = -0.435$, independent of the large scales initial conditions σ and σ_T, which means that statistical properties of the scalar mixing are converged, and can be interpreted as a small scales equilibrium in the viscous-convective range. (ii) The Re_λ^{-1} scaling for S_T (and S), coming from self-similarity theory, was numerically assessed. These numerical and theoretical results exhibit some robust asymptotic states at very large Reynolds and Prandtl numbers for scalar third-order statistics.

Finally, we characterized the decay of a passive scalar field in HIT by extending the Comte-Bellot and Corrsin (CBC) analysis and comparing it to EDQNM simulations. Namely, a scalar backscatter parameter p_T was defined to take into account strong scalar inverse non-linear transfers when $\sigma_T = 4$: p_T is found to depend much more on σ than on Pr. The important result is that the theoretical scalar decay exponents of the extended CBC theory are valid whatever the Prandtl number is in high and low Reynolds and Péclet regimes: indeed, a broad range of Prandtl numbers ($10^{-5} \leq Pr \leq 10^5$) was investigated. The main finding of this study is that the Prandtl number only affects small scales of the scalar spectrum E_T, but not the asymptotic time evolution of scalar one-point statistics: indeed, the large scales ($k < k_L$) depend only on the infrared slopes σ and σ_T. In addition, it was shown numerically that neither the Prandtl number nor the initial position of $L_T(t = 0)$ affect the asymptotic dynamics of the passive scalar decay as soon as the Reynolds and Péclet numbers are large enough. In other words, the problem of the passive scalar decay in HIT has been simplified, reducing the relevant parameters from (Re, Pr, σ, σ_T, $L_T(t = 0)$) to (Pe, σ, σ_T) at large Reynolds numbers. In the continuity of this study, a law able to predict the relative position of the peaks of both kinetic and scalar spectra k_L and k_T was proposed. The consistency of the results over a wide range of Prandtl and Reynolds numbers shows that the decay of the passive scalar is driven only by the most energetic large scales of the initial spectra.

Chapter 2

Spectral Modelling of the Velocity Field in Homogeneous Turbulence

In the previous chapter, the transport of a passive scalar field in HIT was investigated using classical EDQNM. The scalar field is left aside for now, and we focus on the modelling of HAT for the velocity field, in order to later combine both anisotropic features and scalar mixing.

The **anisotropic EDQNM modelling** for the velocity field, introduced in Cambon *et al.* (1981), and recently improved in Mons *et al.* (2016), is presented: details about calculations are gathered in Appendix C. The model consists in two steps: first, a classical EDQNM procedure is used to close the non-linear terms of the exact evolution equations of the spectral second-order moments. Secondly, anisotropy is modelled through spherically-averaged descriptors, following an expansion into spherical harmonics of the spectral Reynolds tensor $\hat{R}_{ij}$, further truncated at the second-order for the sake of simplicity.

The spectral formalism is presented here, along with the main evolution equations, the basics of EDQNM, and the detailed expressions of the spherically averaged production terms and non-linear transfers. New theoretical considerations with respect to Mons *et al.* (2016) are proposed as well regarding the expansion of $\hat{R}_{ij}$. In what follows, non-rotating flows are considered. Direct applications of the anisotropic EDQNM modelling for the velocity field are proposed in Chapter 3.

2.1 Equations in physical space

In turbulence, the **Reynolds decomposition** is used to represent a field as the sum of a mean value and a fluctuating one. Thus, the velocity field $v_i = u_i + U_i$, where u_i is the fluctuating velocity, verifies the Navier-Stokes equation with a non-zero mean field U_i

$$\left(\frac{\partial}{\partial t} + u_j \frac{\partial}{\partial x_j}\right) u_i + U_j \frac{\partial u_i}{\partial x_j} + u_j \frac{\partial U_i}{\partial x_j} = -\frac{\partial p}{\partial x_i} + \nu \frac{\partial^2 u_i}{\partial x_j \partial x_j}, \tag{2.1}$$

where p is the fluctuating pressure and ν the kinematic viscosity. For the sake of clarity, the time dependence was omitted. The two-point velocity correlation, or **Reynolds stress tensor**,

R_{ij} is now introduced

$$R_{ij}(\boldsymbol{x}, \boldsymbol{r}, t) =< u_i(\boldsymbol{x}, t) u_j(\boldsymbol{x} + \boldsymbol{r}, t) >, \tag{2.2}$$

where $\boldsymbol{r}$ is the distance between two points and $< . >$ an ensemble average. In homogeneous turbulence, R_{ij} only depends on the separation vector $\boldsymbol{r}$, and all spatial derivatives of second-order moments (and higher) are zero. Hence, the evolution equation of the one-point correlation $R_{ij}(0, t)$ is

$$\frac{\partial R_{ij}}{\partial t} = \mathfrak{P}_{ij}(t) + \Pi_{ij}(t) - \epsilon_{ij}(t), \tag{2.3}$$

where $\mathfrak{P}_{ij}$ is the production tensor

$$\mathfrak{P}_{ij}(t) = -\frac{\partial U_i}{\partial x_k} R_{kj}(t) - \frac{\partial U_j}{\partial x_k} R_{ki}(t), \tag{2.4}$$

which arises directly from velocity gradients, Π_{ij} is the **pressure strain tensor** given by

$$\Pi_{ij}(t) =< p(t) \left(\frac{\partial u_i}{\partial x_j} + \frac{\partial u_j}{\partial x_i} \right) >, \tag{2.5}$$

which will be investigated in the next chapter, and ϵ_{ij} is the **dissipation tensor**

$$\epsilon_{ij}(t) = 2\nu < \frac{\partial u_i}{\partial x_k} \frac{\partial u_j}{\partial x_k} > . \tag{2.6}$$

Surprisingly, the evolution equation of ϵ_{ij} is not often investigated, as pointed out in Piquet (2001). Its equation is consequently derived and simplified in (A.21) for homogeneous turbulence in Appendix A. The mean velocity gradients are represented by the space-uniform matrix A_{ij}

$$A_{ij} = \frac{\mathrm{d}U_i}{\mathrm{d}x_j}. \tag{2.7}$$

Then, one can develop $U_i(\boldsymbol{x}, t) = A_{ij}(t) x_j + u_i^0$ where u_i^0 expresses the effect of a solid-body motion. The **kinetic energy** $K(t)$ is defined as

$$K(t) = \frac{1}{2} < u_i u_i >= \frac{1}{2} R_{ii}(\boldsymbol{r} = \boldsymbol{0}, t), \tag{2.8}$$

and its evolution can be obtained from (2.3)

$$\frac{\partial K}{\partial t} = \frac{\mathfrak{P}_{ii}}{2} - \frac{\epsilon_{ii}}{2}. \tag{2.9}$$

The evolution equation of $R_{ii}(r \neq 0)$, the so-called **von Kármán-Howarth equation** (von Karman & Howarth, 1938), is addressed in Appendix A. Consistently, the **kinetic energy dissipation rate** is then defined as $\epsilon = \epsilon_{ii}/2$. Finally, to follow the time evolution of global anisotropy, one uses the **anisotropy indicator**

$$b_{ij}(t) = \frac{R_{ij}(t)}{2K(t)} - \frac{\delta_{ij}}{3}, \tag{2.10}$$

which is the normalized deviatoric part of R_{ij}. It will be shown hereafter that b_{ij} contains in fact two types of anisotropy.

2.2 Spectral equations and transfers

In this section, the exact evolution equation of the spectral Reynolds tensor $\hat{R}_{ij}$ is derived, and a decomposition in terms of directional and polarization anisotropies is presented. There are no assumptions, except homogeneity, in this part: the modelling begins in the next section.

2.2.1 Craya equation for $\hat{R}_{ij}$

The counterpart of (2.1) in Fourier space is

$$\left(\frac{\partial}{\partial t} - A_{ln}k_l\frac{\partial}{\partial k_n} + \nu k^2\right)\hat{u}_i(\boldsymbol{k}) + A_{ij}\hat{u}_j(\boldsymbol{k}) + \mathrm{i}k_j\widehat{u_iu_j}(\boldsymbol{k}) = -\mathrm{i}k_i\hat{p}(\boldsymbol{k}), \tag{2.11}$$

where $\hat{u}_i$ is the Fourier transform of u_i and k is the wavenumber: $\hat{u}_i$, and most of the spectral quantities studied in this work, verifies the Hermitian symmetry, *i.e.* $\hat{u}_i^*(\boldsymbol{k}) = \hat{u}_i(-\boldsymbol{k})$, where $()^*$ is the complex conjugate. For the sake of clarity, the time-dependence was omitted; $\widehat{u_mu_n}(\boldsymbol{k})$ is the convolution product that can be written as

$$\widehat{u_mu_n}(\boldsymbol{k}) = \int_{\boldsymbol{k}=\boldsymbol{p}+\boldsymbol{q}} \hat{u}_i(\boldsymbol{p})\hat{u}_m(\boldsymbol{q})\mathrm{d}^3\boldsymbol{p}. \tag{2.12}$$

Thanks to the incompressibility condition $\hat{u}_ik_i = 0$ in Fourier space, the pressure term can be erased by projecting (2.11) on the plane perpendicular to $\hat{p}$. This further yields the so-called **Craya equation** for $\hat{R}_{ij}$

$$\left(\frac{\partial}{\partial t} - A_{ln}k_l\frac{\partial}{\partial k_n} + 2\nu k^2\right)\hat{R}_{ij}(\boldsymbol{k}) + M_{in}(\boldsymbol{k})\hat{R}_{nj}(\boldsymbol{k}) + M_{jn}(\boldsymbol{k})\hat{R}_{ni}(\boldsymbol{k}) = T_{ij}^{\mathrm{NL}}(\boldsymbol{k}), \tag{2.13}$$

where $\hat{R}_{ij}$ in Fourier space is given by

$$\hat{R}_{ij}(\boldsymbol{k},t)\delta(\boldsymbol{k}-\boldsymbol{p}) =< \hat{u}_i^*(\boldsymbol{p},t)\hat{u}_j(\boldsymbol{k},t) >= \left(\frac{1}{2\pi}\right)^3\delta(\boldsymbol{k}-\boldsymbol{p})\int e^{-\mathrm{i}k_pr_p}R_{ij}(\boldsymbol{r})\mathrm{d}^3\boldsymbol{r}, \tag{2.14}$$

and where $M_{ij}(\boldsymbol{k}) = (\delta_{in} - 2\alpha_i\alpha_n)A_{nj}$ with $\alpha_i = k_i/k$. The **total non-linear transfer** reads

$$\boxed{T_{ij}^{\mathrm{NL}}(\boldsymbol{k},t) = P_{imn}(\boldsymbol{k})\int S_{njm}(\boldsymbol{k},\boldsymbol{p},t)\mathrm{d}^3\boldsymbol{p} + P_{jmn}(\boldsymbol{k})\int S_{nim}^*(\boldsymbol{k},\boldsymbol{p},t)\mathrm{d}^3\boldsymbol{p},} \tag{2.15}$$

where $P_{imn}(\boldsymbol{k})$ is the **Kraichnan's operator**, and P_{ij} the projector

$$2P_{imn}(\boldsymbol{k}) = k_mP_{in}(\boldsymbol{k}) + k_nP_{im}(\boldsymbol{k}), \qquad P_{ij}(\boldsymbol{k}) = \delta_{ij} - \alpha_i\alpha_j, \tag{2.16}$$

with S_{ijn} is the spectral three-point third-order correlation

$$S_{ijn}(\boldsymbol{k},\boldsymbol{p},t)\delta(\boldsymbol{k}+\boldsymbol{p}+\boldsymbol{q}) = \mathrm{i} < \hat{u}_i(\boldsymbol{q},t)\hat{u}_j(\boldsymbol{k},t)\hat{u}_n(\boldsymbol{p},t) > . \tag{2.17}$$

The non-linear total transfer T_{ij}^{NL} can be written in a form that includes a conservative part with zero integral over k, and a "slow pressure" term that is responsible for a **return to isotropy**

(RTI) mechanism and interactions between components

$$T_{ij}^{\mathrm{NL}}(\boldsymbol{k},t) = \underbrace{\tau_{ij}(\boldsymbol{k},t) + \tau_{ji}^{*}(\boldsymbol{k},t)}_{\text{Conservative transfer}} + \underbrace{W_{ij}(\boldsymbol{k},t)}_{\text{Return to isotropy}} = P_{in}\tau_{nj}(\boldsymbol{k},t) + P_{jn}\tau_{ni}^{*}(\boldsymbol{k},t), \tag{2.18}$$

where

$$\tau_{ij}(\boldsymbol{k},t) = k_n \int S_{ijn}(\boldsymbol{k},\boldsymbol{p},t)\mathrm{d}^3\boldsymbol{p}, \tag{2.19}$$

and

$$W_{ij} = -\alpha_i\alpha_n\tau_{nj}(\boldsymbol{k},t) - \alpha_j\alpha_n\tau_{ni}^{*}(\boldsymbol{k},t), \tag{2.20}$$

with $W_{ii} = 0$ (because $k_j\tau_{ij} = 0$, but $k_i\tau_{ij} \neq 0$). The conservative part is $\tau_{ij}(\boldsymbol{k},t) + \tau_{ji}^{*}(\boldsymbol{k},t)$, meaning that its integral over k is 0. However, integral over k for W_{ij} is different from 0 since it is the spectral counterpart of the slow-part of the pressure-strain tensor Π_{ij}.

2.2.2 Craya-Herring frame - $\mathcal{E} - Z$ decomposition

An optimal decomposition of $\hat{R}_{ij}$ results from a trace-deviator splitting on the plane perpendicular to the wavevector $\boldsymbol{k}$ (Cambon & Rubinstein, 2006; Cambon *et al.*, 2013). Without helicity, which is the topic of Chapter 8, the spectral Reynolds tensor can be written as follows

$$\boxed{\hat{R}_{ij}(\boldsymbol{k},t) = \underbrace{\frac{E(k,t)}{4\pi k^2}P_{ij}(\boldsymbol{k})}_{\text{Isotropic}} + \underbrace{\left(\mathcal{E}(\boldsymbol{k},t) - \frac{E(k,t)}{4\pi k^2}\right)P_{ij}(\boldsymbol{k})}_{\text{Directional anisotropy}} + \underbrace{\Re\Big(Z(\boldsymbol{k},t)N_i(\boldsymbol{k})N_j(\boldsymbol{k})\Big)}_{\text{Polarization anisotropy}},} \tag{2.21}$$

where $\mathcal{E}$ is the **kinetic energy density**

$$\boxed{\mathcal{E}(\boldsymbol{k},t) = \frac{\hat{R}_{ii}(\boldsymbol{k},t)}{2},} \tag{2.22}$$

linked to the **kinetic energy spectrum** E through a surface integral on a spherical shell S_k of radius k

$$E(k,t) = \int_{S_k} \mathcal{E}(\boldsymbol{k},t)\mathrm{d}^2\boldsymbol{k}. \tag{2.23}$$

The energy density $\mathcal{E}$ is the distribution of energy along the wavevector $\boldsymbol{k}$, and $\mathcal{E} - E/(4\pi k^2)$ reflects the **directional anisotropy**, *i.e.* the difference between energy in one direction and the spherical average. Then, Z represents **polarization anisotropy** and reflects the difference of anisotropy between two components of the spectral Reynolds tensor

$$\boxed{Z(\boldsymbol{k},t) = \frac{\hat{R}_{ij}(\boldsymbol{k},t)}{2}N_i^{*}(\boldsymbol{k})N_j^{*}(\boldsymbol{k}).} \tag{2.24}$$

Both $\mathcal{E}$ and Z must verify the **realizability condition**

$$|Z(\boldsymbol{k},t)| \leq \mathcal{E}(\boldsymbol{k},t), \qquad \forall(\boldsymbol{k},t). \tag{2.25}$$

Without helicity, $\hat{R}_{ij}$ is real and thus $\hat{R}_{ij}(\boldsymbol{k}) = \hat{R}_{ij}(-\boldsymbol{k})$. In the isotropic case, $Z = 0$ and $\mathcal{E} = \mathcal{E}_0 = E/(4\pi k^2)$. Finally, N_j are the **helical modes** (Cambon & Jacquin, 1989; Waleffe,

1992), perpendicular to k_j, and linked to the Craya-Herring frame $(\boldsymbol{e^{(1)}}, \boldsymbol{e^{(2)}}, \boldsymbol{e^{(3)}})$ and to the fixed reference direction $\boldsymbol{n}$, illustrated in Fig. 2.1, through

$$e_i^{(3)} = \frac{k_i}{k}, \qquad e_i^{(2)} = \epsilon_{ijl} e_j^{(3)} e_l^{(1)}, \qquad e_i^{(1)} = \epsilon_{ijl} \frac{k_j n_l}{|\boldsymbol{k} \times \boldsymbol{n}|} = \epsilon_{ijl} \frac{k_j n_l}{k_\perp}, \tag{2.26}$$

$$N_j(\boldsymbol{k}) = e_j^{(2)}(\boldsymbol{k}) - i e_j^{(1)}(\boldsymbol{k}). \tag{2.27}$$

In the Craya-Herring frame, the fluctuating spectral velocity $\hat{u}_i$ is contained in the plane $(\boldsymbol{e^{(1)}}, \boldsymbol{e^{(2)}})$ and can be decomposed into **toroidal** and **poloidal** components according to

$$\hat{u}_i(\boldsymbol{k}) = \hat{u}^{(\text{toro})}(\boldsymbol{k}) e_i^{(1)}(\boldsymbol{k}) + \hat{u}^{(\text{polo})}(\boldsymbol{k}) e_i^{(2)}(\boldsymbol{k}). \tag{2.28}$$

Note that unlike other spectral classical quantities, the toroidal component does not verify the Hermitian symmetry since $e_i^{(1)}(-\boldsymbol{k}) = -e_i^{(1)}(\boldsymbol{k})$, so that $\hat{u}^{(\text{toro})*}(\boldsymbol{k}) = -\hat{u}^{(\text{toro})}(-\boldsymbol{k})$. The toroidal and poloidal potentials $\mathcal{E}^{(\text{toro})}$ and $\mathcal{E}^{(\text{polo})}$ are simply linked to $\mathcal{E}$ and Z through

$$\begin{cases} \mathcal{E}^{(\text{toro})}(\boldsymbol{k})\delta(\boldsymbol{k}-\boldsymbol{p}) =< \hat{u}^{(\text{toro})}(\boldsymbol{k})\hat{u}^{(\text{toro})*}(\boldsymbol{p}) > \\ \mathcal{E}^{(\text{polo})}(\boldsymbol{k})\delta(\boldsymbol{k}-\boldsymbol{p}) =< \hat{u}^{(\text{polo})}(\boldsymbol{k})\hat{u}^{(\text{polo})*}(\boldsymbol{p}) > \end{cases}, \qquad \begin{cases} \mathcal{E}(\boldsymbol{k}) = \mathcal{E}^{(\text{polo})}(\boldsymbol{k}) + \mathcal{E}^{(\text{toro})}(\boldsymbol{k}) \\ Z(\boldsymbol{k}) = \mathcal{E}^{(\text{polo})}(\boldsymbol{k}) - \mathcal{E}^{(\text{toro})}(\boldsymbol{k}). \end{cases} \tag{2.29}$$

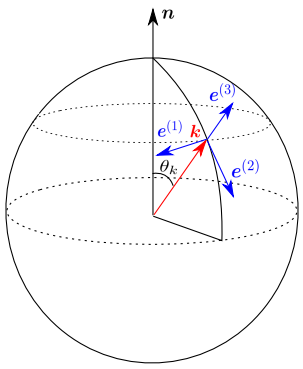

Figure 2.1: Craya-Herring frame $(\boldsymbol{e^{(1)}}, \boldsymbol{e^{(2)}}, \boldsymbol{e^{(3)}})$ in blue, defined in (2.26); in red the wavevector $\boldsymbol{k}$. The fluctuating spectral velocity $\hat{\boldsymbol{u}}$ is contained in the plane $(\boldsymbol{e^{(1)}}, \boldsymbol{e^{(2)}})$.

At this point, it is of interest to mention that the general decomposition (2.21) could also be applied in magnetohydrodynamics (MHD): indeed, the magnetic spectral tensor, defined as $\hat{B}_{ij}(\boldsymbol{k})\delta(\boldsymbol{k}-\boldsymbol{p}) =< \hat{b}_i^*(\boldsymbol{p})\hat{b}_j(\boldsymbol{k}) >$, is also real, symmetric, and solenoidal. This might be interesting to apply this spectral anisotropic formalism to strong MHD turbulence where a mean magnetic field makes the conductive flow axisymmetric (Boldyrev *et al.*, 2011).

2.2.3 Generalized Lin equations

Let's now write the evolution equations for $\mathcal{E}$ and Z, called here the generalized Lin equations. One can rewrite (2.21) as

$$\hat{R}_{ij}(\boldsymbol{k}, t) = \mathcal{E}(\boldsymbol{k}, t) P_{ij}(\boldsymbol{k}) + \Re\Big(Z(\boldsymbol{k}, t) N_i(\boldsymbol{k}) N_j(\boldsymbol{k})\Big). \tag{2.30}$$

With this decomposition and the definition of $\mathcal{E}$, the $\mathcal{E}$-Lin equation reads

$$\boxed{\left(\frac{\partial}{\partial t} - A_{ln}k_l\frac{\partial}{\partial k_n} + 2\nu k^2\right)\mathcal{E} - A^+_{mn}\alpha_n\alpha_m\mathcal{E} + A^+_{mn}\Re(ZN_nN_m) = T_{\mathcal{E}},} \tag{2.31}$$

where A^+_{ij} is the symmetric part of A_{ij}, and where the directional transfer $T_{\mathcal{E}}$, is

$$T_{\mathcal{E}}(\boldsymbol{k},t) = \frac{T^{\mathrm{NL}}_{ii}(\boldsymbol{k},t)}{2} = \frac{1}{2}\Big(\tau_{ii}(\boldsymbol{k},t) + \tau^*_{ii}(\boldsymbol{k},t)\Big). \tag{2.32}$$

Similarly, the Z-Lin equation reads

$$\boxed{\left(\frac{\partial}{\partial t} - A_{ln}k_l\frac{\partial}{\partial k_n} + 2\nu k^2\right)Z + 2\mathrm{i}Z\Omega_{\mathrm{CH}} + A_{in}N^*_i(\mathcal{E}N^*_n + ZN_n) = T_Z,} \tag{2.33}$$

where Ω_{CH}, linked to both the frame and the velocity gradients, is computed in Appendix C, and where the polarization transfer T_Z is

$$T_Z(\boldsymbol{k},t) = \frac{T^{\mathrm{NL}}_{ij}(\boldsymbol{k},t)}{2}N^*_i(\boldsymbol{k})N^*_j(\boldsymbol{k}) = \frac{1}{2}\Big(\tau_{ij}(\boldsymbol{k},t) + \tau^*_{ji}(\boldsymbol{k},t)\Big)N^*_i(\boldsymbol{k})N^*_j(\boldsymbol{k}). \tag{2.34}$$

The effects of a mean rotation on these equations are considered in Appendix C.

2.3 The closure problem

In this section, the eddy-damped quasi-normal Markovian (EDQNM) approach is briefly recalled: since details on the procedure can be found in many references, only the main steps are presented here, and all the calculations specific to homogeneous anisotropic turbulence are detailed in the appendices. The EDQNM procedure is applied to close the Craya equation and to compute analytically the directional and polarization non-linear transfers $T_{\mathcal{E}}$ and T_Z. This step is then combined in the next section with a modelling of anisotropy, so that the $\boldsymbol{k}$-dependence of the spectral second-order moments is transformed into a k-one.

2.3.1 The EDQNM approximation

Similarly to HIT, there is here a need to model the transfer term T^{NL}_{ij}. In order to do so, the evolution equation of the three-point third-order velocity correlation S_{ijn}, defined in (2.17), is investigated. After some algebra, one gets

$$\begin{aligned}&\left(\frac{\partial}{\partial t} + \nu(k^2+p^2+q^2) - A_{lm}\left(k_l\frac{\partial}{\partial k_m} + p_l\frac{\partial}{\partial p_m}\right)\right)S_{ijn}(\boldsymbol{k},\boldsymbol{p},t) + M_{im}(\boldsymbol{q})S_{mjn}(\boldsymbol{k},\boldsymbol{p},t)\\ &+ M_{jm}(\boldsymbol{k})S_{imn}(\boldsymbol{k},\boldsymbol{p},t) + M_{nm}(\boldsymbol{p})S_{ijm}(\boldsymbol{k},\boldsymbol{p},t) = \mathfrak{T}_{ijn}(\boldsymbol{k},\boldsymbol{p},t),\end{aligned} \tag{2.35}$$

where $\mathfrak{T}_{ijn}$ will be submitted to the EDQNM approximation. So far, previous equations were exact. From this point, the modelling begins. Fluctuating velocity probability distributions are assumed to be close to normal distributions. Hence, one can express $\mathfrak{T}_{ijn}$ as the sum of a

quasi-normal part, and a modelled departure from normal laws part, namely

$$\mathfrak{T}_{ijn}(\boldsymbol{k},\boldsymbol{p},t) = \mathfrak{T}^{\mathrm{QN}}_{ijn}(\boldsymbol{k},\boldsymbol{p},t) - \Big(\mu_1(k,t) + \mu_1(p,t) + \mu_1(q,t)\Big) S_{ijn}(\boldsymbol{k},\boldsymbol{p},t). \tag{2.36}$$

The quasi-normal part $\mathfrak{T}^{\mathrm{QN}}_{ijn}$ is expressed as a function of $\hat{R}_{ij}$ according to

$$\begin{aligned}\mathfrak{T}^{\mathrm{QN}}_{ijl}(\boldsymbol{k},\boldsymbol{p},t) = 2\Big(&P_{imn}(\boldsymbol{q})\hat{R}_{mj}(\boldsymbol{k},t)\hat{R}_{nl}(\boldsymbol{p},t)\\ &+ P_{jmn}(\boldsymbol{k})\hat{R}_{ml}(\boldsymbol{p},t)\hat{R}_{ni}(\boldsymbol{q},t) + P_{lmn}(\boldsymbol{p})\hat{R}_{mi}(\boldsymbol{q},t)\hat{R}_{nj}(\boldsymbol{k},t)\Big).\end{aligned} \tag{2.37}$$

The second part $\Big(\mu_1(k,t) + \mu_1(p,t) + \mu_1(q,t)\Big) S_{ijn}(\boldsymbol{k},\boldsymbol{p},t)$ takes into account and models the departure from a normal law: this is the **eddy-damping** contribution where

$$\mu_1(k,t) = A_1\sqrt{\int_0^k x^2 E(x,t)\mathrm{d}x}, \tag{2.38}$$

as defined in Pouquet *et al.* (1975); Orszag (1970). The constant A_1 was originally chosen to be $A_1 = 0.355$ and we keep this value, which provides a Kolmogorov constant so that $K_0 \simeq 1.4$. Choosing a different value, such as $A_1 = 0.49$, yields $K_0 \simeq 1.6$ (Bos *et al.*, 2012).

Now, the evolution equation of S_{ijn} (2.35) with (2.36) can be solved. The resulting expression of S_{ijn} is then simplified using the **Markovianisation** step: the characteristic time of the eddy-damping is very small with respect to the turbulence characteristic time. This constitutes the classical **EDQNM closure**. In the homogeneous isotropic turbulence (HIT) framework, the expression of $\hat{R}_{ij}$ is rather straightforward so that the analytical expression of (2.37) remains quite simple. In homogeneous anisotropic turbulence, the quasi-normal expression $\mathfrak{T}^{\mathrm{QN}}_{ijl}$ is further combined with the decomposition (2.21) and with the modelling of anisotropy for $\mathcal{E}$ and Z, so that the full anisotropic EDQNM modelling contains more complex features than in HIT.

Indeed, in HIT, there is only one EDQNM formalism (Lesieur, 2008). In HAT on the contrary, three versions can be found (Sagaut & Cambon, 2008), so called EDQNM-1,2,3. For non-rotating turbulence and in the presence of strong production mechanisms, the present EDQNM1 (Cambon *et al.*, 1981), in terms of spherically-averaged spectra, is relevant enough. However, rotating turbulence, among other configurations such as stably stratified turbulence for example, requires the use of the EDQNM2 or EDQNM3, which is out of the scope of the present work, and models the effects of interacting inertial dispersive waves on the dynamics of the three-point third-order correlations.

More precisely, the Green's tensor of the rapid distortion regime is used to solve the linear operator in the equation for the three-point third-order correlations (Cambon & Jacquin, 1989). As a consequence, in the EDQNM2 framework, the modelled non-linear transfers contain linear terms (with respect to the mean-velocity gradient) coming from the third-order correlations equations. This is at variance with EDQNM1, where these terms are discarded: a review of various models of turbulence can be found in Cambon & Scott (1999). Then, for a complete match in the asymptotic case of vanishing non-linearity between **wave turbulence theory** and EDQNM, the EDQNM3 was derived, which only slightly differs from EDQNM2 (Cambon *et al.*, 1997, 2004): the separation of rapid and slow variables is refined in the quasi-normal procedure, so that $\mathcal{E}$ is treated as a slow variable, and the rapid phase of Z is accounted for. These different

approaches were recently discussed in Cambon *et al.* (2017) where it is for instance shown how to move from EDQNM2 to EDQNM1 for stratified turbulence.

In what follows, since rotation is not considered, only the EDQNM1 approximation is used. Thanks to the whole EDQNM procedure, it is possible to express τ_{ij}, coming from (2.18), as function of the second-order moments and of the characteristic time θ_{kpq} containing the eddy-damping term:

$$\tau_{ij}(\boldsymbol{k},t) = k_l \int \theta_{kpq} \mathfrak{T}^{\mathrm{QN}}_{ijl}(\boldsymbol{k},\boldsymbol{p},t)\mathrm{d}^3\boldsymbol{p}, \tag{2.39}$$

where θ_{kpq} is the characteristic relaxation time of the third-order correlations

$$\theta_{kpq} = \frac{1-e^{-\mu_{kpq}t}}{\mu_{kpq}}, \qquad \mu_{kpq} = \nu(k^2+p^2+q^2) + \mu_1(k,t) + \mu_1(p,t) + \mu_1(q,t). \tag{2.40}$$

Even for HAT and for consistency with previous studies, an isotropic eddy-damping term is kept, meaning in particular that each component of $\hat{R}_{ij}$ has the same θ_{kpq}. Also, this avoids the introduction of arbitrary constants at this level of the modelling.

It is worth noting that within the EDQNM1 framework, the characteristic time θ_{kpq} can be tuned to take into account different effects. For unstably stratified turbulence, addressed later in Chapter 7, the stratification frequency $N(t)$ was added to the viscous and inertial terms to match better with DNS in Burlot *et al.* (2015*a*): $\theta^{(\mathrm{USHT})}_{kpq} = \theta_{kpq} + a_1 N(t)$, where a_1 is a constant, of order 0.25, which depends on the flow. In isotropic magnetohydrodynamics turbulence, a magnetic correction was added in Pouquet *et al.* (1976) to take into account the propagation of Alfvèn waves: $\theta^{(\mathrm{MHD})}_{kpq} = \theta_{kpq} + \sqrt{2/3}k\sqrt{\int_0^k E_B(x,t)\mathrm{d}x}$, where E_B is the magnetic energy spectrum.

2.3.2 Directional and Polarization transfers $T_{\mathcal{E}}$ and T_Z

The aim of the EDQNM1 approximation is to provide an explicit formula for both the directional and polarization transfers $T_{\mathcal{E}}$ and T_Z given in (2.32) and (2.34). For this purpose, a more convenient frame $(\boldsymbol{\beta},\boldsymbol{\gamma},\boldsymbol{\alpha})$ must be used, attached to the planed formed by the triad $\boldsymbol{k}+\boldsymbol{p}+\boldsymbol{q}=\boldsymbol{0}$, where $\boldsymbol{\gamma}$ is perpendicular to this plane. From now, the following notations are used: $'$ and $''$ refer to quantities expressed in $\boldsymbol{p}$ and $\boldsymbol{q}$ respectively. Useful vectors and angles are gathered in Fig. 2.2. a, b and c are the angles formed by $\boldsymbol{p}$ and $\boldsymbol{q}$, $\boldsymbol{q}$ and $\boldsymbol{k}$, and $\boldsymbol{k}$ and $\boldsymbol{p}$. Finally, $x=\cos a$, $y=\cos b$ and $z=\cos c$. The new frame $(\boldsymbol{\beta},\boldsymbol{\gamma},\boldsymbol{\alpha})$ is obtained from Craya frame $(\boldsymbol{e^{(1)}},\boldsymbol{e^{(2)}},\boldsymbol{e^{(3)}}=\boldsymbol{\alpha})$ by rotations of angles λ, λ' and λ'' around $\boldsymbol{k}$, $\boldsymbol{p}$ and $\boldsymbol{q}$. All the details of the computation of τ_{ij} from (2.18) are given in Appendix C. The final results for the **polarization** and the **directional transfers** are

$$\begin{aligned} T_{\mathcal{E}}(\boldsymbol{k},t) = 2\int \theta_{kpq}kp\Big[&(\mathcal{E}''+\Re X'')\Big((xy+z^3)(\mathcal{E}'-\mathcal{E}) - z(1-z^2)(\Re X'-\Re X)\Big) \\ &+ \Im X''(1-z^2)(x\Im X - y\Im X')\Big]\mathrm{d}^3\boldsymbol{p}, \end{aligned} \tag{2.41}$$

$$\begin{aligned} T_Z(\boldsymbol{k},t) = 2\int \theta_{kpq}kpe^{-2i\lambda}\Big[&(\mathcal{E}''+\Re X'')\Big((xy+z^3)(\Re X'-X) - z(1-z^2)(\mathcal{E}'-\mathcal{E}) \\ &+ i(y^2-z^2)\Im X'\Big) + i\Im X''(1-z^2)\Big(x(\mathcal{E}+X) - iy\Im X'\Big)\Big]\mathrm{d}^3\boldsymbol{p}, \end{aligned} \tag{2.42}$$

with $\mathcal{E}(\boldsymbol{k},t) = \mathcal{E}$, $\mathcal{E}(\boldsymbol{p},t) = \mathcal{E}'$, $\mathcal{E}(\boldsymbol{q},t) = \mathcal{E}''$, $X = Z(\boldsymbol{k},t)e^{2\mathrm{i}\lambda}$, $X' = Z(\boldsymbol{p},t)e^{2\mathrm{i}\lambda'}$ and $X'' = Z(\boldsymbol{q},t)e^{2\mathrm{i}\lambda''}$. The expressions of $T_{\mathcal{E}}$ and T_Z can also be found in Cambon *et al.* (1997); Mons *et al.* (2016).

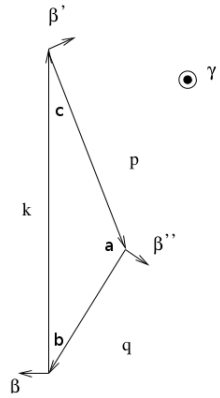

Figure 2.2: The triad $\boldsymbol{k}+\boldsymbol{p}+\boldsymbol{q}=\boldsymbol{0}$ and useful vectors and angles

2.4 Spherically-averaged equations

The generalized $\mathcal{E}$-Lin and Z-Lin equations, along with explicit directional and polarization transfers $T_{\mathcal{E}}$ and T_Z, can be solved. In order to considerably reduce computational time, spherically-averaged descriptors are used, which depend only on the modulus k of the wavevector $\boldsymbol{k}$. The procedure is to integrate analytically the generalized Lin equations over a sphere of radius k. To do so, the expansion of $\hat{R}_{ij}$ into spherical harmonics is truncated at the second-order.

2.4.1 Spherically-averaged descriptors

The decomposition of $\hat{R}_{ij}$ provided by Cambon & Rubinstein (2006) is now used. As seen in (2.21), one has

$$\hat{R}_{ij}(\boldsymbol{k}) = \hat{R}_{ij}^{(\mathrm{iso})}(\boldsymbol{k}) + \hat{R}_{ij}^{(\mathrm{dir})}(\boldsymbol{k}) + \hat{R}_{ij}^{(\mathrm{pol})}(\boldsymbol{k}) = \Big(\mathcal{E}_0(k) + \mathcal{E}^{(\mathrm{dir})}(\boldsymbol{k})\Big)P_{ij}(\boldsymbol{k}) + \Re\Big(Z(\boldsymbol{k})N_i(\boldsymbol{k})N_j(\boldsymbol{k})\Big), \tag{2.43}$$

where $\mathcal{E}_0 = E/(4\pi k^2)$ and $\mathcal{E}^{(\mathrm{dir})} = \mathcal{E} - \mathcal{E}_0$. The complete expansion of $\mathcal{E}$ and Z into spherical harmonics at the second-order was done in Mons *et al.* (2016), and all the details and technical steps are gathered in Appendix C. Here, for theoretical considerations, the fourth-order is briefly presented, even though only the second-order will be used in the numerical simulations. After some algebra, one gets the fourth-order expansion of $\hat{R}_{ij}$ into spherical harmonics

$$\boxed{\begin{aligned} \mathcal{E}(\boldsymbol{k},t) &= \mathcal{E}_0\Big(1 - 15H_{ij}^{(\mathrm{dir})}(k,t)\alpha_i\alpha_j + \frac{945}{12}H_{ijpq}^{(\mathrm{dir})}(k,t)\alpha_i\alpha_j\alpha_p\alpha_q\Big), && (2.44)\\ Z(\boldsymbol{k},t) &= \frac{1}{2}\mathcal{E}_0\Big(5H_{ij}^{(\mathrm{pol})}(k,t) + \frac{21}{2}H_{ijpq}^{(\mathrm{pol})}(k,t)\alpha_p\alpha_q\Big)N_i^*(\boldsymbol{k})N_j^*(\boldsymbol{k}). && (2.45)\end{aligned}}$$

The possibility of a third-order contribution in the expansion of Z is only discussed in the next chapter in section 3.4.3, since the results are not satisfactory for the time being. At this

point, some words need to be said about the new fourth-order tensors. One can remark that at the fourth-order, the polarization part $H_{ijpq}^{(\mathrm{pol})}$ is contracted with both normalized wavevectors $\alpha_p\alpha_q$ and helical modes $N_i^*N_j^*$, unlike the directional part $H_{ijpq}^{(\mathrm{dir})}$ which is only contracted with $\alpha_i\alpha_j\alpha_p\alpha_q$, and is therefore fully symmetric in its indices, as reported in Rubinstein *et al.* (2015). The latter property of full-symmetry is thus *a priori* not verified by $H_{ijpq}^{(\mathrm{pol})}$, but we nonetheless make this assumption. Indeed, the analytical calculations are already very complex and lengthy, and this approximation renders the developments a bit easier. In addition, we assume that both $H_{ijpq}^{(\mathrm{dir})}$ and $H_{ijpq}^{(\mathrm{pol})}$ are trace-free, meaning that any contraction of two indices yields zero. For $H_{ijpq}^{(\mathrm{dir})}$, this is verified according to Rubinstein *et al.* (2015), but for $H_{ijpq}^{(\mathrm{pol})}$ this is a supplementary assumption, again for the sake of simplicity. All these spectral anisotropy descriptors are defined as

$$2E(k,t)H_{ij}^{(\mathrm{dir})}(k,t) = \int_{S_k} \hat{R}_{ij}^{(\mathrm{dir})}(\boldsymbol{k},t)\mathrm{d}^2\boldsymbol{k}, \qquad 2E(k,t)H_{ij}^{(\mathrm{pol})}(k,t) = \int_{S_k} \hat{R}_{ij}^{(\mathrm{pol})}(\boldsymbol{k},t)\mathrm{d}^2\boldsymbol{k}, \tag{2.46}$$

$$2E(k,t)H_{ijpq}^{(\mathrm{dir})}(k,t) = \int_{S_k} \mathcal{E}(\boldsymbol{k},t)\, P_{ijpq}(\boldsymbol{k})\, \mathrm{d}^2\boldsymbol{k}, \tag{2.47}$$

$$2E(k,t)H_{ijpq}^{(\mathrm{pol})}(k,t) = \int_{S_k} \Re\Big(Z(\boldsymbol{k},t)N_{ijpq}(\boldsymbol{k})\Big)\, \mathrm{d}^2\boldsymbol{k}, \tag{2.48}$$

where S_k is the sphere of radius k, and where P_{ijpq} and N_{ijpq} are generalized operators

$$P_{ijpq} = \alpha_i\alpha_j\alpha_p\alpha_q - \frac{1}{7}(\delta_{ij}\alpha_p\alpha_q + 5 \text{ perm.}) + \frac{1}{35}(\delta_{ij}\delta_{pq} + \delta_{ip}\delta_{jq} + \delta_{iq}\delta_{jp}), \tag{2.49}$$

$$N_{ijpq} = (N_iN_j\alpha_p\alpha_q + N_pN_q\alpha_i\alpha_j + 4 \text{ perm.}) - \frac{1}{7}(\delta_{ij}N_pN_q + \delta_{pq}N_iN_j + 4 \text{ perm.}). \tag{2.50}$$

Additional details about the fourth-order expansion, such as the evolution equations of $H_{ijpq}^{(\mathrm{dir})}$, and $H_{ijpq}^{(\mathrm{pol})}$, their linear and non-linear transfers, can be found in Appendix C.

Obviously, the truncation of the expansion into spherical harmonics of the exact decomposition (2.21) provokes a loss of angular information about the anisotropy of the flow. Part of this information is nevertheless restored thanks to the spherically averaged-descriptors $H_{ij}^{()}$ and $H_{ijpq}^{()}$. However, it is complicated to quantify what is lost because of this truncation. It will be shown in Chapter 3 that a consequence is that the exponential growth rate of the kinetic energy in shear flows is too large compared to values obtained in DNS and experiments, and that taking into account the fourth-order expansion tends to reduce this exponential growth rate. On the contrary, the second-order expansion seems to be sufficient for quantitative comparisons in multiple configurations involving the transport of a passive (Chapter 5) and active (Chapter 7) scalar field.

From now, in the context of moderate anisotropy, only the second order expansion of $\hat{R}_{ij}$ is kept. In this framework, all quadratic contributions $H_{ij}^{()}H_{ij}^{()}$ are discarded: nevertheless, these second-order contributions in anisotropy have been computed in Appendix C and it is shown that they are negligible, at least in shear flows. Note that the same kind of second-order truncations will be performed for the modelling of a scalar field in Chapter 4.

The indicator of anisotropy defined in (2.10) can be expanded into $b_{ij} = b_{ij}^{(\mathrm{dir})} + b_{ij}^{(\mathrm{pol})}$ thanks to the previous decomposition

$$b_{ij}^{(\mathrm{dir})}(t) = \frac{1}{K(t)} \int_0^\infty E(k,t) H_{ij}^{(\mathrm{dir})}(k,t) \mathrm{d}k, \qquad b_{ij}^{(\mathrm{pol})}(t) = \frac{1}{K(t)} \int_0^\infty E(k,t) H_{ij}^{(\mathrm{pol})}(k,t) \mathrm{d}k. \tag{2.51}$$

Finally, a limit can be derived from the realizability condition (2.25)

$$\max_i(L_i) \leq \frac{1}{15}, \tag{2.52}$$

where L_i are eigenvalues of $H_{ij}^{(\mathrm{dir})}$. This condition, obviously valid when only the second-order expansion is considered, was shown to hold true in multiple configurations in Mons *et al.* (2016).

2.4.2 Spherically-averaged final Lin equations

In this part, the final spherically-averaged Lin equations of the main spectra, namely E, $EH_{ij}^{(\mathrm{dir})}$, and $EH_{ij}^{(\mathrm{pol})}$, are derived: details of the calculations are given in Appendix C. It is recalled that only the second-order expansion of $\hat{R}_{ij}$ is considered, and that quadratic anisotropic contributions in the non-linear transfers are discarded. The following compact equations were derived in Mons *et al.* (2016), and read

$$\boxed{\begin{aligned} \left(\frac{\partial}{\partial t} + 2\nu k^2\right) E(k,t) &= S^{\mathrm{L(iso)}}(k,t) + S^{\mathrm{NL(iso)}}(k,t), && (2.53)\\ \left(\frac{\partial}{\partial t} + 2\nu k^2\right) E(k,t) H_{ij}^{(\mathrm{dir})}(k,t) &= S_{ij}^{\mathrm{L(dir)}}(k,t) + S_{ij}^{\mathrm{NL(dir)}}(k,t), && (2.54)\\ \left(\frac{\partial}{\partial t} + 2\nu k^2\right) E(k,t) H_{ij}^{(\mathrm{pol})}(k,t) &= S_{ij}^{\mathrm{L(pol)}}(k,t) + S_{ij}^{\mathrm{NL(pol)}}(k,t), && (2.55) \end{aligned}}$$

where $S^{\mathrm{NL(iso)}}(k,t)$ is the classical **non-linear spherically-averaged isotropic transfer** term

$$S^{\mathrm{NL(iso)}}(k,t) = \int_{S_k} T_{\mathcal{E}}(\boldsymbol{k},t) \mathrm{d}^2\boldsymbol{k} \tag{2.56}$$

$$= 16\pi^2 \int_{\Delta_k} \theta_{kpq} k^2 p^2 q (xy + z^3) \mathcal{E}_0''(\mathcal{E}_0' - \mathcal{E}_0) \mathrm{d}p\mathrm{d}q, \tag{2.57}$$

with Δ_k the domain where k, p and q are the lengths of the sides of the triangle formed by the triad. The **non-linear spherically-averaged directional transfer** $S_{ij}^{\mathrm{NL(dir)}}(k,t)$ is

$$S_{ij}^{\mathrm{NL(dir)}}(k,t) = \frac{1}{2} \int_{S_k} T_{\mathcal{E}}(\boldsymbol{k},t) P_{ij}(\boldsymbol{k}) \, \mathrm{d}^2\boldsymbol{k} - \frac{\delta_{ij}}{3} S^{\mathrm{NL(iso)}}(k,t) \tag{2.58}$$

$$\begin{aligned} &= 4\pi^2 \int_{\Delta_k} \theta_{kpq} k^2 p^2 q \mathcal{E}_0'' \left[(y^2-1)(xy+z^3)(\mathcal{E}_0' - \mathcal{E}_0) H_{ij}^{(\mathrm{pol})''} + z(1-z^2)^2 \mathcal{E}_0' H_{ij}^{(\mathrm{pol})'} \right] \mathrm{d}p\mathrm{d}q \\ &+ 8\pi^2 \int_{\Delta_k} \theta_{kpq} k^2 p^2 q (xy+z^3) \mathcal{E}_0'' \left[(3y^2-1)(\mathcal{E}_0' - \mathcal{E}_0) H_{ij}^{(\mathrm{dir})''} + (3z^2-1)\mathcal{E}_0' H_{ij}^{(dir)'} - 2\mathcal{E}_0 H_{ij}^{(\mathrm{dir})} \right] \mathrm{d}p\mathrm{d}q. \end{aligned} \tag{2.59}$$

And $S_{ij}^{\mathrm{NL(pol)}}(k,t)$ is the **non-linear spherically-averaged polarization transfer**

$$S_{ij}^{\mathrm{NL(pol)}}(k,t) = \frac{1}{2}\int_{S_k} \Re\Big(T_Z(\boldsymbol{k},t)N_i(\boldsymbol{k})N_j(\boldsymbol{k})\Big)\mathrm{d}^2\boldsymbol{k} \tag{2.60}$$

$$\begin{aligned}
&= 4\pi^2\int_{\Delta_k}\theta_{kpq}k^2p^2q\mathcal{E}_0''\Bigg[(xy+z^3)\Big((1+z^2)\mathcal{E}_0'H_{ij}^{(\mathrm{pol})'} - 4\mathcal{E}_0H_{ij}^{(\mathrm{pol})}\Big)\\
&+ z(z^2-1)(1+y^2)(\mathcal{E}_0'-\mathcal{E}_0)H_{ij}^{(\mathrm{pol})''} + 2z(z^2-y^2)\mathcal{E}_0'H_{ij}^{(\mathrm{pol})'} + 2xy(z^2-1)\mathcal{E}_0H_{ij}^{(\mathrm{pol})''}\Bigg]\mathrm{d}p\mathrm{d}q\\
&+ 24\pi^2\int_{\Delta_k}\theta_{kpq}k^2p^2qz(z^2-1)\mathcal{E}_0''\Big[(y^2-1)(\mathcal{E}_0'-\mathcal{E}_0)H_{ij}^{(\mathrm{dir})''} + (z^2-1)\mathcal{E}_0'H_{ij}^{(\mathrm{dir})'}\Big]\mathrm{d}p\mathrm{d}q.
\end{aligned} \tag{2.61}$$

For the linear production terms, A_{ij}^+ and A_{ij}^- are respectively the symmetric and antisymmetric parts of A_{ij}. First, $S^{\mathrm{L(iso)}}(k,t)$ is the **linear spherically-averaged isotropic transfer**

$$S^{\mathrm{L(iso)}}(k,t) = \frac{1}{2}\int_{S_k}\left(A_{ln}k_l\frac{\partial\hat{R}_{ii}}{\partial k_n} - 2M_{in}\hat{R}_{ni}\right)\mathrm{d}^2\boldsymbol{k} \tag{2.62}$$

$$= -2A_{lm}^+\left(\frac{\partial}{\partial k}(kEH_{lm}^{(\mathrm{dir})}) + E(H_{lm}^{(\mathrm{dir})} + H_{lm}^{(\mathrm{pol})})\right). \tag{2.63}$$

Then, $S_{ij}^{\mathrm{L(dir)}}(k,t)$ is the **linear spherically-averaged directional transfer**

$$S_{ij}^{\mathrm{L(dir)}}(k,t) = \frac{1}{4}\int_{S_k}\left(A_{ln}k_l\frac{\partial\hat{R}_{mm}}{\partial k_n} - 2M_{mn}(\boldsymbol{k})\hat{R}_{nm}(\boldsymbol{k})\right)P_{ij}(\boldsymbol{k})\mathrm{d}^2\boldsymbol{k} - \frac{\delta_{ij}}{3}S^{\mathrm{L(iso)}}(k,t) \tag{2.64}$$

$$\begin{aligned}
&= \frac{2}{15}A_{ij}^+E - \frac{2}{7}E\Big(A_{lj}^+H_{il}^{(\mathrm{pol})} + A_{li}^+H_{jl}^{(\mathrm{pol})} - \frac{2}{3}A_{ln}^+\delta_{ij}H_{ln}^{(\mathrm{pol})}\Big) - \frac{1}{15}A_{ij}^+\frac{\partial(kE)}{\partial k}\\
&+ \frac{2}{7}\left(A_{il}^+\frac{\partial}{\partial k}(kEH_{jl}^{(\mathrm{dir})}) + A_{jl}^+\frac{\partial}{\partial k}(kEH_{il}^{(\mathrm{dir})}) - \frac{2}{3}A_{lm}^+\delta_{ij}\frac{\partial}{\partial k}(kEH_{lm}^{(\mathrm{dir})})\right)\\
&- \frac{1}{7}E\left(A_{jl}^+H_{il}^{(\mathrm{dir})} + A_{il}^+H_{jl}^{(\mathrm{dir})} - \frac{2}{3}A_{lm}^+H_{lm}^{(\mathrm{dir})}\delta_{ij}\right) + E\Big(A_{jn}^-H_{ni}^{(\mathrm{dir})} + A_{in}^-H_{nj}^{(\mathrm{dir})}\Big).
\end{aligned} \tag{2.65}$$

Finally, $S_{ij}^{\mathrm{L(pol)}}(k,t)$ is the **linear spherically-averaged polarization transfer**

$$S_{ij}^{\mathrm{L(pol)}}(k,t) = \frac{1}{4}\int_{S_k}\Re\left[\left(A_{ln}k_l\frac{\partial\hat{R}_{rs}}{\partial k_n} - 2M_{rn}(\boldsymbol{k})\hat{R}_{ns}(\boldsymbol{k})\right)N_r^*(\boldsymbol{k})N_s^*(\boldsymbol{k})N_i(\boldsymbol{k})N_j(\boldsymbol{k})\right]\mathrm{d}^2\boldsymbol{k} \tag{2.66}$$

$$\begin{aligned}
&= -\frac{2}{5}A_{ij}^+E - \frac{12}{7}E\left(A_{jl}^+H_{il}^{(\mathrm{dir})} + A_{il}^+H_{jl}^{(\mathrm{dir})} - \frac{2}{3}A_{lm}^+H_{lm}^{(\mathrm{dir})}\delta_{ij}\right)\\
&- \frac{2}{7}\Big(A_{il}^+\frac{\partial}{\partial k}(kEH_{lj}^{(\mathrm{pol})}) + A_{jl}^+\frac{\partial}{\partial k}(kEH_{li}^{(\mathrm{pol})}) - \frac{2}{3}\delta_{ij}A_{lm}^+\frac{\partial}{\partial k}(kEH_{lm}^{(\mathrm{pol})})\Big)\\
&+ \frac{1}{7}E\Big(A_{lj}^+H_{il}^{(\mathrm{pol})} + A_{li}^+H_{jl}^{(\mathrm{pol})} - \frac{2}{3}A_{lm}^+H_{lm}^{(\mathrm{pol})}\delta_{ij}\Big) - \frac{1}{3}E\Big(A_{jl}^-H_{li}^{(\mathrm{pol})} + A_{il}^-H_{lj}^{(\mathrm{pol})}\Big).
\end{aligned} \tag{2.67}$$

2.4.3 Return to isotropy - Spectral tensor

In order to investigate more precisely the return to isotropy (RTI) mechanism, a specific transfer term $T^{(\mathrm{RTI})}$ was introduced in Mons *et al.* (2016): the slow-pressure terms (contained in the pressure-strain tensor Π_{ij}) are at the origin of the return to isotropy and drive this mechanism.

Thus, the non-conservative transfer term W_{ij} can be linked to the RTI mechanism as follows

$$W_{ij}(\boldsymbol{k},t) = -\Re\Big(T^{(\mathrm{RTI})}(\boldsymbol{k},t)[\alpha_i N_j(\boldsymbol{k}) + \alpha_j N_i(\boldsymbol{k})]\Big), \quad T^{(\mathrm{RTI})}(\boldsymbol{k},t) = \alpha_i \tau_{ij}(\boldsymbol{k},t) N_j^*(\boldsymbol{k}), \tag{2.68}$$

so that

$$\begin{aligned} T^{(\mathrm{RTI})}(\boldsymbol{k},t) =& 2\int \theta_{kpq} e^{-i\lambda} p(xy+z)\sqrt{1-z^2}(\mathcal{E}'' + \Re X'') \\ & \Big[(\mathcal{E}+X)(zk-qx) - k(z(\mathcal{E}' + \Re X') - i\Im X')\Big]\mathrm{d}^3\boldsymbol{p}, \end{aligned} \tag{2.69}$$

with details given at the end of Appendix C. Regarding the **spherically-averaged RTI transfer**, defined as follows

$$S_{ij}^{(\mathrm{RTI})}(k,t) = -\int_{S_k} \Re\Big(T^{(\mathrm{RTI})}(\boldsymbol{k},t)[\alpha_i N_j(\boldsymbol{k}) + \alpha_j N_i(\boldsymbol{k})]\Big)\mathrm{d}^2\boldsymbol{k}, \tag{2.70}$$

similar calculations yield

$$\begin{aligned} S_{ij}^{(\mathrm{RTI})}(k,t) = 16\pi^2 \int_{\Delta_k} \theta_{kpq} k^2 p^2 q (x+yz)\mathcal{E}_0''\Big[& -y(z^2-x^2)\mathcal{E}_0(6H_{ij}^{(\mathrm{dir})''} + H_{ij}^{(\mathrm{pol})''}) \\ & + \mathcal{E}_0'\Big(y(z^2-y^2)(6H_{ij}^{(\mathrm{dir})''} + H_{ij}^{(\mathrm{pol})''}) - (xz+y)H_{ij}^{(\mathrm{pol})''}\Big)\Big]\mathrm{d}p\mathrm{d}q. \end{aligned} \tag{2.71}$$

Now that all transfer terms have been defined, and that the formalism has been presented, it is convenient to introduce the **spherically-averaged spectral tensor**

$$\phi_{ij}(k,t) = \int_{S_k} \hat{R}_{ij}(\boldsymbol{k},t)\mathrm{d}^2\boldsymbol{k} = 2E(k,t)\left(\frac{\delta_{ij}}{3} + H_{ij}^{(\mathrm{dir})}(k,t) + H_{ij}^{(\mathrm{pol})}(k,t)\right). \tag{2.72}$$

Because of the spherical-average, even if the fourth-order expansion was considered in $\hat{R}_{ij}$, the equation would be the same since the $H_{ijpq}^{()}$ contributions vanish. The evolution equation of ϕ_{ij} is then

$$\left(\frac{\partial}{\partial t} + 2\nu k^2\right)\phi_{ij}(k,t) = S_{ij}^{\mathrm{NL(tot)}} + S_{ij}^{\mathrm{L(tot)}} = S_{ij}^{\mathrm{NL}} + S_{ij}^{(\mathrm{RTI})} + S_{ij}^{\mathrm{L(tot)}}. \tag{2.73}$$

The **total non-linear spherically-averaged transfer** and can be expressed as

$$S_{ij}^{\mathrm{NL(tot)}}(k,t) = \int_{S_k} T_{ij}^{\mathrm{NL}}(\boldsymbol{k},t)\mathrm{d}^2\boldsymbol{k} = S_{ij}^{\mathrm{NL}}(k,t) + S_{ij}^{(\mathrm{RTI})}(k,t) \tag{2.74}$$

$$= 2\left(\frac{\delta_{ij}}{3}S^{\mathrm{NL(iso)}}(k,t) + S_{ij}^{\mathrm{NL(dir)}}(k,t) + S_{ij}^{\mathrm{NL(pol)}}(k,t)\right), \tag{2.75}$$

with $\int_0^\infty S_{ij}^{\mathrm{NL}}(k,t)\mathrm{d}k = 0$. The **total linear spherically-averaged transfer**, which depends linearly on the mean-velocity gradient matrix, is

$$S_{ij}^{\mathrm{L(tot)}}(k,t) = \int_{S_k} T_{ij}^{\mathrm{L}}(\boldsymbol{k},t)\mathrm{d}^2\boldsymbol{k} \tag{2.76}$$

$$= 2\left(\frac{\delta_{ij}}{3}S^{\mathrm{L(iso)}}(k,t) + S_{ij}^{\mathrm{L(dir)}}(k,t) + S_{ij}^{\mathrm{L(pol)}}(k,t)\right). \tag{2.77}$$

If one considers the fourth-order expansion: $S_{ij}^{\mathrm{L(tot)}}$ contains both contributions from the second and fourth orders, whereas $S_{ij}^{\mathrm{NL(tot)}}$ contains only second-order contributions.

Chapter 3

Dynamics of the Velocity Field in Shear-driven Turbulence

The spectral modelling for anisotropy presented in Chapter 2 is now applied. Validation of the model, by comparisons with DNS and experiments, can be found both in Mons *et al.* (2016) and hereafter. This chapter mainly focuses on shear flows: nevertheless, others configurations such as axisymmetric contractions, expansions, and plane distortion, are presented in Appendix D, along with pressure spectra.

> Most of the contents presented in this chapter were published in:
> Briard, Gomez, Mons, & Sagaut, "Decay and growth laws in homogeneous shear turbulence", *Journal of Turbulence*, **17** (07), 699-726 (2016)

The study of homogeneous anisotropic turbulence is of great interest for a deeper understanding of the different mechanisms that occur in anisotropic turbulent flows. The specific case of homogeneous shear flows has been particularly investigated since it exhibits different fundamental physical processes: anisotropic production of turbulent kinetic energy, interaction between linear and non-linear mechanisms, return to isotropy process... Since Kolmogorov (1941 *b*), it is known that small scales should return to an isotropic state, meaning that even with a mean shear applied on large scales that strongly modifies their properties, there is a **return to isotropy** (RTI) mechanism of the small scales. This RTI process and the modelling of the so-called slow-part of the pressure-strain tensor $\Pi_{ij}^{(s)}$ is a challenging issue. The total pressure strain tensor $\Pi_{ij} =< p(\partial_j u_i + \partial_i u_j) >$, where p and u_i are the fluctuating pressure and velocity, intervenes in the evolution equation (2.3) of the Reynolds stress tensor $R_{ij} =< u_i u_j >$. Several models were proposed for the slow part $\Pi_{ij}^{(s)}$ and have been improved in the past decades. The most popular are the LRR model (Launder *et al.*, 1975), the one of Shih & Lumley (1985), the SSG model (Sarkar & Speziale, 1990), and an improved version of the SSG model by Warrior *et al.* (2014). These models rely on a Taylor series expansion around the isotropic state of the dimensionless tensor $\Pi_{ij}^{(s)}/\epsilon$, where ϵ is the kinetic energy dissipation rate. The small parameter in this expansion is the anisotropy tensor b_{ij}, defined in (2.10). These models yield good results in the early times of the flow dynamics. Indeed the arbitrary parameters introduced in these models are tuned in order to fit experimental data. However, a weakness of these models is their lack

of universality: values of their parameters strongly depend on the choice of the experimental data, often obtained at moderate Reynolds numbers. Consequently, the analysis of long-time behaviour of b_{ij} in the RTI process remains an interesting and open question. In the asymptotic case of high Reynolds numbers, this mechanism should be universal and thus should not require any adjustable constants.

In addition to the modelling of $\Pi_{ij}^{(s)}$ and the RTI mechanism, a fundamental feature to investigate is the influence of anisotropy on the decay of integrated quantities such as the kinetic energy $K(t)$. It follows, from the pioneering work of Corrsin (1951*a*); Comte-Bellot & Corrsin (1966) (CBC) relying on dimensional analysis, and self-preservation analysis George (1992*a*), that the kinetic energy decays in power laws in the isotropic framework, $K(t) \sim t^{\alpha}$. This has been recovered recently for very large Reynolds numbers with a classical EDQNM closure for HIT (Meldi & Sagaut (2012, 2013*a*) and Chapter 1).

To quantify the impact of anisotropy on the decay regime, comparisons are usually made with HIT. Moreover, the case of axisymmetric contraction (or expansion), which is representative of grid turbulence, has already received some attention. Notably, it has been shown (Chasnov, 1995; Davidson *et al.*, 2012; Mons *et al.*, 2014*b*) for this configuration that an initial axisymmetry does not modify the decay exponent in the asymptotic regime, *i.e.* for Saffman turbulence $K(t) \sim t^{-6/5}$.

An original configuration to explore, which has not been investigated yet in direct numerical simulations (DNS) nor in experiments, is the case of a mean shear which is suddenly released. This case could be physically interpreted as a volume of fluid that experiences an intense shear, and which is then convected in an almost shearless region. Characteristic time scales in these two different phases are of great importance, as shown later on. Is the decay of kinetic energy modified in such a homogeneous shear-released turbulence (HSRT), with respect to HIT? This fundamental question is of theoretical interest, since HSRT, unlike axisymmetric turbulence, creates a purely anisotropic correlation $R_{13} =< u_1 u_3 >$. The understanding of such a correlation dynamics could provide relevant information on anisotropy.

Another relevant case to focus on is the homogeneous shear turbulence (HST) where the mean velocity gradient is maintained throughout the evolution of the flow. In this configuration, partially representative of atmospheric flows, kinetic energy is continuously produced by the mean shear. This framework is commonly studied in experiments (Tavoularis & Corrsin, 1981; Tavoularis & Karnik, 1989; De Souza *et al.*, 1995) and in DNS (Pumir & Shraiman, 1995; Pumir, 1996; Gualtieri *et al.*, 2002; Brethouwer, 2005). Notably, it is found that the small scales of the velocity field second-order moments return to isotropy, and that kinetic energy grows exponentially (Tavoularis, 1985; George, 1992*a*; Sagaut & Cambon, 2008) when the anisotropy indicators b_{ij} have reached an asymptotic state. Despite all these works, some discrepancies still remain, whose origin is not completely understood. For instance, in the DNS of Brethouwer (2005), the anisotropy tensor b_{ij} does not reach an asymptotic state as required by theory (Sagaut & Cambon, 2008) when the exponential growth rate γ of the kinetic energy is evaluated. Indeed, the dimensionless time St, or **accumulated anisotropy**, where S is the **shear rate**, is not high enough ($St \simeq 12$ only). The issue is similar in most of the DNS and experiments, thus leading to a large dispersion of the growth rates (from $\gamma = 0.07$ to 0.33, see Table 3.1). Moreover, especially in experimental works, the question of homogeneity can be raised: inhomogeneous flows are not studied in the present chapter, but their influence on the growth rate of the kinetic

energy is an open question and deserves further investigations. In addition, the mean velocity gradient strongly varies near the boundaries, possibly inducing a different phenomenology in the growth of the kinetic energy. Finally, in DNS, the finite size of the box could alter the kinetic energy growth rate in a manner difficult to quantify. These aspects could explain the current dispersion of growth rates.

In both HST and HSRT, the mean-velocity gradient matrix reads

$$A_{ij} = \frac{\mathrm{d}U_i}{\mathrm{d}x_j}, \qquad A_{ij} = -S\delta_{1i}\delta_{3j}, \tag{3.1}$$

with S expressed in units of τ_0^{-1}, where τ_0 is the eddy turn-over time $K(0)/\epsilon(0)$, so that $S = \mathcal{S}\tau_0^{-1}$, where $\mathcal{S}$ is the dimensionless mean velocity gradient. The evolution equation of the kinetic energy in homogeneous shear turbulence reads

$$\frac{\mathrm{d}K}{\mathrm{d}t} = SR_{13}(t) - \epsilon(t) = 2SK(t)b_{13}(t) - \epsilon(t), \tag{3.2}$$

where K and its dissipation rate ϵ are linked to the kinetic energy spectrum E through

$$K(t) = \int_0^\infty E(k,t)\mathrm{d}k, \qquad \epsilon(t) = 2\nu\int_0^\infty k^2 E(k,t)\mathrm{d}k. \tag{3.3}$$

The chapter is structured as follows. The case of homogeneous shear-released turbulence (HSRT) is firstly investigated: the return to isotropy, the modelling of the slow part of the pressure strain tensor and decay laws are addressed. Then, the emphasis is put on sustained shear flows (HST). In this part, the results of the present anisotropic modelling are discussed and put into perspective with review of various DNS and experiments. Finally, the most important points developed in this chapter are recalled in the concluding section, and some considerations about the fourth-order expansion are discussed.

3.1 Homogeneous Shear-Released Turbulence (HSRT)

In this section, the emphasis is put on HSRT: this is an original configuration where the shear S is non zero only in the early times. During this phase, linear transfers defined in (2.76) increase the anisotropy and produce kinetic energy. Then, after the release of the velocity gradients, the velocity field freely decays and there is a RTI mechanism: non-linear transfers defined in (2.74) tend to isotropize small scales, decreasing as a consequence both $K(t)$ and $R_{13}(t)$.

This framework, firstly presented in Mons *et al.* (2016), has never been investigated in DNS nor in experiments. This section is divided into five parts. Firstly, rapid distortion theory (RDT) is used to validate the model at short times, when the linear effects are dominant. Then, classical scalings for the different spectra involved in shear-driven turbulence are addressed. Afterwards, the RTI mechanism, once the shear is released, is investigated, with a particular attention on the difference between Saffman and Batchelor turbulence. Then, a model is proposed for the slow-part of the pressure-strain tensor in the RTI phase. Finally, effects of infrared exponent σ and shear rate S, along with the case of anisotropy at low Reynolds numbers, are discussed.

3.1.1 Validation of HSRT with Rapid Distortion Theory

In this part, the anisotropic EDQNM modelling is assessed by comparisons with RDT as done in (Mons *et al.*, 2016). The main calculations coming from RDT are given in Appendix D. In RDT, non-linear terms are discarded: this theory is valid for short times only, when linear processes dominate the flow. Moreover, at short times (for large Reynolds numbers), viscous effects are also negligible with respect to inertial ones. Two different simulations are presented in Fig. 3.1: one with an initial isotropic kinetic spectrum $E(k,t)$ in which linear transfers produce energy and anisotropy. And a second one where these linear transfers are set to zero and the initial spectral tensor ϕ_{ij} is analytically determined thanks to RDT. It is clear that the two different initial conditions collapse into the same behaviour when the shear is released, for both $\sigma = 2$ and $\sigma = 4$. This validates our spectral transfers. Another point of interest is that with RDT, ϕ_{13} displays an inertial $k^{-5/3}$ range instead of an inertial anisotropic $k^{-7/3}$ range, which proves that non-linear transfers are responsible for the anisotropic range.

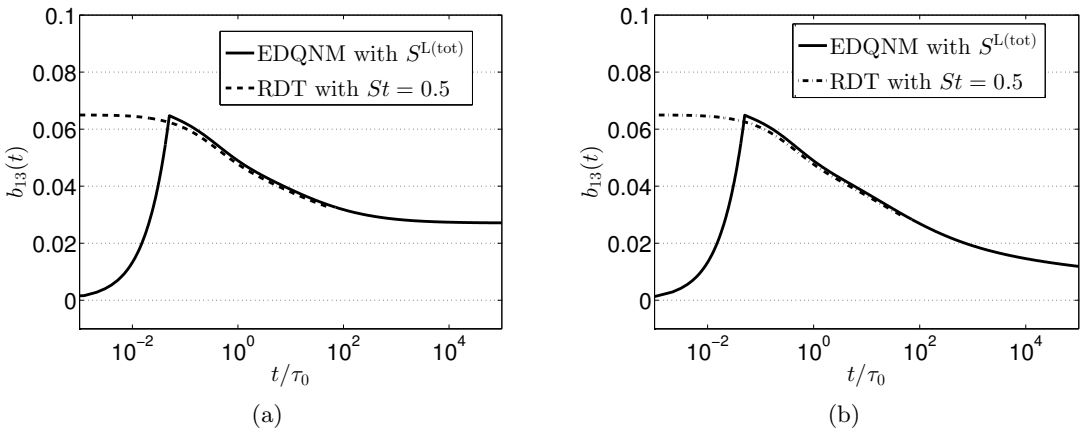

Figure 3.1: Comparison of b_{13} with RDT initial conditions ($S_{ij}^{\mathrm{L(tot)}} = 0$) and with isotropic initial conditions with $St = 0.1$. (a) For $\sigma = 2$. (b) For $\sigma = 4$.

3.1.2 Kinetic energy spectrum $E(k,t)$ and spectral tensor $\phi_{ij}(k,t)$

In Fig. 3.2a, diagonal components of the spectral tensor $\phi_{ij}(k,t)$ (only ϕ_{11} is shown) display a $k^{-5/3}$ scaling in the inertial range, as in the purely isotropic case, from the integral wavenumber $k_L(t) \simeq 1/L(t)$ to the Kolmogorov wavenumber k_η, where $L(t)$ is the kinetic integral scale.

The cross-tensor $\phi_{13}(k,t)$ is also presented, and exhibits a $k^{-7/3}$ scaling in the inertial range. This scaling comes from $E(k,t)H_{ij}^{()}(k,t)$ spectra exclusively since $E\delta_{13} = 0$. The spectral scaling of the cross-tensor can be found by dimensional analysis, assuming that $\phi_{13}(k,t)$ depends on the k, ϵ, and linearly on the shear rate S

$$\phi_{13}(k,t) \sim S\epsilon^{1/3}k^{-7/3}. \tag{3.4}$$

This result was firstly found by Lumley (1967) and derived in a different way by Ishihara *et al.* (2002). The $k^{-7/3}$ slope has also been obtained in DNS (Shen & Warhaft, 2000; Ishihara *et al.*, 2002; Sukheswalla *et al.*, 2013).

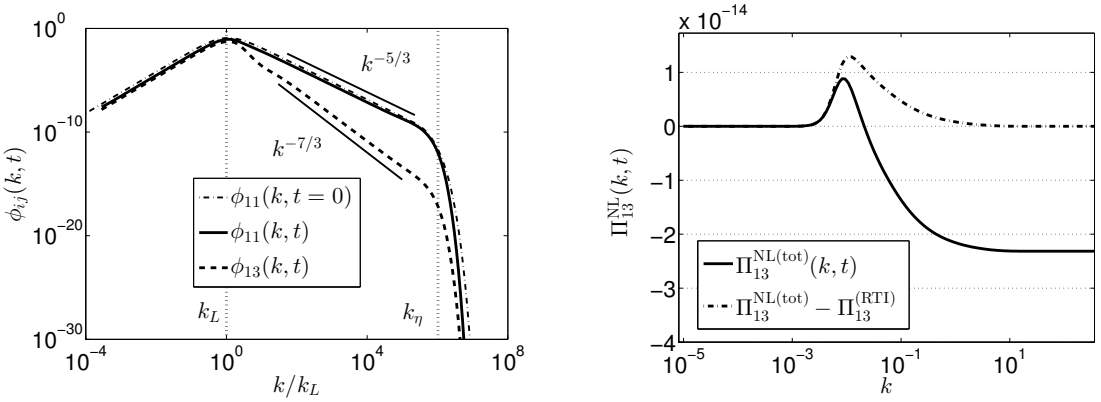

(a) (b)

Figure 3.2: (a) Spectral tensors $\phi_{13}(k,t)$ and $\phi_{11}(k,t)$. (b) Total non-linear flux and RTI flux. Both for $\sigma = 2$ with $St = 1$.

The total non-linear and RTI transfers are now investigated in Fig. 3.2b, and more precisely their corresponding flux, computed according to

$$\Pi_{ij}^{\mathrm{NL}()}(k,t) = -\int_0^k S_{ij}^{\mathrm{NL}()}(u,t)\mathrm{d}u. \tag{3.5}$$

The total non-linear flux is not conservative (meaning that $\Pi_{ij}(k=\infty) \neq 0$) because of the RTI mechanism, originating from "slow pressure" terms. Nevertheless, when the RTI flux is subtracted, a conservative non-linear flux is recovered, as illustrated in Fig. 3.2b. Such a test case is an accurate validation of the previous analytical calculations of Chapter 2 for the non-linear transfers.

3.1.3 Anisotropy descriptors $b_{ij}(t)$ and $H_{ij}^{()}(k,t)$

In this part, the emphasis is put on the RTI mechanism in HSRT. The case of Saffman turbulence has been presented in Mons *et al.* (2016), and is compared here with Batchelor turbulence. Conclusions with regard to the permanence of large eddies are drawn.

The shear is maintained during a small number of turn-over times and is then released. For high Reynolds numbers, it is well known that the anisotropy tensor b_{ij} defined in (2.10) reaches an **asymptotic anisotropic state** in the RTI process. This has already been observed in DNS (Sarkar & Speziale, 1990) and is recovered here in Fig. 3.3a for Saffman turbulence. The initial spectrum $E(k,t=0)$ being isotropic, one has $b_{ij}(t=0)=0$. Because of linear shear effects, a strong departure from the isotropic state is observed: the $|b_{ij}|$ increase up to the shear release, and then reach constant values. The interesting result here at high Reynolds numbers is that the final state of the anisotropy tensor b_{ij}^{∞}, reached from $t = 10^3\tau_0$, is not zero. This means that there is still some anisotropy left in the flow. The anisotropy tensor $b_{ij}(t)$ being an average in space, it hides where the remaining anisotropy is. Therefore, spectral anisotropy descriptors $H_{ij}^{()}(k,t)$ are used to provide information on the localization of anisotropy in wavenumber space: Fig. 3.3b reveals that $H_{ij}^{()} = 0$ only at small scales. This shows that there is a complete RTI of small scales in Saffman turbulence, whereas large scales keep their anisotropy. This behaviour

is in agreement with Kolmogorov (1941*b*) local isotropy theory and with results of DNS (Sarkar & Speziale, 1990) as well.

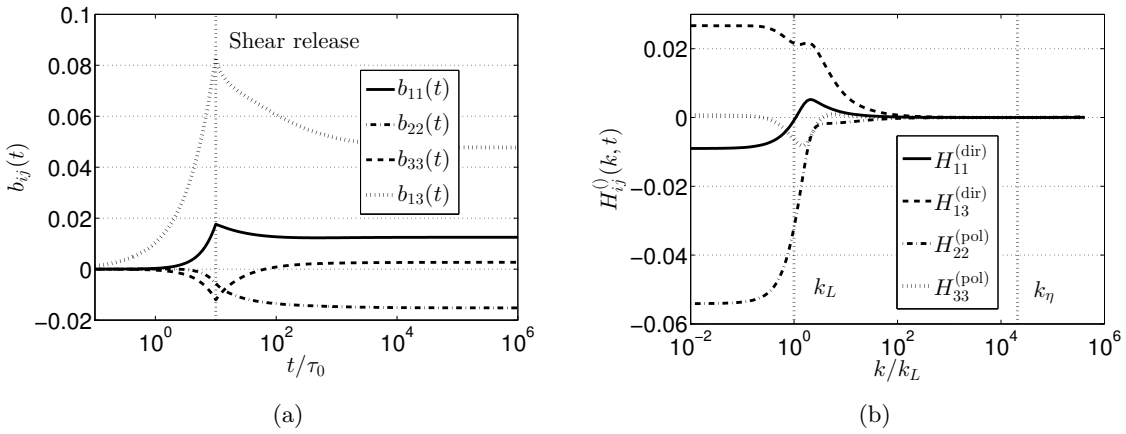

(a) (b)

Figure 3.3: Anisotropy for $\sigma = 2$ with $S = 0.1\tau_0^{-1}$ and $St = 1$. (a) Anisotropy tensor $b_{ij}(t)$. (b) Various spectral anisotropy indicators $H_{ij}^{()}(k,t)$ at $t = 100\tau_0$, along with the integral and Kolmogorov wavenumbers k_L and k_η.

Batchelor turbulence is now addressed. Simulations show that the b_{ij} continuously return to zero, as illustrated in Fig. 3.4a: this means that anisotropy globally decreases over time, unlike Saffman turbulence. Spatial information about the localization of anisotropy is available in Fig. 3.4b: the spectral anisotropy descriptor $H_{13}^{(\mathrm{pol})}(k,t)$ reveals that large scales anisotropy decreases with time for Batchelor turbulence, whereas it remains constant for Saffman turbulence. Other components of $H_{ij}^{(\mathrm{pol})}$ and $H_{ij}^{(\mathrm{dir})}$ behave similarly. Therefore, because of this continuous loss of anisotropy in Batchelor turbulence, a complete RTI of all scales is theoretically possible, even though physically unreachable. Indeed, it would require an infinite Reynolds number in order to stay in the high Reynolds numbers regime: with a larger Reynolds number comes a greater quantity of anisotropy to evacuate.

The large scales loss of anisotropy in Batchelor HSRT is due to the classical backscatter of energy that already occurs in Batchelor HIT (Eyink & Thomson, 2000; Lesieur & Ossia, 2000; Meldi & Sagaut, 2012). Indeed, strong inverse non-linear transfers, from small scales to large ones, tend to isotropize the large scales, which causes the anisotropy to decrease. This is consistent with non-linear mechanisms being responsible for the return-to-isotropy process. Moreover, these strong inverse non-linear transfers result into the breakdown of the PLE in Batchelor turbulence.

3.1.4 Modelling of the pressure-strain tensor $\Pi_{ij}^{(\mathrm{s})}$

The modelling of the pressure-strain tensor Π_{ij}, which directly intervenes in the evolution equation (2.3) of R_{ij}, is a challenging topic. Indeed, the velocity-pressure correlation is complex, and its prediction is of particular interest for the development of RANS models. This term is commonly divided into two parts: a slow one $\Pi_{ij}^{(\mathrm{s})}$, responsible for the redistribution of energy between components, and a rapid one $\Pi_{ij}^{(\mathrm{r})}$, linked to the linear effects of mean-velocity gradients. The latter part is rigorously zero when the shear is released. This is why the emphasis is put

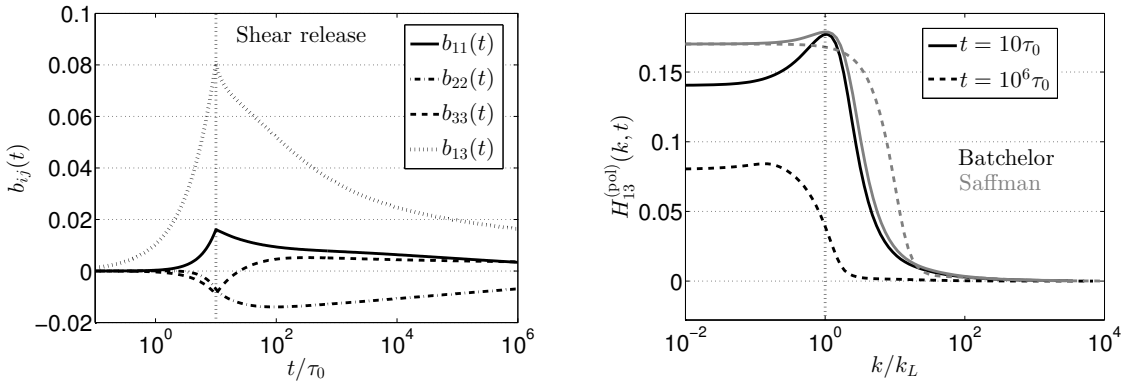

(a) (b)

Figure 3.4: (a) Anisotropy tensor $b_{ij}(t)$ for $\sigma = 4$. (b) Spectral anisotropy indicator $H_{13}^{(\mathrm{pol})}(k,t)$ for $\sigma = 2$ (grey lines) and $\sigma = 4$ (black lines), at $t = 10\tau_0$ and $t = 10^6\tau_0$. Both with $S = 0.1\tau_0^{-1}$ and an injected anisotropy $St = 1$.

on the slow-part $\Pi_{ij}^{(\mathrm{s})}$ which is at the origin of the RTI mechanism highlighted in the previous part.

The slow part of the pressure-strain tensor can be written (Sarkar & Speziale, 1990)

$$\Pi_{ij}^{(\mathrm{s})}(t) = -\epsilon(t)\left(C_{\mathrm{RTI}}^{(1)} b_{ij}(t) + C_{\mathrm{RTI}}^{(2)}\left(b_{il}(t)b_{lj}(t) - \frac{1}{3}b_{kl}(t)b_{kl}(t)\delta_{ij}\right)\right). \tag{3.6}$$

EDQNM simulations at high Reynolds numbers show that powers of b_{ij} are much lower than b_{ij} alone. This would imply, at first order in anisotropy, that $\Pi_{ij}^{(\mathrm{s})}/\epsilon = -C_{\mathrm{RTI}}^{(1)} b_{ij}$. Such a linear relation between the normalized pressure-strain tensor and the anisotropy indicator b_{ij} can be recovered starting from the evolution equation of R_{ij}. Replacing R_{ij} by its expression as a function of b_{ij}, given in (2.10), yields

$$\frac{\mathrm{d}b_{ij}}{\mathrm{d}t} = -\frac{2}{3}A_{ij}^{+} - A_{ik}b_{kj} - A_{jk}b_{ki} + 2A_{kl}b_{lk}\left(\frac{\delta_{ij}}{3} + b_{ij}\right) + \frac{\Pi_{ij}}{2K} + \frac{\epsilon}{K}b_{ij}, \tag{3.7}$$

which can be found as well in Sarkar & Speziale (1990); Warrior *et al.* (2014). The dissipation tensor ϵ_{ij} was assumed to be isotropic, *i.e.* $3\epsilon_{ij} = 2\epsilon\delta_{ij}$. This is a reasonable assumption for moderately anisotropic flows: indeed, simulations at high Reynolds numbers show that the non-diagonal components of ϵ_{ij} are negligible with respect to diagonal ones. Moreover, when the shear is released, $A_{ij} = 0$ and only the slow part of the velocity-pressure correlation remains, $\Pi_{ij} = \Pi_{ij}^{(\mathrm{s})}$. In addition, it has been shown in the previous part that the b_{ij} reach an asymptotic state when the PLE is verified: this implies that $\mathrm{d}b_{ij}/\mathrm{d}t = 0$. Thus, the evolution equation (3.7) of b_{ij} becomes

$$\boxed{\Pi_{ij}^{(\mathrm{s})}(t) = -2\epsilon(t)b_{ij}(t) = -C_{\mathrm{RTI}}\epsilon(t)b_{ij}(t).} \tag{3.8}$$

Consequently, for large times, large Reynolds numbers, an initial moderate mean-velocity gradient which is then released, and when the PLE is verified, this model predicts $C_{\mathrm{RTI}} = 2$ as an - universal - constant of the RTI mechanism. C_{RTI} will be shown hereafter to be independent

of both the large scales initial conditions and of the mean flow gradient A_{ij}. The case of pure rotation is not considered here, and this will be briefly justified later.

Existing models (Shih & Lumley, 1985; Sarkar & Speziale, 1990; Warrior *et al.*, 2014) are intrinsically different since there are designed to capture the short time dynamics of the flow when the mean-velocity gradients are active, *i.e.* when $A_{ij} \neq 0$ and $\Pi_{ij}^{(\mathrm{r})} \neq 0$, whereas the emphasis in this work is put on a freely decaying turbulence initially submitted to mean-velocity gradients, at large times and Reynolds numbers. For instance, in the strongly non-linear model of Shih & Lumley (1985), C_{RTI} is not constant and depends on b_{ij} through $C_{\mathrm{RTI}} = 2+$(terms in $b_{ij}b_{ij}$ and $b_{ik}b_{kj}b_{ij}$), and in Sarkar & Speziale (1990); Warrior *et al.* (2014), one has $3.1 \leq C_{\mathrm{RTI}} \leq 3.4$. The modelling for $\Pi_{ij}^{(\mathrm{s})}$ proposed here is consequently complementary to existing models, and investigates the asymptotic RTI mechanism when the mean-velocity gradients are released.

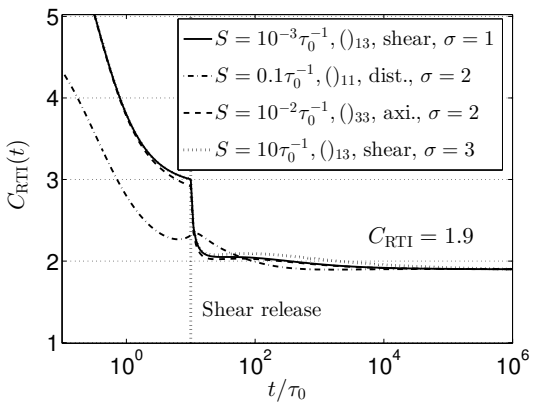

Figure 3.5: Constant of the $\Pi_{ij}^{(\mathrm{s})}$ model for different shear rate S, infrared exponents σ, components $()_{ij}$ and kinds of anisotropy. The asymptotic value at $t = 10^6\tau_0$ is $C_{\mathrm{RTI}} = 1.9$.

In Fig. 3.5, the time evolution of $C_{\mathrm{RTI}}(t)$, computed thanks to (3.8), is displayed. $\Pi_{ij}^{(\mathrm{s})}$ is the integral over k of the RTI non-linear transfer $S_{ij}^{(\mathrm{RTI})}$ defined in (2.71). To assess the relevance of the value $C_{\mathrm{RTI}} = 2$, several cases are presented. C_{RTI} is evaluated with different mean velocity gradient intensities S, for infrared slopes $\sigma = 1$, 2 and 3, for various components of the tensor $\Pi_{ij}^{(\mathrm{s})}$, and several kinds of anisotropy: shear, axisymmetry ($A_{11} = A_{22} = -A_{33}/2$) and distortion ($A_{13} = A_{31}$). The main result is that in all these cases $C_{\mathrm{RTI}}(t) \to 1.9$ which is very close to the theoretical value $C_{\mathrm{RTI}} = 2$ expected from the previous development. Hence, the model $\Pi_{ij}^{(\mathrm{s})}(t) = -2\epsilon(t)b_{ij}(t)$ is assessed numerically. Moreover, this model seems to be robust since it holds for various initial parameters and kinds of anisotropy. The case of Batchelor turbulence is not presented in Fig. 3.5 since $\mathrm{d}b_{ij}/\mathrm{d}t \neq 0$ which is an assumption of the model. Consequently, in Batchelor HSRT, C_{RTI} continuously decreases. But, on a strictly quantitative point on view, the value obtained at $t = 10^6\tau_0$ is $C_{\mathrm{RTI}} = 1.87$, which is close to 2 as well.

The slight difference between the expected value 2 and the 1.9 obtained numerically for C_{RTI} could be, at least partially, attributed to the isotropic approximation for the dissipation rate tensor ϵ_{ij}. Such large times ($t = 10^6\tau_0$) are never reached in practice in experimental works, even though they are essential at high Reynolds numbers to make sure that the decay follows completely the theoretical decay exponents of the CBC theory. Nevertheless, $C_{\mathrm{RTI}} = 2$ remains a

relevant value as all our different curves in Fig. 3.5, corresponding to various initial parameters, are almost equal to $C_{\mathrm{RTI}} = 2$ within 5% from $t = 10^2\tau_0$, which is a reasonable time.

This model mainly relies on two aspects: (i) The isotropic shape of the dissipation tensor ϵ_{ij}, which is well assessed numerically: indeed, ϵ_{ij} strongly depends on small scales, see equation (3.12), which return to isotropy according to Fig. 3.3b, meaning that extra-diagonal components are very small with respect to diagonal ones. (ii) The asymptotic behaviour of the b_{ij} which become constant for large times, which implies $\mathrm{d}b_{ij}/\mathrm{d}t = 0$. Numerically, constant values at large times for the b_{ij} seem to be strongly associated to cases where the PLE is verified. It is worth noting that these two hypothesis are independent of the mean-velocity gradient intensity S and of the mean flow shape (shear, axisymmetry, distortion), which explains the consistency of the results of Fig. 3.5.

These hypothesis are notably satisfied for any flows dominated by production mechanisms, such as shear flows. Consequently, there is no guarantee that this model would work for rotating mean flows for instance: indeed, such a configuration involves turbulent waves which alter the third-order correlations dynamics (Cambon *et al.*, 2013). Therefore, further investigations are needed to fully understand the impact of rotation on the eddy-damping terms and its consequences on the RTI process.

3.1.5 Additional remarks on HSRT

Effects of infrared exponent σ and shear rate S: it has been shown that the global indicators b_{ij} reach asymptotic anisotropic values for large times, except in the case of Batchelor turbulence $\sigma = 4$ where they continuously decrease. In Fig. 3.6a, the emphasis is put on b_{13}. The first obvious remark is that the stronger the anisotropy, *i.e.* the larger the shear rate S (at constant accumulated anisotropy), the more the asymptotic value b_{ij}^{lim} is far from zero. This is expected: if the initial anisotropy is strong, the residues will be important. Finally, in Fig. 3.6b, one can note that the rapider the decay, *i.e.* the larger σ, the more b_{ij}^{lim} is close to zero. Once again, this is consistent with the fact that when the decay is faster, small scales have a more efficient RTI process.

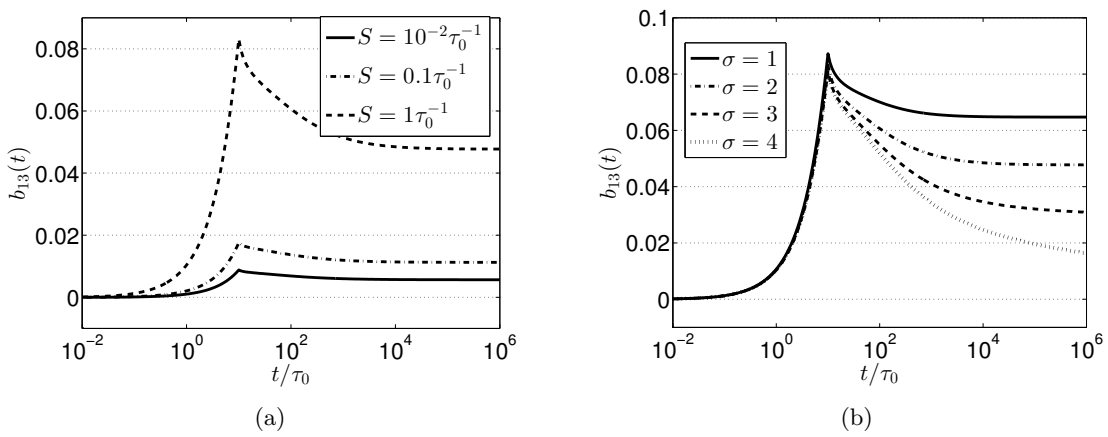

Figure 3.6: Asymptotic anisotropic state for b_{13}. (a) With $\sigma = 2$ for various shear rates S at constant $St = 10$. (b) With $S = 1\tau_0^{-1}$, $St = 10$ for various σ.

Anisotropy at low Reynolds numbers: an interesting behaviour is illustrated in Fig. 3.7a where anisotropy increases at low Reynolds numbers. This is expected since the kinetic energy spectrum $E(k,t)$ no longer displays an inertial range when $Re_\lambda \to 0$: indeed, all anisotropy is gathered at large scales, and b_{ij} being an integral over k, it eventually represents the initial anisotropy injected in the flow: at low Reynolds numbers, the asymptotic values of b_{ij} and $H_{ij}^{(\mathrm{dir})} + H_{ij}^{(\mathrm{pol})}$ coincide. The increase of b_{ij} at low Re_λ is in agreement with Davidson *et al.* (2012) where axisymmetric anisotropic Saffman turbulence is considered. And one can note that in Figure 1.e) therein, for the low Reynolds simulation (Run 5), anisotropy (observed through $u_\perp^2/u_\parallel^2$) slightly increases. There is no explanation in the paper but this phenomenon is in good agreement with our simulations: anisotropy increases with diminishing Reynolds number. In Batchelor turbulence, because of the continuous loss of anisotropy, a complete return to isotropy is possible at low Reynolds numbers as revealed in Fig. 3.7b where $H_{13}^{(\mathrm{dir})} + H_{13}^{(\mathrm{pol})} \to 0$.

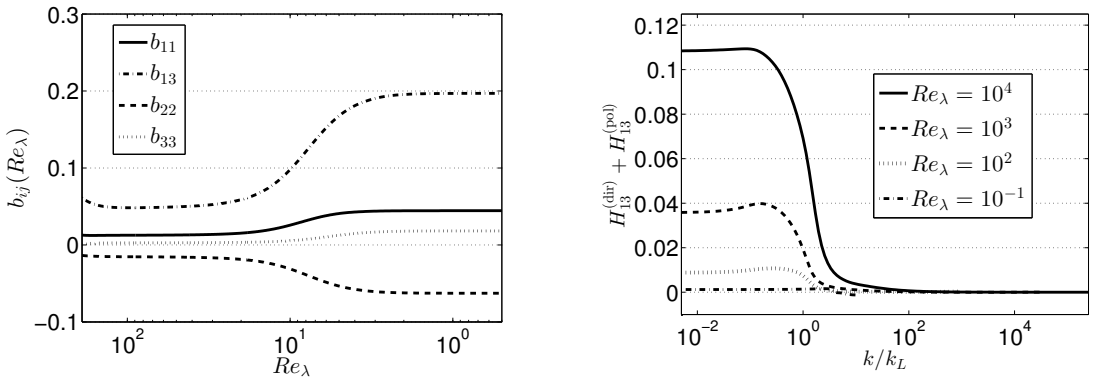

(a) (b)

Figure 3.7: (a) b_{ij}: transition towards low Reynolds numbers for $\sigma = 2$ with $St = 1$. (b) $H_{13}^{()}$ for different Reynolds numbers with $\sigma = 4$.

3.2 Decay of $K(t)$ and $R_{13}(t)$ in Saffman and Batchelor HSRT

In this section, the general decay exponent for the anisotropic correlation R_{13} in Batchelor HSRT is investigated. First, it is recalled that in HIT, following the Comte-Bellot and Corrsin (CBC) theory (Comte-Bellot & Corrsin, 1966; Corrsin, 1951*a*), the kinetic energy and integral scale decay as

$$K(t) \sim t^\alpha, \quad \alpha = -2\frac{\sigma - p + 1}{\sigma - p + 3}, \qquad L(t) \sim t^{n_L}, \quad n_L = \frac{2}{\sigma - p + 3}, \tag{3.9}$$

where the backscatter parameter $p(\sigma = 4) = 0.55$ and $p(\sigma \leq 3) = 0$ takes into account the classical Batchelor breakdown of the PLE (Eyink & Thomson, 2000; Meldi & Sagaut, 2012).

In Fig. 3.8, the theoretical decay exponent α of the kinetic energy is still valid in Saffman HSRT at high Reynolds numbers (and low Reynolds numbers as well, even though it is not presented). The fact that the kinetic energy decay exponent is not affected by anisotropy in Saffman turbulence has already been found in DNS in the case of homogeneous axisymmetric turbulence (Davidson *et al.*, 2012). In the case of Batchelor HSRT, α is also recovered thanks to

the parameter p, as in HIT. However, when it comes to the decay exponent α_{13} of the correlation $R_{13} =< u_1 u_3 >$, one has $\alpha_{13} = \alpha$ only in the case of Saffman HSRT. Indeed, in Batchelor HSRT, one has $\alpha_{13}(\sigma = 4) \neq \alpha(\sigma = 4)$.

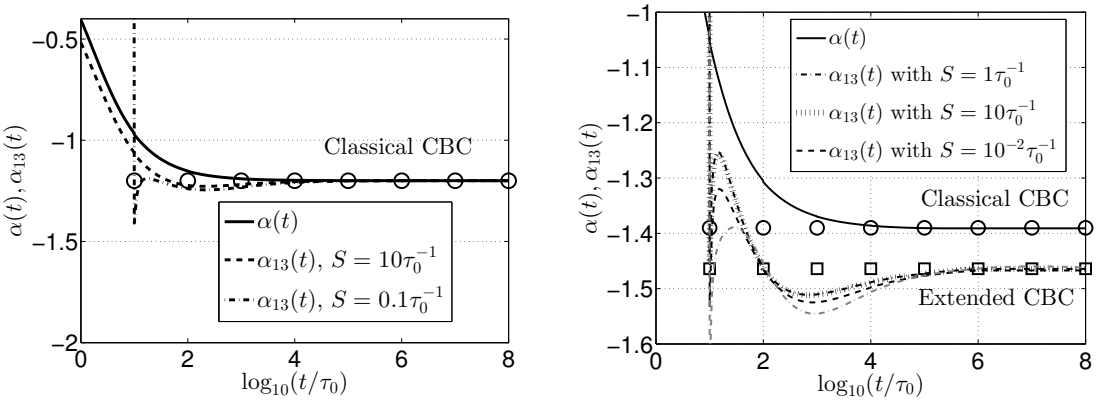

(a) (b)

Figure 3.8: Decay exponents of $K(t)$ and $R_{13}(t)$ for various shear intensity S. ◯: Classical CBC exponents; □: Extended CBC exponents. (a) Saffman HSRT: $\alpha = \alpha_{13} = -6/5$. (b) Batchelor HSRT: $\alpha = -1.38$ is recovered. $\alpha_{13} = -1.464$ with $p_S = 0.279$. The grey dash-dot curve $-\cdot$ corresponds to a distortion simulation with $S = 1\tau_0^{-1}$.

This difference is due to anisotropy which modifies the classical back transfer of energy through non-linear transfers. Because of strong inverse non-linear transfers which tend to isotropize large scales, there is a global loss of anisotropy. Thus, the decay of R_{13} is accelerated in Batchelor HSRT: the correlation R_{13} experiences pressure effects in addition of viscous dissipation, and consequently $|\alpha_{13}| > |\alpha|$, as revealed in Fig. 3.8. It is proposed to model this phenomenon very specific to Batchelor HSRT.

A wise approach is to adopt the same method as in the isotropic case: in HIT, the parameter p is introduced to take into account the breaking of the PLE. This allows to recover the kinetic energy decay exponent $\alpha(\sigma = 4) = -1.38$ obtained numerically (see Fig. 3.8). Without p, the analytical expression gives $\alpha(\sigma = 4, p = 0) = -10/7$. A similar idea is to modify this parameter p into a new one p_S that additionally takes into account effects of initial anisotropy for purely anisotropic quantities.

The kinetic energy $K(t)$ and the anisotropic correlation $R_{13}(t)$ follow the evolution equations

$$\frac{\mathrm{d}K}{\mathrm{d}t} = SR_{13}(t) - \epsilon(t), \qquad \frac{\mathrm{d}R_{13}}{\mathrm{d}t} = SR_{33} + \Pi_{13} - \epsilon_{13}. \tag{3.10}$$

When the shear is released, $S = 0$ and only the slow-part of Π_{13} remains. It is clear that ϵ_{13} is very weak because of the small scales return to isotropy: consequently, unlike K whose decay is driven by ϵ, the destruction of R_{13} is led by the slow part of Π_{13}, *i.e.* pressure effects. Purely anisotropic quantities

$$R_{13}(t) = \int_0^\infty \phi_{13}(k,t)\mathrm{d}k \sim t^{\alpha_{13}}, \tag{3.11}$$

$$\epsilon_{13}(t) = 2\nu \int_0^\infty k^2 \phi_{13}(k,t)\mathrm{d}k, \tag{3.12}$$

$$\Pi_{13}^{(\mathrm{s})}(t) = \int_0^\infty S_{13}^{(\mathrm{RTI})}(k,t)\mathrm{d}k, \tag{3.13}$$

have different decay exponents in Batchelor HSRT than the classical ones of HIT. To determine the theoretical expression of α_{13}, the continuity of $\phi_{13}(k,t)$ at the integral wavenumber is used, similarly to what is done to obtain α. The first assumption is that the integral scale $L(t)$ is the same for all components of $\phi_{ij}(k,t)$, which is reasonable as they all depend on $E(k,t)$. Then, one has to determine the new scaling of ϕ_{13} once the shear is released. Indeed, when $S=0$ one has $\phi_{13} \neq 0$, which is in contradiction with (3.4). Nevertheless, the $k^{-7/3}$ scaling is still observed after the shear release. The solution to reconcile the persistence of $\phi_{13}(k,t)$ and the $k^{-7/3}$ scaling is to replace S^{-1} by another time scale: S being a large scale quantity, the intuitive time scale is the non-linear one $\tau(k_L) = (k_L^2\epsilon)^{-1/3}$ evaluated at the integral wavenumber k_L. Then, numerical simulations show that the destruction mechanism for $\phi_{13}(k,t)$ is the pressure rather than viscosity. This is notably illustrated in Fig. 3.9 where the budget terms of the evolution equations of ϕ_{11} and ϕ_{13} are displayed after the release of the shear, at $t = 10\tau_0$, so that small scales have already returned to isotropy. This explains why $kS_{11}^{(\mathrm{RTI})}$ is very small compared to the other contributions. Moreover, it appears that the viscous dissipation $-2\nu k^3\phi_{11}$ is the destruction mechanism for ϕ_{11}, whereas it is pressure through $kS_{13}^{(\mathrm{RTI})}$ for ϕ_{13}. Indeed, the viscous term $-2\nu k^3\phi_{13}$ is negligible compared to $kS_{13}^{(\mathrm{RTI})}$. This also confirms that neglecting ϵ_{13} in the previous part was a reasonable assumption. Hence, ϵ is accordingly replaced by $\Pi_{13}^{(\mathrm{s})}$ which has the same dimension.

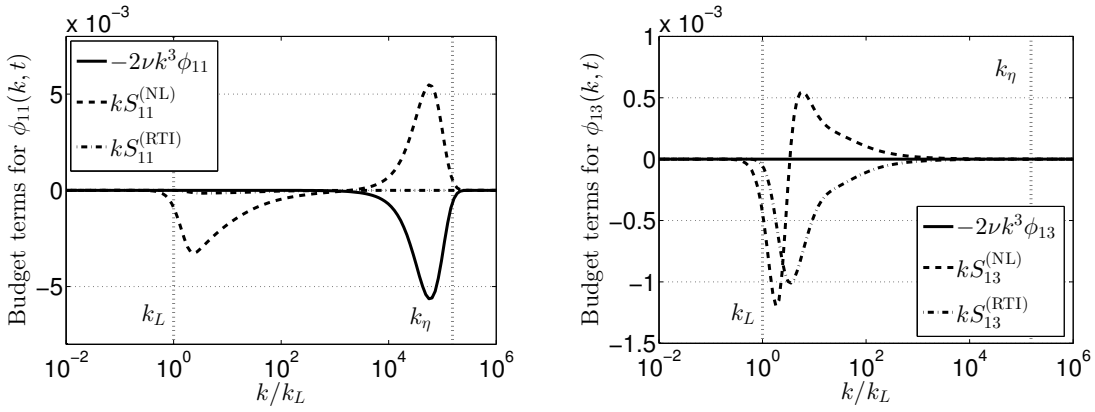

Figure 3.9: Budget terms of the evolution equation of the spectral tensor after the release of the shear: $\partial_t\phi_{ij} = -2\nu k^2\phi_{ij} + S_{ij}^{(\mathrm{NL})} + S_{ij}^{(\mathrm{RTI})}$, at $t = 10\tau_0$ for Saffman HSRT, where $Re_\lambda = 7.10^3$. $S_{ij}^{(\mathrm{NL})}$ is the conservative part of the non-linear transfers, with zero integral over k, and $S_{ij}^{(\mathrm{RTI})}$ is the remaining part, responsible for the RTI mechanism. (a) For ϕ_{11}. (b) For ϕ_{13}.

This finally yields

$$\boxed{\phi_{13}(k,t) \sim {\Pi_{13}^{(\mathrm{s})}}^{2/3}\, k_L^{2/3}\, k^{-7/3}.} \tag{3.14}$$

Then, a new coefficient p_{S} is introduced for the purely anisotropic quantities in Batchelor HSRT, to reflect the effect of anisotropy on the backscatter of energy. Consequently, the continuity of

ϕ_{13} at the integral wavenumber k_L yields $k_L^{\sigma-p_S} \sim \Pi_{13}^{(s)^{2/3}} k_L^{-5/3}$. Hence, one obtains straightforwardly the theoretical decay exponent of $\Pi_{13}^{(s)}$. The resulting expression for the anisotropic decay exponent is then

$$\boxed{R_{13}(t) \sim t^{\alpha_{13}}, \qquad \alpha_{13} = -2\frac{\sigma - p_S + 1}{\sigma - p + 3}, \qquad p_S = \begin{cases} 0 & ,\sigma \leq 3 \\ 0.279 & ,\sigma = 4. \end{cases}} \tag{3.15}$$

Simulations show that α_{13} does not depend on the initial shear rate S in Fig. 3.8, from $S = 10^{-2}\tau_0^{-1}$ to $S = 10\tau_0^{-1}$. This anisotropic decay exponent is found numerically to be $\alpha_{13} = -1.464$. This implies the strong result that p_S does not depend on the shear intensity. The corresponding value of p_S is deduced using (3.15): $p_S = 0.279$. Moreover, p_S is not only independent of S, but also independent of the kind of anisotropy considered. Indeed, for distortion, $\alpha_{13} = -1.464$ as well (grey dash-dot line in Fig. 3.8). All these decay exponents are gathered in Table 5.1.

The value $p_S = 0.279$ is close to the value of the backscatter parameter of a passive scalar field in decaying Batchelor HIT (see Chapter 1). This could be interpreted as ϕ_{13} being almost passively convected by the turbulent velocity field, which is consistent with the production terms being zero once the shear is released.

In conclusion, p_S must be seen as a supplementary parameter for purely anisotropic quantities when the PLE is not verified, as in Batchelor turbulence. p_S is valid in the general case where the mean-gradient matrix A_{ij} has non-diagonal components. From a physical point of view, it has been shown that in Batchelor HSRT, purely anisotropic quantities, such as the correlation $R_{13}(t)$, decay faster than the isotropic ones, such as the kinetic energy $K(t)$. This is because of the continuous loss of large scales anisotropy, induced by strong inverse non-linear transfers. Moreover, the decay of R_{13} is driven by pressure effects rather than viscous ones.

3.3 Homogeneous Shear Turbulence

In this part, the case of homogeneous shear turbulence (HST) is addressed, where the shear is maintained throughout the simulation.

3.3.1 Exponential growth of the kinetic energy $K(t)$

In sustained shear flows, the kinetic energy grows exponentially (Sagaut & Cambon, 2008) as a consequence of anisotropy production and non-linear redistribution. Because of the exponential growth of the integral scale $L(t)$, DNS are quite limited in accumulated anisotropy St. The evolution equation of $K(t)$ in HST is given by (3.2). The dimensionless **shear rapidity** is now introduced

$$S_R(t) = \frac{\epsilon(t)}{SK(t)}, \tag{3.16}$$

which is the ratio of shear and non-linear characteristic times. The evolution equation of K can be written

$$\frac{1}{KS}\frac{\mathrm{d}K}{\mathrm{d}t} = \underbrace{2b_{13} - \frac{\epsilon}{KS}}_{\text{Constant for } St \gg 1.} = \gamma. \tag{3.17}$$

For $St \gg 1$, anisotropy indicators b_{ij} and S_R reach an asymptotic anisotropic state, as in the case of HSRT. So, for large St ($St \geq 25$), the quantity $2b_{13} - \epsilon/KS = \gamma$ becomes constant, as revealed in Fig. 3.10a. The existence of a transient regime of order $St \simeq 30$ has already been found in DNS (Pumir & Shraiman, 1995; Pumir, 1996; Gualtieri *et al.*, 2002). From the previous equation, the exponential growth of kinetic energy

$$K(t) = K(0)\exp(\gamma St), \tag{3.18}$$

is assessed by the present anisotropic EDQNM modelling in Fig. 3.10b. The growth exponent is $\gamma = 0.33$. However, asymptotic values of b_{ij} and S_R are different from those of reported in Sagaut & Cambon (2008), certainly because St was not high enough and thus anisotropy indicators were not constant yet. This will be discussed later. The exponential growth of $K(t)$ has also been assessed in the DNS of Brethouwer (2005), where $St_\mathrm{max} = 12$ only, and so the γ is different from ours, probably because once again b_{ij} is not constant yet; in experiments (Tavoularis, 1985; De Souza *et al.*, 1995); and in another spectral modelling (Clark & Zemach, 1995), where $\gamma = 0.332$ is found as well.

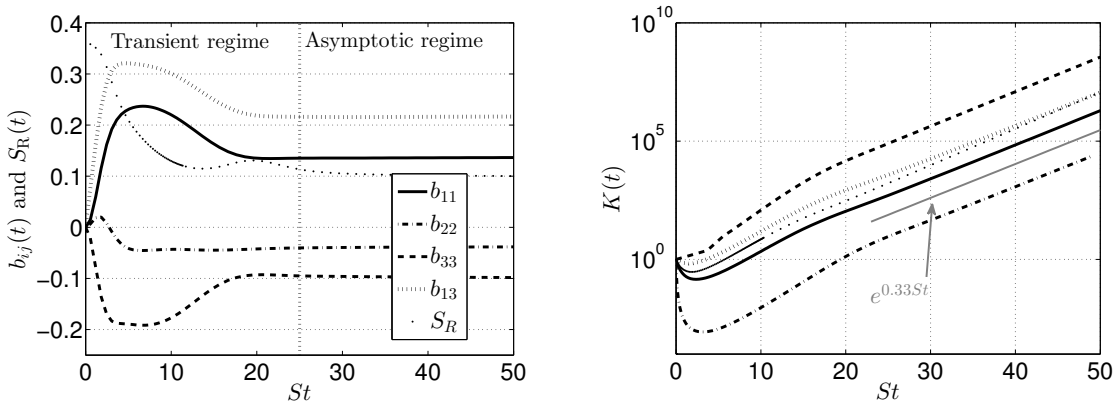

(a) (b)

Figure 3.10: (a) Anisotropy indicators b_{ij} and S_R in Saffman HST with $S = 1\tau_0^{-1}$. (b) Evolution of $K(t)$ for various S and σ. The grey line indicates $\exp(0.33St)$. From top to bottom, the different cases are: $\sigma = 2$ and $S = 10\tau_0^{-1}$; $\sigma = 4$ and $S = 1\tau_0^{-1}$; $\sigma = 1$ and $S = 0.1\tau_0^{-1}$; $\sigma = 2$ and $S = 0.1\tau_0^{-1}$; $\sigma = 3$ and $S = 10^{-2}\tau_0^{-1}$.

It is argued in Pumir & Shraiman (1995); Pumir (1996); Gualtieri *et al.* (2002) that for a finite domain, *i.e.* wall-bounded shear flows, there are kinetic energy bursts since the kinetic energy cannot grow exponentially for very large St. These bursts are periodic (every $St \simeq 20$) and result from the cyclic deformation and stretching of elongated structures in the flow. In our simulations, the shear applies on an infinite length, meaning that there are no boundaries, theoretically allowing $K(t)$ to become infinite. It has been shown by Lee *et al.* (1990) that a very high shear rate creates streaks in the flow, as would do physical boundaries at a more

moderate shear rate. However, high shear rates are not reachable with the present anisotropic EDQNM modelling, in the assumption of moderate anisotropy.

In Fig. 3.10b, it is also revealed that the growth rate exponent γ seems to be quite robust within the present EDQNM modelling: indeed, it appears that $\gamma = 0.33$ is both independent of the shear rate S and the infrared slope σ. In particular, the kinetic energy grows exponentially at the same rate in Saffman and Batchelor turbulence. Moreover, the b_{ij} in Batchelor HST are very similar to those in Saffman HST.

In addition to the exponential growth of $K(t)$, the behaviour of the dissipation rate $\epsilon(t)$, the integral scale $L(t)$ and the anisotropic component $R_{13}(t)$ are investigated. They also grow exponentially as revealed in Fig. 3.11a. In addition to the exponential growth, it is possible to determine the growth rate γ_ϵ and γ_L. From the main equation (3.2), ϵ and K are linked through a time-derivative, then $\gamma_\epsilon = \gamma$. Finally, from the dimensional analysis $L \sim K^{3/2}/\epsilon$, $\gamma_L = \gamma/2$ is straightforward. This is recovered numerically in Fig. 3.11a. Finally, ϵ_{13} strongly decreases, which is expected: indeed, at high Reynolds number, isotropization of small scales tend to strongly reduce ϵ_{13}.

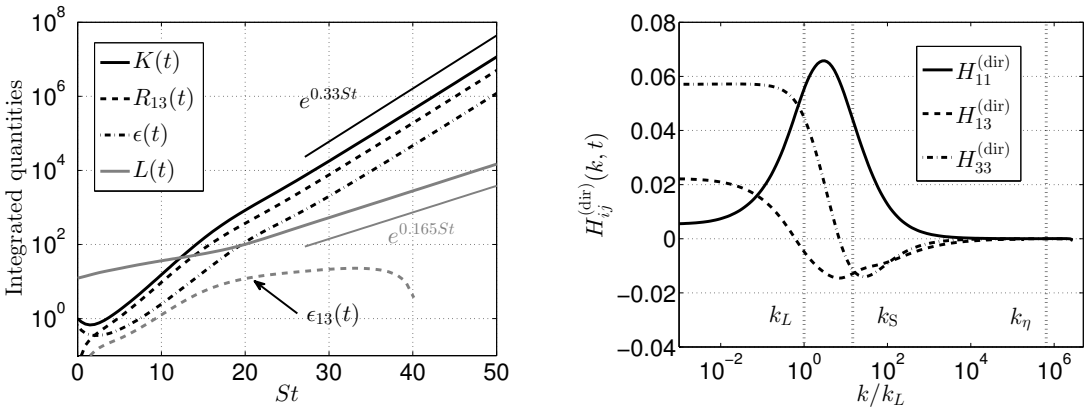

(a) (b)

Figure 3.11: (a) Time evolution of $K(t)$, $\epsilon(t)$, $L(t)$, $R_{13}(t)$ and $\epsilon_{13}(t)$ for $\sigma = 4$ with $S = 1\tau_0^{-1}$. For clarity, $L(t)$ has been increased by a factor 1000. (b) Anisotropy descriptors $H_{ij}^{(\mathrm{dir})}$ for $\sigma = 2$ at $St = 50$.

In Fig. 3.11b, small scales of the velocity second-order moments have completely returned to isotropy, as in HSRT. Hence, our results are in agreement with Pumir & Shraiman (1995); Pumir (1996); Shen & Warhaft (2000); Gualtieri *et al.* (2002) where velocity second-order moments are found to be isotropic at small scales. This is consistent with the fact that at small scales non-linear processes dominate the dynamics. This also explains why ϵ_{13} is destroyed instead of growing exponentially, as illustrated in Fig. 3.11a. Following the definition (3.12), $k^2\phi_{13}$ is larger at small scales: but ϵ_{13} is a purely anisotropic quantity and since small scales return to isotropy, it is continuously destroyed.

A brief comparison with the DNS of Isaza & Collins (2009) for a sustained shear flow is presented in Fig. 3.12. The evolution of the shear parameter $S^* = 2/S_\mathrm{R}$ is investigated for various initial values $S_0^* = [3; 15; 27]$. This is of particular interest since this parameter is discussed later on. The initial Reynolds number is $Re_\lambda(0) \simeq 20$. An initial isotropic field is considered, and the

infrared slope of the kinetic energy spectrum is $E(k < k_L, t = 0) \sim k^2$. It is revealed in Fig. 3.12 that the evolution of $S^*(t)$ at moderate St and Re_λ, which is the domain of accurate DNS, is well-captured in all of the three cases by the present anisotropic EDQNM modelling. A slightly higher final value for the case $S_0^* = 3$ is obtained here, but not significant.

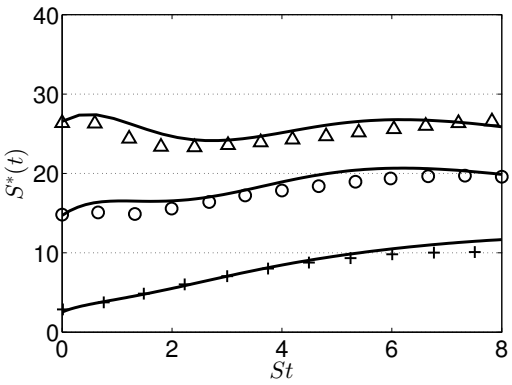

Figure 3.12: Evolution of the shear parameter $S^*(t)$: comparison to the sustained shear flow DNS of Isaza & Collins (2009) with three different initial values S_0^*. Lines and symbols represent respectively the present EDQNM simulations and DNS: $+$, $S_0^* = 3$; $\circ$, $S_0^* = 15$; and $\triangle$, $S_0^* = 27$.

3.3.2 Non-linear transfers and the shear wavenumber

The **shear wavenumber**, or Corrsin wavenumber, is defined as

$$k_\mathrm{S} = \sqrt{\frac{S^3}{\epsilon}}. \tag{3.19}$$

For wavenumbers $k \leq k_\mathrm{S}$, linear effects dominate, meaning that production processes lead the dynamics. In the opposite case, for $k \geq k_\mathrm{S}$, non-linear processes become significant, distribute energy from the main direction to other components through the spectral tensor ϕ_{13}, thus participating into the restoration of isotropy at small scales. Note that other similar wavenumbers exist which indicate the beginning of an efficient RTI, for instance the Zeman wavenumber in rotating turbulence, or the Ozmidov one in USHT, where S is accordingly replaced by the mean rotation or the mean stratification respectively.

In Fig. 3.13, budget terms at $St = 50$ are displayed, when the anisotropic asymptotic state is reached, along with k_S. Before k_S, linear transfers $S_{13}^{\mathrm{L(tot)}}$ dominates whereas for $k \geq k_\mathrm{S}$ pressure strain and non-linear transfers become strong. From the evolution equations of $K(t)$ (3.2) and $R_{13}(t)$ (3.10), the exponential growth of the kinetic energy can be understood thanks to transfer terms. The flow is heading toward the main direction $()_{11}$: thus ϕ_{33} do not receive as much energy as ϕ_{11}. But $S_{33}^{(\mathrm{RTI})}$ being positive, it takes energy from ϕ_{11} and ϕ_{22}, allowing ϕ_{33} to grow. The growth of ϕ_{33} implies the growth of ϕ_{13} and thus the growth of $K(t)$. Hence, the exponential growth of the kinetic energy is the result of non-linear processes and redistribution of energy between components. Moreover, there is a non-negligible dissipation effect for ϕ_{33} in Fig. 3.13. Similar dissipation processes are obtained for ϕ_{11} and ϕ_{22} whereas it does not appear for ϕ_{13}. It justifies *a posteriori* the assumption that the dissipation is nearly isotropic.

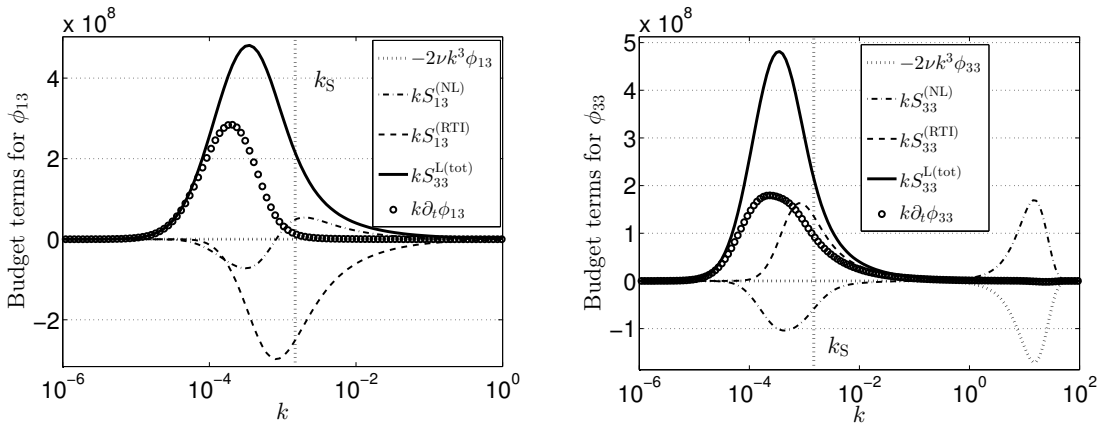

(a) (b)

Figure 3.13: Budget terms with the shear wavenumber k_S at $St = 50$ with $\sigma = 2$. $S_{ij}^{(NL)}$ represents the conservative part of the total non-linear transfer. (a) For ϕ_{13}. (b) For ϕ_{33}.

3.3.3 Discussion on the scattering of integrated quantities in HST

In this section, explanations to the scattering of quantities measured in DNS and experiments in shear flows are proposed. The quantitative discrepancy between the $\gamma = 0.33$ obtained with the present anisotropic EDQNM modelling and the smaller common values is also discussed. One can note that EDQNM simulations are able to reach $St = 50$, which is much higher than DNS, even the most recent ones. This is one of the strength of the current modelling, *i.e.* investigating the asymptotic states of shear-driven flows.

As mentioned previously, weaker values of γ (roughly between 0.07 and 0.20) are found in DNS and experiments, with a noteworthy dispersion, which is now addressed. This could be, for some of these works, the consequence of a too low final St for which the b_{ij} and $\epsilon/(KS)$ are not constant yet, resulting in a value of γ not converged, that reflects transitional effects of initial conditions. Indeed, in the numerical work of Brethouwer (2005), the last dimensionless time is $St = 12$ which is not enough to ensure that b_{ij} and S_R are constant. Other low values of St are reported by Sagaut & Cambon (2008), along with various values of the b_{ij} and γ coming from DNS and experiments. Therefore, moderate values of the final St could be an explanation for the scattering of the experimental and numerical measured γ. It is also argued in Isaza & Collins (2009) that re-meshing, in older DNS, led to loss of kinetic energy and dissipation rate: this could be an explanation as well, rather difficult to quantify.

Several relevant quantities such as γ, b_{13}, $Re_\lambda(0)$, $(St)_{\max}$, $S^*(0)$ and S^*_{end}, coming from different DNS and experiments, are gathered in Table 3.1 to illustrate the noteworthy dispersion of integrated quantities. Qualitatively, it is interesting to point out that for small initial $S^*(0)$, the final value of $|b_{13}|$ is higher, whereas for high initial $S^*(0)$, the final value of γ is higher: this is expected since it corresponds to a strong initial production of kinetic energy, which is recovered with our anisotropic EDQNM modelling in Fig. 3.10b. There is also a slight tendency to increasing $|b_{13}|$ and γ in average in more recent DNS, very likely because of the better spatial resolution of small scales. Nevertheless, the maximum values are $\gamma = 0.18$, still much lower than our $\gamma = 0.33$, and $|b_{13}| = 0.19$, close to our 0.21.

Authors	Kind	$Re_\lambda(0)$	$S^*(0)$	S^*_{end}	b_{13}	γ	$(St)_{\max}$
Tavoularis & Corrsin (1981)	Exp	245	12.5	/	−0.14	0.12	11.6
Shirani *et al.* (1981)	DNS	20	3.3	16.328	−0.147	/	7
Tavoularis & Karnik (1989)	Exp	160	5.6	/	−0.149	0.08	8
Tavoularis & Karnik (1989)	Exp	310	8.4	/	−0.165	0.09	8
Lee *et al.* (1990)	DNS	40	33.5	36.2	−0.1	/	12
De Souza *et al.* (1995)	Exp	1050	11.9	/	−0.121	0.07	12
De Souza *et al.* (1995)	Exp	1010	21.8	/	−0.093	0.10	9
Ferchihi & Tavoularis (2002)	Exp	253	/	/	/	0.0846	23
Schumacher (2004)	DNS	55	0.8	8.2	/	/	10
Brethouwer (2005)	DNS	32	36	/	−0.14	0.178	12
Isaza & Collins (2009)	DNS	26	3	26.6	−0.165	0.10	9
Isaza & Collins (2009)	DNS	26	27	10.3	−0.126	0.18	9
Sukheswalla *et al.* (2013)	DNS	50	3	7.14	−0.19	0.12	20
Sukheswalla *et al.* (2013)	DNS	50	27	21.43	−0.135	0.13	20
Average				17.11	−0.139	**0.114**	
Standard deviation				10.55	0.027	0.037	

Table 3.1: Summary of measured global quantities in existing DNS and experiments for shear flows, classified by date. For experiments, $Re_\lambda(0)$ and $S^*(0)$ refer to estimated values throughout the measurements. The cases presented for Sukheswalla *et al.* (2013) correspond to filtered simulations (see text). When two results from the same work are presented, they correspond to lowest shear and highest shear cases.

Recent DNS studies have focused on the influence of initial parameters, such as the Reynolds number $Re_\lambda(0)$ or the shear parameter $S^*(0)$, on the final state of the flow. Notably, it is reported that there is a tendency toward an almost independence with regard to $Re_\lambda(0)$ and a noteworthy sensitivity to $S^*(0)$. Hereafter, possible explanations for this dependence on initial conditions are proposed. Let's mention that in numerical works, the infrared slope σ is a supplementary initial condition that defines large scales. However, the infrared slopes are not often investigated nor reported, which makes the comparisons and discussions complicated. EDQNM simulations revealed in Fig. 3.10b that the growth rate γ does not depend on σ: therefore in what follows $\sigma = 2$ is chosen.

In Schumacher *et al.* (2003*a*); Schumacher (2004); Isaza & Collins (2009); Sukheswalla *et al.* (2013), the final value of S^* seems to depend on the initial conditions. This is not necessarily in contradiction with our EDQNM results, as revealed in Fig. 3.14a, where the shear parameter $S^* = 2/S_{\text{R}}$ is displayed for various initial $S^*(0)$. Indeed for $St \leq 30$, S^* strongly depends on its initial value for both DNS (see the standard deviation in Table 3.1) and EDQNM. Incidentally, the dispersion of the S^* computed with EDQNM at moderate St (≤ 20) is comparable to the dispersion obtained in DNS and experiments. Then, for sufficiently high $St \geq 30$, S^* becomes independent of initial conditions. Therefore, one could conclude that an universal asymptotic state could be reached only for sufficiently high St, or equivalently at very high Reynolds numbers. Similar assessments are made in Isaza & Collins (2009). At moderate St and Re_λ, the comparison of the present anisotropic model to the recent DNS in Fig. 3.12 shows that the early dynamics of S^* is well captured.

Another point of interest in Isaza & Collins (2009); Sukheswalla *et al.* (2013) is that the average value of the measured γ seems slightly higher (with a maximum of 0.18) than older ones, very likely because of the better spatial resolution. In Sukheswalla *et al.* (2013), small scales had to be

filtered. But, from the present study and Clark & Zemach (1995), it appears that large scales are not determinant in the final value of γ (γ is found to be independent of σ). This directly means that the inertial range scales have a preponderant influence on γ. Hence, the low resolution of small scales in some DNS could result in *slightly* imprecise values for γ, partially responsible for the scattering. This interpretation is confirmed in Figure 18.a of Sukheswalla *et al.* (2013) where the non-filtered kinetic energy is displayed and evolves with a growth rate somewhat higher to those of filtered kinetic energies. In addition, one can note that the unfiltered value of S^* from Sukheswalla *et al.* (2013) reported in Fig. 3.14a would give a value not far from ours ($S^* \to 20$) at a higher St. For the other S^* reported in Schumacher (2004); Isaza & Collins (2009), the $(St)_{\max}$ is to low to conclude.

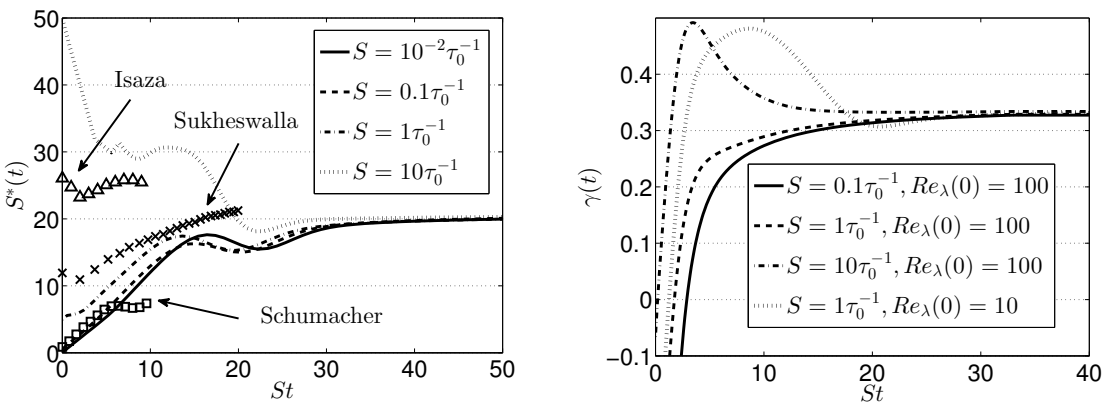

(a) (b)

Figure 3.14: (a) Evolution of the shear parameter $S^* = 2/S_{\mathrm{R}}$ for various S with $\sigma = 2$. The lines correspond to EDQNM simulations with $Re_\lambda(0) = 1$ and symbols to DNS. Crosses refer to Sukheswalla *et al.* (2013), run 256_30 without filtering; triangles to Isaza & Collins (2009); squares to Schumacher (2004), run 4. (b) Evolution of the kinetic energy exponential growth rate γ for various shear intensity S. The initial Reynolds number is either $Re_\lambda(0) = 10$ or $Re_\lambda(0) = 100$ and $\sigma = 2$. The average exponential growth rate is $\gamma_{\mathrm{av}} = 0.114$.

The influence of the initial Reynolds number $Re_\lambda(0)$ is now discussed. It has been reported in Sukheswalla *et al.* (2013) that $Re_\lambda(0)$ had not much impact on the final state of the flow. This is recovered in Fig. 3.14b where the kinetic energy exponential growth rate γ is displayed at $Re_\lambda(0) = 10$ and $Re_\lambda(0) = 100$ for various initial shear intensities S. The important result is that a different initial Reynolds number changes very slightly the final growth rate exponent γ: indeed, $\gamma \simeq 0.33$ was obtained previously for $Re_\lambda(0) = 1$. Here, for $S \leq 1\tau_0^{-1}$ and both $Re_\lambda(0) = 10$ and $Re_\lambda(0) = 100$, one has $\gamma \simeq 0.330$, whereas $\gamma \simeq 0.334$ for $S = 10\tau_0^{-1}$ and $Re_\lambda(0) = 100$. This underlines that for sufficiently high final St, or equivalently sufficiently high Reynolds numbers, an asymptotic state independent of initial conditions is obtained. This result is consistent with what is observed in DNS, *i.e.* the independence with regard to $Re_\lambda(0)$. Let's mention that the $Re_\lambda(0) = 100$ chosen here is higher than common initial Reynolds numbers for DNS, as revealed in Table 3.1. Moreover, Fig. 3.14b reveals that at comparable St, our γ is much higher than common ones and almost constant. Hence, it is very likely that γ in DNS and experiments would not increase for higher St. Therefore, the moderate St reached in DNS and experiments can only explain the scattering around the average value $\gamma_{\mathrm{av}} = 0.114$.

The results of this discussion, summarized hereafter, are twofold. Firstly, Fig. 3.14a and 3.14b exhibited interesting behaviours: firstly, an unique asymptotic value for the shear parameter $S^* = 2KS/\epsilon$ is obtained only at high values of St. For typical final values of DNS and experiments ($St \leq 20$) at an initial moderate Reynolds number $Re_\lambda(0)$, it appears that S^* still depends on initial conditions. Furthermore, in agreement with existing works, an independence with regard to the initial Reynolds number has been obtained. Thus, high St can limit the dispersion of the results by erasing effects of initial conditions. Secondly, it has been pointed out that the present anisotropic EDQNM modelling provides higher values for the growth rate γ than DNS and experiments do. Even though similar values are found in the spectral model of Clark & Zemach (1995), our numerical $\gamma = 0.33$ is much higher than common ones, gathered around $\gamma_{\text{av}} = 0.114$.

The practical input of this numerical work is notably indications for future DNS. According to the previous discussion and Table 3.1, it seems crucial to reach final values of the accumulated anisotropy $25 \leq (St)_{\max} \leq 30$ to limit the scattering of the results and transitional effects from initial conditions, and to systematically investigate the dependence in ($Re_\lambda(0)$, $S^*(0)$), as reported in Schumacher *et al.* (2003*a*).

3.4 Conclusion and perspectives

Firstly, the main features of this chapter are recalled hereafter: results regarding decay and growth laws in shear-driven flows are gathered in Table 5.1, along with similar results for the passive scalar field addressed in the next chapters. Secondly, we come back on the value of the kinetic energy exponential growth rate $\gamma = 0.33$. Finally, some perspectives are drawn for future works.

3.4.1 Conclusions on HST and HSRT

Homogeneous anisotropic turbulence has been investigated with the anisotropic EDQNM modelling in the particular case of shear flows, when mean-velocity gradients are both released (HSRT) and sustained (HST). In this framework, we have revisited classical phenomena and provided results obtained at high Reynolds numbers, qualitatively in agreement with existing ones in DNS and experiments.

In the shear-released turbulence configuration, a model was derived for the slow-part of the pressure strain-tensor $\Pi_{ij}^{(\text{s})}$, which is responsible for the return to isotropy mechanism, valid once the mean-velocity gradients are released. This model is in agreement with our simulations and must be seen as complementary to existing ones, since it focuses on the asymptotic anisotropic state at large times for high Reynolds numbers. Then, the present model allows to understand deeply the RTI mechanism: spectral descriptors show that small scales of the velocity second-order moments completely return to isotropy in both Saffman and Batchelor turbulence, leading to a global partial return to isotropy, which is in agreement with experiments and DNS. Regarding large scales, they keep their anisotropy in Saffman turbulence, whereas they continuously evacuate anisotropy in Batchelor turbulence, because of strong inverse non-linear transfers. In

addition, the decay of the kinetic energy $K(t)$ and of the anisotropic correlation R_{13} was investigated in both Saffman and Batchelor HSRT. The decay of the kinetic energy is not modified by the initial shear, whereas R_{13}, which also decays in $t^{-6/5}$ in Saffman HSRT, decays faster than $K(t)$ in Batchelor HSRT, because of the RTI mechanism driven by pressure effects.

At last, the case of the sustained shear turbulence was addressed. The original aspect highlighted here is that with the present modelling the growth rate γ seems to not depend on large scales initial condition (the infrared slope σ) nor on the shear rate intensity S, provided a sufficiently high accumulated anisotropy St, or equivalently a high Reynolds numbers, is reached. Quantitative differences have been exhibited, especially for the exponential growth rate γ of the kinetic energy, which is found to be two to three times higher than existing values. Nonetheless, as for the shear parameter S^*, its dynamics seems to be well described by the present model. The dispersion of integrated quantities obtained in DNS and experiments has been discussed, and the main result of this work regarding sustained shear flows lies in the explanations proposed: it has been shown notably that moderate values of the final accumulated anisotropy St may be responsible for the scattering of integrated quantities, reported in Table 3.1, and that higher values of St, or higher Reynolds numbers, could limit this dispersion by erasing initial conditions effects. Another parameter that could be of importance is the nature of the initial flow, that we choose to be isotropic for simplicity reasons. In experiments for instance, the initial condition is clearly not isotropic. EDQNM simulations with an initial condition slightly anisotropic, as in Davidson *et al.* (2012), show that for instance γ slightly varies by $\pm 5\%$. This indicates a small dependence on initial anisotropy, but not significant.

3.4.2 Exponential growth rate γ

This part aims at answering two questions of fundamental interest for the modelling of shear flows: (i) Why is the exponential growth rate γ of the kinetic energy not depending on the infrared slope σ whereas it strongly does in unstably stratified homogeneous turbulence (see Chapter 7) ? (ii) Is the value $\gamma = 0.33$ predictable? Theoretical considerations about shear flows which were found after the publication of the contents of this chapter in *Journal of Turbulence* are thus presented here.

The independence of γ with σ in HST is not a consequence of the modelling of anisotropy, since in Chapter 7, the kinetic energy exponential growth rate in USHT strongly depends on σ. Assuming self-similarity of the kinetic energy spectrum and a linear dynamics of large scales in both HST and USHT, one has $K \sim \exp(\gamma St)$, $L \sim \exp(\gamma St/2)$, so that

$$E(k,t) \sim k^{\sigma} \exp\left[\frac{\sigma+3}{2}\gamma St\right]. \tag{3.20}$$

Following the method proposed in Poujade & Peybernes (2010); Soulard *et al.* (2014), the time evolution of E is also given at large scales by the largest eigenvalue of the linear operator of the generalized Lin equations system (2.53)-(2.55). The linear operator of HST verifies, dropping

the non-linear and viscous terms,

$$\frac{\partial}{\partial t}\begin{pmatrix} E \\ EH_{11}^{(\mathrm{dir})} \\ EH_{13}^{(\mathrm{dir})} \\ EH_{33}^{(\mathrm{dir})} \\ EH_{11}^{(\mathrm{pol})} \\ EH_{13}^{(\mathrm{pol})} \\ EH_{33}^{(\mathrm{pol})} \end{pmatrix} = S \begin{pmatrix} 0 & 0 & 2(\sigma+2) & 0 & 0 & 2 & 0 \\ 0 & 0 & -\frac{2(\sigma+11)}{21} & 0 & 0 & \frac{2}{21} & 0 \\ \frac{(\sigma-1)}{30} & \frac{3-\sigma}{7} & 0 & -\frac{4+\sigma}{7} & \frac{1}{7} & 0 & \frac{1}{7} \\ 0 & 0 & \frac{2(10-\sigma)}{21} & 0 & 0 & \frac{2}{21} & 0 \\ 0 & 0 & \frac{4}{7} & 0 & 0 & \frac{2(\sigma+4)}{21} & 0 \\ \frac{1}{5} & \frac{6}{7} & 0 & \frac{6}{7} & \frac{3\sigma-2}{21} & 0 & \frac{3\sigma+5}{21} \\ 0 & 0 & \frac{4}{7} & 0 & 0 & \frac{2(\sigma-3)}{21} & 0 \end{pmatrix} \begin{pmatrix} E \\ EH_{11}^{(\mathrm{dir})} \\ EH_{13}^{(\mathrm{dir})} \\ EH_{33}^{(\mathrm{dir})} \\ EH_{11}^{(\mathrm{pol})} \\ EH_{13}^{(\mathrm{pol})} \\ EH_{33}^{(\mathrm{pol})} \end{pmatrix}. \tag{3.21}$$

It is worth noting that the linear operator, because of the space-derivative $\partial/\partial k$ production terms, depends explicitly on σ, unlike the linear operator of USHT, whose maximum eigenvalue is $4/\sqrt{5}$. Consequently, the largest eigenvalue of the linear operator in HST almost balances the self-similar expression (3.20) for $E(k,t)$, thus strongly reducing the dependence of γ with σ.

The maximum real eigenvalue $\Gamma_{\max}(\sigma)$ of the linear operator being a rather lengthy expression, only the final growth rate is given here, obtained by equalizing (3.20) and $E \sim \exp(\Gamma_{\max} St)$, so that

$$\gamma = \begin{cases} 0.358 & \text{for} \quad \sigma = 1, \\ 0.339 & \text{for} \quad \sigma = 2, \\ 0.346 & \text{for} \quad \sigma = 3, \\ 0.367 & \text{for} \quad \sigma = 4. \end{cases} \tag{3.22}$$

This result answers the two questions (i) and (ii) of the beginning of this part. First, the numerical simulations presented so far recover a value around $0.33 \leq \gamma \leq 0.34$ for all σ, which is close to the linear prediction (3.22): this means that the non-linear redistribution of energy through scales permits to maintain this exponential growth rate, obtained by self-similar arguments and the linear dynamics of large scales where anisotropic mechanisms dominate. Secondly, the fact that the maximum eigenvalue of the linear operator depends on σ explains why γ hardly varies with σ in HST, unlike USHT where the maximum eigenvalue is independent of the large scales initial conditions, so that the exponential growth rate in USHT (7.26) varies a lot with σ.

3.4.3 Perspectives

In this section, two perspectives for future works regarding shear flows are proposed. The first one, already introduced in Chapter 2, is the consideration of the fourth-order expansion for $\mathcal{E}$ and Z. The second one is to consider that the mean-shear intensity $S(t)$ can vary with time, *i.e.* to model the retro-action of the fluctuating turbulent quantities on the mean-field, similarly to what is done at the end of Chapter 7 for a variable stratification frequency $N(t)$.

Fourth-order expansion: In Chapter 2, the formalism of the fourth-order expansion into spherical harmonics has been presented, with details in Appendix C. The fourth-order contributions $EH_{ijpq}^{(\mathrm{dir})}$ and $EH_{ijpq}^{(\mathrm{pol})}$ have their own evolution equations (C.59) and (C.60): their non-linear transfers depend only on fourth-order contributions, whereas their linear production terms are modified by the second-order ones. The impact of $EH_{ijpq}^{(\mathrm{dir})}$ and $EH_{ijpq}^{(\mathrm{pol})}$ on the second-order spectra $EH_{ij}^{(\mathrm{dir})}$ and $EH_{ij}^{(\mathrm{pol})}$ is uniquely done through the linear transfers $S_{ij}^{\mathrm{L(dir4)}}$ and $S_{ij}^{\mathrm{L(pol4)}}$, which add to the previous ones (2.65) and (2.65), now written $S_{ij}^{\mathrm{L(dir2)}}$ and $S_{ij}^{\mathrm{L(pol2)}}$. In

the end, the total linear directional and polarization transfers with the fourth-order expansions are $S_{ij}^{\mathrm{L(dir)}} = S_{ij}^{\mathrm{L(dir2)}} + S_{ij}^{\mathrm{L(dir4)}}$, and $S_{ij}^{\mathrm{L(pol)}} = S_{ij}^{\mathrm{L(pol2)}} + S_{ij}^{\mathrm{L(pol4)}}$.

The main consequence of the fourth-order contributions is that the kinetic energy exponential growth rate is decreased in Fig. 3.15 from $\gamma = 0.33$ to $\gamma = 0.28$. Even though the value of γ remains rather large, the significant decrease by 15% with the fourth-order expansion of $\mathcal{E}$ and Z perfectly illustrates that taking into account more spherical harmonics goes into the good direction, *i.e.* diminishes γ towards smaller values obtained in DNS, as reported in Table 3.1. The joint result is, in Fig. 3.15 as well, the decrease of b_{13} from 0.215 to 0.18, which is a noteworthy feature as well. One can further remark that on the contrary, the fourth-order contributions increase $|b_{11}|$ and $|b_{33}|$, which is expected. Indeed, taking into account more harmonics reduces the loss of information due to the spherical integration by restoring part of the anisotropic angular information. As a consequence, the strong anisotropy of the shear flow between the streamwise and transverse directions is better captured.

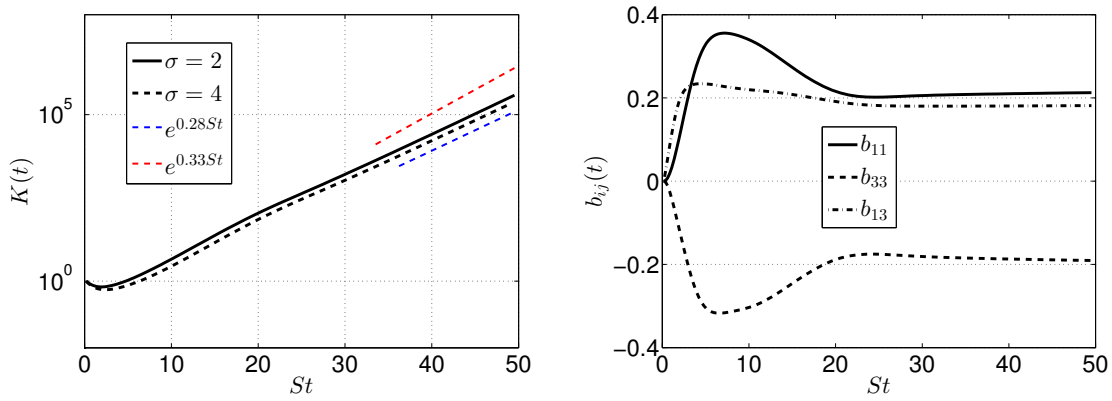

(a) (b)

Figure 3.15: Effects of the fourth-order expansion on the growth of the kinetic energy $K(t)$ and the anisotropy tensor b_{ij}. (a) $K(t)$ for $\sigma = 2$ and $\sigma = 4$. (b) b_{ij} for $\sigma = 2$.

To better illustrate the impact of the fourth-order contributions, we investigate the detailed linear transfers in Figure 3.16, with the directional and polarization parts of the streamwise, transverse and cross components in Saffman turbulence. In the this figure, the black curves represent simulations with the fourth-order contributions, at $Re_\lambda = 9.10^3$. Whereas the grey curves indicate simulations with only the second-order expansion, as in MCS. Since the Reynolds number increases faster in the latter case, the results are presented at $St = 43$ where $Re_\lambda \simeq 9.10^3$ as well.

One can remark that the effects are different for the directional and polarization parts: indeed, the fourth-order contributions tend to decrease the intensity of the directional linear transfers for the streamwise $()_{11}$ and transverse $()_{33}$ components, while increasing it for the $()_{13}$ component. The opposite happens for the linear polarization transfers. In particular, the strongest difference is observed for the transverse directional transfer $S_{33}^{\mathrm{L(dir)}}$, which is positive without the fourth-order contributions, and becomes mostly negative with them.

The practical input of this section in terms of modelling is that it is much more important to improve the linear production terms through the fourth-order expansion than considering

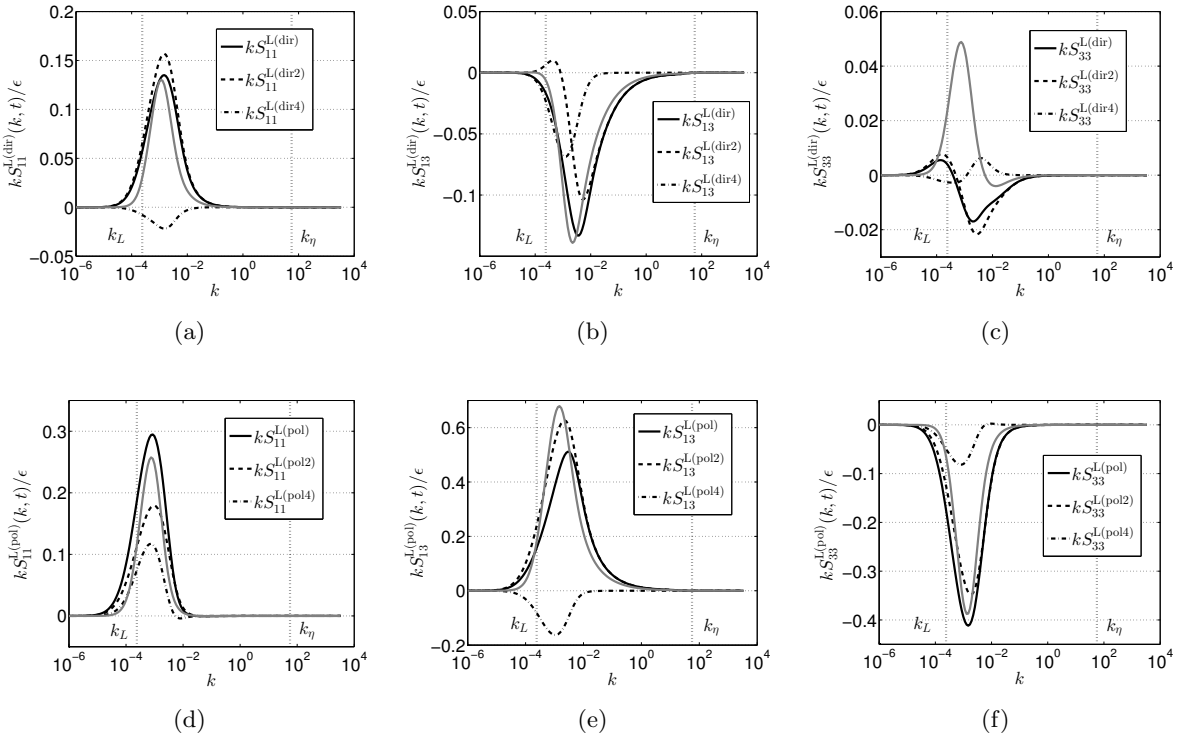

Figure 3.16: Effects of the fourth-order expansion on the linear transfers of $EH_{ij}^{(\mathrm{dir})}$ and $EH_{ij}^{(\mathrm{pol})}$, for $\sigma = 2$, at $Re_\lambda(St = 50) = 9.10^3$. The terms $S_{ij}^{\mathrm{L(dir2)}}$ and $S_{ij}^{\mathrm{L(pol2)}}$ contain the second-order contributions, and the terms $S_{ij}^{\mathrm{L(dir4)}}$ and $S_{ij}^{\mathrm{L(pol4)}}$ the fourth-order contributions. (a) $S_{11}^{\mathrm{L(dir)}}$, (b) $S_{13}^{\mathrm{L(dir)}}$, (c) $S_{33}^{\mathrm{L(dir)}}$, (d) $S_{11}^{\mathrm{L(pol)}}$, (e) $S_{13}^{\mathrm{L(pol)}}$, and (f) $S_{33}^{\mathrm{L(pol)}}$. In each case, the grey curves indicate simulations without the fourth-order contributions at $Re_\lambda(St = 43) = 9.10^3$.

the quadratic anisotropic contributions in the classical non-linear transfers (see Appendix C). Another approach could be to solve directly the evolution equations of $\mathcal{E}(\boldsymbol{k}, t)$ and $Z(\boldsymbol{k}, t)$ with the exact linear terms, and to keep the modelled non-linear transfers with the second-order expansion: this is currently the topic of a PhD under the direction of Claude Cambon.

Third-order expansion: Some considerations are now presented about the third-order expansion of Z: even though they are not conclusive right now, they could be of interest for future works. There are two reasons why we wish to further consider odd-order terms in the expansion of Z: (i) Odd-order expansions could improve the modelling of the $2\mathrm{i}Z\Omega_{\mathrm{CH}}$ term in the evolution equation (2.33) of Z; (ii) Recent results by Claude Cambon show that the main difference between the MCS model with an exact treatment of linear terms lies in the polarization anisotropy.

Up to the fourth-order, the expansion of Z can be written

$$Z(\boldsymbol{k}, t) = \frac{1}{2}\mathcal{E}_0\Big(5H_{ij}^{(\mathrm{pol})}(k, t) + 7\mathrm{i}H_{ijk}^{(\mathrm{pol})}\alpha_k + \frac{21}{2}H_{ijpq}^{(\mathrm{pol})}(k, t)\alpha_p\alpha_q\Big)N_i^*(\boldsymbol{k})N_j^*(\boldsymbol{k}), \tag{3.23}$$

where $H_{ijk}^{(\mathrm{pol})}$ is a tensor which verifies, for simplicity reasons as before, full symmetry under any change of indices, and is zero when two indices are equal. Note that the expression of the third-order contribution differs from the one in Mons *et al.* (2016) because of the imaginary

number i. The latter is crucial, otherwise it can be shown that the third-order of Z never contributes. Two features are needed to prove this statement. First, one requires the following equation when computing the polarization part $\hat{R}_{ij}^{(\mathrm{pol})} = \Re[ZN_iN_j]$:

$$N_iN_jN_p^*N_q^* = \Big[P_{ip}P_{jq} + P_{iq}P_{jp} - P_{ij}P_{pq}\Big] - \frac{1}{2}\mathrm{i}\alpha_a\Big[P_{jq}\epsilon_{ipa} + P_{ip}\epsilon_{jqa} + P_{iq}\epsilon_{jpa} + P_{jp}\epsilon_{iqa}\Big],$$

where ϵ_{ijk} is the Levi-Civita permutation tensor. The second one is that the spherical average of an odd number of normalized wavevectors α_i is zero, as explained for instance in Pope (2000). Consequently, without the i, $\Re[ZN_iN_j]$ has an odd number of α_i so that it vanishes with the spherical-average. Therefore, the present expansion of Z (3.23) corrects the equation (3.15) of Mons *et al.* (2016).

Then, as for the second and fourth-order terms, one needs an operator which gives only the third-order contribution and erases the others. This operator is $N_{ijk} = \alpha_kN_iN_j + \alpha_jN_iN_k + \alpha_iN_jN_k$, and we further define $H_{ijk}^{(\mathrm{pol})}$ as

$$2E(k,t)H_{ijk}^{(\mathrm{pol})}(k,t) = \int_{S_k} \Im\Big[Z(\boldsymbol{k},t)N_{ijk}(\boldsymbol{k})\Big]\mathrm{d}^2\boldsymbol{k}. \tag{3.24}$$

Similarly to the fourth-order expansion, the third-order expansion of Z does not modify the spectral tensor ϕ_{ij}, which is still expressed as function of $H_{ij}^{(\mathrm{dir})}$ and $H_{ij}^{(\mathrm{pol})}$ only.

Finally, the third-order expansion of Z gives a new contribution in the modelled spectral Reynolds tensor $\hat{R}_{ij}$, which reads

$$\hat{R}_{ij}^{\mathrm{z3}}(\boldsymbol{k},t) = \frac{7}{2}\mathcal{E}_0(k,t)H_{pql}^{(\mathrm{pol})}(k,t)\alpha_l\alpha_n\Big(\epsilon_{ipn}P_{jq}(\boldsymbol{k}) + \epsilon_{jqn}P_{ip}(\boldsymbol{k})\Big). \tag{3.25}$$

<u>Remark</u>: It is worth noting that the third-order expansion of polarization can be related to the stropholysis tensor of Kassinos *et al.* (2001), defined as

$$Q_{ijk} = \epsilon_{ipq}\int \alpha_p\alpha_k\hat{R}_{jq}(\boldsymbol{k})\mathrm{d}^3\boldsymbol{k} = -\int \epsilon_{ijp}\alpha_p\alpha_k\mathcal{E}(\boldsymbol{k})\mathrm{d}^3\boldsymbol{k} + \int \alpha_k\Im\Big(Z(\boldsymbol{k})N_i(\boldsymbol{k})N_j(\boldsymbol{k})\Big)\mathrm{d}^3\boldsymbol{k}. \tag{3.26}$$

The final expression of Q_{ijk} using the second-order expansions can be found in Mons *et al.* (2016). Interestingly, the symmetric stropholysis $Q_{ijk}^* = (Q_{ijk} + Q_{ikj} + 4 \text{ perm.})/6$ erases the directional anisotropy and depends only on polarization. More specifically, only odd-order terms of the Z expansion can contribute in Q_{ijk}^*, which further justifies the interest of odd-order contributions.

Now, we determine the explicit expressions of the production terms linked to the third-order contributions in the expansion (3.23) of Z. As before, there are three different kinds of terms: the third-order contributions in the equations of $EH_{ij}^{(\mathrm{dir})}$ and $EH_{ij}^{(\mathrm{pol})}$ and in the equation of $EH_{ijk}^{(\mathrm{pol})}$, and finally the second-order contributions in the equations of $EH_{ijk}^{(\mathrm{pol})}$. There are no third-order contributions in the Lin equation for E, and for simplicity reasons, we further discard the third-order contributions in the evolution equations of $EH_{ijpq}^{(\mathrm{dir})}$ and $EH_{ijpq}^{(\mathrm{pol})}$, and the fourth-order contributions in the equation of $EH_{ijk}^{(\mathrm{pol})}$: thus there is no direct linear coupling between the third and fourth orders.

First, the contributions of the third-order expansion in the equations of $EH_{ij}^{(\mathrm{dir})}$ and $EH_{ij}^{(\mathrm{pol})}$ are, after some algebra,

$$S_{ij}^{\mathrm{L(dir3)}}(k,t) = \frac{1}{6}A_{ln}^{+}E\Big(\epsilon_{ilp}H_{jnp}^{(\mathrm{pol})} + \epsilon_{jlp}H_{inp}^{(\mathrm{pol})}\Big), \tag{3.27}$$

$$\begin{aligned} S_{ij}^{\mathrm{L(pol3)}}(k,t) &= \frac{1}{3}A_{ln}^{-}E\Big(\epsilon_{lnp}H_{ijp}^{(\mathrm{pol})} - \epsilon_{ilp}H_{jnp}^{(\mathrm{pol})} - \epsilon_{jlp}H_{inp}^{(\mathrm{pol})}\Big) \\ &\quad - \frac{1}{6}A_{ln}^{+}\Big(\frac{\partial}{\partial k}\Big[kE(\epsilon_{ilp}H_{jnp}^{(\mathrm{pol})} + \epsilon_{jlp}H_{inp}^{(\mathrm{pol})})\Big] + E(\epsilon_{ilp}H_{jnp}^{(\mathrm{pol})} + \epsilon_{jlp}H_{inp}^{(\mathrm{pol})})\Big). \end{aligned} \tag{3.28}$$

Note that unlike $S_{ij}^{\mathrm{L(dir4)}}$ and $S_{ij}^{\mathrm{L(pol4)}}$, $S_{ij}^{\mathrm{L(dir3)}}$ and $S_{ij}^{\mathrm{L(pol3)}}$ depend on the antisymmetric part A_{ln}^{-} of the mean-velocity gradient. The linear polarization transfer $S_{ijk}^{\mathrm{L(pol)}}$ of $EH_{ijk}^{(\mathrm{pol})}$ is defined as

$$S_{ijk}^{\mathrm{L(pol)}}(k) = \frac{1}{4}\int_{S_k} \Im\left[\left(A_{ln}k_l\frac{\partial \hat{R}_{rs}}{\partial k_n} - 2M_{rn}(\boldsymbol{k})\hat{R}_{ns}(\boldsymbol{k})\right)N_r^*(\boldsymbol{k})N_s^*(\boldsymbol{k})N_{ijk}(\boldsymbol{k})\right]\mathrm{d}^2\boldsymbol{k}. \tag{3.29}$$

This production term is divided into two contributions resulting from the second and third order expansions. First, we determine the impact of the second-order contributions $EH_{ij}^{(\mathrm{dir})}$ and $EH_{ij}^{(\mathrm{pol})}$ on the linear transfer of $EH_{ijk}^{(\mathrm{pol})}$. For this purpose, we introduce two trace-free and symmetric operators, namely

$$\begin{aligned} \mathcal{H}_{ijk}^{2,+}[EH^{()}] &= 5E\Big[A_{il}^{+}\Big(\epsilon_{jln}H_{nk}^{()} + \epsilon_{kln}H_{nj}^{()}\Big) + A_{jl}^{+}\Big(\epsilon_{iln}H_{nk}^{()} + \epsilon_{kln}H_{ni}^{()}\Big) \\ &\quad + A_{kl}^{+}\Big(\epsilon_{iln}H_{nj}^{()} + \epsilon_{jln}H_{ni}^{()}\Big)\Big] - 2EA_{ln}^{+}H_{np}^{()}E\Big[\delta_{ij}\epsilon_{klp} + \delta_{ik}\epsilon_{jlp} + \delta_{jk}\epsilon_{ilp}\Big] \end{aligned} \tag{3.30}$$

$$\begin{aligned} \mathcal{H}_{ijk}^{2,-}[EH^{()}] &= 5E\Big[A_{il}^{-}\Big(\epsilon_{jln}H_{nk}^{()} + \epsilon_{kln}H_{nj}^{()}\Big) + A_{jl}^{-}\Big(\epsilon_{iln}H_{nk}^{()} + \epsilon_{kln}H_{ni}^{()}\Big) \\ &\quad + A_{kl}^{-}\Big(\epsilon_{iln}H_{nj}^{()} + \epsilon_{jln}H_{ni}^{()}\Big) - A_{ln}^{-}\Big(\epsilon_{iln}H_{jk}^{()} + \epsilon_{jln}H_{ik}^{()} + \epsilon_{kln}H_{ij}^{()}\Big)\Big] \\ &\quad + 2EA_{ln}^{-}H_{np}^{()}E\Big[\delta_{ij}\epsilon_{klp} + \delta_{ik}\epsilon_{jlp} + \delta_{jk}\epsilon_{ilp}\Big]. \end{aligned} \tag{3.31}$$

After complex calculations, one gets

$$S_{ijk}^{\mathrm{L(pol2)}} = -\frac{1}{7}\mathcal{H}_{ijk}^{(2,+)}[EH^{(\mathrm{dir})}] + \frac{1}{21}\Big[\mathcal{H}_{ijk}^{(2,-)}[EH^{(\mathrm{pol})}] - \mathcal{H}_{ijk}^{(2,+)}[EH^{(\mathrm{pol})}]\Big] + \frac{1}{42}\mathcal{H}_{ijk}^{(2,+)}[\partial_k(kEH^{(\mathrm{pol})})]. \tag{3.32}$$

Now, we proceed similarly to determine the impact of the third-order expansion on the linear transfers of $EH_{ijk}^{(\mathrm{pol})}$. After some algebra, one gets

$$S_{ijk}^{\mathrm{L(pol3)}} = \frac{1}{3}\Big[A_{il}^{-}H_{jlk}^{(\mathrm{pol})} + A_{jl}^{-}H_{ilk}^{(\mathrm{pol})} + A_{kl}^{-}H_{ijl}^{(\mathrm{pol})}\Big], \tag{3.33}$$

where notably the symmetric part of the mean-velocity gradient matrix does not intervene. The third-order polarization non-linear transfer is defined as

$$S_{ijk}^{\mathrm{NL(pol)}}(k,t) = \frac{1}{2}\int_{S_k} \Im\Big(T_Z(\boldsymbol{k},t)N_{ijk}(\boldsymbol{k},t)\Big)\,\mathrm{d}^2\boldsymbol{k}. \tag{3.34}$$

For the sake of simplicity, quadratic anisotropic contributions are discarded, as for the second and fourth orders: therefore, only the third-order terms contribute in $S_{ijk}^{\mathrm{NL(pol)}}$. Furthermore, because $H_{ijk}^{(\mathrm{pol})}$ is symmetric and trace-free, it follows that third-order expansions vanish in

$S_{ij}^{\mathrm{NL(dir)}}$ and $S_{ij}^{\mathrm{NL(pol)}}$. Eventually, injecting the third-order expansion into the expression (2.42) of T_Z gives the spherically-averaged non-linear polarization transfer

$$S_{ijk}^{\mathrm{NL(pol)}} = 4\pi^2 \int_{\Delta_k} \theta_{kpq} k^2 p^2 q \mathcal{E}_0'' \Bigg[H_{ijk}^{(\mathrm{pol})''} (1-z^2)\Big(2z(1-2y^2)(\mathcal{E}_0' - \mathcal{E}_0) + xy(1-3y^2)\mathcal{E}_0\Big)$$
$$- 4(xy+z^3)\mathcal{E}_0 H_{ijk}^{(\mathrm{pol})} + H_{ijk}^{(\mathrm{pol})'} \mathcal{E}_0' \Big(2(xy+z^3)(2z^2-1) - z(3z^2-1)(y^2-z^2)\Big)\Bigg] \mathrm{d}p\mathrm{d}q. \quad (3.35)$$

The evolution equation of the third-order anisotropic descriptor $EH_{ijk}^{(\mathrm{pol})}$ reads

$$\left(\frac{\partial}{\partial t} + 2\nu k^2\right) E(k) H_{ijk}^{(\mathrm{pol})}(k) = S_{ijk}^{\mathrm{L(pol2)}}(k) + S_{ijk}^{\mathrm{L(pol3)}}(k) + S_{ijk}^{\mathrm{NL(pol)}}(k). \quad (3.36)$$

Moreover, the Lin equations of $EH_{ij}^{(\mathrm{dir})}$ and $EH_{ij}^{(\mathrm{pol})}$ derived are modified accordingly into

$$\left(\frac{\partial}{\partial t} + 2\nu k^2\right) E(k,t) H_{ij}^{(\mathrm{dir})}(k) = S_{ij}^{\mathrm{L(dir2)}}(k) + S_{ij}^{\mathrm{L(dir3)}}(k) + S_{ij}^{\mathrm{NL(dir)}}(k), \quad (3.37)$$
$$\left(\frac{\partial}{\partial t} + 2\nu k^2\right) E(k) H_{ij}^{(\mathrm{pol})}(k) = S_{ij}^{\mathrm{L(pol2)}}(k) + S_{ij}^{\mathrm{L(pol3)}}(k) + S_{ij}^{\mathrm{NL(pol)}}(k). \quad (3.38)$$

Note that the retro-action of the third-order contributions on the second-order ones is uniquely done through the linear transfers $S_{ij}^{\mathrm{L(dir3)}}$ and $S_{ij}^{\mathrm{L(pol3)}}$, and that inversely, the impact of the second-order contributions on the third-order ones is uniquely done through the linear transfers $S_{ijk}^{\mathrm{L(dir2)}}$ and $S_{ijk}^{\mathrm{L(pol2)}}$.

Variable shear: We consider a free-shear mixing layer created by two parallel streams of different uniform speeds U_h and U_l in the direction x_1, with $U_h > U_l$, both independent of time and space. The notations of Dimotakis (1991) are used: the characteristic mean velocity is $\Delta U = U_h - U_l$, and the mean velocity at the center of the mixing layer is $U_c = (U_h + U_l)/2$. In the turbulent mixing layer, the mean flow is in the streamwise x_1-direction and varies along the vertical x_3-direction, from U_l to U_h according to

$$U_1(x_3,t) = \frac{\Delta U}{L_S(t)} x_3 + U_l = S(t) x_3 + U_l, \quad (3.39)$$

where L_S is the free-shear layer length. The total turbulent velocity field can be decomposed, in the shear layer, as

$$u_i^{(\mathrm{tot})}(\boldsymbol{x},t) = U_1(x_3,t)\delta_{1i} + u_i(\boldsymbol{x},t). \quad (3.40)$$

One can further define the dimensionless mean streamwise velocity as $\tilde{U}_1 = U_1/\Delta U$, so that $\partial_3 \tilde{U}_1 = 1/L_S$, and the definition of L_S is analogous to the one of the mixing length L of an unstably stratified flow (see the end of Chapter 7)

$$L_S(t) = \frac{6}{\Delta U^2} \int_{-\infty}^{+\infty} (U_1 - U_l)(U_h - U_1) \mathrm{d}x_3, \quad (3.41)$$

and is proportional to the momentum thickness θ, with $L_S = 6\theta$. The evolution equation of the streamwise mean velocity reads

$$\frac{\partial U_1}{\partial t} = -\frac{\partial P}{\partial x_1} - \frac{\partial R_{11}}{\partial x_1} - \frac{\partial R_{13}}{\partial x_3} + \nu \frac{\partial^2 U_1}{\partial x_l \partial x_l}. \tag{3.42}$$

Assuming that the viscous term is negligible at large Reynolds numbers, that there is no horizontal mean pressure gradient, and that the variations along x_3 are stronger than along x_1, one gets

$$\frac{\partial U_1}{\partial t} \simeq -\frac{\partial R_{13}}{\partial x_3}, \tag{3.43}$$

which was also obtained in Galmiche & Hunt (2002). Further using (3.43) in the time derivative of (3.41), one gets

$$\frac{\mathrm{d}L_S}{\mathrm{d}t} = -\frac{12}{\Delta U^2}\Big[(U_c - U_1)R_{13}\Big]_{-\infty}^{+\infty} - \frac{12}{\Delta U^2}\int_{-\infty}^{+\infty} R_{13}\frac{\partial U_1}{\partial x_3}\mathrm{d}x_3 = -\frac{12}{L_S \Delta U}\int_{-\infty}^{+\infty} R_{13}\,\mathrm{d}x_3, \tag{3.44}$$

The first term is zero since it is assumed that there is no turbulent fluctuations outside the shear layer of extent $L_S(t)$. Then, choosing a parabolic shape for the Reynolds stress tensor R_{13}, with $x_3 \in [-L_S/2; L_S/2]$, one gets

$$\frac{\mathrm{d}L_S}{\mathrm{d}t} = -\frac{8}{\Delta U} < u_1 u_3 > = -\frac{8}{S L_S} < u_1 u_3 > . \tag{3.45}$$

Finally, since $\Delta U = -S(t)L_S(t)$ is constant, one gets

$$\frac{\mathrm{d}S}{\mathrm{d}t} = -\frac{S}{L}\frac{\mathrm{d}L_S}{\mathrm{d}t} = \frac{8}{L_S^2} < u_1 u_3 > = -\frac{\partial^2 R_{13}}{\partial x_3^2}. \tag{3.46}$$

Since most of the experimental studies investigate the development of a spatial free-shear layer, it is worth noting that the spatial extent L_S can be obtained with a **Taylor frozen-flow assumption**, which transforms the streamwise spatial coordinate into a temporal one, according to

$$x_1 \to U_c\, t, \qquad U_c \frac{\partial}{\partial x_1} \to \frac{\partial}{\partial t}. \tag{3.47}$$

The local spatial extent $\delta(x_1)$ of the shear layer could be assimilated to L_S with a Taylor frozen-flow hypothesis, *i.e.* $\delta(x_1) \sim L_S(t)$. In Dimotakis (1991), the growth rate of the mixing layer region, for two fluids of equal density $\rho_h = \rho_l = \rho_0$, is given by

$$\frac{\delta(x_1)}{x_1} = \frac{1-r}{1+r}\, C_\delta, \tag{3.48}$$

with the ratio $r = U_l/U_h$, and C_δ is a constant. In the latter reference, a noteworthy scattering of the values of C_δ are reported, $0.25 \leq C_\delta \leq 0.45$, with possible values outside these bounds. Further, one gets

$$C_\delta = \frac{1+r}{1-r}\frac{\delta(x_1)}{x_1} = \frac{2U_c}{\Delta U}\frac{L_S}{U_c\, t} = \frac{2}{S(t)\, t}. \tag{3.49}$$

Here, we choose to define the self-similar free-shear layer length as

$$L_S(t) = \alpha_S\, \Delta U\, t. \tag{3.50}$$

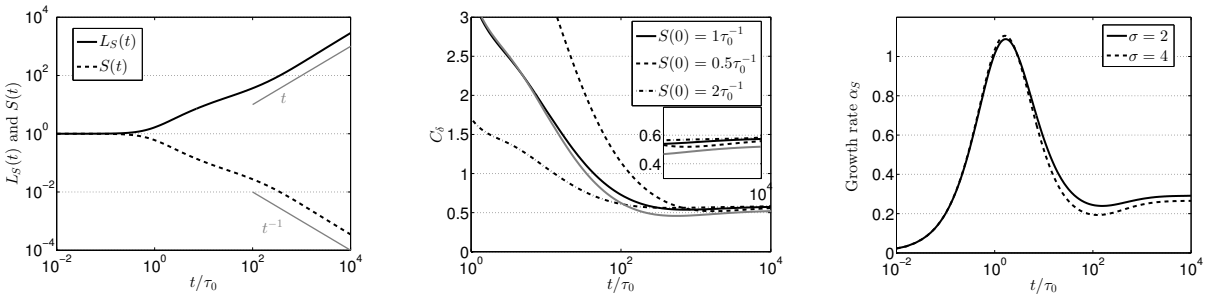

(a) (b) (c)

Figure 3.17: (a) Shear length $L_S(t)$ and shear rate $S(t)$ for Saffman turbulence ($\sigma = 2$). (b) C_δ, defined in (3.49), for $\sigma = 2$ (black), $L_S(0) = 1$ and various $S(0)$; and for $\sigma = 4$ (grey).

The linear dependence in time of the free-shear layer length L_S is assessed in Fig. 3.17a, for Saffman turbulence (Batchelor turbulence can be hardly distinguished from Saffman turbulence, thus it is not presented). The mean velocity gradient $S(t) = \Delta U/L_S(t)$ is also presented and obviously evolves in t^{-1}.

The parameter C_δ is presented in Fig. 3.17b for various initial values of the shear intensity $S(0)$. It seems that at sufficiently large Reynolds numbers, in the self-similar regime where $L_S \sim t$, C_δ does not depend on $S(0)$: a similar conclusion is obtained if $L_S(0)$ is varied instead of $S(0)$. The values of C_δ are such that $0.5 \leq C_\delta \leq 0.6$, higher than what is reported in Dimotakis (1991).

Finally, the growth rate α_S can be simply evaluated as

$$\alpha_S = \frac{\dot{L}_S}{\Delta U} = -\frac{8R_{13}}{(SL_S)^2}, \tag{3.51}$$

and is presented in Fig. 3.17c for both Saffman and Batchelor turbulence. It appears that there is a slight dependance of the free-shear layer length L_S on the infrared slope σ: indeed, it is slightly larger for $\sigma = 2$ ($\alpha_L = 0.29$) than for $\sigma = 4$ ($\alpha_L = 0.265$).

Part II

Transport and Mixing in Homogeneous Anisotropic Turbulence

Chapter 4

Spectral Modelling of a Passive Scalar in Homogeneous Turbulence

"I am among those who think that science has great beauty."

– Marie Curie

This chapter aims at modelling the transport of a passive scalar field and its associated scalar flux in homogeneous anisotropic turbulence (HAT), in order to address two configurations: homogeneous isotropic turbulence with a mean scalar gradient (HITSG), and homogeneous shear turbulent with a mean scalar gradient (HSTSG). Cases of shear-driven turbulence without a mean scalar gradient will also be studied. This part is an extension of the previous modelling dedicated to the velocity field. A similar two-step approach, called anisotropic EDQNM modelling, is consistently applied here. Firstly, dynamical equations that govern the passive scalar and scalar flux fields are closed using a quasi-normal approximation and an isotropic eddy-damping procedure without any assumption regarding anisotropy. Then, for moderately anisotropic flows, scalar spherically-averaged descriptors that depend only on the wavenumber modulus k are defined. In the end, the dynamics of the velocity, passive scalar and scalar flux fields is described by six generalized spherically-averaged Lin equations: three for the velocity field, two for the passive scalar, and one for the scalar flux. These equations are valid for arbitrary mean velocity and scalar gradients of moderate intensity.

The contents of this chapter and the following one were published in:
Briard, Gomez, & Cambon, "Spectral modelling for passive scalar dynamics in homogeneous anisotropic turbulence", *Journal of Fluid Mechanics*, **799**, 159-199 (2016)

Details on the calculations are provided in Appendix E along with additional considerations about the modelling of the scalar flux, and basic results about passive scalar dynamics in HIT framework are recalled in Chapter 1.

4.1 Scalar and scalar flux generalized Lin equations

The Reynolds decomposition for the scalar field T reads

$$T = \Theta + \theta, \qquad < \theta >= 0. \tag{4.1}$$

The mean-scalar gradient vector is written $\lambda_i = \partial_i \Theta$ so that $\Theta = \lambda_i x_i$. In physical space, the evolution equation of the scalar fluctuation θ in the homogeneous framework is

$$\frac{\partial \theta}{\partial t} + A_{jl} x_l \frac{\partial \theta}{\partial x_j} + u_j \lambda_j + \frac{\partial}{\partial x_j}(\theta u_j) = a \frac{\partial^2 \theta}{\partial x_j \partial x_j}. \tag{4.2}$$

The Fourier transform of the previous equation gives

$$\left(\frac{\partial}{\partial t} - A_{jl} k_j \frac{\partial}{\partial k_l} + a k^2 \right) \hat{\theta}(\boldsymbol{k}) + \lambda_j \hat{u}_j(\boldsymbol{k}) = -\mathrm{i} k_j \widehat{\theta u_j}(\boldsymbol{k}), \tag{4.3}$$

with the convolution product

$$\widehat{\theta u_j}(\boldsymbol{k}) = \int_{\boldsymbol{k}=\boldsymbol{p}+\boldsymbol{q}} \hat{\theta}(\boldsymbol{p}) \hat{u}_j(\boldsymbol{q}) \mathrm{d}^3 \boldsymbol{p}. \tag{4.4}$$

The spectral scalar-scalar correlation $\mathcal{E}^T$ is defined as

$$< \hat{\theta}^*(\boldsymbol{p}) \hat{\theta}(\boldsymbol{k}) >= \mathcal{E}^T(\boldsymbol{k}) \delta(\boldsymbol{k} - \boldsymbol{p}), \tag{4.5}$$

which corresponds to the two-point correlation $R^T(\boldsymbol{r}) =< \theta(\boldsymbol{x}) \theta(\boldsymbol{x} + \boldsymbol{r}) >$ in physical space. Its evolution is given by the **Yaglom equation** (A.97), firstly derived in Yaglom (1949), and recovered in Appendix A. The correlation $\mathcal{E}^T$ is real, satisfies $\mathcal{E}^T(\boldsymbol{k}) = \mathcal{E}^T(-\boldsymbol{k})$, and verifies the **scalar Craya equation**

$$\left(\frac{\partial}{\partial t} - A_{jl} k_j \frac{\partial}{\partial k_l} + 2 a k^2 \right) \mathcal{E}^T(\boldsymbol{k}, t) + 2 \lambda_j F_j(\boldsymbol{k}, t) = T^{\mathrm{T,NL}}(\boldsymbol{k}, t). \tag{4.6}$$

The **total non-linear scalar transfer** $T^{\mathrm{T,NL}}$ reads

$$\boxed{T^{\mathrm{T,NL}}(\boldsymbol{k}, t) = 2 k_i \Re \left(\int S_i^T(\boldsymbol{k}, \boldsymbol{p}, t) \mathrm{d}^3 \boldsymbol{p} \right).} \tag{4.7}$$

where $S_i^T(\boldsymbol{k}, \boldsymbol{p}, t)$ is the three-point third-order spectral velocity-scalar-scalar correlation

$$S_i^T(\boldsymbol{k}, \boldsymbol{p}, t) \delta(\boldsymbol{k} + \boldsymbol{p} + \boldsymbol{q}) = \mathrm{i} < \hat{u}_i(\boldsymbol{q}) \hat{\theta}(\boldsymbol{k}) \hat{\theta}(\boldsymbol{p}) > . \tag{4.8}$$

The spectral scalar-velocity correlation F_i - or the **scalar flux** - is defined as

$$< \hat{u}_i^*(\boldsymbol{p}) \hat{\theta}(\boldsymbol{k}) >= F_i(\boldsymbol{k}) \delta(\boldsymbol{k} - \boldsymbol{p}), \tag{4.9}$$

which corresponds to the two-point correlation $R_i^F(\boldsymbol{r}) =< u_i(\boldsymbol{x}) \theta(\boldsymbol{x} + \boldsymbol{r}) >$ in physical space. The scalar flux F_i is solenoidal and verifies the **scalar flux Craya equation**

$$\left(\frac{\partial}{\partial t} - A_{jl} k_j \frac{\partial}{\partial k_l} + (\nu + a) k^2 \right) F_i(\boldsymbol{k}, t) + M_{ij}(\boldsymbol{k}) F_j(\boldsymbol{k}, t) + \lambda_j \hat{R}_{ij}(\boldsymbol{k}, t) = T_i^{\mathrm{F,NL}}(\boldsymbol{k}, t). \tag{4.10}$$

The **non-linear scalar flux transfer** $T_F^{\mathrm{T,NL}}$ reads

$$\boxed{T_i^{\mathrm{F,NL}}(\boldsymbol{k},t) = P_{inm}(\boldsymbol{k}) \int S_{nm}^F(\boldsymbol{k},\boldsymbol{p},t)\mathrm{d}^3\boldsymbol{p} + k_j \int S_{ji}^{F*}(\boldsymbol{p},\boldsymbol{k},t)\mathrm{d}^3\boldsymbol{p},} \tag{4.11}$$

where $S_{nm}^F(\boldsymbol{k},\boldsymbol{p},t)$ is the three-point third-order spectral velocity-velocity-scalar correlation

$$S_{nm}^F(\boldsymbol{k},\boldsymbol{p},t)\delta(\boldsymbol{k}+\boldsymbol{p}+\boldsymbol{q}) = \mathrm{i} < \hat{u}_n(\boldsymbol{q})\hat{\theta}(\boldsymbol{k})\hat{u}_m(\boldsymbol{p}) > . \tag{4.12}$$

The expression of the non-linear scalar flux transfer (4.11) has also been obtained in recent study for active scalar dynamics (Burlot *et al.*, 2015*a*). Furthermore, $T_i^{\mathrm{F,NL}}$ can be written in a way similar to τ_{ij} for the kinetic case, namely

$$\tau_i^F(\boldsymbol{k},\boldsymbol{p},t) = k_n \int S_{ni}^F(\boldsymbol{k},\boldsymbol{p},t)\mathrm{d}^3\boldsymbol{p}, \tag{4.13}$$

so that the non-linear scalar flux transfer is

$$T_i^{\mathrm{F,NL}}(\boldsymbol{k},t) = \underbrace{\tau_i^F(\boldsymbol{k},\boldsymbol{p},t) + \tau_i^{*F}(\boldsymbol{p},\boldsymbol{k},t)}_{\text{True transfer}} + \underbrace{W_i^F(\boldsymbol{k},t)}_{\text{Pressure effects}} . \tag{4.14}$$

The term $W_i^F(\boldsymbol{k},t) = -\alpha_i\alpha_m\tau_m^F(\boldsymbol{k},\boldsymbol{p},t)$ is responsible for the return to isotropy of the cross-correlation F_i, *i.e.* the destruction of the scalar flux since it does not exist in the isotropic framework. The generalized Lin equations for the passive scalar and scalar flux are then

$$\left(\frac{\partial}{\partial t} + 2ak^2\right)\mathcal{E}^T(\boldsymbol{k},t) = T^{\mathrm{T,NL}}(\boldsymbol{k},t) + T^{\mathrm{T,L}}(\boldsymbol{k},t), \tag{4.15}$$

$$\left(\frac{\partial}{\partial t} + (\nu+a)k^2\right)F_i(\boldsymbol{k},t) = T_i^{\mathrm{F,NL}}(\boldsymbol{k},t) + T_i^{\mathrm{F,L}}(\boldsymbol{k},t), \tag{4.16}$$

where $T^{\mathrm{T,L}}$ is the **linear scalar transfer** and $T_i^{\mathrm{F,L}}$ the **linear scalar flux transfer**

$$T^{\mathrm{T,L}}(\boldsymbol{k},t) = A_{jl}k_j\frac{\partial\mathcal{E}^T(\boldsymbol{k},t)}{\partial k_l} - 2\lambda_l F_l(\boldsymbol{k},t), \tag{4.17}$$

$$T_i^{\mathrm{F,L}}(\boldsymbol{k},t) = A_{jl}k_j\frac{\partial F_i(\boldsymbol{k},t)}{\partial k_l} - M_{ij}(\boldsymbol{k})F_j(\boldsymbol{k},t) - \lambda_j\hat{R}_{ij}(\boldsymbol{k},t). \tag{4.18}$$

4.2 EDQNM closure for $\mathcal{E}^T$ and F_i

Now that the evolution equations of $\mathcal{E}^T$ and F_i have been derived, the next step is to close the non-linear terms with the EDQNM procedure described in Chapter 2. Then, in the following section, the resulting closed expressions of the non-linear terms will be combined with a consistent modelling for anisotropy.

The quasi-normal expressions for the passive scalar and scalar flux non-linear transfers $T^{\mathrm{T,NL}}$ and $T_i^{\mathrm{F,NL}}$ are

$$T^{\mathrm{T,NL}}(\boldsymbol{k},t) = 2k_i \int \theta_{kpq}^T \mathfrak{T}_i^{\mathrm{T,QN}}(\boldsymbol{k},t)\mathrm{d}^3\boldsymbol{p}, \tag{4.19}$$

$$T_i^{\mathrm{F,NL}}(\boldsymbol{k},\boldsymbol{p},t) = P_{imn}(\boldsymbol{k})\int \theta_{kpq}^F \mathfrak{T}_{nm}^{\mathrm{F,QN}}(\boldsymbol{k},\boldsymbol{p},t)\mathrm{d}^3\boldsymbol{p} + k_j \int \theta_{kpq}^{\mathrm{F,QN}} \mathfrak{T}_{ji}^{*F}(\boldsymbol{p},\boldsymbol{k},t)\mathrm{d}^3\boldsymbol{p}, \tag{4.20}$$

where θ_{kpq}^T and θ_{kpq}^F are the characteristic times of the third-order scalar and scalar flux correlations respectively

$$\theta_{kpq}^T = \frac{1-\exp\left[-(a(k^2+p^2)+\nu q^2+\mu_2(k)+\mu_2(p)+\mu_3(q))t\right]}{a(k^2+p^2)+\nu q^2+\mu_2(k)+\mu_2(p)+\mu_3(q)}, \tag{4.21}$$

$$\theta_{kpq}^F = \frac{1-\exp\left[-(ak^2+\nu(p^2+q^2)+\mu_2(k)+\mu_3(p)+\mu_3(q))t\right]}{ak^2+\nu(p^2+q^2)+\mu_2(k)+\mu_3(p)+\mu_3(q)}. \tag{4.22}$$

Both θ_{kpq}^T and θ_{kpq}^F are obtained by writing the evolution equation of the passive scalar and scalar flux third-order correlations defined in (4.8) and (4.12) respectively. Such an approach for the scalar case has already been performed by Bos *et al.* (2005) in the framework of homogeneous isotropic turbulence with a mean scalar gradient (HITSG). The eddy-damping terms μ_2 and μ_3 reflect departure from normal laws according to

$$\mu_i(k) = A_i\sqrt{\int_0^k u^2 E(u,t)\mathrm{d}u}, \qquad i=2,3, \tag{4.23}$$

with $A_2 = 0$ and $A_3 = 1.3$. The setting of A_2 and A_3 is discussed in Herring *et al.* (1982); Lesieur (2008), along with the choice of the eddy-damping terms μ_2 and μ_3. These two constants, also based on experimental considerations, are set to recover the Corrsin-Obukhov constant $K_{\mathrm{CO}} \simeq 0.75$, and no new constants are necessary for the scalar flux. Nevertheless, a different choice, for instance the setting $A_1 = A_2 = A_3$ which will be addressed in Chapter 7 for USHT, would lead to similar results; an alternative configuration is discussed by Bos (2005) to account for pressure effects in the damping. But here, with the present definition of the scalar flux third-order correlation (4.12), pressure effects are already taken into account: $A_2 = 0$ affects the equation involving $u_i(x_3)u_j(x_2)\partial_1\theta(x_1)$ which does not contain the fluctuating pressure. As a result of the quasi-normal approximation, $\mathfrak{T}_i^{\mathrm{T,QN}}$ and $\mathfrak{T}_{ij}^{\mathrm{F,QN}}$ can be written

$$\begin{aligned}\mathfrak{T}_i^{\mathrm{T,QN}}(\boldsymbol{k},\boldsymbol{p},t) &= 2P_{imn}(\boldsymbol{q})F_n(\boldsymbol{k},t)F_m(\boldsymbol{p},t)\\ &\quad + F_i^*(\boldsymbol{q},t)\Big(k_nF_n(\boldsymbol{p},t)+p_nF_n(\boldsymbol{k},t)\Big) - k_n\hat{R}_{ni}(\boldsymbol{q},t)\Big(\mathcal{E}^T(\boldsymbol{k},t)-\mathcal{E}^T(\boldsymbol{p},t)\Big),\end{aligned} \tag{4.24}$$

$$\begin{aligned}\mathfrak{T}_{ij}^{\mathrm{F,QN}}(\boldsymbol{k},\boldsymbol{p},t) &= k_n\Big(\hat{R}_{ni}(\boldsymbol{q},t)F_j^*(\boldsymbol{p},t)+\hat{R}_{nj}(\boldsymbol{p},t)F_i^*(\boldsymbol{q},t)\Big)\\ &\quad + 2F_m(\boldsymbol{k},t)\Big(P_{imn}(\boldsymbol{q})\hat{R}_{nj}(\boldsymbol{p},t)+P_{jmn}(\boldsymbol{p})\hat{R}_{ni}(\boldsymbol{q},t)\Big).\end{aligned} \tag{4.25}$$

With this closure, and using calculations similar to the kinetic case detailed in Appendix E, the non-linear scalar transfer becomes

$$\begin{aligned}T^{\mathrm{T,NL}}(\boldsymbol{k},t) &= 2\int \theta_{kpq}^T kp(xy+z)(\mathcal{E}''+\Re X'')(\mathcal{E}^{T'}-\mathcal{E}^T)\mathrm{d}^3\boldsymbol{p}\\ &\quad + 2\int \theta_{kpq}^T\Big(k_nF_n''^*(p_mF_m+k_mF_m')+p_mF_mk_nF_n'\frac{ky-px}{q}\Big)\mathrm{d}^3\boldsymbol{p}.\end{aligned} \tag{4.26}$$

Since the contributions of the velocity-scalar correlation F_i are quadratic in anisotropy, they are neglected in what follows in the moderate anisotropy framework. These quadratic contributions of anisotropy in the non-linear transfers for the scalar and the scalar flux are nevertheless calculated in Appendix E. The modelling of $F_i(\boldsymbol{k})$ is developed with an appropriate decomposition

in the following section.

4.3 Final spherically-averaged scalar Lin equations

This section presents the final step of the modelling: combining the modelling of anisotropy with the closed expressions of the transfers obtained by EDQNM. Spherically averaged evolution equations for the scalar variance spectrum, the scalar directional anisotropy and the scalar flux are derived from the previous generalized scalar Lin equations: these final scalar equations depend only on the modulus k of the wavevector $\boldsymbol{k}$.

4.3.1 Modelling of $\mathcal{E}^T$ and F_i

A decomposition similar to the one of $\mathcal{E}$ in the kinetic case is used for the scalar correlation $\mathcal{E}_T$ since both $\mathcal{E}$ and $\mathcal{E}^T$ verify the same properties

$$\boxed{\mathcal{E}^T(\boldsymbol{k},t) = \frac{E_T(k,t)}{4\pi k^2}\Big(1 - 15H_{ij}^{(T)}(k,t)\alpha_i\alpha_j\Big) = \mathcal{E}_0^T + \mathcal{E}^{(\mathrm{T,dir})},} \tag{4.27}$$

with $\mathcal{E}^{(\mathrm{T,dir})} = -15\mathcal{E}_0^T H_{ij}^{(T)}\alpha_i\alpha_j$ and $\mathcal{E}_0^T = E_T/(4\pi k^2)$. One can remark that the fourth-order expansion of $\mathcal{E}^T$ would be similar to the one of $\mathcal{E}$. The following expansion is chosen for the scalar flux

$$\boxed{F_i(\boldsymbol{k},t) = \frac{3}{2}\mathcal{E}_j^F(k,t)P_{ij}(\boldsymbol{k}) + (\text{Antisymmetric contribution}).} \tag{4.28}$$

This decomposition is consistent with the scalar flux being a solenoidal field ($k_iF_i = 0$). Hermitian symmetry for the scalar flux, $F_i(-\boldsymbol{k}) = F_i^*(\boldsymbol{k})$, is straightforward from the decomposition of a vector into helical modes. Notably, it implies that the vector $\mathcal{E}_j^F$ is purely real and that the antisymmetric contribution is purely imaginary. The antisymmetric part brings an imaginary contribution to the scalar flux, which is zero in isotropic turbulence with or without mean scalar gradient, and which will be discussed in Chapter 8. Consequently, without helicity, only the projection part of (4.28) is considered here. Using a helical decomposition for F_i shows that (see Appendix E) the scalar flux has a poloidal structure. Moreover, one can derive a realizability condition for the scalar field, starting from the decomposition (4.27) of $\mathcal{E}^T$, analogous to (2.52) for the kinetic field

$$\max_i(L_i^T) \leq \frac{1}{15}, \tag{4.29}$$

where L_i^T are eigenvalues of $H_{ij}^{(T)}$.

The decompositions (4.27) and (4.28) are exact in the framework of homogeneous isotropic turbulence with a mean scalar gradient (Herr *et al.*, 1996). Whereas they are truncations at the the second order of the scalar correlation $\mathcal{E}^T$ and scalar flux F_i expansions in shear-driven turbulence, consistently with the modelling for the velocity field of $\mathcal{E}$ and Z done in (2.44) and (2.45).

About the distinction between directional and polarization anisotropies: scalars admit directional anisotropy only. Consequently, $H_{ij}^{(T)}$, which appears in the expansion of $\mathcal{E}^T$, reflects directional anisotropy, as $H_{ij}^{(\mathrm{dir})}$ in the decomposition (2.44) of $\mathcal{E}$. Then, since F_i is a vector, $\mathcal{E}_j^F$ represents polarization anisotropy. Finally, a solenoidal second-order tensor such as $\hat{R}_{ij}$ admits both contributions. This classification is summarized in Table 4.1.

The scalar variance spectrum is given by

$$E_T(k,t) = \int_{S_k} \mathcal{E}^T(\boldsymbol{k},t)\mathrm{d}^2\boldsymbol{k}. \tag{4.30}$$

The spectral scalar directional anisotropy descriptor $H_{ij}^{(T)}$ and the spherically-averaged scalar flux E_i^F verify

$$2E_T(k,t)H_{ij}^{(T)}(k,t) = \int_{S_k} \mathcal{E}^{(\mathrm{T,dir})}(\boldsymbol{k},t)P_{ij}(\boldsymbol{k})\mathrm{d}^2\boldsymbol{k}, \tag{4.31}$$

$$E_i^F(k,t) = \int_{S_k} F_i(\boldsymbol{k},t)\mathrm{d}^2\boldsymbol{k}, \tag{4.32}$$

where $4\pi k^2\mathcal{E}_i^F = E_i^F(k,t)$. The scalar anisotropy tensor b_{ij}^T is defined as

$$b_{ij}^T(t) = \frac{1}{K_T(t)}\int_0^\infty E_T(k,t)H_{ij}^{(T)}(k,t)\mathrm{d}k, \tag{4.33}$$

where K_T is the **scalar variance**,

$$K_T(t) =< \theta^2 >= \int_0^\infty E_T(k,t)\mathrm{d}k. \tag{4.34}$$

The global anisotropy indicators b_{ij}^T have a function analogous to the kinetic ones b_{ij}. Similar anisotropy descriptors were introduced by Kassinos *et al.* (2007) with a different convention. Finally, the **second-order spectral scalar tensor** ϕ_{ij}^T can then be written

$$\phi_{ij}^T(k,t) = 2E_T(k,t)\left(\frac{\delta_{ij}}{3} + H_{ij}^{(T)}(k,t)\right). \tag{4.35}$$

One can note that these definitions for the passive scalar field are very similar to the kinetic one.

4.3.2 Spherical average of the passive scalar and scalar flux

The **spherically-averaged scalar and scalar flux Lin equations** are then

$$\boxed{\begin{aligned}
\left(\frac{\partial}{\partial t} + 2ak^2\right)E_T(k,t) &= S^{\mathrm{T,L(iso)}}(k,t) + S^{\mathrm{T,NL(iso)}}(k,t), && (4.36)\\
\left(\frac{\partial}{\partial t} + 2ak^2\right)E_T(k,t)H_{ij}^{(T)}(k,t) &= S_{ij}^{\mathrm{T,L(dir)}}(k,t) + S_{ij}^{\mathrm{T,NL(dir)}}(k,t), && (4.37)\\
\left(\frac{\partial}{\partial t} + (a+\nu)k^2\right)E_i^F(k,t) &= S_i^{\mathrm{F,L}}(k,t) + S_i^{\mathrm{F,NL}}(k,t). && (4.38)
\end{aligned}}$$

The usual **non-linear spherically-averaged isotropic scalar transfer** term $S^{\mathrm{T,NL(iso)}}$ is

$$S^{\mathrm{T,NL(iso)}}(k,t) = \int_{S_k} T^{\mathrm{T,NL}}(\boldsymbol{k},t)\mathrm{d}^2\boldsymbol{k} \tag{4.39}$$

$$= 16\pi^2 \int_{\Delta_k} \theta^T_{kpq} k^2 p^2 q(xy+z)\mathcal{E}''_0(\mathcal{E}^{T'}_0 - \mathcal{E}^T_0)\mathrm{d}p\mathrm{d}q, \tag{4.40}$$

in agreement with Lesieur (2008). The **non-linear spherically-averaged directional scalar transfer** term $S^{\mathrm{T,NL(dir)}}_{ij}$ reads

$$S^{\mathrm{T,NL(dir)}}_{ij}(k,t) = \frac{1}{2}\int_{S_k} T^{\mathrm{T,NL}}(\boldsymbol{k},t)P_{ij}(\boldsymbol{k})\,\mathrm{d}^2\boldsymbol{k} - \frac{\delta_{ij}}{3}S^{\mathrm{T,NL(iso)}}(k,t) \tag{4.41}$$

$$\begin{aligned}
&= 4\pi^2 \int_{\Delta_k} \theta^T_{kpq} k^2 p^2 q(xy+z)(y^2-1)\mathcal{E}''_0(\mathcal{E}^{T'}_0 - \mathcal{E}^T_0)H^{(\mathrm{pol})''}_{ij}\mathrm{d}p\mathrm{d}q \\
&+ 8\pi^2 \int_{\Delta_k} \theta^T_{kpq} k^2 p^2 q(xy+z)(3y^2-1)\mathcal{E}''_0(\mathcal{E}^{T'}_0 - \mathcal{E}^T_0)H^{(\mathrm{dir})''}_{ij}\mathrm{d}p\mathrm{d}q \\
&+ 8\pi^2 \int_{\Delta_k} \theta^T_{kpq} k^2 p^2 q(xy+z)\mathcal{E}''_0\Big((3z^2-1)\mathcal{E}^{T'}_0 H^{(T)'}_{ij} - 2\mathcal{E}^T_0 H^{(T)}_{ij}\Big)\mathrm{d}p\mathrm{d}q.
\end{aligned} \tag{4.42}$$

The isotropic term $S^{\mathrm{T,NL(iso)}}$ is a conservative transfer, meaning that its integral over k is zero. However, the integral of $S^{\mathrm{T,NL(dir)}}_{ij}$ is different from zero, as the directional transfer in the kinetic case. This means that there is a return to isotropy of the passive scalar. Nevertheless, it is not possible to extract an explicit RTI term from $S^{\mathrm{T,NL(dir)}}_{ij}$, since this mechanism is led by the pressure field which is absent of the scalar equations. This means that the RTI of the scalar field is driven by the velocity field. The production terms depend linearly both on the mean velocity and scalar gradients: the **linear spherically-averaged isotropic scalar transfer** $S^{\mathrm{T,L(iso)}}$ is

$$S^{\mathrm{T,L(iso)}}(k,t) = \int_{S_k} T^{\mathrm{T,L}}(\boldsymbol{k},t)\mathrm{d}^2\boldsymbol{k} \tag{4.43}$$

$$= -2A^+_{ln}\frac{\partial}{\partial k}(kE_T H^{(T)}_{ln}) - 2\lambda_l E^F_l. \tag{4.44}$$

The **linear spherically-averaged directional scalar transfer** $S^{\mathrm{T,L(dir)}}_{ij}$ is

$$S^{\mathrm{T,L(dir)}}_{ij}(k,t) = \frac{1}{2}\int_{S_k} T^{\mathrm{T,L}}(\boldsymbol{k},t)P_{ij}(\boldsymbol{k})\mathrm{d}^2\boldsymbol{k} - \frac{\delta_{ij}}{3}S^{\mathrm{T,L(iso)}}(k,t) \tag{4.45}$$

$$\begin{aligned}
&= -\frac{3}{7}E_T\Big(A^+_{lj}H^{(T)}_{il} + A^+_{li}H^{(T)}_{jl} - \frac{2}{3}A^+_{ln}\delta_{ij}H^{(T)}_{ln}\Big) + \frac{1}{5}A^+_{ij}E_T \\
&- \frac{1}{15}A^+_{ij}\frac{\partial}{\partial k}(kE_T) - E_T\Big(A^-_{lj}H^{(T)}_{il} + A^-_{li}H^{(T)}_{jl}\Big) - \frac{1}{10}\Big(\lambda_i E^F_j + \lambda_j E^F_i - \frac{2}{3}\lambda_l E^F_l\delta_{ij}\Big) \\
&+ \frac{2}{7}\left(A^+_{il}\frac{\partial}{\partial k}(kE_T H^{(T)}_{jl}) + A^+_{jl}\frac{\partial}{\partial k}(kE_T H^{(T)}_{il}) - \frac{2}{3}A^+_{lm}\delta_{ij}\frac{\partial}{\partial k}(kE_T H^{(T)}_{lm})\right).
\end{aligned} \tag{4.46}$$

At first order in anisotropy, with the decomposition (4.28), the non-linear scalar flux transfer becomes

$$T^{\mathrm{F,NL}}_i(\boldsymbol{k},t) = \frac{3}{2}\int \theta^F_{kpq} k\mathcal{E}'_0\Bigg[\mathcal{E}^F_j\Bigg(2px(\alpha_i + z\alpha'_i)(\alpha''_j + y\alpha_j)$$

$$
\begin{aligned}
&+ q(y+xz)\Big(2\alpha_i''(\alpha_j''+y\alpha_j)-P_{ij}\Big)\Big) + k\mathcal{E}_j^{F''}\Big((1-z^2)P_{ij}''+(\alpha_i+z\alpha_i')(\alpha_j+y\alpha_j'')\Big)\Big]\mathrm{d}^3\boldsymbol{p}\\
&+\frac{3}{2}\int\theta_{pkq}^F k\Big[q\mathcal{E}_0\mathcal{E}_j^{F'}(\alpha_i''+y\alpha_i)\Big(\alpha_j+z\alpha_j'+2y(\alpha_j''+x\alpha_j')\Big)\\
&+k\mathcal{E}_0''\mathcal{E}_j^{F'}\Big((\alpha_i+y\alpha_i'')(\alpha_j+z\alpha_j')+(1-y^2)\Big(P_{ij}'-2\alpha_i(\alpha_j+z\alpha_j')\Big)\Big)\\
&+p\Big(\mathcal{E}_0\mathcal{E}_j^{F''}(\alpha_i'+z\alpha_i)(\alpha_j+y\alpha_j'')-(xy+z)\mathcal{E}_0''\mathcal{E}_j^F P_{ij}\Big)\Big]\mathrm{d}^3\boldsymbol{p}\\
&-3\int\theta_{kpq}^F k\alpha_i\Big[k(1-y^2)\mathcal{E}_0''\mathcal{E}_j^{F'}(\alpha_j+z\alpha_j')+q\mathcal{E}_0'\mathcal{E}_j^F(1-z^2-2y(y+xz))(\alpha_j''+y\alpha_j)\Big]\mathrm{d}^3\boldsymbol{p}.
\end{aligned}
\tag{4.47}
$$

Since quadratic contributions of anisotropy are discarded, but nevertheless computed in Appendix E, only the isotropic part of the kinetic field appears. The **non-linear spherically-averaged scalar flux transfer** is thus

$$
S_i^{\mathrm{F,NL}}(k,t)=\int_{S_k}T_i^{\mathrm{F,NL}}(\boldsymbol{k},t)\mathrm{d}^2\boldsymbol{k} \tag{4.48}
$$

$$
\begin{aligned}
&=4\pi^2\int_{\Delta_k}\theta_{kpq}^F k^2pq\mathcal{E}_0'\Big[k\mathcal{E}_i^{F''}(1+y^2-z^2-xyz-2y^2z^2)-2q(y^3+xz)\mathcal{E}_i^F\Big]\mathrm{d}p\mathrm{d}q\\
&+4\pi^2\int_{\Delta_k}\theta_{pkq}^F k^2pq\Big[\mathcal{E}_0\Big(qz(2xy^2+yz-x)\mathcal{E}_i^{F'}-py(x+yz)\mathcal{E}_i^{F''}\Big)\\
&+k\mathcal{E}_0''\Big((1-y^2+z^2-xyz-2y^2z^2)\mathcal{E}_i^{F'}-2(1-y^2)\mathcal{E}_i^F\Big)\Big]\mathrm{d}p\mathrm{d}q.
\end{aligned}
\tag{4.49}
$$

One can extract from the non-linear scalar-flux transfer the **spherically-averaged scalar flux RTI transfer**

$$
S_i^{\mathrm{F,RTI}}(k,t)=-8\int_{\Delta_k}\pi^2\theta_{kpq}^F k^3pq\mathcal{E}_0'\mathcal{E}_i^{F''}(1-y^2)(1-z^2)\mathrm{d}p\mathrm{d}q. \tag{4.50}
$$

The **linear spherically-averaged scalar flux transfer** reads

$$
S_i^{\mathrm{F,L}}(k,t)=\int_{S_k}T_i^{\mathrm{F,L}}(\boldsymbol{k},t)\mathrm{d}^2\boldsymbol{k} \tag{4.51}
$$

$$
=-2\lambda_jE\Big(\frac{1}{3}\delta_{ij}+H_{ij}^{(\mathrm{dir})}+H_{ij}^{(\mathrm{pol})}\Big)-\frac{1}{5}A_{ij}^{+}\Big(2E_j^F+\frac{\partial}{\partial k}(kE_j^F)\Big). \tag{4.52}
$$

As a conclusion, the whole dynamics of a passive scalar field in homogeneous anisotropic turbulence is driven by six spherically-averaged compact equations. Three for the velocity field coming from Chapter 2, two for the passive scalar and one for the scalar flux. The last three ones are original results of the present work. The different anisotropy descriptors are gathered in Table 4.1.

$\boldsymbol{k}$-vectors descriptors	Spherically averaged descriptors		
	Isotropy	Directional anisotropy	Polarization anisotropy
$\mathcal{E}(\boldsymbol{k},t)$	$E(k,t)$	$H_{ij}^{(\mathrm{dir})}(k,t)$	0
$Z(\boldsymbol{k},t)$	0	0	$H_{ij}^{(\mathrm{pol})}(k,t)$
$\mathcal{E}^T(\boldsymbol{k},t)$	$E_T(k,t)$	$H_{ij}^{(T)}(k,t)$	0
$F_i(\boldsymbol{k},t)$	0	0	$E_i^F(k,t)$

Table 4.1: Description of anisotropy at the velocity, passive scalar and scalar flux levels, using $\boldsymbol{k}$-vectors descriptors and their corresponding spherically-averaged contributions.

4.4 Cospectrum for an uniform mean scalar gradient

In this section, the emphasis is put on homogeneous isotropic turbulence with a mean scalar gradient (HITSG). The scalar flux is created by an uniform mean gradient

$$\boldsymbol{\lambda} = (0, 0, -\Lambda), \qquad \Lambda > 0, \tag{4.53}$$

whereas the kinetic field remains fully isotropic, and thus decays with time. In this framework, which has been widely investigated notably by Bos and coworkers, turbulent eddies bring the hot fluid to the cooler parts of the flow (and the opposite), thus creating a heat flux. Some definitions are given before starting the numerical study in the next chapter. Firstly, when the kinetic field is isotropic, it tends to destroy the scalar flux, created by the scalar gradient. Given the expression of the production term $S_i^{\mathrm{F,L}}$, only the third component of E_i^F is non-zero, and its sign is opposite to the one of Λ. Thus, the **cospectrum** is defined as

$$\mathcal{F}(k,t) = E_3^F(k,t), \tag{4.54}$$

the **mixed velocity-scalar correlation** as

$$K_{\mathcal{F}}(t) =< u_3\theta >= \int_0^\infty \mathcal{F}(k,t)\mathrm{d}k, \tag{4.55}$$

and the **cospectrum dissipation rate** as

$$\epsilon_{\mathcal{F}}(t) = (\nu + a)\int_0^\infty k^2\mathcal{F}(k,t)\mathrm{d}k. \tag{4.56}$$

Finally, the time evolution of the velocity-scalar correlation $R_i^F(t) =< u_i(t)\theta(t) >$, for $\boldsymbol{r} = \boldsymbol{0}$, is given by

$$\frac{\mathrm{d}R_i^F}{\mathrm{d}t} + R_{ij}\lambda_j + A_{ij}R_j^F =< p\frac{\partial\theta}{\partial x_i} > -2\epsilon_i^F - a < \theta\frac{\partial^2 u_i}{\partial x_l\partial x_l} > -\nu < u_i\frac{\partial^2\theta}{\partial x_l\partial x_l} >,$$

with

$$\epsilon_i^F(t) = (\nu + a) < \frac{\partial u_i}{\partial x_l}\frac{\partial\theta}{\partial x_l} > . \tag{4.57}$$

The last three rhs terms of the equation for R_i^F simplify into $-\epsilon_i^F$ using homogeneity. The evolution equation of ϵ_i^F has not received much attention, and is therefore derived and simplified for homogeneous turbulence in Appendix A, and then for HITSG in (A.34). In the classical case

of a (vertical) mean scalar gradient, $R_3^F = K_{\mathcal{F}}$ and the previous evolution equation simplifies into

$$\frac{\mathrm{d}K_{\mathcal{F}}}{\mathrm{d}t} = P_{\mathcal{F}}(t) - \epsilon_{\mathcal{F}}(t) + \Pi_{\mathcal{F}}(t), \tag{4.58}$$

where

$$\Pi_{\mathcal{F}}(t) = \int_0^\infty S_3^{\mathrm{F,NL}}(k,t)\mathrm{d}k \tag{4.59}$$

is the **cospectrum destruction**, or cospectrum pseudo return to isotropy, driven by the kinetic field. And $P_{\mathcal{F}}$ is the **cospectrum production** term

$$P_{\mathcal{F}}(t) = \int_0^\infty S_3^{\mathrm{F,L}}(k,t)\mathrm{d}k = \frac{2}{3}\Lambda K(t), \tag{4.60}$$

which decays with time along with the kinetic energy.

Chapter 5

Dynamics of a Passive Scalar in Homogeneous Turbulence

In this chapter, the complete anisotropic EDQNM modelling is used to investigate the dynamics of a scalar field and its flux, passively advected by the homogeneous turbulent flow. The Prandtl number Pr is set to unity, and cases of $Pr \ll 1$ and $Pr \gg 1$ are addressed in Chapter 6. The extension to active scalar dynamics in homogeneous unstably stratified turbulence is presented in Chapter 7.

> The contents of this chapter and the previous one were published in:
> Briard, Gomez, & Cambon, "Spectral modelling for passive scalar dynamics in homogeneous anisotropic turbulence", *Journal of Fluid Mechanics*, **799**, 159-199 (2016)

The study of a passive scalar, such as small temperature fluctuations θ, convected by a turbulent velocity field u_i, is of interest for several reasons. From a fundamental point of view: though HAT has been at the center of many theoretical, numerical and experimental works for almost 40 years, numerous questions still remain without clear answers. How does the energy, mainly produced at large scales by mean velocity and scalar gradients, affect the small scales dynamics? Is there a complete return to isotropy of small scales? Is the growth or decay of integrated quantities, such as the kinetic energy and the scalar variance, predictable?

Upstream to these fundamental questions, there are practical reasons to the investigation of HAT. Indeed, taking into account anisotropy created by non-zero mean fields is an important feature to describe real flows by comparison to the classical case of HIT. Notably, the deep understanding of homogeneous turbulence dynamics could provide further insights into the analysis of high Reynolds numbers natural flows such as atmospheric and oceanic ones. Such flows are complex for multiple reasons, one being that their Reynolds numbers are much higher than the ones currently reachable in DNS and experiments. For instance, Re_λ can be of order 10^4 in atmospheric flows. Such large Reynolds numbers simulations without modelling would require huge computational resources to capture only the early stage of the dynamics, and would need a fine description of all scales, from the most energetic ones to the dissipative ones at the level of the Kolmogorov wavenumber k_η. In addition to very high Reynolds numbers involved in atmospheric flows, the nature itself of such flows is complex since it contains many different

physical phenomena. Indeed, a fine description of atmospheric dynamics would require to take into account rotation, helicity, stratification, shear, and mean scalar gradient from the ground to high altitude (Wyngaard & Coté, 1972).

Mean velocity and scalar gradients are also deeply associated to production mechanisms in the turbulence dynamics regardless of the flow type. Indeed, they play a fundamental role in the energy transfers through scales. Therefore, insights concerning the role of mean velocity and scalar gradients are of great interest for turbulent flows, and specifically the ones where departure from isotropy is generated by anisotropic forces or by solid walls giving rise to shearing stresses. Moreover, a better understanding of all these anisotropic turbulent flows could be obtained by making separate investigations of isolated mechanisms at high Reynolds numbers, which are still quite unreachable using DNS. This is the approach followed in this study. In order to achieve this objective, the dynamics of a passive scalar field θ and its flux $< u_i\theta >$ in HAT is addressed with the use of the anisotropic EDQNM modelling developed in Chapters 2 and 4. It is worth noting that the present model is developed for arbitrary mean velocity gradients that produce energy: consequently it is not adapted to the case of purely rotating turbulence in which there is no energy production and where the dynamics is dominated by dispersive inertial waves interacting non-linearly, requiring even more complex tools (Cambon & Jacquin, 1989; Sagaut & Cambon, 2008). The emphasis is thus put on three different configurations: Homogeneous Isotropic Turbulence with a mean Scalar Gradient (HITSG), Homogeneous Shear Turbulence (HST), and finally, these two frameworks are combined into Homogeneous Shear Turbulence with mean Scalar Gradient (HSTSG) as notably encountered in atmospheric flows.

In HITSG, the mean scalar gradient produces scalar fluctuations so that the scalar variance $< \theta^2 >$ can increase whereas the isotropic velocity field is decaying. This mean scalar gradient creates an anisotropic flux $< u_3\theta >$, called the cospectrum in spectral space, which has received a lot of attention: with spectral closures (Herr *et al.*, 1996; Bos *et al.*, 2004, 2005; O'Gorman & Pullin, 2005), with DNS (Pumir, 1994; Overholt & Pope, 1996), theoretically (Lumley, 1967), and experimentally (Venkataramani & Chevray, 1978; Warhaft, 1980; Sirivat & Warhaft, 1983; Mydlarski & Warhaft, 1998; Mydlarski, 2003). In all these studies, the scaling of the cospectrum is uncertain in the inertial range, $k^{-7/3}$ or k^{-2}: this point is addressed hereafter.

The case of a mean velocity gradient without mean scalar gradient, has been less studied: a rapid decrease of $K_T =< \theta^2 >$ was observed experimentally (Warhaft, 1980; Karnik & Tavoularis, 1989), and this has been confirmed theoretically (Gonzalez, 2000). Interestingly, in such a configuration, the evolution of the passive scalar field is completely different from the one of the velocity field.

Finally, when both mean velocity and scalar gradients are applied, there is a continuous production of kinetic energy $K(t)$ which grows exponentially for large dimensionless times St. Consequently, thanks to interactions with the scalar flux, K_T grows exponentially as well. The HSTSG configuration has been at the center of many works as well: with a classical EDQNM approach (Bos & Bertoglio, 2007), with DNS (Shirani *et al.*, 1981; Rogers *et al.*, 1989; Brethouwer, 2005; Kassinos *et al.*, 2007) and experimentally (Tavoularis & Corrsin, 1981; Danaila *et al.*, 1999*b*; Ferchihi & Tavoularis, 2002). Even without rotation, the HSTSG configuration remains quite representative of atmospheric flows (Wyngaard & Coté, 1972). Another configuration where the kinetic energy, the scalar variance and the mixed-correlation grow exponentially conjointly is analyzed in Chapter 7 for active scalar dynamics.

Besides, the small scales RTI for each of the three cases presented is of primary importance: indeed, according to Kolmogorov (1941*b*), small scales of the flow should return to isotropy whatever the large scales are. While the small scales RTI of second-order moments of the velocity field is well-admitted (Sarkar & Speziale, 1990; Pumir, 1996; Garg & Warhaft, 1998; Shen & Warhaft, 2000), the case of third-order moments - such as the velocity derivative skewness in shear flows - is still an open question. Some considerations about statistics in HST are proposed in A. Moreover, it appeared that the scalar case is even more complicated, since the conclusion is not clear regarding second-order moments: departure from isotropy are observed experimentally and numerically at small scales with a mean scalar gradient only, in shear-driven flows, in boundary layers and in jets (Sreenivasan *et al.*, 1979; Sreenivasan & Tavoularis, 1980; Sreenivasan, 1991; Pumir, 1994; Danaila *et al.*, 1999*b*).

Consequently, and in order to clarify the RTI of the scalar small scales, high Reynolds numbers anisotropic flows are investigated thanks to the present anisotropic EDQNM modelling. For the different configurations (HST, HITSG, HSTSG, HSRT), comparisons with DNS and experiments are proposed in order to validate the model. Then, new numerical and theoretical results at very high Reynolds numbers are presented. The evolution equation of the scalar variance $K_T(t)$ in homogeneous turbulence reads

$$\frac{\mathrm{d}K_T}{\mathrm{d}t} = -2\lambda_j R_j^F(t) - \epsilon_T(t), \tag{5.1}$$

where the scalar variance dissipation rate ϵ_T is

$$\epsilon_T(t) = 2a\int_0^\infty k^2 E_T(k,t)\mathrm{d}k = 2a < \frac{\partial\theta}{\partial x_l}\frac{\partial\theta}{\partial x_l} > . \tag{5.2}$$

The evolution equation of ϵ_T in homogeneous turbulence is derived in Appendix A.

5.1 Homogeneous shear-driven turbulence

In this section, the effects of a mean shear on the passive scalar dynamics are studied. Firstly, the scalar variance spectrum $E_T(k,t)$ is briefly investigated. Then, HSRT is addressed. Finally, the emphasis is put on HST, which presents an interesting result regarding the different behaviours of the kinetic energy and the scalar variance. All results regarding the passive scalar decay and growth laws in HSRT and HST are gathered in Table 5.1.

5.1.1 Scalar spectrum $E_T(k,t)$ and non-linear transfers

It can be shown by dimensional analysis that the scalar spectral tensor linked to the shear extra-diagonal component ϕ_{13}^T also evolves as $k^{-7/3}$ in the inertial range between the scalar integral wavenumber $k_T = 1/L_T$ and the Kolmogorov wavenumber k_η. One has to assume that ϕ_{13}^T depends on the kinetic energy dissipation rate ϵ, the scalar variance dissipation rate ϵ_T, the wavenumber k and the shear rate S. Since the transport equation of a passive scalar is linear with u_i, it is assumed that $\phi_{13}^T(k^a, \epsilon^b, \epsilon_T^c, S^d) = \phi_{13}^T(k^a, \epsilon^b, \epsilon_T^c, S)$. Dimension analysis yields

$$\phi_{13}^T(k,t) \sim S\epsilon^{-2/3}\epsilon_T k^{-7/3}. \tag{5.3}$$

This $k^{-7/3}$ range is recovered both in HSRT and HST. Only the case of HSRT is presented in Fig. 5.1a. It has been said in Chapter 4 that the spherically-averaged non-linear directional scalar transfer $S_{ij}^{\mathrm{T,NL(dir)}}$ has a non-zero integral over k because the RTI process is driven by the kinetic field only. This is illustrated in Fig. 5.1b along with the isotropic scalar transfer $S^{\mathrm{T,NL(iso)}}$ which has zero integral over k.

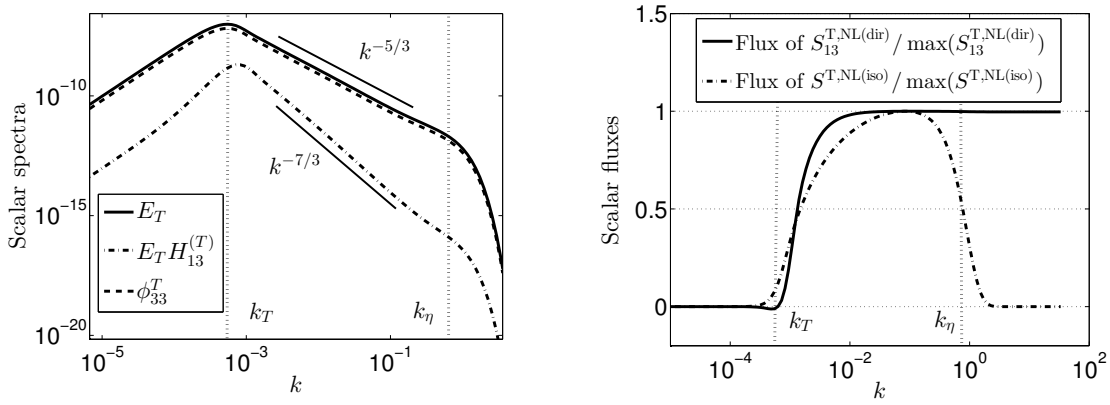

(a) (b)

Figure 5.1: (a) Scalar variance spectrum $E_T(k,t)$ and spectral tensors $\phi_{13}^T(k,t)$ and $\phi_{33}^T(k,t)$ for $\sigma = 2$ with $St = 1$. (b) Fluxes of $S_{13}^{\mathrm{T,NL(dir)}}$ and $S^{\mathrm{T,NL(iso)}}$.

5.1.2 Scalar decay laws and RTI in HSRT

The scalar decay exponent α_T of the scalar variance K_T is well-known thanks to the CBC theory. This decay exponent has been extended to the case of Batchelor HIT for a passive scalar field in Chapter 1, using a scalar backscatter parameter p_T similar to p for the kinetic field

$$K_T(t) \sim t^{\alpha_T}, \qquad \alpha_T = -2\frac{\sigma_T - p_T + 1}{\sigma - p + 3}, \tag{5.4}$$

where $p_T(\sigma = \sigma_T = 4) = 0.27$ and $p_T(\sigma = \sigma_T \leq 3) = 0$. This parameter p_T slightly depends on the Prandtl number and much more on the kinetic infrared slope σ. In Fig. 5.2, both low and large Reynolds numbers scalar decay exponents are recovered for Saffman and Batchelor HSRT.

Then, the return to isotropy of the scalar field is driven by the kinetic one: the consequence of this is that no explicit scalar RTI transfer term can be derived. Nevertheless, the RTI mechanism can be observed thanks to the anisotropy indicators b_{ij}^T in Fig. 5.3a for Saffman turbulence. An asymptotic anisotropic state is reached, similar to the kinetic one. The final non-zero values of b_{ij}^T indicate that there is still anisotropy left after the release of the velocity gradients. Batchelor turbulence is not presented, but the b_{ij}^T are found to continuously decrease, like the kinetic case in Chapter 3.

As revealed in Fig. 5.3b, the anisotropy of the scalar field is mostly contained in large scales around the scalar integral wavenumber k_T. Small scales have almost returned to isotropy ($H_{ij}^{(T)} \simeq 0$), but not completely for the extra-diagonal component, as revealed by the zoom near k_η. The kinetic indicator $H_{ij}^{()}$ are zero at small scales, whereas there is some anisotropy left

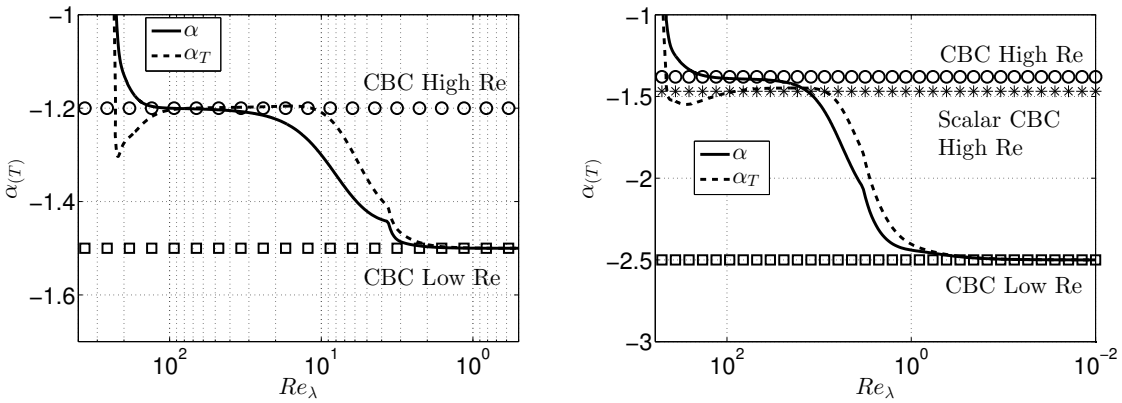

(a) (b)

Figure 5.2: Scalar and kinetic decay exponents α_T and α in both high and low Reynolds regimes, with $St = 1$, where symbols represent theoretical predictions. (a) $\sigma = 2$; (b) $\sigma = 4$.

here in the scalar small scales. This is consistent with most of the numerical and experimental observations, as it will be discussed later on. A deeper investigation of local isotropy is proposed at the end of this chapter for HSTSG.

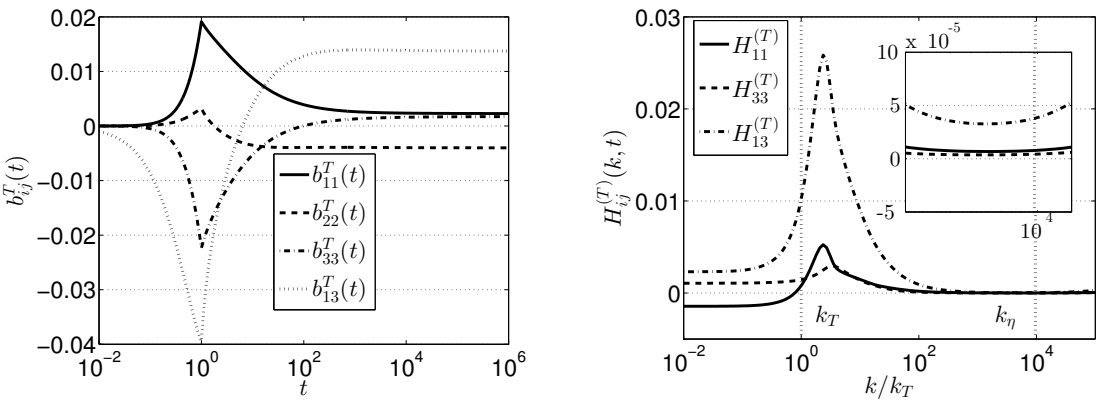

(a) (b)

Figure 5.3: Scalar anisotropy indicators for $\sigma = 2$ with $St = 1$. (a) $b^T_{ij}(t)$. (b) $H^{(T)}_{ij}(k,t)$ at $t = 10^6\tau_0$ ($Re_\lambda = 800$).

The case of an axisymmetric contraction was studied by Gylfason & Warhaft (2009), where the temperature fluctuations are created by a mean gradient that increases during the effective contraction. Although no quantitative comparison is possible because of the "moderate anisotropy" limitation of the present model, interesting qualitative facts can be reported. The measure of anisotropy is done using the **fluctuating covariance** $C_{ij}(t) =< \xi_i\xi_j >$, where $\xi_i = \partial_i\theta$, which brings comparable information as the b^T_{ij}. During the contraction, $|C_{ij}|$ increases, and at the exit of the contraction, it converges to a constant value, different from zero. This behaviour is similar to the one of b^T_{ij}, and the authors concluded that there is a partial return to isotropy,

which is in agreement with the presents results: however, there is no spectral information in Gylfason & Warhaft (2009) to locate the remaining anisotropy.

5.1.3 Sustained shear (HST)

In this part, the shear is maintained. It has been shown in Chapter 3 that there is an exponential growth of the kinetic energy $K(t)$ due to non-linear transfers. Is there a similar growth of the scalar variance? In the evolution equation of K_T (5.1), there are no production terms unlike the evolution equation of $K(t)$. This means that anisotropy only produces energy for the kinetic field. Hence, there should be no growth of $K_T(t)$ even if the shear is maintained. Fig. 5.4a exhibits a remarkable behaviour: b_{ij}^T and the **scalar shear rapidity**

$$S_{\mathrm{R}}^T(t) = \frac{\epsilon_T(t)}{SK_T(t)} \tag{5.5}$$

reach constant values for $St \geq 30$, as in the kinetic case. Moreover, it is revealed that the scalar variance K_T decreases exponentially in Fig. 5.4b, with a decay rate $\gamma_T \simeq -0.52$. Let's replace K_T and ϵ_T in (5.1) (with $\Lambda = 0$) by

$$K_T(t) = K_T^\infty \exp(\gamma_T St), \qquad \epsilon_T(t) = \epsilon_T^\infty \exp(\gamma_T St).$$

An analytical expression for γ_T is obtained

$$\boxed{\gamma_T = -\frac{\epsilon_T}{SK_T} = -0.52, \qquad K_T(t) \sim K_T(0)\exp(\gamma_T St).} \tag{5.6}$$

The scalar exponential exponent found by plotting K_T is in good agreement with the asymptotic value of S_{R}^T, which gives $\gamma_T = -0.52$. The important result is that the value of γ_T does not depend on the shear rate S nor on the infrared exponents σ and σ_T (and neither does γ for the exponential growth of $K(t)$). The scalar dissipation ϵ_T, also displayed in Fig. 5.4b, exponentially decreases with the same rate $\gamma_T = -0.52$, which is consistent with the evolution equation (5.1).

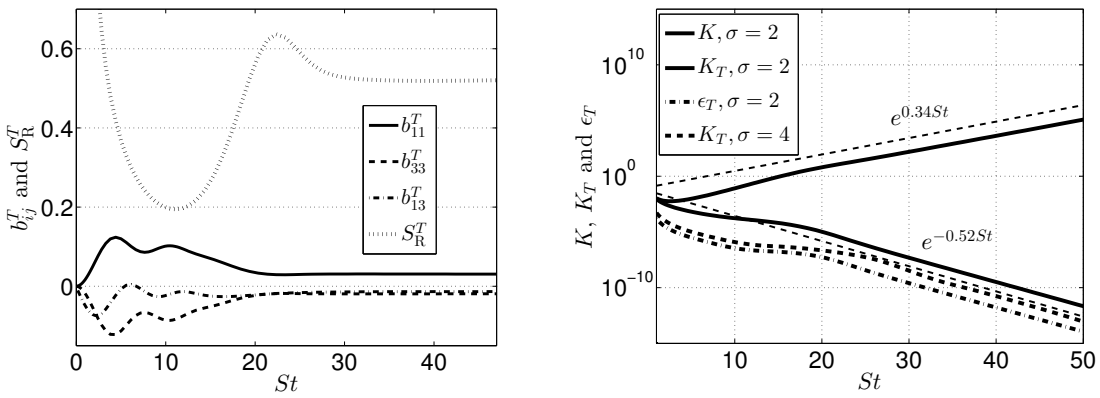

(a) (b)

Figure 5.4: (a) Scalar anisotropy indicators b_{ij}^T along with S_{R}^T for $\sigma = 2$. (b) Kinetic energy K, scalar variance K_T, and scalar dissipation rate ϵ_T, for $\sigma = 2$ and $\sigma = 4$.

/	Algebraic exponents $\forall S$ in HSRT	Exp. rates $\forall(S,\sigma,\sigma_T,Pr)$ in HST
$K(t)$	$\alpha = -2\frac{\sigma-p+1}{\sigma-p+3}, \quad p = \begin{cases} 0 & ,\sigma \leq 3 \\ 0.55 & ,\sigma = 4 \end{cases}$	$\gamma = 2b_{13} - \epsilon/KS$
$\epsilon(t)$	$n_\epsilon = -3\frac{\sigma-p+5/3}{\sigma-p+3}$	γ
$L(t)$	$n_L = \frac{2}{\sigma-p+3}$	$\gamma/2$
$R_{13}(t)$	$\alpha_{13} = -2\frac{\sigma-p_S+1}{\sigma-p+3}, \quad p_S = \begin{cases} 0 & ,\sigma \leq 3 \\ 0.279 & ,\sigma = 4 \end{cases}$	γ
$\epsilon_{13}(t)$	$n_{\epsilon_{13}} = \alpha_{13} - 1$	Destruction
$K_T(t)$	$\alpha_T = -2\frac{\sigma_T-p_T+1}{\sigma-p+3}$	$\gamma_T = -\epsilon_T/K_TS = -0.52$
$\epsilon_T(t)$	$n_{\epsilon_T} = -\frac{\sigma-p+5+2\sigma_T-2p_T}{\sigma-p+3}$	γ_T
$L_T(t)$	$n_{L_T} = n_L$	$\gamma/2$

Table 5.1: Decay and growth laws of kinetic and scalar integrated quantities in HSRT and HST. Note that the time exponents for K, ϵ, L, K_T, ϵ_T and L_T of HSRT are also valid in HIT.

The fact that anisotropy accelerates the decay of the scalar field has been observed experimentally by Warhaft (1980) with a contraction. Moreover, such an exponential decrease of $< \theta^2 >$ has been found theoretically by Pierrehumbert (1994); Gonzalez (2000) using a self-preservation analysis. In the latter reference, the decay rate of Karnik & Tavoularis (1989) is computed by fitting the experimental data $K_T^{\text{exp}} \sim \exp(-0.037x_\theta/M)$. From this, it is possible to determine the associated γ_T^{exp} according to

$$K_T^{\text{exp}}(t) \sim \exp(\gamma_T^{\text{exp}} St), \qquad \gamma_T^{\text{exp}} = \frac{-0.037U_c}{M\mathrm{d}U_1/\mathrm{d}x_2}.$$

The parameters are $U_c = 13\text{m.s}^{-1}$, $M = 0.0254\text{m}$ and $\mathrm{d}U_1/\mathrm{d}x_2 = k_sU_c = 8.06\text{s}^{-1}$ with the shear generator parameter $k_S = 0.62\text{m}^{-1}$. Hence $\gamma_T^{\text{exp}} = -2.35$. This value seems very large and may come from a too low $\mathrm{d}U_1/\mathrm{d}x_2$. Indeed, details about the shear generation are provided in Karnik & Tavoularis (1987) where velocity gradients $\mathrm{d}U_1/\mathrm{d}x_2$ from $43.5s^{-1}$ to 84s^{-1} are reported, which would respectively give $\gamma_T^{\text{exp}} = -0.435$, closer to the present value, and $\gamma_T^{\text{exp}} = -0.235$. Whatever it be, $|\gamma_T^{\text{exp}}| < |\gamma_T|$.

5.1.4 Decay and growth laws for the passive scalar in HSRT and HST

The decay and growth laws of the kinetic and scalar fields, obtained theoretically and assessed numerically, valid not only in HSRT and HST, but also in HIT, are gathered in the following Table 5.1.

5.2 Isotropic Turbulence with a mean Scalar Gradient

The cospectrum $\mathcal{F}(k,t)$ is now investigated in the case of homogeneous turbulence submitted to a mean scalar gradient $\lambda_3 = -\Lambda$ with an isotropic kinetic field (HITSG). The scalar gradient accounts for a production term of scalar fluctuations, and initially the cospectrum $\mathcal{F} = 0$. In

these conditions, the study of the cospectrum, the only non-zero component of the scalar flux, amounts to the investigation of another passive scalar.

5.2.1 Spectra and transfers

The inertial scaling of the cospectrum can be found by dimensional analysis (Lumley, 1967). One has to assume that $\mathcal{F}$ only depends on the scalar gradient Λ, the wavenumber k and the kinetic energy dissipation rate ϵ so that

$$\mathcal{F}(k,t) = C_{\mathcal{F}} \Lambda \epsilon^{1/3} k^{-7/3}, \tag{5.7}$$

where $C_{\mathcal{F}}$ is the cospectrum constant, found to be $C_{\mathcal{F}} \simeq 3$ in the present work. Bos (2005) reported $C_{\mathcal{F}} \simeq 1.5$ whereas O'Gorman & Pullin (2005) computed $C_{\mathcal{F}} = 3.5$ with their model. The $k^{-7/3}$ dependence is similar to the fully anisotropic spectral tensor ϕ_{13} in shear-driven turbulence. If one assumes that $\mathcal{F}$ depends on ϵ, k and its dissipation rate $\epsilon_{\mathcal{F}}$, then $\mathcal{F} \sim \epsilon^{-1/3} \epsilon_{\mathcal{F}} k^{-5/3}$, like a passive scalar. This would imply that $\epsilon_{\mathcal{F}}$ is conserved throughout the cascade and this cannot be satisfied due to the pressure effects.

In what follows for numerical simulations, one needs to define a dimensionless mean scalar gradient $\mathcal{S}_\theta$. There are different possibilities to define a reference mean scalar gradient Λ_{ref}, unlike the mean velocity gradient which is unambiguously defined (De Souza *et al.*, 1995). We choose

$$\mathcal{S}_\theta = \frac{\Lambda}{\Lambda_{\text{ref}}}. \tag{5.8}$$

The reference mean scalar gradient Λ_{ref} is defined explicitly in the following comparisons. If not mentioned otherwise, $\mathcal{S}_\theta = 1$ is chosen.

In Fig. 5.5a, the $k^{-7/3}$ scaling clearly appears for the cospectrum. However, it requires a very high Reynolds number ($Re_\lambda \geq 10^4$ here). Without it, it is hard to distinguish the theoretical power law $k^{-7/3}$ from k^{-2}, as revealed in figure 5.5b for the moderate Reynolds number case $Re_\lambda = 100$, where the inertial range is rather narrow. The $k^{-7/3}$ scaling has also been obtained experimentally by Mydlarski (2003), in DNS by O'Gorman & Pullin (2005); Watanabe & Gotoh (2007) or with EDQNM by Bos *et al.* (2005).

An interesting point to mention that has not been reported so far is the infrared range of the cospectrum; indeed, since $\mathcal{F} = 0$ in the initial isotropic flow, one can wonder how it evolves at very large scales. The result is displayed in Fig. 5.6a: the cospectrum infrared exponent is the same as the kinetic one σ. Moreover, the $k^{-7/3}$ scaling is recovered for all the σ presented. Finally, the linear and non-linear transfers associated to the cospectrum are presented in Fig. 5.6b: $S_3^{\text{F,NL}} - S_3^{\text{F,RTI}}$ represents the conservative non-linear transfer with zero integral over k. $S_3^{\text{F,RTI}}$ is the RTI term associated with the pressure effects. $S_3^{\text{F,NL}}$ is the total non-linear transfer that corresponds to a non-conservative flux. Finally, $S_3^{\text{F,L}}$ is the linear transfer responsible for production of anisotropy through the scalar gradient, that decreases along time with the kinetic spectrum $E(k,t)$. This is in agreement with similar results presented in Bos *et al.* (2005).

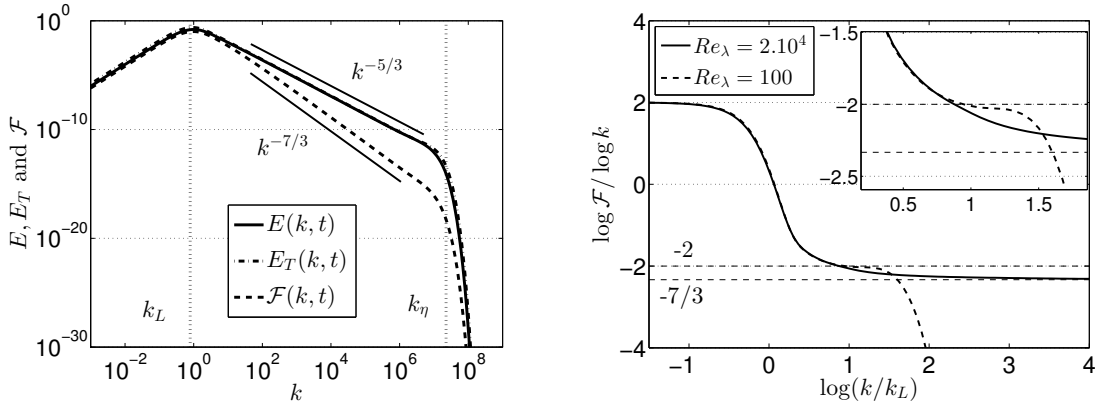

(a) (b)

Figure 5.5: (a) Cospectrum, kinetic energy and scalar variance spectra $\mathcal{F}$, E and E_T for $Re_\lambda = 2.10^5$, along with the integral and Kolmogorov wavenumbers k_L and k_η. (b) Effect of low Reynolds numbers on the scaling of $\mathcal{F}$, with a zoom on the narrow inertial range for the case $Re_\lambda = 100$. Both for $\sigma = 2$.

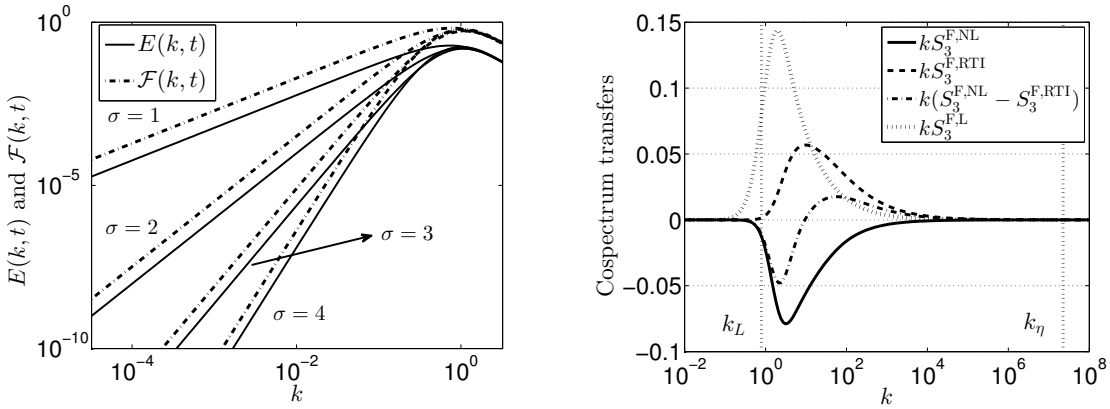

(a) (b)

Figure 5.6: (a) Large scales behaviour of the cospectrum $\mathcal{F}$ for different infrared kinetic exponents σ. (b) Linear and non-linear transfers of the cospectrum for $\sigma = 2$, at $Re_\lambda = 2.10^5$.

5.2.2 Comparisons with experimental and numerical results

This section aims at assessing the anisotropic EDQNM modelling in the HITSG framework by comparisons with one DNS and one experiment.

Overholt and Pope (1996): in this part, the emphasis it put on the ratio of the cospectrum dissipation $\epsilon_{\mathcal{F}}$ and cospectrum production $P_{\mathcal{F}}$ defined in (4.56) and (4.60). In the DNS of Overholt & Pope (1996), it is shown that the cospectrum dissipation is not negligible at low Reynolds numbers even though it decreases with Re_λ. The following power law is found

$$\left(\frac{\epsilon_{\mathcal{F}}}{P_{\mathcal{F}}}\right)^{\mathrm{DNS}} = 4.61 Re_\lambda^{-0.769},$$

reported in Fig. 5.7, from $Re_\lambda = 28$ to 185. Results coming from EDQNM simulations are also presented for comparison purposes

$$\left(\frac{\epsilon_{\mathcal{F}}}{P_{\mathcal{F}}}\right)^{\text{EDQNM}} = 11.6 Re_\lambda^{-0.760}.$$

The ratio is evaluated for Reynolds numbers such that the kinetic field decreases according to CBC theory. It is observed that for $Re_\lambda = 28$ the kinetic field is in the transition towards low Reynolds numbers regime. This is why here the minimum value for the ratio is at $Re_\lambda = 40$. This agreement with DNS regarding the Re_λ power law in low Reynolds numbers regime partially validates the model for the cospectrum. The discrepancy for the numerical factor arises from the fact that initial conditions are different, and mainly because in the DNS the velocity field is forced, whereas it is freely decaying here. Nevertheless, the Re_λ power law is recovered.

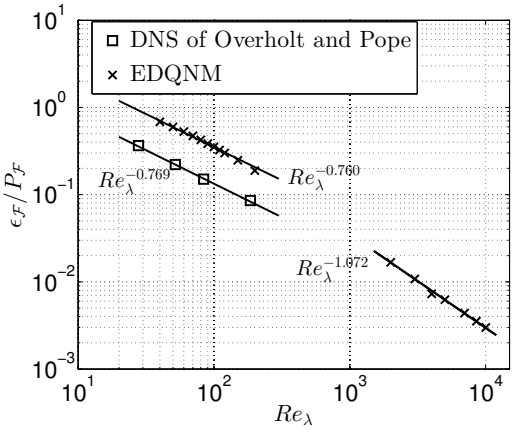

Figure 5.7: Comparison of the ratio of cospectrum dissipation and production with the DNS of Overholt & Pope (1996) for $\sigma = 2$ in high and low Reynolds numbers regimes.

As for the high Reynolds numbers regime, the Re_λ^{-1} predicted by Bos *et al.* (2005) is recovered numerically in Fig. 5.7 as well. This scaling law can be obtained analytically, assuming that in high Reynolds numbers regime the dominant region of the kinetic spectrum and cospectrum is the inertial range

$$\frac{\epsilon_{\mathcal{F}}(t)}{P_{\mathcal{F}}(t)} = \frac{3(\nu + a)}{2\Lambda} \frac{\int_0^\infty k^2 \mathcal{F}(k,t)\mathrm{d}k}{\int_0^\infty E(k,t)\mathrm{d}k} \sim \frac{\int_{k_L}^{k_\eta} \epsilon^{1/3} k^{-1/3}\mathrm{d}k}{\int_{k_L}^{k_\eta} \epsilon^{2/3} k^{-5/3}\mathrm{d}k}. \tag{5.9}$$

Then, using classical relations such as $(k_\eta/k_L) = Re_L^{3/4}$ where Re_L is the integral Reynolds number so that $\sqrt{Re_L} \sim Re_\lambda$, and $\nu k_\eta^{4/3} = \epsilon^{1/3}$, one finds $\epsilon_{\mathcal{F}}/P_{\mathcal{F}} \sim Re_\lambda^{-1}$.

Sirivat and Warhaft (1983): in this part, the results provided by the current model are compared with the experimental work of Sirivat & Warhaft (1983). The case where the scalar gradient is created with a mandoline (a screen of thin heated wires) is chosen. The parameters of the experiment are the following ones: the input speed is $U = 3.4\text{m.s}^{-1}$ and the meshsize $M = 0.024\text{m}$. For this configuration, the initial Reynolds number is $Re_\lambda(0) = 26.4$ and the turn-over time $\tau_{\text{exp}} = 1.14\text{s}$. The scalar dissipation rate, written ϵ_θ for the experiment, is $\epsilon_\theta \simeq 10^{-2}\,{}^\circ\text{C}^2.\text{s}^{-1}$ for a scalar gradient $\beta = 1.78^\circ\text{C.m}^{-1}$. Assuming that for this experiment the

Prandtl number is about 0.7, a reference fluctuating scalar gradient is computed as

$$\left(\frac{\partial\theta}{\partial x}\right)_{\text{ref}} = \Lambda_{\text{ref}} = \sqrt{\frac{\epsilon_\theta}{3a}},$$

so that the dimensionless scalar gradient is $\mathcal{S}_\theta = \beta/\Lambda_{\text{ref}} = 0.152$. Temporal results are transposed to spatial ones through

$$\frac{x}{M} = \frac{t}{\tau_0}\frac{U\tau_{\text{exp}}}{M},$$

where τ_0 is the kinetic characteristic time K/ϵ evaluated numerically after two turn-over times, so that transition effects from the initial conditions are erased. The experimental decay rate of the kinetic field being $\alpha_{\text{exp}} = -1.3$, Saffman turbulence ($\sigma = 2$) is an appropriate large scales initial condition for the simulations. The **cospectrum correlation**

$$\rho_{u_i\theta} = \frac{< u_i\theta >}{\sqrt{< u_i^2 >< \theta^2 >}}, \qquad \rho_{u_3\theta} = \rho_{w\theta}, \tag{5.10}$$

is well recovered in Fig. 5.8a, and $\rho_{w\theta} \to -0.7$. The ratio of scalar production $-\Lambda K_{\mathcal{F}}$ and dissipation ϵ_T is also in agreement with the present results in Fig. 5.8c. The final value of the characteristic times ratio

$$R_T = \frac{K\,\epsilon_T}{K_T\,\epsilon} \tag{5.11}$$

matches quite well experimental data in Fig. 5.8d. However, there is a slight discrepancy in Fig. 5.8b for the ratio of integral scales L_T/L defined in (1.37) ($\simeq 0.7$ with EDQNM, and $\simeq 0.9$ experimentally). Since no definitions are given in the experiment, there could be a difference in the definitions. Nevertheless, the fact that $L_T < L$ is recovered. Let's underline that initial conditions are isotropic, which is not the case in the experiment: as mentioned by Sirivat & Warhaft (1983), the initial fluctuating temperature field is slightly inhomogeneous, and because of the grid itself the kinetic field contains some anisotropy. But still, the "early times" of $\rho_{w\theta}$ and $-\Lambda K_{\mathcal{F}}/\epsilon_T$ are well captured by the anisotropic EDQNM modelling.

About the cospectrum correlation $\rho_{w\theta}$, it has to be pointed out that there exists a large scatter, since measured values span from $\simeq -0.19$ to $\simeq -0.8$, with an average around $\simeq -0.65$ (Venkataramani & Chevray, 1978; Sirivat & Warhaft, 1983; Overholt & Pope, 1996; Mydlarski, 2003). It appears in EDQNM simulations that $\rho_{w\theta}$ strongly varies for $5 \leq Re_\lambda \leq 300$, roughly from 0.6 to $\simeq 0.71$ for decreasing Reynolds numbers. This is the classical range of Reynolds numbers covered by experiments and DNS. Consequently, the reason for the scattering of $\rho_{w\theta}$ could be moderate Reynolds numbers, where it becomes more sensitive to the intensity of the mean-scalar gradient. Another explanation is proposed in Chapter 6.

5.2.3 Decay and growth laws for the cospectrum and passive scalar

In this section, the anisotropic EDQNM modelling is used to address the high Reynolds numbers regimes of HAT. The satisfactory agreements obtained at moderate Reynolds numbers in the previous comparisons give confidence in the following investigation. The main contribution of this chapter is the new results presented in HITSG, which aim at predicting the decay and growth of the mixed-correlation and scalar variance. These results, gathered in Table 5.2, also exhibit the dominant mechanisms during the decay.

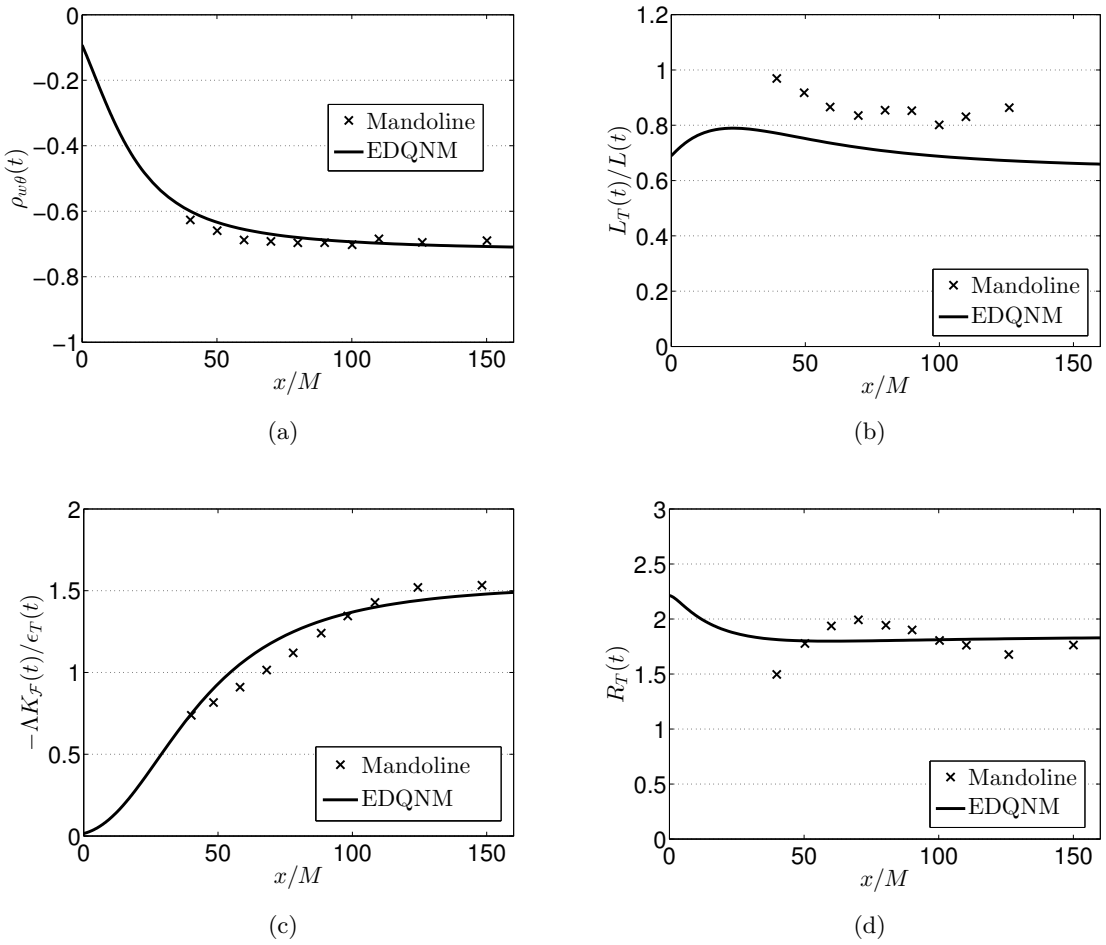

Figure 5.8: Comparisons with the experiment of Sirivat & Warhaft (1983) with the mandoline configuration, for $\sigma = 2$ and $\mathcal{S}_\theta = 0.152$. (a) Cospectrum correlation $\rho_{w\theta}$ defined in (5.10). (b) Scalar to kinetic integral scales ratio L_T/L. (c) Ratio of production and dissipation of the passive scalar $-\Lambda K_{\mathcal{F}}/\epsilon_T$. (d) Kinetic to scalar time scales ratio R_T defined in (5.11).

Decay of $K_{\mathcal{F}}(t)$ and $\epsilon_{\mathcal{F}}(t)$: the scalar flux $\mathcal{F}$ is destroyed by the classical decay of the kinetic field and consequently experiences a decay itself. Is it possible to derive theoretical decay exponents based on CBC theory for $< u_3\theta >$? Two assumptions based on physical arguments for high Reynolds numbers regime need to be made: (i) It has been shown in Fig. 5.6a that the cospectrum does not have a specific infrared exponent and is completely controlled by the kinetic field. Therefore, only the inertial $k^{-7/3}$ range, starting at the integral wavenumber k_L, should be taken into account into the cospectrum decay process. (ii) In the case of Batchelor turbulence, backscatter parameters p and p_T are introduced for the kinetic and scalar fields respectively. Since the cospectrum $\mathcal{F}$ is the spectral counterpart of the velocity-scalar cross correlation, its backscatter parameter $p_{\mathcal{F}}$ should contain both effects. Hence, the simplest form is chosen: $p_{\mathcal{F}} = (p + p_T)/2$ for $\sigma = 4$, which gives $p_{\mathcal{F}} = 0.4075$ with $Pr = 1$.

With these reasonable assumptions, one can write

$$K_{\mathcal{F}}(t) = \int_{k_L}^{\infty} \mathcal{F}(k,t)\mathrm{d}k \sim k_L^{-4/3}\epsilon^{1/3}. \tag{5.12}$$

Injecting in this equation decay exponents of kinetic integrated quantities recalled in Table 5.1, and using $p_{\mathcal{F}}$, one finds

$$\boxed{K_{\mathcal{F}}(t) \sim t^{\alpha_{\mathcal{F}}}, \qquad \alpha_{\mathcal{F}} = -\frac{\sigma - p_{\mathcal{F}} - 1}{\sigma - p + 3}.} \tag{5.13}$$

It can be deduced from the scaling (5.12) that the dominant mechanism in the decay of $\mathcal{F}$ at high Reynolds numbers is not production, but inertial effects of the velocity field. This is not true anymore in the low Reynolds numbers regime, where the production term $P_{\mathcal{F}}$ leads the dynamics. From the evolution equation (4.58) of the mixed-correlation, only $\mathrm{d}K_{\mathcal{F}}/\mathrm{d}t \sim P_{\mathcal{F}} = 2\Lambda K/3$ remains. The return to isotropy term $\Pi_{\mathcal{F}}$, or cospectrum destruction, is weak and $\epsilon_{\mathcal{F}}$ is also negligible: indeed, given the shape of the cospectrum dissipation (4.56), this term is strong in the inertial range, which does not exist anymore in the low Reynolds regime. This immediately yields

$$\boxed{\alpha_{\mathcal{F}} = -\frac{\sigma - 1}{2}.} \tag{5.14}$$

These decay exponents do not depend on the scalar gradient Λ, and are assessed numerically in Fig. 5.9a in the high and low Reynolds numbers regimes. The agreement is excellent even for the particular case of Batchelor turbulence. This is the first time such a result is presented: indeed, in existing DNS, the kinetic field is forced or artificially frozen so that no decay can occur. From (5.13) and (5.14), it follows that $K_{\mathcal{F}}$ does not decay for $\sigma = 1$. In this case, the Reynolds number Re_λ remains constant and so the dynamics of the inertial range, on which is based $\alpha_{\mathcal{F}}$, remains unchanged. These theoretical decay exponents, assessed numerically, give further insights into the prediction of high Reynolds numbers decay in HITSG: this is also an extension of an analysis previously applied to the passive scalar in HIT in Chapter 1.

Regarding the cospectrum dissipation rate: since the scalar flux is a purely anisotropic quantity, $\epsilon_{\mathcal{F}}$ is not a conserved quantity unlike ϵ and ϵ_T. Therefore, it is not possible to express it under the shape of a power law. Nevertheless, as the inertial range disappears in the low Reynolds numbers regime, it is possible to compute the decay exponent $n_{\epsilon_{\mathcal{F}}}$ of $\epsilon_{\mathcal{F}}$ from the evolution equation (4.58) so that

$$\boxed{\epsilon_{\mathcal{F}}(t) \sim t^{n_{\epsilon_{\mathcal{F}}}}, \qquad n_{\epsilon_{\mathcal{F}}} = \alpha_{\mathcal{F}} - 1 = -\frac{\sigma + 1}{2}.} \tag{5.15}$$

The agreement between this theoretical result and numerical simulations is displayed in Fig. 5.9b.

Growth of $K_T(t)$ and $\epsilon_T(t)$: the effect of the mean scalar gradient Λ on the passive scalar itself is now addressed. Such a study was not performed in previous references. The scalar spectrum still displays a $k^{-5/3}$ inertial-convective range despite the mean gradient, as obtained experimentally by Mydlarski & Warhaft (1998). In the HITSG framework, the evolution equation (5.1) of K_T is driven by both dissipation and production. In the presence of a mean scalar gradient Λ, the production term leads the dynamics of the passive scalar field. Using the previous results regarding the decay exponents of $K_{\mathcal{F}}$, one can compute the exponent of K_T in presence of a mean scalar gradient α_T^{Λ}. One gets in high and low Reynolds numbers regimes

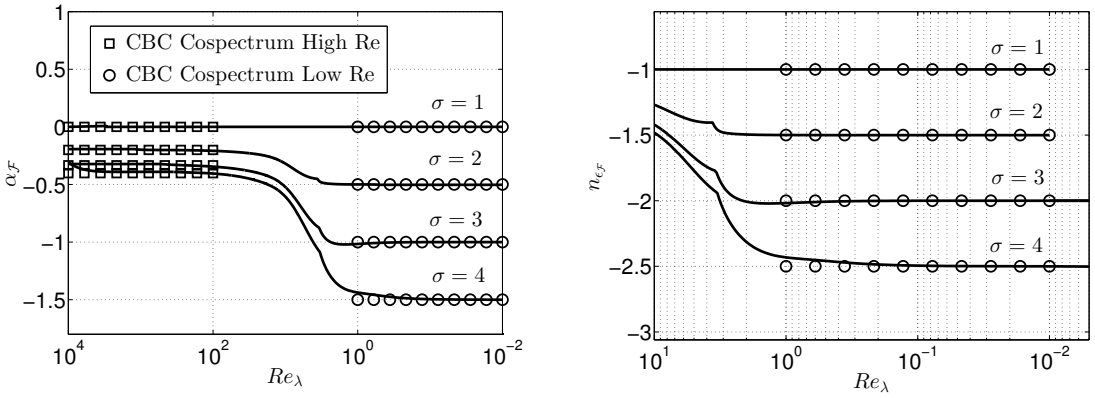

(a) (b)

Figure 5.9: Decay exponents for the scalar flux for various σ; Symbols represent theoretical predictions, □ for large Reynolds numbers and ∘ for low Reynolds numbers. (a) Mixed-correlation decay exponent $\alpha_{\mathcal{F}}$ in high and low Reynolds numbers regimes. (b) Cospectrum dissipation rate decay exponent $n_{\epsilon_{\mathcal{F}}}$ in the low Reynolds numbers regime.

respectively

$$K_T(t) \sim t^{\alpha_T^\Lambda}, \qquad \alpha_T^\Lambda = \frac{4 + p_{\mathcal{F}} - p}{\sigma - p + 3}, \tag{5.16}$$

$$K_T(t) \sim t^{\alpha_T^\Lambda}, \qquad \alpha_T^\Lambda = -\frac{\sigma - 3}{2}. \tag{5.17}$$

The agreement between these theoretical expressions of α_T^Λ and numerical simulations is presented in Fig. 5.10a for both high and low Reynolds numbers regimes. The exponents do not depend on the scalar gradient Λ. For high Reynolds numbers, the scalar variance grows in time whatever σ is, whereas for low Reynolds numbers, it decays for $\sigma = 4$. This can be explained with the following arguments. The theoretical prediction (5.17) of α_T^Λ is based on the fact that the dynamics of K_T is driven by the production term $2\Lambda K_{\mathcal{F}}$, and $K_{\mathcal{F}}$ is stronger for smaller σ. Consequently, for a large infrared slope such as $\sigma = 4$, the spectrum $E(k,t)$, and thus $\mathcal{F}(k,t)$, has less energy in large scales, resulting into a weak production term for the scalar variance that does not balance dissipation. This is consistent with HITSG experimental results at moderate Re_λ, where the scalar variance can grow or decay depending on the intensity of Λ: with a weak Λ, K_T still decays (nevertheless more slowly than in HIT). Therefore, there is a link between physical and spectral spaces: a strong mean scalar gradient Λ corresponds to a small infrared slope σ, or equivalently to energetic large scales.

Moreover, in the particular case of Saffman turbulence ($\sigma = 2$), the value $\alpha_T^\Lambda = 4/5$ was already found by Chasnov (1995). Therein, the decay and growth laws of passive and active scalar fields, with and without mean gradient, are studied. Power laws for the active scalar fields were assessed by Large Eddy Simulations (LES). Hence, the present EDQNM simulations valid the power laws for the passive scalar field, with an explicit dependence on the initial large scales conditions σ. Consequently, this result can be seen as an extension of Chasnov (1995) on the passive scalar.

Finally, the dissipation rate of the passive scalar field is investigated. From the scalar variance evolution equation (5.1), it can be deduced that ϵ_T should evolve as $K_{\mathcal{F}}$, meaning

$$\epsilon_T(t) \sim t^{n^{\Lambda}_{\epsilon_T}}, \qquad n^{\Lambda}_{\epsilon_T} = \alpha_{\mathcal{F}} \tag{5.18}$$

in both high and low Reynolds numbers regimes. This is assessed in Fig. 5.10b.

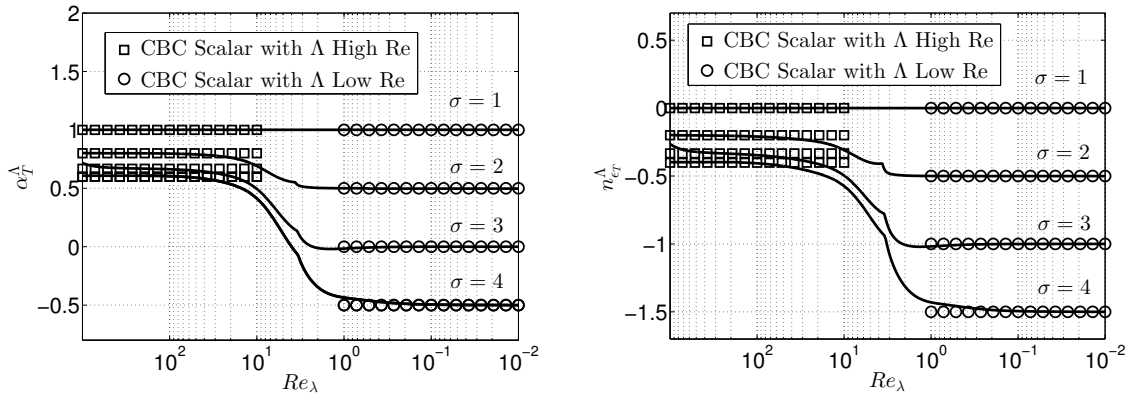

(a) (b)

Figure 5.10: Time exponents for the scalar field for various σ; Symbols represent theoretical predictions, □ for large Reynolds numbers and ∘ for low Reynolds numbers. (a) Scalar variance growth exponent α_T^{Λ}. (b) Scalar dissipation rate decay exponent $n_{\epsilon_T}^{\Lambda}$.

All these new and partially new results regarding decay and growth exponents for K_T and $K_{\mathcal{F}}$ and their dissipation rates are gathered in Table 5.2. They notably permit to explain why the cospectrum correlation (5.10) does not depend on σ in both high and low Reynolds numbers regimes: indeed, the computation using the previous exponents shows that the time evolution of $\rho_{w\theta}$ does not depend on σ anymore for very large or small Reynolds numbers.

When a passive scalar is forced with a mean gradient, it is fully dominated by the decaying isotropic velocity field which completely leads the dynamics of the flow. Indeed, the infrared scalar exponent σ_T has no influence on the decay and growth exponents. A similar result was obtained by De Marinis *et al.* (2013) in HIT where the passive scalar field experiences a Joule heat production. Therefore, it can be concluded that in a presence of a production mechanism, the velocity field completely dominates the passive scalar dynamics. This will not be true anymore for an active scalar in Chapter 7.

	High Reynolds regime $\forall(\Lambda, \sigma_T, Pr)$	Low Reynolds regime $\forall(\Lambda, \sigma_T, Pr)$
$K_T(t)$	$\alpha_T^{\Lambda} = \frac{4+p_{\mathcal{F}}-p}{\sigma-p+3}, \quad p_{\mathcal{F}} = \begin{cases} 0 & ,\sigma \leq 3 \\ \frac{1}{2}(p+p_T) & ,\sigma = 4 \end{cases}$	$\alpha_T^{\Lambda} = -\frac{\sigma-3}{2}$
$\epsilon_T(t)$	$n^{\Lambda}_{\epsilon_T} = \alpha_{\mathcal{F}} = -\frac{\sigma-p_{\mathcal{F}}-1}{\sigma-p+3}$	$n^{\Lambda}_{\epsilon_T} = \alpha_{\mathcal{F}} = -\frac{\sigma-1}{2}$
$K_{\mathcal{F}}(t)$	$\alpha_{\mathcal{F}} = -\frac{\sigma-p_{\mathcal{F}}-1}{\sigma-p+3}$	$\alpha_{\mathcal{F}} = -\frac{\sigma-1}{2}$
$\epsilon_{\mathcal{F}}(t)$	not defined	$n_{\epsilon_{\mathcal{F}}} = -\frac{\sigma+1}{2}$

Table 5.2: Decay and growth exponents of integrated quantities in HITSG for the cospectrum and scalar fields.

Remark on the scalar large scales in HITSG: the mean scalar gradient Λ results in a production term in the passive scalar equation. This scalar production is linked to the cospectrum, itself linked to the kinetic energy spectrum. Hence, the "minimum of energy" of the flow is imposed by the infrared range of the kinetic spectrum, *i.e.* imposed by σ. So, the scalar infrared exponent σ_T changes if initially different from σ. There are two cases: (i) $\sigma_T(t=0) > \sigma$ rapidly results into $\sigma_T = \sigma$. Indeed, $\sigma_T > \sigma$ means $K_T < K$: since the kinetic field imposes the minimum of energy, σ_T decreases. For instance, if one has $\sigma_T(t=0) = 4$ and $\sigma = 2$, the self-similar regime is $\sigma = \sigma_T = 2$. (ii) For $\sigma_T < \sigma$, then $\sigma_T = \sigma$ but it takes more time, as revealed in Fig. 5.11. Without the scalar gradient, the scalar variance would decrease more slowly than the kinetic energy. The production term being proportional to $K(t)$, it forces the scalar field to grow with the infrared slope $\sigma_T = \sigma$.

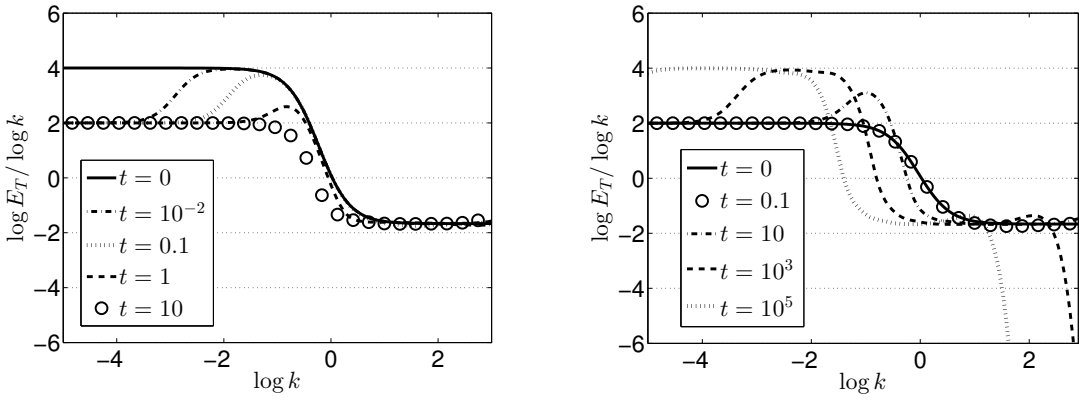

(a) (b)

Figure 5.11: Evolution of the scalar infrared slope σ_T with $\Lambda = -1$. (a) $\sigma_T(t=0) = 4$ and $\sigma = 2$. (b) $\sigma_T(t=0) = 2$ and $\sigma = 4$.

5.2.4 Return to isotropy in HITSG

The small scales RTI is briefly addressed for HITSG at the level of scalar second-order moments. Since only the third component of the mean scalar gradient is non-zero, this is an axisymmetric configuration, meaning that the scalar anisotropy indicators verify $2H_{11}^{(T)} = 2H_{22}^{(T)} = -H_{33}^{(T)}$. In Fig. 5.12a, the b_{ij}^T are presented: they become constant both in Saffman and Batchelor turbulence. This is qualitatively the same behaviour as the b_{ij} in a sustained shear flow. Then, in the low Reynolds numbers regime, the b_{ij}^T increase and reach a constant asymptotic value, meaning that there is anisotropy left in the flow. The fact that anisotropy increases in the low Reynolds numbers regime has already been observed for the velocity field in Chapter 3. The spectral anisotropy tensor $H_{ij}^{(T)}$ reveals that small scales of the scalar second-order moments completely return to isotropy in Fig. 5.12b. Moreover, it has been pointed in experiments and DNS (Pumir, 1994; Danaila *et al.*, 1999*b*) that at the level of scalar third-order moments, anisotropy remains in the small scales. This is not incompatible with small-scales isotropic second-order moments as shown recently by Bos (2014).

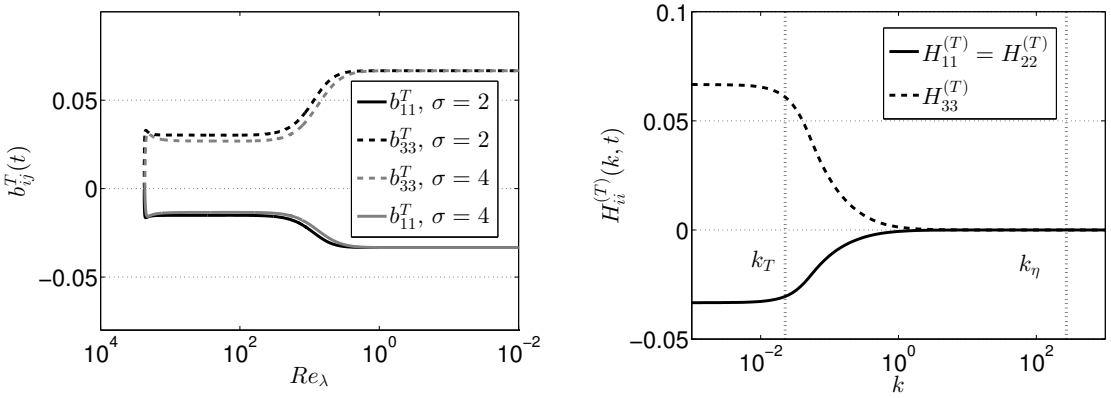

(a) (b)

Figure 5.12: (a) Scalar anisotropy indicators b_{ii}^T (no summation) from high to low Reynolds numbers regimes, for both Saffman (black) and Batchelor (grey) turbulence. (b) $H_{ii}^{(T)}$ (no summation) at $Re_\lambda = 10^3$ for $\sigma = 2$, along with the Kolmogorov and scalar integral wavenumbers k_η and k_T.

An interesting analogy can be made between the velocity field in a sustained shear flow and the scalar field in HITSG. For both fields, (i) there is a complete return to isotropy of small scales; (ii) there are no significant differences between Saffman and Batchelor turbulence: in both cases b_{ij} and b_{ij}^T reach constant values (see Fig. 5.12a for the b_{ij}^T and Fig. 3.10a for the b_{ij}). (iii) Anisotropy fills large scales and does not remain around the integral wavenumber as in HSRT.

5.3 Homogeneous Shear Turbulence with Scalar Gradient

This final part focuses on homogeneous shear turbulence with a mean scalar gradient (HSTSG). The emphasis is put on the impact of both mean velocity and scalar gradients on the scalar flux and the passive scalar.

5.3.1 Definitions and transfers

Previously, it has been shown that with a mean scalar gradient Λ, only the third component of the scalar flux is non-zero, namely the cospectrum $\mathcal{F}$. With a mean velocity gradient only, no scalar flux appears at all, and the scalar variance decays exponentially. With both mean velocity and scalar gradients, the first component of the scalar flux is also non-zero. Thus, the **streamwise flux** is defined as

$$E_1^F(k,t) = \mathcal{F}_S(k,t), \tag{5.19}$$

and arises only due to the combined presence of a both mean velocity and scalar gradients. The **streamwise mixed-correlation** reads

$$K_{\mathcal{F}}^{S}(t) = \int_0^\infty \mathcal{F}_S(k,t)\mathrm{d}k. \tag{5.20}$$

In Fig. 5.13, both linear and non-linear spherically averaged transfers are presented for the cospectrum and the streamwise flux in HSTSG. One can note that they are very similar and slightly differ in intensity.

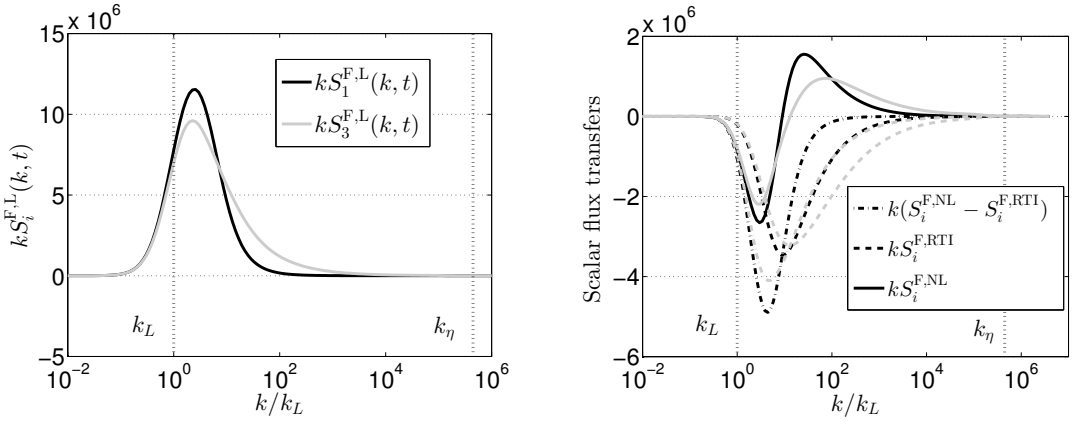

(a) (b)

Figure 5.13: Transfers for the cospectrum (grey) and streamwise flux (black) for $\sigma = 2$ at $St = 50$ where $Re_\lambda = 2.10^4$. (a) Linear transfers. (b) Non-linear transfers.

5.3.2 Comparisons with experimental and numerical results

This part aims at assessing the anisotropic EDQNM modelling in HSTSG - a configuration which combines various mechanisms at stake in atmospheric flows - by comparisons to two DNS and one experiment.

Tavoularis and Corrsin (1981): EDQNM simulations are compared to the experiment of Tavoularis & Corrsin (1981). Such a comparison has also been performed by Bos (2005) and the conclusions will be discussed. The mean speed is $U_c = 12.4\mathrm{m.s}^{-1}$ and the characteristic length is the shear generator one $h = 0.305\mathrm{m}$. The mean velocity and scalar gradients are $\mathrm{d}U_1/\mathrm{d}x_2 = 46.8\mathrm{m.s}^{-1}$ and $\mathrm{d}T/\mathrm{d}x_2 = 9.5°\mathrm{C.m}^{-1}$. From the data of the kinetic characteristic time written $\tau_u = 2\tau_0 = 0.26\mathrm{s}$, one has $S = 6.19\tau_0^{-1}$. Then, from the scalar characteristic time τ_θ and $< \theta^2 >$, it is possible to evaluate the scalar dissipation rate $\epsilon_\theta = 0.128°\mathrm{C}^2.\mathrm{s}^{-1}$ at $x_1/h = 7.5$, and thus to compute the reference scalar gradient $(\partial\theta/\partial x)_{\mathrm{ref}} = \sqrt{\epsilon_\theta/(2a)} = 52.1°\mathrm{C.m}^{-1}$ so that $\mathcal{S}_\theta = 0.1823$. It is worth noting that initial isotropic conditions are used here, which is clearly not the case in the experiment. Two final Reynolds numbers are given in (Tavoularis & Corrsin, 1981): $R_{\lambda_g} = 160$ scaled for an isotropic framework, and $R_{\lambda_{11}} = 266$ for inhomogeneous flows. The comparisons are presented in Fig. 5.14a to 5.14d. Data is available at three locations: $x_1/h = 7.5$, 9.5 and 11. Using the appropriate conversion in dimensionless time, written τ in

(Tavoularis & Corrsin, 1981; De Souza *et al.*, 1995), one has

$$\tau = St = \frac{x_1}{U_c}\frac{\mathrm{d}U_1}{\mathrm{d}x_2},$$

which provides experimental information at $St = 8.63$, 10.94 and 12.66. There are satisfactory agreements in Fig. 5.14a for the cospectrum and streamwise flux correlations $\rho_{u\theta}$ and $\rho_{v\theta}$. Similar values for $\rho_{u\theta}$ and $\rho_{v\theta}$ are reported in Ferchihi & Tavoularis (2002) which once again confirms the relevance of the present EDQNM closure for the passive scalar and scalar flux. A satisfactory agreement is also obtained in Fig 5.14b for the characteristic times ratio R_T defined in (5.11). A first discrepancy is observed for

$$B(t) = \frac{\Lambda}{S}\sqrt{\frac{2K}{K_T}}, \tag{5.21}$$

which is underestimated in Fig. 5.14d, whereas it is overestimated in Bos (2005). $B(t)$ seems to be very dependent on initial conditions, which could explain the discrepancy. One has to keep in mind that here initial conditions are isotropic, whereas in the experiment there is initial anisotropy in the flow, difficult to model. Finally, in Fig. 5.14c a difference is observed for the **turbulent Prandtl number**

$$Pr_T(t) = \frac{\Lambda}{S}\frac{R_{12}(t)}{K_{\mathcal{F}}(t)}, \tag{5.22}$$

where $Pr_T^{\mathrm{exp}} \simeq 1.1$ and $Pr_T^{\mathrm{EDQNM}} \simeq 0.74$. The value obtained experimentally seems quite large: indeed, atmospheric data and theoretical considerations suggest that one should obtain $0.6 \leq Pr_T \leq 0.8$ (Herring *et al.*, 1982; Lesieur, 2008), in agreement with existing values (Shirani *et al.*, 1981; Rogers *et al.*, 1989). The comparison with the results of Bos & Bertoglio (2007) is not relevant here because a constant of their model for linear transfers is set so that $Pr_T = 1.1$ is recovered.

Rogers, Mansour and Reynolds (1989): The comparison is made with the DNS of Rogers *et al.* (1989). There, the mean velocity gradient $\mathrm{d}U_1/\mathrm{d}x_2 = S = \mathcal{S}\tau_0^{-1}$ is such that the dimensionless shear is $\mathcal{S} = 14.142$. Three cases for the scalar gradient are performed, one in each direction x_1, x_2 and x_3, with $\mathcal{S}_\theta = 2.5$. Comparisons are made with the **diffusivity tensor** defined as

$$D_{ij}(t) = -<\theta u_i>\left(\frac{\mathrm{d}T}{\mathrm{d}x_j}\right)^{-1}. \tag{5.23}$$

Each column of D_{ij} refers to a different simulation where the direction of the scalar gradient changes. For instance, D_{13} refers to the third case. The agreement between EDQNM simulations and DNS is revealed in Fig. 5.15a where D_{ij} is normalized by D_{22}. A difference is observed along the flow direction for D_{11}/D_{22} where DNS predicts a higher value. This discrepancy may come from the limited DNS resolution that alters the dynamics in the streamwise direction. For each simulation, the turbulent Prandtl number is defined by

$$Pr_T(t) = -\frac{R_{12}(t)}{SD_{ii}(t)}, \tag{5.24}$$

where D_{ii} (no summation) is the **turbulent diffusivity**, with $i = 1$, 2 or 3 depending on the case considered. The agreement is rather good in Fig. 5.15b: the classical asymptotic value of $Pr_T = 0.8$ is recovered in the second case, whereas the general behaviour is captured for the

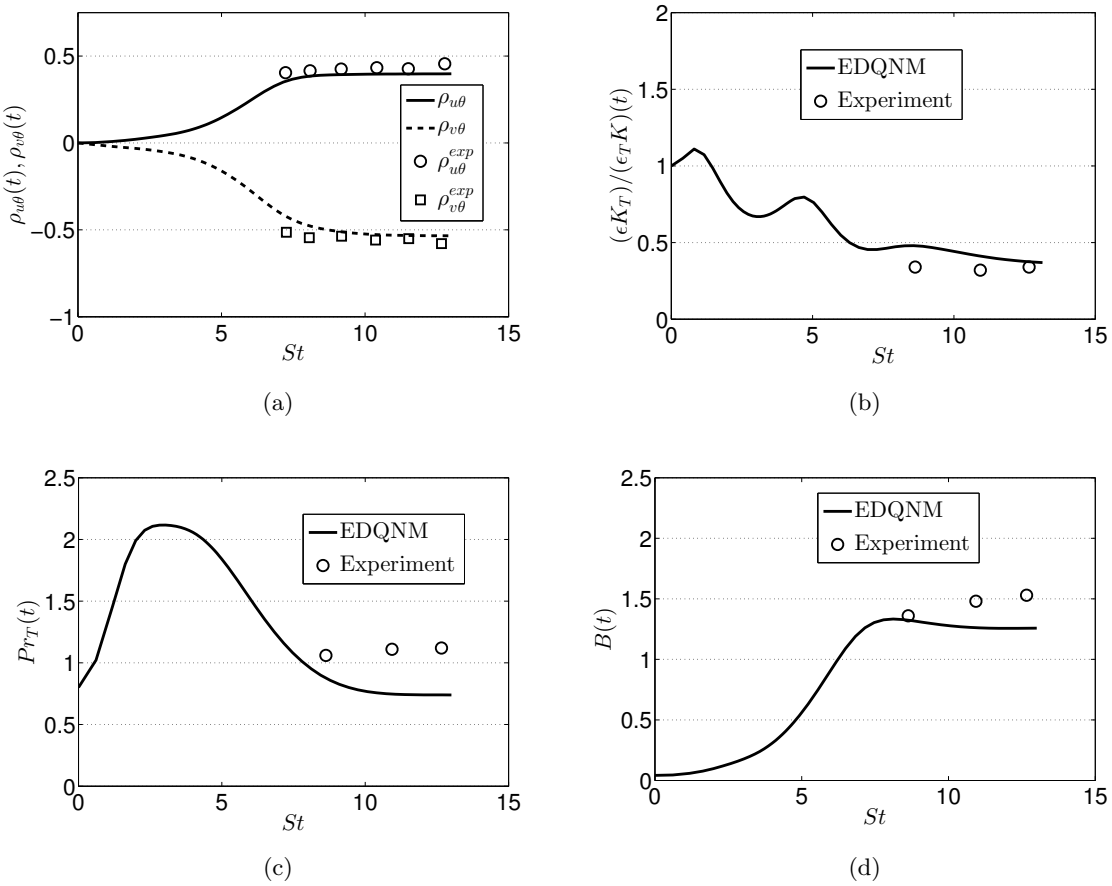

Figure 5.14: Comparisons with the experiment of Tavoularis & Corrsin (1981), for $\sigma = 2$, $S = 6.19\tau_0^{-1}$ and $\mathcal{S}_\theta = 0.1823$. (a) Scalar flux correlations $\rho_{u_i\theta}$ defined in (5.10). (b) Inverse of the time scales ratio defined in (5.11). (c) Turbulent Prandtl number Pr_T defined in (5.22). (d) Relative strength of the fluctuations B defined in (5.21).

first and third cases: $Pr_T^{(1)} < Pr_T^{(3)} < Pr_T^{(2)}$. Nevertheless, the present simulations seem less sensitive to the mean scalar gradient intensity than experiments. Moreover, for larger St, $Pr_T^{(2)}$ would be quite smaller, which indicates that the present anisotropic EDQNM modelling slightly underestimates the turbulent Prandtl number. A possibility to correct these lower values of Pr_T is to set the eddy-damping constants as $A_1 = A_2 = A_3 = 0.355$.

Kassinos, Knaepen and Carati (2007): a last comparison is performed with the DNS of Kassinos *et al.* (2007). This work deals about MHD but the validation is made in the purely hydrodynamic case with the data of Brethouwer (2005). Hence, only the case where the magnetic field is zero and where there is no rotation is considered. The mean velocity and scalar gradients are along x_2 such that $\mathcal{S} = 8.95$ and $\mathcal{S}_\theta = 1$. The kinetic field is allowed to decay without any forcing before velocity and scalar gradients are applied at t_0. There, the Reynolds number is $Re_\lambda = 45$ with $SK/\epsilon(t = t_0) = 18$. The scalar fluctuations are set to 0 at $t = t_0$: this is why initially $\rho_{v\theta}(t = t_0) = -1$. For EDQNM simulations, S and Λ are applied after two turn-over times and there $SK/\epsilon = 13$ and $Re_\lambda = 50$. The two correlations $\rho_{u\theta}$ and $\rho_{v\theta}$ are presented in Fig. 5.16a along with

$$\beta = \frac{S}{\Lambda}\sqrt{\frac{3K_T}{2K}}, \tag{5.25}$$

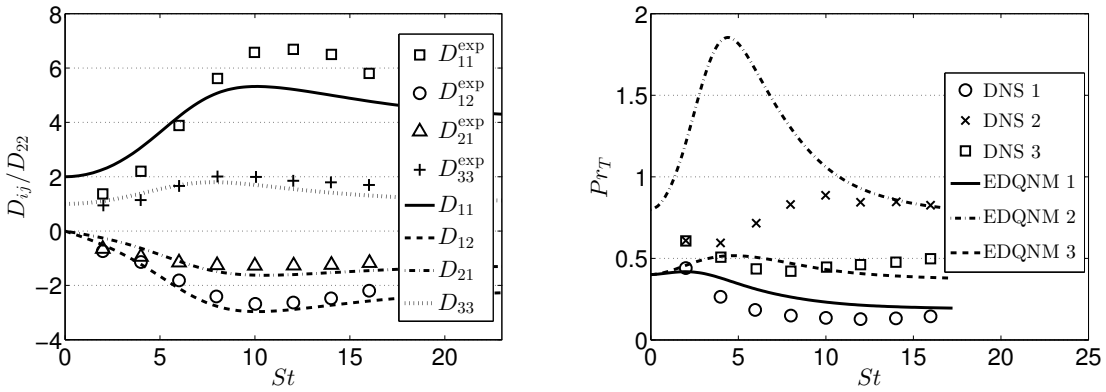

(a) (b)

Figure 5.15: Comparisons with the DNS of Rogers *et al.* (1989), with $\sigma = 2$, $\mathcal{S} = 14.142$ and $\mathcal{S}_\theta = 2.5$. (a) Normalized diffusivity tensor, defined in (5.23), for the three orientations of the mean scalar gradient. (b) Turbulent Prandtl number Pr_T, defined in (5.24), for these three cases.

which characterizes the relative strengths of the velocity and scalar fluctuations. There is a good agreement for the asymptotic values of $\rho_{u\theta}$ and $\rho_{v\theta}$. Our weaker value for $\rho_{u\theta}$ at moderate St may be the consequence of a slightly too strong growth of $R_{11} =< u_1^2 >$. This does not prevent to reach the correct value at larger St in the asymptotic state. As for β, EDQNM simulations slightly differ from the DNS in Fig. 5.16b, where β is over-estimated and has almost reached a constant value whereas it slightly decreases in Kassinos *et al.* (2007). Nevertheless, in both cases $\beta \sim 1$ at large St, which indicates that the velocity and scalar fluctuations have a similar contribution to the anisotropic asymptotic state.

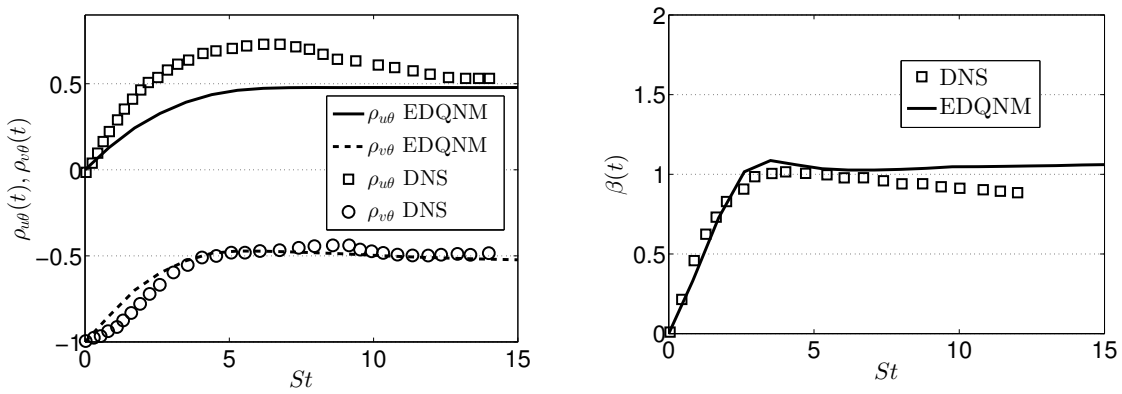

(a) (b)

Figure 5.16: Comparisons with the DNS of Kassinos *et al.* (2007), for $\sigma = 2$, $\mathcal{S} = 8.95$ and $\mathcal{S}_\theta = 1$. (a) $\rho_{u\theta}$ and $\rho_{w\theta}$, defined in (5.10). (b) β defined in (5.25).

5.3.3 Growth of K, K_T, $K_\mathcal{F}$ and $K_\mathcal{F}^S$

In this part, the emphasis is put on the growth of the scalar variance and its interactions with the scalar flux. Some additional results about the passive scalar and the scalar flux are presented, which may be of interest for one-point modelling, such as negligible quantities at high shear rates. The scalar anisotropy tensors b_{ij}^T are presented in Fig. 5.17 along with the **scalar flux shear rapidities**

$$S_\mathrm{R}^\mathcal{F}(t) = \frac{\epsilon_\mathcal{F}}{K_\mathcal{F} S}, \qquad S_\mathrm{R}^{\mathcal{F},S}(t) = \frac{\epsilon_\mathcal{F}^S}{K_\mathcal{F}^S S}. \tag{5.26}$$

As in the HST framework without mean scalar gradient, the scalar indicators reach constant values for large St, and the ratio $\mathcal{S}_\theta/\mathcal{S}$ impacts only the short time dynamics without modifying the asymptotic state. There is a noteworthy similarity with the behaviour of b_{ij} in shear flows.

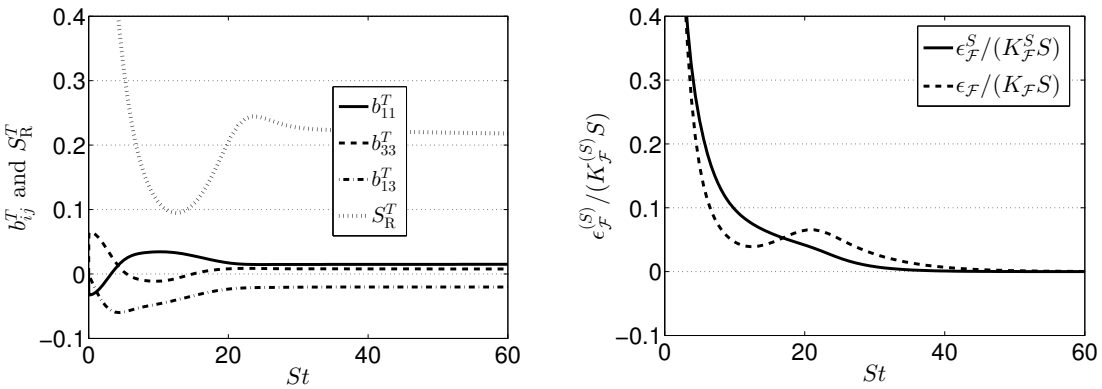

(a) (b)

Figure 5.17: (a) Scalar anisotropy indicators b_{ij}^T and scalar shear rapidity S_R^T. (b) Scalar flux shear rapidities $S_\mathrm{R}^\mathcal{F}$ and $S_\mathrm{R}^{\mathcal{F},S}$. Both for $\sigma = 2$ and $S = 10^{-2}\tau_0^{-1}$.

An interesting feature is that $S_R^\mathcal{F}$ and $S_R^{\mathcal{F},S}$ tend to zero for large St, whereas their kinetic and scalar counterparts do not. This means that the linear effects of shear are preponderant over non-linear exchanges: this is in agreement with figure 5.13, where the scalar flux transfers of energy are gathered at large scales, dominated by linear mechanisms. The evolution of the scalar variance and mixed-correlations are given by

$$\frac{\mathrm{d}K_T}{\mathrm{d}t} = 2\Lambda K_\mathcal{F} \qquad -\epsilon_T \tag{5.27}$$

$$\frac{\mathrm{d}K_\mathcal{F}}{\mathrm{d}t} = \Lambda R_{33} \qquad +\Pi_\mathcal{F} \quad -\epsilon_\mathcal{F} \tag{5.28}$$

$$\frac{\mathrm{d}K_\mathcal{F}^S}{\mathrm{d}t} = \Lambda R_{13} \quad +SK_\mathcal{F} \quad +\Pi_\mathcal{F}^S \quad -\epsilon_\mathcal{F}^S, \tag{5.29}$$

Here is what happens simultaneously: the cross-correlation R_{13} produces $K_\mathcal{F}^S$ through the mean scalar gradient Λ. Then, R_{13} brings energy to the transverse component R_{33} thanks to non-linear redistribution, which causes $K_\mathcal{F}$ to grow as well through Λ. Finally, $K_\mathcal{F}$ provokes the growth of K_T. It is possible to compute the rapid pressure parts of the scalar flux $\Pi_\mathcal{F}$ and $\Pi_\mathcal{F}^S$. Details are given in Appendix E. This gives for the cospectrum $5\Pi_\mathcal{F}^\mathrm{r}(t) = SK_\mathcal{F}^S$. The

numerical factor 0.08 obtained by Bos & Bertoglio (2007) is far from the present 0.2. However, the streamwise part, $5\Pi^{\mathrm{r,S}}_{\mathcal{F}}(t) = -4SK_{\mathcal{F}}$, is closer from 0.62 of the latter reference.

The main result here is that the scalar variance K_T, which was exponentially decreasing in HST, now grows exponentially in HSTSG, as revealed in Fig. 5.18a. Its scalar exponential growth rate γ_T is identical to the kinetic one γ so that $\gamma_T = \gamma = 0.34$. This is qualitatively in agreement with the experimental work of Ferchihi & Tavoularis (2002): they found that K and K_T grow with the same rate in the presence of scalar and velocity gradients (with $\gamma^{\mathrm{exp}} \simeq 0.085$, which is far inferior to $\gamma = 0.34$, and lower than common experimental ones). Moreover, both $K_{\mathcal{F}}$ and $K^S_{\mathcal{F}}$ grow exponentially with the rate γ as well. Growths of the mixed-correlations have been obtained numerically by Rogers (1991), even though it is complicated to determine if the growth is algebraic or exponential due to the DNS limitation. The fact that all these correlations grow exponentially with the same rate is consistent with the constant scalar flux correlations $\rho_{u_i\theta}$ obtained experimentally and in DNS for sufficiently high St.

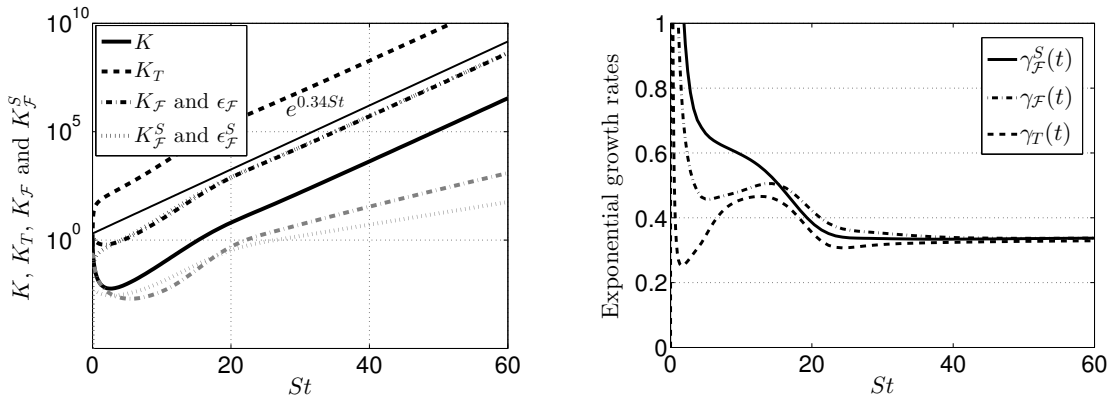

Figure 5.18: (a) Exponential growth of the kinetic, scalar, cospectrum and streamwise flux correlations. The cospectrum and streamwise flux dissipation rates $\epsilon_{\mathcal{F}}$ and $\epsilon^S_{\mathcal{F}}$ are displayed in grey. (b) Exponential growth rates $\gamma_{\mathcal{F}}$, $\gamma^S_{\mathcal{F}}$ and γ_T. Both for $\sigma = 2$ and $S = 10^{-2}\tau_0^{-1}$.

From the equations (5.27)-(5.29), it is possible to determine the expression of the cospectrum, streamwise flux and scalar exponential growth rates $\gamma_{\mathcal{F}}$, $\gamma^S_{\mathcal{F}}$ and γ_T. Using the fact that $\epsilon_{\mathcal{F}}/(K_{\mathcal{F}}S) \to 0$ and $\epsilon^S_{\mathcal{F}}/(K^S_{\mathcal{F}}S) \to 0$, one has

$$\frac{1}{K_{\mathcal{F}}S}\frac{\mathrm{d}K_{\mathcal{F}}}{\mathrm{d}t} = \underbrace{\frac{\Lambda}{S}\frac{R_{33}}{K_{\mathcal{F}}} + \frac{\Pi_{\mathcal{F}}}{K_{\mathcal{F}}S}}_{\text{Constant for } St \gg 1} = \gamma_{\mathcal{F}}, \tag{5.30}$$

$$\frac{1}{K^S_{\mathcal{F}}S}\frac{\mathrm{d}K^S_{\mathcal{F}}}{\mathrm{d}t} = \underbrace{\frac{K_{\mathcal{F}}}{K^S_{\mathcal{F}}}(1+Pr_T) + \frac{\Pi^S_{\mathcal{F}}}{K^S_{\mathcal{F}}S}}_{\text{Constant for } St \gg 1} = \gamma^S_{\mathcal{F}}, \tag{5.31}$$

$$\frac{1}{K_TS}\frac{\mathrm{d}K_T}{\mathrm{d}t} = \underbrace{2\frac{\Lambda}{S}\frac{K_{\mathcal{F}}}{K_T} - \frac{\epsilon_T}{K_TS}}_{\text{Constant for } St \gg 1} = \gamma_T. \tag{5.32}$$

The agreement between the asymptotic values of these quantities and the 0.34 expected are presented in Fig. 5.18b. Moreover, simulations show that $\gamma_{\mathcal{F}}$, $\gamma^S_{\mathcal{F}}$ and γ_T do not depend on

large scales initial conditions σ, as for the kinetic rate γ. The definitions (5.30) and (5.31) are not convenient for calculations since the slow-part of $\Pi_{\mathcal{F}}^{(S)}$ cannot be expressed explicitly. One could want to use one-point modelling, such as the ones proposed by Wikström *et al.* (2000). The simplest model that can be found is

$$\Pi_i^{F,\text{slow}}(t) - \epsilon_i^F(t) = -c_1 \frac{\epsilon}{K} < u_i \theta >, \tag{5.33}$$

where $c_1 = 3.2$ is calibrated on experimental data. Injecting this model in (5.30) and (5.31), and using the previous explicit calculations of the rapid contribution, yields

$$\gamma_{\mathcal{F}} = \frac{\Lambda}{S}\frac{R_{33}}{K_{\mathcal{F}}} + \frac{1}{5}\frac{K_{\mathcal{F}}^S}{K_{\mathcal{F}}} - 3.2\frac{\epsilon}{KS} \simeq 0.2827 \tag{5.34}$$

$$\gamma_{\mathcal{F}}^S = \frac{K_{\mathcal{F}}}{K_{\mathcal{F}}^S}\left(\frac{1}{5} + Pr_T\right) - 3.2\frac{\epsilon}{KS} \simeq 0.2122. \tag{5.35}$$

The obtained values of $\gamma_{\mathcal{F}}$ and $\gamma_{\mathcal{F}}^S$ are not too far from 0.34. However, $\gamma_{\mathcal{F}} \neq \gamma_{\mathcal{F}}^S$, which shows that the simplest models cannot handle such complex flows.

5.3.4 Streamwise flux spectrum $\mathcal{F}_S(k,t)$

The inertial scaling of the streamwise flux $\mathcal{F}_S$ has not received much attention yet. Wyngaard & Coté (1972) proposed a scaling in k^{-3}. However such a slope did not agree well with atmospheric data and they concluded that a $k^{-5/2}$ range would be more appropriate. The k^{-3} slope is obtained by assuming that $\mathcal{F}_S$ depends on ϵ, k, S and Λ, so that

$$\mathcal{F}_S(k,t) \sim \Lambda S k^{-3}. \tag{5.36}$$

This expression can also be found starting from $\mathcal{F}_S \sim \Lambda \epsilon^{1/3} k^{-7/3}$ and replacing $\epsilon^{1/3}$ by its expression as a function of the shear scale defined in (3.19), $\epsilon^{1/3} \sim k^{-2/3} S$. Bos & Bertoglio (2007) derived a $k^{-23/9}$ range both analytically and numerically based on tensorial arguments. $\epsilon^{1/3}$ is replaced by $\epsilon_{ij}^{1/3}(k)$ so that the scalar flux is written

$$F_i(k,t) \sim \lambda_j \epsilon_{ij}^{1/3} k^{-7/3}, \tag{5.37}$$

with $\epsilon_{ij}(k)E(k) = 3\phi_{ij}(k)\epsilon$. This recovers the classical scaling for $\mathcal{F}$ and yields

$$\boxed{\mathcal{F}_S(k,t) = C_{\mathcal{F}}^S \, \Lambda \, S^{1/3} \, \epsilon^{2/9} \, k^{-23/9}.} \tag{5.38}$$

In a recent paper, Knaus & Pantano (2009) studied reactive and non-reactive scalar flux spectra with DNS and found that a $k^{-7/3}$ range was a satisfactory scaling. Such a spectral behaviour can be recovered assuming that $\mathcal{F}_S$ depends on ϵ, k, S and $\epsilon_{\mathcal{F}}^S$

$$\mathcal{F}_S(k,t) \sim S \epsilon^{-2/3} \epsilon_{\mathcal{F}} k^{-7/3}. \tag{5.39}$$

But this is not consistent with the fact that ϵ_i^F is not conserved (and consequently that the scalar flux does not exist in the isotropic framework). Older atmospheric measurements reported a $k^{-5/3}$ scaling (Antonia & Zhu, 1994). Numerically, it is revealed in Fig. 5.19 that there is a

good agreement for the streamwise flux $\mathcal{F}_S$ with the $k^{-23/9}$ scaling predicted by Bos & Bertoglio (2007). Numerically, the constant is found to be $C_{\mathcal{F}}^S \simeq 1.5$.

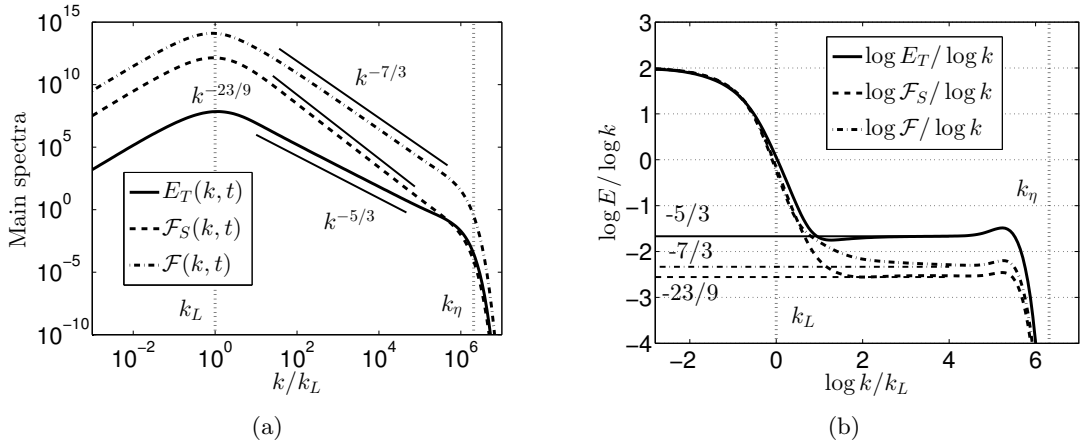

Figure 5.19: (a) Scalar variance, cospectrum and streamwise flux spectra E_T, $\mathcal{F}$ and $\mathcal{F}_S$. (b) Associated spectral scalings: the horizontal dashed lines correspond to $-5/3$, $-7/3$, $-23/9$. Both at $St = 60$ with $\sigma = 2$ and $Re_\lambda = 4.10^4$.

5.3.5 Return to isotropy in HSTSG

The small scales RTI is finally addressed for HSTSG at the level of the scalar second-order moments. In Fig. 5.20, the scalar anisotropy tensors $H_{ij}^{(T)}$ are presented at large St for HSTSG, at two different Reynolds numbers: local isotropy is almost respected for second-order moments of the scalar field as in the inertial range one has $H_{ij}^{(T)}(k \to k_\eta, t) \to 0$. Nevertheless, $H_{ij}^{(T)}$ is not rigorously zero at small scales, especially the extra-diagonal component $H_{13}^{(T)}$. This shows that in the presence of shear, and in agreement with most of the DNS and experiments, some anisotropy persists at the scalar small scales, even at the second-order moments level. Furthermore, the Reynolds number is found to have a non-negligible impact on the small scales anisotropy: indeed, small scales anisotropy reduces from $Re_\lambda = 2400$, which is slightly higher than Reynolds numbers reached in DNS, to $Re_\lambda = 1,5.10^4$. The shear wavenumber $k_S = \sqrt{S^3/\epsilon}$ is displayed as well: for wavenumbers $k > k_S$, non-linear effects are dominant, consistent with the RTI of small scales, whereas for $k < k_S$, linear effects are stronger are carry most of the anisotropy. A last remark is that the presence of a mean scalar gradient seems to smooth the scalar large scales anisotropy: indeed, for shear-driven flows without mean scalar gradient, anisotropy is gathered around the scalar peak of energy k_T and is weaker in the infrared range (see Fig. 5.3b). Whereas for HSTSG, anisotropy progressively increases from moderate to large scales.

5.4 Conclusions for the passive scalar at $Pr = 1$

This chapter was an application of the anisotropic EDQNM modelling. Three different configurations were considered, whose comprehension is crucial to understand the dynamics of complex flows such as atmospheric ones: isotropic turbulence with a mean scalar gradient

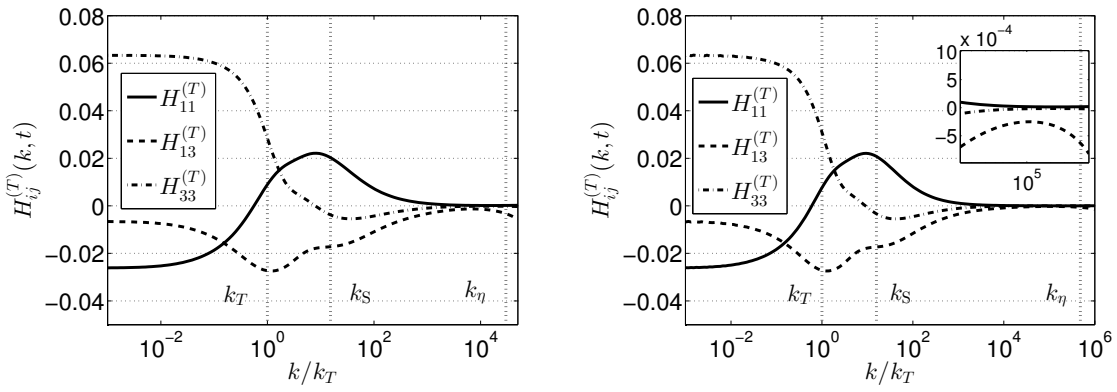

(a) (b)

Figure 5.20: Scalar anisotropy tensors $H_{ij}^{(T)}$ with Kolmogorov, shear and scalar integral wavenumbers k_η, k_S and k_T for $\sigma = 2$ at two different Reynolds numbers. (a) $St = 40$ where $Re_\lambda = 2400$. (b) $St = 50$ where $Re_\lambda = 2.10^4$. The zoom represents the small scales before k_η where the persistence of anisotropy is clear.

(HITSG), shear turbulence (HST) and shear turbulence with a scalar gradient (HSTSG). The anisotropic EDQNM modelling was assessed by detailed comparisons with several DNS and experiments at moderate Reynolds numbers in HITSG and HSTSG: asymptotic values of scalar flux correlations, turbulent Prandtl numbers and diffusivity tensors are well recovered, and the agreement at short time is satisfactory as well. Then, the model was used to address high Reynolds numbers flows which are not accessible by DNS yet.

In HITSG, the scalar flux along the mean scalar gradient, the cospectrum $\mathcal{F}(k,t)$, is found to scale as $k^{-7/3}$ in the inertial range for very large Reynolds numbers $Re_\lambda \geq 10^4$. New results are proposed regarding the decay and growth of $< u_3\theta >$ and $< \theta^2 >$, gathered in Table 5.2: theoretical exponents are derived using physical arguments, and are then assessed numerically. Such results were not provided before and complete the work of Chasnov (1995). This theoretical contribution provides further insights into the prediction of high Reynolds numbers decaying turbulence. In HST, the exponential decrease of the scalar variance was recovered, and furthermore, algebraic decay laws for K_T were provided in HSRT, unchanged with respect to HIT. All these results for shear-driven flows without a mean scalar gradient are gathered in Table 5.1. In HSTSG, the inertial scaling of the streamwise flux $\mathcal{F}_S(k,t)$ in $k^{-23/9}$ is recovered (Bos & Bertoglio, 2007), and alternative scalings are briefly discussed. The interesting result of this part is the exponential growth of the scalar variance and mixed-correlations $< u_1\theta >$ and $< u_3\theta >$, at a rate equal to the one of the kinetic energy.

In these three configurations, the small scales RTI of scalar second-order moments was investigated, and the conclusions are threefold. (i) Scalar small scales return completely to isotropy in HITSG, which is not surprising since the velocity field remains isotropic. (ii) On the contrary, when there is a mean velocity gradient (with or without an additional mean scalar gradient), some anisotropy persists in the scalar small scales even at high Reynolds numbers, which is consistent with DNS and experiments. This persistent small scale anisotropy for the passive scalar is nevertheless found to diminish with an increasing Reynolds number. (iii) When the anisotropy consists of velocity gradients only, anisotropy is gathered around the scalar integral

wavenumber k_T, whereas when a mean scalar gradient is present, anisotropy fills more the large scales.

Rotation was not investigated in this work, because its effects on triple correlations are not clear, and as mentioned earlier, interacting waves require additional theoretical tools, such as EDQNM2 (Cambon & Jacquin, 1989; Sagaut & Cambon, 2008), to be properly captured. It is nevertheless a necessary step to the deep understanding of atmospheric flows: the DNS by Brethouwer (2005) suggests that the effects of a rotating shear on the passive scalar transport and its flux are multiple and rather complex. Finally, the present modelling is further extended to unstably stratified homogeneous turbulence in Chapter 7, since stratification amounts only to additional linear transfers, much simpler than the ones induced by mean-velocity gradients.

In conclusion, the anisotropic EDQNM modelling seems promising since it recovers quite well previous experimental and numerical results, and additionally permits to explore large Reynolds numbers. It can predict the velocity and scalar fields dynamics for various kinds of anisotropy with the same consistent method and does not rely on adjustable constants, except the classical ones used in the eddy-damping terms.

Chapter 6

Prandtl Number Effects on Passive Scalar Dynamics

Here, the anisotropic EDQNM modelling assessed and used for $Pr = 1$ in Chapter 5 is applied to the case of a Prandtl number different from unity: the frameworks of a highly diffusive scalar $Pr \ll 1$, and of a weakly diffusive scalar $Pr \gg 1$, are investigated. For these two configurations, the scalar variance spectrum $E_T(k,t)$ is known to scale differently at small scales in HIT (see Chapter 1). Consequently, one can wonder if these scalings for the scalar variance spectrum are modified when anisotropy appears at the velocity and scalar levels, and what happens for the scalar flux as well.

This chapter is divided into two parts: section 6.1 focuses on the HITSG framework, whereas section 6.2 addresses shear-driven flows. The first section is the main contribution of this chapter. For shear-driven turbulence, varying the Prandtl number while adding a shear seems to be a limit of the present spectral modelling, especially when $Pr \ll 1$. Nevertheless, some cases with mean velocity gradients in HST, HSRT and HSTSG are briefly presented afterwards.

The contents of this chapter for HITSG were published in:
Briard & Gomez, "Prandtl number effects in decaying homogeneous isotropic turbulence with a mean scalar gradient", *Journal of Turbulence*, **18** (5), 418-442 (2017)

For $Pr \ll 1$, it is recalled that the inertial-diffusive range (IDR) spans from $k_{\mathrm{CO}} = Pr^{3/4} k_\eta$, where diffusion effects become dominant, to k_η. One can define $k_{\mathrm{CD}} = \sqrt{Pr} k_\eta$ from which convection from small scales balances diffusion effects (see Chapter 1). And for $Pr \gg 1$, the viscous-convective range (VCR) spans from k_η, the smallest active turbulent scale for the velocity field, to $k_{\mathrm{B}} = \sqrt{Pr} k_\eta$. In this region, small scalar fluctuations are advected by the velocity field of the Kolmogorov scale. Then, beyond k_{B}, scalar fluctuations are destroyed by diffusive processes. Interactions that are at the origin of the VCR are strongly non-local: indeed, the cascade of energy computed with EDQNM does not reach scales much smaller than k_η because of the logarithmic discretization of the wavenumber space. Non-local transfers have been studied notably by Lesieur & Schertzer (1978); Métais & Lesieur (1986); Lesieur (2008), and the derivation of the non-local fluxes for the velocity and passive scalar fields is proposed in Appendix B.

6.1 Prandtl number effects in HITSG

Most of the papers dealing with a Prandtl number different from unity in HITSG were done at moderate Reynolds numbers, and focused on its effects on (i) high-order scalar statistics, and on (ii) the cospectrum $\mathcal{F}(k,t)$ and scalar variance spectrum $E_T(k,t)$ spectral scalings (Chasnov, 1991; Yeung *et al.*, 2002; O'Gorman & Pullin, 2005; Bos *et al.*, 2009; Yeung & Sreenivasan, 2014). The aim of the present study is to explore asymptotic regimes of HITSG, at very large Reynolds numbers and either very high or small Prandtl numbers, in order to predict the growth and decay rates of the scalar variance $< \theta^2 >$ and mixed-correlation $< u_3\theta >$ of highly and weakly diffusive scalars, which is a new feature, and to verify the proposed spectral scalings as well. This is of theoretical interest since these regimes cannot be reached experimentally nor in DNS yet. In addition, this permits to analyze the combined effects of anisotropy that mainly affect large scales, and Pr which dominantly modifies small scales of the spectra. Furthermore, it has been shown numerically in Chapter 1 that the Prandtl number did not affect the theoretical decay exponent of the scalar variance in HIT at large Reynolds numbers. Consequently, a natural extension of this work is to address effects of Prandtl numbers on the time evolution of $< \theta^2 >$ and $< u_3\theta >$ in an anisotropic framework such as HITSG at large Reynolds numbers.

In the previous Chapter 5, only the case $Pr = 1$ was addressed: theoretical decay and growth exponents for $< u_3\theta >$ and $< \theta^2 >$ respectively were derived for HITSG, and assessed numerically. Therefore, the present work is an application of the anisotropic EDQNM modelling when the Prandtl number strongly departs from unity, basically from 10^{-5} to 10^4. Investigating an anisotropic configuration such as HITSG at large Reynolds numbers, with either very large or small Prandtl numbers, with an approach previously validated in more complex configurations such as shear-driven flows, is an important contribution in terms of modelling.

First, the theoretical spectral scalings of the cospectrum and scalar variance spectrum are derived in HITSG for $Pr \ll 1$ and $Pr \gg 1$, and four comparisons are performed to assess the relevance of the model when the Prandtl number strongly departs from unity: this part serves as a new and additional validation of the present anisotropic EDQNM modelling. Then, original numerical results are exposed. Effects of both very large and very small Prandtl numbers on the time evolution of $< \theta^2 >$ and $< u_3\theta >$ are investigated. Afterwards, the normalized mixed correlation $\rho_{w\theta}$ is studied as a function of the Reynolds and Prandtl numbers, and compared to results obtained in DNS. Furthermore, the effects of varying the Prandtl number on the small scales return to isotropy of the scalar second-order moments are analyzed. Finally, these different features are discussed in the concluding section.

6.1.1 Inertial scalings for $E_T(k,t)$ and $\mathcal{F}(k,t)$ - Comparisons

The emphasis is put on the inertial scaling of the scalar variance spectrum $E_T(k,t)$ and cospectrum $\mathcal{F}(k,t)$ when the Prandtl number is either very low or very large. These theoretical scalings are recovered analytically and numerically, and are then compared with recent numerical studies, such as DNS, LES and other spectral models. The fact that the present results are not always compared with DNS is because in most of the DNS, either the Reynolds number is not high enough, or the Prandtl number is too close to unity.

6.1.1.1 Highly diffusive passive scalar $Pr \ll 1$

Scaling of the scalar spectrum $E_T(k,t)$: in the inertial-diffusive range for HIT, the scalar spectrum scales as

$$E_T(k,t) = \frac{K_0}{3}\,\epsilon_T\,a^{-3}\,\epsilon^{2/3}\,k^{-17/3}. \tag{6.1}$$

It has been shown by Chasnov (1991) that with a mean scalar gradient Λ, the scalar dissipation rate ϵ_T should take into account this production effect, thus leading to

$$\epsilon_T \to \epsilon_T + 2a\Lambda^2, \tag{6.2}$$

where $2a\Lambda^2$ is a pseudo scalar dissipation rate arising from the mean gradient. The HIT scaling for E_T given in (6.1) is thus modified in HITSG into

$$E_T(k,t) = \frac{K_0}{3}\,\epsilon_T\,a^{-3}\,\epsilon^{2/3}\,k^{-17/3}\left(1 + 2\frac{a\Lambda^2}{\epsilon_T}\right). \tag{6.3}$$

Such a result was recovered analytically by O'Gorman & Pullin (2005) with their Sparse Direct-Interaction Perturbation (SDIP) model. Here, an alternative method is proposed, based on dimensional analysis and physical arguments that will be consistent with further developments. In the HITSG framework, the integration of the scalar Lin equation (4.36) yields

$$\frac{\partial K_T}{\partial t} = -\epsilon_T - 2\lambda_3 K_{\mathcal{F}} = -\epsilon_T\left(1 + \frac{2\lambda_3 K_{\mathcal{F}}}{\epsilon_T}\right).$$

The whole rhs term can be seen as a general scalar dissipation rate. Moreover, dimensional analysis gives $K_{\mathcal{F}} \sim \lambda_3 a$ which results into (6.2). The present simulations, at very low Prandtl numbers and very large Reynolds numbers, show that $2a\Lambda^2/\epsilon_T \ll 1$, so that the classical scaling (6.1) is still relevant. This is consistent with the RTI of small scales in the IDR: this feature will be illustrated later on. However, when a moderate Reynolds number is combined with a very small Pr, this ratio becomes greater than unity, so that the isotropic scaling is modified into

$$E_T(k,t) \sim \Lambda^2\,a^{-2}\,\epsilon^{2/3}\,k^{-17/3}, \tag{6.4}$$

derived in Bos *et al.* (2009); Yeung & Sreenivasan (2014), and is notably obtained by neglecting the non-linear contribution in the scalar Lin equation with respect to production and dissipation. It is worth noting that in Yeung & Sreenivasan (2014), the Prandtl number is very low, and the Reynolds number moderate, so that very likely small scales are still anisotropic due to production mechanisms. Consequently, the general expression (6.3) should be kept.

The $k^{-17/3}$ scaling of the scalar spectrum in low Pr HITSG has been assessed recently in a DNS by Yeung & Sreenivasan (2014). Present results are compared with the latter DNS in Fig. 6.1a. The final Reynolds number is $Re_\lambda = 240$ after ten turn-over times. The Prandtl number is $Pr = 1/2048$ and the initial integral scales are $L(0) = 1.346$ and $L_T(0) = 3.468$. $E_T(k, t = 0) = 0$ and scalar fluctuations arise from a unit mean scalar gradient. A good agreement is found for the scalar spectrum. Near the Kolmogorov wavenumber ($k\eta = 1$), the scalar spectrum slightly increases: this is due to small scale convection, as discussed in Chapter 1. This phenomenon increases with higher Reynolds numbers and lower Prandtl numbers. This does not happen in the DNS result, may be because small scales are not completely resolved beyond k_η. Nevertheless, the $k^{-17/3}$ is well recovered.

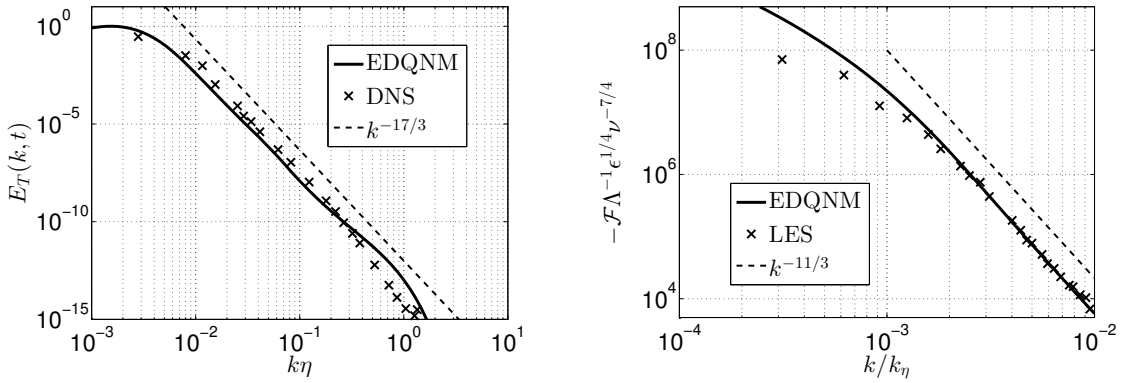

(a) (b)

Figure 6.1: (a) Scalar spectrum E_T obtained with EDQNM compared to Yeung & Sreenivasan (2014): with $Pr = 1/2048$ and $\sigma = 2$ at $Re_\lambda = 240$. (b) Cospectrum $\mathcal{F}$ compared with O'Gorman & Pullin (2005), with $Pr = 2.10^{-4}$, $Re_\lambda = 1500$ and $\sigma = 2$.

Scaling of the cospectrum $\mathcal{F}(k,t)$: the starting point to determine the cospectrum scaling is the scalar flux Lin equation

$$\left(\frac{\partial}{\partial t} + (a+\nu)k^2\right)\mathcal{F}(k,t) = \frac{2}{3}\Lambda E(k,t) + S_3^{\mathrm{F,NL}}(k,t). \tag{6.5}$$

A reasonable assumption is to say that the diffusive timescale $(ak^2)^{-1}$ is much smaller than the non linear time scale defined as

$$\tau(k) = \left(k^3 E(k)\right)^{-1/2} = \left(k^2\epsilon\right)^{-1/3} = \frac{kE(k)}{\epsilon}. \tag{6.6}$$

This is obvious at large k for high thermal diffusivity a. Therefore, non-linear contributions can be neglected, as previously mentioned for the scalar spectrum. Then, for scaling considerations, the time derivative is dropped off, so that

$$ak^2\mathcal{F}(k,t) = \frac{2}{3}\Lambda E(k,t),$$

which yields the IDR scaling for the cospectrum

$$\boxed{\mathcal{F}(k,t) = \frac{2}{3}K_0\Lambda a^{-1}\epsilon^{2/3}k^{-11/3}.} \tag{6.7}$$

A similar process was performed by Bos *et al.* (2009); Yeung & Sreenivasan (2014). O'Gorman & Pullin (2005) obtained this result with other analytical considerations. The key point being to neglect the non-linear transfers in both cases. Another approach is possible. Thanks to the previous work performed in Chapter 5, let's assume that the **spectral cospectrum correlation** is constant in the inertial range

$$\rho_{w\theta}(k) \simeq \rho_{w\theta} = \frac{\mathcal{F}(k)}{\sqrt{E(k)E_T(k)}}. \tag{6.8}$$

Hence, using Kolmogorov scaling for E, and Batchelor (1959) scaling (6.1) for E_T, one gets

$$\mathcal{F}(k,t) \sim a^{-3/2}\epsilon_T^{1/2}\epsilon^{2/3}k^{-11/3}. \tag{6.9}$$

Moreover, since the scalar field as no retro-action on the velocity one, ϵ_T should not appear in (6.9). Consequently, equalizing (6.7) and (6.9) gives $\epsilon_T \sim a\Lambda^2$. This is consistent with the additional scalar dissipation rate coming from mean scalar gradient effect explained previously in (6.2).

The $k^{-11/3}$ inertial-diffusive scaling of the cospectrum for $Pr \ll 1$ is assessed in Fig. 6.1b: our EDQNM simulation is compared to the LES of O'Gorman & Pullin (2005) where $Pr = 2.10^{-4}$ and $Re_\lambda = 1500$ (after 10 turn-over times for EDQNM). The agreement with the $k^{-11/3}$ scaling is rather good at this Reynolds number, and the agreement between EDQNM and LES is excellent in the inertial-diffusive range.

6.1.1.2 Weakly diffusive passive scalar $Pr \gg 1$

The case $Pr \gg 1$ is now considered: small scales of the scalar variance spectrum experience convection from the velocity field of the Kolmogorov scale, which results in a viscous-convective range from k_η, the smallest active turbulent scale for the velocity field, to the Batchelor wave-number $k_\mathrm{B} = \sqrt{Pr}k_\eta$, where E_T scales as (Batchelor, 1959)

$$E_T(k,t) = K_\mathrm{B}\epsilon_T\sqrt{\frac{\nu}{\epsilon}}k^{-1}, \tag{6.10}$$

where K_B is the Batchelor constant, found to be $\simeq 2.5$ in the present simulations. This value is close to the first proposal $K_\mathrm{B} = 2$ by Batchelor (1959), and in agreement with predictions of Gibson (1968): $\sqrt{3} \leq K_\mathrm{B} \leq 2\sqrt{3}$ for HIT. Other values measured in the ocean are slightly higher (see Qian (1995) and values reported therein) even though other mechanisms may play a non-negligible role in the ocean. Values obtained in DNS at moderate Re_λ are also higher (Yeung *et al.*, 2002).

The scaling of the cospectrum $\mathcal{F}(k,t)$ for a weakly diffusive passive scalar field has been discussed notably in O'Gorman & Pullin (2005) and it has been found that the spectral velocity-scalar correlation is not strongly modified in the framework $Pr \gg 1$, unlike the case $Pr \ll 1$. This is expected if one compares the cospectrum Lin equations (6.5) for $Pr = 1$ where $a = \nu$, so that the dissipative term is $2\nu k^2\mathcal{F}$, and for $Pr \gg 1$, where $a \ll \nu$, which yields for the dissipative term only $\nu k^2\mathcal{F}$. Hence, for a weakly diffusive scalar, the cospectrum still scales in $k^{-7/3}$ in the inertial-convective range.

Finally, two comparisons are proposed hereafter. Since in DNS when the Prandtl number increases the Reynolds number conjointly decreases for numerical resolution issues, we first propose a large Reynolds number comparison with the SDIP model (O'Gorman & Pullin, 2005) at $Pr = 100$ in Fig. 6.2a. However, since the SDIP is an asymptotic model, the Reynolds number is unknown. The agreement is acceptable, and the slight discrepancy may be attributed to the uncertainty for the Reynolds numbers, which is $Re_\lambda = 2.10^4$ here with the present anisotropic EDQNM modelling.

Then, in Fig. 6.2b, the compensated scalar variance spectrum is compared with the low Reynolds number DNS of Yeung *et al.* (2004), where $Re_\lambda \simeq 8$ and $Pr = 1024$. Initially, the scalar variance spectrum is zero, and the Reynolds number is chosen so that after ten turnover times the Reynolds number is $Re_\lambda = 10$. Our minimum wavenumber was decreased on purpose to match with the DNS configuration, and the reason for the slight discrepancy at large wavenumbers could be that the DNS is forced at large scales, whereas here we have a freely decaying Saffman turbulence. This does not prevent us from getting a very good agreement, both in the viscous convective range and further in the viscous-dissipative range, which validates our approach, even at low Reynolds numbers.

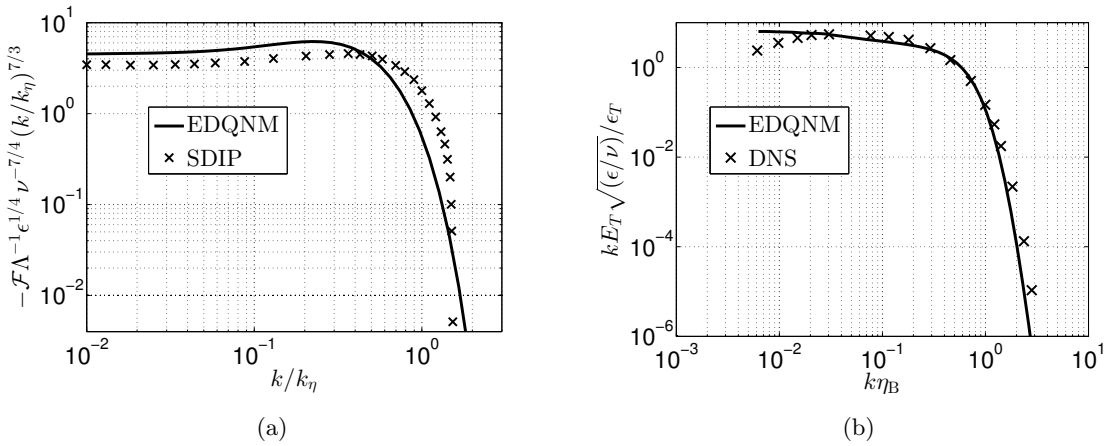

Figure 6.2: (a) Compensated cospectrum compared with the SDIP model (O'Gorman & Pullin, 2005) at $Re_\lambda = 2.10^4$ and $Pr = 100$. (b) Compensated scalar variance spectrum compared with the DNS of Yeung *et al.* (2004) at $Re_\lambda \simeq 8$ and $Pr = 1024$.

6.1.1.3 Spectral transfers and conclusions for the inertial scalings

The inertial scalings of the cospectrum $\mathcal{F}(k,t)$ and scalar variance spectrum $E_T(k,t)$ were investigated for both low and large Prandtl numbers in subsections 6.1.1.1 and 6.1.1.2, where a mean scalar gradient Λ sustains the fluctuations in a homogeneous isotropic decaying turbulence. The theoretical predictions were recovered analytically, and more importantly, assessed numerically over a wide range of Reynolds and Prandtl numbers, which illustrates the relevance of our anisotropic EDQNM modelling.

Finally, the budget terms of the evolution equation of $E_T(k,t)$ are analyzed in Fig. 6.4, for large (left column) and low (right column) Reynolds numbers, at high (top line) and small (bottom line) Prandtl numbers. The first observation is that for all four cases, the linear production term is more intense than the non-linear transfer at large scales, and then is negligible at smaller scales, meaning that production of scalar fluctuations through the mean gradient is dominant at large scales, where anisotropy is consistently gathered. In the very large Péclet number case (a) where $Pe_\lambda = Re_\lambda\sqrt{Pr} = 1.8.10^5$, there is a clear separation of three domains, in agreement with Yeung & Sreenivasan (2014), even though freely decaying turbulence is considered here: at low wavenumbers, one has almost $-S^{\mathrm{T,NL(iso)}} \simeq 2\Lambda\mathcal{F}$, and the difference is due to the term $\partial_t E_T \neq 0$; at intermediate wavenumbers, all three contributions are very small and of the same order; finally, at large wavenumbers, there is a balance between non-linear transfer and

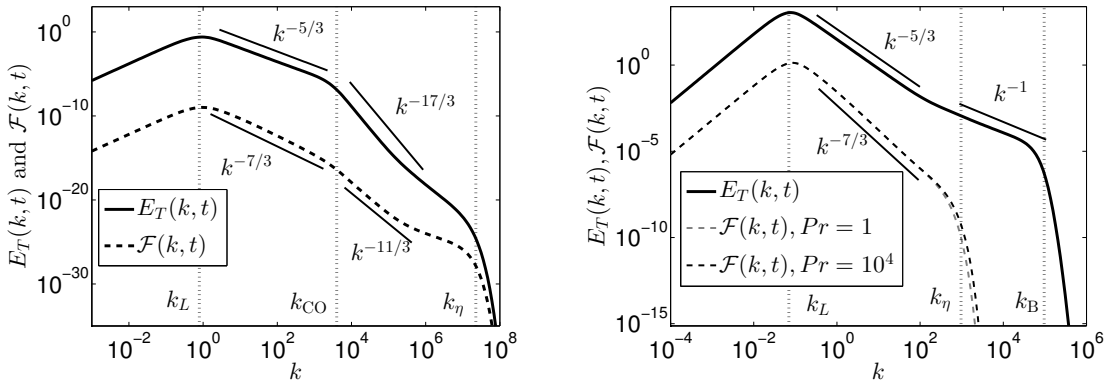

(a) (b)

Figure 6.3: Scalar variance spectrum $E_T(k,t)$ and cospectrum $\mathcal{F}(k,t)$ at large Reynolds numbers for $\sigma = 2$. (a) $Re_\lambda = 2.10^5$ and $Pr = 10^{-5}$, along with the integral, Corrsin-Obukhov and Kolmogorov wavenumbers k_L, k_{CO} and k_η. (b) $Re_\lambda = 10^4$ and $Pr = 10^4$, along with the integral, Kolmogorov and Batchelor wavenumbers k_L, k_η and k_{B}. The cospectrum at $Pr = 1$ at the same Reynolds numbers is displayed in grey as well.

dissipation $S^{\mathrm{T,NL(iso)}} \simeq 2ak^2E_T$. In the opposite case (d) where $Pe_\lambda \to 0$, non-linear transfers are small and production balances well dissipation, in agreement with the prediction of Yeung & Sreenivasan (2014). Furthermore, in the two low Prandtl number cases (c) and (d), the insets show that the dissipation term is always more intense that non-linear transfers, even in the high Re_λ configuration, in accord with the latter reference. For the two high Prandtl number cases (a) and (b), non-linear transfers are more intense around k_η, and then dissipation takes over while approaching k_B at larger wavenumbers.

6.1.2 Numerical results - Time evolution and anisotropy

In the previous section, the anisotropic EDQNM modelling was assessed for small and large Prandtl numbers in HITSG by investigating the inertial scalings of the scalar variance spectrum $E_T(k,t)$ and cospectrum $\mathcal{F}(k,t)$. In this part, effects of the Prandtl number Pr on the time evolution of the scalar variance K_T, the mixed-correlation $K_\mathcal{F}$, the normalized cospectrum correlation $\rho_{w\theta}$, and the Nusselt number Nu, are analyzed, along with the small scales return to isotropy of the flow.

6.1.2.1 Prandtl effects on the decay and growth of $< u_3\theta >$ and $< \theta^2 >$

The growth of $K_T =< \theta^2 >$ and decay of $K_\mathcal{F} =< u_3\theta >$ are addressed for both highly and weakly diffusive passive scalars. In Cahpter 5, for $Pr = 1$, one had $p_\mathcal{F} = 0.4075$. Here, for $Pr \ll 1$ and $Pr \gg 1$, it is found that $p_\mathcal{F}$ slightly increases to $p_\mathcal{F} \simeq 0.42$ when Pr departs from unity, consistently with the variations of the scalar backscatter parameter p_T in HIT with Pr. It makes sense that $p_\mathcal{F}$ varies less with Pr than p_T since $< u_3\theta >$ is a mixed correlation where the velocity field is not affected at all by a change in Pr.

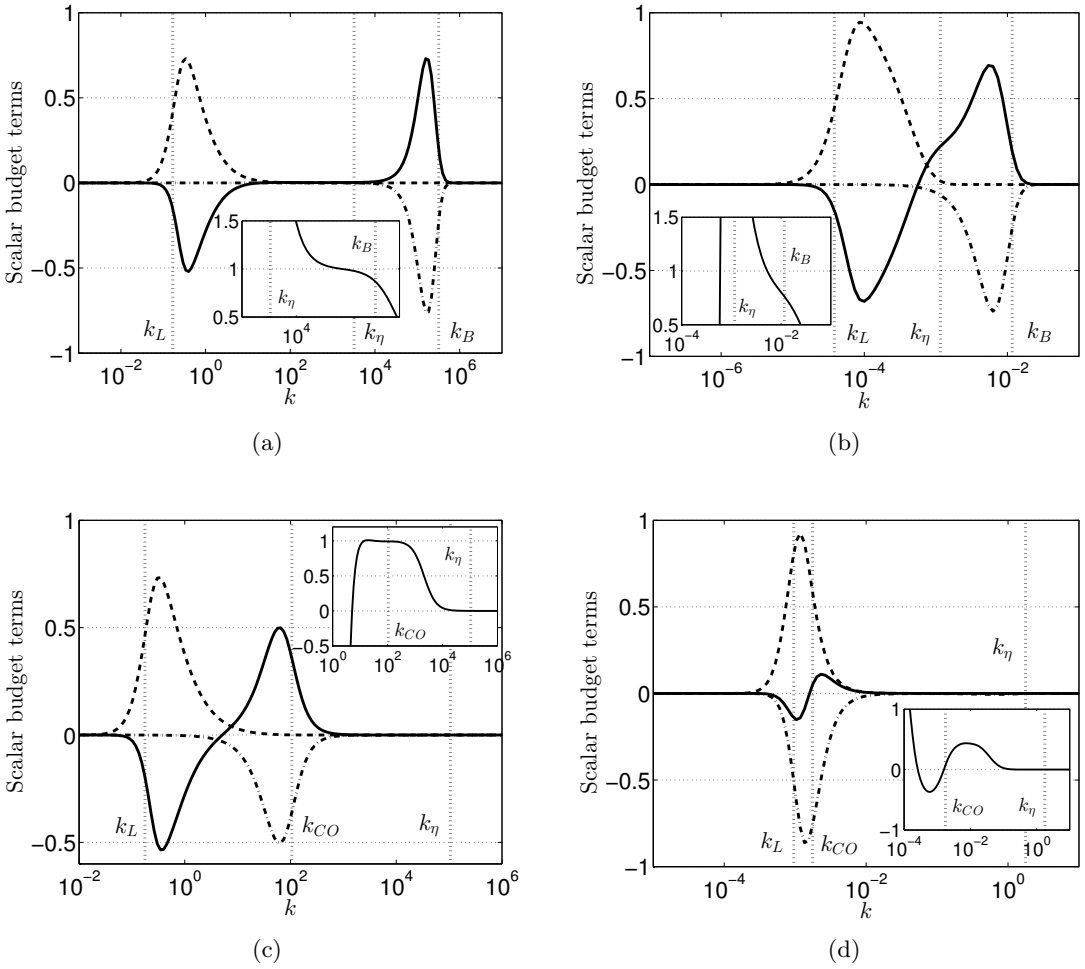

Figure 6.4: Budget terms of the evolution equation (4.36) of the scalar variance spectrum $E_T(k,t)$, along with the previous characteristic wavenumbers, for $\sigma = 2$. $-$ Non-linear term $kS^{\mathrm{T,NL(iso)}}$; $--$ Production term $2k\Lambda\mathcal{F}$; $-\cdot$ Dissipation term $-2ak^3E_T$. The insets represent the ratio $S^{\mathrm{T,NL(iso)}}/2ak^2E_T$. (a) $Re_\lambda = 1800$ and $Pr = 10^4$, (b) $Re_\lambda = 23$ and $Pr = 10^2$, (c) $Re_\lambda = 2.10^4$ and $Pr = 10^{-4}$, and (d)$Re_\lambda = 400$ and $Pr = 10^{-4}$.

In Fig. 6.5a and 6.5b, both theoretical predictions for $\alpha_{\mathcal{F}}$ and α_T^Λ given in (5.13) and (5.16) are recovered numerically. The Reynolds number Re_λ is much higher for $Pr \ll 1$ than for $Pr \gg 1$ in order to keep a sufficiently high Péclet number. One can say from Fig. 6.5a and 6.5b that the respective decay and growth of $K_{\mathcal{F}}$ and K_T in HITSG is not affected by high or small Prandtl numbers at large Reynolds numbers. A similar result was obtained for scalar integrated quantities such as K_T in decaying HIT in Chapter 1.

In addition, α_T^Λ is presented in Fig. 6.5c at moderate Reynolds numbers, typical of DNS and experiments, for various Prandtl numbers. This figure should be compared to the case $Pr = 1$ presented in Chapter 5, where a monotonic decrease of α_T^Λ was observed from the high Reynolds to the low Reynolds predictions (recalled in grey in Fig. 6.5c for Batchelor turbulence). Therefore, this figure clearly illustrates that even though a Pr strongly different from unity does not modify the asymptotic theoretical predictions at very large Reynolds numbers, it significantly alters the decay of the scalar variance K_T at moderate ones. For $Pr \gg 1$, the growth exponent α_T^Λ slightly increases before diminishing toward the low Reynolds numbers

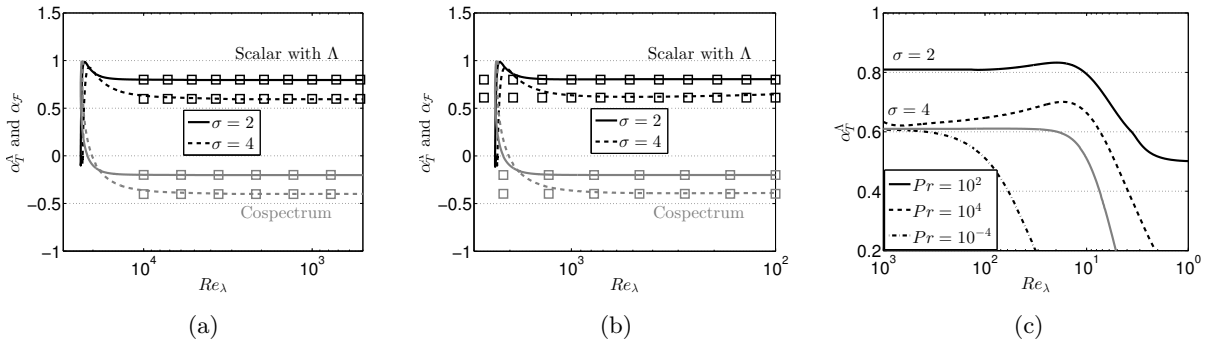

Figure 6.5: Scalar decay exponent α_T^Λ defined in (5.16) (black lines), and cospectrum decay exponent $\alpha_\mathcal{F}$ defined in (5.13) (grey lines). Simulations $\sigma = 2$ (-) and $\sigma = 4$ (- -), with □ the theoretical predictions, for (a) $Pr = 10^{-4}$, and (b) $Pr = 10^4$. (c) α_T^Λ at intermediate Reynolds numbers, for both $\sigma = 2$ and $\sigma = 4$ and various Pr (in black); the case $\sigma = 4$ and $Pr = 1$ is recalled in grey.

($Re_\lambda \leq 1$) predictions of Chapter 5: this is because when Re_λ decreases, the $k^{-5/3}$ inertial range vanishes. However, the k^{-1} viscous range survives, thus slightly slowing down the decay. Whereas for $Pr \ll 1$, the decrease of α_T^Λ starts at quite high Reynolds numbers, because the Péclet number is very small. The same observations are made for the decay exponent $\alpha_\mathcal{F}$ of the mixed-correlation.

Consequently, one could conclude from Fig. 6.5a, 6.5b and 6.5c that the Prandtl number does not affect the time exponent at very large Reynolds numbers, but at moderate ones. This is of importance because it could explain why in DNS there is a significant scatter of the normalized mixed-correlation $\rho_{w\theta}$.

6.1.2.2 Cospectrum correlation $\rho_{w\theta}$, pressure-scalar correlation $\Pi_\mathcal{F}$, and Nusselt number Nu

The normalized correlation $\rho_{w\theta}$, defined in (5.10), is addressed in Fig. 6.6a. Some values of this quantity at $Pr = 1$ were reported in Chapter 5: therefore, the emphasis is put here on the influence of Pr on $\rho_{w\theta}$. The first feature to point out is that at large Reynolds numbers, either with a small or large Prandtl number, $\rho_{w\theta}$ is constant: this can be obtained analytically by considering the expressions of the exponents α, α_T^Λ and $\alpha_\mathcal{F}$. Then, $\rho_{w\theta}$ diminishes with decreasing Reynolds numbers because of the joint decay of $< u_3\theta >$ and growth of the scalar variance, both studied in the previous part. It is worth noting that the magnitude of $\rho_{w\theta}$ strongly depends on Pr at moderate Re_λ, because the Prandtl number affects decay exponents in this region of moderate Reynolds numbers, as revealed previously in Fig. 6.5c.

In addition, several low Pr values from Yeung & Sreenivasan (2014) are included in Fig. 6.6a, and there is a good quantitative agreement with the present anisotropic EDQNM modelling: the three simulations of Yeung & Sreenivasan (2014), for $Pr = 1/2048$, $Pr = 1/512$, and $Pr = 1/128$, are almost all consistently contained within our EDQNM simulations at $Pr = 10^{-4}$ and $Pr = 10^{-2}$. Moreover, at these moderate Re_λ, it is recovered that $\rho_{w\theta}$ increases in magnitude with the Reynolds number at a given Pr. Furthermore, an interesting behaviour is recovered,

which is the decrease in magnitude of $\rho_{w\theta}$ when Pr departs from unity, either for $Pr \ll 1$ or $Pr \gg 1$, at a fixed moderate Re_λ: this notably confirms the DNS results of Yeung *et al.* (2002); Yeung & Sreenivasan (2014), and can be interpreted in terms of loss of phase alignment between spectral velocity and scalar fluctuations: indeed, for both $Pr \ll 1$ and $Pr \gg 1$, there exists a subrange in wavenumber space (the inertial-diffusive and viscous-convective ranges respectively) where the scalar variance spectrum strongly depart from the kinetic energy one. This phenomenon is much more visible for $Pr \ll 1$.

This decrease in magnitude of $\rho_{w\theta}$ with a Prandtl number different from unity is of practical interest since it happens at moderate Reynolds numbers only, and this might be the reason for the scattering of the obtained values of the cospectrum normalized correlation, as already mentioned in Chapter 5.

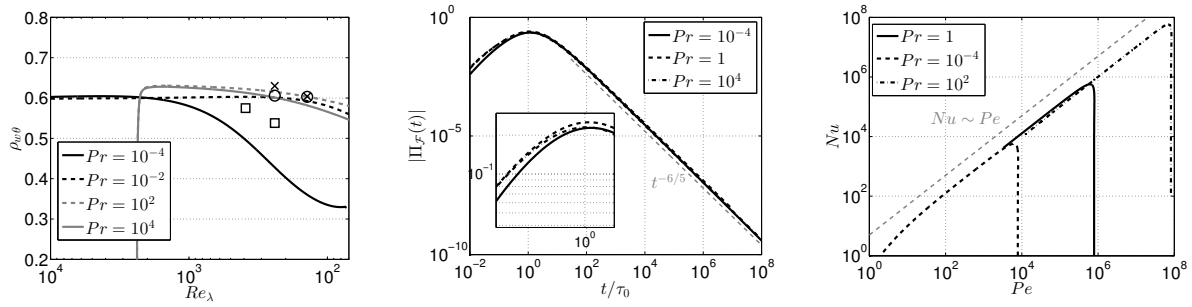

(a) (b) (c)

Figure 6.6: (a) Normalized correlation $\rho_{w\theta}$ for $\sigma = 4$ at various Prandtl numbers as a function of Re_λ. Symbols correspond to the DNS of Yeung & Sreenivasan (2014): □ $Pr = 1/2048$; ○ $Pr = 1/512$; × $Pr = 1/128$. Black and grey lines are respectively for small and large Prandtl numbers. (b) Pressure-scalar correlation $\Pi_{\mathcal{F}}$ for $\sigma = 2$ at various Prandtl numbers. The grey dashed line corresponds to the theoretical prediction. The zoom focuses on small times to illustrate the difference with varying Pr. (c) Nusselt number Nu, defined in (6.11), as a function of the Péclet number Pe, for various Pr.

Furthermore, the scalar-pressure correlation $\Pi_{\mathcal{F}} =< p\partial_3\theta >$ is investigated: this correlation has not received much attention, even though it is the destruction mechanism of the scalar flux, and was not addressed in Chapter 5. There, it was shown that one cannot define a decay rate for the dissipation $\epsilon_{\mathcal{F}}$ at large Reynolds numbers, because it is not conserved in the inertial range unlike ϵ and ϵ_T. But it is possible for $\Pi_{\mathcal{F}}$: indeed, according to the evolution equation (4.58) of $< u_3\theta >$, $\Pi_{\mathcal{F}}$ should evolve as the production mechanism, proportional to the kinetic energy $K(t)$. This is confirmed numerically in Fig. 6.6b for Saffman turbulence: $\Pi_{\mathcal{F}}$ is found to decay in $t^{-6/5}$, similarly to the kinetic energy. Furthermore, Fig. 6.6b once more illustrates that the theoretical decay rate does not depend on the Prandtl number.

Finally, the Nusselt number, defined as

$$Nu = -\frac{< u_3\theta >}{a\Lambda}, \tag{6.11}$$

is investigated for various Prandtl numbers. Nu is in fact another normalization of the mixed-correlation $< u_3\theta >$ which is of practical interest for heat transfers. The theoretical prediction for the Nusselt number, detailed and assessed in Gotoh & Watanabe (2012), is that it should

vary as $Nu \sim Pe$, where the Péclet number is $Pe = PrRe_T$, with the turbulent Reynolds number $Re_T = 3Re_\lambda^2/20$. This scaling is successfully recovered in Fig. 6.6c for a wide range of Péclet and Prandtl numbers.

6.1.2.3 Return to isotropy of small scales

The anisotropy of the flow is briefly investigated here, at the level of the scalar second-order moments: it is recalled that in Chapter 4, it was shown that small scales completely returned to isotropy, which was expected since the velocity field remains isotropic in HITSG. Consequently, one can wonder if the Prandtl number has an influence on the scalar small scales return to isotropy. Not surprisingly, it is found that the impact of the Prandtl number on the global anisotropy is comparable to moderate Reynolds numbers effects for the kinetic field: indeed, the relevant dimensionless parameter for the scalar is not only Re_λ, but the product $Re_\lambda\sqrt{Pr}$, which could be called a Taylor Péclet number Pe_λ.

Thus, even with a large Re_λ, if the Prandtl number is as small as 10^{-4}, Pe_λ will be moderately small, so that scalar small scales may not be not completely isotropic, in addition to other issues, such as the lack of scale separation in the spectra (Yeung & Sreenivasan, 2014). Consequently, very large Re_λ are required for highly diffusive passive scalars. This is illustrated in Fig. 6.7a, where the Taylor Reynolds number is very large $Re_\lambda \sim 10^5$, so that even at small Prandtl numbers of order $\sim 10^{-4}$, the Péclet number based on the Taylor scale is still sufficiently high $Pe_\lambda \sim 10^3$: this is an important condition for weakly diffusive passive scalars to obtain clear scalings, as underlined in Yeung & Sreenivasan (2014). This allows to observe in Fig. 6.7a that there is a complete return to isotropy of scalar second-order moments small scales. It is worth noting that from the Corrsin-Obukhov wavenumber k_{CO}, *i.e.* in the inertial-diffusive range, there is no more anisotropy: the non-linearity being much stronger in the inertial-convective range, for $k_L < k < k_{\mathrm{CO}}$, the return to isotropy mechanism occurs dominantly in this region of the wavenumber space.

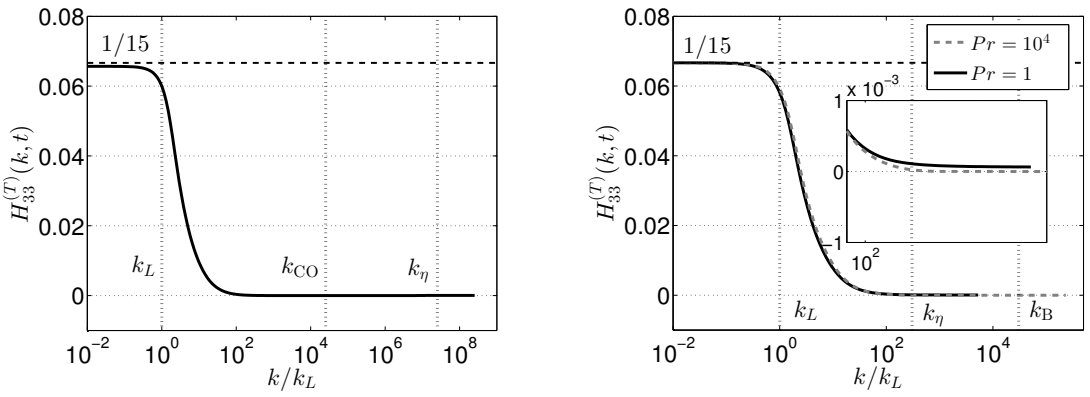

(a) (b)

Figure 6.7: Effects of Pr on $H_{33}^{(T)}$ for $\sigma = 2$ along with the integral, Kolmogorov, Corrsin-Obukhov and Batchelor wavenumbers k_L, k_η, k_{CO} and k_{B}. (a) $Pr = 10^{-4}$ and $Re_\lambda = 2,1.10^5$ so that $Pe_\lambda = 2,1.10^3$. (b) $Pr = 1$ in black and $Pr = 10^4$ in grey, both at $Re_\lambda = 100$, so that the Péclet number varies from $Pe_\lambda = 10^2$ to 10^4.

For weakly diffusive scalar, analogous assessments leading to a similar conclusion are made in Yeung *et al.* (2002), where it is shown numerically that even with a moderate Re_λ, increasing the Pr - which amounts to increase Pe_λ - allows to recover scalar isotropic small scales. It is proposed to illustrate this feature in Fig. 6.7b, where $H_{33}^{(T)}$ is displayed for Saffman turbulence at $Re_\lambda = 100$, for $Pr = 1$ and $Pr = 10^4$. It is clear, notably with the zoom around the Kolmogorov wavenumber k_η, that increasing the Prandtl number at a fixed Reynolds number participates into restoring isotropy at small scales.

Finally, it is worth noting that within our modelling, according to Fig. 6.7a and 6.7b, the large scales level of anisotropy seems to be independent of the Prandtl number in Saffman turbulence, and always very close to 1/15, with $1/15 \geq H_{33}^{(T)}$. This value of 1/15 is interesting because it is the maximum level of anisotropy that the scalar field can handle according to the realizability condition (4.29). Using the axisymmetric relations $H_{11}^{(T)} = H_{22}^{(T)} = -H_{33}^{(T)}/2$, one obtains that the largest eigenvalue is $H_{33}^{(T)}$. Thus, in HITSG, the realizability condition is verified (otherwise one would get negative scalar spectra) and the important feature is that the anisotropy reaches its maximal value at large scales in Saffman turbulence.

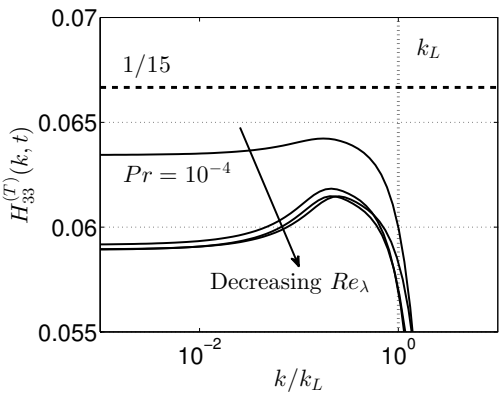

Figure 6.8: Zoom at large scales for $H_{33}^{(T)}$ in Batchelor turbulence ($\sigma = 4$) for $Pr = 10^{-4}$, along with the integral wavenumber k_L. The four different curves are at $Pe_\lambda = 193$, 87, 36 and 15.

The case of Batchelor turbulence is a bit different: indeed, because of classical backscatter of energy, strong inverse transfers initiate a return to isotropy mechanism at large scales (Eyink & Thomson, 2000), so that the large scales level of anisotropy can decrease with time (or equivalently can decrease when Re_λ decreases). This is more visible in the case $Pr \ll 1$ because the Péclet number is in general lower than in the case $Pr \gg 1$, as illustrated in Fig. 6.8. There, $H_{33}^{(T)}$ for $Pr = 10^{-4}$ is displayed at different times during the decay, or equivalently at various decreasing Reynolds numbers, so that the Péclet number goes from $Pe_\lambda = 193$ down to $Pe_\lambda = 15$. Even though the large scales level of anisotropy remains close to 1/15, it nevertheless slightly diminishes.

6.1.3 Conclusions for $Pr \neq 1$ in HITSG

Decaying homogeneous isotropic turbulence with a mean scalar gradient (HITSG) that sustains scalar fluctuations has been investigated numerically at large Reynolds numbers with the anisotropic EDQNM modelling. The present work is a direct application of Chapter 5 for a Prandtl

number either very small or very large: first, four quantitative comparisons are proposed. The good agreement between the present results and DNS, LES and other models, permits to assess the relevance of the model at $Pr \ll 1$ and $Pr \gg 1$ over a wide range of Reynolds numbers. This notably confirms numerically theoretical spectral scalings for the scalar variance spectrum $E_T(k,t)$ and the cospectrum $\mathcal{F}(k,t)$. Hence, in HITSG, at large Reynolds numbers, it is notably recovered that for $Pr \ll 1$, E_T and $\mathcal{F}$ scale respectively in $k^{-5/3}$ and $k^{-7/3}$ in the inertial-convective range, and then, from the Corrsin-Obukhov wavenumber k_{CO}, in $k^{-17/3}$ and $k^{-11/3}$ in the inertial-diffusive range. Moreover, when $Pr \gg 1$, the k^{-1} viscous convective range beyond k_η for E_T is not modified with the presence of a mean scalar gradient. For both low and large Prandtl numbers, budget terms of the evolution equation of $E_T(k,t)$ were analyzed as well: it was shown that at large scales, the production is always stronger than non-linear transfers. At small scales for $Pr \ll 1$, even at large Re_λ, dissipation is stronger than non-linear transfers: in the limit where the Péclet number tends to zero, dissipation balances production.

Secondly, the time evolution of the scalar variance $< \theta^2 >$ and the mixed-correlation $< u_3\theta >$ was investigated at large Reynolds numbers: it was shown numerically that the theoretical predictions of Chapter 5 for the algebraic time exponents are still valid for $Pr \ll 1$ and $Pr \gg 1$, consistently with a similar result for the scalar variance decay in HIT: the Prandtl number does not affect the asymptotic time evolution of $< \theta^2 >$ and $< u_3\theta >$ at large Reynolds numbers, only at moderate ones. In addition, it was shown numerically that the pressure-scalar correlation $< p\partial_3\theta >$, which is responsible for the destruction of the scalar flux, decays with the same rate as the kinetic energy, independently of the Prandtl number.

Afterwards, the Reynolds and Prandtl numbers dependence of the normalized cospectrum correlation $\rho_{w\theta}$ was addressed as well: the present spectral modelling provides good quantitative results with respect to DNS. Notably, it was found that at a fixed moderate Reynolds number, say $Re_\lambda \sim 100$, $\rho_{w\theta}$ decreases in magnitude when the Prandtl number either increases or decreases, in agreement with the prediction of Yeung & Sreenivasan (2014). The linear dependence of the Nusselt number with the Péclet number is also recovered.

Finally, it was shown numerically that the small scales of the scalar second-order moments return to isotropy, provided the Péclet number is large enough. This notably implies, for highly diffusive passive scalars, the need to reach very high Taylor Reynolds numbers Re_λ when one wants to obtain a clear $k^{-17/3}$ inertial-diffusive scaling, which numerically requires that $Pr \leq 10^{-3}$.

6.2 Prandtl number effects in shear-driven turbulence

In this section, HSRT, HST and HSTSG are addressed. The results regarding the impact of a Prandtl number strongly different from unity are less conclusive than in the previous section dedicated to HITSG. There are mainly two reasons for this: (i) First, for $Pr \ll 1$, huge initial Reynolds numbers are needed, which make the simulations really long when St increases. This is particularly true when there is no mean scalar gradient, *i.e.* in HST, since K_T decreases exponentially whereas K increases exponentially. Nevertheless, a new result regarding the inertial-diffusive scaling of $\mathcal{F}_S$ is proposed for HSTSG when $Pr \ll 1$. (ii) Secondly, when $Pr \gg 1$, it is not clear if the use of non-local transfers, detailed in Appendix B, to sustain the k^{-1} viscous-convective range remains appropriate when a sustained shear is applied. Indeed,

the non-local transfers were first derived for isotropic turbulence: since in HITSG the velocity field remains isotropic, it seemed relevant enough to use the non-local expansions in the previous section. But a sustained shear is the most anisotropic case. Hence, it is not straightforward to quantify how the anisotropic non-linear transfers "disturb" the isotropic scalar non-local transfer in the presence of shear.

Whatever framework is considered, HSRT, HST, or HSTSG, the $k^{-17/3}$ inertial-diffusive scaling when $Pr \ll 1$ and the k^{-1} viscous convective scaling when $Pr \gg 1$ for $E_T(k,t)$ are not modified by the presence of shear. For the cospectrum $\mathcal{F}(k,t)$, the $k^{-11/3}$ inertial-diffusive scaling when $Pr \ll 1$ is also not modified by the presence of shear.

6.2.1 Homogeneous shear-released turbulence

In this section, the decay of K_T in HSRT is addressed when either $Pr \ll 1$ or $Pr \gg 1$. It is revealed in Fig. 6.9 that the Prandtl number does not affect the decay of the scalar variance K_T in HSRT, as previously shown in HIT in Chapter 1 for asymptotically large or small Reynolds numbers. Saffman and Batchelor turbulence are presented. It is notably found that K_T decays faster with $Pr = 10^{-4}$ than with $Pr = 1$, which is consistent with a moderate Péclet number: the low Reynolds numbers regime is reached more rapidly than with $Pr \geq 1$.

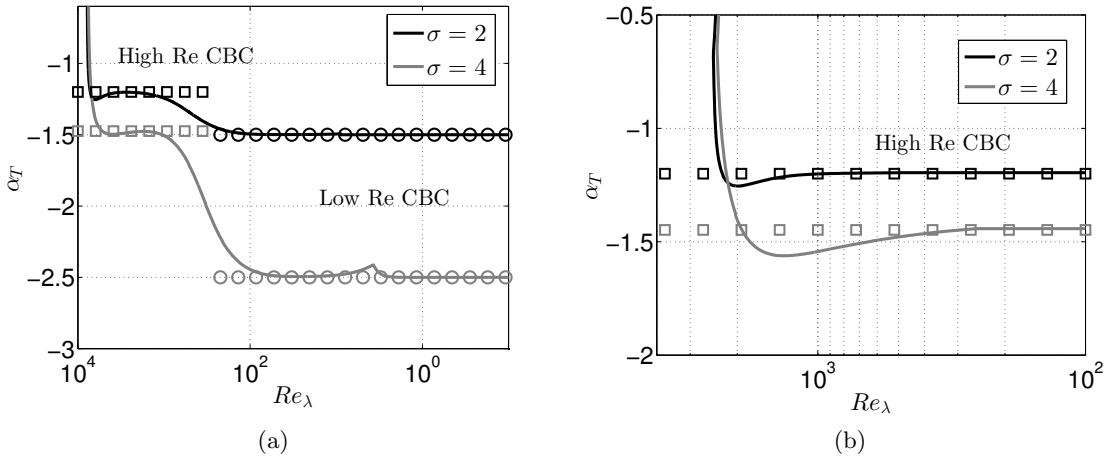

Figure 6.9: Scalar variance decay exponent α_T, with $\sigma = 2$ in black and $\sigma = 4$ in grey, with $St = 1$; □: high Reynolds predictions; ○: low Reynolds predictions. (a) From high to low Reynolds numbers regimes for $Pr = 10^{-4}$. (b) For $Pr = 10^4$.

The scalar global anisotropy indicators b_{ij}^T are then displayed in Fig. 6.10 for both very large and very small Prandtl numbers, and they have the same behaviour as in the case $Pr = 1$, *i.e.* an asymptotic state different from zero, meaning that there is still anisotropy left in the flow, gathered at large scales.

6.2.2 Sustained shear flow

The case of sustained shear flows is now addressed. It is revealed in Fig. 6.11 that even with $Pr \ll 1$ or $Pr \gg 1$, the scalar variance K_T still decays exponentially with $\gamma_T = -0.52$. This is

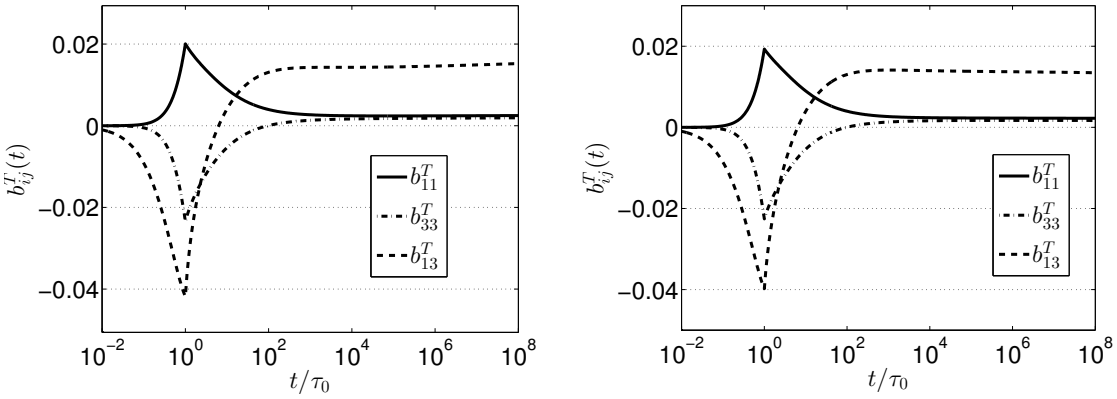

(a) (b)

Figure 6.10: b_{ij}^T for $\sigma = 2$ and $St = 1$. (a) $Pr = 10^{-4}$. (b) $Pr = 10^4$.

consistent with the Prandtl number dominantly affecting the small scales of the scalar variance spectrum. Nevertheless, for $Pr \ll 1$, with an initial $Re_\lambda(0) = 1$, the associated Péclet number would be too small and consequently the transitional state before reaching the asymptotic anisotropic state would be rather large: furthermore, a too low $Re_\lambda(0)$ causes some numerical issues. Therefore, for a sustained shear flow and $Pr \ll 1$, the initial Reynolds number is chosen much higher ($Re_\lambda(0) = 100$) to ensure an initial moderate Péclet number. Whereas in the configuration $Pr \gg 1$, the initial Péclet number is sufficiently large so that no specific precautions have to be taken.

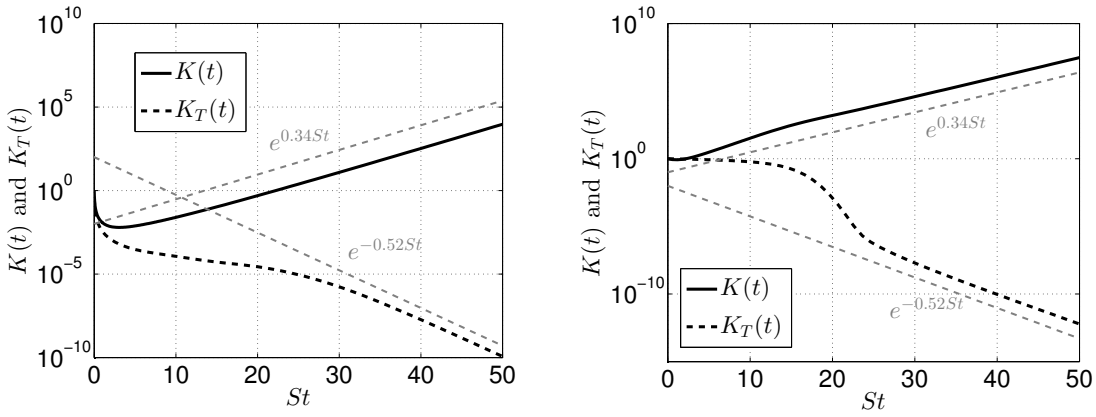

(a) (b)

Figure 6.11: Scalar variance K_T in Saffman HST. (a) For $S = 10^{-2}\tau_0^{-1}$, $Re_\lambda(0) = 100$ and $Pr = 10^{-4}$. (b) For $S = 1\tau_0^{-1}$ and $Pr = 10^4$.

Afterwards, the time evolution of the b_{ij}^T and of the scalar shear rapidity $S_{\mathrm{R}}^T = \epsilon_T/(K_T S)$ are displayed in Fig. 6.12 for Saffman HST, for both $Pr = 10^{-4}$ and $Pr = 10^4$. They all reach the same asymptotic anisotropic state, independently of the value of the Prandtl number, which is similar to the previous findings about anisotropy in HITSG.

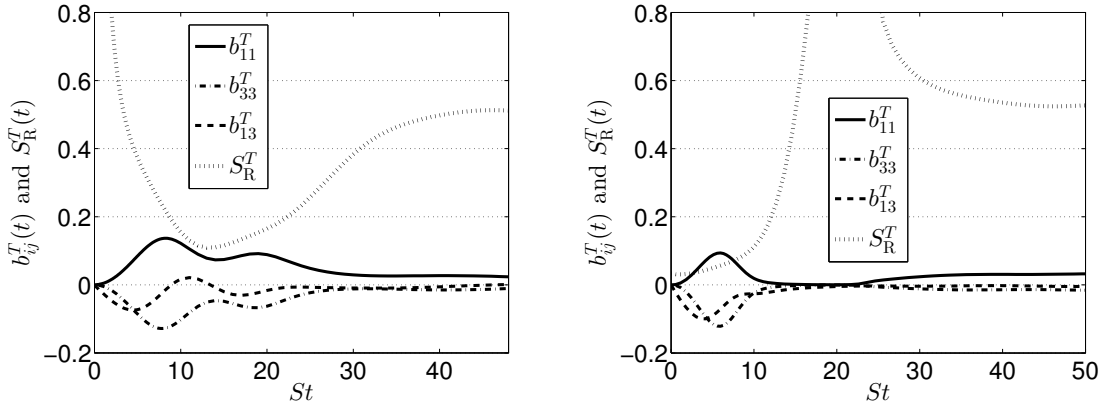

(a) (b)

Figure 6.12: Scalar global anisotropy indicators $b_{ij}^T(t)$ and scalar shear rapidity $S_R^T(t)$. (a) For $S = 10^{-2}\tau_0^{-1}$, $Re_\lambda(0) = 100$ and $Pr = 10^{-4}$. (b) For $S = 1\tau_0^{-1}$ and $Pr = 10^4$.

Finally, for illustration purposes in the high Prandtl case, the scalar variance spectrum E_T is presented in Fig. 6.13a at $St = 50$ and displays a clear k^{-1} scaling in the VCR. This scaling is obviously not modified by anisotropy, because mean velocity gradients mainly apply on large scales. In addition, the scalar fluxes are displayed in Fig 6.13b: the impact of the direct non-local part T_T^+ of the non-linear scalar transfer, which results in the non-local flux Π_T^+ after integration, is clear on the scalar non-linear isotropic flux $\Pi_T^{\mathrm{NL(iso)}}$: energy is brought beyond the Kolmogorov wavenumber and the total resulting flux is found to be constant through k_η. This non-local transfer allows to maintain, as in HIT, the k^{-1} viscous-convective range.

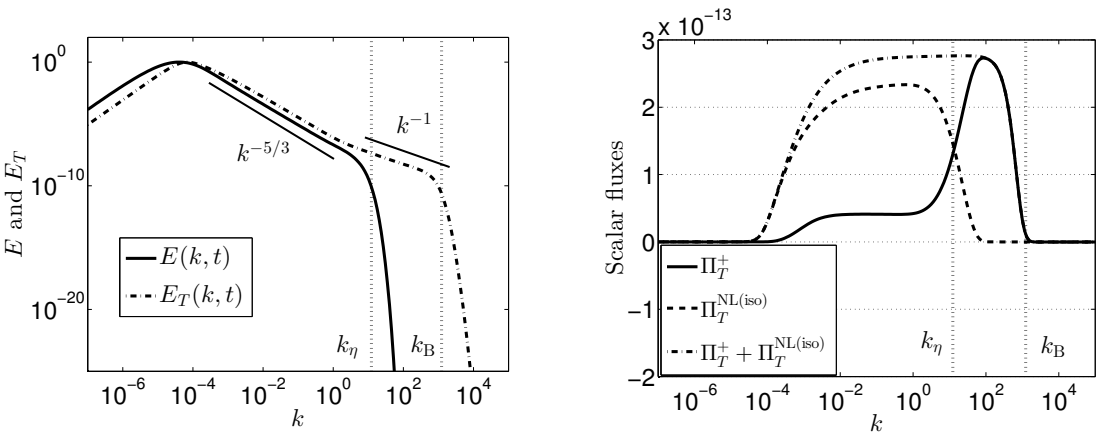

(a) (b)

Figure 6.13: (a) Normalized kinetic energy and scalar variance spectra $E(k,t)$ and $E_T(k,t)$. (b) Scalar fluxes: non-linear isotropic $\Pi_T^{\mathrm{NL(iso)}}$ and non-local (direct) Π_T^+ contributions. Both with the Kolmogorov and Batchelor wavenumbers k_η and k_B, at $Pr = 10^4$, $\sigma = 2$ and at $St = 50$ ($Re_\lambda \sim 10^4$).

6.2.3 Homogeneous Shear Turbulence with a mean Scalar Gradient

The HSTSG framework is now studied. For $Pr \ll 1$, the scaling of the streamwise flux spectrum $E_1^F = \mathcal{F}_S$ in the inertial range can be easily predicted using arguments similar to the ones of Bos & Bertoglio (2007) in the case $Pr = 1$. Starting from the scaling of the cospectrum for a highly conductive passive scalar field (6.7), and replacing ϵ by ϵ_{ij}, which is justified by the presence of the main shear $\mathrm{d}U_1/\mathrm{d}x_3$, yields

$$E_i^F(k,t) = \frac{2}{3} K_0 a^{-1} \lambda_j \epsilon_{ij}^{2/3}(k) k^{-11/3}. \tag{6.12}$$

Then, the scaling of the spectral tensor is used $\epsilon_{ij}(k)E(k) = 3\phi_{ij}(k)\epsilon$, where $\epsilon_{ii} = 2\epsilon$. This gives in the inertial range $\epsilon_{ij}(k) \sim S\epsilon^{2/3}k^{-2/3}$. Finally, for very low Prandtl numbers, the streamwise scalar flux is, in the inertial-diffusive range,

$$\boxed{\mathcal{F}_S(k,t) = -C_{\mathcal{F}}^S \Lambda a^{-1} \epsilon^{4/9} k^{-37/9}.} \tag{6.13}$$

In Fig. 6.14a, the $k^{-37/9}$ scaling for the streamwise flux $\mathcal{F}_S$ is assessed over two decades in the IDR (the two components of the scalar flux have been decreased for readability reasons), and the $k^{-23/9}$ slope in the ICR is recovered as well. The scalar spectrum E_T and cospectrum $\mathcal{F}$ display the same scaling as in HITSG and are not modified by shear, similarly to the case of $Pr = 1$. For weakly diffusive passive scalars $Pr \gg 1$, E_T still displays a k^{-1} slope in the VCR, whereas $\mathcal{F}$ and $\mathcal{F}_S$ scale similarly to the case $Pr = 1$ in HSTSG. This is also illustrated in Fig. 6.14b.

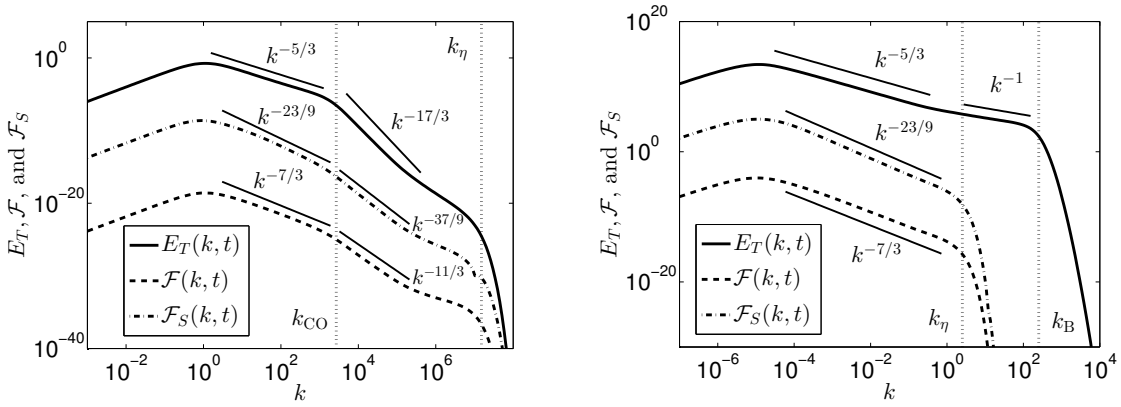

(a) (b)

Figure 6.14: Scalar variance, cospectrum and streamwise flux spectra E_T, $\mathcal{F}$ and $\mathcal{F}_S$ in Saffman HSTSG. (a) For $Pr = 10^{-5}$ and $S = 1\tau_0^{-1}$, at $Re_\lambda = 2.10^5$, along with the Corrsin-Obukhov and Kolmogorov wavenumbers k_{CO} and k_η. (b) For $Pr = 10^4$ and $S = 10^{-2}\tau_0^{-1}$, along with the Kolmogorov and Batchelor wavenumbers k_η and k_{B}.

Finally, the exponential growth of K, K_T, $K_{\mathcal{F}}$ and $K_{\mathcal{F}}^S$ at the rate $\gamma = 0.34$ is presented in Fig. 6.15. In the latter figure, $K_{\mathcal{F}}$ and $K_{\mathcal{F}}^S$ can hardly be distinguished. There is no strong differences with the case $Pr = 1$, except that the transitory state for the scalar variance and mixed correlations $< u_1\theta >$ and $< u_3\theta >$ is longer for the case $Pr \ll 1$, as noted previously

in HST for K_T. One can nevertheless remark that either in the case $Pr \ll 1$ or $Pr \gg 1$, the kinetic energy is always less intense than K_T, $K_{\mathcal{F}}$ and $K_{\mathcal{F}}^S$, as in the case $Pr = 1$.

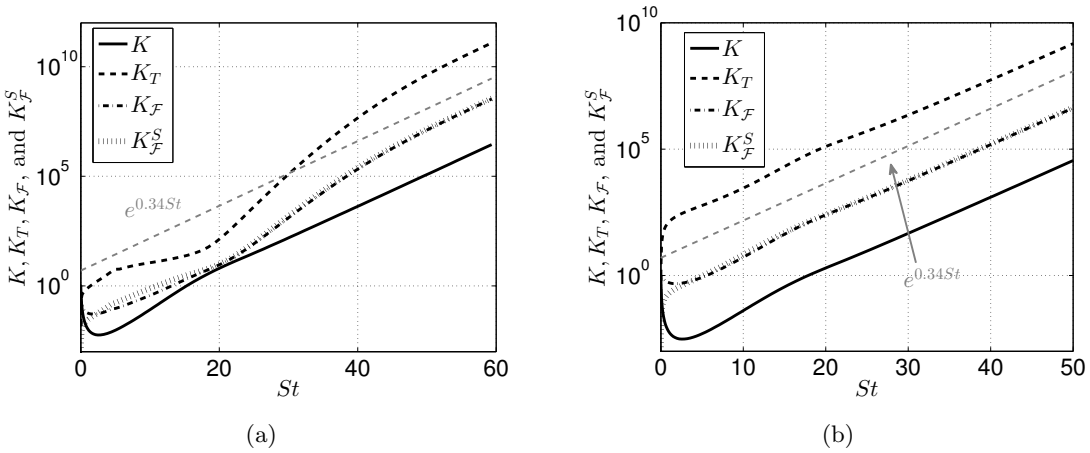

Figure 6.15: Kinetic energy K, scalar variance K_T, and mixed-correlations $K_{\mathcal{F}}$ and $K_{\mathcal{F}}^S$, in Saffman HSTSG. (a) For $Pr = 10^{-5}$ and $S = 1\tau_0^{-1}$. (b) For $Pr = 10^4$ and $S = 10^{-2}\tau_0^{-1}$.

6.2.4 Conclusions about shear-driven turbulence for $Pr \neq 1$

As specified at the beginning of this chapter, the results for highly and weakly diffusive passive scalars in shear-driven turbulence are less conclusive than in HITSG. The lack of accurate data for these regimes is flagrant since it was impossible to perform quantitative comparisons against DNS and experiments.

Therefore, this section should be considered as a guide for future works, and may be some of the results presented here will be of use. Nevertheless, the noteworthy findings are twofold: (i) the Prandtl number does not affect the exponential rate of the scalar and scalar flux fields in HST and HSTSG. (ii) For $Pr \ll 1$, a new IDR scaling was derived for the streamwise flux $\mathcal{F}_S$ based on the arguments of Bos & Bertoglio (2007) for $Pr = 1$, which reads $\mathcal{F}_S \sim k^{-37/9}$.

On a theoretical point of view, as mentioned earlier, it is not clear if the use of isotropic non-local transfers for the scalar field in the case $Pr \gg 1$ remains relevant in the presence of shear. Anisotropic non-local transfers were derived (but not presented in Appendix B) following the methodology of Lesieur & Schertzer (1978), but they proved to be completely negligible with respect to the scalar isotropic transfer. What are the reasons for doubting of these non-local transfers? First, the direct non-local transfer T_T^+ brings strongly "anisotropic scalar variance" from large scales to almost isotropic small scales, and this transfer only depends on E and E_T, not on the anisotropic descriptors $H_{ij}^{()}$. Secondly, in some configurations, the inverse non-local scalar transfers T_T^- caused some numerical issue, probably because it only affects the isotropic spectrum E_T at larges scales (by bringing small scales "isotropic scalar variance") and not $E_T H_{ij}^{(T)}$.

Chapter 7

Spectral Modelling for Unstably Stratified Homogeneous Turbulence

In this section, the anisotropic EDQNM modelling is extended to the case of active scalar dynamics.

> The contents of this chapter, except the variable stratification part, were published in: Briard, Iyer & Gomez, "Anisotropic spectral modeling for unstably stratified homogeneous turbulence", *Physical Review Fluids*, **2** (4), 044604 (2017)

Unstably Stratified Homogeneous Turbulence (USHT) can be seen as a simplified approach for Rayleigh-Taylor instability (Soulard & Griffond, 2012; Gréa, 2013; Soulard *et al.*, 2016), which is a phenomenon occurring for fluid of variable density. This instability can be found in various areas, such as geophysical, astrophysical and confined industrial flows: more specifically, the Rayleigh-Taylor instability can happen in natural flows such as atmospheric ones because of the mean vertical temperature gradient, when the heavy fluid, located above the lighter one, pushes it downward due to gravitational acceleration, which creates a mixing zone.

To investigate both numerically and theoretically a mechanism as complex as Rayleigh-Taylor instability, it is convenient to work in the framework of USHT, which notably discards inhomogeneity, uses the Boussinesq approximation to reflect the retro-action of the convected buoyant field on the velocity one, and assumes that the mixing length L is constant in time, and larger than the turbulent integral scale (Soulard *et al.*, 2014; Burlot *et al.*, 2015*a*,*b*; Gréa *et al.*, 2016*a*). It follows that the stratification frequency N is constant as well. One has to point out that frameworks different from USHT can be considered as well, for instance variable-density flows where the Boussinesq approximation is not used anymore (Livescu & Ristorcelli, 2007; Chung & Pullin, 2010).

The USHT framework has been addressed recently, thanks to the *axisymmetric EDQNM model* (Burlot *et al.*, 2015*a*,*b*; Gréa *et al.*, 2016*a*) to analyze the large Reynolds numbers regimes. As specified by its name, this spectral approach is dedicated to axisymmetric configurations and permits an accurate investigation of the scale-by-scale anisotropy distribution, and of the time evolution of one-point statistics such as the Froude number Fr and the mixing intensity Λ,

which will be defined later on. The strength of the axisymmetric EDQNM is that production terms, linear with N, are exactly treated, whereas the non-linear transfers are closed by a classical EDQNM procedure, which is the most costly step in terms of computational resources. However, this approach cannot handle, at least in the present form, shear flows, where there is no particular symmetry, unlike the present anisotropic EDQNM modelling. For this reason, the latter model is extended here to the case of active scalar dynamics, and compared to the results obtained with the axisymmetric EDQNM of Burlot and coworkers. Furthermore, throughout this chapter, USHT is qualitatively compared to results obtained with the anisotropic EDQNM modelling in the frameworks of HST and HITSG (Chapters 3 and 5). In addition, both the effects of large Schmidt numbers Sc on the inertial scaling of the scalar flux spectrum, and pressure spectra, are addressed on a fundamental point of view.

The extension of the anisotropic EDQNM modelling to unstable stratification is a step further towards the modelling and understanding of high Reynolds geophysical flows, such as atmospheric and oceanic ones. Indeed, under the assumption of homogeneity, such flows contain effects of shear, temperature and concentration gradients, stratification, rotation, and helicity. Shear and mean scalar gradient mechanisms have already been addressed with our model, and helicity is the topic of Chapter 8, so that stratification appears to be an natural extension, whereas effects of rotation were addressed independently with EDQNM2 (Cambon *et al.*, 2013).

Then, a step further toward the modelling of Rayleigh-Taylor instability is crossed by allowing the stratification frequency $N(t)$ to vary with time, with a retro-action of the fluctuating quantities on the mean field. In such a configuration, the dynamics is completely different, and the mixing length $L(t)$ is known to evolve in t^2 (Soulard & Griffond, 2012; Gréa, 2013; Soulard *et al.*, 2016).

7.1 Evolution equations in USHT

In this section, the spectral anisotropic modelling developed in Chapters 2 and 4 for passive scalar dynamics is extended to the case of unstably stratified turbulence: the additional linear transfers linked to the Boussinesq approximation are presented hereafter.

7.1.1 Additional coupling terms

As commonly done for USHT, one has to scale the scalar fluctuations θ, which is usually a concentration, as a buoyant velocity $\mathfrak{v}$ (Soulard *et al.*, 2014) according to

$$\mathfrak{v} = \frac{2\mathcal{A}g\theta}{N}, \tag{7.1}$$

where N is the stratification characteristic time, or buoyancy frequency

$$N = \sqrt{2\mathcal{A}g\frac{\mathrm{d}\mathfrak{V}}{\mathrm{d}x_3}}, \tag{7.2}$$

where $\mathfrak{V}$ is the mean buoyant field, g the gravitational acceleration, $\mathcal{A}$ the Atwood number $\mathcal{A} = (\rho_1 - \rho_2)/(\rho_1 + \rho_2)$, assumed to be small or the Boussinesq approximation, with ρ_1 and ρ_2

the densities of the heavy and light fluid respectively. The evolution equations of the fluctuating velocity and scalar fields are then

$$\frac{\partial \mathfrak{v}}{\partial t} + u_j \frac{\partial \mathfrak{v}}{\partial x_j} = a \frac{\partial^2 \mathfrak{v}}{\partial x_j \partial x_j} + N u_3, \tag{7.3}$$

$$\frac{\partial u_i}{\partial t} + u_j \frac{\partial u_i}{\partial x_j} = -\frac{\partial p}{\partial x_i} + \nu \frac{\partial^2 u_i}{\partial x_j \partial x_j} + N \mathfrak{v}\, \delta_{i3}. \tag{7.4}$$

The spectral counterpart of these equations are straightforward (see Appendices C and E). In what follows, one has to replace $\hat{\theta}$ by $\hat{\mathfrak{v}}$ in the definitions of the spectral quantities introduced in Chapter 4. The evolution equations of the two-point second-order correlations $\hat{R}_{ij}$, F_i and $\mathcal{E}^T$ are then

$$\left(\frac{\partial}{\partial t} + 2\nu k^2\right) \hat{R}_{ij}(\boldsymbol{k}, t) = T_{ij}^{\mathrm{NL}}(\boldsymbol{k}, t) + \underbrace{N\Big(P_{j3}(\boldsymbol{k}) F_i(\boldsymbol{k}, t) + P_{i3}(\boldsymbol{k}) F_j(\boldsymbol{k}, t)\Big)}_{\text{Additional stratification coupling}}, \tag{7.5}$$

$$\left(\frac{\partial}{\partial t} + (\nu + a) k^2\right) F_i(\boldsymbol{k}, t) = T_i^{\mathrm{F,NL}}(\boldsymbol{k}, t) + N \hat{R}_{i3}(\boldsymbol{k}, t) + \underbrace{N P_{i3}(\boldsymbol{k})\, \mathcal{E}^T(\boldsymbol{k}, t)}_{\text{Additional coupling}}, \tag{7.6}$$

$$\left(\frac{\partial}{\partial t} + 2a k^2\right) \mathcal{E}^T(\boldsymbol{k}, t) = T^{\mathrm{T,NL}}(\boldsymbol{k}, t) + 2N F_3(\boldsymbol{k}, t). \tag{7.7}$$

7.1.2 Spherically-averaged Lin equations for USHT

The computation of the new linear transfers linked to the buoyancy frequency N amounts to only two additional production terms with respect to HITSG, as seen just before: the retro-action of the scalar field on the cospectrum, and the retro-action of the scalar flux on the kinetic energy spectrum. The resulting four new linear spherically-averaged transfers for unstably stratified turbulence are, for a vertical scalar gradient (along x_3),

$$S^{\mathrm{L,USHT(iso)}}(k) = N \int_{S_k} P_{i3}(\boldsymbol{k}) F_i(\boldsymbol{k}) \mathrm{d}^2\boldsymbol{k} = N \mathcal{F}(k), \tag{7.8}$$

$$\begin{aligned} S_{ij}^{\mathrm{L,USHT(dir)}}(k) &= \frac{N}{2} \int_{S_k} P_{l3}(\boldsymbol{k}) F_l(\boldsymbol{k}) P_{ij}(\boldsymbol{k}) \mathrm{d}^2\boldsymbol{k} - \frac{\delta_{ij}}{3} N \mathcal{F}(k) \\ &= \frac{N}{20}\Big(E_i^F(k)\delta_{j3} + E_j^F(k)\delta_{i3} - \frac{2}{3}\mathcal{F}(k)\delta_{ij}\Big), \end{aligned} \tag{7.9}$$

$$\begin{aligned} S_{ij}^{\mathrm{L,USHT(pol)}}(k) &= \frac{N}{4} \int_{S_k} \Big(P_{l3}(\boldsymbol{k}) F_n(\boldsymbol{k}) + P_{n3}(\boldsymbol{k}) F_l(\boldsymbol{k})\Big) N_l^*(\boldsymbol{k}) N_n^*(\boldsymbol{k}) N_i(\boldsymbol{k}) N_j(\boldsymbol{k}) \mathrm{d}^2\boldsymbol{k} \\ &= \frac{3N}{10}\Big(E_i^F(k)\delta_{j3} + E_j^F(k)\delta_{i3} - \frac{2}{3}\mathcal{F}(k)\delta_{ij}\Big), \end{aligned} \tag{7.10}$$

$$S_i^{\mathrm{F,L,USHT}}(k) = N \int_{S_k} \mathcal{E}^T(\boldsymbol{k}) P_{i3}(\boldsymbol{k}) \mathrm{d}^2\boldsymbol{k} = 2N E_T(k,t)\Big(\frac{1}{3}\delta_{i3} + H_{i3}^{(T)}(k)\Big). \tag{7.11}$$

Consequently, the spherically-averaged Lin equations for USHT are

$$\left(\frac{\partial}{\partial t} + 2\nu k^2\right) E(k,t) = S^{\mathrm{NL(iso)}}(k,t) + N \mathcal{F}(k,t), \tag{7.12}$$

$$\left(\frac{\partial}{\partial t} + 2\nu k^2\right) E(k,t) H_{33}^{(\mathrm{dir})}(k,t) = S_{33}^{\mathrm{NL(dir)}}(k,t) + \frac{N}{15}\mathcal{F}(k,t), \tag{7.13}$$

$$\left(\frac{\partial}{\partial t}+2\nu k^2\right)E(k,t)H_{33}^{(\mathrm{pol})}(k,t)=S_{33}^{\mathrm{NL(pol)}}(k,t)+\frac{2N}{5}\mathcal{F}(k,t), \tag{7.14}$$

$$\left(\frac{\partial}{\partial t}+2ak^2\right)E_T(k,t)=S^{\mathrm{T,NL(iso)}}(k,t)+2N\mathcal{F}(k,t), \tag{7.15}$$

$$\left(\frac{\partial}{\partial t}+2ak^2\right)E_T(k,t)H_{33}^{(T)}(k,t)=S_{33}^{\mathrm{T,NL(dir)}}(k,t)+\frac{2}{15}N\mathcal{F}(k,t), \tag{7.16}$$

$$\left(\frac{\partial}{\partial t}+(\nu+a)k^2\right)\mathcal{F}(k,t)=S_3^{\mathrm{F,NL}}(k,t)+N\phi_{33}(k,t)+2NE_T(k,t)\Big(\frac{1}{3}+H_{33}^{(T)}(k,t)\Big). \tag{7.17}$$

The non-linear transfers are the same as in passive scalar dynamics, since the linear operators of the three-point third-order correlations equations are not taken into account in the non-linear closure. Quadratic anisotropic contributions in the non-linear transfers for the scalar and cospectrum can be found in Appendix E along with some illustrations for USHT.

In the following sections, high Reynolds USHT is investigated and results are qualitatively compared with the axisymmetric EDQNM developed in Burlot *et al.* (2015*a*,*b*). Only the component along the mean gradient $()_{33}$ will be presented since one has $()_{11}=()_{22}=-()_{33}/2$ because of axisymmetry. Furthermore, to be consistent with the development of the present spectral modelling, the same set of eddy-damping constants is kept: $A_1=0.355$, $A_2=0$ and $A_3=1.3$. Differences between this set of constants, and $A_1=A_2=A_3=0.355$ used in Burlot *et al.* (2015*a*), are illustrated hereafter in section 7.3.7.

First, inertial scaling of the kinetic energy, scalar variance and scalar flux spectra are addressed, along with some considerations about the large scales initial conditions σ and σ_T. Then, the time evolution of one-point statistics is studied, such as the kinetic energy and its exponential growth rate, the Froude number, the mixing parameter, and global anisotropy indicators. Influence of large scales initial conditions σ and of the intensity of the stratification N on the asymptotic anisotropic states of the previous quantities is also analyzed. Afterwards, a quantitative comparison with Burlot *et al.* (2015*b*) is proposed, to illustrate that our model is able to recover, with satisfactory quantitative agreement, some features obtained by a model without any truncation of the expansion in spherical harmonics specific for axisymmetric turbulence. The scale-by-scale repartition of anisotropy in spectral space is then addressed and some considerations on the structure of the flow are proposed. These different parts constitute a complete validation of our anisotropic EDQNM modelling. Furthermore, qualitative comparisons with the cases of passive scalar dynamics and shear flows, which have been addressed with the same consistent closure, are proposed. Finally, in section 7.5, two new applications are presented: first, the pressure spectrum, and more specifically its anisotropic part resulting from stratification, is investigated. Then, effects of large Schmidt numbers, notably on the inertial scaling of the cospectrum $\mathcal{F}$, are revealed.

7.2 Spectral scaling and infrared dynamics

In this part, the emphasis is put on on the three main spectra of USHT: the kinetic energy spectrum $E(k,t)$, the scalar variance spectrum $E_T(k,t)$ and the cospectrum $\mathcal{F}(k,t)$, which are investigated at large Reynolds numbers. First, the inertial scaling is discussed, and then, we focus on the infrared dynamics.

7.2.1 Spectral scaling of E, E_T and $\mathcal{F}$

Firstly, the scaling of the main spectra is investigated. As in HITSG, E and E_T scale in $k^{-5/3}$ in the inertial range, and $\mathcal{F}$ in $k^{-7/3}$, as revealed in Fig. 7.1. Moreover, the peaks of the three spectra evolve in k^{-3} with increasing Nt, as assessed in Figure 11 of Burlot *et al.* (2015*a*). This can be shown easily, and the idea of the proof is inspired from a Rayleigh-Taylor analysis by Poujade (2006). Let's call $E_{\max}$ the maximum of the kinetic energy spectrum. Dimensional arguments yield $E_{\max}(t) \sim L(t)K(t)$. Using the self-similar exponential growth of integrated quantities gives $E_{\max}(t) \sim \exp(3\beta Nt/2)$, where β is the exponential growth rate of the kinetic energy. Then, at high Reynolds numbers, one can assume that $k_{\max}(t) \sim k_L(t)$ so that the time t can be expressed as follows: $t \sim -2\ln(k_L)/(\beta N)$. Injecting this formula into $E_{\max}$ finally provides

$$E_{\max}(t) \sim k_L^{-3}, \tag{7.18}$$

in agreement with numerical simulations.

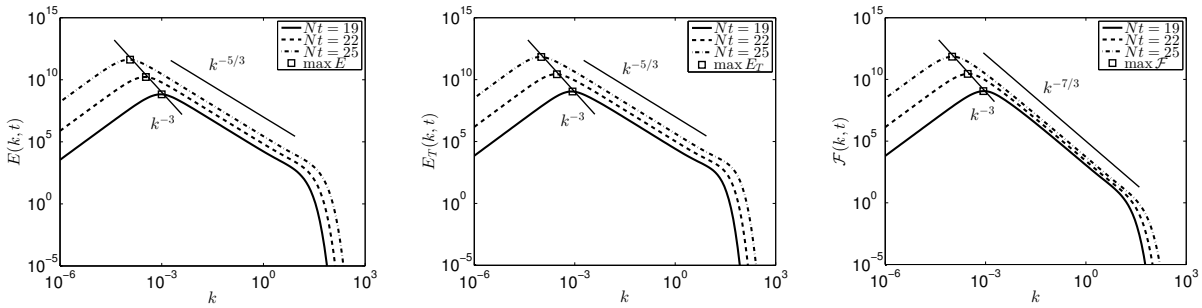

(a) (b) (c)

Figure 7.1: Evolution of the spectra in Saffman USHT. The □ denotes the peak of the spectra, which are represented at three dimensionless times $Nt = 19$, $Nt = 22$ and $Nt = 25$, and $Re_\lambda(Nt = 25) = 3.10^4$. (a) Kinetic energy spectrum $E(k,t)$; (b) Scalar variance spectrum $E_T(k,t)$; (c) Cospectrum $\mathcal{F}(k,t)$.

Furthermore, the possibility of an anisotropic correction to the Kolmogorov spectra is discussed in Burlot *et al.* (2015*b*), and it is shown numerically in the latter reference that the anisotropic part of $\phi_{33}(k,t)$ scales in k^{-3} (mostly at the beginning of the inertial range). Nevertheless, if one zooms in in the corresponding Figure 12, it appears that k^{-3} is steeper than the real inertial range slope. This is in agreement with our numerical simulations displayed in Fig. 7.2a, where the isotropic, directional and polarization parts of $\phi_{33}(k,t)$ are presented. Clearly, the isotropic part $\phi_{33}^{(\mathrm{iso})}$ scales in $k^{-5/3}$. Whereas one has for $\phi_{33}^{(\mathrm{pol})}$ (and $\phi_{33}^{(\mathrm{dir})}$) a spectral slope steeper than $k^{-7/3}$, but not as sharp as k^{-3}. Numerically, $k^{-2.52}$ is found here, in good agreement with the recent DNS of Gréa *et al.* (2016*a*), where the spectral scaling of $\phi_{33}^{(\mathrm{pol})}$ is also closer to $k^{-7/3}$ than k^{-3}. Furthermore, it is recovered, in agreement with Burlot *et al.* (2015*b*), that the polarization part is more intense at large scales than the directional one.

In Fig. 7.2b, for illustration purposes, the linear and non-linear transfers of kinetic energy are displayed for Saffman turbulence. It is revealed that at large scales, linear production mechanisms dominate over non-linear transfers which take energy from these large scales and bring it to smaller scales. This feature, that production is strong at large scales and thus that anisotropy is dominant at large scales, will be used later on.

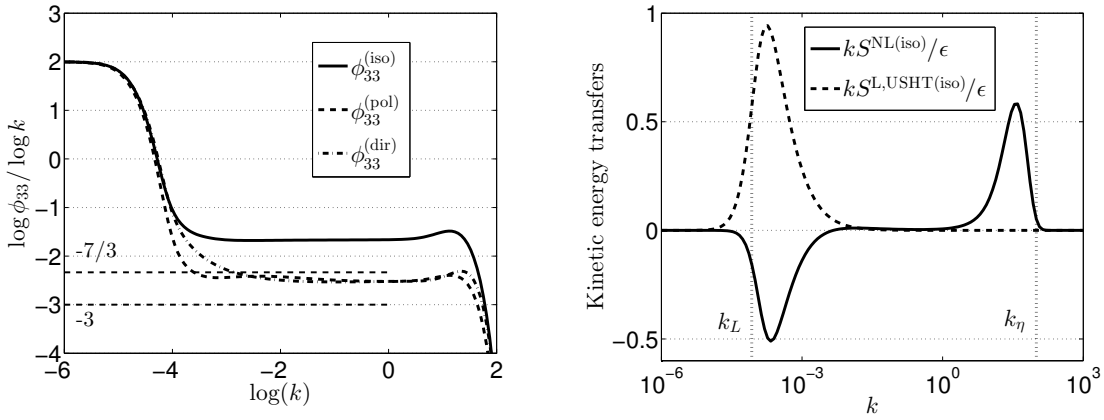

(a) (b)

Figure 7.2: (a) Spectral slope of the isotropic, directional and polarization parts of the spectral tensor $\phi_{33}(k,t)$. (b) Normalized linear and non-linear transfers of kinetic energy. Both in Saffman USHT at $Nt = 25$ where $Re_\lambda = 3.10^4$.

Now, we investigate in detail the inertial scaling of $E(k,t)$, $E_T(k,t)$ and $\mathcal{F}(k,t)$, and more precisely the value of the Kolmogorov and Corrsin-Obukhov constants K_0 and K_{CO} respectively. These constants are obtained by compensating the spectra with an adapted scaling. For the kinetic energy and buoyancy spectra, it is shown in Fig. 7.3a that the usual isotropic inertial scalings

$$E_{\mathrm{inertial}}(k,t) = E(k,t)\,\epsilon^{-2/3}\,k^{5/3}, \tag{7.19}$$

$$E_{\mathrm{T,inertial}}(k,t) = E_T(k,t)\,\epsilon_T^{-1}\,\epsilon^{1/3}\,k^{5/3}, \tag{7.20}$$

are relevant and allow to recover classical values for the constants, $K_0 = 1.31$ and $K_{\mathrm{CO}} = 0.76$, similar to what is obtained for passive scalar dynamics. This is completely different when it comes to the cospectrum $\mathcal{F}$. First, let's point out that there exist two different inertial scalings: the classical one proposed by Lumley (1967) which was shown to work nicely for passive scalar dynamics in HITSG in Chapter 5, with a constant $C_{\mathcal{F}} \simeq 3$, and a more recent one, derived by Burlot *et al.* (2015*b*), which unlike Lumley's, takes into account the scalar dissipation rate ϵ_T, which seems *a priori* relevant for an active scalar field

$$\mathcal{F}_{\mathrm{inertial}}^{\mathrm{Lumley}}(k,t) = \mathcal{F}(k,t)\,N^{-1}\epsilon^{-1/3}\,k^{7/3}, \tag{7.21}$$

$$\mathcal{F}_{\mathrm{inertial}}^{\mathrm{Burlot}}(k,t) = \mathcal{F}(k,t)\,N^{-1}\Big(K_0\epsilon^{1/3} + K_{\mathrm{CO}}\epsilon_T\epsilon^{-2/3}\Big)^{-1}k^{7/3}. \tag{7.22}$$

The inertial scaling $\mathcal{F}_{\mathrm{inertial}}^{\mathrm{Burlot}}$, first derived in Soulard & Griffond (2012), is presented in Fig. 7.3b: the plateau of the compensated cospectrum only starts appearing at Reynolds numbers as large as $Re_\lambda \sim 3.10^6$. Whereas for the passive scalar case, at a similar Reynolds number, $\mathcal{F}$ was displaying a clear plateau around $C_{\mathcal{F}} \simeq 3$ in the inertial range. Nevertheless, the scaling proposed by Burlot and coworkers $\mathcal{F}_{\mathrm{inertial}}^{\mathrm{Burlot}}$ seems to be more relevant than Lumley's: indeed, for $\mathcal{F}_{\mathrm{inertial}}^{\mathrm{Burlot}}$, a plateau seems to appear around 3.7, whereas $\mathcal{F}_{\mathrm{inertial}}^{\mathrm{Lumley}}$ settles around 12, which is too high, and consequently not displayed in Fig. 7.3b. The fact the scaling (7.22) is better than $\mathcal{F}_{\mathrm{inertial}}^{\mathrm{Lumley}}$ is very likely because it takes the scalar dissipation rate ϵ_T into account.

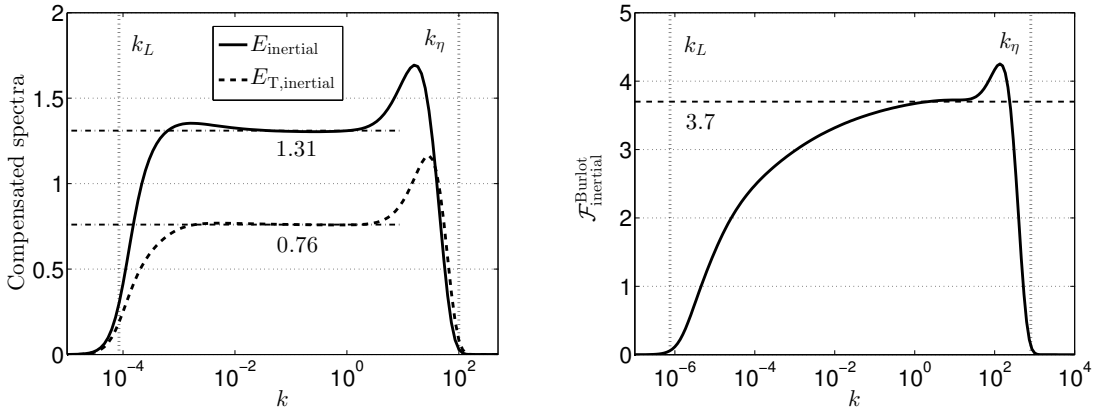

(a) (b)

Figure 7.3: Compensated spectra in the inertial range for Saffman USHT, with the integral and Kolmogorov wavenumbers k_L and k_η. (a) Compensated kinetic energy spectrum (7.19) and scalar variance spectrum (7.20) at $Re_\lambda = 3.10^4$, along with the Kolmogorov constant $K_0 = 1.31$ and Corrsin-Obukhov constant $K_{\text{CO}} = 0.76$. (b) Compensated cospectrum with Burlot scaling (7.22) at $Re_\lambda = 3.10^6$. The Lumley scaling (7.21) is not displayed since the curve is similar, but the plateau is located around 12.

7.2.2 Infrared dynamics

Now that the inertial range of the spectra has been investigated, the infrared dynamics is considered. It is recalled that in HITSG for a passive scalar, if initially σ_T is different from σ, greater or lesser it does not matter, it always results in $\sigma_T = \sigma$ after a few turnover times (see Chapter 5). In USHT, it is fundamentally different since because of stratification, all of the three main spectra E, E_T and $\mathcal{F}$ are coupled through the linear production terms at large scales. Hence, the most energetic initial spectrum, the one with the smallest infrared slope, imposes the minimum of energy to the others, so that in the end one has always $\sigma = \sigma_T = \min(\sigma(t = 0), \sigma_T(t = 0))$. This is completely different from HITSG where the passive scalar field has no effect on the kinetic field. Two examples are presented. First, in Fig. 7.4a, one has $\sigma(t = 0) = 2$ and $\sigma_T(t = 0) = 4$. The minimum of energy is thus imposed by E so that the scalar infrared slope results very rapidly, within one dimensionless time Nt, in $\sigma_T = 2$. This is identical to what happens in HITSG. In the opposite case illustrated in Fig. 7.4b, one has $\sigma(t = 0) = 4$ and $\sigma_T(t = 0) = 2$: the minimum of energy is this time imposed by E_T so that after one Nt, $\sigma = 2$. This case is completely different from HITSG where σ_T would have changed to 4.

A last aspect is presented in Fig. 7.4c: because of strong backscatter of energy towards large scales when $\sigma \geq 4$, if the slope is initially $\sigma = 5$, it eventually becomes $\sigma = 4$ in a few dimensionless times Nt. The same mechanism of strong inverse transfers of energy occurs in decaying isotropic turbulence (Lesieur & Ossia, 2000).

From this analysis, one can choose, without any loss of generality, $\sigma = \sigma_T \leq 4$. This result for USHT infrared dynamics notably simplifies the study of asymptotic anisotropic states of the flow: in particular, we choose to investigate only integer values of the infrared slopes: $\sigma = \sigma_T = \{1; 2; 3; 4\}$.

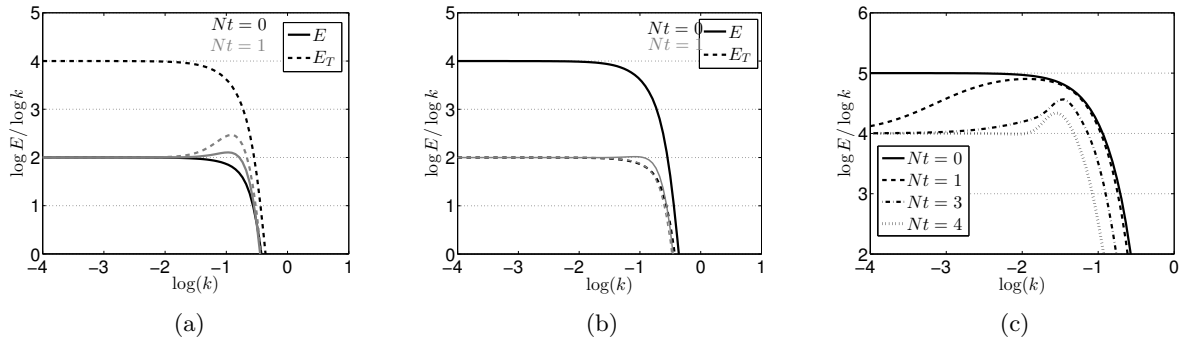

Figure 7.4: Infrared dynamics of $E(k,t)$ and $E_T(k,t)$ with $N = 1\tau_0^{-1}$. (a) $\sigma(t=0) = 2$ and $\sigma_T(t=0) = 4$: black curves at $Nt = 0$ and grey ones at $Nt = 1$. (b) $\sigma(t=0) = 4$ and $\sigma_T(t=0) = 2$: black curves at $Nt = 0$ and grey ones at $Nt = 1$. (c) Initially $\sigma(t=0) = 5$, and then σ varies from $Nt = 0$ to $Nt = 4$.

7.3 One-point statistics

Here, two important quantities of unstably stratified turbulence are firstly addressed, namely the Froude number

$$Fr(t) = \frac{\epsilon(t)}{K(t)N}, \tag{7.23}$$

which is the ratio of the stratification characteristic time $1/N$ on the inertial one K/ϵ, and the mixing parameter

$$\Lambda(t) = \frac{K_T(t)}{K(t)}, \tag{7.24}$$

which is the ratio of the scalar variance to kinetic energy. Since the scalar field is scaled as a buoyant velocity, Λ is dimensionless. Then, the exponential growth rate β of the kinetic energy $K =< u_i u_i > /2$ is analyzed, along with the time evolution of global anisotropy using the normalized deviatoric Reynolds stress tensor b_{ij}. More precisely, the influence of N and σ on the asymptotic values reached by Fr, Λ, β and b_{33} at large Nt and Re_λ is studied. Finally, a quantitative comparison with the axisymmetric EDQNM (Burlot *et al.*, 2015*b*) is proposed. Additional considerations about the modelling are also briefly presented.

7.3.1 The Froude number Fr

The Froude number can be interpreted as a ratio of characteristic time scales. As such, it could be qualitatively compared to the shear rapidity $S_\mathrm{R} = \epsilon/(KS)$ in shear flows, notably addressed with the same anisotropic EDQNM modelling in Chapter 3. In Fig. 7.5a it is revealed that Fr, unlike S_R, depends on σ in the asymptotic anisotropic state. Final values of Fr spans from 0.44 for $\sigma = 1$ to 0.66 for $\sigma = 4$. The smaller σ, the smaller Fr: this is expected since for small σ, large scales contain more energy and consequently are more anisotropic, because of the production terms which act dominantly at large scales, as illustrated in Fig. 7.2b. With the production terms being dynamically dominant with a small σ, the characteristic time scale $1/N$ diminishes, thus making Fr decrease. Nevertheless, the values reached here by Fr are slightly higher than the values obtained in Burlot *et al.* (2015*b*) ($Fr = 0.3$ for $\sigma = 1$). This means that

the flow within the present approach is less sensitive to stratification than with the axisymmetric EDQNM. It is shown in section 7.3.7 that by changing the eddy damping constants, we can increase the impact of stratification and thus reduce the Froude number: asymptotic values of Fr are gathered in Table 7.2.

However, in Fig. 7.5b it is shown that Fr, similarly to S_{R}, does not depend on the intensity of the mean gradient N, except at small Nt in the transitory regime. At short times, the larger N, the smaller Fr: this is consistent with a strong stratification intensity making production of buoyant fluctuations dominant initially.

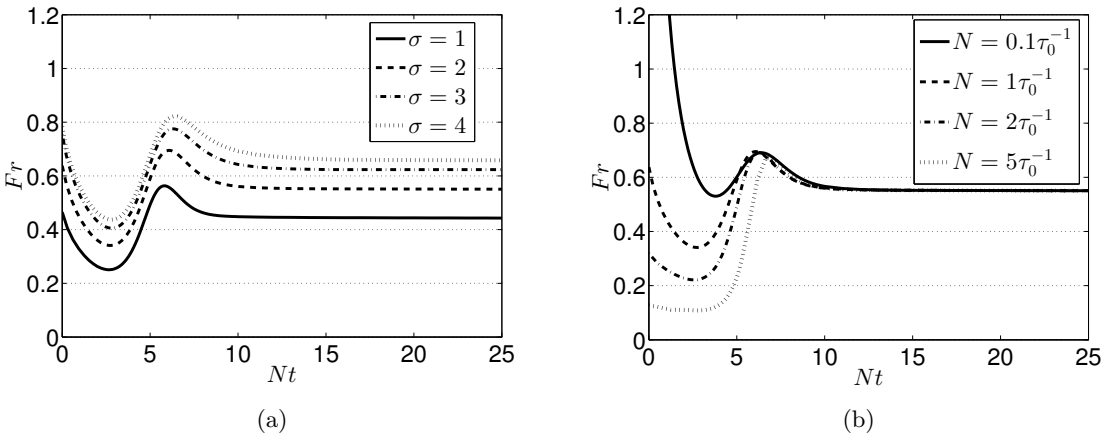

Figure 7.5: Influence of initial parameters σ and N on the Froude number $Fr = \epsilon/(KN)$. (a) Various σ at $N = 1\tau_0^{-1}$. (b) Various N for $\sigma = 2$.

7.3.2 The mixing intensity Λ

Now, the mixing intensity Λ is addressed. Similarly to Fr, its asymptotic value depends on σ, but not on its initial value, except for short times of course, as revealed in Fig. 7.6a and 7.6b. The dependence with N is not presented since it is very similar to what happens for Fr, *i.e.* a dependence on N only at short times. The final values of Λ are contained between 1.6 for $\sigma = 1$ and 1.4 for $\sigma = 4$, which is quantitatively in agreement with Burlot *et al.* (2015*b*): asymptotic values of Λ are gathered in Table 7.2.

One can remark that K_T/K depends strongly on initial conditions at a fixed σ, such as the initial Reynolds number $Re_\lambda(0)$ and the stratification frequency N. Indeed, Λ initially decreases in Burlot *et al.* (2015*b*), whereas it initially increases here. The reason is the following: here, $Re_\lambda(0) \simeq 5$ implies that linear production mechanisms dominate whatever the value of N is, roughly for $N \geq 0.1\tau_0^{-1}$. For the axisymmetric EDQNM, $Re_\lambda(0) \simeq 70$, which requires at least $N = 1\tau_0^{-1}$ to make Λ increase initially, meaning that linear production overcomes non-linearity. This is illustrated in Fig. 7.6c.

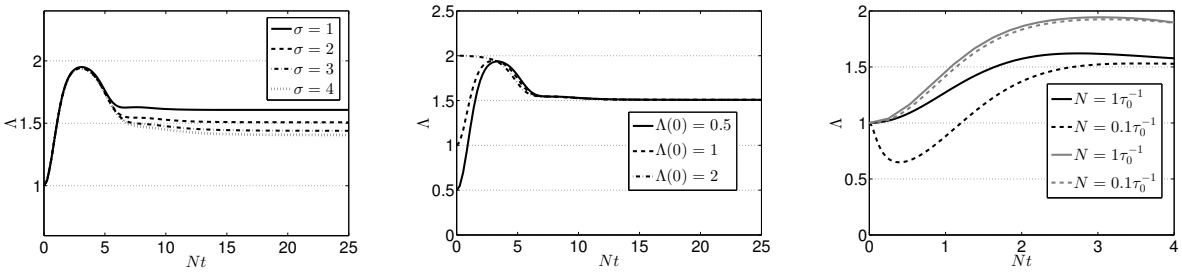

(a) (b) (c)

Figure 7.6: Mixing intensity $\Lambda = K_T/K$ for: (a) various σ at $N = 1\tau_0^{-1}$; (b) various initial values $\Lambda(0)$ for $\sigma = 2$ and $N = 1\tau_0^{-1}$; (c) various N and $Re_\lambda(0)$ with $\sigma = 2$: $Re_\lambda(0) = 70$ in black and $Re_\lambda(0) = 5$ in grey.

7.3.3 Growth of the kinetic energy $K(t)$

The emphasis is now put on the exponential growth rate β of the kinetic energy $K(t)$ in USHT. It was assessed by Burlot *et al.* (2015*b*) that this growth rate strongly depends on the large scales initial condition σ, according to the theoretical prediction

$$K(t) \sim K(0)\exp(\beta_{\text{Burlot}} Nt), \qquad \beta_{\text{Burlot}} = \frac{4}{\sigma + 3}, \tag{7.25}$$

which comes from the more general work of Soulard *et al.* (2014) where the stratification frequency N can vary: (7.25) corresponds to the specific case where N is constant. Furthermore, (7.25) relies on the fact that the largest eigenvalue of the linear operator of the evolution equations of the axisymmetric EDQNM is $2N$: indeed, equalizing the growth rate of the linear limit $E \sim \exp(2Nt)$ with the one coming from self-similar analysis $E \sim KL \sim \exp((\sigma + 3)\beta Nt/2)$ directly yields (7.25). In our case, because of the anisotropy modelling through a truncated expansion into spherical harmonics, our evolution equations (7.12) to (7.17) are different from those of Burlot and coworkers. The largest eigenvalue of the linear operator associated to (7.12)-(7.17) is $4N/\sqrt{5}$ here, against $2N$ for Burlot *et al.* (2015*a*,*b*); Gréa *et al.* (2016*a*). This leads to a different theoretical prediction for the exponential growth rate of the kinetic energy

$$K(t) \sim K(0)\exp(\beta_{\text{th}} Nt), \qquad \beta_{\text{th}} = \frac{8}{\sqrt{5}(\sigma + 3)}. \tag{7.26}$$

The present theoretical predictions and those of Burlot *et al.* (2015*a*) are gathered in Table 7.1, and it is worth noting that for a given large scales initial condition σ, our predictions yield a smaller growth rate than in the axisymmetric EDQNM: this is very likely due to our truncated expansion into spherical harmonics of the spectral correlations. Moreover, this is consistent with our flow being less anisotropic. We could conjecture that taking into account more spherical harmonics would increase the exponential growth rate of the kinetic energy up to the limit β_{Burlot}.

Large scales initial condition	$\sigma = 1$	$\sigma = 2$	$\sigma = 3$	$\sigma = 4$
Present prediction : β_{th}	0.894	0.716	0.596	0.511
Present EDQNM : β	0.893	0.715	0.596	0.540
Burlot's prediction : β_{Burlot}	1	4/5	2/3	4/7

Table 7.1: Comparison between the theoretical prediction β_{th} for the kinetic energy exponential growth rate, and the numerical result β obtained with our anisotropic EDQNM modelling.

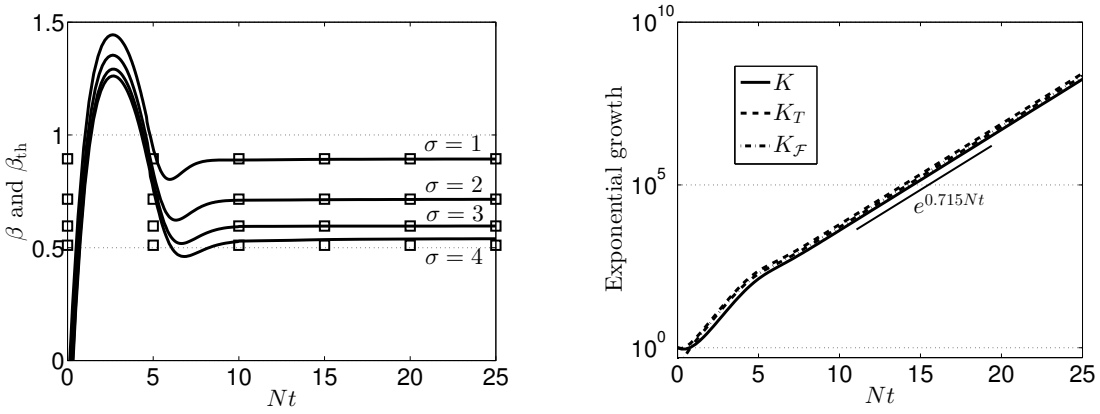

(a) (b)

Figure 7.7: (a) Kinetic energy exponential growth rate β for $\sigma = 1$, 2, 3 and 4. Straight lines indicate the numerical results, and □ the theoretical prediction (7.26), without the correction p_{USHT}. (b) Exponential growth of K, K_T and $K_{\mathcal{F}}$ for $\sigma = 2$.

In fact, the evolution equations (7.5) to (7.7) of $\hat{R}_{ij}$, $\mathcal{E}^T$, and F_i reveal that contributions of the fourth order expansion for $\mathcal{E}$, Z and $\mathcal{E}^T$ bring no contribution in (7.6). A higher-order expansion for the scalar flux F_i is required to modify the production terms and thus get closer to the exact value $2N$ of the maximal eigenvalue of the linear operator.

The predictions for the exponential growth rate of the kinetic energy are compared to our numerical results in Fig. 7.7a. The agreement is excellent: for $\sigma = 1, 2, 3$, the prediction β_{th} is recovered within 1%. There is a slight difference in the case of Batchelor turbulence, where the numerical result is 5% higher than the prediction: this is very likely because of the strong inverse non-linear transfers which naturally occur in Batchelor turbulence (Lesieur & Ossia, 2000). One could add a backscatter parameter, *i.e.* a correction for Batchelor turbulence, to the prediction (7.26) in the specific case $\sigma = 4$, as usually done for decaying HIT. Here for USHT, in order to adapt the theoretical prediction in Batchelor turbulence to our numerical result, a least square fit leads to the backscatter parameter $p_{\text{USHT}} = 0.37$, so that

$$\boxed{\beta_{\text{th}} = \frac{8}{\sqrt{5}(\sigma - p_{\text{USHT}} + 3)}, \qquad \begin{cases} p_{\text{USHT}} = 0 & \text{for} \quad \sigma \leq 3, \\ p_{\text{USHT}} = 0.37 & \text{for} \quad \sigma = 4. \end{cases}} \tag{7.27}$$

It is revealed in Fig. 7.7b that the scalar variance K_T and the mixed correlation $K_{\mathcal{F}}$ both grow

at the same rate β, in agreement with Burlot *et al.* (2015*a*,*b*); Gréa *et al.* (2016*a*). This can be qualitatively compared with the case of a passive scalar field advected by a turbulent shear flow with an imposed mean scalar gradient, where K_T and $K_{\mathcal{F}}$ also grow exponentially with the same rate as K, as revealed in Chapter 5.

In conclusion, the kinetic energy exponential growth rate strongly depends on the large scales initial conditions σ in the asymptotic states of USHT. This is interesting, since for shear flows, $K(t)$ was growing at the same rate independently of σ, at least within the same anisotropic EDQNM modelling (further explanations were provided at the end of Chapter 3). This illustrates two intrinsically different mechanisms of kinetic energy production in shear flows and USHT.

7.3.4 Global anisotropy

The time evolution of global anisotropy is now addressed: the scale-by-scale distribution of anisotropy is the subject of the next part. In Fig. 7.8a to 7.8d, b_{33} and b_{33}^T first increase, which shows the departure from the isotropic state, and then decrease and reach a final non-zero value. This decrease is the signature of a return to isotropy of the small scales when the Reynolds number increases. More specifically, it is revealed that polarization anisotropy for b_{33} is stronger than the directional one, in agreement with Burlot *et al.* (2015*b*). The strong anisotropy in the component $()_{33}$ furthermore shows that turbulent structures mainly align with the mean scalar gradient. In addition, the values reached by b_{33}^T are quite similar to the ones reached by $b_{33}^{(\mathrm{dir})}$. Another important feature is to study the influence of initial conditions, such as σ and N, on the final state of anisotropy. The same conclusions as for Fr and Λ are drawn for b_{33} and b_{33}^T: as shown in Fig. 7.8d, varying N affects only the short time dynamics of b_{33} and b_{33}^T, whereas increasing σ decreases the asymptotic values of the velocity and scalar anisotropy indicators. The latter feature is expected because by decreasing σ, one diminishes the large scales energy and consequently the amount of anisotropy of the flow. The results obtained here are quite different from shear flows, where the asymptotic anisotropic state of b_{ij} does not depend anymore on σ. Whereas for both shear flows and USHT, varying the mean gradient intensity impacts only short times of b_{ij}.

Hence, the main difference with the axisymmetric EDQNM is that the present anisotropic EDQNM modelling under-estimates the global anisotropy of the flow, so that asymptotic anisotropic states of b_{33} are lower in our case: values are reported in Table 7.2. It is shown in part 7.3.7 that we can slightly increase the global anisotropy of the flow by changing the eddy-damping constants.

Finally, in addition to these global anisotropy indicators, the pressure-velocity Π_{33} and pressure-scalar $\Pi_{\mathcal{F}}$ correlations are presented in Fig. 7.8e, whose definitions are respectively

$$\Pi_{\mathcal{F}}(t) =< p\frac{\partial \mathfrak{v}}{\partial x_3} >= \int_0^\infty S_3^{\mathrm{F,NL}}(k,t)\mathrm{d}k, \tag{7.28}$$

$$\Pi_{33}(t) =< 2p\frac{\partial u_3}{\partial x_3} >= 2\int_0^\infty \left(\frac{1}{3}S^{\mathrm{NL(iso)}} + S_{33}^{\mathrm{NL(dir)}} + S_{33}^{\mathrm{NL(pol)}}\right)\mathrm{d}k. \tag{7.29}$$

The return to isotropy at the level of the scalar flux is found to be more intense than the one of the velocity field: this is expected since the cospectrum is a purely anisotropic quantity,

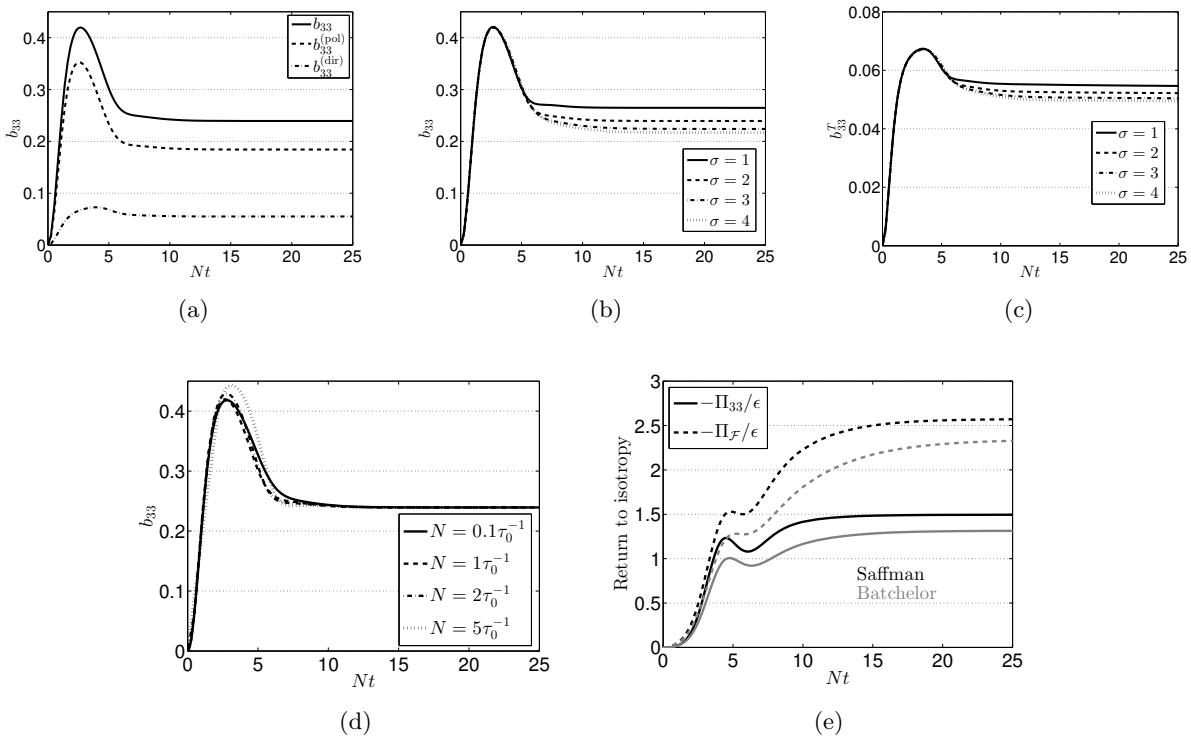

Figure 7.8: Global anisotropy indicators for the velocity and scalar fields. (a) Polarization and directional anisotropy parts of b_{33} for $N = 1\tau_0^{-1}$ and $\sigma = 2$. (b) b_{33} at $N = 1\tau_0^{-1}$ for various σ. (c) b_{33}^T at $N = 1\tau_0^{-1}$ for various σ. (d) b_{33} at $\sigma = 2$ for various N (the same behaviour is observed for b_{33}^T). (e) Return to isotropy: normalized pressure-velocity Π_{33} and pressure-scalar $\Pi_{\mathcal{F}}$ correlations in Saffman (black) and Batchelor (grey) turbulence.

for which pressure is the destructive mechanism. Furthermore, in agreement with previous statements, the return to isotropy mechanism is stronger for Saffman turbulence than Batchelor turbulence, because large scales are less anisotropic in the latter case than in the former.

7.3.5 Comparison with Burlot *et al.* (2015*b*)

In this part, we compare quantitatively the results of our anisotropic EDQNM modelling to the axisymmetric EDQNM (Burlot *et al.*, 2015*a*,*b*) specifically for two one-point statistics investigated in the previous sections: the Froude number Fr, defined in (7.23), and the mixing intensity Λ defined in (7.24). First, it was observed previously that the asymptotic anisotropic states obtained with the present anisotropic EDQNM modelling are less anisotropic than the ones obtained in Burlot *et al.* (2015*b*): this was notably seen through Fr and b_{33} which were higher and smaller respectively. In order to provide here a meaningful comparison, and only for this part, we use the eddy-damping constants of the axisymmetric EDQNM, *i.e.* $A_1 = A_2 = A_3 = 0.355$. The impact on USHT dynamics of the two different settings of eddy-damping constants ([EDC1]: $A_1 = 0.355$, $A_2 = 0$, $A_3 = 1.3$; [EDC2]: $A_1 = A_2 = A_3 = 0.355$) is discussed in section 7.3.7.

So, for the comparison, we use the setting [EDC2] in Saffman turbulence ($\sigma = 2$), an initial turbulent Reynolds number close to $Re_T = 833$, with $Re_\lambda = \sqrt{20 Re_T/3}$, and the initial peak of energy is $k_{\mathrm{peak}} = 40 k_L(0)$. Even though it is stated in Burlot *et al.* (2015*a*) that the initial

Froude number is $Fr = 1.2$, it seems to not be the case in Figure 1(a) therein. Consequently, we choose the stratification frequency $N = 4\tau_0^{-1}$ so that the initial behaviour of Fr is recovered: taking $N = 1\tau_0^{-1}$ would not have changed much.

The results are presented in Fig. 7.9. For the Froude number, the overall agreement is excellent: the transient regime is correctly captured and notably the strong decrease; the asymptotic value of Fr is quite well recovered. For the mixing ratio Λ, the initial behaviour is quite well captured, with a very good agreement for the asymptotic value. In conclusion, there is a satisfactory agreement with the axisymmetric EDQNM if one changes the eddy-damping constants from [EDC1] to [EDC2]. The drawback is that, as illustrated in section 7.3.7, by doing so the Corrsin-Obukhov constant decreases.

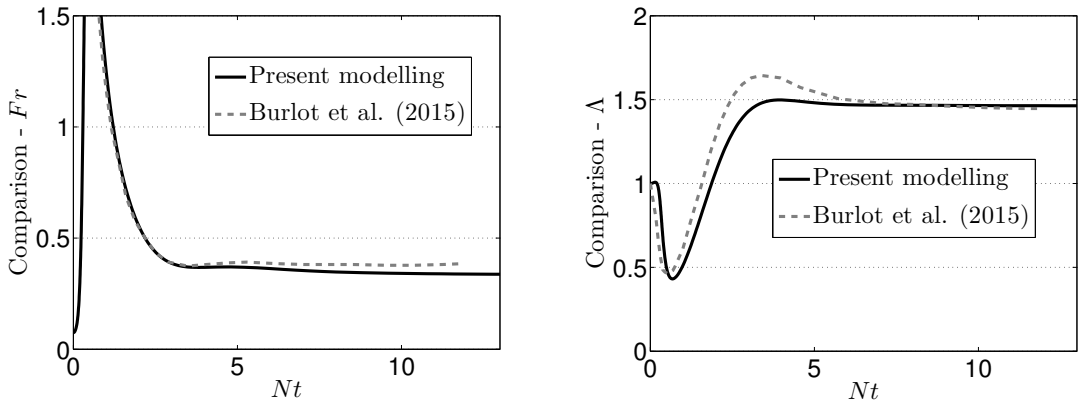

(a) (b)

Figure 7.9: Comparison of the present anisotropic EDQNM modelling with the axisymmetric EDQNM of Burlot *et al.* (2015*b*): $\sigma = 2$, $Re_\lambda(0) \simeq 70$, $N = 4\tau_0^{-1}$, and $k_{\text{peak}} = 40k_L(0)$. (a) Froude number Fr. (b) Mixing intensity Λ.

7.3.6 Conclusions on one-point statistics

In this part, various one-point statistics of crucial importance in unstably stratified turbulence have been studied: the Froude number Fr, the mixing intensity Λ, the growth rate β of the kinetic energy, scalar variance and scalar flux, and the velocity and scalar global anisotropy indicators b_{33} and b_{33}^T. The different results could be summarized as follows: (i) All these quantities strongly depend on σ in the asymptotic anisotropic state at large Nt, or equivalently at large Reynolds numbers. When σ increases, the large scales energy diminishes along with the quantity of anisotropy injected in the flow, so that Fr increases, and Λ, β, b_{33} and b_{33}^T decrease. (ii) On the contrary, the asymptotic anisotropic state does not depend on N: changing the intensity of the mean scalar gradient only impacts the short time dynamics.

Finally, the main difference between the two approaches is that the flow is less anisotropic in our case, probably due to the truncation of the spherical harmonics expansion of spectral correlations for the modelling of anisotropy. The principal consequences are (i) an exponential growth rate of the kinetic energy 10% lower than in Burlot *et al.* (2015*a*), but nevertheless in agreement with our new theoretical prediction, and (ii) smaller values for b_{33} as well. Asymptotic values of the

	Froude number Fr		Mixing intensity Λ		Growth rate β		Global anisotropy b_{33}	
σ	Present	Burlot	Present	Burlot	Present	Burlot	Present	Burlot
1	0.443-0.265	0.306	1.607-1.580	1.56	0.893	1	0.265-0.287	0.410
2	0.551-0.337	0.385	1.508-1.466	1.45	0.715	4/5	0.239-0.260	0.375
3	0.624-0.387	0.435	1.440-1.387	1.37	0.596	2/3	0.224-0.242	0.346
4	0.659-0.412	0.460	1.407-1.347	1.31	0.540	4/7	0.217-0.234	0.323

Table 7.2: Comparisons of the asymptotic values at large Re_λ of one-point statistics, obtained with the present anisotropic EDQNM modelling, and with the axisymmetric EDQNM. For the present modelling, values at left correspond to the setting of eddy-damping constants [EDC1], and at right to [EDC2] (see section 7.3.7 for details).

one-point statistics analyzed so far, and obtained with both the present anisotropic EDQNM modelling and the axisymmetric EDQNM, are gathered in Table 7.2.

Furthermore, throughout this part, qualitative comparisons were made with the cases of passive scalar dynamics (HITSG) and shear flows. It notably appeared that the asymptotic anisotropic states in USHT and shear flows strongly differ: indeed, in shear flows, at least within the same anisotropic EDQNM modelling, the asymptotic anisotropic state does not depend on the mean-field gradient intensity, nor on the large scales initial conditions σ.

7.3.7 Eddy-damping constants

In this section, we briefly discuss the impact of changing the eddy-damping constants on the dynamics of USHT. First, we recall that for consistency with the development of the present anisotropic EDQNM modelling, the same eddy-damping constants are kept here for the extension to the case of active scalar dynamics, *i.e.* $A_1 = 0.355$, $A_2 = 0$, $A_3 = 1.3$ [EDC1], where A_1 is for the velocity field, and A_2 and A_3 for the scalar field. The setting [EDC1] was consequently kept so far, except for the quantitative comparison against the axisymmetric EDQNM: indeed, in the latter work, a different choice of eddy-damping constants was made, *i.e.* $A_1 = A_2 = A_3 = 0.355$ [EDC2]. Furthermore, in Burlot *et al.* (2015*a*), a correction to the eddy-damping term is added to match with DNS: this is not considered here, since it only slightly affects the early dynamics.

With the present setting [EDC1], the Kolmogorov and Corrsin-Obukhov constants are consistent with those obtained for passive scalar dynamics, $K_0 = 1.31$ and $K_{\mathrm{CO}} = 0.76$, as presented before. Choosing [EDC2] as in Burlot *et al.* (2015*a*,*b*), tends first to decrease K_{CO} to values smaller than usual ones ($K_{\mathrm{CO}} = 0.6$), as revealed in Fig. 7.10a, whereas K_0 remains unchanged. Furthermore, with [EDC2], the flow is slightly more anisotropic in Fig. 7.10b: indeed, b_{33} increases a bit from [EDC1] to [EDC2]. The main difference is observed on Fr, which is reduced with [EDC2]: this means that the latter choice of eddy-damping constants enhance the importance of stratification in the dynamics, without increasing significantly the global anisotropy. Hence, changing the eddy-damping constants from [EDC1] to [EDC2] slightly increases the global anisotropy of the flow, and reduces Fr, which makes our results closer to Burlot *et al.* (2015*a*,*b*). But the counterpart is a decrease of the Corrsin-Obukhov constant, which is another reason why [EDC1] is preferred here. Moreover, whether [EDC1] or [EDC2] is chosen, it does not improve the plateau for the cospectrum $\mathcal{F}$ nor change the exponential growth rate β of the kinetic energy.

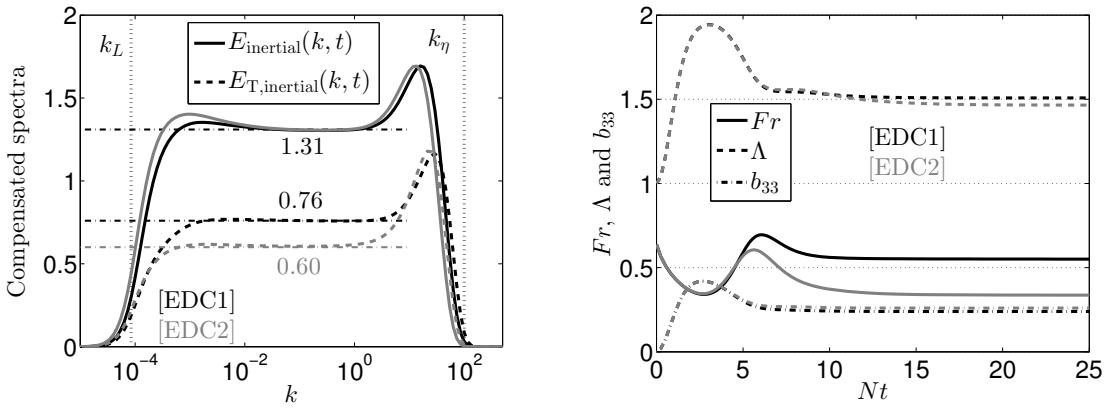

(a) (b)

Figure 7.10: Comparisons of the eddy-damping constants settings in Saffman turbulence: $A_1 = 0.355$, $A_2 = 0$ and $A_3 = 1.3$ [EDC1] (black lines) and $A_1 = A_2 = A_3 = 0.355$ [EDC2] (grey lines). (a) Kinetic energy and scalar variance compensated spectra with $Re_\lambda(Nt = 20) = 3.10^4$. Straight line (−) for $Ek^{5/3}\epsilon^{-2/3}$, dashed line (−−) for $E_T k^{5/3}\epsilon_T^{-1}\epsilon^{1/3}$. (b) Fr, Λ and b_{33}.

7.4 Scale by scale anisotropy and structure of the flow

In this part, the scale by scale distribution of anisotropy is investigated for the velocity and scalar fields, at the level of the second-order moments, thanks to $H_{33}^{(\text{dir})}(k,t)$, $H_{33}^{(\text{pol})}(k,t)$ and $H_{33}^{(T)}(k,t)$. More precisely, we use, instead of $H_{33}^{(T)}$, the **scale-by-scale dimensionality parameter**, another indicator of anisotropy often used

$$\sin^2\gamma_T(k,t) = \frac{1}{E_T(k,t)}\int_{S_k}\sin^2\theta_k(\boldsymbol{k})\ \mathcal{E}^T(\boldsymbol{k},t)\mathrm{d}^2\boldsymbol{k} = 2H_{33}^{(T)}(k,t) + \frac{2}{3}, \tag{7.30}$$

where $\theta_k(\boldsymbol{k})$ is the angle between the vertical axis and the wavevector $\boldsymbol{k}$. When the considered scales are isotropic, the value of $\sin^2\gamma_T$ is 2/3, whereas it is 0 for $H_{ij}^{(T)}$.

It was shown in Fig. 7.8a to Fig. 7.8d that in the asymptotic anisotropic state, the global anisotropy indicators b_{33} and b_{33}^T are non-zero, meaning that there is anisotropy in the flow. First, it is revealed in Fig. 7.11a, that anisotropy is mainly gathered at large scales for the velocity field, where $H_{33}^{(\text{dir})}$ and $H_{33}^{(\text{pol})}$ are different from zero, unlike small scales which have returned to isotropy. One can remark that, as previously, polarization anisotropy is much stronger that directional one at large scales. An interpretation of this is provided a bit later. Similarly, for the scalar field in Fig. 7.11b, small scales have returned to isotropy ($\sin^2\gamma_T = 2/3$), whereas anisotropy is gathered at large scales. This figure additionally illustrates further that Saffman turbulence is globally more anisotropic than Batchelor turbulence, because the linear production at large scales is stronger in Saffman than in Batchelor turbulence. Interestingly, for both the velocity and scalar fields, Fig. 7.11a and 7.11b show that from the longitudinal Taylor scale $\lambda = \sqrt{20\nu K/\epsilon}$, the scales have completely returned to isotropy: in particular, this indicates that even in USHT, isotropic statistics could be used for scales smaller than λ. The Ozmidov wavenumber, defined in Gréa *et al.* (2016*a*) $k_O = 2\pi\sqrt{N^3/\epsilon}$, is displayed as well: it is

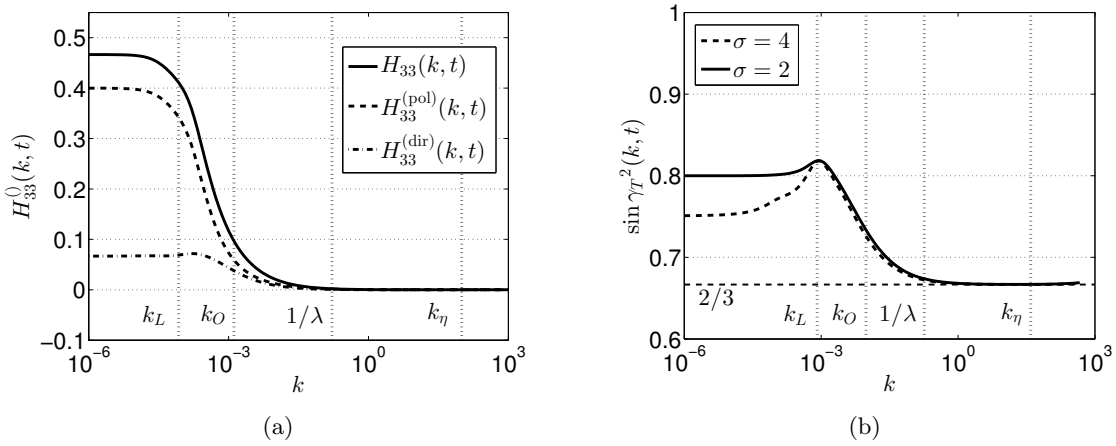

Figure 7.11: Spectral anisotropy indicators, along with the integral, Ozmidov, and Kolmogorov wavenumbers k_L, k_O, k_η; the Taylor scale λ is displayed as well. (a) $H_{33}^{(\mathrm{dir})}$ and $H_{33}^{(\mathrm{pol})}$ for $\sigma = 2$ at $Re_\lambda(Nt = 25) = 3.10^4$. (b) $\sin^2\gamma_T$ for $\sigma = 2$ and $\sigma = 4$ at different Nt so that for both $Re_\lambda = 3500$.

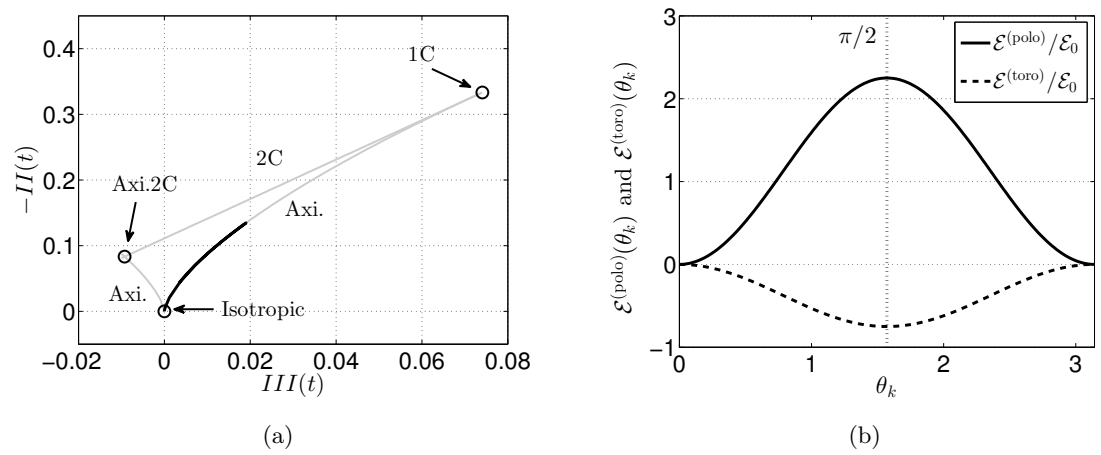

Figure 7.12: (a) Lumley triangle: grey lines correspond to the boundaries between the isotropic, two-components axisymmetric (Axi.2C) and one-component (1C) configurations, and the black line to a EDQNM simulation. (b) Normalized potentials $\mathcal{E}^{(\mathrm{toro})}/\mathcal{E}_0$ and $\mathcal{E}^{(\mathrm{polo})}/\mathcal{E}_0$, for $\sigma = 2$, at a wavenumber located in the infrared range.

clear that for scales larger than k_O, stratification and anisotropy dominate, whereas for scales smaller, non-linear transfers drive the return to isotropy mechanism.

It is possible to obtain some qualitative information about the spatial structure of anisotropy. If one considers the Lumley triangle (Simonsen & Krogstad, 2005) which displays the second invariant of b_{ij}, $-2II = b_{ij}b_{ij}$, as a function of the third one, $3III = b_{ij}b_{il}b_{jl}$, one obtains the grey curves of Fig. 7.12a. In our simulation (black curve), the flow evolves from an isotropic state toward a one component state (poloidal component) following an axisymmetric configuration, and tends to be 2D (invariance along the direction of the mean scalar gradient): accordingly, the Reynolds stresses have a rod-like shape.

Another possibility is to investigate the energy contained in the toroidal and poloidal modes, defined in (2.28), using the Craya-Herring frame illustrated in Fig. 2.1. First thing to do is to link the spherically-averaged spectra $EH_{33}^{(\mathrm{dir})}$ and $EH_{33}^{(\mathrm{pol})}$ to θ_k, the angle between the vertical axis (the mean scalar gradient direction) and the wavevector $\boldsymbol{k}$. After some algebra, one gets a relation between directional and polarization anisotropies $\mathcal{E}^{(\mathrm{dir})}$ and Z, and θ_k

$$\mathcal{E}^{(\mathrm{dir})}(k,\theta_k) = -\frac{15}{2}\mathcal{E}_0(k)H_{33}^{(\mathrm{dir})}(k)(3\cos^2\theta_k - 1), \qquad Z(k,\theta_k) = \frac{15}{2}\mathcal{E}_0(k)H_{33}^{(\mathrm{pol})}(k)\sin^2\theta_k. \tag{7.31}$$

Finally, this permits to obtain $\mathcal{E}^{(\mathrm{toro})}$ and $\mathcal{E}^{(\mathrm{polo})}$, defined in (2.29), as functions of the spherically averaged spectra

$$\mathcal{E}^{(\mathrm{toro})}(k,\theta_k) = \frac{\mathcal{E}_0(k)}{2}\Big[1 - \frac{15}{2}\Big(H_{33}^{(\mathrm{pol})}(k)\sin^2\theta_k + H_{33}^{(\mathrm{dir})}(k)(3\cos^2\theta_k - 1)\Big)\Big], \tag{7.32}$$

$$\mathcal{E}^{(\mathrm{polo})}(k,\theta_k) = \frac{\mathcal{E}_0(k)}{2}\Big[1 + \frac{15}{2}\Big(H_{33}^{(\mathrm{pol})}(k)\sin^2\theta_k - H_{33}^{(\mathrm{dir})}(k)(3\cos^2\theta_k - 1)\Big)\Big]. \tag{7.33}$$

At this point, it is of interest to point out that in Burlot *et al.* (2015*a*), instead of considering the equations of $\mathcal{E}$ and Z, the equations of $\mathcal{E}^{(\mathrm{toro})}$ and $\mathcal{E}^{(\mathrm{polo})}$ are solved, along with those of $\mathcal{E}^T$ and F_3. The variations of both $\mathcal{E}^{(\mathrm{toro})}$ and $\mathcal{E}^{(\mathrm{polo})}$ as functions of θ_k are displayed in Fig. 7.12b for a wavenumber located in the infrared range: this is where the anisotropy is gathered, as shown in Fig. 7.11a. For $0 \leq \theta_k \leq \pi$, one has $\mathcal{E}^{(\mathrm{polo})} > \mathcal{E}^{(\mathrm{toro})}$, and the poloidal and toroidal potentials are maximum for $\theta_k = \pi/2$. The poloidal mode being more intense, this means that in the configuration $\theta_k = \pi/2$, spectral velocity fluctuations are preferentially aligned in the mean scalar gradient direction. This is an interesting feature: indeed, in the previous sections it was underlined that polarization anisotropy is stronger than directional one at large scales. This is assessed in Fig. 7.12b, where in the infrared range one has clearly $Z > \mathcal{E}^{(\mathrm{dir})}$. Consequently, the present results show that in USHT, a dominant polarization anisotropy corresponds to spectral velocity fluctuations mainly aligned with the mean scalar gradient, so that the principal component is the poloidal one, in agreement with Fig. 7.12a, where our simulation goes toward the (1C) state. Also, for $\theta_k = 0$ or $\theta_k = \pi$, in a plane perpendicular to the mean scalar gradient, $\mathcal{E}^{(\mathrm{toro})} = \mathcal{E}^{(\mathrm{polo})}$ so that there is no polarization anisotropy.

7.5 Pressure spectra and high Schmidt numbers

So far, the dynamics of USHT at a unit Schmidt number $Sc = 1$ was addressed at large Reynolds numbers, and the strong dependence of the asymptotic anisotropic state on the infrared slope σ was recovered, with a good overall agreement with the axisymmetric EDQNM. In the present section, the anisotropic EDQNM modelling is applied to two new cases: first, the pressure spectrum is studied, and in particular its anisotropic part resulting from stratification, with a qualitative comparison to the pressure spectrum in shear flows. Then, the case of very large Schmidt numbers $Sc \gg 1$, corresponding for instance to saltwater, is analyzed on a fundamental point of view, with the emphasis put on the scaling of the cospectrum.

7.5.1 Pressure spectra

The emphasis is put on the pressure spectra, which have not been investigated in USHT in previous references. This study is done in the spirit of the work by George *et al.* (1984) who analyzed the anisotropic part of the pressure spectrum for shear flows. This is notably presented, within the present anisotropic EDQNM modelling, in Appendix D. The same method is applied here for USHT. The Poisson equation in USHT is obtained by taking the divergence of (7.4), which yields

$$-\Delta p = \frac{\partial^2 u_i u_j}{\partial x_i \partial x_j} + \lambda_i \frac{\partial \mathfrak{v}}{\partial x_i}. \tag{7.34}$$

Then, with the definition of the two-point second-order pressure correlation (D.19), one gets

$$\boxed{\mathcal{E}_P(\boldsymbol{k},t) = 2\alpha_i\alpha_j\alpha_p\alpha_q \int_{\boldsymbol{k}=\boldsymbol{p}+\boldsymbol{q}} \hat{R}_{iq}(\boldsymbol{p},t)\hat{R}_{jp}(\boldsymbol{q},t)\mathrm{d}^3\boldsymbol{p} + \frac{\alpha_i\alpha_j}{k^2}\lambda_i\lambda_j\mathcal{E}^T(\boldsymbol{k},t).} \tag{7.35}$$

The isotropic part remains unchanged with respect to HST, only the anisotropic part is different. The spherical average of this equation eventually gives

$$E_P(k,t) = 16\pi^2 \int_{\Delta_k} kpq(1-y^2)(1-z^2)\mathcal{E}_0'\mathcal{E}_0''\mathrm{d}p\mathrm{d}q + \frac{E_T}{k^2}\lambda_i\lambda_j\left(\frac{\delta_{ij}}{3} - 2H_{ij}^{(T)}\right), \tag{7.36}$$

where we call the second-contribution $E_P^{(\mathrm{USHT})}$ the turbulence-unstable-stratification interaction. One can note that the total pressure spectrum $E_P(k,t)$ for USHT is similar, in its structure, to the one in HST.

First, in Fig. 7.13a, the scaling of the isotropic and anisotropic parts of E_P are presented. The turbulence-turbulence interaction spectrum scales in $E_P^{(\mathrm{iso})} \sim k^{-7/3}$: the constant $C_P = 2.3$ in Fig. 7.13b is close to the value obtained in shear flows which indicates some universality of the isotropic pressure spectrum. Then, the anisotropic part resulting from stratification is presented in Fig. 7.13a and scales in $E_P^{(\mathrm{USHT})} \sim k^{-11/3}$. The $k^{-11/3}$, analogous to the anisotropic part in shear flow, is expected from the expression (7.36), because $E_T \sim k^{-5/3}$ in the inertial range. And similarly to shear flows, the anisotropic part has a quadratic dependence on the mean-field gradient, given its expression (7.36). Thus, only the dependence on the dissipation rates remains to be determined. Since the scalar field is rescaled as a buoyant velocity, there are infinite possibilities of the form $\epsilon^a\epsilon_T^b$, with $a+b=2/3$, by dimensional analysis. One could choose the inertial scaling of E_T, *i.e.* $a=-1/3$ and $b=1$, but this yields in Fig. 7.13b (in grey) a constant quite small of order 0.25: this is not satisfactory since for shear flows the constant was very close to Kolmogorov. Given the similarities pointed out so far, we choose $a=2/3$ and $b=0$, as for $E_P^{(\mathrm{S})}$, which provides in Fig. 7.13b (in black) a constant $C_P^{(\mathrm{USHT})} \simeq 0.7$. This seems convenient because it is close to the Corrsin-Obukhov constant, consistently with $E_P^{(\mathrm{USHT})}$ depending on E_T. In the end, the scaling of the anisotropic part of the pressure spectrum in USHT reads

$$\boxed{E_P^{(\mathrm{USHT})}(k,t) = C_P^{(\mathrm{USHT})} N^2 \epsilon^{2/3} k^{-11/3}, \qquad C_P^{(\mathrm{USHT})} \simeq 0.7.} \tag{7.37}$$

This scaling is a new fundamental result, interesting for two reasons: first, it is strongly analogous to the inertial scaling of the anisotropic part of the pressure spectrum in shear flows

($\epsilon^{2/3}k^{-11/3}$); secondly, $C_P^{(\mathrm{USHT})}$ is close to the Corrsin-Obukhov constant, similarly to $C_P^{(\mathrm{S})}$ being close to the Kolmogorov one (see Appendix D).

Finally, the time evolution of the isotropic and anisotropic parts $K_P^{(\mathrm{iso})}$ and $K_P^{(\mathrm{USHT})}$ of the pressure variance are displayed in Fig. 7.13c: it is found, similarly to shear flows, that the pressure variances grow exponentially at a rate 2β, where β is the exponential growth rate of the kinetic energy. Interestingly, the exponential growth rate of the pressure variance still depends on the infrared slope σ of the kinetic energy spectrum, even though the infrared slope of the isotropic pressure spectrum is $E_P^{(\mathrm{iso})} \sim k^2$.

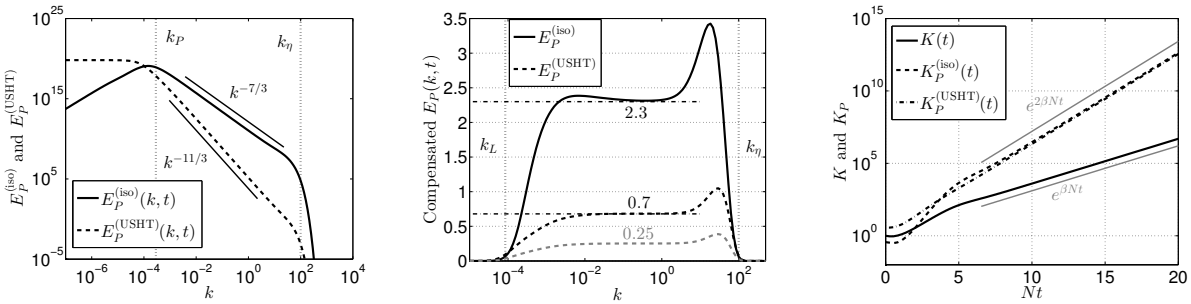

(a) (b) (c)

Figure 7.13: Pressure spectra in USHT, for $\sigma = 2$ at $Re_\lambda = 2.10^4$. (a) Isotropic and anisotropic pressure spectra $E_P^{(\mathrm{iso})}$ and $E_P^{(\mathrm{USHT})}$, along with the pressure integral wavenumber k_P and the Kolmogorov wavenumber k_η, at $Re_\lambda \simeq 3.10^4$. (b) Compensated pressure spectra $E_P^{(\mathrm{iso})}k^{7/3}\epsilon^{-4/3}$ and $E_P^{(\mathrm{USHT})}k^{11/3}\epsilon^{-2/3}/N^2$ in black, and $E_P^{(\mathrm{USHT})}k^{11/3}\epsilon^{1/3}/(\epsilon_T N^2)$ in grey. (c) Isotropic and anisotropic parts $K_P^{(\mathrm{iso})}$ and $K_P^{(\mathrm{USHT})}$ of the pressure variance, along with the kinetic energy K: the grey lines indicate $\exp(\beta Nt)$ and $\exp(2\beta Nt)$.

7.5.2 Cospectrum at high Schmidt numbers

In this section, the case of a weakly diffusive active scalar with $Sc \gg 1$ is addressed (instead of considering the Prandtl number, the Schmidt number Sc is used, which is equivalent for a being the molecular diffusivity). This configuration is representative of unstably stratified water columns in the ocean generated by double diffusion mechanisms: at the ocean surface, hot salty water is on top of cooler and saltier water, so that the stratification is stable. But when the temperature drops off in the air layer above the ocean, the upper salty water cools down very rapidly, because heat transfers are much more efficient than mass transfers. In the end, one has a heavier fluid on top, causing unstably stratified water columns (Sigman *et al.*, 2004).

For $Sc \gg 1$, the scalar flux $\mathcal{F}$ was found to decrease sharply after k_η in Chapter 6, similarly to the kinetic energy spectrum. It appears that in USHT, the behaviour of the cospectrum beyond k_η is completely different, as revealed in figure 7.14a: indeed, unlike passive scalar dynamics, the scalar flux survives in the viscous-convective range. The buoyant spectrum E_T still scales in k^{-1}, and there are also small scales fluctuations for E beyond k_η, but they are much less intense than for E_T and $\mathcal{F}$, and are therefore neglected.

The scaling of $\mathcal{F}$ in the viscous-convective range is not clear, but it seems to be close to k^{-1}, slightly steeper, as revealed in the zoom in Fig. 7.14b. Around k_η, the cospectrum seems

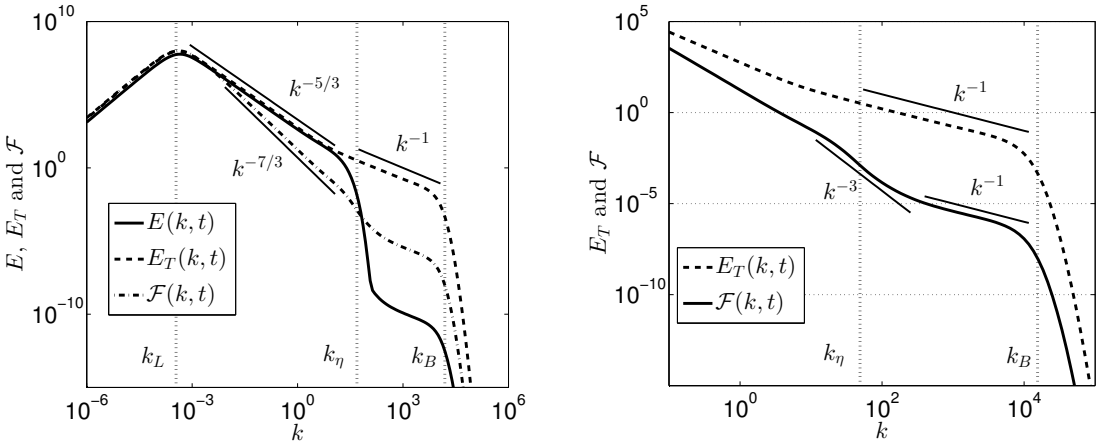

(a) (b)

Figure 7.14: Saffman USHT for $Sc = 10^5$ at $Re_\lambda = 10^4$, along with the integral, Kolmogorov and Batchelor wavenumbers k_L, k_η and k_B. (a) E, E_T and $\mathcal{F}$, along with the $k^{-5/3}$ inertial scaling for E and E_T, the $k^{-7/3}$ inertial scaling for $\mathcal{F}$, and the k^{-1} viscous-convective scaling for E_T. (b) Zoom in the viscous-convective range for E_T and $\mathcal{F}$, with different scalings explained in the text.

to scale in k^{-3}, but this is very likely just a transition toward the viscous-convective scaling. Nevertheless, both the k^{-1} and k^{-3} scalings are briefly justified using classical arguments. The k^{-3} scaling can be obtained by assuming that at small scales, there is a balance between dissipation and production of buoyant fluctuations in (7.17), so that

$$(\nu + a)k^2\mathcal{F} \sim \frac{2}{3}NE_T \Leftrightarrow \mathcal{F}(k,t) \sim N\frac{\epsilon_T}{\sqrt{\nu\epsilon}}k^{-3}. \tag{7.38}$$

In this expression, $E_T H_{33}^{(T)}$ was neglected compared to E_T. For reasons which are explained hereafter, it is preferred to express this new scaling as follows

$$\boxed{\mathcal{F}(k,t) \sim N\sqrt{\frac{\epsilon}{\nu}}\frac{\epsilon_T}{\epsilon}k^{-3},} \tag{7.39}$$

where the inverse of the Kolmogorov time scale $\sqrt{\nu/\epsilon}$ appears, consistently with the dynamics of the viscous-convective range. Then, after k_η, the scaling is slightly steeper than k^{-1}, but nevertheless the Batchelor scaling seems relevant if one assumes, as for E_T, that the characteristic time scale of $\mathcal{F}$ in the viscous-convective range is also independent of k: since this new range exists only thanks to the small scales coupling through N, it makes sense to assume that it depends linearly on N, and also on ϵ and ν: this provides $N\nu/\epsilon$ as the characteristic time scale of the cospectrum in the viscous-convective range. Further assuming that $\mathcal{F}$ depends only on this time scale, k and ϵ_T, yields

$$\boxed{\mathcal{F}(k,t) \sim \sqrt{\frac{\nu}{\epsilon}}\epsilon_T k^{-1}.} \tag{7.40}$$

It is worth noting that, unlike E_T for which non-local transfers are at the origin of the viscous

convective range, the new range for $\mathcal{F}$ beyond k_η is created by local production of buoyant fluctuations through the term NE_T. Direct non-local expansions ($q \ll k \sim p$) were performed for the non-linear transfers of $\mathcal{F}$ but they are negligible.

The change from the scaling in k^{-3}, around k_η, to k^{-1}, just after k_η, can be understood in terms of characteristic time scales: for the scaling (7.39), the characteristic time is $\sqrt{\nu/\epsilon}$, which is the classical characteristic time of the Kolmogorov scale. For smaller scales, viscous dissipation becomes more and more important, so that the characteristic time evolves from $\sqrt{\nu/\epsilon}$ toward $(\nu k^2)^{-1}$, which directly yields (7.40). Then, the characteristic time scale saturates to $N\nu/\epsilon$. These two scalings and their characteristic times are consistent with the Kolmogorov scale being the wavenumber around which the cospectrum changes from k^{-3} to k^{-1}: indeed, equating (7.39) and (7.40) yields $k = k_\eta$.

About the one-point statistics: obviously, even with high Schmidt numbers, simulations show that the asymptotic anisotropic state still depend on σ and not on N, and the exponential growth rate β is not modified with respect to the case $Sc = 1$. Nevertheless, it is proposed to illustrate in figure 7.15 the impact of a large Sc on the early dynamics of the scalar anisotropy indicator b_{33}^T and the mixing parameter Λ (the effects are negligible for Fr and b_{33}). The main result is that a large Sc does not change the asymptotic values with respect to the case $Sc = 1$. However, specifically for b_{33}^T and Λ which depend explicitly on the scalar field unlike b_{33} and Fr, a large Schmidt number strongly impacts the transient regime as well: Λ initially increases much more with $Sc = 10^4$ than with $Sc = 1$, whereas on the contrary, b_{33}^T is always smaller at $Sc = 10^4$.

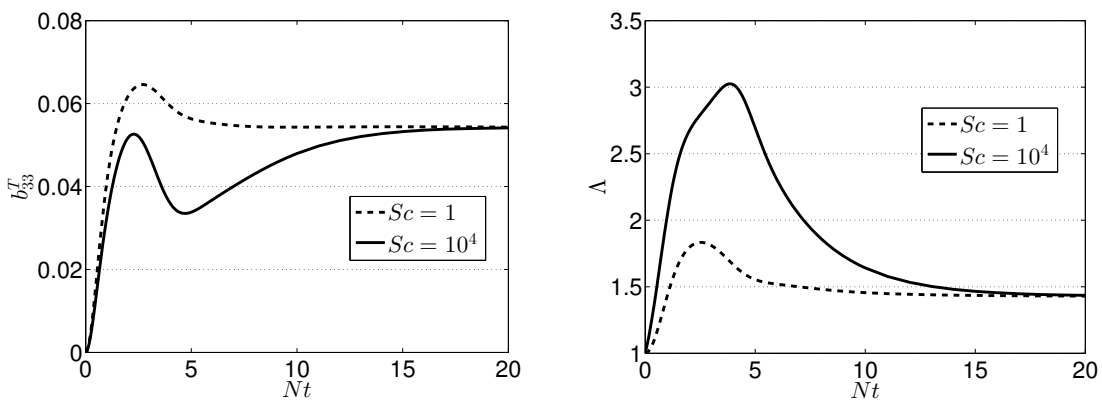

(a) (b)

Figure 7.15: Saffman USHT for $Sc = 1$ and $Sc = 10^4$. (a) Scalar anisotropy indicator b_{33}^T. (b) Mixing intensity Λ.

At $Sc = 10^4$, even if there is no inertial range initially for E_T, the viscous convective range spans almost two decades: this is completely different from the case $Sc = 1$. This initial viscous-convective range thus contributes greatly to Λ because it gives large initial values of K_T, which explains the strong increase at small Nt. Then, when the Reynolds number increases, the inertial ranges of E and E_T become dominant in the integrals for K and K_T, so that eventually, the same asymptotic value as for $Sc = 1$ is recovered. Whereas for b_{33}^T, the viscous-convective range initially adds isotropic small scales, thus reducing the early global anisotropy over the whole wavenumber space.

As a conclusion, unlike passive scalar dynamics, the cospectrum survives in the viscous-convective range for USHT for large Schmidt numbers, and scales in k^{-1}, similarly to the scalar variance spectrum, after a transient k^{-3} subrange around the Kolmogorov wavenumber. Finally, large Schmidt numbers strongly affect the early dynamics of b_{33}^T and Λ, nevertheless without changing the asymptotic state.

7.6 Conclusion on USHT

Unstably stratified homogeneous turbulence (USHT) was investigated at large Reynolds numbers with the anisotropic EDQNM modelling extended to the case of active scalar dynamics. Moreover, since the present modelling was applied previously for different configurations - notably transport of passive scalar in an isotropic turbulence with a mean scalar gradient and shear flows - qualitative comparisons are also made with these cases and some interesting differences and similarities were found between shear-driven flows and unstably stratified turbulence.

The time evolution of the kinetic energy, scalar variance (or buoyancy) and scalar flux spectra $E(k,t)$, $E_T(k,t)$ and $\mathcal{F}(k,t)$ were first addressed: the $k^{-5/3}$ inertial scaling of E and E_T was recovered, along with the $k^{-7/3}$ inertial scaling of the cospectrum $\mathcal{F}$. For the latter compensated spectrum, a plateau starts appearing at the highest Reynolds numbers reached here ($Re_\lambda \sim 10^6$). The k^{-3} time evolution of the peak of the three previous spectra was also recovered and justified analytically. For the infrared dynamics, it is found that because of the strong coupling between E, E_T and $\mathcal{F}$ due to stratification, the spectrum with initially the smallest infrared slope σ imposes the minimum of energy to the others, which significantly differs from passive scalar dynamics.

Then, the effects of varying the stratification frequency N and the infrared slope σ on the asymptotic anisotropic states of one-point statistics in USHT were studied, specifically the Froude number Fr, the mixing intensity Λ, global anisotropy indicators for the velocity and scalar fields b_{33} and b_{33}^T, and the exponential growth rate β of the kinetic energy, scalar variance and mixed-correlation. The conclusion is, in agreement with Burlot and coworkers, that the asymptotic states of these quantities strongly depend on σ. This feature is completely different from shear flows where one-point statistics do not depend anymore on σ asymptotically, at least within the same modelling. However, for both shear flows and USHT, varying the mean gradient intensity impacts only short times. In particular, it is recovered that the more energy initially in large scales, *i.e.* the smaller σ, the more anisotropic the flow: furthermore, at large Reynolds numbers, anisotropy is gathered at large scales whereas small scales return to isotropy for both the velocity and buoyancy fields (at least at the level of second-order moments). A satisfactory agreement is found in the quantitative comparison with the axisymmetric EDQNM, but nevertheless one can point out some differences between the two approaches: (i) with our anisotropic EDQNM modelling, the flow is less anisotropic than in Burlot *et al.* (2015*a*,*b*); Gréa *et al.* (2016*a*), meaning notably that our anisotropy indicator b_{33} is slightly smaller; (ii) a new theoretical prediction for the exponential growth rate β of kinetic energy is proposed, based on the linear operator of our evolutions equations, and assessed numerically. Whatever the large scales initial conditions σ are, our growth rate is 10% smaller than the one of Burlot and coworkers, consistently with our flow being less anisotropic; (iii) the Froude number is higher

with the anisotropic EDQNM modelling, but can be decreased by changing the eddy-damping constants, as exposed in section 7.3.7.

To recover the exact theoretical prediction (7.25) for β, it is possible to multiply the production terms of the anisotropic EDQNM modelling for USHT, in equations (7.12)-(7.17), by $\sqrt{5}/2$, so that the maximal eigenvalue $2N$ of the linear operator is recovered. This procedure artificially corrects the exponential growth rate of the kinetic energy, nevertheless without increasing the global anisotropy of the flow since it is already maximal.

Finally, two applications of our anisotropic EDQNM modelling were proposed, which constitute new fundamental results. First, pressure spectra in USHT were investigated, and it was found that the anisotropic part, resulting from stratification, scales in $k^{-11/3}$ in the inertial range, whereas the isotropic part scales in $k^{-7/3}$: these scalings are completely similar to pressure spectra in shear flows, investigated in Appendix D. It is also shown that the pressure variance grows exponentially at a rate 2β, where β is the growth rate of the kinetic energy. Then, high Schmidt numbers were considered: the scalar variance spectrum still scales in k^{-1} in the viscous-convective range beyond the Kolmogorov wavenumber, as in HIT. The main result here is that the cospectrum, which was strongly decreasing in passive scalar dynamics, now also displays a viscous-convective range with a scaling close to k^{-1}, after a transient k^{-3} subrange around k_η. It is worth noting that large Schmidt numbers do not affect the asymptotic values of one-point statistics, nor the exponential growth rate β, but only the transient regime of Λ and b_{33}^T.

7.7 Perspective - Variable stratification $N(t)$

In this section, the mixing length $L(t)$ is not fixed anymore, unlike USHT, which causes the stratification frequency $N(t)$ to vary as well. The active scalar field is now a dimensionless concentration c, and we do not consider anymore the rescaled buoyant-velocity $\mathfrak{v}$. This part is thus a step further toward the modelling of Rayleigh-Taylor instability: the fluctuating quantities now impact the dynamics of the mean dimensionless concentration field C according to

$$\frac{\partial C}{\partial t} = -\frac{\partial < u_3 c >}{\partial x_3} + a\frac{\partial^2 C}{\partial x_3^2} \underbrace{\simeq}_{Re_\lambda \gg 1} -\frac{\partial < u_3 c >}{\partial x_3}. \tag{7.41}$$

It is assumed that the Reynolds number is large enough to neglect diffusion effects, and in addition inside the mixing zone, one has $\partial_3 C = -1/L$. Hereafter, a new prediction for the growth rate of the mixing length is derived within the anisotropic EDQNM modelling framework.

7.7.1 Evolution equations with variable stratification

In what follows, the Boussinesq approximation is still considered. In the self-similar state, the mixing length evolves according to (Poujade, 2006; Gréa, 2013)

$$L(t) = 2\alpha^{\mathrm{RT}}\mathcal{A}gt^2, \tag{7.42}$$

where α^{RT} is the Rayleigh-Taylor growth rate, whose theoretical prediction was derived by Poujade & Peybernes (2010) in the limit of small Atwood number $\mathcal{A} \ll 1$,

$$\alpha_{\mathrm{th}}^{\mathrm{RT}} = \frac{1}{(\sigma+2)(\sigma+3)}. \tag{7.43}$$

In what follows, it will be shown that this prediction relies on two crucial features and needs to be adapted to the anisotropic EDQNM modelling. The mixing length is defined as

$$L(t) = 6 \int_{-\infty}^{+\infty} C(1-C)\mathrm{d}x_3. \tag{7.44}$$

Assuming that $x_3 = 0$ is at the center of the mixing zone, and that $< u_3\theta >$ has a parabolic evolution from $-L/2$ to $L/2$ (Soulard *et al.*, 2014), the time derivative of this equation becomes, with the equation of the mean field (7.41),

$$\frac{\mathrm{d}L}{\mathrm{d}t} = \dot{L}(t) = 8 < u_3 c > . \tag{7.45}$$

There exists another possibility, proposed in Soulard *et al.* (2016) for instance, where $\dot{L} = 12\widetilde{< u_3\theta >}$, with $\widetilde{\cdot}$ referring to the average along the inhomogeneous direction x_3. In what follows, the first equation (7.45) is kept. Then, since the mixing length $L(t)$ and the stratification frequency $N(t)$ are linked through

$$N(t) = \sqrt{\frac{2\mathcal{A}g(t)}{L(t)}}, \qquad \frac{\dot{N}}{N} = \frac{1}{2}\left(\frac{\dot{g}}{g} - \frac{\dot{L}}{L}\right). \tag{7.46}$$

If the gravitational acceleration is assumed to be constant, one further gets

$$\dot{N}(t) = -\frac{4N(t)}{L(t)} < u_3 c >, \tag{7.47}$$

so that the growth rate of the mixing zone can be computed according to

$$\alpha^{\mathrm{RT}} = \frac{(\dot{L})^2}{8\mathcal{A}gL(t)} = \left(\frac{4 < u_3 c >}{N(t)L(t)}\right)^2. \tag{7.48}$$

The evolution equations, in physical space, of the fluctuating velocity and concentration u_i and c are

$$\frac{\partial u_i}{\partial t} + u_j\frac{\partial u_i}{\partial x_j} = -\frac{\partial p}{\partial x_i} + \nu\frac{\partial^2 u_i}{\partial x_j \partial x_j} + 2\mathcal{A}gc\delta_{i3}, \tag{7.49}$$

$$\frac{\partial c}{\partial t} + u_j\frac{\partial c}{\partial x_j} = a\frac{\partial^2 c}{\partial x_j \partial x_j} + \frac{1}{L(t)}u_3. \tag{7.50}$$

If one wants to work with the buoyant velocity $\mathfrak{v}$, the equations becomes more complex because an additional term, linked to the variable stratification, appears

$$\frac{\partial \mathfrak{v}}{\partial t} + u_j\frac{\partial \mathfrak{v}}{\partial x_j} = a\frac{\partial^2 \mathfrak{v}}{\partial x_j \partial x_j} + Nu_3 - \mathfrak{v}\left(\frac{\dot{N}}{N} - \frac{\dot{g}}{g}\right). \tag{7.51}$$

7.7.2 Prediction of the growth rate α^{RT}

In this section, a new prediction for the growth rate α^{RT} is derived, like what was done before for USHT, where a theoretical exponential growth rate β_{th} for the kinetic energy was proposed, based on the linear operator of our equations within the anisotropic EDQNM modelling. The prediction (7.43) by Poujade & Peybernes (2010) relies on two crucial features: (i) foliated average in the inhomogeneous direction. This foliated average notably causes the scalar variance $< c^2 >$ to evolve in t^2, like the mixing length $L(t)$, whereas the classical scalar variance is constant in the self-similar regime of Rayleigh-Taylor turbulence, since it is bounded by 0 (light fluid) and 1 (heavy fluid); (ii) the fact that at large scales $\mathcal{F}^2/(\phi_{33}E_T) = 1$. This result is essential to link α^{RT} to the infrared slope σ (in Poujade & Peybernes (2010), one has for the vertical foliated averaged spectrum $2\mathcal{E}_z \sim \phi_{33}$). This ratio $\mathcal{F}^2/(\phi_{33}E_T) = 1$ is recovered in the present simulations.

Here are the main steps to derive a new prediction for the Rayleigh-Taylor growth rate. First, at large scales, the self-similar spectra can be written

$$\phi_{33}(k,t) = E^0 k^\sigma t^{n_E}, \qquad E_T(k,t) = E_T^0 k^\sigma t^{n_T}, \qquad \mathcal{F}(k,t) = F^0 k^\sigma t^{n_F}, \tag{7.52}$$

where E^0, E_T^0 and F^0 are independent of time and space. At large scales, the evolution equations of ϕ_{33} and E_T (7.12) and (7.15) read, neglecting the non-linear transfers,

$$\frac{\partial \phi_{33}}{\partial t} \simeq \frac{16}{5}\mathcal{A}g\mathcal{F}(k,t), \qquad \frac{\partial E_T}{\partial t} \simeq \frac{2}{L(t)}\mathcal{F}(k,t), \tag{7.53}$$

which directly yields $n_E = n_F + 1$ and $n_F = n_T + 1$, since E^0, E_T^0 and F^0 do not depend on time. The equation of $\mathcal{F}$ cannot be used similarly since the production terms depend on both the kinetic and scalar variance spectra. From these equations, one obtains

$$\frac{E_0}{E_T^0} = \frac{16}{5}(\mathcal{A}g)^2 \alpha^{\mathrm{RT}} \frac{n_T}{n_E}. \tag{7.54}$$

The exponent n_T is determined using the fact that $< c^2 >$ is eventually constant in time

$$< c^2 > = \int_0^\infty E_T(k,t)\mathrm{d}k \simeq \int_0^{1/L(t)} E_T^0 k^\sigma t^{n_T}\mathrm{d}k = \frac{E_T^0}{\sigma+1} t^{n_T - 2(\sigma+1)}, \tag{7.55}$$

which provides $n_T = 2(\sigma+1)$, and consequently $n_E = 2(\sigma+2)$ and $2n_F = n_E + n_T$. Afterwards, from (7.53), one gets at large scales

$$\frac{\mathcal{F}^2(k,t)}{\phi_{33}(k,t)E_T(k,t)} = \frac{5}{16}\alpha^{\mathrm{RT}} n_E\, n_T. \tag{7.56}$$

This finally yields a new theoretical prediction for the growth rate

$$\boxed{\alpha_{\mathrm{th}}^{\mathrm{RT}} = \frac{4}{5(\sigma+1-p_{\mathrm{USHT}})(\sigma+2-p_{\mathrm{USHT}})},} \tag{7.57}$$

which gives values 33.3% higher than the expression of Poujade & Peybernes (2010). One can remark that unlike the original prediction of the latter reference, a backscatter parameter was added here, in order to take into account strong inverse non-linear transfers in Batchelor turbulence. The noteworthy feature is that numerically $p_{\mathrm{USHT}} = 0.37$ is obtained, meaning that the intensity of the back transfers in Batchelor turbulence is similar between fixed (USHT) and variable stratification frequency. This new prediction (7.57) relies on $< c^2 >$ being constant in the self-similar regime, unlike Poujade & Peybernes (2010) where $< c^2 > \sim t^2$ with the foliated average, and $\mathcal{F}^2/(\phi_{33}E_T) = 1$ at large scales.

The theoretical prediction (7.43) for $\alpha_{\mathrm{th}}^{\mathrm{RT}}$ by Poujade & Peybernes (2010) becomes, without the foliated-average,

$$\alpha_{\mathrm{th}}^{\mathrm{RT}} = \frac{1}{(\sigma+1)(\sigma+2)}, \tag{7.58}$$

as in Soulard *et al.* (2014); Griffond *et al.* (2015). This prediction can be recovered by multiplying the linear production terms by $\sqrt{5}/2$ in the Lin equations of USHT obtained with the anisotropic EDQNM modelling, as mentioned earlier for USHT.

7.7.3 Numerical results

In what follows, if not mentioned otherwise, the initial Reynolds number is $Re_\lambda(0) = 10$, the mixing parameter is $\Lambda(0) = 1$, $N(0) = N_0 = 1\tau_0^{-1}$ and $L(0) = L_0 = 1$, so that $\mathcal{A} = 5, 1.10^{-2}$, in agreement with the assumption of small Atwood numbers. First, spectral scalings are addressed and are compared with the results obtained with the anisotropic EDQNM modelling for USHT. Then, one-point statistics are investigated.

Spectral scalings: The inertial scalings of the three main spectra $E(k,t)$, $E_T(k,t)$, and $\mathcal{F}(k,t)$, are firstly addressed. It has been shown that for USHT, the classical inertial scalings for E and E_T, (7.19) and (7.20) respectively, are relevant, and this is still the case for variable $N(t)$, as revealed in Fig. 7.16a. For the scalar flux, as for USHT, the scaling initially proposed by Lumley (7.21) is not well-suited, because in particular it does not take into account the concentration dissipation rate ϵ_T. On the other hand, the scaling derived for Rayleigh-Taylor turbulence in Soulard & Griffond (2012), and used in Burlot *et al.* (2015*b*) with the buoyant velocity (7.22) was shown to be satisfactory for USHT, and this is still valid for variable $N(t)$, as revealed in Fig. 7.16b. To obtain this compensated cospectrum, the inertial scaling (7.22) is adapted because the scalar field is now a dimensionless concentration: in Soulard & Griffond (2012), the square of the stratification velocity V_N^2 appears; here, instead of $V_N = \sqrt{gL}$, $V_N = NL$ is chosen, so that the Rayleigh-Taylor inertial scaling becomes

$$\mathcal{F}_{\mathrm{inertial}}^{\mathrm{Soulard}}(k,t) = \mathcal{F}(k,t)\, L\Big(K_0\epsilon^{1/3} + K_{\mathrm{CO}}(NL)^2\epsilon_T\epsilon^{-2/3}\Big)^{-1} k^{7/3}. \tag{7.59}$$

Simulations also show in Fig. 7.16b that a simpler expression for the inertial scaling of $\mathcal{F}$ can also be considered, namely

$$\mathcal{F}_{\mathrm{inertial}}^{\mathrm{RT}}(k,t) = \mathcal{F}(k,t)\, N^{-2}\, L^{-1}\epsilon_T^{-1}\epsilon^{2/3}k^{7/3}. \tag{7.60}$$

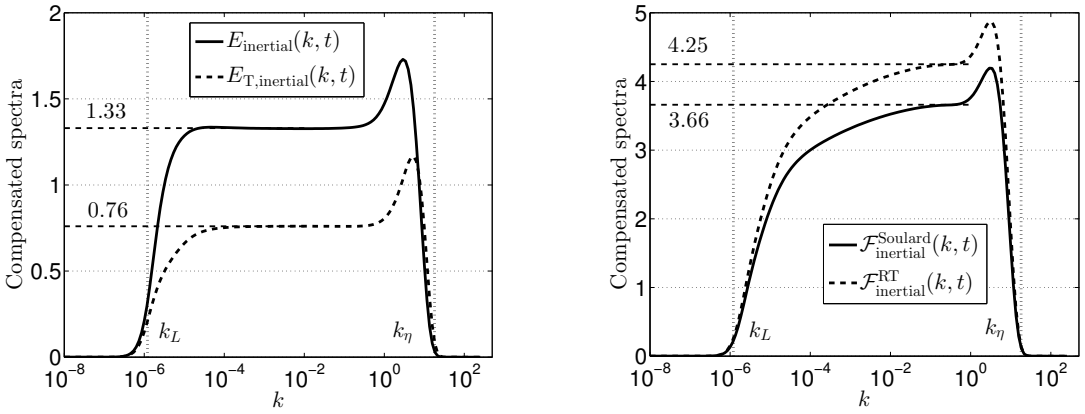

(a) (b)

Figure 7.16: Compensated spectra at $Re_\lambda(N_0 t = 10^4) = 1,6.10^5$ for $\sigma = 2$. (a) Compensated kinetic energy and scalar variance spectra, given by (7.19) and (7.20). (b) Compensated cospectrum, given by (7.59) and (7.60).

Since for $\mathcal{F}^{\text{Soulard}}_{\text{inertial}}$ the plateau approaches a value closer to the one obtained in USHT, this inertial scaling is kept for consistency.

One-point statistics: It is shown in Fig. 7.17a for Saffman turbulence that the mixing length reaches the self-similar state $L \sim t^2$ after a transient regime of about $N_0 t \simeq 100$. From the same point, the stratification frequency evolves as $N \sim t^{-1}$, which is straightforward using (7.46). Moreover, it is shown that in the self-similar regime, the scalar variance $< c^2 >$ is constant, in agreement with what was discussed earlier. In Fig. 7.17b, the prediction (7.57) is assessed numerically for various infrared slopes σ. It is worth noting that for $\sigma = 4$, the backscatter parameter $p_{\text{USHT}} = 0.37$, previously introduced for USHT, is still relevant, which shows that unstably stratified turbulence and the variable stratification case share some infrared dynamics properties.

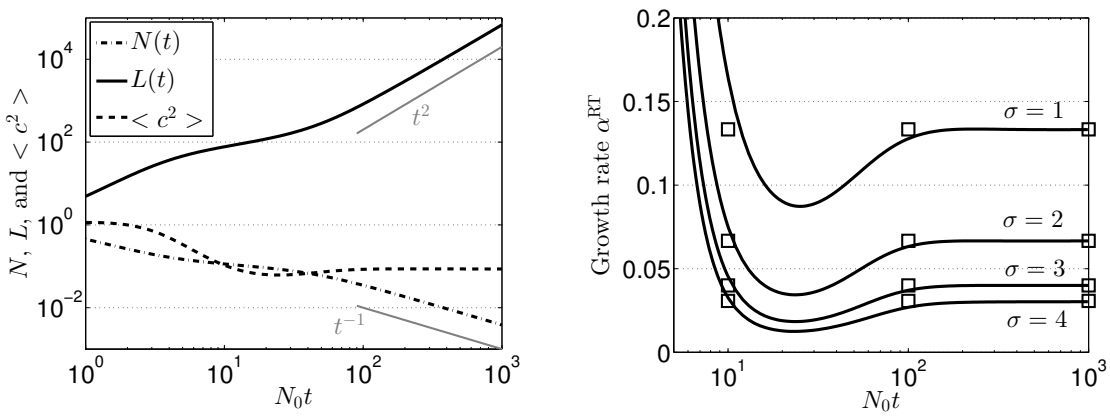

(a) (b)

Figure 7.17: (a) Stratification frequency N, mixing length L, and concentration variance $K_T =< c^2 >$ for $\sigma = 2$, and $Re_\lambda(N_0 t = 10^3) = 5.10^3$. (b) Growth rate α^{RT} for various σ: – computed with (7.48); □ prediction (7.57).

The emphasis is now put on the kinetic energy K, the scalar variance K_T and the mixed-correlation $K_{\mathcal{F}} =< u_3 c >$, whose evolution equations are

$$\frac{\partial K_T}{\partial t} = -\epsilon_T + \frac{2}{L} < u_3 c >, \tag{7.61}$$

$$\frac{\partial K}{\partial t} = -\epsilon + 2\mathcal{A}g < u_3 c >, \tag{7.62}$$

$$\frac{\partial < u_3 c >}{\partial t} = -\epsilon_{\mathcal{F}} + 2\mathcal{A}g K_T + \frac{R_{33}}{L}. \tag{7.63}$$

Since the scalar variance becomes eventually constant in the asymptotic state, it means that dissipation balances production, so that $\epsilon_T = 2 < u_3 c > /L$, and $< u_3 c > \sim t$. It then follows that the kinetic energy evolves in $K \sim t^2$ similarly to $L(t)$. These different time-dependencies are assessed in Fig. 7.18a.

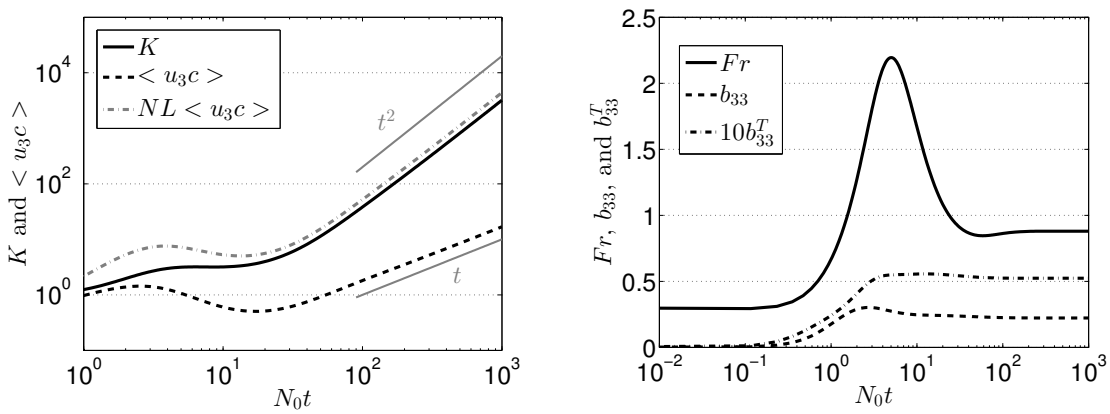

(a) (b)

Figure 7.18: One-point statistics for $\sigma = 2$. (a) Time dependence of K and $K_{\mathcal{F}}$; $NL < u_3 c >$ is displayed as well in a grey dash-dot line. (b) Fr, b_{33} and b_{33}^T: b_{33}^T is increased by a factor 10 for readability.

Consequently, because of the continuous production of kinetic energy, it is reasonable to assume that $\partial_t K \simeq 2\mathcal{A}g < u_3 c >$. Furthermore, in agreement with Fig. 7.18b where Fr is displayed, stratification dominates over turbulence in the self-similar regime, so that with a rough approximation, $\partial_t K \sim KN$. This provides an approximation of the kinetic energy in the self-similar regime

$$K(t) \sim N(t) L(t) < u_3 c > . \tag{7.64}$$

This approximation, which involves the characteristic stratification velocity $V_N = NL$, is well assessed in Fig. 7.18a in grey. In addition, it is revealed in Fig. 7.18b that both b_{33} and b_{33}^T, like Fr, become constant at large Reynolds numbers. The asymptotic value of the global anisotropy for $\sigma = 2$ with variable $N(t)$ is $b_{33}^{\infty} = 0.223$, slightly lower than in USHT where $b_{33}^{\infty} = 0.239$, meaning that the variable stratification tends to decrease the global anisotropy. This is expected since the mixing length grows in time, thus reducing the intensity of the mean concentration gradient, which is the source term of anisotropy in the equations.

Chapter 8

Dynamics of Helicity in Skew-Isotropic Turbulence

In this chapter, the transport of a scalar field is put aside to investigate the dynamics of helicity: this is of fundamental interest since helicity can be considered as the "smoothest" kind of anisotropy, since it breaks only mirror-symmetry with respect to HIT.

The contents of this chapter were published in:
Briard & Gomez, "Dynamics of helicity in homogeneous skew-isotropic turbulence ", *Journal of Fluid Mechanics*, **821**, 539-581 (2017)

Helicity is a quantity of interest since it is an invariant of the 3D inviscid Navier-Stokes equations (Moffatt, 1969) and has been consequently at the center of a great amount of theoretical (Brissaud *et al.*, 1973; Moffatt & Tsinober, 1992; Chkhetiani, 1996; Gomez *et al.*, 2000; Ditlevsen & Giuliani, 2001) and numerical (André & Lesieur, 1977; Polifke & Shtilman, 1989; Borue & Orszag, 1997; Chen *et al.*, 2003; Baerenzung *et al.*, 2008*b*; Biferale *et al.*, 2012) studies. Nevertheless, despite all the attention helicity has received for more than forty years, it remains a quantity quite complex, whose effects on the transfers of energy are not completely understood, as stated in Chen *et al.* (2003): indeed, helicity $K_H =< u_i\omega_i > /2$, unlike kinetic energy $K(t) =< u_iu_i > /2$, is not positive definite since it is the scalar product of the fluctuating velocity u_i and vorticity $\omega_i = \epsilon_{ijk}\partial_j u_k$, so that it can be either positive or negative. It is worth noting that inviscid 3D turbulence has two invariants, kinetic energy and helicity, and 2D turbulence has two as well, kinetic energy and enstrophy $< \omega_i\omega_i >$. Therefore, some authors have evoked the possibility of interpreting helicity as a 3D analogous of enstrophy, despite the fact that the latter quantity is positive definite. Since enstrophy is responsible for an inverse cascade of energy in 2D (Kraichnan, 1967), it has been concluded that helicity could also be associated to inverse cascade mechanisms in 3D (Brissaud *et al.*, 1973; Chen *et al.*, 2003).

Consequently, since the pioneering work of Brissaud *et al.* (1973), the possibility of inverse energy cascades has been a crucial point of discussion. At this time, two different scenarios were proposed: (i) Joint cascades of helicity and energy towards small scales with non zero kinetic and helical dissipation rates, respectively ϵ and ϵ_H, so that the kinetic and helical spectra scale in $E(k) \sim \epsilon^{2/3}k^{-5/3}$ and $H(k) \sim \epsilon_H\epsilon^{-1/3}k^{-5/3}$. (ii) A pure helicity cascade, with

no energy transfer $\epsilon = 0$, so that the kinetic and helical spectra scale in $E(k) \sim \epsilon_H^{2/3} k^{-7/3}$ and $H(k) \sim \epsilon_H^{2/3} k^{-4/3}$ in the forward cascade. In such a configuration, there would be an inverse cascade of kinetic energy in $k^{-5/3}$. This second scenario was proven to be impossible in decaying turbulence by André & Lesieur (1977) in the EDQNM framework. However, for instance in rotating turbulence with a non-vanishing helical forcing, and in other very specific configurations, an inverse energy cascade is observed (Biferale *et al.*, 2013). Furthermore, one must point out that recently, it was shown that the Navier-Stokes equations intrinsically contain this inverse energy cascade mechanism (Biferale *et al.*, 2012): indeed, when considering specific triadic interactions between only positive (or negative) helical modes, there is an inverse kinetic energy cascade $E(k) \sim \epsilon^{2/3} k^{-5/3}$. Still, as soon as there is a single helical mode of opposite sign, this inverse cascade vanishes.

On a practical point of view, large Reynolds numbers helical flows can be found notably in atmospheric turbulence, where helicity is naturally present and may be the reason for the persistence of tornadoes (Moffatt & Tsinober, 1992; Lesieur, 2008). On a theoretical point of view, the high Reynolds numbers regime is of interest since the classical scalings, phenomenology and mechanisms of turbulence were developed in this framework, where small scales should always be isotropic and forget the effects of large scales (Kolmogorov, 1941*b*). The review of the different studies involving helicity shows that, except the early and pioneering work of André & Lesieur (1977), there were no further attempts to investigate the dynamics of the helical spectrum $H(k,t)$ at very large Reynolds numbers ($Re_\lambda \geq 10^3$). In addition, it appears that the long-time decay of helicity has not been addressed. Yet, the knowledge of the decay rate of integrated quantities, such as the inviscid invariants, is crucial for the understanding and prediction of the turbulence dynamics in asymptotic regimes at large Reynolds numbers. Therefore, it could be interesting to have clear decay exponents for helicity: indeed, there were no studies providing decay exponents for helicity, except the theoretical one by Levshin & Chkhetiani (2013), which is not fully satisfactory as explained later on. Consequently, this chapter first focuses on two fundamental questions: is the decay of helicity predictable? How does helicity modify non-linear transfers and the decay of kinetic energy?

Since mean helicity can be created in homogeneous turbulence, from non-zero spectral helical modes (André & Lesieur, 1977), the knowledge of its decay law is of great interest when it is initially present in the flow. This is why the authors choose to focus on a classical configuration at large Reynolds numbers, namely Homogeneous Helical Turbulence (HHT), which is basically a skew-isotropic turbulence, *i.e.* HIT without mirror symmetry. In particular, there are no magnetic fields, so that only the kinetic helicity is considered: this is precisely the framework addressed by André & Lesieur (1977), and unlike recent studies, no distinctions are made here between positive and negative helical modes (Biferale *et al.*, 2013).

In such a fundamental configuration, several crucial theoretical results in physical space were derived regarding two-point third-order correlations: notably, Chkhetiani (1996) proposed an inertial scaling for the triple velocity correlation $S(r) =< u_L u_2 u_3' >$, where r is the distance between two points located in $\boldsymbol{x}$ and $\boldsymbol{x'} = \boldsymbol{x} + \boldsymbol{r}$, the prime $'$ refers to quantities expressed in $\boldsymbol{x'}$, and the $()_L$ to the component along $\boldsymbol{r}$: $S(r)$ appears in the evolution equation of the antisymmetric part of $< u_i u_j' >$, and is found to scale, neglecting the temporal and viscous dissipation terms, as $S(r) \sim \epsilon_H r^2/30$. In addition, mixed velocity-velocity-vorticity structure functions were analyzed in Gomez *et al.* (2000), and it was found that $< \delta u_L \delta u_i \delta \omega_i > - < \delta \omega_L \delta u_i \delta u_i > /2 = -4r\epsilon_H/3$ in the inertial range, where $\delta u_i = u_i' - u_i$. These two laws are

equivalent, and result from the conservation of helicity in inviscid flows. This is why the second law is analogous to the "four-thirds" laws for the kinetic energy and scalar variance, which both come from conservation laws as well (Antonia *et al.*, 1997). Whereas an equivalent of the first law for $S(r)$ has been assessed in DNS (Kurien *et al.*, 2004), it is not the case for the helical "four-thirds" law. Both these fundamental relations are assessed numerically here at high Reynolds numbers, and statistics of helical flows will be further investigated, notably the evolution equation of the helical dissipation rate ϵ_H and derivatives of skew-isotropic tensors.

Finally, a new configuration is addressed, combining both a mean scalar gradient and helicity. This case, which could be of interest for the modelling of atmospheric turbulence where these two features may be present, permits to illustrate the subtle effects of helicity on the scalar flux. Indeed, unlike a passive scalar field where there is no explicit contributions of helicity in its evolution equations, the coupling of helicity and mean scalar gradient creates the quadrature spectrum $Q(k,t)$, linked to the imaginary antisymmetric part of the scalar flux. The appearance of this additional contribution parallel to the cospectrum is called "skew-diffusion" by Moffatt & Tsinober (1992).

8.1 Spectral modelling of helicity

In this part, the evolution equations of the kinetic and helical spectra are derived starting from the spectral counterpart of the Navier-Stokes equation. The EDQNM approach is presented as well. In the following, helicity is injected initially at large scales along with kinetic energy so that both decay freely: there is no forcing mechanism nor rotation, and no magnetic field. Historically, this is the framework investigated by Brissaud *et al.* (1973) and it will be shown that even in such a classical case, there are still some important open questions which are tackled in the following sections, such as the prediction of the helicity decay and its impact on kinetic energy transfers.

8.1.1 The $\mathcal{E}$-$\mathcal{H}$ decomposition

With helicity, the spectral Reynolds tensor $\hat{R}_{ij}$ has an imaginary part, and is consequently not symmetric anymore. In the framework of homogeneous helical turbulence (HHT), $\hat{R}_{ij}$ can be decomposed as

$$\hat{R}_{ij}(\boldsymbol{k},t) = \mathcal{E}(\boldsymbol{k},t)P_{ij} + \Re(Z(\boldsymbol{k},t)N_iN_j) + \mathrm{i}\epsilon_{ijk}\alpha_k\frac{\mathcal{H}(\boldsymbol{k},t)}{k}, \tag{8.1}$$

following the formalism of Cambon & Jacquin (1989). For simplicity reasons, mean velocity gradients are not considered, which simplifies the previous expression into the $\mathcal{E}$-$\mathcal{H}$ decomposition which reads

$$\boxed{\hat{R}_{ij}(\boldsymbol{k},t) = \hat{R}_{ij}^{(\mathrm{iso})}(\boldsymbol{k},t) + \hat{R}_{ij}^{(\mathrm{hel})}(\boldsymbol{k},t) = \mathcal{E}_0(k,t)P_{ij} + \mathrm{i}\epsilon_{ijk}\alpha_k\frac{\mathcal{H}(\boldsymbol{k},t)}{k}} \tag{8.2}$$

where $\mathcal{H}$ is a pseudo-scalar, real, not positive-definite, and reflects the **density of helicity**, defined as

$$\mathcal{H}(\boldsymbol{k},t)\delta(\boldsymbol{k}-\boldsymbol{p}) = \frac{1}{2} < \hat{u}_i^*(\boldsymbol{p},t)\hat{\omega}_i(\boldsymbol{k},t) > \tag{8.3}$$

where $\omega_i = \epsilon_{ijk}\partial_j u_k$ is the **vorticity**. Similar $\mathcal{E}$-$\mathcal{H}$ decompositions were used by Borue & Orszag (1997); Chen *et al.* (2003). The inverse relation for the energy density is straightforward, $\mathcal{E}_0 = \hat{R}_{ii}/2$, whereas the one for the helical density is more complex (Moffatt, 1983; Cambon *et al.*, 2013)

$$\mathcal{H}(\boldsymbol{k},t) = -\frac{1}{2} i k_m \epsilon_{ijm} \hat{R}_{ij}(\boldsymbol{k},t). \tag{8.4}$$

The $\mathcal{E}$-$\mathcal{H}$ decomposition could also be applied in isotropic MHD to the spectral second-order magnetic correlation $R_{ij}^M(\boldsymbol{k})\delta(\boldsymbol{k}-\boldsymbol{p}) =< \hat{a}_i^*(\boldsymbol{p},t)\hat{a}_j(\boldsymbol{k},t) >$, with $\hat{a}_i$ the magnetic potential, where the antisymmetric part would be linked to the magnetic helicity $\mathcal{H}^M$, related to R_{ij}^M through an equation analogous to (8.4).

Using the equations of the fluctuating spectral velocity and vorticity given in Appendix D, one obtains the **helical Craya equation**

$$\frac{\partial \mathcal{H}}{\partial t} + 2\nu k^2 \mathcal{H}(\boldsymbol{k},t) = T_H(\boldsymbol{k},t). \tag{8.5}$$

The **non-linear helical transfer** T_H can be expressed as a function of the τ_{ij}, defined in (2.39), using the relation (8.4) so that

$$\boxed{T_H(\boldsymbol{k},t) = -\frac{1}{2}\mathrm{i}\epsilon_{ijl}k_l\Big(\tau_{ij}(\boldsymbol{k},t) + \tau_{ji}^*(\boldsymbol{k},t)\Big).} \tag{8.6}$$

This expression (8.6) links the helical transfer to the total non-linear one defined in (2.18), similar to what was done for $T_{\mathcal{E}}$ and T_Z in (2.32) and (2.34) respectively. The **helical spectrum** is further defined as

$$H(k,t) = \int_{S_k} \mathcal{H}(\boldsymbol{k},t)\mathrm{d}^2\boldsymbol{k} = 4\pi k^2 \mathcal{H}(k,t), \tag{8.7}$$

and is linked to helicity and the helical dissipation rate through

$$K_H(t) = \frac{1}{2} < u_i\omega_i >= \int_0^\infty H(k,t)\mathrm{d}k, \tag{8.8}$$

$$\epsilon_H(t) = \nu < \frac{\partial u_i}{\partial x_j}\frac{\partial \omega_i}{\partial x_j} >= 2\nu \int_0^\infty k^2 H(k,t)\mathrm{d}k. \tag{8.9}$$

The time evolution of helicity is thus given by

$$\frac{\mathrm{d}K_H}{\mathrm{d}t} = \frac{1}{2}A_{ij}\Big(< u_i\omega_j > - < u_j\omega_i > \Big) - \epsilon_H. \tag{8.10}$$

Without mean-velocity gradients, $A_{ij} = 0$ and consequently the helicity follows the same evolution equation as the kinetic energy in HIT.

8.1.2 Spherically-averaged helical Lin equations for $E(k,t)$ and $H(k,t)$

In this part, the explicit spherically-averaged transfer terms for HHT are derived within the EDQNM framework, as in André & Lesieur (1977). Using (8.6) and the details provided in Appendix D, the **non-linear spherically-averaged helical transfer** reads

$$S_H^{\mathrm{NL}}(k,t) = \int_{S_k} T_H(\boldsymbol{k},t)\mathrm{d}^2\boldsymbol{k} = S_{\mathrm{H1}}^{\mathrm{NL}}(k,t) + S_{\mathrm{H2}}^{\mathrm{NL}}(k,t), \tag{8.11}$$

with

$$\begin{aligned} S_{\mathrm{H1}}^{\mathrm{NL}}(k,t) &= 16\pi^2 \int_{\Delta_k} \theta_{kpq}^H k^2 p^2 q (xy + z^3)\mathcal{E}_0''(\mathcal{H}' - \mathcal{H})\mathrm{d}p\mathrm{d}q \\ S_{\mathrm{H2}}^{\mathrm{NL}}(k,t) &= -16\pi^2 \int_{\Delta_k} \theta_{kpq}^H k^2 pz(x + yz)\mathcal{H}''(p^2\mathcal{E}_0' - k^2\mathcal{E}_0)\mathrm{d}p\mathrm{d}q. \end{aligned} \tag{8.12}$$

Moreover, from the $\mathcal{E}$-$\mathcal{H}$ decomposition, the kinetic non-linear transfers now contain a helical part coming from products of $\hat{R}_{ij}^{(\mathrm{hel})}$: details of the calculations are given in Appendix D. The **non-linear spherically averaged purely helical transfer** is

$$S^{\mathrm{NL(hel)}}(k,t) = \int_{S_k} T_{\mathcal{E}}(\boldsymbol{k},t)\mathrm{d}^2\boldsymbol{k} - S^{\mathrm{NL(iso)}}(k,t) \tag{8.13}$$

$$= -16\pi^2 \int_{\Delta_k} \theta_{kpq} k^2 pz(x + yz)\mathcal{H}''(\mathcal{H}' - \mathcal{H})\mathrm{d}p\mathrm{d}q, \tag{8.14}$$

with $S^{\mathrm{NL(iso)}}$ given by (2.57). These three new transfer terms, $S_{\mathrm{H1}}^{\mathrm{NL}}$, $S_{\mathrm{H2}}^{\mathrm{NL}}$, and $S^{\mathrm{NL(hel)}}$, are independently conservative. The characteristic time of the third-order correlations is the same for the kinetic and helical fields: it is shown later on that such an assumption is consistent with joint cascades for the kinetic and helical spectra, and can be a posteriori justified with physical arguments. Beyond these physical justifications, it seems relevant to choose θ_{kpq} for both the kinetic and helical fields since the closure comes from the same evolution equation, which is the one of the spectral velocity third-order correlation (2.17). One can further remark that the form of $S_{\mathrm{H1}}^{\mathrm{NL}}$ is similar to the scalar non-linear transfer $S^{\mathrm{T,NL(iso)}}$. It will be shown numerically that $S_{\mathrm{H1}}^{\mathrm{NL}}$ corresponds in fact to a direct transfer, whereas both $S_{\mathrm{H2}}^{\mathrm{NL}}$ and $S^{\mathrm{NL(hel)}}$ to inverse ones.

The spherically-averaged Lin equations for the kinetic and helical spectra are

$$\boxed{\begin{aligned} &\left(\frac{\partial}{\partial t} + 2\nu k^2\right) H(k,t) = S_H^{\mathrm{NL}}(k,t), && (8.15) \\ &\left(\frac{\partial}{\partial t} + 2\nu k^2\right) E(k,t) = S^{\mathrm{NL(iso)}}(k,t) + S^{\mathrm{NL(hel)}}(k,t) = S_E^{\mathrm{NL}}(k,t). && (8.16) \end{aligned}}$$

Finally, the helical spectrum $H(k,t)$ must satisfy the realizability condition

$$|H(k,t)| \leq kE(k,t), \tag{8.17}$$

which was derived by Kraichnan (1973). When this equation is an equality, this condition is called the **maximal helicity condition**.

8.2 Numerical results on the helical and kinetic fields

In this part, the kinetic energy and helical spectra $E(k,t)$ and $H(k,t)$ are investigated numerically at very large Reynolds numbers thanks to the EDQNM modelling presented in the previous section. After a short discussion on initial conditions, basic properties of homogeneous skew-isotropic flows are recovered and some features regarding inverse transfers are addressed. Then, non-local interactions are considered in the infrared range of the spectra (for wavenumbers smaller than the integral one k_L) and non-local expansions are made in order to study the large scales dynamics. These results are directly used to predict the decay of kinetic energy and helicity in homogeneous turbulence.

8.2.1 The importance of initial conditions $H(k, t = 0)$

The initial condition for the helical spectrum is (8.17). One has to be careful with this initial condition, which increases the infrared slope σ_H of the helical spectrum, and thus accelerates the decay of helicity. Indeed, in Saffman HHT for instance, at large scales $H(k < k_H, t) \sim k^3$ whereas $E(k < k_L, t) \sim k^2$, where k_H is the **helical integral wavenumber**, defined similarly to the kinetic one

$$L_H(t) = \frac{1}{k_H} = \frac{3\pi}{4K_H(t)} \int_0^\infty k^{-1} H(k,t) \mathrm{d}k. \tag{8.18}$$

The last point to define is the shape of $E(k, t = 0)$, which is of primary importance. So far, the initial condition (1.10) was used, called (IC1) from now, which corresponds to a spectrum with energy at all scales at $t = 0$. In particular, (IC1) implies that helicity is initially present at all scales as well: this strongly minimizes the impact of helicity on the kinetic energy cascade and decay. Hence, the initial condition (IC2) is used instead

$$\text{(IC2)}: \qquad E(k, t = 0) = k^\sigma \exp\Big(- \frac{\sigma}{2} \Big(\frac{k}{k_L} \Big)^2 \Big). \tag{8.19}$$

One can wonder if $H(k, t = 0) = E(k, t = 0)$ is an acceptable initial condition, even if for $k \geq k_L$ this breaks (8.17). Fig. 8.1a reveals that the latter initial condition is physically unacceptable: indeed, after a hundred turn-over times, one has $kE - H \leq 0$ around the integral wavenumber k_L. Whereas for the maximal helicity condition, for all k one has $kE - H \geq 0$, for both (IC1) and (IC2). Consequently, from this point, all the computations presented are initialized with the maximal helicity condition.

Unlike the kinetic energy spectrum $E(k,t)$, the helical spectrum $H(k,t)$ is not restricted to positive values: it was notably found by André & Lesieur (1977) that negative values appeared at the beginning of the dissipative range near k_η. This is also observed here with the present EDQNM simulations in Fig. 8.1b, where the helical spectrum has negative values while approaching k_η. Positive and negative values for $H(k,t)$ were reported in DNS (Polifke & Shtilman, 1989; Polifke, 1991).

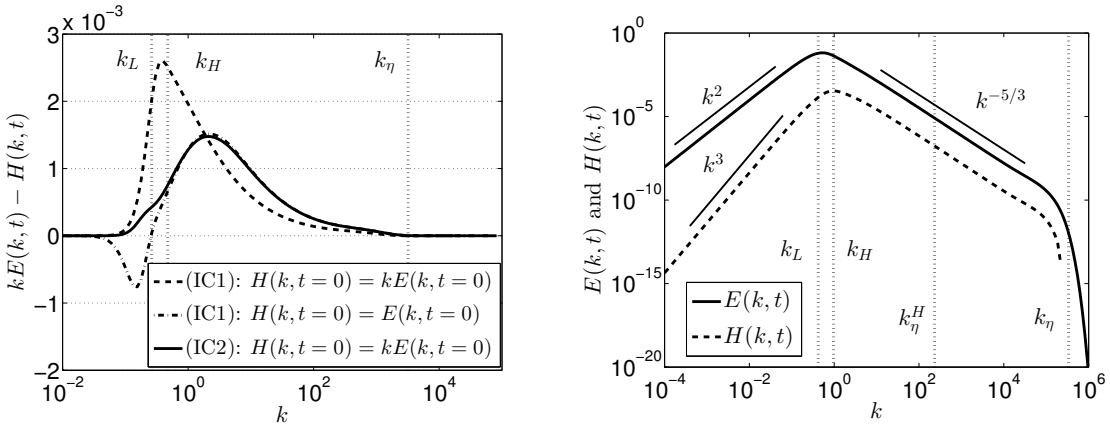

(a) (b)

Figure 8.1: (a) $kE - H$ for three different initial conditions, with $\sigma = 4$ at $Re_\lambda = 1400$. (b) Kinetic and helical spectra $E(k,t)$ and $H(k,t)$ with $\sigma = 2$ at $Re_\lambda = 2.10^4$. k_η^H is defined in (8.22). Both along with the kinetic and helical integral wavenumbers k_L and k_H, and the Kolmogorov wavenumber k_η.

8.2.2 Helical spectrum $H(k,t)$ and non-linear transfers

In this section, the inertial scaling of $H(k,t)$ and the non-linear helical transfers are addressed. Fig. 8.1b reveals that after a few turn-over times the helical spectrum scales in $k^{-5/3}$ in the inertial range. This scaling assesses the joint cascades mentioned earlier for kinetic energy and helicity. The $k^{-5/3}$ scaling can be deduced from dimensional analysis. The main hypothesis is that the characteristic time in the inertial range $\tau(k,t) = (k^2\epsilon(t))^{-1/3}$ is the same for both the kinetic and helical spectra. From this assumption results an "Obukhov-like" scaling, $\epsilon_H(t) = kH(k,t)/\tau(k,t)$, which directly yields in the inertial range

$$H(k,t) = C_H\, \epsilon_H\, \epsilon^{-1/3}\, k^{-5/3}. \tag{8.20}$$

The constant $C_H = 2$ is obtained by investigated the compensated spectra in Fig. 8.2a at high Reynolds number $Re_\lambda = 2.10^4$. The Kolmogorov constant $K_0 = 1.3$ remains unchanged with respect to HIT. It is worth noting that similarly to K_0, the value of C_H depends on the choice of the eddy-damping constant. The present value $C_H \simeq 2$ is in agreement with André & Lesieur (1977), somehow higher that $C_H \simeq 1$ obtained in Borue & Orszag (1997).

One can remark that the inertial scaling (8.20) of $H(k,t)$ is similar to the one of a passive scalar convected by a turbulent velocity field; this is the reason why it is often said that helicity *cascades linearly* with the kinetic energy. Such a scaling can also be obtained by considering that non-linear transfers in the inertial range are mainly local: $k \sim p \sim q$. By dimensional analysis and dropping all geometric factors in (8.11), this yields for the fluxes $\Pi(k) \sim \theta\, E(k)^2\, k^4$ and $\Pi_H(k) \sim \theta\, E(k)\, H(k)\, k^4$, where $\theta_{kkk} = \theta$ is the same for E and H, as assumed earlier. Then, for high Reynolds numbers, one has in the inertial range $\Pi \simeq \epsilon$ and $\Pi_H \simeq \epsilon_H$, which is well assessed in Fig. 8.2b. Thus, one has $\theta = \epsilon/(k^4E^2) = \tau(k)$ so that

$$\epsilon(t)\, H(k,t) \sim E(k,t)\epsilon_H(t) \qquad \rightarrow \int_0^\infty \mathrm{d}k \rightarrow \qquad \epsilon(t)\, K_H(t) \sim K(t)\epsilon_H(t). \tag{8.21}$$

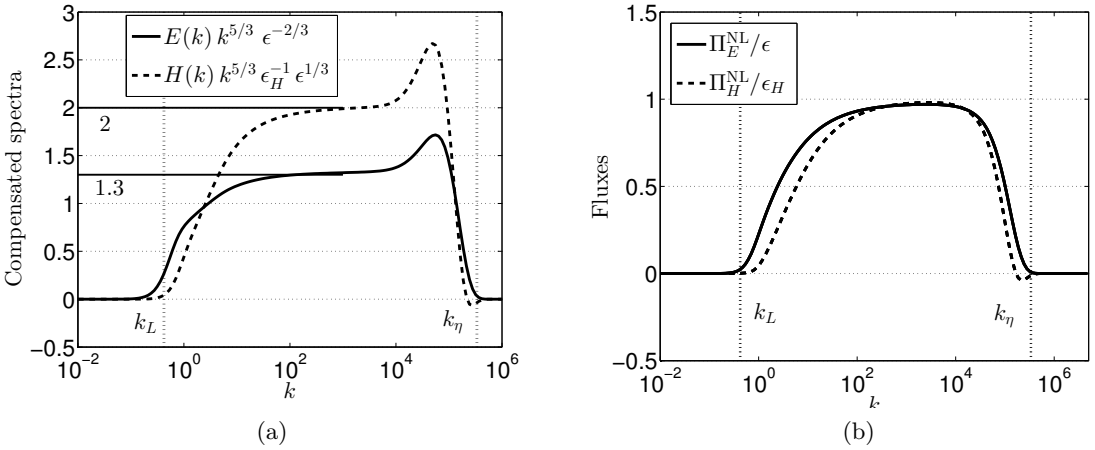

Figure 8.2: (a) Compensated kinetic and helical spectra. (b) Normalized kinetic and helical fluxes. Both with $\sigma = 2$, at $Re_\lambda = 2.10^4$, and along with the integral and Kolmogorov wavenumbers k_L and k_η.

In addition, a specific wavenumber k_η^H is displayed in Fig. 8.1b. This wavenumber was derived theoretically by Ditlevsen & Giuliani (2001)

$$k_\eta^H = \left(\frac{\epsilon_H^3}{\nu^3\epsilon^2}\right)^{1/7}, \tag{8.22}$$

and is supposed to mark the end of the helical inertial range, which is clearly not the case here. The helical inertial range spans from the helical integral wavenumber $k_H \sim k_L$ to k_η, similarly to the kinetic energy spectrum. This was also assessed both numerically and theoretically by Chen *et al.* (2003). A different interpretation of k_η^H is proposed in Appendix D.

The total non-linear kinetic and helical transfers $S_E^{\rm NL}$ and $S_H^{\rm NL}$ are now investigated in Fig. 8.3a to 8.3c for Batchelor turbulence (results are similar for Saffman turbulence). In the previous part, $S_E^{\rm NL}$ was decomposed into the sum of a purely kinetic contribution $S^{\rm NL(iso)}$, identical to the non-linear transfer in HIT, and a purely helical contribution $S^{\rm NL(hel)}$. It is found in the EDQNM simulations that the latter part corresponds in fact to a transfer of energy from small to large scales. This inverse transfer is nevertheless less intense than the direct one, so that the total kinetic transfer $S_E^{\rm NL}$ is direct, as observed in Fig. 8.3b. Moreover, whereas the direct non-linear transfer $S^{\rm NL(iso)}$ spans all scales of the wavenumber space, the inverse transfer $S^{\rm NL(hel)}$ is very localized at large scales, which creates a small region where $S^{\rm NL(iso)}$ is positive at large scales, which is different from HIT. Nevertheless, the total kinetic energy transfer $S_E^{\rm NL}$ is completely similar to the one in HIT.

Similarly, $S_H^{\rm NL}$ was decomposed into two contributions $S_{\rm H1}^{\rm NL}$ and $S_{\rm H2}^{\rm NL}$, which both span the entire inertial range. It is revealed in Fig. 8.3a that these two parts correspond to direct and inverse transfers respectively. Once again, the inverse transfer is weaker than the direct one, so that the total transfer of helicity $S_H^{\rm NL}$ goes from large to small scales. One can observe in Fig. 8.3c that $S_H^{\rm NL}$ is negative around k_η, and this explains the negative values of the helical spectrum $H(k,t)$ at the dissipative scales observed in Fig. 8.1b: this can be interpreted as viscous production of helicity, since $-2\nu k^3 H(k)$ is positive in this region. The fact that inverse transfers of kinetic

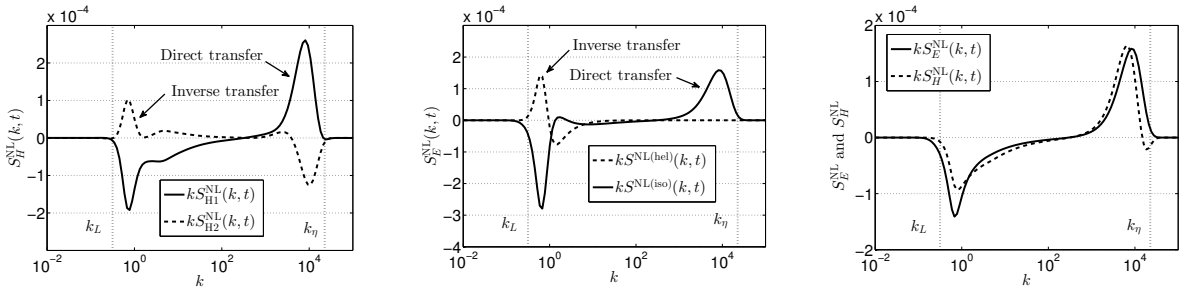

(a) (b) (c)

Figure 8.3: (a) Helical non-linear transfers $S_{\mathrm{H1}}^{\mathrm{NL}}$ and $S_{\mathrm{H2}}^{\mathrm{NL}}$. (b) Purely helical and isotropic non-linear transfers $S^{\mathrm{NL(hel)}}$ and $S^{\mathrm{NL(iso)}}$. (c) Non-linear kinetic and helical transfers S_E^{NL} and S_H^{NL}. All for $\sigma = 4$ at $Re_\lambda = 5.10^3$, along with the integral and Kolmogorov wavenumbers k_L and k_η.

energy and helicity are hidden in the total direct cascade is in agreement with the recent results of Alexakis (2017).

In this part, it was recovered that in freely decaying HHT, there is a joint cascade of kinetic energy and helicity towards small scales. The main assumption behind the $k^{-5/3}$ inertial scaling is that the kinetic and helical fields have the same inertial characteristic time. Finally, it was shown numerically that despite a direct cascade of kinetic energy and helicity, some inverse non-linear transfers occur, less intense than direct ones.

8.2.3 Infrared dynamics and non-local transfers

This section focuses on the permanence of large eddies (PLE) in the presence of helicity, and on non-local interactions between small and large scales. The starting point is Fig. 8.4a and 8.4b, where the time evolution of the kinetic energy and helical spectra $E(k,t)$ and $H(k,t)$ is displayed for Batchelor turbulence. Two features need to be underlined: firstly, it appears that H experiences no backscatter in Fig. 8.4b, so that the PLE hypothesis is verified in Batchelor HHT for the helical spectrum, unlike E. Secondly, the backscatter for E in Fig. 8.4a is weaker in presence of helicity than in HIT, as revealed by the grey curve corresponding to a HIT simulation for E, at the same time and Reynolds number. These two features can be explained analytically, using non-local expansions. These important results, and especially the fact that the PLE hypothesis is verified for H even in Batchelor turbulence, are applied in the next section to determine theoretical decay exponents for $K(t)$ and $K_H(t)$.

Firstly, Lesieur (2008) showed that the kinetic non-local transfers acting in the infrared range are

$$T^{(\mathrm{iso})-}(k,t) = \frac{14}{15}k^4 \int_{k_L}^{\infty} \theta_{0pp} \frac{E(p)^2}{p^2} \mathrm{d}p - \frac{2}{15}k^2 E(k) \int_{k_L}^{\infty} \theta_{0pp} \left(5E(p) + p\frac{\partial E}{\partial p}\right) \mathrm{d}p. \tag{8.23}$$

These terms come from the space derivative $\partial\Pi^-/\partial k$, with $\Pi^{(\mathrm{iso})-} = \Pi^-$ defined in (B.17), evaluated at the lowest order in k/k_L, with the non-local parameter $a = k/k_L$. The first rhs term is responsible for the backscatter of energy that breaks the PLE hypothesis. The second rhs term can be written under the eddy-viscous form $-2\nu_t k^2 E$, and represents a pseudo kinetic

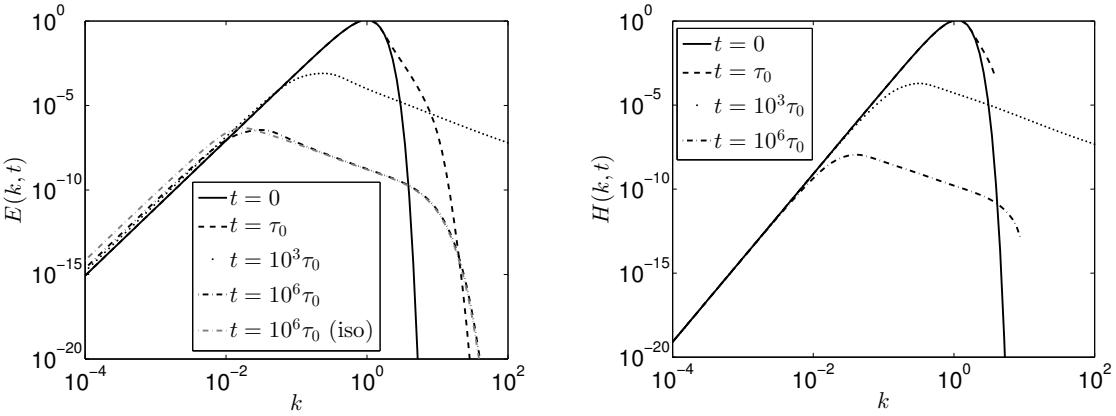

(a) (b)

Figure 8.4: Decaying spectra in Batchelor turbulence with $Re_\lambda(0) = 3400$. (a) Kinetic energy spectrum $E(k,t)$: at $t = 10^6\tau_0$, $E(k,t)$ for HIT is displayed as well in grey. (b) Helical spectrum $H(k,t)$.

energy dissipation, *i.e.* the damping of large scales by turbulence. To understand why back transfers of energy on $E(k,t)$ are decreased with helicity, one has to expand $S^{\mathrm{NL(hel)}}$ when $k \ll p \sim q$, using calculations similar to those presented in Appendix B. This gives

$$\Pi^{(\mathrm{hel})-}(k,t) = -\frac{14}{15}\int_0^k k'^4 \int_{\sup(k,k'/a)}^{\infty} \theta_{k'pp}\frac{H(p)^2}{p^4}\mathrm{d}p\mathrm{d}k' \tag{8.24}$$

$$+\frac{2}{15}\int_0^k k'^2 H(k') \int_{\sup(k,k'/a)}^{\infty} \frac{\theta_{k'pp}}{p^2}\left(9H(p) - p\frac{\partial H}{\partial p}\right)\mathrm{d}p\mathrm{d}k'. \tag{8.25}$$

The spatial derivative of $\Pi^{(\mathrm{hel})-}$, with the same assumptions, yields

$$T^{(\mathrm{hel})-}(k,t) = -\frac{14}{15}k^4\int_{k_L}^{\infty}\theta_{0pp}\frac{H(p)^2}{p^4}\mathrm{d}p + \frac{2}{15}k^2H(k)\int_{k_L}^{\infty}\frac{\theta_{0pp}}{p^2}\left(9H(p) - p\frac{\partial H}{\partial p}\right)\mathrm{d}p. \tag{8.26}$$

The first rhs term modifies the backscatter of energy whereas the second one can also be interpreted as a pseudo helical dissipation term in $-2\nu_t^H k^2 H$. Combining this expression with (8.23) reveals the impact of helicity on the total **inverse non-local kinetic transfer** in HHT

$$T_E^-(k,t) = \underbrace{\frac{14}{15}k^4\int_{k_L}^{\infty}\theta_{0pp}\frac{E(p)^2}{p^2}\left(1-\left(\frac{H(p)}{pE(p)}\right)^2\right)\mathrm{d}p}_{k^4\text{ backscatter}}\underbrace{-2\nu_t k^2E(k) - 2\nu_t^H k^2 H(k)}_{\text{damping of large scales}}. \tag{8.27}$$

The second term indicates a change in the effects of viscous damping on large-scales, difficult to quantify. However, for the first rhs term, using the realizability condition $0 \le |H|/kE \le 1$, one has

$$\frac{14}{15}k^4\int_{k_L}^{\infty}\theta_{0pp}\frac{E(p)^2}{p^2}\underbrace{\left(1-\left(\frac{H(p)}{pE(p)}\right)^2\right)}_{\le 1}\mathrm{d}p \le \underbrace{\frac{14}{15}k^4\int_{k_L}^{\infty}\theta_{0pp}\frac{E(p)^2}{p^2}\mathrm{d}p}_{\text{Non-local transfer in HIT}}. \tag{8.28}$$

Consequently, the k^4 backscatter of energy of $E(k,t)$ is decreased by helicity, with respect to HIT. Then, similar expansions of S_H^{NL} give

$$\begin{aligned}
&\Pi_H^-(k,t) = \Pi_{H1}^-(k,t) + \Pi_{H2}^-(k,t) \\
&= \frac{14}{15}\int_0^k k'^4 \int\limits_{\sup(k,k'/a)}^{\infty} \theta_{k'pp}\frac{H(p)E(p)}{p^4}\mathrm{d}p\mathrm{d}k' - \frac{2}{15}\int_0^k k'^2 H(k') \int\limits_{\sup(k,k'/a)}^{\infty} \theta_{k'pp}\left(5E(p) + p\frac{\partial E}{\partial p}\right)\mathrm{d}p\mathrm{d}k' \\
&- \frac{14}{15}\int_0^k k'^4 \int\limits_{\sup(k,k'/a)}^{\infty} \theta_{k'pp}\frac{H(p)E(p)}{p^4}\mathrm{d}p\mathrm{d}k' + \frac{14}{15}\int_0^k k'^4 E(k') \int\limits_{\sup(k,k'/a)}^{\infty} \theta_{k'pp}\frac{H(p)}{p^2}\mathrm{d}p\mathrm{d}k'. \qquad (8.29)
\end{aligned}$$

The two terms responsible for the k^4 backscatter cancel, which explains that in the end, $H(k,t)$ does not experience any strong back transfer of energy, so that the PLE hypothesis holds true for the helical spectrum. The space derivative of the inverse non-local helical flux yields

$$T_H^-(k,t) = -\frac{2}{15}k^2 H(k)\int_{k_L}^{\infty}\theta_{0pp}\left(5E(p) + p\frac{\partial E}{\partial p}\right)\mathrm{d}p + \frac{14}{15}k^4 E(k)\int_{k_L}^{\infty}\theta_{0pp}\frac{H(p)}{p^2}\mathrm{d}p. \qquad (8.30)$$

This **inverse non-local helical transfer** T_H^- indicates that there is no strong k^4 backscatter. The first term can be written $-2\nu_t k^2 H$ (and was found also in Baerenzung *et al.* (2008*b*)), and the second one is quite original since it makes intervene a pseudo-enstrophy dissipation and could consequently be written $-2\nu_t^\omega k^4 E$.

The method used now to describe analytically the infrared dynamics of the kinetic energy and helical spectra in HHT - at first order - is inspired from Lesieur (2008), where a similar reasoning is performed for HIT. When the turbulence is fully developed, both spectra scale in $E(k,t) \sim A(t)k^\sigma$ and $H(k,t) \sim A_H(t)k^{\sigma_H}$ at large scales. In this infrared range, viscous dissipation is negligible, and inverse non-local transfers T_E^- and T_H^- dominate with respect to local ones S_E^{NL} and S_H^{NL}. Thus, the simplified Lin equations in the infrared range are $\partial_t E = T_E^-$ and $\partial_t H = T_H^-$, which yields

$$\frac{\mathrm{d}A}{\mathrm{d}t} = \frac{14}{15}k^{4-\sigma}\int_{k_L}^{\infty}(...)\mathrm{d}p - 2\nu_t k^2 A(t) - 2\nu_t^H k^{2+\sigma_H-\sigma}A_H(t) \qquad (8.31)$$

$$\frac{\mathrm{d}A_H}{\mathrm{d}t} = -\frac{2}{15}k^2 A_H(t)\int_{k_L}^{\infty}(...)\mathrm{d}p + \frac{14}{15}k^{4+\sigma-\sigma_H}A(t)\int_{k_L}^{\infty}(...)\mathrm{d}p. \qquad (8.32)$$

With the present initial conditions (8.19), one has $\sigma_H = \sigma + 1$, but one could think of different initial conditions that would result in a more complex infrared dynamics for E and B: this is the object of section 8.2.5. For now, one has $\sigma_H = \sigma + 1$, and in this case, whatever the infrared slope σ is, the dissipation terms involving the turbulent eddy viscosities ν_t, ν_t^ω and ν_t^H are negligible because $k \ll 1$, so that

$$\boxed{\forall\sigma, \qquad \frac{\mathrm{d}A_H}{\mathrm{d}t} \simeq 0.} \qquad (8.33)$$

$\mathrm{d}A_H/\mathrm{d}t$ is not rigorously zero since the non-local expansion is kept at the lowest order in $k/p \ll 1$ in the infrared range, as done in Lesieur & Schertzer (1978), but is equal to some subdominant terms for the dynamics of A_H, as assessed by Fig. 8.4b. This means that whatever the large scales initial conditions σ are, the PLE hypothesis holds for the helical spectrum

Expression	Physical meaning	Appears in eqs for ...
$15\nu_t = \int_{k_L}^{\infty} \theta_{0pp}(5E(p) + p\frac{\partial E}{\partial p})\mathrm{d}p$	Dissip. of $K(t)$ and $K_H(t)$	$E(k,t)$ and $H(k,t)$
$15\nu_t^H = \int_{k_L}^{\infty} \frac{\theta_{0pp}}{p^2}(p\frac{\partial H}{\partial p} - 9H(p))\mathrm{d}p$	Dissip. of $K_H(t)$	$E(k,t)$
$15\nu_t^\omega = -7\int_{k_L}^{\infty} \theta_{0pp}\frac{H(p)}{p^2}\mathrm{d}p$	Dissip. of enstrophy	$H(k,t)$

Table 8.1: Summary of the different eddy-viscosities ν_t, ν_t^H, and ν_t^ω, that intervene in the non-local expansions $k \ll p \sim q$ of the non-linear transfers S_E^{NL} and S_H^{NL} in HHT.

$H(k,t)$. Regarding $E(k,t)$, for $\sigma \leq 3$, the rhs terms of (8.31) are negligible, meaning that the PLE hypothesis holds true, whereas for $\sigma = 4$, $A(t)$ truly depends on time since the first rhs term is stronger than the two others $-2\nu_t k^2 A$ and $-2\nu_t^H k^3 A_H$, so that

$$\boxed{\begin{aligned} &\frac{\mathrm{d}A}{\mathrm{d}t} \simeq 0, \qquad \forall \sigma \leq 3, && (8.34)\\ &\frac{\mathrm{d}A}{\mathrm{d}t} \simeq \frac{14}{15}\int_{k_L}^{\infty} \theta_{0pp}\frac{E(p)^2}{p^2}\Big(1 - \Big(\frac{H(p)}{pE(p)}\Big)^2\Big)\mathrm{d}p, \qquad \text{for } \sigma = 4. && (8.35)\end{aligned}}$$

The latter result contains the fact that helicity decreases the backscatter of $E(k,t)$ in Batchelor HHT. The different turbulent spectral viscosity introduced previously are summarized in Table 8.1.

8.2.4 Decay laws in helical flows

In this part, the emphasis is put on both the impact of helicity on the kinetic energy decay, and on the decay of the helicity K_H itself. It is obvious that K_H will decay faster than the kinetic energy, because of the large scales initial condition (8.19) $\sigma_H = \sigma + 1$.

Remarks about the decay of helicity and kinetic energy: it has been said in the introduction that helicity is known to slow down transfers. This result comes from André & Lesieur (1977), and was also observed in DNS (Polifke & Shtilman, 1989; Polifke, 1991; Moffatt & Tsinober, 1992). One must be precise to characterize this phenomenon: indeed, this does not concern the theoretical decay exponent α of the kinetic energy $K(t)$, but only the cascade of kinetic energy: with helicity, it takes more time for the non-linear transfers to fill in the small scales of the kinetic spectrum with energy coming from larger ones. This phenomenon, which cannot be observed with (IC1) since all scales already contained energy initially, is illustrated with (IC2) in Fig. 8.5 for Batchelor turbulence (the result is identical for Saffman turbulence). The kinetic energy is constant during the first turn-over times with and without helicity, which corresponds to the filling of the small scales. It is then clear that the filling of small scales is slightly longer in presence of helicity.

EDQNM has been intensively used to determine theoretical decay exponents in different configurations, at high Reynolds numbers and after a large number of turnover times: the decay of kinetic integrated quantities in HIT (Meldi & Sagaut, 2013*a*), the decay of the scalar variance in HIT (Lesieur *et al.*, 1987) and other scalar quantities in Chapter 1, the decay of the kinetic energy in a turbulence initially submitted to mean-velocity gradients (see Chapter 3), and finally the decay of the velocity-scalar correlation in an isotropic turbulence with a mean scalar

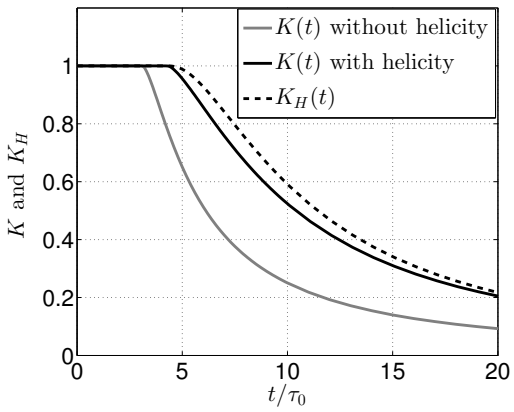

Figure 8.5: Kinetic energy $K(t)$ in HIT (grey line) and in HHT (black line) along with helicity $K_H(t)$ for $\sigma = 4$.

gradient (see Chapter 5). The study of the helical case is therefore a natural extension, and our predictions are compared to those of Levshin & Chkhetiani (2013) later on.

Impact of helicity on the decay of $K(t)$: The effects of helicity on the kinetic energy decay are firstly addressed. Simulations show that the decay exponent α of the kinetic energy, where $K(t) \sim t^{\alpha}$, is not modified by helicity, except in the case of Batchelor turbulence because of the reduction of the non-local inverse transfers analyzed in the previous section. Hence, one would expect the decay of $K(t)$ to be rapider in Batchelor HHT than in Batchelor HIT: indeed, the non-local inverse transfers bring back less energy to the large scales. This is recovered in Fig. 8.6b.

To analytically take into account the breakdown of the PLE hypothesis, the backscatter parameter p usually introduced in HIT is modified. In HIT, one has $p(\sigma = 4) = 0.55$ and $p(\sigma \leq 3) = 0$: in particular, in Batchelor HIT $K(t) \sim t^{-1.38}$. Here, in Batchelor HHT, $K(t) \sim t^{-1.417}$ is obtained, and a least-square fit provides a new backscatter parameter $p_H = 0.14$ for HHT. Consequently, with respect to HIT, only the backscatter parameter changes from p to p_H in HHT for the decay of kinetic energy

$$\boxed{\alpha = -2\frac{\sigma - p_H + 1}{\sigma - p_H + 3}, \qquad \begin{cases} p_H(\sigma = 4) = 0.14 \\ p_H(\sigma \leq 3) = 0 \end{cases}.} \tag{8.36}$$

These decay exponents for the kinetic energy are assessed in Fig 8.6b in Saffman and Batchelor turbulence: only the case $\sigma = 4$ differs from HIT, where here in HHT the decay of $K(t)$ is slightly rapider. The fact that helicity does not influence much the energy cascade once the turbulence is fully developed is in good agreement with conclusions drawn by Polifke (1991); Borue & Orszag (1997).

Decay of helicity: Helicity was shown to impact the kinetic energy decay only in Batchelor turbulence. The emphasis is now put on the decay of K_H itself. The method to predict the decay of helicity is similar to the one of an advected passive scalar, and even more simple. Indeed, as revealed in Fig. 8.4b, the helical spectrum $H(k, t)$ experiences no strong back transfers, so that the PLE hypothesis holds even in Batchelor turbulence. Therefore, there is no need to

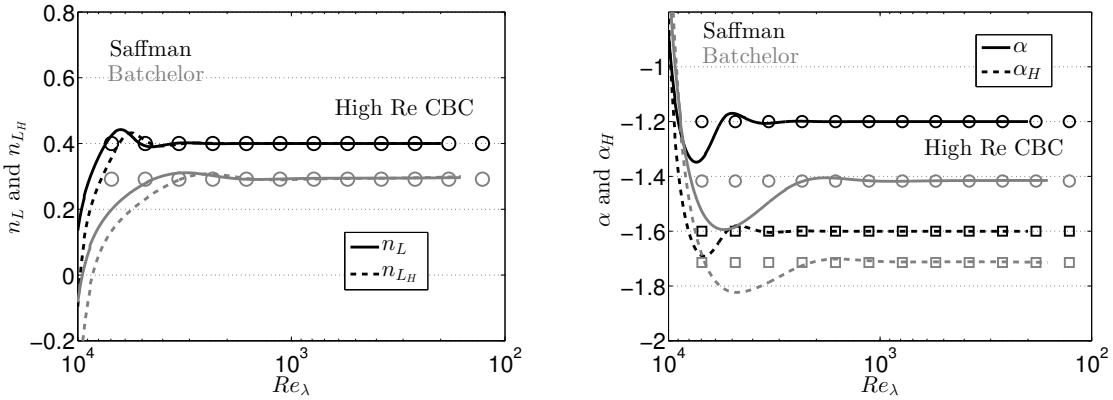

(a) (b)

Figure 8.6: Algebraic laws for the kinetic (−) and helical (−−) fields, in Saffman (black) and Batchelor (grey) turbulence. Symbols refer to the theoretical predictions: (8.36) for α, (8.38) for α_H, and (8.37) for L and L_H. (a) Growth exponents of the kinetic and helical integral scales L and L_H. At a given σ, the kinetic and helical theoretical exponents cannot be distinguished. (b) Decay exponents of the kinetic energy and helicity K and K_H, where ∘ and □ refer to kinetic and helical theoretical exponents.

introduce a helical backscatter parameter. Then, it is reasonable to assume that the kinetic and helical integral scales $L(t)$ and $L_H(t)$ decay similarly, so that their algebraic exponents n_L and n_{L_H} are equal

$$L_H(t) \sim t^{n_{L_H}}, \qquad n_{L_H} = \frac{2}{\sigma+3} \simeq n_L = \frac{2}{\sigma - p_H + 3}. \tag{8.37}$$

This assumption is completely assessed in Fig. 8.6a. Then, using either the continuity of $H(k,t)$ in $k = k_H$ to determine the decay law for ϵ_H, or dimensional analysis with $K_H \sim K/L_H$, or (8.21), one finds

$$\boxed{\alpha_H = -2\frac{\sigma+2}{\sigma+3}.} \tag{8.38}$$

Theoretical values of this expression for α_H, gathered in the last line of Table 8.2, are in excellent agreement with simulations presented in Fig. 8.6b for Saffman and Batchelor turbulence. Interestingly, α_H is equivalent to α_T in HIT with $\sigma_T = \sigma + 1$ without backscatter. The decay exponent of ϵ_H is then simply $\alpha_H - 1$. Moreover, Fig. 8.6b shows that the more σ increases, the more K_H decays rapidly, similarly to $K(t)$.

Comparison with Levshin & Chkhetiani (2013): Our results for the decay of kinetic energy and helicity are now compared with the predictions of Levshin & Chkhetiani (2013) (LC13): this work contains vagueness since the initial conditions are not defined, and it is well-known that they are crucial since large scales are determinant for the decay rate. Indeed, in LC13, for a given decay exponent α of the kinetic energy, two different decay exponents α_H of the helicity are proposed, which makes no sense (Tables 1 and 2 therein). The present theoretical predictions for the decay of helicity are gathered in Table 8.2, along with the two propositions made by LC13. To fill in Table 8.2, a very reasonable assumption is made: as pointed out earlier, initial conditions are not defined in LC13, so that there is no infrared slope σ. Hence, when in LC13 a decay exponent for the kinetic energy is proposed, it is associated

Decay exponent of helicity α_H				
	$\sigma = 1$	$\sigma = 2$	$\sigma = 3$	$\sigma = 4$
LC13 Table 1	/	$-3/2$	$-8/5$	$-5/3$
LC13 Table 2	$-8/5$	$-5/3$	$-12/7$	/
(8.38) assessed by EDQNM	$-3/2$	$-8/5$	$-5/3$	$-12/7$

Table 8.2: Comparison of the different decay exponents α_H obtained by EDQNM with (IC2) and by Levshin & Chkhetiani (2013) (LC13).

here with its corresponding infrared slope according to the CBC theory: $K \sim t^{-1} \to \sigma = 1$, $K \sim t^{-6/5} \to \sigma = 2$, $K \sim t^{-4/3} \to \sigma = 3$, and $K \sim t^{-10/7} \to \sigma = 4$ (backscatter is not taken into account in LC13). The values of α_H from LC13 are the same as the ones coming from (8.38) ($-3/2$, $-8/5$, $-5/3$ and $-12/7$), but there are not associated with the correct infrared slopes. For instance in Saffman turbulence, two laws are proposed in LC13 for helicity: $K_H^{\mathrm{LC13}}(t) \sim t^{-3/2}$ and $K_H^{\mathrm{LC13}}(t) \sim t^{-5/3}$. This is impossible: using our theoretical prediction (8.38), $K_H^{\mathrm{LC13}}(t) \sim t^{-3/2}$ implies that $\sigma = 1$, and $K_H^{\mathrm{LC13}}(t) \sim t^{-5/3}$ implies that $\sigma = 3$, whereas $\sigma = 2$ in Saffman turbulence. In conclusion, it seems that the results of Levshin & Chkhetiani (2013) correspond to infrared slopes of E and H chosen independently, without respecting the realizability condition (8.17) which fixes σ_H once and for all as soon as σ is chosen for E: (8.17) forbids initial conditions such as $\sigma_H = \sigma$ and $\sigma_H = \sigma - 1$. In addition, helical decay exponents gathered in LC13 seems to be erroneously reported.

8.2.5 Robustness of the decay exponents - Altered infrared dynamics

In the previous section, for kinetic energy and helical spectra scaling in $E = Ak^{\sigma}$ and $H = A_H k^{\sigma_H}$ in fully developed turbulence, the evolution equations of $A(t)$ and $A_H(t)$ were derived in (8.31)-(8.32) in the infrared range, assuming the dominance of inverse non-local transfers T_E^- and T_H^- on local ones. For the initial conditions (8.19) where $\sigma_H = \sigma + 1$, it was notably found that the permanence of large eddies holds for Batchelor turbulence ($\sigma = 4$).

Nevertheless, one can wonder if other initial conditions would produce a different infrared dynamics, and this could be relevant to test the robustness of the decay exponents α and α_H derived in the previous sections. One can remark that in (8.31), the term responsible for the backscatter of E is the one where the $k^{()}$ factor vanishes. Thus, it is legitimate to wonder if in (8.32) one could have $4 + \sigma - \sigma_H = 0$ in order to obtain $\mathrm{d}_t A_H \neq 0$, and consequently to create backscatter for the helical spectrum. It is worth noting that $2 + \sigma_H - \sigma = 0$ is impossible in (8.31) because of the realizability condition (8.17).

In order to simplify this study and to point out one original case, the maximal helicity condition $H = kE$ is kept, but the initial kinetic energy spectrum is now changed into a sharply peaked Gaussian one

$$E(k, t = 0) = C_1 \exp\left(-\frac{1}{(C_2)^2}\left[\ln\left(\frac{k}{k_L}\right)\right]^2\right), \tag{8.39}$$

with C_1 so that one has a unit initial kinetic energy, and $C_2 = 0.1$. After a few turnover times, the kinetic energy spectrum scales in $E \sim Ak^4$ in the infrared range (Lesieur & Ossia, 2000). Unlike (8.19), the helical infrared slope σ_H is now different from $\sigma + 1$. As a consequence of

(8.32), it follows that $\sigma_H = \sigma + 4 = 8$, and that the helical spectrum experiences backscatter with

$$\sigma = 4, \qquad \frac{\mathrm{d}A_H}{\mathrm{d}t} = \frac{14}{15} A(t) \int_{k_L}^{\infty} \theta_{0pp} \frac{H(p)}{p^2} \mathrm{d}p. \tag{8.40}$$

The theoretical infrared scaling prediction $H \sim k^8$ is assessed in figure 8.7a, along with the k^4 infrared scaling of $E(k,t)$: in this case, the permanence of large eddies is not verified anymore for $H(k,t)$ for the initial conditions (8.39). Nevertheless, it is shown in figure 8.7b as well that the previous theoretical decay exponents for kinetic energy and helicity are still valid, which implies that the backscatter of $H(k,t)$ is negligible in the decay. This case further illustrates the robustness of the theoretical predictions for the decay exponents.

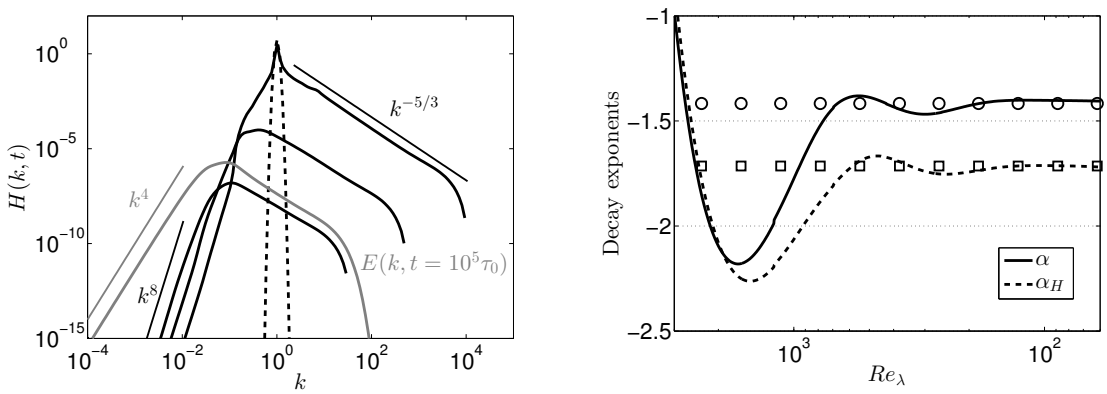

(a) (b)

Figure 8.7: (a) Helical spectrum $H(k,t)$ (black) for the initial condition (8.39) (−−) at various times $t/\tau_0 = 10$, 10^3 and 10^5; the kinetic energy spectrum $E(k,t)$ is displayed as well (grey) at $t/\tau_0 = 10^5$. (b) Decay exponents α (−) and α_H (−−), where ∘ and □ refer to the kinetic and helical theoretical predictions (8.36) and (8.38) respectively.

Simulations not presented here show that for Saffman turbulence ($E \sim k^2$), a k^6 infrared scaling for H could be created, but this is out of the maximal helicity framework: indeed, $H(k, t = 0)$ should be Gaussian with $E(k, t = 0) \sim k^2 \exp(-k^2)$, and the theoretical decay exponents are still verified.

8.3 Structure functions in helical turbulence

In the introduction, the main theoretical results for high Reynolds numbers HHT in physical space were recalled: notably two equivalent laws, found independently, which result from the conservation of helicity in inviscid flows. These two laws are the inertial scaling for the two-point triple velocity correlation (Chkhetiani, 1996)

$$\boxed{S(r) =< u_{\mathrm{L}} u_2 u_3' >= \frac{r^2}{30} \epsilon_H,} \tag{8.41}$$

and the inertial scaling for the third-order velocity-velocity-vorticity structure function (Gomez *et al.*, 2000)

$$\boxed{D^{(uu\omega)}(r) =< \delta u_{\mathrm{L}} \delta u_i \delta \omega_i > -\frac{1}{2} < \delta u_i \delta u_i \delta \omega_{\mathrm{L}} >= -\frac{4}{3} r \epsilon_H.} \tag{8.42}$$

The formalism of structure functions is detailed in Appendix A: the separation vector between two points located in $\boldsymbol{x}$ and $\boldsymbol{x'}$ is written $\boldsymbol{r} = \boldsymbol{x'} - \boldsymbol{x}$, and x'_j and x_j are independent variables. The prime $'$ refers to quantities expressed in $\boldsymbol{x'}$, which should not be misunderstood with the prime of correlations functions, such as $f'(r)$, $h'(r)$, which is the spatial derivative $\partial/\partial r$.

For HIT, the Kármán-Howarth and Yaglom equations for the third-order structure functions $D_{\mathrm{LLL}} =< \delta u_{\mathrm{L}}^3 >$ and $D_{\mathrm{LTT}} =< \delta u_{\mathrm{L}} \delta \theta^2 >$ are recovered analytically in Appendix A, along with the equations that permit to compute D_{LLL} and D_{LTT} from spectral non-linear transfers. These two equations, and their multiple formulations, are very well-known and have been assessed numerous times, mostly in DNS (Yeung *et al.*, 2002; Watanabe & Gotoh, 2004; Yeung *et al.*, 2005; Bos *et al.*, 2012; Gotoh & Watanabe, 2015). A numerical validation using high Reynolds EDQNM simulations is proposed as well in Appendix A. The helical "four-thirds" law (8.42) is similar to the "four-thirds" laws for the kinetic energy and scalar variance in HIT, since they all come from conservation laws (Antonia *et al.*, 1997).

In this section, formula that allow to compute helical structure functions from spectral quantities are derived, similarly to what is usually done for velocity and scalar statistics in HIT (Monin & Yaglom, 1971). This further permits, using the EDQNM model presented in the previous sections, to assess numerically at high Reynolds numbers the two laws (8.41) and (8.42). In continuity of these developments in physical space, the evolution equation of the helical dissipation rate ϵ_H is addressed: ϵ_H itself and its production term are simplified, similarly to what is usually done for the kinetic energy dissipation rate in HIT. These analytical considerations provide further insights on the derivatives of helical correlations and skew-isotropic tensors, and leads to the definition of a helical Taylor scale and a helical derivative skewness.

8.3.1 Inertial scaling for $S(r)$ and $D^{(uu\omega)}(r)$

This part aims at recalling the main steps of the derivation of the laws (8.41) and (8.42), linking $S(r)$ and $D^{(uu\omega)}(r)$, and finally assessing their inertial scalings at large Reynolds numbers.

The law of Chkhetiani (1996): The Reynolds tensor reads

$$R_{ij}(r) =< u_i u'_j >= u^2 \Big[f(r)\delta_{ij} + \frac{r}{2} f'(r) \left(\delta_{ij} - \frac{r_i r_j}{r^2} \right) \Big] + \frac{h(r)}{r} \epsilon_{ijl} r_l, \tag{8.43}$$

where $f =< u_{\mathrm{L}} u'_{\mathrm{L}} > /u^2$ is the second-order longitudinal correlation (see Appendix A for details), with $u^2 = 2K/3$, and $h(r) = R_{23}$. The **mixed velocity-vorticity correlation** is defined as

$$R^H_{ij} =< u_i \omega'_j >= \epsilon_{jln} \frac{\partial R_{in}}{\partial x'_l} = u^2 \epsilon_{ijl} \left(\frac{r_l}{r} f' + \frac{r_l}{2} f'' \right) - 2\delta_{ij} \frac{h}{r} + \left(\frac{h}{r} - h' \right) \left(\delta_{ij} - \frac{r_i r_j}{r^2} \right), \tag{8.44}$$

with $< u_i\omega_i >= 2K_H$. Also,

$$R^H_{ii}(r) = -4\frac{h}{r} - 2h', \qquad h(r) = -\frac{1}{3}rK_H. \tag{8.45}$$

The latter expression shows that $h(0) = 0$. The two-point third-order velocity correlation contains an additional antisymmetric part with respect to HIT, so that

$$< u_i u_j u'_k >= \frac{k - rk'}{2r^3} r_i r_j r_k - \delta_{ij}\frac{k}{2r} r_k + \frac{2k + rk'}{4r}(\delta_{ik} r_j + \delta_{jk} r_i) + S(r)\frac{r_l}{r^2}(\epsilon_{ikl} r_j + \epsilon_{jkl} r_i), \tag{8.46}$$

where $k(r) =< u_{\mathrm{L}} u_{\mathrm{L}} u'_{\mathrm{L}} >$ and $S(r) =< u_{\mathrm{L}} u_2 u'_3 >$: in particular, $< u_2 u_3 u_{\mathrm{L}}' >= 0$ and $< u_{\mathrm{L}} u_3 u'_2 >= -S(r)$, which gives $S(0) = 0$. Thus, from the evolution equation (A.75) of $R_{ij}(r)$, it is possible to compute the evolution equation of the antisymmetric part $(R_{ij} - R_{ji})/2 = h\epsilon_{ijl} r_l/r$ linked to helicity. The spatial derivative ∂_{r_j} erases the part which contains the third-order longitudinal correlation $k(r)$, so that, after some algebra and using $\mathrm{d}_t K_H = -\epsilon_H$, one gets

$$\frac{r}{3}\epsilon_H = \frac{2}{r^3}\frac{\partial}{\partial r}(r^3 S) + 2\nu\left(-\frac{2}{r^2}h(r) + \frac{2}{r}\frac{\partial h}{\partial r} + \frac{\partial^2 h}{\partial r^2}\right). \tag{8.47}$$

Further neglecting the viscous effects in the inertial range and integrating over r, one obtains (8.41).

The law of Gomez *et al.* (2000): The equation for $< \delta\omega_i >$ is derived analogously to the one for δu_i (A.85), starting from (D.27):

$$\partial_t \delta\omega_i + \delta u_j \frac{\partial}{\partial r_j}(\delta\omega_i) = \delta\omega_j \frac{\partial}{\partial r_j}(\delta u_i) + 2\nu \frac{\partial^2}{\partial r_j \partial r_j}(\delta u_i). \tag{8.48}$$

Combining (A.85) and (D.27) yields

$$\frac{\partial < \delta u_i \delta\omega_i >}{\partial t} + \frac{\partial}{\partial r_j}\Big(< \delta u_j \delta u_i \delta\omega_i > - \frac{1}{2} < \delta u_i \delta u_i \delta\omega_j > \Big) = 2\nu \frac{\partial^2 < \delta u_i \delta\omega_i >}{\partial r_j \partial r_j} - 4\,\underbrace{\nu < \frac{\partial \delta u_i}{\partial r_j}\frac{\partial \delta\omega_i}{\partial r_j} >}_{=\epsilon_H}. \tag{8.49}$$

Then, $< \delta u_j \delta u_i \delta\omega_i >= r_j < \delta u_{\mathrm{L}} \delta u_i \delta\omega_i > /r$, and $\partial_{r_j}(D^{(uu\omega)} r_j/r) = \partial_r(r^2 D^{(uu\omega)})/r^2$. Further neglecting the time dependance and the viscous term in the inertial range, integration over r yields (8.42). Interestingly, the Gomez and Chkhetiani laws can be linked. Remarking that $< \delta u_i \delta\omega_i >= 2 < u_i\omega_i > -2 < u_i\omega'_i >$, $\partial_t R^H_{11} = -2\epsilon_H/3$, with $R^H_{11} = -2h/r$, this provides

$$\frac{1}{r^2}\frac{\partial}{\partial r}(r^3 R^H_{11}) =< u_i\omega'_i >= R^H_{ii}, \qquad \frac{1}{r}\frac{\partial}{\partial r}\left(\frac{1}{r^2}\frac{\partial(r^3 R^H_{11})}{\partial r}\right) = \frac{1}{r^4}\frac{\partial}{\partial r}\left(r^4 \frac{\partial R^H_{11}}{\partial r}\right),$$

one gets by identification

$$D^{(uu\omega)} =< \delta u_{\mathrm{L}} \delta u_i \delta\omega_i > - \frac{1}{2} < \delta u_i \delta u_i \delta\omega_{\mathrm{L}} >= -\frac{8}{r^3}\frac{\partial}{\partial r}(r^3 S(r)), \tag{8.50}$$

from which (8.41) immediately follows using (8.42).

Link between spectral and physical space: The equations to compute D_{LLL} and D_{LTT} from spectral quantities are well known, even-though the second-one is much less documented: see for instance Monin & Yaglom (1971) and Appendix A for details. Here, the equations to

obtain both $S(r)$ and $D^{(uu\omega)}$ from S_H^{NL} are presented. First, one needs to derive the evolution equations of $< u_i\omega_i' > /2$: this is done starting from (8.47). Since

$$\frac{< u_i\omega_i' >}{2} = -\frac{1}{r^2}\frac{\partial(r^2 h)}{\partial r}, \qquad \frac{r\epsilon_H}{3} = \frac{\partial h}{\partial t}, \tag{8.51}$$

one obtains

$$\frac{\partial}{\partial t}\left(\frac{< u_i\omega_i' >}{2}\right) = -\frac{2}{r^2}\frac{\partial}{\partial r}\left(\frac{1}{r}\frac{\partial}{\partial r}(r^3 S)\right) - \frac{2\nu}{r^4}\frac{\partial}{\partial r}\left(r^4\frac{\partial^2 h}{\partial r^2}\right). \tag{8.52}$$

This equations needs to be identified with the helical Lin equation (8.15), so that

$$-\frac{2}{r^2}\frac{\partial}{\partial r}\left(\frac{1}{r}\frac{\partial}{\partial r}(r^3 S(r))\right) = \int_0^\infty S_H^{\mathrm{NL}}(k)\frac{\sin(kr)}{kr}\mathrm{d}k.$$

This yields, after some algebra,

$$\boxed{\begin{aligned} S(r) &= \frac{1}{2}\int_0^\infty \frac{S_H^{\mathrm{NL}}}{k^2}\left[\frac{\sin(kr)}{kr} - 3\frac{\sin(kr)}{(kr)^3} + 3\frac{\cos(kr)}{(kr)^2}\right]\mathrm{d}k, && (8.53)\\ D^{(uu\omega)}(r) &= 4\int_0^\infty \frac{S_H^{\mathrm{NL}}}{k}\left[\frac{\sin(kr)}{(kr)^2} - \frac{\cos(kr)}{kr}\right]\mathrm{d}k. && (8.54)\end{aligned}}$$

The formula for $D^{(uu\omega)}$ is very similar to the ones for $< \delta u_{\mathrm{L}}\delta q^2 >$ and D_{LTT}, which is expected since they all refer to conservation laws. The relevance of the two previous formula is illustrated in Fig. 8.8a and 8.8b, where the compensated helical third-order correlations $-D^{(uu\omega)}/(r\epsilon_H)$ and $S/(r^2\epsilon_H)$ are displayed at high Reynolds numbers. The theoretical values 4/3 and 1/30 are almost recovered at $Re_\lambda = 3.10^4$: the slight difference is comparable to the difference observed for the $-4/5$ law in decaying turbulence (Bos *et al.*, 2012; Tchoufag *et al.*, 2012). Interestingly, $D^{(uu\omega)}$ is closer to 4/3 than $< \delta u_{\mathrm{L}}\delta q^2 >$ in HHT. Let's mention that an equivalent scaling for S (the 2/15 law) was already assessed in DNS (Kurien *et al.*, 2004). But so far, to our knowledge, the scaling for $D^{(uu\omega)}$ was not verified numerically, at least for freely decaying turbulence: the present simulations show a very good agreement between EDQNM results and the theoretical expectations. Finally, it is revealed in Fig. 8.8c that $S \sim r^4$ at small scales, which is straightforward using (8.50), unlike $< \delta u_{\mathrm{L}}^3 >$, $< \delta u_{\mathrm{L}}\delta q^2 >$, $< \delta u_{\mathrm{L}}\delta\theta^2 >$ and $D^{(uu\omega)}$ which scale in r^3.

8.3.2 Evolution equation of ϵ_H

In this part, the evolution equation of the helical dissipation rate is addressed. The objective is to simplify its equation, in a manner similar to what is usually done for the kinetic energy dissipation rate ϵ in HIT (Pope, 2000). More precisely, ϵ_H itself and its production term are greatly simplified, and expressed as functions of the derivatives of the fluctuating velocity and vorticity fields. The final expressions (8.58) and (8.67) constitute one of the main new theoretical contributions of the present work, and applications are proposed as well. The calculations being rather lengthy, the intermediate steps are gathered in Appendix D for the sake of clarity. The evolution equation of ϵ_H reads

$$\frac{\partial}{\partial t}\left(\frac{\epsilon_H}{\nu}\right) + D[u,\omega] = -2\nu < \frac{\partial^2 u_i}{\partial x_j \partial x_l}\frac{\partial^2 \omega_i}{\partial x_j \partial x_l} >, \tag{8.55}$$

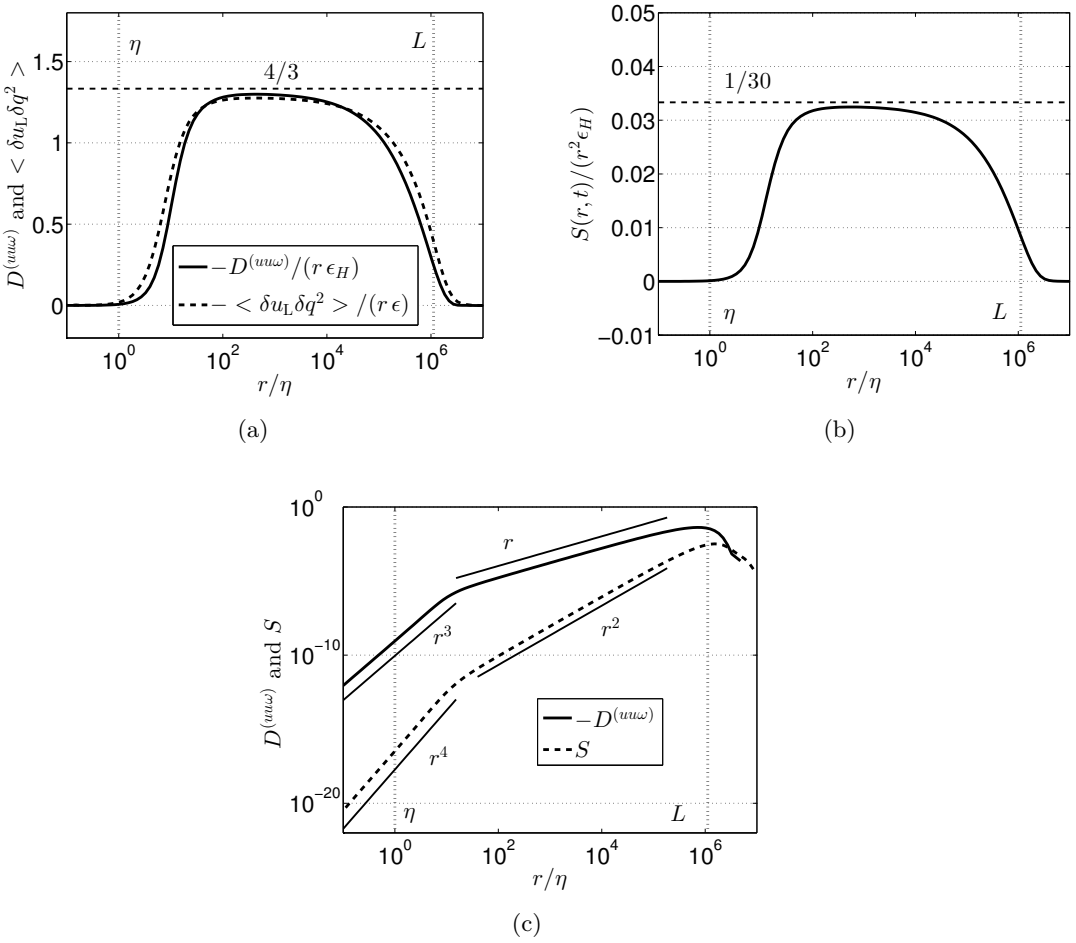

Figure 8.8: Third-order helical correlations $D^{(uu\omega)}$ and S, for $\sigma = 2$ at $Re_\lambda = 3.10^4$, along with the integral and Kolmogorov scales L and η. (a) $-D^{(uu\omega)}/(r\epsilon_H)$ and $- < \delta u_L \delta q^2 > /(r\epsilon)$. (b) $S/(r^2\epsilon_H)$. (c) The different scalings of $D^{(uu\omega)}$ and S.

$$D[u,\omega] =< \frac{\partial u_i}{\partial x_j}\frac{\partial u_l}{\partial x_j}\frac{\partial \omega_i}{\partial x_l} > + < \frac{\partial u_i}{\partial x_l}\frac{\partial u_l}{\partial x_j}\frac{\partial \omega_i}{\partial x_j} > - < \frac{\partial u_i}{\partial x_j}\frac{\partial u_i}{\partial x_l}\frac{\partial \omega_l}{\partial x_j} >, \tag{8.56}$$

where the production term $D[u,\omega]$ contains contributions from spatial derivatives of skew-isotropic tensors such as $< u_i u_j \omega_l' >$ and $< \omega_i u_j u_l' >$. In what follows, both ϵ_H and $D[u,\omega]$ are simplified. This procedure consists into two steps: first, expressing ϵ_H and $D[u,\omega]$ as functions of the derivatives of $h(r)$ and $S(r)$ respectively, and then expressing these derivatives as functions of particular components of the fluctuating velocity and vorticity fields. Obviously, this is much more lengthy for $D[u,\omega]$ since it is a third-order moment, composed of three different terms.

Derivatives of $R^H_{ij}(r)$: The first step to simplify ϵ_H consists into expressing it as a function of the derivatives of $h(r)$. To do so, one first needs to know the derivatives of R^H_{ij}, analogously to what George & Hussein (1991) did for ϵ in axisymmetric turbulence. One has

$$\frac{\partial^2 R^H_{ij}}{\partial r_p \partial r_q} = - < \frac{\partial u_i}{\partial x_p}\frac{\partial \omega_j'}{\partial x_q'} >, \qquad \frac{\epsilon_H}{\nu} = - \left(\frac{\partial^2 R^H_{ii}}{\partial r_j \partial r_j}\right)_{r=0} =< \frac{\partial u_i}{\partial x_j}\frac{\partial \omega_i}{\partial x_j} > . \tag{8.57}$$

After some algebra gathered in Appendix D, one gets the general expression of $\partial^2_{pq} R^H_{ij}$, from

which one can obtain some relations between the derivatives of $h(r)$. Then, using a Taylor expansion of $h(r)$ for $r \to 0$ (with $h(0) = 0$) yields the important theoretical result

$$\boxed{\epsilon_H = 10\nu h'''(0) = 15\nu < \frac{\partial u_1}{\partial x_1}\frac{\partial \omega_1}{\partial x_1} > .} \tag{8.58}$$

This expression permits to determine the helicity dissipation rate with one term instead of nine, and is equivalent to $\epsilon = 15\nu < (\partial_1 u_1)^2 >$ for the kinetic energy dissipation rate in HIT.

The natural extension of the previous calculations for ϵ_H is the definition of a helical Taylor scale λ_H. Its expression is found analogously to what is usually done for the longitudinal Taylor scale λ (Pope, 2000), *i.e.* considering the osculating curve $P_H(r)$ of $h(r)$ in $r = 0$, which reads

$$P_H(r) = h(0) + rh'(0) + \frac{r^2}{2}h''(0) + \frac{r^3}{6}h'''(0) = -r\frac{K_H}{3} + r^3\frac{\epsilon_H}{60\nu}, \tag{8.59}$$

and λ_H is further defined by $P_H(\lambda_H) = 0$ and $\lambda_H \neq 0$, which yields

$$\boxed{\lambda_H = \sqrt{\frac{20\nu K_H}{\epsilon_H}}.} \tag{8.60}$$

It is worth noting that this new expression is completely equivalent to the classical one for the velocity $\lambda = \sqrt{20\nu K/\epsilon}$. The relevance of this formula is illustrated in Fig. 8.9. Both λ and λ_H are displayed, at large and moderate Reynolds numbers for Saffman turbulence. Both scales indicate the beginning of a region where viscous dissipation balances non-linear transfers. At high Reynolds numbers, λ and λ_H cannot be distinguished, whereas λ_H is a bit smaller at moderate Reynolds numbers. The wavenumber k_η^H, defined in (8.22) and proposed by Ditlevsen & Giuliani (2001), is presented as well: it seems to have a similar physical meaning as λ_H, at least at large Reynolds numbers, and some explanations are provided in Appendix D. Moreover, Fig. 8.9 illustrates the viscous production of helicity, already observed in Fig. 8.1b where the helical spectrum was negative around k_η: indeed, $-2\nu k^3 H$ is positive near k_η here.

A secondary application of these calculations is to express analytically the impact of helicity on the second-order longitudinal correlation $f(r \to 0)$. Indeed, unlike HIT where all odd derivatives of $f(r)$ for $r = 0$ are zero, one can show that $f'''(0)$ is a priori different from zero in HHT (one has always $f'(0) = 0$ because of homogeneity). Expressing $\partial_{11}^2 R_{23}^H$ and $\partial_{33}^2 R_{23}^H$ thanks to (D.33) yields

$$f'''(0) = -\frac{1}{2} < \frac{\partial u_2}{\partial x_1}\frac{\partial \omega_3}{\partial x_1} >= - < \frac{\partial u_2}{\partial x_3}\frac{\partial \omega_3}{\partial x_3} >, \tag{8.61}$$

so that the Taylor expansion of $f(r)$ reads

$$f(r) = 1 - \frac{r^2}{2}\frac{\epsilon}{15\nu u^2} \underbrace{+\frac{r^3}{6}f'''(0)}_{\text{Additional HHT term}} + \frac{r^4}{24}\frac{2}{35u^2}\int_0^\infty k^4 E(k)\mathrm{d}k. \tag{8.62}$$

Determination of the production term $D[u, \omega]$: The procedure used to determine ϵ_H is now applied to the production term $D[u, \omega]$: since this term is complex and involves derivatives of two different tensors $< u_i u_j \omega_l' >$ and $< \omega_i u_j u_l' >$, the determination is divided into two steps. First, $D[u, \omega]$ is expressed as a function of the derivatives of $S(r)$, and it will be shown that only

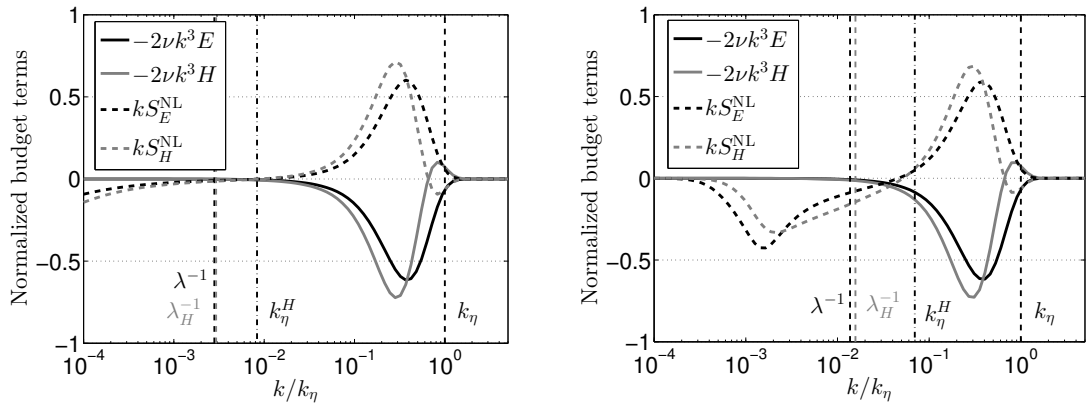

(a) (b)

Figure 8.9: Taylor scales for kinetic energy and helicity λ and λ_H, along with the corresponding spectral viscous fluxes $-2\nu k^3 E$ and $-2\nu k^3 H$ and the non-linear transfers $kS_E^{\rm NL}$ and $kS_H^{\rm NL}$ for $\sigma = 2$. The wavenumbers k_η^H (8.22) and k_η are displayed as well. The black curves are for the kinetic field, and the grey ones for the helical one. (a) $Re_\lambda = 10^4$. (b) $Re_\lambda = 400$.

$S^{(iv)}(0)$ remains. Then, $S^{(iv)}(0)$ is expressed as a function of the derivatives of the fluctuating velocity and vorticity fields.

As pointed out in Gomez *et al.* (2000), the tensor $< \omega_i u_j u'_l >$ is much more complicated to handle than $< u_i u_j \omega'_l >$, which can be linked easily to $< u_i u_j u'_l >$ given in (8.46)

$$\phi_{ijl}^{(uu\omega)} =< u_i u_j \omega'_l >= \epsilon_{lpq} \frac{\partial < u_i u_j u'_q >}{\partial r_p}, \qquad \phi_{ijl}^{(\omega uu)} =< \omega_i u_j u'_l > . \tag{8.63}$$

Calculations detailed in Appendix D first permit to link derivatives of $\phi_{ijl}^{(uu\omega)}$ and $\phi_{ijl}^{(\omega uu)}$ to $D[u,\omega]$ according to

$$D[u,\omega] = \left(\frac{\partial^3}{\partial r_j \partial r_j \partial r_l} \left[\phi_{ili}^{(uu\omega)} + \phi_{ili}^{(\omega uu)} - \phi_{lii}^{(\omega uu)} \right] \right)_{r=0}, \tag{8.64}$$

where the derivatives of $\phi_{ijl}^{(uu\omega)}$ and $\phi_{ijl}^{(\omega uu)}$ contain derivatives of $S(r)$. Taylor expansions of $S(r)$ for $r \to 0$ further give

$$D[u,\omega] =< \frac{\partial u_i}{\partial x_j} \frac{\partial u_l}{\partial x_j} \frac{\partial \omega_i}{\partial x_l} > + < \frac{\partial u_i}{\partial x_l} \frac{\partial u_l}{\partial x_j} \frac{\partial \omega_i}{\partial x_j} > - < \frac{\partial u_i}{\partial x_j} \frac{\partial u_i}{\partial x_l} \frac{\partial \omega_l}{\partial x_j} >= -35 S^{(iv)}(0). \tag{8.65}$$

Now that $D[u,\omega]$ has been linked to $S^{(iv)}(0)$, the final step is to express the fourth derivative of $S(r)$ as derivatives of the fluctuating velocity and vorticity fields, so that $D[u,\omega]$ can be evaluated in DNS for instance. For this purpose, the explicit sixth-order tensor $\partial^3_{npq} \phi_{ijl}^{(uu\omega)}$ is needed, and given in Appendix D. From this lengthy expression, one notably gets

$$\left(\frac{\partial^3 \phi_{111}^{(uu\omega)}}{\partial r_1^3} \right)_{r=0} = -S^{(iv)}(0), \tag{8.66}$$

from which one finally obtains the second important result of this section

$$\boxed{D[u,\omega] = -35S^{(iv)}(0) = 35 < \frac{\partial^2 u_1^2}{\partial x_1^2}\frac{\partial \omega_1}{\partial x_1} >,} \tag{8.67}$$

which permits notably to compute $D[u,\omega]$ with only one term, instead of eighty-one. Further proceeding as in Kerr (1985), *i.e.* identifying (8.55) with the spectral evolution equation of ϵ_H

$$\frac{\partial \epsilon_H}{\partial t} = 2\nu \int_0^\infty k^2 S_H^{\mathrm{NL}}(k,t)\mathrm{d}k - 4\nu^2 \int_0^\infty k^4 H(k,t)\mathrm{d}k, \tag{8.68}$$

provides

$$S^{(iv)}(0) = \frac{2}{35}\int_0^\infty k^2 S_H^{\mathrm{NL}}(k,t)\mathrm{d}k. \tag{8.69}$$

Hence, one can define, analogously to the mixed-derivative skewness of a passive scalar in HIT, a **helical derivative skewness** as

$$S_{uu\omega} = < \frac{\partial^2 u_1^2}{\partial x_1^2}\frac{\partial \omega_1}{\partial x_1} > \Big/ \left(< \frac{\partial u_1}{\partial x_1}\frac{\partial \omega_1}{\partial x_1} > \sqrt{< \left(\frac{\partial u_1}{\partial x_1}\right)^2 >} \right) \tag{8.70}$$

$$= -\frac{3\sqrt{30}}{14}\frac{\int_0^\infty k^2 S_H^{\mathrm{NL}}\mathrm{d}k}{\sqrt{\int_0^\infty k^2 E dk}\int_0^\infty k^2 H \mathrm{d}k}. \tag{8.71}$$

Interestingly, the numerical factor $3\sqrt{30}/14$ is identical to the one of the velocity derivative skewness in HIT.

The helical derivative skewness $S_{uu\omega}$ is displayed in Fig. 8.10 as a function of the Reynolds number Re_λ. Only Saffman turbulence is presented, because the curve for Batchelor turbulence is identical at high Reynolds numbers, similarly to the velocity and mixed derivative skewnesses in HIT (see Chapter 1 and Appendix A). The initial oscillations at large Re_λ correspond to the first turnover times of the simulation, when the turbulence is not fully developed yet. As for the velocity and mixed derivative skewnesses, $S_{uu\omega}$ is negative and reaches an asymptotic value at large Reynolds numbers $S_{uu\omega}^\infty = -0.141$. This value $S_{uu\omega}^\infty$ is lower in magnitude than asymptotic values for the velocity and mixed derivative skewnesses in HIT which are around $\simeq -0.5$. The knowledge of the helical derivative skewness is of importance, for two reasons: it is of theoretical interest since it permits to have a strong analogy between the evolution equations of ϵ in HIT and ϵ_H in HHT. On a more practical point of view, the previous developments which led to $S_{uu\omega}$ show that there exists, in homogeneous helical turbulence, a quantity which is constant at large Reynolds numbers: such a result could be used to improve RANS models for helical flows, where the production term would be linked to $S_{uu\omega}$.

8.4 Effect of helicity on the scalar flux

In this section, the transport of a passive scalar field θ is addressed. However, since there are no explicit contributions of helicity in its evolution equation, a vertical mean scalar gradient

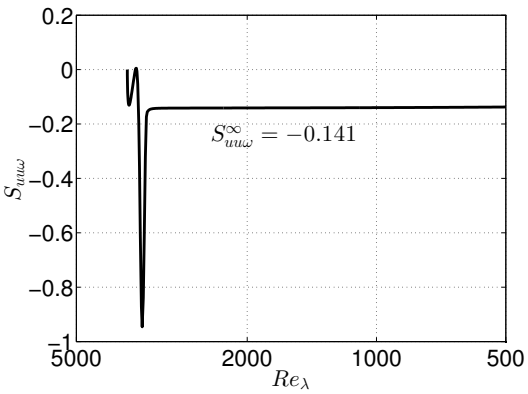

Figure 8.10: Helical derivative skewness $S_{uu\omega}(t)$ in HHT for $\sigma = 2$.

$\boldsymbol{\lambda} = (0, 0, -\Lambda)$ is added. In purely isotropic turbulence with a mean scalar gradient, the well-known cospectrum $\mathcal{F}$ is created (see Chapter 5). When both helicity and a mean scalar gradient are combined, a second spectrum is created, called the quadrature spectrum $Q(k,t)$, linked to the imaginary antisymmetric part of the scalar flux $F_i(\boldsymbol{k})$. This quadrature spectrum was reported in Mydlarski & Warhaft (1998), and shown to be zero in non-helical turbulence with a mean scalar gradient in O'Gorman & Pullin (2005). Consequently, we choose here the framework of Helical Homogeneous Turbulence with a mean Scalar Sradient (HHTSG) in order to create this quadrature spectrum and analyze its properties. In the two next parts, it is first proposed to derive the evolution equation of $Q(k,t)$ and its non-linear transfer terms within the EDQNM framework, and secondly to investigate its inertial scaling. Analogies with the effects of helicity on the kinetic energy spectrum are pointed out, and the decay exponent of helicity along with the helical Taylor scale given previously are used. A unit Prandtl number is considered, and simulations not presented here have revealed that the scalar variance spectrum still scales in $k^{-5/3}$ in the inertial range despite the presence of helicity.

8.4.1 Modelling of the quadrature spectrum

When the decomposition of the scalar flux (4.28) was introduced in Chapter 4, it was mentioned that in presence of helicity there could be an additional antisymmetric contribution. Thus, without mirror symmetry, the new decomposition of the scalar flux reads

$$F_i(\boldsymbol{k},t) = \frac{3}{2}\mathcal{E}^F_j(k,t)P_{ij}(\boldsymbol{k}) + \frac{3}{2}\mathrm{i}\varepsilon_{ijn}\alpha_n\frac{\mathcal{E}^Q_j(k,t)}{k}, \tag{8.72}$$

which is quite similar to the decomposition (8.2) of $\hat{R}_{ij}$. Both $\mathcal{E}^Q_j$ and $\mathcal{E}^F_j$ are real vectors. The imaginary antisymmetric part is linked to the quadrature spectrum $Q(k,t)$, which is zero in HITSG and arises only with the additional presence of helicity, and is defined as

$$Q(k,t) = 4\pi k^2\mathcal{E}^Q_3(k,t) = \int_{S_k} \mathrm{i}\epsilon_{3jl}k_l F_j(\boldsymbol{k},t)\mathrm{d}^2\boldsymbol{k}. \tag{8.73}$$

It appears that the quadrature spectrum was never analytically investigated, and is only reported to be zero in HIT and HITSG by Mydlarski (2003); O'Gorman & Pullin (2005). The mechanism

which creates an additional contribution to the scalar flux, parallel to the mean gradient in the presence of helicity, is called **skew-diffusion** by Moffatt & Tsinober (1992). It is worth noting that from the decomposition (8.72) and (8.73), imaginary components of the scalar flux, perpendicular to the mean scalar gradient, are non-zero. Nevertheless, these components vanish after spherical averaging. Hence, in HHTSG, the evolution equation of the cospectrum given in (4.38) is modified into

$$\boxed{\left(\frac{\partial}{\partial t}+(a+\nu)k^2\right)\mathcal{F}(k,t)=\frac{2}{3}\Lambda E(k,t)+\underbrace{S_3^{\mathrm{F,NL}}(k,t)+S_3^{\mathrm{F,NL(hel)}}(k,t)}_{S_F^{\mathrm{NL}}(k,t)},} \tag{8.74}$$

where $S_i^{\mathrm{F,NL(hel)}}$ is the additional contribution arising from the presence of helicity, the **non-linear spherically-averaged helical scalar flux transfer**

$$\begin{aligned}S_i^{\mathrm{F,NL(hel)}}(k,t)&=4\pi^2\int_{\Delta_k}\theta^F_{kpq}k^2(x+yz)\mathcal{H}''\Big(2pz\mathcal{E}_i^Q-k\mathcal{E}_i^{Q'}\Big)\mathrm{d}p\mathrm{d}q\\&+4\pi^2\int_{\Delta_k}\theta^F_{pkq}k(x+yz)\Big[\mathcal{H}\Big(p^2\mathcal{E}_i^{Q''}-q(q-2ky)\mathcal{E}_i^{Q'}\Big)-k^2\mathcal{H}''\mathcal{E}_i^{Q'}\Big]\mathrm{d}p\mathrm{d}q.\end{aligned} \tag{8.75}$$

The remarkable feature about $S_i^{\mathrm{F,NL(hel)}}$ is that, unlike $S_i^{\mathrm{F,NL}}$ which contains a RTI part, it is a conservative transfer, with zero integral over the whole wavenumber space. Then, the evolution equation of the quadrature spectrum reads

$$\boxed{\left(\frac{\partial}{\partial t}+(a+\nu)k^2\right)Q(k,t)=\frac{2}{3}\Lambda H(k,t)+S_Q^{\mathrm{NL}}(k,t),} \tag{8.76}$$

where the production term is linked to helicity, and $S_Q^{\mathrm{NL}}=S_3^{\mathrm{Q,NL}}$ is the **non-linear spherically-averaged quadrature transfer**

$$\begin{aligned}S_i^{\mathrm{Q,NL}}(k,t)&=4\pi^2\int_{\Delta_k}\theta^F_{kpq}k^3pq\Big[\mathcal{E}_0''\Big(\mathcal{E}_i^{Q'}(xyz+2z^2-y^2)-2z(xy+z)\mathcal{E}_i^Q\Big)\\&+z(xy+z)\mathcal{H}''(2\mathcal{E}_i^F-\mathcal{E}_i^{F'})\Big]\mathrm{d}p\mathrm{d}q\\&+4\pi^2\int_{\Delta_k}\theta^F_{pkq}k^2q\Big[kp\mathcal{E}_0''\Big(\mathcal{E}_i^{Q'}(xyz+2z^2-y^2)-2(1-y^2)\mathcal{E}_i^Q\Big)-kpz(xy+z)\mathcal{H}''\mathcal{E}_i^{F'}\\&+k\mathcal{E}_0\Big(\mathcal{E}_i^{Q''}p(1-y^2)-\mathcal{E}_i^{Q'}q(x-yz-2xy^2)\Big)\\&-pq\mathcal{H}\Big(\mathcal{E}_i^{F''}y(1-y^2)+\mathcal{E}_i^{F'}(xz+y^3-y(1-x^2))\Big)\Big]\mathrm{d}p\mathrm{d}q.\end{aligned} \tag{8.77}$$

Similarly to $S_3^{\mathrm{F,NL}}$, S_Q^{NL} is not a conservative transfer. Some details are provided in Appendix E for $S_i^{\mathrm{F,NL(hel)}}$ and $S_i^{\mathrm{Q,NL}}$.

8.4.2 Decay of $<\omega_3\theta>$ and inertial scaling of $Q(k,t)$

For these numerical simulations, one has initially $Q=\mathcal{F}=E_T=0$, E is given by (8.19), and $H=kE$. First, let's consider the evolution equation in physical space of the one-point mixed

vorticity-scalar correlation

$$K_Q(t) =< \omega_3\theta >= \int_0^\infty Q(k,t)\mathrm{d}k, \qquad \epsilon_Q(t) = (\nu + a) < \frac{\partial\omega_3}{\partial x_l}\frac{\partial\theta}{\partial x_l} >= 2(\nu + a)\int_0^\infty k^2 Q(k,t)\mathrm{d}k, \tag{8.78}$$

which reads

$$\frac{\partial < \omega_3\theta >}{\partial t} = \frac{2}{3}\Lambda K_H + < \theta\omega_j\frac{\partial u_3}{\partial x_j} > -(\nu + a) < \frac{\partial\theta}{\partial x_j}\frac{\partial\omega_3}{\partial x_j} >, \tag{8.79}$$

where $< \theta\omega_l\partial_l u_3 >$ is the destruction term of $< \omega_3\theta >$, and is given by the integral of S_Q^{NL} over the whole wavenumber space. From this evolution equation, it directly follows that the decay exponent of K_Q is $\alpha_Q = \alpha_H + 1$, because the production term linked to helicity is the one responsible for the creation of the quadrature spectrum. This yields

$$K_Q(t) \sim t^{\alpha_Q}, \qquad \alpha_Q = -\frac{\sigma + 1}{\sigma + 3}, \tag{8.80}$$

which is assessed, for both Saffman and Batchelor turbulence, in Fig. 8.11a. The decay exponent $\alpha_{\mathcal{F}}$, derived in (5.13) for HITSG is still valid, using the helical backscatter parameter $p_H = 0.14$. For a given infrared slope σ, the decay of $< \omega_3\theta >$ is faster than $< u_3\theta >$, similarly to the decay of K_H being faster than K.

Regarding the non-linear transfers: the impact of the quadrature spectrum on the cospectrum can be observed through the conservative non-linear transfer $S_3^{\mathrm{F,NL(hel)}}$. This transfer is linked to an inverse cascade of $< u_3\theta >$, localized at large scales, between the integral and the helical Taylor scales. This can be qualitatively compared to the impact of helicity on the kinetic energy spectrum dynamics through $S^{\mathrm{NL(hel)}}$ in Fig. 8.3b. One could conclude that helicity only slightly reduces the non-linear transfers of the cospectrum at large scales. Then, the quadrature non-linear transfer S_Q^{NL} itself is similar to the cospectrum one $S_3^{\mathrm{F,NL}}$, but less intense.

Finally, in Fig. 8.11c, the quadrature spectrum is presented. In the infrared range, it scales in $Q \sim k^3$ for Saffman turbulence, because the helical spectrum itself evolves in $H \sim k^3$: indeed, helicity, through the mean scalar gradient, is the production term of the quadrature spectrum. In the inertial range, $Q(k,t)$ is first positive for scales larger than the helical Taylor scale λ_H, and scales in $k^{-7/3}$ similarly to $\mathcal{F}$. Whereas for scales smaller than λ_H, the spectral slope is close to $k^{-5/3}$ and the quadrature spectrum is negative: it is recalled that around k_η, $H(k,t)$ is also negative.

One can propose a theoretical inertial scaling for the positive region of the quadrature spectrum: assuming in (8.76) that $\partial_t Q \sim \Lambda H$, with the characteristic inertial time $(k^2\epsilon)^{-1/3}$, this gives

$$\boxed{Q(k,t) \sim \Lambda\,\epsilon_H\,\epsilon^{-2/3}\,k^{-7/3}, \qquad k_L < k < \lambda_H^{-1}.} \tag{8.81}$$

For the negative region of $Q(k,t)$, the quadrature spectrum should only depend on ϵ_H, and not anymore on ϵ, since this is the negative small scales of $H(k,t)$ which are responsible for this **inertial-helical range** of $Q(k,t)$. Thus, one gets

$$\boxed{Q(k,t) \sim \Lambda\,\epsilon_H^{1/3}\,k^{-5/3}, \qquad \lambda_H^{-1} < k < k_\eta.} \tag{8.82}$$

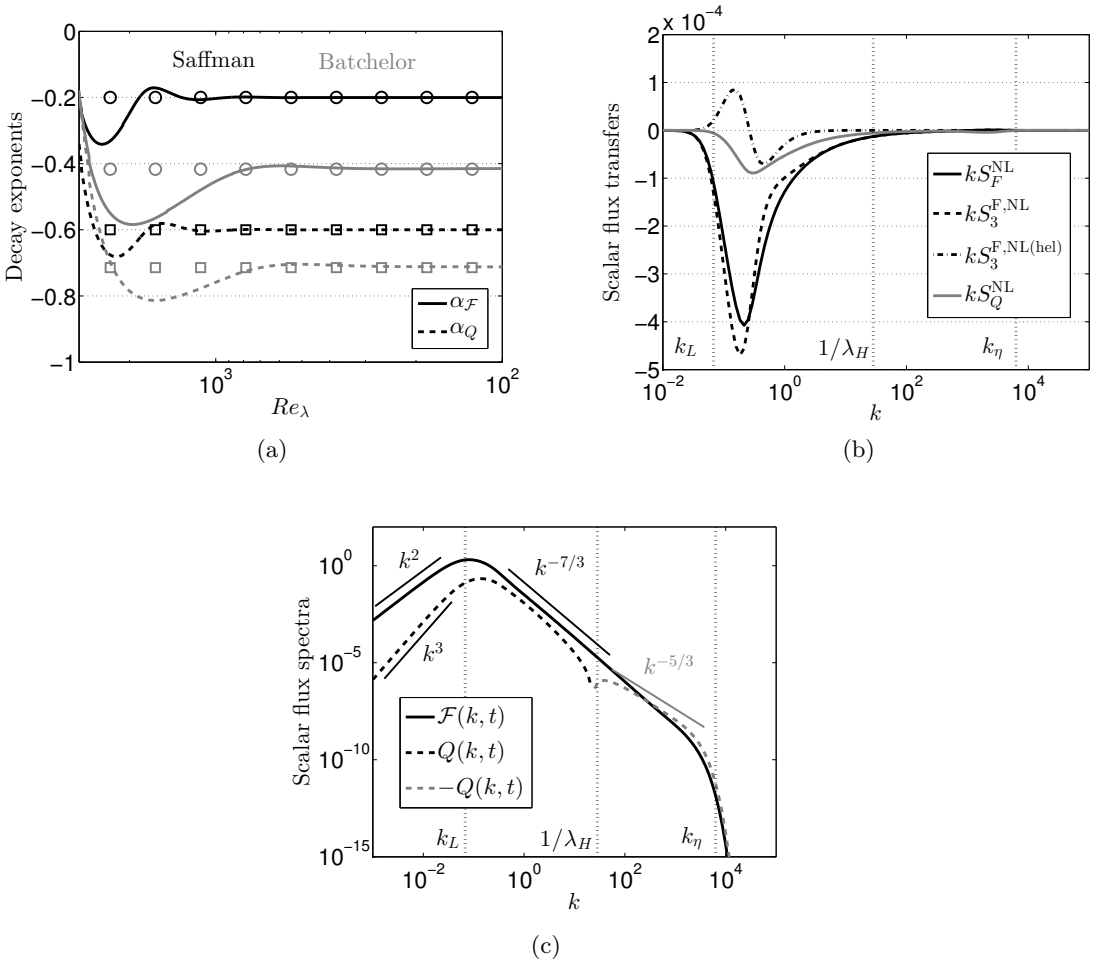

Figure 8.11: (a) Decay exponents α_Q and $\alpha_{\mathcal{F}}$ of $< \omega_3\theta >$ $(--)$ and $< u_3\theta >$ $(-)$ respectively, for $\sigma = 2$ (black) and $\sigma = 4$ (grey); theoretical predictions, $\square$ for α_Q (8.80), and $\circ$ for $\alpha_{\mathcal{F}}$ (5.13). (b) Cospectrum and quadrature non-linear transfers, for $\sigma = 2$ at $Re_\lambda = 5.10^3$, along with the integral, helical Taylor and Kolmogorov wavenumbers k_L, $1/\lambda_H$ and k_η. (c) Cospectrum $\mathcal{F}(k,t)$ and quadrature spectrum $Q(k,t)$; $-Q(k,t)$ is displayed in grey. Same configuration as (b).

This change of slope, from $k^{-7/3}$ for $k\lambda_H < 1$, to $k^{-5/3}$ for $k\lambda_H > 1$, observed in figure 8.11c, and justified with dimensional and physical arguments, can also be interpreted in terms of a change in characteristic time scales, from $\tau = (k^2\epsilon)^{-1/3}$ to $\tau_H = (k\epsilon_H)^{-1/3}$. The latter time scale was notably proposed by Kurien *et al.* (2004) for an alternative scaling of $H(k,t)$ at small scales. This characteristic time scale τ_H is relevant for the inertial-helical scaling of Q when it is negative: indeed, for $k\lambda_H > 1$, the equation (8.76) of Q can be written $\partial_t Q \sim S_Q^{\mathrm{NL}}$. Using the characteristic time scale τ_H, the classical inertial scaling (8.20) of H and $\mathcal{F}$, one gets for the non-linear quadrature transfer $S_Q^{\mathrm{NL}} \sim \Lambda k^{-4/3}\epsilon_H^{2/3}$, so that (8.82) is recovered.

8.5 Conclusion on homogeneous skew-isotropic turbulence

The classical framework of decaying homogeneous helical turbulence (HHT) where mirror symmetry is broken at large Reynolds numbers was addressed using the anisotropic EDQNM modelling.

Some existing results were recovered here for decaying skew-isotropic turbulence, in order to validate the use of EDQNM for HHT, which could be summarized in three features. First, when helicity is initially present at large scales, helicity cascades towards small scales along with the kinetic energy, creating a $k^{-5/3}$ inertial range that extends up to the Kolmogorov wavenumber k_η. The $k^{-5/3}$ scaling of the helical spectrum $H(k,t)$ is similar to the one of an advected passive scalar, also obtained with dimensional analysis by assuming that the inertial characteristic time $\tau(k) = (k^2\epsilon)^{-1/3}$ is identical for both the kinetic and helical fields. Secondly, in the early stage of the decay, helicity slows down the filling of the kinetic energy spectrum at small scales. Consequently, there is an initial reduction of the kinetic energy transfers: this is a transitory effect, since once the turbulence is fully developed, the effects of helicity on the kinetic energy decay are rather weak. Finally, two-point third-order helical correlations were investigated: notably, the "four-thirds" law for helical structure functions, and the 1/30 law for the helical correlation $S(r)$, were assessed with EDQNM at very high Reynolds numbers in decaying turbulence. It is worth noting that the two formula linking helical correlations in physical space and spectral non-linear helical transfers are new results of this work.

Then, EDQNM simulations were used to assess some new theoretical predictions of fundamental interest for helical turbulence. First, the infrared dynamics of the kinetic energy and helical spectra was investigated theoretically using non-local expansions in the non-linear transfers. It clearly appears that in Batchelor HHT, helicity reduces the back transfers of kinetic energy with respect to HIT: consequently, inverse non-local transfers are weakened and bring back less energy to large scales. Furthermore, the permanence of large eddies is shown to be verified for $H(k,t)$, even in Batchelor turbulence, with classical initial conditions such that the kinetic and helical infrared slopes are $\sigma_H = \sigma + 1$. These two features are assessed numerically with EDQNM. An original configuration, with different initial conditions, also exhibited a k^8 infrared scaling for $H(k,t)$, along with some helical backscatter.

Secondly, as a direct application of the previous infrared dynamics analysis, the impact of helicity on the long-time kinetic energy decay was shown to be quite subtle: indeed, the decay of $K(t)$ is not modified with regard to HIT, except in the case of Batchelor turbulence where it is slightly accelerated, because of the less-intense inverse transfers. In addition, in agreement with dimensional analysis, theoretical decay exponents for helicity were derived, and assessed numerically at large Reynolds numbers: in particular, it is found that helicity decays faster than the kinetic energy.

Thirdly, the evolution equation of the helicity dissipation rate ϵ_H was studied, with a particular attention on the derivatives of second and third order skew-isotropic tensors such as $< u_i\omega'_j >$, $< u_iu_j\omega'_l >$ and $< \omega_iu_ju'_l >$. As an important result of these analytical developments, ϵ_H itself is expressed as a function of $h'''(0)$ only, where $h = R_{23}(r)$, and its production term $D[u,\omega]$ as a function of $S^{(iv)}(0)$ only, where $S =< u_Lu_2u'_3 >$. It follows that ϵ_H and $D[u,\omega]$ can be expressed with only one term, instead of nine and eighty-one respectively.

Fourthly, as a direct application of these fundamental results, a helical Taylor scale was defined $\lambda_H = \sqrt{20\nu K_H/\epsilon_H}$, whose expression is analogous to the longitudinal Taylor scale λ for kinetic energy. Such a scale is new for the helical field, and its relevance was illustrated numerically: λ_H is the scale from which viscous dissipation of helicity becomes dynamically important, and at large Reynolds numbers, it is very close to λ. Moreover, a helical derivative skewness was defined and is negative and constant at large Reynolds numbers, similarly to the velocity derivative and mixed-derivative skewnesses in HIT.

Finally, it was shown that combining a mean scalar gradient and helicity produces the quadrature spectrum $Q(k,t)$, linked to the imaginary antisymmetric part of the scalar flux. As a consequence, the large scales non-linear transfers of the cospectrum are slightly reduced. The main result is that $Q(k,t)$ has two different scalings in the inertial range: for $k\lambda_H < 1$, $Q \sim k^{-7/3}$, and then for $k\lambda_H > 1$, $Q \sim k^{-5/3}$: this change in the spectral slope can be interpreted as the characteristic time evolving from $(k^2\epsilon)^{-1/3}$ to $(k\epsilon_H)^{-1/3}$ at smaller scales.

Chapter 9

General Conclusions and Perspectives

"Do. Or do not. There is no try."

– Master Yoda, *Star Wars V*

The main objective of this thesis was to understand the fundamental turbulent mechanisms occurring in natural flows at large Reynolds numbers, such as atmospheric and oceanic ones. For this purpose, we established a methodology which could be summarized as follows: we worked in the framework of homogeneous turbulence, with the spectral formalism, and aimed at modelling the various processes at stake in turbulent anisotropic flows. The resulting model, called **anisotropic EDQNM modelling** throughout the manuscript, was assessed by multiple comparisons against DNS and experiments. Then, theoretical predictions were derived, based on both physical arguments and analytical calculations, which were successfully verified by the model.

The starting point of this complex task was the pioneering study of Cambon *et al.* (1981), further developed and improved in Mons *et al.* (2016). The general concept of the spectral modelling relies on two steps: (i) a classical EDQNM procedure to close the non-linear terms in the evolution equations of the two-point second-order moments; and (ii) a modelling of anisotropy through truncated expansions in spherical harmonics of the spectral second-order moments. The final model is not an end in itself, but rather a general and robust method to address complex flows, which eventually requires no more adjustable constants than the eddy-damping one, chosen once and for all on the well-known and accepted isotropic value. Consequently, the model is relevant to explore configurations unreachable by DNS and experiments.

Since detailed conclusions were provided at the end of each chapter, it would be redundant to recall them here. Instead, we prefer to briefly put the emphasis on the main findings of the thesis. In the eight previous chapters, we tackled isotropic turbulence (HIT), isotropic turbulence with a mean scalar gradient (HITSG), isotropic helical turbulence (HHT), helical turbulence with a mean scalar gradient (HHTSG), turbulence initially submitted to shear (HSRT), sustained shear flows (HST), shear flows with a mean scalar gradient (HSTSG), and unstably stratified turbulence (USHT). For each of these configurations:

- Lengthy and complex analytical calculations have been performed to determine the non-linear transfers and production terms of the anisotropic EDQNM model...
- ... which was compared, when possible, to DNS, experiments and other models.
- The infrared and inertial scalings of the main spectra were accurately investigated.
- The scale-by-scale distribution of anisotropy was analyzed.
- Theoretical time exponents, assessed numerically, were derived for one-point statistics such as the kinetic energy, the scalar variance, the mixed velocity-scalar correlation, and the helicity.

Among these numerous features, the three most important findings would be, very likely:

- The new algebraic decay exponents for $< \theta^2 >$ and $< u_3\theta >$ in HITSG, and for $< u_i\omega_i >$ in HHT, and when combining both, the creation of the quadrature spectrum.
- The profound difference between the asymptotic anisotropic states of shear flows and unstably stratified turbulence: the former is almost independent of large scales initial conditions σ, whereas the latter strongly depend on them, and this was justified analytically.
- The effects of moderate Reynolds numbers on the scattering of global quantities in shear flows and on persistent small scales anisotropy at the level of the scalar second-order moments.

In addition to all the points mentioned above, detailed appendices are provided which contain all the calculations needed to understand the anisotropy modelling, the establishment of the quasi-normal normal expressions of the non-linear transfers within the EDQNM procedure (along with all the tricky but essential geometrical relations), the spherical and λ integrations, the non-local expansions, and statistics of second and third order moments in homogeneous turbulence. These appendices are rather long on purpose, in order to allow this work to be continued conveniently.

Further theoretical considerations were also proposed, such as the pressure spectra, quadratic anisotropic contributions in the non-linear transfers, and last but not least, the third and fourth orders expansions of $\mathcal{E}$ and Z for the kinetic field. This last remark makes the transition with the possible perspectives that I can imagine:

- Pursue the work, started Chapter 2 and Appendix C, about the third and fourth orders expansions of $\mathcal{E}$ and Z for the velocity field, and find some configurations, in addition to the sustained shear flow, where it could be of of importance. This is a promising track since first results in Chapter 3 indicate that fourth-order contributions tend to reduce the kinetic energy exponential growth rate γ. The extension to the scalar field through $\mathcal{E}^T$ would be rather straightforward. But more interestingly, some work needs to be done regarding the higher-order expansion of the scalar flux. Indeed, given the equations of USHT, it could improve the theoretical linear prediction for the kinetic energy exponential growth rate β, and consequently makes it closer to the exact value $2N$.

- Since shear was already combined to a mean scalar gradient for passive scalar dynamics in Chapter 5, and helicity to a mean scalar gradient in Chapter 8, a natural extension could be to combine both shear and USHT. First results tend to indicate that stratification overcomes shear, with an exponential growth rate for K which depends on σ. At a comparable level, it would be interesting to go further with the variable mean-fields $S(t)$ and $N(t)$, with some details and equations already provided at the end of Chapters 3 and 7. This could extend the reach of the anisotropic EDQNM modelling to address mixing and free-shear layers within a homogeneous framework.

- For the long-term perspective, it would be of great theoretical interest to extend the concept of the modelled anisotropy through spherical harmonics expansion to EDQNM2, in order to deal with rotating turbulence. Of course, this is a complex task which would require significant analytical developments to take into account the linear operators of the third-order correlations into the non-linear transfers. But it could permit to model more accurately geophysical flows by combining shear, stratification and rotation.

- Finally, the case of MHD turbulence could be addressed again thanks to the present anisotropic EDQNM modelling, in line with the pioneering works of Pouquet *et al.* (1976); Grappin *et al.* (1982). Indeed, the spectral two-point magnetic-magnetic correlation verifies the same properties as $\hat{R}_{ij}$, and thus can be decomposed as well into directional and polarization parts, which could be of use to address strong MHD, where a mean magnetic field breaks the isotropy of the flow. Before that, it appears to be essential to focus first on isotropic MHD, with the effects of kinetic helicity, magnetic helicity, and cross-helicity combined. In the last months of this thesis, I started studying isotropic MHD in presence of cross-helicity, without a mean magnetic field, and despite some analogies with the kinetic helicity in hydrodynamics turbulence, it is much more complex and there is still a great amount of work to be done.

Appendix A

Statistics and Structure Functions

The first objective of this appendix is to gather equivalences between physical and spectral formulations, in order to compute third-order statistical quantities with EDQNM, such as derivative skewnesses, in homogeneous turbulence. Equivalences in homogeneous isotropic turbulence (HIT) are not that straightforward, and thus deserve some details, since errors are found in reference papers (Pope, 2000; Antonia & Orlandi, 2004; Ristorcelli, 2006). In the following sections, as many details as possible are given, that could be used for other purposes as well. Extensions to homogeneous turbulence without any particular symmetries are proposed. The second objective is to recall some basic results about structure functions.

A.1 Evolution equations and definitions

The fluctuating vorticity ω_i is divergence-free and the vorticity tensor is defined as

$$\mathcal{W}_{ij} =< \omega_i \omega_j > . \tag{A.1}$$

The enstrophy $\mathcal{W}_{ii} =< \omega^2 >$ is linked to the kinetic energy dissipation rate through

$$< \omega_i \omega_i >=< \omega^2 >= \frac{\epsilon}{\nu}. \tag{A.2}$$

This is always valid in homogeneous turbulence, as shown hereafter. The evolution equations of the fluctuating velocity and vorticity are given in (2.1) and (D.27). Let's define as well the two useful symmetric and antisymmetric tensors

$$s_{ij} = \frac{\partial u_i}{\partial x_j} + \frac{\partial u_j}{\partial x_i}, \qquad a_{ij} = \frac{\partial u_i}{\partial x_j} - \frac{\partial u_j}{\partial x_i}. \tag{A.3}$$

For the scalar field, the evolution equation of the fluctuating part is given in (4.2). Let's define as well the scalar covariance tensor $< \partial_i \theta \, \partial_j \theta >=< \xi_i \xi_j >$ and the derivative scalar variance

$$< \xi_i \xi_i >=< \xi^2 >= \frac{\epsilon_T}{a}, \qquad \xi_i = \frac{\partial \theta}{\partial x_i}. \tag{A.4}$$

The evolution equations of the enstrophy $< \omega^2 >$ and $< \xi^2 >$ are detailed for homogeneous flows in section A.2, and then for HIT in section A.3.

A.2 Tensorial relations for homogeneous turbulence

In this part, the emphasis is put on homogeneous turbulence to provide general relations between sixth order tensors involving second and third order moments of the fluctuating velocity and scalar fields. In what follows, only homogeneity is assumed.

A.2.1 Dissipation ϵ and enstrophy $< \omega^2 >$

Expanding $< \partial_l(u_i\,\partial_k u_j) = 0 >$ and $< \partial_k(u_i\,\partial_l u_j) = 0 >$ yields the important result detailed in George & Hussein (1991)

$$< \frac{\partial u_i}{\partial x_l}\frac{\partial u_j}{\partial x_k} >=< \frac{\partial u_i}{\partial x_k}\frac{\partial u_j}{\partial x_l} > . \tag{A.5}$$

Let's call this result the 2nd **order law**, since it involves second-order moments of the velocity field through a rank-4 tensor. Then, multiplying the incompressibility condition $\partial_i u_i = 0$ by $\partial_1 u_1$, $\partial_2 u_2$ and $\partial_3 u_3$ provides, after ensemble average,

$$< \partial_2 u_1\,\partial_1 u_2 > + < \partial_3 u_1\,\partial_1 u_3 >= - < (\partial_1 u_1)^2 >,$$

$$< \partial_2 u_1\,\partial_1 u_2 > + < \partial_3 u_2\,\partial_2 u_3 >= - < (\partial_2 u_2)^2 >,$$

$$< \partial_3 u_1\,\partial_1 u_3 > + < \partial_3 u_2\,\partial_2 u_3 >= - < (\partial_3 u_3)^2 > .$$

This gives the relation always valid in homogeneous turbulence

$$< \frac{\partial u_1}{\partial x_2}\frac{\partial u_2}{\partial x_1} > + < \frac{\partial u_1}{\partial x_3}\frac{\partial u_3}{\partial x_1} > + < \frac{\partial u_2}{\partial x_3}\frac{\partial u_3}{\partial x_2} >= -\frac{1}{2}\left(< \left(\frac{\partial u_1}{\partial x_1}\right)^2 > + < \left(\frac{\partial u_2}{\partial x_2}\right)^2 > + < \left(\frac{\partial u_3}{\partial x_3}\right)^2 > \right), \tag{A.6}$$

so that

$$< \omega^2 >= \frac{\epsilon}{\nu} =< \frac{\partial u_i}{\partial x_j}\frac{\partial u_i}{\partial x_j} >= \frac{1}{2} < \left(\frac{\partial u_i}{\partial x_j} + \frac{\partial u_j}{\partial x_i}\right)\left(\frac{\partial u_i}{\partial x_j} + \frac{\partial u_j}{\partial x_i}\right) >= \frac{1}{2} < s_{ij}s_{ij} > . \tag{A.7}$$

A.2.2 Identities for the velocity field

Let's define the sixth order tensor

$$B_{ijkpqr} =< \frac{\partial u_i}{\partial x_p}\frac{\partial u_j}{\partial x_q}\frac{\partial u_k}{\partial x_r} > . \tag{A.8}$$

This tensor appears notably in the numerator of the velocity derivative skewness $S(t)$, and on the evolution equation of the dissipation rate $\epsilon(t)$. In a manner similar to George & Hussein (1991) with the 2nd order law (A.5), there is a need to find different relations involving B_{ijkpqr}.

Firstly, the use of homogeneity, through the difference of $< \partial_j(u_i\,\partial_q u_p\,\partial_q u_p) >= 0$ and $< \partial_j(u_i\,\partial_q u_p\,\partial_p u_q) >= 0$, gives

$$< \frac{\partial u_i}{\partial x_j}\frac{\partial u_q}{\partial x_p}\frac{\partial u_q}{\partial x_p} >=< \frac{\partial u_i}{\partial x_j}\frac{\partial u_q}{\partial x_p}\frac{\partial u_p}{\partial x_q} > . \tag{A.9}$$

This is similar to (A.5), but for third-order moments of the velocity field, and thus this result is called the 3rd **order first law**. One can also derive a second relation for third-order moments of the velocity field: $< \partial_p(u_i u_q \, \partial^2_{jq} u_p) >= 0$ and $< \partial_q(u_q \, \partial_p u_i \, \partial_j u_p) >= 0$ yield

$$< u_q \frac{\partial u_i}{\partial x_p} \frac{\partial^2 u_p}{\partial x_j \partial x_q} >= - < u_i \frac{\partial u_p}{\partial x_q} \frac{\partial^2 u_q}{\partial x_j \partial x_p} >= - < u_q \frac{\partial u_p}{\partial x_j} \frac{\partial^2 u_i}{\partial x_p \partial x_q} >,$$

which allows, from $< \partial^2_{pq}(u_i u_p \partial_j u_q) >= 0$, to obtain

$$< \frac{\partial u_i}{\partial x_p} \frac{\partial u_q}{\partial x_j} \frac{\partial u_p}{\partial x_q} > + < u_q \frac{\partial u_p}{\partial x_j} \frac{\partial^2 u_i}{\partial x_p \partial x_q} >= 0.$$

Injecting the two previous equations into the development of $< \partial_q(u_p \, \partial_j u_i \, \partial_p u_q) >= 0$, and using the fact that $< \partial_j(u_q \, \partial_p u_i \, \partial_p u_q) >= 0$, yields the 3rd **order second law**

$$< \frac{\partial u_i}{\partial x_j} \frac{\partial u_q}{\partial x_p} \frac{\partial u_q}{\partial x_p} >= 2 < \frac{\partial u_i}{\partial x_p} \frac{\partial u_p}{\partial x_q} \frac{\partial u_q}{\partial x_j} > . \tag{A.10}$$

Then, combining $< \partial_i(u_k \, \partial_j u_i \, \partial_k u_j) >= 0$ and $< \partial^3_{ijk}(u_i u_j u_k) >= 0 = 4 < u_k \, \partial_j u_i \, \partial^2_{ik} u_j >$, provides

$$< \frac{\partial u_i}{\partial x_j} \frac{\partial u_j}{\partial x_k} \frac{\partial u_k}{\partial x_i} >= 0, \tag{A.11}$$

which is consistent with (A.10). This result is often used in the isotropic framework. Finally, it is possible to derive one more relation for B_{ijkpqr} : let's consider the following system

$$\begin{array}{lll} [1] < \partial_p(u_i \, \partial_q u_j \, \partial_r u_k) >= 0, & [2] < \partial_p(u_i \, \partial_r u_j \, \partial_q u_k) >= 0, & [3] < \partial_q(u_i \, \partial_p u_j \, \partial_r u_k) >= 0, \\ [4] < \partial_q(u_i \, \partial_r u_j \, \partial_p u_k) >= 0, & [5] < \partial_r(u_i \, \partial_q u_j \, \partial_p u_k) >= 0, & [6] < \partial_r(u_i \, \partial_p u_j \, \partial_q u_k) >= 0. \end{array}$$

Each equation creates three terms, with one involving a particular permutation of B_{ijkpqr}. Combining these six equations, in the specific order [2]+[3]+[5]-[1]-[4]-[6], yields the **permutation law**

$$B_{ijkpqr} + B_{ijkqrp} + B_{ijkrpq} = B_{ijkprq} + B_{ijkqpr} + B_{ijkrqp}. \tag{A.12}$$

Let's now define another sixth order tensor

$$C_{ijkpqr} =< \frac{\partial^2 u_i}{\partial x_k \partial x_p} \frac{\partial^2 u_j}{\partial x_q \partial x_r} > . \tag{A.13}$$

This tensor appears notably in the numerator of the kinetic palinstrophy $G(t)$, and on the evolution equation of the dissipation rate $\epsilon(t)$. Firstly, the equations $< \partial^2_{jk}(u_i \, \partial^2_{jk} u_i) >= 0$ and $< \partial^2_{jj}(u_i \, \partial^2_{kk} u_i) >= 0$ provide

$$< \frac{\partial^2 u_i}{\partial x_j \partial x_j} \frac{\partial^2 u_i}{\partial x_k \partial x_k} >=< \frac{\partial^2 u_i}{\partial x_j \partial x_k} \frac{\partial^2 u_i}{\partial x_j \partial x_k} >, \tag{A.14}$$

Then, $< \partial^2_{ij}(\partial_k u_i \, \partial_k u_j) >= 0$ gives

$$< \frac{\partial^2 u_i}{\partial x_k \partial x_j} \frac{\partial^2 u_j}{\partial x_k \partial x_i} >= 0. \tag{A.15}$$

These two equations will be used in the HIT framework. Finally, with the difference of $< \partial^2_{kk}(u_j\,\partial^2_{pp}u_i) >= 0$ and $< \partial^2_{kp}(u_j\,\partial^2_{kp}u_i) >= 0$, a more general result can be obtained

$$< \frac{\partial^2 u_i}{\partial x_k \partial x_p}\frac{\partial^2 u_j}{\partial x_k \partial x_p} >=< \frac{\partial^2 u_i}{\partial x_k \partial x_k}\frac{\partial^2 u_j}{\partial x_p \partial x_p} > . \tag{A.16}$$

A.2.3 Evolution equations of $\mathcal{W}_{ij}$ and $< \omega^2 >$

In the homogeneous framework, the vorticity tensor $\mathcal{W}_{ij}$ evolution equation reads

$$\frac{\partial \mathcal{W}_{ij}}{\partial t} = \mathcal{W}_{il}A_{jl} + \mathcal{W}_{jl}A_{il} + < \omega_l\Big(\omega_j\frac{\partial u_i}{\partial x_l} + \omega_i\frac{\partial u_j}{\partial x_l}\Big) > -\epsilon^{\omega}_{ij}, \tag{A.17}$$

where the vorticity dissipation rate is $\epsilon^{\omega}_{ij} = 2\nu < \partial_l\omega_i\partial_l\omega_j >$. Using (A.5), one obtains directly

$$\mathcal{W}_{ij} = \delta_{ij} < \frac{\partial u_q}{\partial x_p}\frac{\partial u_q}{\partial x_p} > - < \frac{\partial u_q}{\partial x_i}\frac{\partial u_q}{\partial x_j} > -\frac{\epsilon_{ij}}{2\nu}. \tag{A.18}$$

It is possible to simplify $< \omega_l\omega_j\partial_l u_i >$. Firstly, the expansion of this term yields

$$< \omega_l\omega_j\frac{\partial u_i}{\partial x_l} >=< \frac{\partial u_i}{\partial x_p}a_{qp}a_{jq} > + < \frac{\partial u_i}{\partial u_j}\frac{\partial u_q}{\partial x_p}a_{qp} >,$$

and the second rhs term is zero thanks to (A.9). Finally, one obtains using (A.10)

$$\begin{aligned} &< \omega_l\left(\omega_j\frac{\partial u_i}{\partial x_l} + \omega_i\frac{\partial u_j}{\partial x_l}\right) >=< \frac{\partial u_i}{\partial x_p}\frac{\partial u_q}{\partial x_j}\frac{\partial u_p}{\partial x_q} > + < \frac{\partial u_q}{\partial x_i}\frac{\partial u_j}{\partial x_p}\frac{\partial u_p}{\partial x_q} > - < \frac{\partial u_i}{\partial x_p}\frac{\partial u_q}{\partial x_j}\frac{\partial u_q}{\partial x_p} > \\ &= - < \frac{\partial u_q}{\partial x_i}\frac{\partial u_j}{\partial x_p}\frac{\partial u_q}{\partial x_p} > + \frac{1}{2} < \frac{\partial u_p}{\partial x_q}\frac{\partial u_p}{\partial x_q}s_{ij} > - < \frac{\partial u_i}{\partial x_p}\frac{\partial u_q}{\partial x_j}\frac{\partial u_q}{\partial x_p} > - < \frac{\partial u_q}{\partial x_i}\frac{\partial u_j}{\partial x_p}\frac{\partial u_q}{\partial x_p} > . \end{aligned} \tag{A.19}$$

Furthermore, using (A.11) and (A.14), one has

$$\begin{aligned} &< \omega_i\omega_j\frac{\partial u_i}{\partial x_j} >=< a_{jq}a_{qi}\frac{\partial u_i}{\partial x_j} >= - < \frac{\partial u_i}{\partial x_j}\frac{\partial u_j}{\partial x_k}\frac{\partial u_i}{\partial x_k} >, \\ &\frac{1}{2\nu}\epsilon^{\omega}_{ii} =< \frac{\partial \omega_i}{\partial x_j}\frac{\partial \omega_i}{\partial x_j} >=< \frac{\partial^2 u_i}{\partial x_p \partial x_p}\frac{\partial^2 u_i}{\partial x_q \partial x_q} >, \end{aligned}$$

so that the enstrophy evolution equation in homogeneous turbulence reads

$$\boxed{\frac{\partial < \omega^2 >}{\partial t} = 2\mathcal{W}_{ij}A^{+}_{ij} - 2 < \frac{\partial u_i}{\partial x_j}\frac{\partial u_j}{\partial x_k}\frac{\partial u_i}{\partial x_k} > -2\nu < \frac{\partial^2 u_i}{\partial x_p \partial x_p}\frac{\partial^2 u_i}{\partial x_q \partial x_q} > .} \tag{A.20}$$

A.2.4 Evolution equation of ϵ_{ij}

The evolution equation of the dissipation tensor ϵ_{ij} is not often investigated, as pointed out in Piquet (2001). The starting point to compute the evolution equation of $\epsilon_{ij} = 2\nu < \partial_k u_i\,\partial_k u_j >$ is to derive the evolution equation (2.1) of u_i with respect to x_k, and to multiply it by $\partial_k u_j$. The same process is done for the evolution equation of u_j and the two resulting expressions are summed. Finally, the ensemble average is applied. Some terms are not straightforward to

simplify, and details are provided hereafter: this yields the evolution equation of the dissipation tensor in the homogeneous framework

$$\frac{\partial}{\partial t}\left(\frac{\epsilon_{ij}}{2\nu}\right) = -<\frac{\partial u_i}{\partial x_k}\frac{\partial u_j}{\partial x_p}\frac{\partial u_p}{\partial x_k}> -<\frac{\partial u_j}{\partial x_k}\frac{\partial u_i}{\partial x_p}\frac{\partial u_p}{\partial x_k}> +<\frac{\partial p}{\partial x_k}\frac{\partial s_{ij}}{\partial x_k}> -2\nu<\frac{\partial^2 u_i}{\partial x_k \partial x_k}\frac{\partial^2 u_j}{\partial x_p \partial x_p}>$$
$$-2<A_{pk}\frac{\partial u_i}{\partial x_p}\frac{\partial u_j}{\partial x_k}> -<A_{ip}\frac{\partial u_p}{\partial x_k}\frac{\partial u_j}{\partial x_k}> -<A_{jp}\frac{\partial u_p}{\partial x_k}\frac{\partial u_i}{\partial x_k}>. \tag{A.21}$$

The term arising from the non-linearity:

$$<\frac{\partial u_i}{\partial x_k}\frac{\partial^2 u_j u_p}{\partial x_p \partial x_k}> +<\frac{\partial u_j}{\partial x_k}\frac{\partial^2 u_i u_p}{\partial x_p \partial x_k}>=$$
$$\Big(<\frac{\partial u_i}{\partial x_k}\frac{\partial u_j}{\partial x_p}\frac{\partial u_p}{\partial x_k}> +<u_p\frac{\partial u_i}{\partial x_k}\frac{\partial^2 u_j}{\partial x_k \partial x_p}>\Big) + \Big(<\frac{\partial u_j}{\partial x_k}\frac{\partial u_i}{\partial x_p}\frac{\partial u_p}{\partial x_k}> +<u_p\frac{\partial u_j}{\partial x_k}\frac{\partial^2 u_i}{\partial x_k \partial x_p}>\Big). \tag{A.22}$$

Considering $<u_p\partial_p(\partial_k u_i\,\partial_k u_j)>=0$ by virtue of homogeneity and incompressibility yields

$$<u_p\frac{\partial u_j}{\partial x_k}\frac{\partial^2 u_i}{\partial x_k \partial x_p}>=-<u_p\frac{\partial u_i}{\partial x_k}\frac{\partial^2 u_j}{\partial x_k \partial x_p}>, \tag{A.23}$$

which simplifies (A.22) into

$$<\frac{\partial u_i}{\partial x_k}\frac{\partial^2 u_j u_p}{\partial x_p \partial x_k}> +<\frac{\partial u_j}{\partial x_k}\frac{\partial^2 u_i u_p}{\partial x_p \partial x_k}>=<\frac{\partial u_i}{\partial x_k}\frac{\partial u_j}{\partial x_p}\frac{\partial u_p}{\partial x_k}> +<\frac{\partial u_j}{\partial x_k}\frac{\partial u_i}{\partial x_p}\frac{\partial u_p}{\partial x_k}>. \tag{A.24}$$

The mean-gradient terms: the terms involving the mean-velocity gradient can be grouped together thanks to (A.5), which yields

$$-<A_{pk}\frac{\partial u_i}{\partial x_p}\frac{\partial u_j}{\partial x_k}> -<A_{pk}\frac{\partial u_j}{\partial x_p}\frac{\partial u_i}{\partial x_k}> -<A_{ip}\frac{\partial u_p}{\partial x_k}\frac{\partial u_j}{\partial x_k}> -<A_{jp}\frac{\partial u_p}{\partial x_k}\frac{\partial u_i}{\partial x_k}>$$
$$=-2<A_{pk}\frac{\partial u_i}{\partial x_p}\frac{\partial u_j}{\partial x_k}> -<A_{ip}\frac{\partial u_p}{\partial x_k}\frac{\partial u_j}{\partial x_k}> -<A_{jp}\frac{\partial u_p}{\partial x_k}\frac{\partial u_i}{\partial x_k}>,$$

and the terms involving only the mean velocity are zero due to (A.23)

$$-<U_p\frac{\partial u_j}{\partial x_k}\frac{\partial^2 u_i}{\partial x_p \partial x_k}> -<U_p\frac{\partial u_i}{\partial x_k}\frac{\partial^2 u_j}{\partial x_p \partial x_k}>=0.$$

The pressure terms: there are several steps: expanding $<\partial^3_{jkk}(pu_i)>=0$ and using $<\partial_k(\partial_k u_i\,\partial_k p)>=0$, $<\partial_k(\partial_j u_i\,\partial_k p)>=0$, and $<\partial_j(\partial_k u_i\,\partial_k p)>=0$, gives

$$<p\frac{\partial^3 u_i}{\partial x_j \partial x_k \partial x_k}> +<u_i\frac{\partial^3 p}{\partial x_j \partial x_k \partial x_k}>=0. \tag{A.25}$$

Then, the sum of $<\partial^2_{kk}(u_i\partial_j p)>=0$ and $<\partial^2_{kk}(\partial_j u_i\,p)>=0$ provides, using (A.25)

$$<\frac{\partial p}{\partial x_k}\frac{\partial^2 u_i}{\partial x_j \partial x_k}> +<\frac{\partial u_i}{\partial x_k}\frac{\partial^2 p}{\partial x_j \partial x_k}>=0. \tag{A.26}$$

Finally, summing the previous equation with $(i \leftrightarrow j)$ yields the simplification

$$- < \frac{\partial u_j}{\partial x_k}\frac{\partial^2 p}{\partial x_i \partial x_k} > - < \frac{\partial u_i}{\partial x_k}\frac{\partial^2 p}{\partial x_j \partial x_k} >=< \frac{\partial p}{\partial x_k}\frac{\partial s_{ij}}{\partial x_k} > . \tag{A.27}$$

The viscous terms: expanding $< \partial^2_{kp}(\partial_k u_j\, \partial_p u_i) >= 0$ and using (A.16) yields

$$\nu < \frac{\partial u_i}{\partial x_k}\frac{\partial^3 u_j}{\partial x_p \partial x_p \partial x_k} > +\nu < \frac{\partial u_j}{\partial x_k}\frac{\partial^3 u_i}{\partial x_p \partial x_p \partial x_k} >= -2\nu < \frac{\partial^2 u_i}{\partial x_k \partial x_k}\frac{\partial^2 u_j}{\partial x_p \partial x_p} > \tag{A.28}$$

A.2.5 Evolution equations of $< \xi_i \xi_j >$ and $< \xi^2 >$

The starting point to compute the evolution equation of the scalar covariance tensor $< \xi_i \xi_j >$ is to derive the evolution equation (4.2) of θ with respect to x_i, and to multiply it by $\partial_j \theta$. Finally, the ensemble average is applied, which yields the evolution equation of the scalar covariance tensor $< \xi_i \xi_j >$ in the homogeneous framework

$$\begin{aligned}
&\frac{\partial < \xi_i \xi_j >}{\partial t} + \lambda_l \Big(< \frac{\partial u_l}{\partial x_i}\frac{\partial \theta}{\partial x_j} > + < \frac{\partial u_l}{\partial x_j}\frac{\partial \theta}{\partial x_i} > \Big) + < \frac{\partial \theta}{\partial x_j}\frac{\partial^2 \theta u_l}{\partial x_l \partial x_i} > + < \frac{\partial \theta}{\partial x_i}\frac{\partial^2 \theta u_l}{\partial x_l \partial x_j} > \\
&+ < A_{li}\frac{\partial \theta}{\partial x_l}\frac{\partial \theta}{\partial x_j} > + < A_{lj}\frac{\partial \theta}{\partial x_l}\frac{\partial \theta}{\partial x_i} > + < U_l \frac{\partial \theta}{\partial x_j}\frac{\partial^2 \theta}{\partial x_i \partial x_l} > + < U_l \frac{\partial \theta}{\partial x_i}\frac{\partial^2 \theta}{\partial x_j \partial x_l} > \\
&= a \Big[< \frac{\partial \theta}{\partial x_j}\frac{\partial^3 \theta}{\partial x_i \partial x_l \partial x_l} > + < \frac{\partial \theta}{\partial x_i}\frac{\partial^3 \theta}{\partial x_j \partial x_l \partial x_l} > \Big].
\end{aligned} \tag{A.29}$$

This equation can be simplified in an analogous manner to what was done for ϵ_{ij}. First, $< \partial_l (U_l\, \xi_i\, \xi_j) >= 0$ which simplifies the two terms in U_l. Then, using $< \partial_l (u_l\, \xi_i\, \xi_j) >= 0$ simplifies the fourth and fifth terms. Finally, the diffusion terms can be grouped remarking that $< \partial^2_{ll}(\xi_i \xi_j) >= 0$. This yields

$$\begin{aligned}
&\frac{\partial < \xi_i \xi_j >}{\partial t} + \lambda_l \Big(< \frac{\partial u_l}{\partial x_i}\frac{\partial \theta}{\partial x_j} > + < \frac{\partial u_l}{\partial x_j}\frac{\partial \theta}{\partial x_i} > \Big) + < \frac{\partial \theta}{\partial x_j}\frac{\partial u_l}{\partial x_i}\frac{\partial \theta}{\partial x_l} > + < \frac{\partial \theta}{\partial x_i}\frac{\partial u_l}{\partial x_j}\frac{\partial \theta}{\partial x_l} > \\
&+ < A_{li}\frac{\partial \theta}{\partial x_l}\frac{\partial \theta}{\partial x_j} > + < A_{lj}\frac{\partial \theta}{\partial x_l}\frac{\partial \theta}{\partial x_i} >= -2a < \frac{\partial^2 \theta}{\partial x_j \partial x_l}\frac{\partial^2 \theta}{\partial x_i \partial x_l} > .
\end{aligned} \tag{A.30}$$

This is notably recovered in Gylfason & Warhaft (2009). In the end, the evolution equation of $< \xi^2 >$ in homogeneous turbulence reads

$$\boxed{\begin{aligned}
&\frac{\partial < \xi^2 >}{\partial t} + 2\lambda_j < \frac{\partial u_j}{\partial x_i}\frac{\partial \theta}{\partial x_i} > +2 < \frac{\partial \theta}{\partial x_i}\frac{\partial u_j}{\partial x_i}\frac{\partial \theta}{\partial x_j} > +2 < A^+_{ij}\frac{\partial \theta}{\partial x_i}\frac{\partial \theta}{\partial x_j} > \\
&\qquad = -2a < \frac{\partial^2 \theta}{\partial x_i \partial x_j}\frac{\partial^2 \theta}{\partial x_i \partial x_j} > .
\end{aligned}} \tag{A.31}$$

A.2.6 Cospectrum in isotropic turbulence with mean scalar gradient

Another quantity which has not been investigated and deserves some interest is the dissipation rate of the scalar flux $< u_3 \theta >$ in HITSG. The evolution equation of the derivative scalar variance in HITSG can be obtained from (A.31) by taking $A_{ij} = 0$ and $\lambda_3 = -\Lambda$. The procedure to

derive the evolution equation of $< \partial_j u_i \, \partial_j \theta >$ is similar to what was done previously: one needs to derive the evolution equation (4.2) of θ with respect to x_j, to multiply it by $\partial_j u_i$, and to sum it with the equation (2.1) of u_i derived by x_j and multiplied by $\partial_j \theta$. This yields

$$\begin{aligned}
&\frac{\partial}{\partial t} < \frac{\partial u_i}{\partial x_j}\frac{\partial \theta}{\partial x_j} > + \lambda_j < \frac{\partial u_j}{\partial x_l}\frac{\partial u_i}{\partial x_l} > + A_{ij} < \frac{\partial u_j}{\partial x_l}\frac{\partial \theta}{\partial x_l} > + A_{jl}\Big(< \frac{\partial \theta}{\partial x_l}\frac{\partial u_i}{\partial x_j} > + < \frac{\partial \theta}{\partial x_j}\frac{\partial u_i}{\partial x_l} > \Big) \\
&+ < u_j \frac{\partial \theta}{\partial x_l}\frac{\partial^2 u_i}{\partial x_j \partial x_l} > + < u_j \frac{\partial u_i}{\partial x_l}\frac{\partial^2 \theta}{\partial x_j \partial x_l} > + < \frac{\partial u_i}{\partial x_j}\frac{\partial \theta}{\partial x_l}\frac{\partial u_j}{\partial x_l} > + < \frac{\partial u_i}{\partial x_l}\frac{\partial \theta}{\partial x_j}\frac{\partial u_j}{\partial x_l} > \\
&+ < U_j \frac{\partial \theta}{\partial x_l}\frac{\partial^2 u_i}{\partial x_j \partial x_l} > + < U_l \frac{\partial u_i}{\partial x_l}\frac{\partial^2 \theta}{\partial x_j \partial x_l} > \\
&= - < \frac{\partial \theta}{\partial x_l}\frac{\partial^2 p}{\partial x_i \partial x_l} > + a < \frac{\partial u_i}{\partial x_l}\frac{\partial^3 \theta}{\partial x_j \partial x_j \partial x_l} > + \nu < \frac{\partial \theta}{\partial x_l}\frac{\partial^3 u_i}{\partial x_j \partial x_j \partial x_l} > .
\end{aligned} \tag{A.32}$$

This equation simplifies using $< \partial_j (u_j \partial_l \theta \, \partial_l u_i) >= 0$ and $< \partial_l (\partial_l u_i \, \partial^2_{jj} \theta) >= 0$, and reads

$$\begin{aligned}
&\frac{\partial}{\partial t} < \frac{\partial u_i}{\partial x_j}\frac{\partial \theta}{\partial x_j} > + \lambda_j < \frac{\partial u_j}{\partial x_l}\frac{\partial u_i}{\partial x_l} > + A_{ij} < \frac{\partial u_j}{\partial x_l}\frac{\partial \theta}{\partial x_l} > + A_{jl}\Big(< \frac{\partial \theta}{\partial x_l}\frac{\partial u_i}{\partial x_j} > + < \frac{\partial \theta}{\partial x_j}\frac{\partial u_i}{\partial x_l} > \Big) \\
&+ < \frac{\partial u_i}{\partial x_j}\frac{\partial \theta}{\partial x_l}\frac{\partial u_j}{\partial x_l} > + < \frac{\partial u_i}{\partial x_l}\frac{\partial \theta}{\partial x_j}\frac{\partial u_j}{\partial x_l} >= - < \frac{\partial \theta}{\partial x_l}\frac{\partial^2 p}{\partial x_i \partial x_l} > - (\nu + a) < \frac{\partial^2 u_i}{\partial x_l \partial x_l}\frac{\partial^2 \theta}{\partial x_j \partial x_j} > .
\end{aligned} \tag{A.33}$$

In HITSG, this equation further simplifies into

$$\boxed{\frac{\partial}{\partial t}\Big(\frac{\epsilon_{\mathcal{F}}}{\nu + a}\Big) = \Lambda \frac{\epsilon}{3\nu} - < \frac{\partial u_3}{\partial x_j}\frac{\partial \theta}{\partial x_l} s_{jl} > + < \frac{\partial p}{\partial x_3}\frac{\partial^2 \theta}{\partial x_l \partial x_l} > - (\nu + a) < \frac{\partial^2 u_3}{\partial x_l \partial x_l}\frac{\partial^2 \theta}{\partial x_j \partial x_j} > .} \tag{A.34}$$

These considerations on the evolution equations of ϵ_T and $\epsilon_{\mathcal{F}}$ were added in the *Journal of Turbulence* of 2017.

A.3 Homogeneous isotropic turbulence

The previous equations and tensorial relations are simplified when the homogeneous turbulence is in addition considered isotropic. This notably yields important results for the second and third order moments of the fluctuating velocity and scalar gradients. From now and for clarity, the non-linear transfers $S^{\mathrm{NL(iso)}}$ and $S^{\mathrm{T,NL(iso)}}$ are called T and T_T respectively. Some of the results of this section were used in 1.

A.3.1 Spectral formalism

In HIT, the enstrophy evolution equation is

$$\frac{\partial < \omega^2 >}{\partial t} = 2 < \omega_j \omega_i \frac{\partial u_i}{\partial x_j} > - 2\nu < \frac{\partial \omega_i}{\partial x_j}\frac{\partial \omega_i}{\partial x_j} >, \tag{A.35}$$

which is (A.20) without the mean velocity gradient. This expression for HIT has been found and developed in Wyngaard (1971); Piquet (2001); Lesieur (2008) notably. The spectral counterpart is

$$\frac{1}{\nu}\frac{\partial \epsilon}{\partial t} = 2\int_0^\infty k^2 T(k,t)\mathrm{d}k - 4\nu\int_0^\infty k^4 E(k,t)\mathrm{d}k. \tag{A.36}$$

Identification between (A.20) and (A.36) provides straightforward equivalences that are detailed hereafter. In an analogous manner, one can write the evolution equation of the derivative scalar variance $< \partial_i\theta\partial_i\theta >$ in the HIT framework

$$\frac{\partial < \xi^2 >}{\partial t} = -2 < \frac{\partial\theta}{\partial x_i}\frac{\partial\theta}{\partial x_j}\frac{\partial u_i}{\partial x_j} > -2a < \frac{\partial^2\theta}{\partial x_i\partial x_j}\frac{\partial^2\theta}{\partial x_i\partial x_j} >, \tag{A.37}$$

which is (A.31) without the mean velocity and scalar gradients. This equation has been found in Wyngaard (1971), and has to be identified with its spectral counterpart

$$\frac{1}{a}\frac{\partial \epsilon_T}{\partial t} = 2\int_0^\infty k^2 T_T(k,t)\mathrm{d}k - 4a\int_0^\infty k^4 E_T(k,t)\mathrm{d}k, \tag{A.38}$$

A.3.2 Second and third-order statistics

In what follows, second-order statistics, such as dissipation rates, and third-order statistics, such as skewnesses, are computed and simplified within the HIT framework. First, the velocity derivative skewness and kinetic palinstrophy are defined as

$$S(t) = \frac{< (\partial u_1/\partial x_1)^3 >}{< (\partial u_1/\partial x_1)^2 >^{3/2}}, \qquad G(t) =< u^2 > \frac{< (\partial^2 u_1/\partial x_1^2)^2 >}{< (\partial u_1/\partial x_1)^2 >^2}. \tag{A.39}$$

The aim of the previous calculations is to express B_{ijkpqr} and C_{ijkpqr}, which appear in the evolution equation of the enstrophy, as a function of B_{111111} and C_{111111} only. One can proceed similarly for the passive scalar field. The mixed-derivative skewness and scalar palinstrophy are defined as

$$S_T(t) = \frac{< (\partial u_1/\partial x_1)(\partial\theta/\partial x_1)^2 >}{\sqrt{< (\partial u_1/\partial x_1)^2 >}< (\partial\theta/\partial x_1)^2 >}, \qquad G_T(t) =< \theta^2 > \frac{< (\partial^2\theta/\partial x_1^2)^2 >}{< (\partial\theta/\partial x_1)^2 >^2}. \tag{A.40}$$

Dissipation rate ϵ and enstrophy $< \omega^2 >$: the fourth order tensor

$$B_{ijkl} =< \frac{\partial u_i}{\partial x_j}\frac{\partial u_k}{\partial x_l} > \tag{A.41}$$

is used to simplify the expression of $\epsilon = \nu < \omega^2 >$. B_{ijkl} can be expanded as

$$B_{ijkl} = a_1\delta_{ij}\delta_{kl} + a_2\delta_{ik}\delta_{jl} + a_3\delta_{il}\delta_{jk}.$$

Then, the incompressibility $B_{iikl} = 0$ gives $3a_1 + a_2 + a_3 = 0$. In addition, $< \partial_j(u_i\,\partial_i u_j) >= 0$ and $< \partial^2_{ij}(u_i u_j) >= 0$ yield $B_{ijji} = 0$ which provides $a_1 + a_2 + 3a_3$. Hence

$$B_{ijkl} = a_2\Big(-\frac{1}{4}\delta_{ij}\delta_{kl} + \delta_{ik}\delta_{jl} - \frac{1}{4}\delta_{il}\delta_{jk}\Big). \tag{A.42}$$

Finally, $B_{1111} =< (\partial u_1/\partial x_1)^2 >= a_2/2$ and $B_{ijij} =< \omega^2 >= 15a_2/2$. This calculation is detailed in Pope (2000) and reported in Ristorcelli (2006); Piquet (2001).

Velocity derivative skewness S: the sixth order tensor B_{ijkpqr} defined in (A.8) is considered to compute the numerator of the derivative skewness. In the isotropic framework, this tensor is the sum of 15 terms, which are products of 3 δ-functions. Nevertheless, with symmetries, some of these terms can be grouped together, which eventually gives

$$\begin{aligned} B_{ijkpqr} &= a_1\delta_{ip}\delta_{jq}\delta_{kr} + a_2\Big(\delta_{ip}\delta_{jk}\delta_{qr} + \delta_{ik}\delta_{jq}\delta_{pr} + \delta_{ij}\delta_{kr}\delta_{pq}\Big) \\ &+ a_3\Big(\delta_{ip}\delta_{jr}\delta_{qk} + \delta_{ir}\delta_{jq}\delta_{pk} + \delta_{iq}\delta_{pj}\delta_{kr}\Big) + a_4\Big(\delta_{iq}\delta_{jr}\delta_{pk} + \delta_{ir}\delta_{jp}\delta_{kq}\Big) \\ &+ a_5\Big(\delta_{ij}\delta_{kp}\delta_{qr} + \delta_{ij}\delta_{kq}\delta_{pr} + \delta_{ik}\delta_{jp}\delta_{rq} + \delta_{ik}\delta_{jr}\delta_{qp} + \delta_{iq}\delta_{jk}\delta_{pr} + \delta_{ir}\delta_{jk}\delta_{pq}\Big) \end{aligned}$$

Then, the incompressibility $B_{ijkiqr} = 0$ gives a set of three equations: $3a_1 + 2a_2 + 2a_3 = 0$, $3a_2 + 4a_5 = 0$ and $3a_3 + 2a_4 + 2a_5 = 0$. In addition, equation (A.11) for the homogeneity yields $a_1 + 3a_2 + 9a_3 + 10a_4 + 12a_5 = 0$, so that

$$\begin{aligned} B_{ijkpqr} = a_1\Bigg[&\delta_{ip}\delta_{jq}\delta_{kr} - \frac{4}{3}\Big(\delta_{ip}\delta_{jk}\delta_{qr} + \delta_{ik}\delta_{jq}\delta_{pr} + \delta_{ij}\delta_{kr}\delta_{pq}\Big) \\ &- \frac{1}{6}\Big(\delta_{ip}\delta_{jr}\delta_{qk} + \delta_{ir}\delta_{jq}\delta_{pk} + \delta_{iq}\delta_{pj}\delta_{kr}\Big) - \frac{3}{4}\Big(\delta_{iq}\delta_{jr}\delta_{pk} + \delta_{ir}\delta_{jp}\delta_{kq}\Big) \\ &+ \Big(\delta_{ij}\delta_{kp}\delta_{qr} + \delta_{ij}\delta_{kq}\delta_{pr} + \delta_{ik}\delta_{jp}\delta_{rq} + \delta_{ik}\delta_{jr}\delta_{qp} + \delta_{iq}\delta_{jk}\delta_{pr} + \delta_{ir}\delta_{jk}\delta_{pq}\Big)\Bigg]. \end{aligned} \tag{A.43}$$

Finally $B_{111111} =< (\partial u_1/\partial x_1)^3 >= a_1$ and $B_{iijjll} = 35a_1/2$. This calculation was done in Pope (2000) (without the details regarding the homogeneity simplifications) and is reported in Ristorcelli (2006); Wyngaard (1971); Piquet (2001). The final expression of B_{ijkpqr} yields results in agreement with the recent work of Vreman & Kuerten (2014).

Kinetic palinstrophy G: the sixth order tensor C_{ijkpqr} defined in (A.13) is now used to compute the numerator of the kinetic palinstrophy. As previously, symmetries allow to group some of the 15 products of δ-functions, which gives

$$\begin{aligned} C_{ijkpqr} &= a_1\delta_{ij}\delta_{kp}\delta_{qr} + a_2\Big(\delta_{ij}\delta_{kq}\delta_{pr} + \delta_{ij}\delta_{kr}\delta_{pq}\Big) + a_3\Big(\delta_{ik}\delta_{jp}\delta_{qr} + \delta_{ip}\delta_{jk}\delta_{qr} + \delta_{iq}\delta_{jr}\delta_{kp} + \delta_{ir}\delta_{jq}\delta_{kp}\Big) \\ &+ a_4\Big(\delta_{iq}\delta_{jk}\delta_{pr} + \delta_{iq}\delta_{jp}\delta_{kr} + \delta_{ir}\delta_{jk}\delta_{pq} + \delta_{ir}\delta_{jp}\delta_{kq}\Big) + a_5\Big(\delta_{ik}\delta_{jq}\delta_{pr} + \delta_{ik}\delta_{jr}\delta_{pq} + \delta_{ip}\delta_{jq}\delta_{kr} + \delta_{ip}\delta_{jr}\delta_{kq}\Big) \end{aligned}$$

Then, the incompressibility $C_{ijipqr} = 0$ gives two equations: $a_1 + 4a_3 + 2a_4 = 0$, and $a_2 + a_3 + a_4 + 4a_5 = 0$. In addition, the homogeneity relations (A.14) and (A.15) provide respectively $6a_1 - 6a_2 + 8a_3 - 4a_4 - 4a_5 = 0$ and $a_1 + 4a_2 + 8a_3 + 16a_4 + 6a_5 = 0$, so that

$$\begin{aligned} C_{ijkpqr} = a_5\Bigg[&-6\delta_{ij}\delta_{kp}\delta_{qr} - 6\Big(\delta_{ij}\delta_{kq}\delta_{pr} + \delta_{ij}\delta_{kr}\delta_{pq}\Big) + \Big(\delta_{ik}\delta_{jp}\delta_{qr} + \delta_{ip}\delta_{jk}\delta_{qr} + \delta_{iq}\delta_{jr}\delta_{kp} + \delta_{ir}\delta_{jq}\delta_{kp}\Big) \\ &+ \Big(\delta_{iq}\delta_{jk}\delta_{pr} + \delta_{iq}\delta_{jp}\delta_{kr} + \delta_{ir}\delta_{jk}\delta_{pq} + \delta_{ir}\delta_{jp}\delta_{kq}\Big) + \Big(\delta_{ik}\delta_{jq}\delta_{pr} + \delta_{ik}\delta_{jr}\delta_{pq} + \delta_{ip}\delta_{jq}\delta_{kr} + \delta_{ip}\delta_{jr}\delta_{kq}\Big)\Bigg]. \end{aligned} \tag{A.44}$$

Finally $C_{111111} =< (\partial^2 u_1/\partial x_1^2)^2 >= -6a_5$ and $C_{iijkjk} = -210a_5$. This result was used (and misreported) in Ristorcelli (2006) without any details. The final expression of C_{ijkpqr} yields results in agreement with the recent work of Vreman & Kuerten (2014).

Mixed-derivative skewness S_T: the tensor

$$B^T_{ijkl} =< \frac{\partial\theta}{\partial x_i}\frac{\partial\theta}{\partial x_j}\frac{\partial u_k}{\partial x_l} > \tag{A.45}$$

is used to compute the numerator of the mixed-derivative skewness. Similarly, B^T_{ijkl} can be expressed as

$$B^T_{ijkl} = a_1\delta_{ij}\delta_{kl} + a_2\delta_{ik}\delta_{jl} + a_3\delta_{il}\delta_{jk},$$

and symmetry $B^T_{ijkl} = B^T_{jikl}$ directly yields $a_2 = a_3$. Then, with incompressibility $B^T_{ijll} = 0$, one has $2a_2 = -3a_1$. Finally, $B^T_{1111} =< (\partial\theta/\partial x_1)^2(\partial u_1/\partial x_1) >= 4a_2/3$ and $B^T_{ijij} = 10a_2$. This relation was used in Wyngaard (1971) without any details.

Scalar palinstrophy $G_T(t)$: the tensor

$$C^T_{ijkl} =< \frac{\partial^2\theta}{\partial x_i\partial x_j}\frac{\partial^2\theta}{\partial x_k\partial x_l} > \tag{A.46}$$

is introduced to compute the numerator of the scalar palinstrophy. C^T_{ijkl} can be expressed as

$$C^T_{ijkl} = a_1\delta_{ij}\delta_{kl} + a_2\delta_{ik}\delta_{jl} + a_3\delta_{il}\delta_{jk},$$

and symmetry directly yields $a_2 = a_3$. Then, with homogeneity, $< \partial^2_{ij}(\partial_i\theta\,\partial_j\theta) >= 0$ and $< \partial^2_{ii}(\partial_j\theta\,\partial_j\theta) >= 0$ which provides $C^T_{iijj} = C^T_{ijij}$ and thus $a_1 = a_2$. Finally, $C^T_{1111} =< (\partial^2\theta/\partial x_1^2)^2 >= 3a_1$ and $C^T_{ijij} = 15a_1$. This result was used in Ristorcelli (2006); Wyngaard (1971) without any details.

A.3.3 Results for the velocity field

Using the results for B_{ijkpqr} and C_{ijkpqr}, along with (A.11), (A.14) and (A.15), gives

$$< \omega_i\omega_i > =< \frac{\partial u_i}{\partial x_j}\frac{\partial u_i}{\partial x_j} > - < \frac{\partial u_i}{\partial x_j}\frac{\partial u_j}{\partial x_i} >= \Big(15 - 0\Big) < \left(\frac{\partial u_1}{\partial x_1}\right)^2 >= 15 < \left(\frac{\partial u_1}{\partial x_1}\right)^2 >, \tag{A.47}$$

$$< \frac{\partial\omega_i}{\partial x_j}\frac{\partial\omega_i}{\partial x_j} > =< \frac{\partial^2 u_i}{\partial x_j\partial x_k}\frac{\partial^2 u_i}{\partial x_j\partial x_k} > - < \frac{\partial^2 u_i}{\partial x_j\partial x_k}\frac{\partial^2 u_j}{\partial x_i\partial x_k} >= 35 < \left(\frac{\partial^2 u_1}{\partial x_1^2}\right)^2 >, \tag{A.48}$$

$$\begin{aligned} < \omega_i\omega_j\frac{\partial u_i}{\partial x_j} > &=< \frac{\partial u_i}{\partial x_j}\frac{\partial u_l}{\partial x_i}\frac{\partial u_j}{\partial x_l} > - < \frac{\partial u_i}{\partial x_j}\frac{\partial u_l}{\partial x_i}\frac{\partial u_l}{\partial x_j} > - < \frac{\partial u_i}{\partial x_j}\frac{\partial u_i}{\partial x_l}\frac{\partial u_j}{\partial x_l} > + < \frac{\partial u_i}{\partial x_j}\frac{\partial u_i}{\partial x_l}\frac{\partial u_l}{\partial x_j} > \\ &= \left(0 - \frac{35}{2} - \frac{35}{2} + \frac{35}{2}\right) < \left(\frac{\partial u_1}{\partial x_1}\right)^3 >= -\frac{35}{2} < \left(\frac{\partial u_1}{\partial x_1}\right)^3 > . \end{aligned} \tag{A.49}$$

The following identification process is more or less done in Piquet (2001). The present results are in agreement with Kerr (1985). Identifying (A.20) and (A.36) yields

$$< \left(\frac{\partial u_1}{\partial x_1}\right)^3 >= -\frac{2}{35}\int_0^\infty k^2 T(k,t)\mathrm{d}k, \qquad < \left(\frac{\partial^2 u_1}{\partial x_1^2}\right)^2 >= \frac{2}{35}\int_0^\infty k^4 E(k,t)\mathrm{d}k. \tag{A.50}$$

Using the previous calculations gives

$$< \left(\frac{\partial u_1}{\partial x_1}\right)^3 >= S\left(\frac{\epsilon}{15\nu}\right)^{3/2}, \qquad < \left(\frac{\partial^2 u_1}{\partial x_1^2}\right)^2 > \frac{2K}{3} = G\left(\frac{\epsilon}{15\nu}\right)^2,$$

where $K = 3 < u_1^2 > /2$ is the kinetic energy. This results in

$$S(t) = -\frac{3\sqrt{30}}{14}\frac{\int_0^\infty k^2 T(k,t)\mathrm{d}k}{\left(\int_0^\infty k^2 E(k,t)\mathrm{d}k\right)^{3/2}}, \qquad G(t) = \frac{30\nu}{7}\frac{K}{\epsilon}\frac{\int_0^\infty k^4 E(k,t)\mathrm{d}k}{\int_0^\infty k^2 E(k,t)\mathrm{d}k}. \tag{A.51}$$

Finally, one can write the spectral evolution equation of the kinetic energy dissipation rate as

$$\frac{\partial \epsilon}{\partial t} = -\left(\frac{7}{3\sqrt{15}}S(t)\sqrt{Re_T} + \frac{7}{15}G(t)\right)\frac{\epsilon^2}{K} = -\frac{7}{15}\left(\frac{1}{2}S(t)Re_\lambda + G(t)\right)\frac{\epsilon^2}{K}, \tag{A.52}$$

where the turbulent (or integral) Reynolds number is Re_T was defined in (1.7). The normalized palinstrophy G can be interpreted as the dissipation of enstrophy, and interestingly can be linked to the dissipation skewness S_ϵ of Kerr (1985) through $G = Re_\lambda S_\epsilon/2$ so that (A.52) becomes

$$\frac{\partial \epsilon}{\partial t} = -\frac{7}{30}Re_\lambda\Big(S(t) + S_\epsilon(t)\Big)\frac{\epsilon^2}{K}. \tag{A.53}$$

A.3.4 Results for the passive scalar field

Using the results for B^T_{ijkl} and C^T_{ijkl} gives

$$\epsilon_T = a < \frac{\partial\theta}{\partial x_i}\frac{\partial\theta}{\partial x_i} >= 3a < \left(\frac{\partial\theta}{\partial x_1}\right)^2 >, \qquad < \frac{\partial^2\theta}{\partial x_i\partial x_j}\frac{\partial^2\theta}{\partial x_i\partial x_j} >= 5 < \left(\frac{\partial^2\theta}{\partial x_1\partial x_1}\right)^2 >,$$
$$< \frac{\partial\theta}{\partial x_i}\frac{\partial\theta}{\partial x_j}\frac{\partial u_i}{\partial x_j} >= \frac{15}{2} < \frac{\partial\theta}{\partial x_1}\frac{\partial\theta}{\partial x_1}\frac{\partial u_1}{\partial x_1} > .$$

The following identification process is done in Kerr (1985). Identifying (A.37) and (A.38) yields

$$< \frac{\partial u_1}{\partial x_1}\left(\frac{\partial\theta}{\partial x_1}\right)^2 >= -\frac{2}{15}\int_0^\infty k^2 T_T(k,t)\mathrm{d}k, \qquad < \left(\frac{\partial^2\theta}{\partial x_1^2}\right)^2 >= \frac{2}{5}\int_0^\infty k^4 E_T(k,t)\mathrm{d}k. \tag{A.54}$$

Using the previous calculations gives

$$< \frac{\partial u_1}{\partial x_1}\left(\frac{\partial\theta}{\partial x_1}\right)^2 >= S_T\sqrt{\frac{\epsilon}{15\nu}}\left(\frac{\epsilon_T}{3a}\right), \qquad < \left(\frac{\partial^2\theta}{\partial x_1^2}\right)^2 > 2K_T = G_T\left(\frac{\epsilon_T}{3a}\right)^2,$$

where $K_T =< \theta^2 > /2$ is the scalar variance [1]. This results in

$$S_T(t) = -\sqrt{\frac{3}{10}}\frac{\int_0^\infty k^2 T_T(k,t)dk}{\sqrt{\int_0^\infty k^2 E(k,t)\mathrm{d}k}\left(\int_0^\infty k^2 E_T(k,t)\mathrm{d}k\right)}, \qquad G_T(t) = \frac{18a}{5}\frac{K_T}{\epsilon_T}\frac{\int_0^\infty k^4 E_T(k,t)\mathrm{d}k}{\int_0^\infty k^2 E_T(k,t)\mathrm{d}k}. \tag{A.55}$$

There is an error in Antonia & Orlandi (2004) regarding the numerical factor of S_T. The present result is in agreement with Kerr (1985). Finally, one can write the spectral evolution

[1] For this section only, we choose $K_T =< \theta^2 > /2$ instead of $K_T =< \theta^2 >$ for consistency with some of the reference papers

equation of the scalar variance dissipation rate, with r the kinetic to scalar time scales ratio $r = (K\,\epsilon_T)/(K_T\,\epsilon)$.

$$\frac{\partial \epsilon_T}{\partial t} = -\left(\sqrt{\frac{5}{3}} S_T(t)\sqrt{Re_T} + r\frac{5}{9}G_T(t)\right)\frac{\epsilon\epsilon_T}{K} = -\left(\frac{1}{2}S_T(t)Re_\lambda + r\frac{5}{9}G_T(t)\right)\frac{\epsilon\epsilon_T}{K}. \tag{A.56}$$

A.4 Structure functions and auto-correlations

This section is dedicated to the investigation of structure functions in HIT. So far, the spectral formalism was preferred, for convenience with EDQNM. Nevertheless, correlation and structure functions which depend on $\boldsymbol{r}$, the separation vector between two points located in $\boldsymbol{x}$ and $\boldsymbol{x'}$ so that $\boldsymbol{r} = \boldsymbol{x'} - \boldsymbol{x}$, are another fundamental aspect of the turbulence theory. For this reason, and to extend a bit the range if this thesis, basic results are recovered: notably, the von Karman & Howarth (1938) equation is derived, and then the famous $4/5^{\text{th}}$ law of Kolmogorov (1941*a*) is recovered. In what follows, the prime refers to a quantity expressed in $\boldsymbol{x'}$, the time dependence is sometimes omitted for clarity, and u refers to the rms of the fluctuating velocity. Part of the results of this appendix, notably the $4/3^{\text{rd}}$ laws for the structure functions inertial scalings , were included in the *Journal of Fluid Mechanics* for helicity.

A.4.1 Second-order longitudinal correlation and structure function

The Reynolds stress tensor, defined in (2.2), can be written

$$R_{ij}(r,t) = u^2\frac{f(r,t)-g(r,t)}{r^2}r_i r_j + u^2 g(r,t)\delta_{ij}, \tag{A.57}$$

where f and g are the longitudinal and transverse correlations functions, linked to $R_{ij}(r)$, if one chooses $\boldsymbol{r}$ along the x_1 direction for instance (Pope, 2000), as

$$f(r,t) = \frac{R_{11}(r,t)}{u^2}, \qquad g(r,t) = \frac{R_{22}(r,t)}{u^2} = \frac{R_{33}(r,t)}{u^2}. \tag{A.58}$$

The expression of R_{ij} being symmetric, f and g are even functions of r, so that a Taylor expansion yields

$$f(r) = 1 + f''(0)\frac{r^2}{2} + f^{(iv)}(0)\frac{r^4}{4!} + \dots, \tag{A.59}$$

and similarly for g. The second and fourth derivatives of f for $r \to 0$ can be linked to quantities previously investigated:

$$-u^2 f''(0) = -\lim_{r\to 0}\frac{\partial^2}{\partial r^2} < u_1 u_1' > = - < u_1 \partial_{11}^2 u_1 > = -\Big[\underbrace{< \partial_1(u_1\partial_1 u_1) >}_{=0} - < (\partial_1 u_1)^2 > \Big] = < (\partial_1 u_1)^2 >,$$

where $\partial_1 = \partial/\partial x_1$. This gives, following the results of section A.3, $f''(0) = -\epsilon/(15\nu u^2)$. Then, for $f^{(iv)}(0)$, one needs to use $< \partial_1(u_1\partial_{111}^3 u_1) > = 0$, which gives

$$u^2 f^{(iv)}(0) = \lim_{r\to 0}\frac{\partial^4}{\partial r^4} < u_1 u_1' > = < u_1 \partial_{1111}^4 u_1 > = \underbrace{< \partial_{11}^2(u_1\partial_{11}^2 u_1) >}_{=0} - < (\partial_{11}^2 u_1)^2 > -2\underbrace{< \partial_1 u_1 \partial_{111}^3 u_1 >}_{=-<u_1\partial_{1111}^4 u_1>}.$$

Using the results of section A.3, $< (\partial_{11}^2 u_1)^2 >= 2P/35$, where $P = \int k^4 E(k)\mathrm{d}k$, so that $u^2 f^{(iv)}(0) = 2P/35$. Hence, the **longitudinal correlation** can be expanded in HIT as

$$f(r,t) \sim_{r\to 0} 1 - \frac{\epsilon(t)}{30\nu u^2} r^2 + \frac{P(t)}{420 u^2} r^4. \tag{A.60}$$

The definition of Bos *et al.* (2012) is used for the **two-point second-order longitudinal structure function**

$$D_{\mathrm{LL}}(r,t) =< \delta u_{\mathrm{L}}^2 >= 2\frac{r_i r_j}{r^2}(R_{ij}(0) - R_{ij}(r)), \qquad \delta u_{\mathrm{L}} = \frac{u_i' r_i}{r} - \frac{u_i r_i}{r}, \tag{A.61}$$

where δu_{L} is the longitudinal velocity increment. It is obviously possible to link D_{LL} and $f(r,t)$, and this deserves some details. Considering x_i and x_i' as independent variables, using $\partial r/\partial r_i = r_i/r$, and expending the incompressibility condition $\partial R_{ji}/\partial r_i = 0$, one gets (von Karman & Howarth, 1938)

$$2f(r,t) - 2g(r,t) = -r\frac{\partial f}{\partial r}, \tag{A.62}$$

so that the Reynolds stress tensor can be expressed only as a function of f:

$$R_{ij}(r) = u^2\left(f(r) + \frac{r}{2}\frac{\partial f}{\partial r}\right)\delta_{ij} - \frac{u^2}{2r}\frac{\partial f}{\partial r} r_i r_j. \tag{A.63}$$

Half the trace, $R(r) = R_{ii}(r)/2$, is important since it was used by Saffman (1967) to demonstrate some invariant properties which will be detailed hereafter. In agreement with Davidson *et al.* (2012), one can write

$$< u_i u_i' >= 2R(r) = \frac{1}{r^2}\frac{\partial}{\partial r}(r^3 u^2 f) = u^2(3f + r\partial_r f). \tag{A.64}$$

Injecting (A.63) into (A.61) gives

$$D_{\mathrm{LL}}(r,t) = 2u^2(1 - f(r,t)), \tag{A.65}$$

in agreement with Saffman & Pullin (1996). Finally, following Kolmogorov (1941*b*), the second-order longitudinal structure function scales in the inertial range as $(\epsilon r)^{2/3}$. Furthermore, since $f(r\to\infty) = 0$, one has also, at large scales, $D_{\mathrm{LL}} \sim 2u^2$. And at small r, typically near the Kolmogorov scale η, $\delta u_{\mathrm{L}} \sim r\partial_1 u_1$, so that $D_{\mathrm{LL}} \sim r^2\epsilon/(15\nu)$. This yields

$$D_{\mathrm{LL}}(r,t) = \begin{cases} 2u^2 & \text{for} \quad r > L, \\ C_2(\epsilon r)^{2/3} & \text{for} \quad L > r \gg \eta, \\ r^2\epsilon/(15\nu) & \text{for} \quad r \sim \eta. \end{cases} \tag{A.66}$$

Finally, it is possible to compute f (and thus D_{LL}) from the kinetic energy spectrum. Details are given for D_{LL} in Bos *et al.* (2012), and one has

$$D_{\mathrm{LL}}(r,t) = 4\int_0^\infty E(k,t)\Big[\frac{1}{3} - \frac{\sin(kr)}{(kr)^3} + \frac{\cos(kr)}{(kr)^2}\Big]\mathrm{d}k, \qquad R(r,t) = \int_0^\infty E(k,t)\frac{\sin(kr)}{kr}\mathrm{d}k, \tag{A.67}$$

consistent with another expression in Saffman & Pullin (1996). This relation allows to determine the structure functions from the high Reynolds numbers kinetic energy spectra obtained with EDQNM, as revealed in Fig. A.1a: the r^2 and $r^{2/3}$ scalings for the inertial range are recovered,

and the value $D_{\mathrm{LL}}(\infty) = 2u^2$ at large scales as well. Furthermore, the constant of D_{LL} is found to be $C_2 = 1.73$ in Fig. A.1b, which is a bit less than in Bos *et al.* (2012).

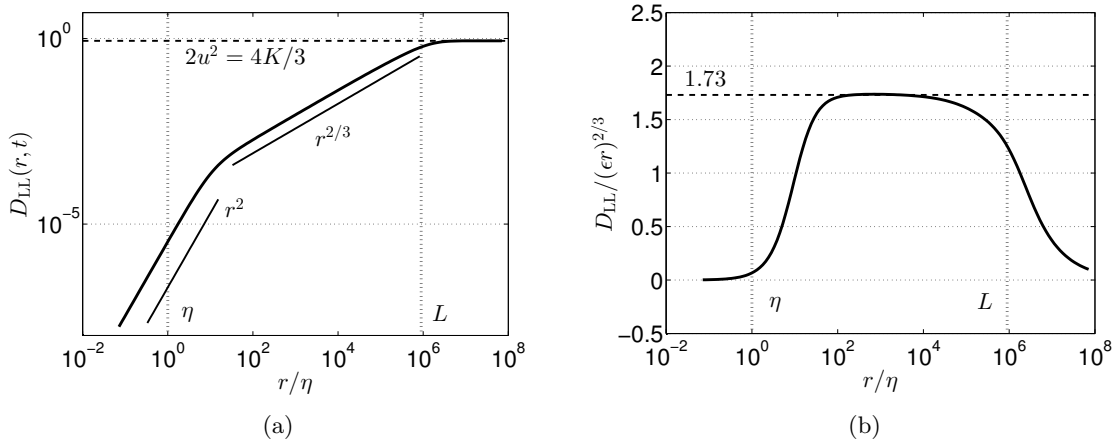

Figure A.1: Longitudinal structure function $D_{\mathrm{LL}}(r,t)$ for $\sigma = 2$ at $Re_\lambda = 2.10^4$. (a) The different scalings. (b) Compensated D_{LL} to obtain $C_2 = 1.73$.

A.4.2 Third-order longitudinal correlation and structure function

The two-point third-order correlation reads (von Karman & Howarth, 1938)

$$< u_i u_j u'_k >= - < u'_i u'_j u_k >= T_{ijk} = r_i r_j r_k \frac{k(r) - h(r) - 2q(r)}{r^3} + \delta_{ij} \frac{r_k h(r)}{r} + \frac{q(r)}{r}(\delta_{ik} r_j + \delta_{jk} r_i), \tag{A.68}$$

and the incompressibility condition $\partial T_{ijk}/\partial r_k = 0$ yields

$$k(r) = -2h(r), \qquad q(r) = -h(r) - \frac{r}{2}\frac{\partial h}{\partial r}, \tag{A.69}$$

so that T_{ijk} can only be expressed as a function of k or h. Of particular interest, k can be expanded, for $r \to 0$, as

$$k(r) = k'''(0)\frac{r^3}{6} + \ldots, \tag{A.70}$$

and $k'''(0)$ is linked to the mixed-derivative skewness $S(t)$ analyzed earlier, using $< \partial_1(u_1 \partial_1 u_1 \partial_1 u_1) >= 0$:

$$k'''(0) = \lim_{r\to 0} \frac{\partial^3}{\partial r^3} < u_1 u_1 u'_1 >=< u_1 u_1 \partial^3_{111} u_1 >= \underbrace{< \partial_1(u_1^2 \partial^2_{11} u_1) >}_{=0} - \underbrace{2 < u_1 \partial_1 u_1 \partial^2_{11} u_1 >}_{=-<(\partial_1 u_1)^3>},$$

so that

$$k'''(0) =< \left(\frac{\partial u_1}{\partial x_1}\right)^3 >= S(t)\left(\frac{\epsilon}{15\nu}\right)^{3/2}. \tag{A.71}$$

Then, the **two-point third-order longitudinal structure function** D_{LLL} can be linked to the third-order correlation k through

$$D_{\mathrm{LLL}}(r,t) =< \delta u_{\mathrm{L}}^3 >= 6\frac{r_i r_j r_k}{r^3} T_{ijk}(r) = 6k(r). \tag{A.72}$$

Interestingly, the velocity derivative skewness can be expressed as

$$S(t) = \lim_{r\to 0} \frac{D_{\mathrm{LLL}}}{D_{\mathrm{LL}}^{3/2}}. \tag{A.73}$$

Finally, $D_{\mathrm{LLL}}(r,t)$ can be computed from the non-linear kinetic energy transfers $T(k,t)$, and details are provided in Bos *et al.* (2012)

$$D_{\mathrm{LLL}}(r,t) = 12r \int_0^\infty T(k,t)\Big[\frac{3(\sin(kr) - (kr)\cos(kr)) - (kr)^2\sin(kr)}{(kr)^5}\Big]\mathrm{d}k. \tag{A.74}$$

A.4.3 Towards the Kármán-Howarth equation

All the ingredients to obtain the evolution equation of $u^2 f$, or equivalently D_{LL}, have been presented. Starting from (2.1), without mean-velocity gradients, and multiplying by u'_k, and then combining it with (2.1) written for u'_k multiplied by u_i yields

$$\frac{\partial R_{ik}}{\partial t} = \frac{\partial}{\partial r_j}(T_{ijk} + T_{kji}) + 2\nu \frac{\partial^2 R_{ik}}{\partial r_j \partial r_j}. \tag{A.75}$$

Here are some details:

$$\begin{aligned}
\frac{1}{u^2}\frac{\partial R_{ik}}{\partial t} &= \frac{r_i r_k}{r^2}\left[\frac{\partial f}{\partial t} - \frac{\partial g}{\partial t}\right] + \delta_{ik}\frac{\partial g}{\partial t},\\
\frac{1}{u^2}\frac{\partial^2 R_{ik}}{\partial r_j \partial r_j} &= \frac{r_i r_k}{r^2}\left[\frac{-6}{r^2}(f-g) + \frac{2}{r}\left(\frac{\partial f}{\partial r} - \frac{\partial g}{\partial r}\right) + \left(\frac{\partial^2 f}{\partial r^2} - \frac{\partial^2 g}{\partial r^2}\right)\right] + \delta_{ik}\left[\frac{2}{r^2}(f-g) + \frac{2}{r}\frac{\partial g}{\partial r} + \frac{\partial^2 g}{\partial r^2}\right],\\
\frac{\partial}{\partial r_j}(T_{ijk} + T_{kji}) &= \frac{r_i r_k}{r^2}\left[\frac{-4}{r}h + 4\frac{\partial h}{\partial r} + r\frac{\partial^2 h}{\partial r^2}\right] + \delta_{ik}\left[\frac{-4}{r}h - 6\frac{\partial h}{\partial r} - r\frac{\partial^2 h}{\partial r^2}\right].
\end{aligned}$$

The equation with δ_{ik} allows to determine $\partial_t g$, and further using (A.62) allows to recover the **Kármán-Howarth equation**

$$\boxed{\frac{\partial(u^2 f)}{\partial t} - \frac{1}{r^4}\frac{\partial r^4 k}{\partial r} = 2\nu \frac{u^2}{r^4}\frac{\partial}{\partial r}\left(r^4 \frac{\partial f}{\partial r}\right).} \tag{A.76}$$

From this, it is possible to express the evolution equation of $R(r)$, defined in (A.64), in agreement with Davidson (2010)

$$\frac{\partial R}{\partial t} - \frac{1}{2r^2}\frac{\partial}{\partial r}\left(\frac{1}{r}\frac{\partial}{\partial r}(r^4 k)\right) = 2\nu \frac{1}{r^2}\frac{\partial}{\partial r}\left(r^2 \frac{\partial R}{\partial r}\right). \tag{A.77}$$

Using the relations between f, k and D_{LL}, D_{LLL}, and $d_t u^2 = -2\epsilon/3$, one obtains the **Kármán-Howarth-Kolmogorov equation**

$$\frac{\partial D_{\mathrm{LL}}}{\partial t} + \frac{1}{3r^4}\frac{\partial}{\partial r}(r^4 D_{\mathrm{LLL}}) = \frac{2\nu}{r^4}\frac{\partial}{\partial r}\left(r^4 \frac{\partial D_{\mathrm{LL}}}{\partial r}\right) - \frac{4}{3}\epsilon. \tag{A.78}$$

Multiplying (A.78) by r^4, and integrating from 0 to r yields (Saffman & Pullin, 1996)

$$\frac{3}{r^4}\int_0^r s^4 \frac{\partial D_{\mathrm{LL}}}{\partial t}\mathrm{d}s + D_{\mathrm{LLL}} = 6\nu \frac{\partial D_{\mathrm{LL}}}{\partial r} - \frac{4}{5}\epsilon r. \tag{A.79}$$

Neglecting the time derivative and viscous dissipation at high Reynolds numbers in the inertial range yields the $4/5^{\mathbf{th}}$ **law**

$$\boxed{D_{\mathrm{LLL}}(r,t) = -\frac{4}{5}\epsilon r.} \tag{A.80}$$

This relation is assessed in Fig. A.2b, along with the scaling for $< \delta u_{\mathrm{L}} \delta q^2 >$ derived hereafter. Even at Reynolds numbers such as 2.10^4, the theoretical expectation $4/5$ is not rigorously reached, as in Bos *et al.* (2012) for freely decaying turbulence. It is noteworthy to remark that unlike D_{LL}, the integration for D_{LLL} requires quadruple precision, otherwise one gets strong oscillations as in Tchoufag *et al.* (2012). Furthermore, the small scale r^3 scaling for both $< \delta u_{\mathrm{L}} \delta q^2 >$ and $< \delta u_{\mathrm{L}}^3 >$ is recovered in Fig. A.2a, followed by the linear dependence in r.

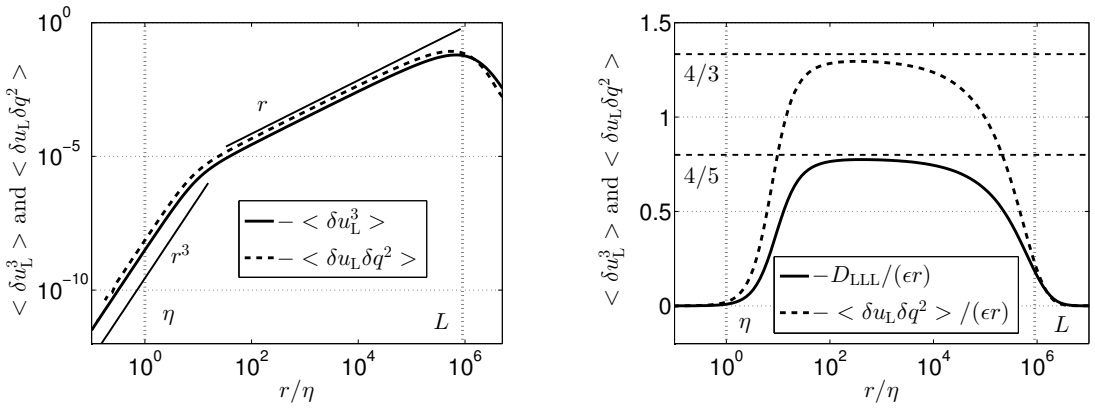

(a) (b)

Figure A.2: Kinetic third-order structure functions $< \delta u_{\mathrm{L}}^3 >$ and $< \delta u_{\mathrm{L}} \delta q^2 >$ for $\sigma = 2$ at $Re_\lambda = 2.10^4$. (a) The different scalings. (b) Compensated kinetic structures functions.

Invariants: Saffman and Batchelor turbulence are now briefly discussed in terms of invariants, as done in Davidson (2010). The expansion of the kinetic energy spectrum for very low wavenumbers yields

$$E(k \to 0) = L\frac{k^2}{4\pi^2} + I\frac{k^4}{24\pi^2}, \tag{A.81}$$

where L and I are the Saffman and Loitsiansky integrals respectively. For the Saffman integral L, associated to the conservation of linear momentum, one has

$$L = \int < u_i u_i' > \mathrm{d}\boldsymbol{r} = 4\pi \int_0^\infty 2r^2 R(r)\mathrm{d}r = 4\pi[r^3 u^2 f]_\infty, \tag{A.82}$$

meaning that when $L \neq 0$ initially (*i.e.* $E(k \to 0) \sim k^2$), the longitudinal function should decrease as $f \sim r^{-3}$ when $r \to \infty$. Furthermore, it was shown by Saffman (1967) that $\int r^2 R\mathrm{d}r$, and so L, is an invariant of motion in freely decaying turbulence: this can be shown by integration of (A.77) multiplied by r^2,

$$\frac{1}{8\pi}\frac{\mathrm{d}L}{\mathrm{d}t} - \frac{1}{2r}\frac{\partial}{\partial r}(r^4 k) = 2\nu r^2 \frac{\partial R}{\partial r},$$

and further neglecting the viscous term for high Reynolds numbers, so that

$$\frac{\mathrm{d}L}{\mathrm{d}t} = 4\pi\left[\frac{1}{r}\frac{\partial}{\partial r}(r^4 k)\right]. \tag{A.83}$$

Since $k \sim r^{-4}$, L is independent of time and is consequently an invariant of motion. For the Loitsiansky integral, linked to the conservation of angular momentum,

$$I = -\int r^2 < u_i u_i' > \mathrm{d}\boldsymbol{r} = -4\pi \int_0^\infty 2r^4 R(r)\mathrm{d}r = -4\pi \int_0^\infty r^2 \frac{\partial}{\partial r}(r^3 u^2 f)\mathrm{d}r \sim -4\pi[r^5 u^2 f], \tag{A.84}$$

meaning that when $L = 0$ initially (*i.e.* $E(k \to 0) \sim k^4$), the longitudinal function should decrease as $f \sim r^{-5}$ when $r \to \infty$.

Kármán-Howarth $4/3^{\mathrm{rd}}$ **equation**: the Kármán-Howarth-Kolmogorov equation (A.78) can be written differently: instead of considering the longitudinal second-order structure function δu_{L}^2, the emphasis is put on the kinetic energy increment $\delta q^2 = \delta u_i \delta u_i$. The method to derive this equation is detailed in Antonia *et al.* (1997), and the procedure is very similar to the $4/3^{\mathrm{rd}}$ law derived in Yaglom (1949) for passive scalar structure function, developed in the next section. For clarity, $\partial_j' = \partial/\partial x_j'$ and $\partial_j = \partial/\partial x_j$. Subtracting the evolution equation of u_i' to the one of u_i, one gets

$$\partial_t \delta u_i + \delta u_j \frac{\partial}{\partial r_j}(\delta u_i) + u_j(\partial_j' + \partial_j)(\delta u_i) = -(\partial_i' + \partial_i)(\delta p) + \nu(\partial_{jj}' + \partial_{jj})(\delta u_i), \tag{A.85}$$

where $\delta u_j \partial_{r_j} \delta u_i + u_j(\partial_j' + \partial_j)(\delta u_i) = \partial_j'(u_i' u_j') - \partial_j(u_i u_j)$. Multiplying the previous equation by $2\delta u_i$ and using ensemble average yields

$$\frac{\partial}{\partial t} < \delta q^2 > + \frac{\partial}{\partial r_j} < \delta u_j \delta q^2 >= 2\nu \frac{\partial^2}{\partial r_j \partial r_j} < \delta q^2 > -4\underbrace{\nu < \frac{\partial \delta u_i}{\partial r_j}\frac{\partial \delta u_i}{\partial r_j} >}_{=\epsilon}. \tag{A.86}$$

Both the $u_j(\partial_j' + \partial_j)$ and pressure terms are zero because $\partial_j' = \partial_{r_j} = -\partial_j$. Further neglecting the time derivative and writing $-4\epsilon = -4/3\partial_{r_j}(\epsilon r_j)$, one gets

$$< \delta u_j \delta q^2 >= 2\nu \frac{\partial}{\partial r_j} < \delta q^2 > -\frac{4}{3}\epsilon r_j, \tag{A.87}$$

where the result of von Karman & Howarth (1938) has been used: $2f/r + f' = 0 \leftrightarrow f = 0$, combined with $\partial^2/(\partial r_j \partial r_j) = (2/r\partial_r + \partial_{rr}^2)$. At high Reynolds numbers in the inertial range, this eventually gives after the use of the divergence theorem

$$\boxed{< \delta u_{\mathrm{L}} \delta q^2 > (r,t) = -\frac{4}{3}\epsilon r.} \tag{A.88}$$

It is possible to make a link between (A.80) and (A.88): using $< \delta q^2 >= 4K - 4R$ and further identifying the evolution equations of $< \delta q^2 >$ and R yields

$$3r^3 < \delta u_{\mathrm{L}} \delta q^2 >= \frac{\partial}{\partial r}(r^4 < \delta u_{\mathrm{L}}{}^3 >). \tag{A.89}$$

A similar reasoning is proposed in Chapter 8 for HHT. Using the previous relation, one gets

$$< \delta u_{\mathrm{L}} \delta q^2 > (r,t) = 4\int_0^\infty \frac{T(k,t)}{k}\left(\frac{\sin(kr)}{(kr)^2} - \frac{\cos(kr)}{kr}\right)\mathrm{d}k, \tag{A.90}$$

which is very similar to the formula for D_{LTT} derived hereafter. Finally, (A.88) is assessed in

Fig. A.2b, along with the r^3 small scale scaling of $< \delta u_{\rm L} \delta q^2 >$ in Fig. A.2a. As remarked before, even at $Re_\lambda = 2.10^4$, the 4/3 is not exactly recovered. Interestingly, double precision is enough to compute $< \delta u_{\rm L} \delta q^2 >$, unlike $D_{\rm LLL}$.

A.4.4 Yaglom and Corrsin equations

The Yaglom (1949) equation can be obtained in a completely analogous manner, by defining the scalar increment, and the **scalar two-points second and third order structure functions**

$$\delta\theta = \theta' - \theta, \qquad D_{\rm TT} =< \delta\theta\delta\theta >, \qquad D_{\rm LTT} =< \delta u_{\rm L}\delta\theta\delta\theta > . \tag{A.91}$$

Interestingly, the mixed derivative skewness can be expressed as

$$S_{u\theta}(t) = \lim_{r\to 0} \frac{D_{\rm LTT}}{D_{\rm TT} D_{\rm LL}^{1/2}}, \tag{A.92}$$

and simple dimensional arguments give

$$D_{\rm TT}(r,t) = \begin{cases} 2\theta^2 & \text{for} \quad r > L, \\ C_2^T r^{2/3}\, \epsilon_T\, \epsilon^{-1/3} & \text{for} \quad L > r \gg \eta, \\ r^2 \epsilon_T/(3a) & \text{for} \quad r \sim \eta, \end{cases} \tag{A.93}$$

and this is illustrated in Fig. A.3, where the three different scalings are recovered. The constant $C_2^T = 1.88$ is slightly higher than C_2, qualitatively in agreement with Watanabe & Gotoh (2004), despite the much highers constant in the latter reference. The present C_2^T is in reasonable agreement with Yeung *et al.* (2002).

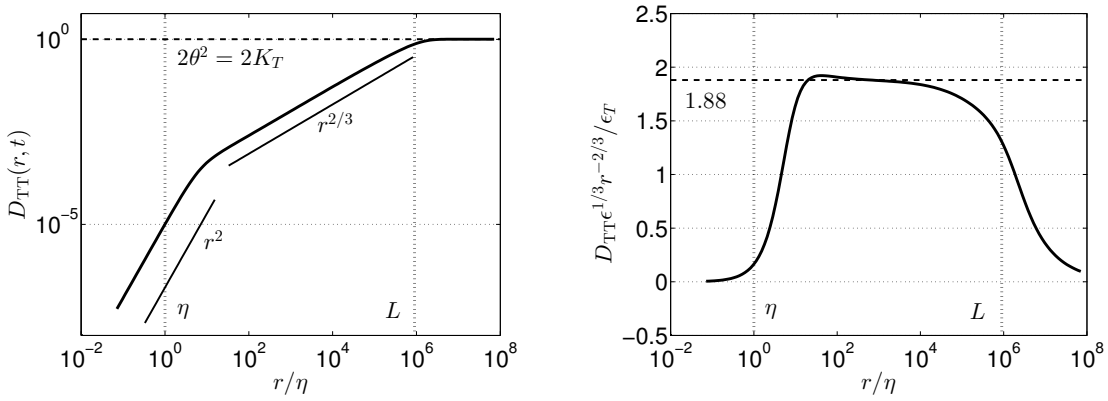

(a) (b)

Figure A.3: Structure function $D_{\rm TT}(r,t)$ for $\sigma = 2$ at $Re_\lambda = 2.10^4$. (a) The different scalings. (b) Compensated $D_{\rm TT}$ to obtain $C_2^T = 1.88$.

A procedure similar to the one done for the equation of $< \delta q^2 >$ yields

$$\frac{\partial}{\partial t} < \delta\theta\delta\theta > + \frac{\partial}{\partial r_j} < \delta u_j \delta\theta\delta\theta >= 2a \frac{\partial^2}{\partial r_j \partial r_j} < \delta\theta\delta\theta > \underbrace{-4a < \frac{\partial \delta\theta}{\partial r_j}\frac{\partial \delta\theta}{\partial r_j} >}_{=-4/3\partial_{r_j}(\epsilon_T r_j)} . \tag{A.94}$$

Neglecting the time derivative and using the previous result of von Karman & Howarth (1938) yields the **Yaglom equation**

$$< \delta u_j \delta\theta\delta\theta >= 2a\frac{\partial}{\partial r_j} < \delta\theta\delta\theta > -\frac{4}{3}\epsilon_T r_j, \tag{A.95}$$

which reduces, in the inertial range, along $\boldsymbol{r}$, to the $4/3^{\mathbf{rd}}$ **law**

$$\boxed{< \delta u_{\mathrm{L}} \delta\theta\delta\theta > (r,t) = -\frac{4}{3}\epsilon_T r.} \tag{A.96}$$

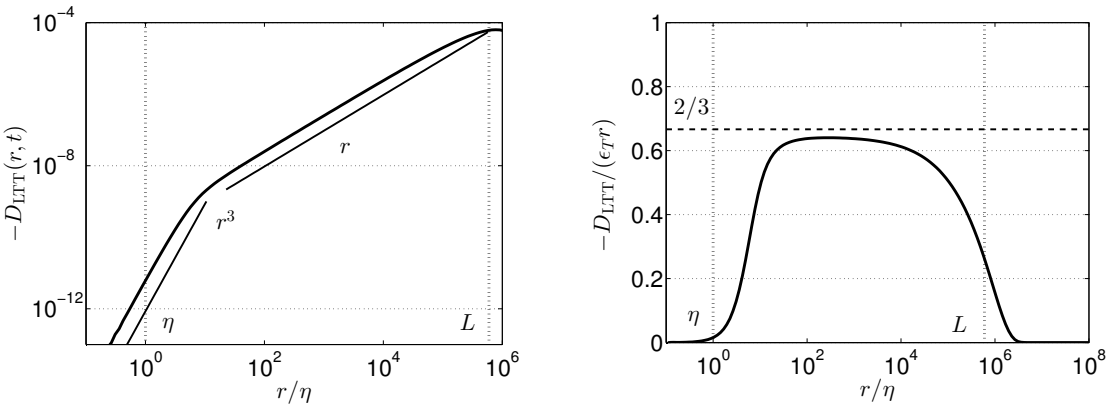

(a) (b)

Figure A.4: Scalar structure function $D_{\mathrm{LTT}}(r,t)$ for $\sigma = 2$ at $Re_\lambda = 2.10^4$. (a) The different scalings. (b) Compensated scalar structure function D_{LTT}.

This result can also be obtained in a way much more similar to von Karman & Howarth (1938), as detailed in Danaila *et al.* (1999*a*). First, one starts with the **Corrsin equation** (Corrsin, 1951*a*)

$$\boxed{\frac{\partial}{\partial t} < \theta\theta' >= 2\left(\frac{2}{r} + \frac{\partial}{\partial r}\right)\left[< u_{\mathrm{L}}\theta\theta' > +a\frac{\partial}{\partial r} < \theta\theta' >\right],} \tag{A.97}$$

The links between correlations and structure functions are

$$R^T(r,t) =< \theta\theta' >=< \theta^2 > -D_{\mathrm{TT}}/2, \qquad D_{\mathrm{LTT}} = 4 < u_{\mathrm{L}}\theta\theta' >, \tag{A.98}$$

and $r_j < u_{\mathrm{L}}\theta\theta' > /r =< u_j\theta\theta' >$. Let's point out that

$$-R^{T''}(0) = -\lim_{r\to 0}\frac{\partial^2}{\partial r^2} < \theta\theta' >= - < \theta\partial_{11}^2\theta >=< (\partial_1\theta)^2 >= \frac{\epsilon_T}{3a}.$$

Then, since $r^2(2/r + \partial_r)[f] = \partial_r(r^2 f)$, (A.97) can be simplified: multiplying by r^2, integrating, and then dividing by r^2, with $\partial_t\theta^2 = -2\epsilon_T$ yields

$$\frac{1}{r^2}\int_0^r s^2\frac{\partial D_{\mathrm{TT}}}{\partial t}\mathrm{d}s = -D_{\mathrm{LTT}} + 2a\frac{\partial D_{\mathrm{TT}}}{\partial r} - \frac{4}{3}r\epsilon_T. \tag{A.99}$$

Finally, the links between structure functions and scalar variance spectra, even though less documented, are simply

$$< \theta\theta' > (r,t) = \int_0^\infty E_T(k,t)\frac{\sin(kr)}{kr}\mathrm{d}k, \qquad D_{\mathrm{TT}}(r,t) = 2\int_0^\infty E_T(k,t)\left(1-\frac{\sin(kr)}{kr}\right)\mathrm{d}k. \tag{A.100}$$

As for the scalar non-linear transfer, it can be found starting from the Corrsin equation (A.97) and identifying with (1.8)

$$\frac{2}{r^2}\frac{\partial}{\partial r}(r^2 < u_{\mathrm{L}}\theta\theta' >) = \int_0^\infty T_T(k)\frac{\sin(kr)}{kr}\mathrm{d}k,$$

so that eventually

$$D_{\mathrm{LTT}}(r,t) = 2\int_0^\infty \frac{T_T(k,t)}{k}\left(\frac{\sin(kr)}{(kr)^2}-\frac{\cos(kr)}{kr}\right)\mathrm{d}k. \tag{A.101}$$

It is revealed in Fig. A.4 that $-D_{\mathrm{LTT}}/(\epsilon_T r)$ closely approaches 2/3 at very large Reynolds numbers (the constant is 2/3 in the present simulations because $\epsilon_T = 2a < (\partial_i\theta)^2 >$). Furthermore, the linear scaling in r in the inertial range is recovered, along with the r^3 scaling at small scales.

Appendix B

Non-local Expansions of the Non-Linear Transfers

In this part, details on the calculation of non-local expansions of the non-linear transfers are given. These non-local expansions are crucial for the scalar field when the Prandtl number is such that $Pr \gg 1$. These expansions where extensively discussed for the velocity field by Lesieur & Schertzer (1978); Métais & Lesieur (1986). The main elements of the computation are gathered here. The need to evaluate these non-local contributions arises from the logarithmic discretization of the wavenumber space that cannot take into account the elongated triads. The criterion to quantify the non-local transfer is

$$\frac{\inf(k,p,q)}{\sup(k,p,q)} \leq a, \tag{B.1}$$

where a is the **non-local parameter**. Numerically, $a = r - 1$ where $k_{i+1} = rk_i$, $r = 10^{1/f}$ with f is the number of discrete points per decade. The regions of the plane (p, q) corresponding to the non-local interactions are displayed in grey in Fig. B.1. For simplicity reasons, only the isotropic parts of the non-linear transfers are firstly expanded, and the third-order correlations characteristic time $\theta^{(T)}_{kpq}$ is always expanded at the lowest order.

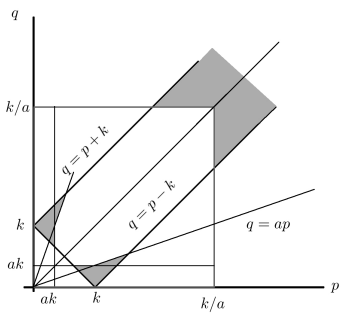

Figure B.1: Non-local interactions (in grey) in the plane (p, q).

B.1 Non-local fluxes

It is recalled that

$$S^{\mathrm{NL(iso)}}(k,t) = \int_{\Delta_k} \theta_{kpq} \frac{(xy+z^3)}{q} E(q)\Big(k^2 E(p) - p^2 E(k)\Big)\mathrm{d}p\mathrm{d}q = \int_{\Delta_k} S(k,p,q)\mathrm{d}p\mathrm{d}q, \tag{B.2}$$

$$S_T^{\mathrm{NL(iso)}}(k,t) = \int_{\Delta_k} \theta^T_{kpq} \frac{(xy+z)}{q} E(q)\Big(k^2 E_T(p) - p^2 E_T(k)\Big)\mathrm{d}p\mathrm{d}q = \int_{\Delta_k} S_T(k,p,q)\mathrm{d}p\mathrm{d}q. \tag{B.3}$$

The non-local transfers from large scales to very small ones are such that $q \ll k \sim p$. They are referred to as $T^+(k,t)$ and $T_T^+(k,t)$, for the velocity and scalar fields respectively. The non-local transfers in the opposite direction are such that $k \ll p \sim q$ and are referred to as $T^-(k,t)$ and $T_T^-(k,t)$. For convenience, these non-local transfers are computed through their associated energy-conservative non-local fluxes, so that

$$\Pi_{(T)}^{\text{Non-Local}}(k,t) = \int_k^\infty T_{(T)}^{\text{Non-Local}}(k',t)\mathrm{d}k', \tag{B.4}$$

$$T_{(T)}^{\pm}(k,t) = -\frac{\partial \Pi_{(T)}^{\pm}(k,t)}{\partial k} = -\frac{\partial}{\partial k}\Big(\Pi_{(T)}^{+}(k,t) - \Pi_{(T)}^{-}(k,t)\Big), \tag{B.5}$$

where the derivation is done numerically. Therefore, the non-local fluxes read (Lesieur & Schertzer, 1978)

$$\begin{aligned}\Pi_{(T)}^{+}(k,t) &= 2\int_0^{ak}\mathrm{d}q\int_k^{k+q}\mathrm{d}k'\int_{k'-q}^{k} S_{(T)}(k',p,q)\mathrm{d}p,\\ \Pi_{(T)}^{-}(k,t) &= 2\int_0^{k}\mathrm{d}k'\int_{\sup(k,k'/a)}^{\infty}\mathrm{d}p\int_{p-k'}^{p} S_{(T)}(k',p,q)\mathrm{d}q.\end{aligned} \tag{B.6}$$

The region of non-local transfers is the grey part of the rectangle Δ_k delimited by $q = p + k$ and $q = p - k$ in Fig. B.1. These regions being symmetric with respect to $q = p$, this justifies the factor 2. The condition (B.1) yields

$$\Pi_{(T)}^{+} : \begin{cases} q < ap \\ q < ak, \end{cases} \qquad \Pi_{(T)}^{-} : \begin{cases} p > k/a \\ q > k/a. \end{cases}$$

Since $k' < k$ for $\Pi_{(T)}^{-}$, it could happen that $k > k'/a$. This is the reason why $\sup(k, k'/a)$ is chosen in the bound. Then, it has been shown (Lesieur & Schertzer, 1978) that

$$S_{(T)}(k,p,q) + S_{(T)}(p,q,k) + S_{(T)}(q,k,p) = 0. \tag{B.7}$$

Because of (p,q) symmetry, one has $S_{(T)}(p,q,k) = 0$. This allows to compute the non-local flux in a symmetric way

$$S_{(T)}(k,p,q) = \frac{1}{2}\Big(S_{(T)}(k,p,q) - S_{(T)}(q,k,p)\Big). \tag{B.8}$$

The final expressions are gathered in Lesieur (2008), and in what follows, these expressions are recovered. Before that, let's discuss the **conservation property** (B.7), which relies on the

(p,q) symmetry: starting from (2.15) for T_{ij}^{NL}, one has

$$T_{ii}^{\mathrm{NL}}(\boldsymbol{k}) = k_n \int S_{nii}(\boldsymbol{k},\boldsymbol{p})\mathrm{d}^3\boldsymbol{p} + k_m \int S_{iim}^*(\boldsymbol{k},\boldsymbol{p})\mathrm{d}^3\boldsymbol{p} = \int s(\boldsymbol{k},\boldsymbol{p},\boldsymbol{q})\mathrm{d}^3\boldsymbol{p},$$

with

$$s(\boldsymbol{k},\boldsymbol{p},\boldsymbol{q}) = k_n < \hat{u}_n''\hat{u}_i\hat{u}_i' > + k_m < \hat{u}_m'\hat{u}_i\hat{u}_i'' > . \tag{B.9}$$

Further using $k_n + q_n = -p_n$ and incompressibility so that $p_n u_n' = 0$ yields

$$s(\boldsymbol{k},\boldsymbol{p},\boldsymbol{q}) + s(\boldsymbol{q},\boldsymbol{k},\boldsymbol{p}) + s(\boldsymbol{p},\boldsymbol{q},\boldsymbol{k}) = 0. \tag{B.10}$$

A similar property can be written for the scalar field. Using (p,q) symmetry, one can write the term under the integral in (4.7) as

$$s^T(\boldsymbol{k},\boldsymbol{p},\boldsymbol{q}) = 2k_j < \hat{u}_j'\hat{\theta}\hat{\theta}'' > + k_j < \hat{u}_j''\hat{\theta}\hat{\theta}' >, \tag{B.11}$$

so that for the same reasons

$$s^T(\boldsymbol{k},\boldsymbol{p},\boldsymbol{q}) + s^T(\boldsymbol{q},\boldsymbol{k},\boldsymbol{p}) + s^T(\boldsymbol{p},\boldsymbol{q},\boldsymbol{k}) = 0. \tag{B.12}$$

B.2 Expansions for $q \ll k \sim p$

The small parameter of the expansion is $\zeta = q/k$. Firstly, p is expanded as

$$p = k\left(1 - y\zeta + \frac{1}{2}(1-y^2)\zeta^2\right), \text{ and } \qquad p^{-1} = k^{-1}\left(1 + y\zeta + \frac{1}{2}(3y^2-1)\zeta^2\right).$$

Then, geometrical relations yield

$$z = 1 - \frac{1}{2}(1-y^2)\zeta^2, \text{ and } \qquad x = \frac{-k^2+p^2+q^2}{2pq} = -y + (1-y^2)\zeta + \frac{3}{2}y(1-y^2)\zeta^2.$$

This gives

$$xy + z^3 = (1-y^2)\left(1 + y\zeta - \frac{3}{2}(1-y^2)\zeta^2\right), \qquad xy + z = (1-y^2)\left(1 + y\zeta + \frac{1}{2}(3y^2-1)\zeta^2\right),$$
$$xz + y^3 = (1-y^2)\left(-y + \zeta + 2y\zeta^2\right), \qquad xz + y = (1-y^2)\zeta(1+2y\zeta).$$

Then, a Taylor expansion provides

$$E_{(T)}(p) = E_{(T)}(k) - qy\frac{\partial E_{(T)}}{\partial k} + \frac{1}{2}\zeta^2\left((1-y^2)k\frac{\partial E_{(T)}}{\partial k} + y^2k^2\frac{\partial^2 E_{(T)}}{\partial k^2}\right).$$

The method is the following one: the different quantities are expressed as a function of y (the cosine of the angle in front of $\boldsymbol{p}$) and the small parameter $\zeta = q/k$. Then, the p-integration is done by using y and the variable

$$y' = \frac{k'^2 - k^2 + q^2}{2k'q}$$

so that

$$\int_{k'-p}^{k} S_{(T)}(k',p,q)\mathrm{d}p = \int_{y'}^{1} \frac{k'q}{p} S_{(T)}(k',p,q)\mathrm{d}y.$$

Finally, the last integration, assuming that $\theta^{(T)}_{k'k'q} \simeq \theta^{(T)}_{kkq}$, is done according to

$$\int_{k}^{k+q} (\ldots)\mathrm{d}k' = q\int_{0}^{1} (\ldots)\mathrm{d}y', \tag{B.13}$$

and one has in particular

$$\int_0^1\int_{y'}^1 y(1-y^2)\mathrm{d}y\mathrm{d}y' = \frac{2}{15}, \qquad \int_0^1\int_{y'}^1 (1-y^2)\mathrm{d}y\mathrm{d}y' = \frac{1}{4},$$

Computation of $\Pi^+(k,t)$: firstly, one has

$$\begin{aligned}
k^2E(p) - p^2E(k) &= k^2\Big[y\zeta\left(2E(k) - k\frac{\partial E}{\partial k}\right) + \zeta^2\left(-E(k) + \frac{1-y^2}{2}k\frac{\partial E}{\partial k} + \frac{y^2}{2}k^2\frac{\partial^2 E}{\partial k^2}\right)\Big],\\
\frac{kq}{p}\frac{(xy+z^3)}{q} &= (1-y^2)\left(1+2y\zeta+2(2y^2-1)\zeta^2\right),\\
\frac{kq}{p}S(k,p,q) &= \theta_{kkq}(1-y^2)E(q)\Bigg[ykq\left(2E(k) - k\frac{\partial E}{\partial k}\right)\\
&\quad + q^2\left((4y^2-1)E(k) + \frac{1}{2}(1-5y^2)k\frac{\partial E}{\partial k} + \frac{y^2}{2}k^2\frac{\partial^2 E}{\partial k^2}\right)\Bigg].
\end{aligned}$$

At the lowest order in q, only the first rhs term remains. Secondly,

$$\begin{aligned}
\frac{kq}{p}\frac{(xz+y^3)}{p} &= \zeta(1-y^2)(-y + (1-2y^2)\zeta + y(5-4y^2)\zeta^2),\\
\frac{kq(xz+y^3)}{p^2}q^2E(p)E(k) &= (1-y^2)E(k)\left(-yq^2\zeta E(k) + q^2\zeta^2\Big[(1-2y^2)E(k) + y^2k\frac{\partial E}{\partial k}\Big]\right),\\
\frac{kq(xz+y^3)}{p^2}k^2E(p)E(q) &= (1-y^2)E(q)\Bigg(-kqy\left(E(k) - qy\frac{\partial E}{\partial k}\right)\\
&\quad + q^2\Big[(1-2y^2)E(k) + \frac{1}{2}qy(5y^2-3)\frac{\partial E}{\partial k} - \frac{1}{2}qky^3\frac{\partial^2 E}{\partial k^2}\Big]\Bigg).
\end{aligned}$$

Using equation (B.8), this yields

$$\begin{aligned}
2\frac{kq}{p}S(k,p,q) &= \theta_{kkq}(1-y^2)\Bigg[E(k)\Big[yq^2\zeta E(k) - q^2\zeta^2\left((1-2y^2)E(k) + y^2k\frac{\partial E}{\partial k}\right)\Big]\\
&\quad + E(q)\Big[kqy\left(E(k) - k\frac{\partial E}{\partial k}\right) + q^2\left(2y^2E(k) + \frac{1}{2}(1-3y^2)k\frac{\partial E}{\partial k} + \frac{1}{2}y^2k^2\frac{\partial^2 E}{\partial k^2}\right)\Big]\Bigg].
\end{aligned}$$

At the lowest order

$$2\frac{kq}{p}S(k,p,q) = \theta_{kkq}y(1-y^2)\Big[E(k)^2q^2\zeta + kqE(q)\left(E(k) - k\frac{\partial E}{\partial k}\right)\Big].$$

Hence, the **direct non-local kinetic flux** is

$$\Pi^+(k,t) = \frac{2}{15}k\left(E(k) - k\frac{\partial E}{\partial k}\right)\int_0^{ak}\theta_{kkq}q^2E(q)\mathrm{d}q + \frac{2}{15}\frac{E(k)^2}{k}\int_0^{ak}\theta_{kkq}q^4\mathrm{d}q. \tag{B.14}$$

Computation of $\Pi_T^+(k,t)$: the calculation is very similar to the previous one. One has

$$\frac{kq}{p}\frac{(xy+z)}{q} = (1-y^2)\left(1+2y\zeta+(4y^2-1)\zeta^2\right),$$

so that

$$\frac{kq}{p}\frac{(xy+z)}{q}E(q)(k^2E_T(p)-p^2E_T(k)) = (1-y^2)\Bigg[kqy\left(2E_T(k)-k\frac{\partial E_T}{\partial k}\right)$$
$$+q^2\left((4y^2-1)E_T(k)+\frac{1-5y^2}{2}k\frac{\partial E_T}{\partial k}+\frac{1}{2}y^2k^2\frac{\partial^2 E_T}{\partial k^2}\right)\Bigg]. \tag{B.15}$$

Then

$$\frac{kq}{p}\frac{(xz+y)}{p}E(p)(q^2E_T(k)-k^2E_T(q)) = (1-y^2)(1+4y\zeta)q^2E(k)\Big[E_T(k)\zeta^2-E_T(q)\Big].$$

Using (B.8), one obtains the **direct non-local scalar flux** at the lowest order

$$\Pi_T^+(k,t) = \frac{2}{15}k\left(2E_T(k)-k\frac{\partial E_T}{\partial k}\right)\int_0^{ak}\theta_{kkq}^Tq^2E(q)\mathrm{d}q$$
$$+\frac{1}{4}E(k)\int_0^{ak}\theta_{kkq}^Tq^3E_T(q)\mathrm{d}q - \frac{1}{4}\frac{E(k)E_T(k)}{k^2}\int_0^{ak}\theta_{kkq}^Tq^5\mathrm{d}q. \tag{B.16}$$

The non-local fluxes are displayed in Fig. B.2 at $Pr = 10^4$. It is clear that they bring energy beyond Kolmogorov wavenumber k_η to sustain the k^{-1} viscous-convective range.

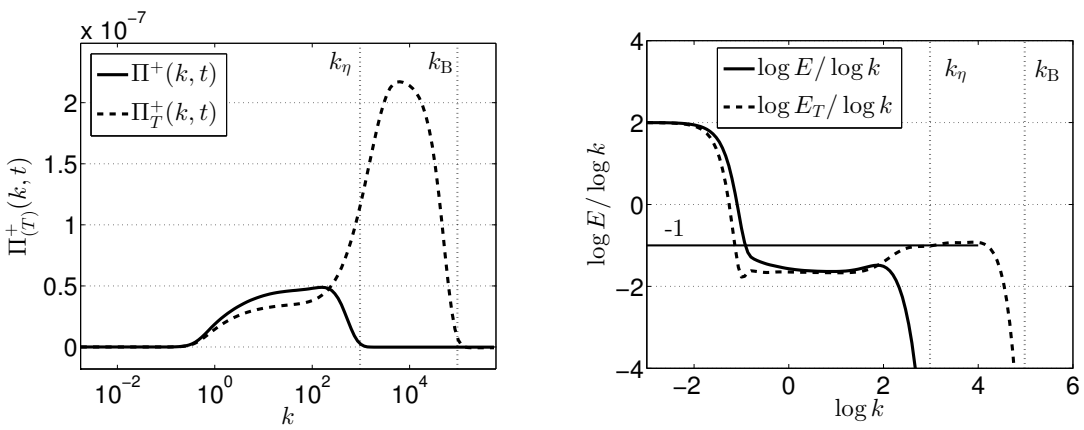

(a) (b)

Figure B.2: (a) Non-local fluxes Π^+ and Π_T^+. (b) Slopes of the kinetic and scalar spectra E and E_T. Both with the Kolmogorov and Batchelor wavenumbers k_η and k_B, at $Pr = 10^4$ and $\sigma = 2$ at $Re_\lambda = 10^3$.

B.3 Expansions for $k \ll p \sim q$

The small parameter of the expansion is $\zeta = k/p$. Firstly, q is expanded as

$$q = p\left(1 - z\zeta + \frac{1}{2}(1-z^2)\zeta^2\right), \text{ and } \qquad q^{-1} = p^{-1}\left(1 + z\zeta + \frac{1}{2}(3z^2-1)\zeta^2\right).$$

Then, geometrical relations yield

$$x = 1 - \frac{1}{2}(1-z^2)\zeta^2, \text{ and } \qquad y = \frac{k^2 - p^2 + q^2}{2kq} = -z + (1-z^2)\zeta - \frac{3}{2}z(z^2-1)\zeta^2.$$

This gives

$$\begin{aligned} xy + z^3 &= (1-z^2)\left(-z + \zeta + 2z\zeta^2\right), \qquad xy + z = (1-z^2)\zeta(1+2z\zeta), \\ xz + y^3 &= z(1-z^2)\left(1 + 3z\zeta + \frac{1}{2}(15z^2-7)\zeta^2\right), \qquad xz + y = (1-z^2)\zeta\left(1+z\zeta\right). \end{aligned}$$

Then, a Taylor expansion provides

$$E_{(T)}(q) = E_{(T)}(p) - kz\frac{\partial E_{(T)}}{\partial p} + \frac{1}{2}\zeta^2\left((1-z^2)p\frac{\partial E_{(T)}}{\partial p} + z^2p^2\frac{\partial^2 E_{(T)}}{\partial p^2}\right).$$

The method is almost the same: the different quantities are expressed as a function of z (the cosine of the angle in front of $\boldsymbol{q}$) and the small parameter $\zeta = k/p$. Then, the q-integration is done by using z, which simplifies, at the first order, into

$$\int_{p-k'}^{p} S_{(T)}(k',p,q)\mathrm{d}q = \int_0^1 \frac{k'p}{q} S_{(T)}(k',p,q)\mathrm{d}z.$$

As previously, it is assumed that $\theta^{(T)}_{k'pp} \simeq \theta^{(T)}_{kpp}$.

Computation of $\Pi^-(k,t)$: firstly,

$$\begin{aligned} \frac{kp}{q}\frac{(xy+z^3)}{q} &= \zeta(1-z^2)(-z + (1-2z^2)\zeta + z(5-4z^2)\zeta^2), \\ \frac{kp}{q}\frac{(xz+y^3)}{p} &= \zeta z(1-z^2)(1 + 4z\zeta + 8(3z^2-1)\zeta^2). \end{aligned}$$

In all the following calculations, the lowest order always simplifies. Hence

$$2\frac{kp}{q}S(k,p,q) = \theta_{kpp}(1-z^2)\left[(1+2z^2)k^2\zeta^2E(p)^2 - k^2E(k)E(p) - z^2k^2E(k)p\frac{\partial E}{\partial p}\right].$$

Then, using

$$\int_0^1 (1-z^2)(1+2z^2)\mathrm{d}z = \frac{14}{15}, \qquad \int_0^1 (1-z^2)\mathrm{d}z = \frac{2}{3}, \qquad \int_0^1 z^2(1-z^2)\mathrm{d}z = \frac{2}{15},$$

one finds the **inverse non-local kinetic flux**

$$\Pi^-(k,t) = \frac{14}{15}\int_0^k k'^4 \left[\int_{\sup(k,k'/a)}^{\infty} \theta_{k'pp} \frac{E(p)^2}{p^2} \mathrm{d}p \right] \mathrm{d}k' - \frac{2}{15}\int_0^k k'^2 E(k') \left[\int_{\sup(k,k'/a)}^{\infty} \theta_{k'pp} \left(5E(p) + p\frac{\partial E}{\partial p} \right) \mathrm{d}p \right] \mathrm{d}k'. \tag{B.17}$$

Computation of $\Pi_T^-(k,t)$: firstly,

$$\frac{kp}{q}\frac{(xy+z)}{q} = \zeta^2(1-z^2)(1+4z\zeta), \qquad \frac{kp}{q}\frac{(xz+y)}{p} = \zeta^2(1-z^2)(1+2z\zeta).$$

This directly yields the **inverse non-local scalar flux**

$$\Pi_T^-(k,t) = -\frac{4}{3}\int_0^k k'^2 E_T(k') \left[\int_{\sup(k,k'/a)}^{\infty} \theta_{k'pp}^T E(p) \mathrm{d}p \right] \mathrm{d}k' + \frac{4}{3}\int_0^k k'^4 \left[\int_{\sup(k,k'/a)}^{\infty} \theta_{k'pp}^T \frac{E_T(p)E(p)}{p^2} \mathrm{d}p \right] \mathrm{d}k'.$$

B.4 Applications of the isotropic non-local transfers

In this section, two brief applications of the non-local transfers, in addition to the classical case for weakly diffusive scalars, are presented.

Spatial resolution: in Fig. B.3, the number of points per decade f is changed. With a better spatial resolution in wavenumbers, $a = 10^{1/f} - 1$ decreases and thus, according to (B.1), the influence of the non-local transfers should decrease: this is assessed in Fig. B.3 where three different resolutions are tested, with the quantity $\Delta[kS^{\mathrm{NL(iso)}}](k,t)$ referring to the difference between a simulation with the non-local expansions and the same simulation without them. This quantity $\Delta[kS^{\mathrm{NL(iso)}}](k,t)$ decreases in intensity with a better spatial resolution. In addition, it appears that the non-local expansions are more important around the integral and Kolmogorov wavenumbers than in the inertial range, which is expected.

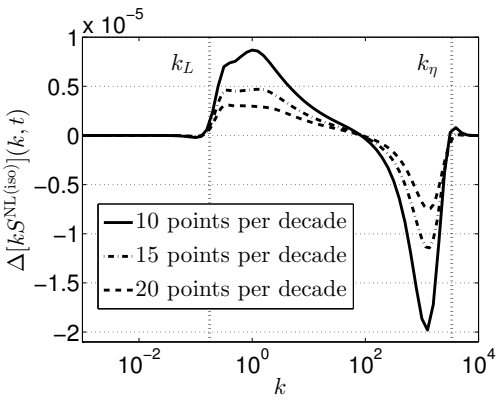

Figure B.3: Influence of the spatial resolution on the non-local transfers in HIT at $Pr = 1$, $\sigma = 2$ and $Re_\lambda = 2.10^3$.

Homogeneous Shear Flows: it is revealed in Fig. B.4 that the isotropic non-local transfers $T^{\pm}(k,t)$ are negligible with respect to the local ones for high Reynolds numbers shear flows (Π^{-} is very small compared to Π^{+}), where $\Pi^{\mathrm{NL(iso)}}$ is the flux of $S^{\mathrm{NL(iso)}}$, following

$$\Pi^{\mathrm{NL(iso)}}(k,t) = -\int_0^k S^{\mathrm{NL(iso)}}(k,t)\mathrm{d}k.$$

This justifies a posteriori why the non-local developments are used only for HIT and more specifically for a scalar field with $Pr \gg 1$.

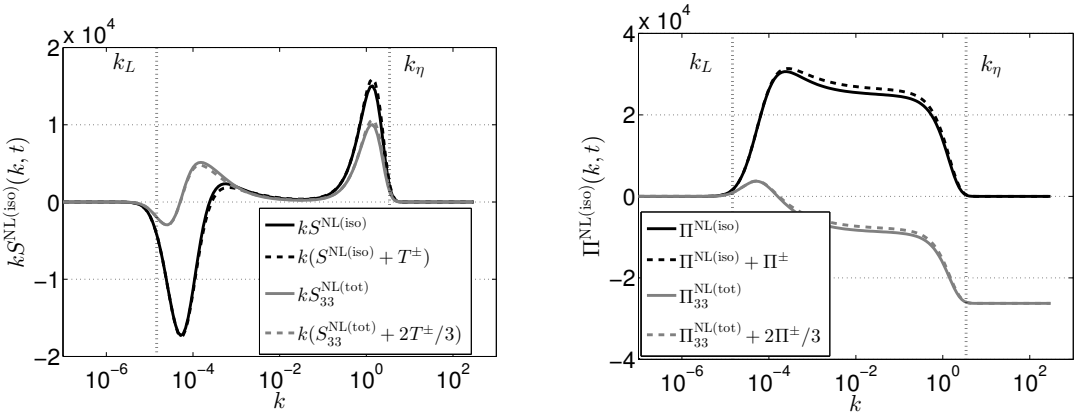

(a) (b)

Figure B.4: Influence of the isotropic non-local transfers in shear flows at $St = 50$ ($Re_\lambda = 10^4$) with $S = 0.1$ and $\sigma = 2$. (a) Budget terms for the isotropic part and the component $()_{33}$. (b) Associated fluxes.

In addition to the usual kinetic and scalar isotropic non-local fluxes presented in this appendix, non-local fluxes were also computed for the non-linear transfers of F_i, and for the non-linear directional and polarization kinetic transfers. These three contributions revealed to be completely negligible with respect to the local ones, and much less intense than the isotropic non-local contributions.

Appendix C

Details on the Spherically-Averaged Lin Equations

Here, all the calculations yielding to the spherically-averaged Lin equations of the velocity field of Chapter 2 are fully detailed. It includes notably the computation of the non-linear and linear transfers, and the complete spherical and λ integrations. Moreover, additional theoretical considerations are developed: (i) quadratic contributions of anisotropy in the non-linear transfers, (ii) the modelling of anisotropy resulting from a truncation at the fourth-order of the expansion into spherical harmonics of the spectral Reynolds tensor.

C.1 Spectral evolution equations

C.1.1 Craya equation

The evolution equation of the fluctuating field in the presence of both mean velocity gradients and rotation is

$$\left(\frac{\partial}{\partial t}+u_j\frac{\partial}{\partial x_j}\right)u_i+U_j\frac{\partial u_i}{\partial x_j}+u_jA_{ij}\underbrace{+2\epsilon_{inj}\Omega_n u_j}_{\text{Solid body rotation}}=-\frac{\partial p}{\partial x_i}+\nu\frac{\partial^2 u_i}{\partial x_j\partial x_j}. \tag{C.1}$$

The counterpart of (2.1) in Fourier space, using $U_i=A_{ij}x_j$ and $\widehat{x_ju_l}=\mathrm{i}\partial_j\hat{u}_l$, is

$$\left(\frac{\partial}{\partial t}-A_{ln}k_l\frac{\partial}{\partial k_n}+\nu k^2\right)\hat{u}_i(\boldsymbol{k})+A_{ij}\hat{u}_j(\boldsymbol{k})+2\epsilon_{inj}\Omega_n\hat{u}_j+\mathrm{i}k_j\widehat{u_iu_j}(\boldsymbol{k})=-\mathrm{i}k_i\hat{p}(\boldsymbol{k}), \tag{C.2}$$

where $\hat{u}_i$ is the Fourier transform of u_i, $A_{ij}=d_jU_i$ is a space uniform gradient matrix, k is the wave-number modulus, and $\widehat{u_mu_n}(\boldsymbol{k})$ is the convolution product

$$\widehat{u_iu_m}(\boldsymbol{k})=\int_{\boldsymbol{k}=\boldsymbol{p}+\boldsymbol{q}}\hat{u}_i(\boldsymbol{p})\hat{u}_m(\boldsymbol{q})\mathrm{d}^3\boldsymbol{p}.$$

Thanks to the incompressibility condition $\hat{u}_ik_i=0$ in Fourier space, the pressure term can be erased by projecting (C.2) on the plane perpendicular to $k_i\hat{p}$. Using the operator $P_{ij}=\delta_{ij}-\alpha_i\alpha_j$ one finds

$$\left(\frac{\partial}{\partial t}-A_{ln}k_l\frac{\partial}{\partial k_n}+\nu k^2\right)\hat{u}_i(\boldsymbol{k})+M_{ij}(\boldsymbol{k})\hat{u}_j(\boldsymbol{k})+\mathrm{i}P_{imn}(\boldsymbol{k})\widehat{u_mu_n}(\boldsymbol{k})=0, \tag{C.3}$$

where $P_{imn}(\boldsymbol{k})$ is the Kraichnan operator $2P_{imn} = k_m P_{in}(\boldsymbol{k}) + k_n P_{im}(\boldsymbol{k})$ and

$$M_{ij}(\boldsymbol{k}) = (\delta_{in} - 2\alpha_i\alpha_n)A_{n_j} \underbrace{+P_{in}\epsilon_{nlj}\Omega_l}_{\text{Rotation effect}}, \tag{C.4}$$

where $\alpha_i = k_i/k$. Writing (C.3) for $\hat{u}_j(\boldsymbol{k})$, multiplying it by $\hat{u}_i^*(p)$, summing it to (C.3) written for $\hat{u}_i^*(p)$ and multiplied by $\hat{u}_j(\boldsymbol{k})$, and finally taking the ensemble average, one obtains the equation of the second-order spectral tensor $\hat{R}_{ij}$, which is, in Fourier space

$$\hat{R}_{ij}(\boldsymbol{k},t)\delta(\boldsymbol{k}-\boldsymbol{p}) =< \hat{u}_i^*(\boldsymbol{p},t)\hat{u}_j(\boldsymbol{k},t) > . \tag{C.5}$$

The previous equation for $\hat{R}_{ij}$ is finally integrated over the whole domain (which simplifies the Dirac function $\delta(\boldsymbol{k}-\boldsymbol{p})$) to obtain the Craya equation. The total derivative reads $\mathrm{d}_t = \partial_t - A_{ij}k_i\partial_j$ so that

$$\frac{\mathrm{d}\hat{R}_{ij}}{\mathrm{d}t} + 2\nu k^2\hat{R}_{ij}(\boldsymbol{k}) + M_{in}(\boldsymbol{k})\hat{R}_{nj}(\boldsymbol{k}) + M_{jn}(\boldsymbol{k})\hat{R}_{ni}(\boldsymbol{k}) = T_{ij}^{\mathrm{NL}}(\boldsymbol{k}). \tag{C.6}$$

C.1.2 Generalized Lin equations for $\mathcal{E}$ and Z

The helical modes

$$N_j(\boldsymbol{k}) = e_j^{(2)}(\boldsymbol{k}) - \mathrm{i}e_j^{(1)}(\boldsymbol{k}). \tag{C.7}$$

are linked to the Craya-Herring frame $(e^{(1)}, e^{(2)}, e^{(3)})$ through

$$e_i^{(3)} = \frac{k_i}{k}, \qquad e_i^{(2)} = \epsilon_{ijn}e_j^{(3)}e_n^{(1)}, \qquad e_i^{(1)} = \epsilon_{ijl}\frac{k_j n_l}{|\boldsymbol{k}\times\boldsymbol{n}|} = \epsilon_{ijl}\frac{k_j n_l}{k_\perp}, \tag{C.8}$$

where $\boldsymbol{n}$ is a fixed reference vector. By definition of these helical modes, one has $N_j k_j = 0$, $N_j N_j = 0$, $N_j N_j^* = 2$ and $N_i N_j^* = P_{ij} - \mathrm{i}\epsilon_{ijn}\alpha_n$. The generalized $\mathcal{E}$-Lin equation is obtained by taking half the trace of (2.13) and replacing $\hat{R}_{ij}$ by the $\mathcal{E} - Z$ decomposition (2.30), so that

$$\frac{\mathrm{d}\mathcal{E}}{\mathrm{d}t} + 2\nu k^2\mathcal{E} + M_{in}\Big(\mathcal{E}P_{in} + \Re(Z(\boldsymbol{k},t)N_i(\boldsymbol{k})N_j(\boldsymbol{k}))\Big) = \frac{T_{ii}^{\mathrm{NL}}}{2}. \tag{C.9}$$

Using the incompressibility condition $A_{ii} = 0$, the $\mathcal{E}$-Lin equation presented in (2.31) is recovered. One can remark that rotation does not intervene directly in the evolution equation of $\mathcal{E}$. The calculation for the Z-Lin equation is more complicated: (2.13) is firstly multiplied by $N_i^*(\boldsymbol{k})N_j^*(\boldsymbol{k})/2$. One has to compute $\hat{R}_{nj}N_j^*$ and $M_{in}N_i^*$ which can be done by using the previous relations on N_j and the fact that $\forall z \in \mathbb{C}, \Re(z) = (z + z^*)/2$. One finds $\hat{R}_{nj}N_j^* = \mathcal{E}N_n^* + ZN_n$ and $M_{in}N_i^* = A_{in}N_i^*$. This yields

$$\frac{\mathrm{d}Z}{\mathrm{d}t} + 2\nu k^2 Z - \frac{\hat{R}_{ij}}{2}\frac{d}{dt}(N_i^*N_j^*) + A_{in}N_i^*(\mathcal{E}N_n^* + ZN_n) = T_Z, \tag{C.10}$$

where the non-linear transfer linked to the polarization anisotropy T_Z is defined in (2.34). Some detailed calculations yields

$$\Re(ZN_nN_j)M_{in}N_i^*N_j^* = -A_{ln}^+\alpha_l\alpha_n Z - 2\mathrm{i}Z\left(2\alpha_l\Omega_l + \frac{1}{2}\epsilon_{lpq}\alpha_l A_{pq}^-\right)$$
$$\mathcal{E}P_{nj}M_{in}N_i^*N_j^* = A_{ln}^+N_l^*N_n^*\mathcal{E}$$

Since the Craya-Herring frame is moving in space with time, the term $d_t(N_i^*N_j^*)$ in (C.10) is evaluated using (2.30) and the previous remark on $\hat{R}_{nj}N_j^*$, so that

$$\hat{R}_{ij}\frac{\mathrm{d}}{\mathrm{d}t}(N_i^*N_j^*) = -ZN_j\frac{\mathrm{d}N_j^*}{\mathrm{d}t}.$$

Finally, to compute $\mathrm{d}N_j^*/\mathrm{d}t$, one has to use

$$\frac{\mathrm{d}}{\mathrm{d}t} = \frac{\partial}{\partial t} - A_{ij}k_i\frac{\partial}{\partial k_j}, \qquad \frac{\mathrm{d}k_i}{\mathrm{d}t} = -A_{ji}k_j.$$

Moreover, similar calculations yield

$$\frac{\partial \alpha_i}{\partial k_j} = \frac{P_{ij}}{k}, \qquad \frac{\partial k}{\partial k_i} = \alpha_i.$$

Finally,

$$N_j\frac{\mathrm{d}N_j^*}{\mathrm{d}t} = 2\mathrm{i}e_p^{(1)}A_{lp}\left(e_l^{(2)} + \frac{n_l k}{k_\perp}\right) = -2\mathrm{i}\Omega_{\mathrm{CH}}, \tag{C.11}$$

where Ω_{CH} expresses the rotation of the Craya-Herring frame. The Z-Lin equation, accounting for rotation, is then

$$\left(\frac{\mathrm{d}}{\mathrm{d}t} + 2\nu k^2\right)Z - A_{ln}^+\alpha_l\alpha_n Z + A_{ln}^+N_l^*N_n^*\mathcal{E} - 2\mathrm{i}Z\Big(\underbrace{2\Omega_l\alpha_l}_{\text{Rotation part}} + \frac{1}{2}\epsilon_{lpq}\alpha_l A_{pq}^- - \Omega_{\mathrm{CH}}\Big) = T_Z, \tag{C.12}$$

in agreement with Cambon *et al.* (2013); Mons *et al.* (2016). One can simplify this expression a bit, using a previous relation that gives

$$A_{ln}N_nN_l^*Z = -\alpha_l\alpha_n A_{ln}^+Z - \mathrm{i}\epsilon_{jnl}\alpha_j A_{nl}^-,$$

so that (2.33) is recovered.

C.1.3 Evolution equation of $S_{ijk}(\boldsymbol{k},\boldsymbol{p},t)$

From (C.3), the evolution equation of the third-order tensor S_{ijk}, defined in (2.17), is obtained by writing (C.3) for $\hat{u}_j$, $\hat{u}_i'$ and $\hat{u}_k''$, and summing these three equations, previously multiplied by $\hat{u}_i'\hat{u}_k''$, $\hat{u}_j\hat{u}_k''$ and $\hat{u}_i'\hat{u}_j$ respectively. Since $S_{ijk}(\boldsymbol{k},\boldsymbol{p},t)$ does not depend on $\boldsymbol{q}$, the term $q_l\frac{\partial}{\partial q_n}$ has to be erased. This is done by using $q_l = -k_l - p_l$ and $\boldsymbol{k}$ and $\boldsymbol{p}$ being independent variables. Hence,

$$u_i'u_k''\frac{\partial u_j}{\partial k_n} = u_k''\frac{\partial u_j u_i'}{\partial k_n}, \qquad u_ju_k''\frac{\partial u_i'}{\partial p_n} = u_k''\frac{\partial u_j u_i'}{\partial p_n}, \qquad \frac{\partial}{\partial q_n} = -\frac{\partial}{\partial p_n} = -\frac{\partial}{\partial k_n}.$$

Averaging and integrating to erase Dirac functions yields

$$\left(\frac{\partial}{\partial t} + \nu(k^2+p^2+q^2) - A_{lm}\left(k_l\frac{\partial}{\partial k_m} + p_l\frac{\partial}{\partial p_m}\right)\right)S_{ijn}(\boldsymbol{k},\boldsymbol{p},t) + M_{im}(\boldsymbol{q})S_{mjn}(\boldsymbol{k},\boldsymbol{p},t)$$
$$+ M_{jm}(\boldsymbol{k})S_{imn}(\boldsymbol{k},\boldsymbol{p},t) + M_{nm}(\boldsymbol{p})S_{ijm}(\boldsymbol{k},\boldsymbol{p},t) = \mathfrak{T}_{ijn}(\boldsymbol{k},\boldsymbol{p},t).$$

Here, some details on the quasi-normal closure $\mathfrak{T}_{ijn}^{\mathrm{QN}}$ (2.37) are provided. For this purpose, the correlation that intervenes in the previous equation is defined as

$$T_{ijn}(\boldsymbol{k},\boldsymbol{p})\delta(\boldsymbol{k}+\boldsymbol{p}+\boldsymbol{q}) = \mathrm{i} < s_i(\boldsymbol{q})\hat{u}_j(\boldsymbol{k})\hat{u}_n(\boldsymbol{p}) >, \tag{C.13}$$

where

$$s_j(\boldsymbol{k}) = -P_{jpq}(\boldsymbol{k})\int_{\boldsymbol{k}=\boldsymbol{r}+\boldsymbol{s}}\hat{u}_p(\boldsymbol{r})\hat{u}_q(\boldsymbol{s})\mathrm{d}^3\boldsymbol{r}. \tag{C.14}$$

Thus, the previous equation becomes

$$\left(\frac{\partial}{\partial t} + \nu(k^2+p^2+q^2)\right)S_{ijn}(\boldsymbol{k},\boldsymbol{p},t) + ... = T_{ijn}(\boldsymbol{k},\boldsymbol{p},t) + T_{jni}(\boldsymbol{p},\boldsymbol{q},t) + T_{nij}(\boldsymbol{q},\boldsymbol{k},t). \tag{C.15}$$

Each of the three rhs terms can be written

$$T_{ijn}(\boldsymbol{k},\boldsymbol{p})\delta(\boldsymbol{k}+\boldsymbol{p}+\boldsymbol{q}) = P_{ipq}(\boldsymbol{q})\int_{\boldsymbol{q}=\boldsymbol{r}+\boldsymbol{s}} < \hat{u}_p(\boldsymbol{r})\hat{u}_q(\boldsymbol{s})\hat{u}_j(\boldsymbol{k})\hat{u}_n(\boldsymbol{p}) > \mathrm{d}^3\boldsymbol{r}.$$

The quasi-normal approximation consists into neglecting the fourth order cumulants, which gives

$$\begin{aligned}T^{\mathrm{QN}}_{ijn}(\boldsymbol{k},\boldsymbol{p})\delta(\boldsymbol{k}+\boldsymbol{p}+\boldsymbol{q}) &= P_{ipq}(\boldsymbol{0})\hat{R}_{jn}(\boldsymbol{k})\hat{R}_{pq}(-\boldsymbol{s})\delta(\boldsymbol{k}+\boldsymbol{p})\\ &+ P_{ipq}(\boldsymbol{q})\hat{R}_{jp}(\boldsymbol{k})\hat{R}_{nq}(\boldsymbol{p})\delta(\boldsymbol{k}+\boldsymbol{p}+\boldsymbol{q}) + P_{ipq}(\boldsymbol{q})\hat{R}_{np}(\boldsymbol{p})\hat{R}_{jq}(\boldsymbol{k})\delta(\boldsymbol{k}+\boldsymbol{p}+\boldsymbol{q}),\end{aligned}$$

and simplifies into

$$T^{\mathrm{QN}}_{ijn}(\boldsymbol{k},\boldsymbol{p}) = 2P_{ipq}(\boldsymbol{q})\hat{R}_{jp}(\boldsymbol{k})\hat{R}_{nq}(\boldsymbol{p}).$$

The quasi-normal term $\mathfrak{T}^{\mathrm{QN}}_{ijn}$ is finally recovered since

$$\mathfrak{T}^{\mathrm{QN}}_{ijn}(\boldsymbol{k},\boldsymbol{p},t) = T^{\mathrm{QN}}_{ijn}(\boldsymbol{k},\boldsymbol{p},t) + T^{\mathrm{QN}}_{jni}(\boldsymbol{p},\boldsymbol{q},t) + T^{\mathrm{QN}}_{nij}(\boldsymbol{q},\boldsymbol{k},t).$$

C.2 Calculations of $T_{\mathcal{E}}$ and T_Z

C.2.1 Relations between frameworks

In Fig. 2.2, a new frame ($\boldsymbol{\beta}$,$\boldsymbol{\gamma}$,$\boldsymbol{\alpha}$) has been presented, attached to the plane of the triad. The new frame ($\boldsymbol{\beta}$,$\boldsymbol{\gamma}$,$\boldsymbol{\alpha}$) is obtained from the Craya frame ($\boldsymbol{e^{(1)}}, \boldsymbol{e^{(2)}}, \boldsymbol{e^{(3)}} = \boldsymbol{\alpha}$) by rotations of angles λ, λ' and λ'' around $\boldsymbol{k}$, $\boldsymbol{p}$ and $\boldsymbol{q}$. Hence, one has

$$\boldsymbol{N}(\boldsymbol{k}) = \boldsymbol{N} = \boldsymbol{e^{(2)}} - \mathrm{i}\boldsymbol{e^{(1)}} = e^{\mathrm{i}\lambda}\underbrace{(\boldsymbol{\beta}+\mathrm{i}\boldsymbol{\gamma})}_{\mathbf{W}}, \tag{C.16}$$

$$\boldsymbol{N}(\boldsymbol{p}) = \boldsymbol{N'} = \boldsymbol{e^{(2)}}' - \mathrm{i}\boldsymbol{e^{(1)}}' = e^{\mathrm{i}\lambda'}\underbrace{(\boldsymbol{\beta'}+\mathrm{i}\boldsymbol{\gamma})}_{\mathbf{W'}}, \tag{C.17}$$

$$\boldsymbol{N}(\boldsymbol{q}) = \boldsymbol{N''} = \boldsymbol{e^{(2)}}'' - \mathrm{i}\boldsymbol{e^{(1)}}'' = e^{\mathrm{i}\lambda''}\underbrace{(\boldsymbol{\beta''}+\mathrm{i}\boldsymbol{\gamma})}_{\mathbf{W''}}, \tag{C.18}$$

where $\boldsymbol{\gamma}$ is normal to the plane of the triad

$$\boldsymbol{\gamma} = \frac{\boldsymbol{k}\times\boldsymbol{p}}{|\boldsymbol{k}\times\boldsymbol{p}|}. \tag{C.19}$$

The vectors $\boldsymbol{\beta}$, $\boldsymbol{\beta'}$ and $\boldsymbol{\beta''}$ are perpendicular to $\boldsymbol{k}$, $\boldsymbol{p}$ and $\boldsymbol{q}$ but still in the plane of the triad

$$\boldsymbol{\beta} = \frac{\boldsymbol{k}\times\boldsymbol{\gamma}}{|\boldsymbol{k}\times\boldsymbol{\gamma}|}, \qquad \boldsymbol{\beta'} = \frac{\boldsymbol{p}\times\boldsymbol{\gamma}}{|\boldsymbol{p}\times\boldsymbol{\gamma}|}, \qquad \boldsymbol{\beta''} = \frac{\boldsymbol{q}\times\boldsymbol{\gamma}}{|\boldsymbol{q}\times\boldsymbol{\gamma}|}. \tag{C.20}$$

With these definitions, one gets

$$\begin{aligned}\boldsymbol{\alpha'} &= -z\boldsymbol{\alpha} - \sqrt{1-z^2}\boldsymbol{\beta}, & \boldsymbol{\alpha''} &= -y\boldsymbol{\alpha} + \sqrt{1-y^2}\boldsymbol{\beta},\\ \boldsymbol{\beta'} &= -z\boldsymbol{\beta} + \sqrt{1-z^2}\boldsymbol{\alpha}, & \boldsymbol{\beta''} &= -y\boldsymbol{\beta} - \sqrt{1-y^2}\boldsymbol{\alpha},\\ \boldsymbol{W'} &= \sqrt{1-z^2}\boldsymbol{\alpha} + \frac{1-z}{2}\boldsymbol{N}e^{-\mathrm{i}\lambda} - \frac{1+z}{2}\boldsymbol{N}^*e^{\mathrm{i}\lambda}, & \boldsymbol{W''} &= -\sqrt{1-y^2}\boldsymbol{\alpha} + \frac{1-y}{2}\boldsymbol{N}e^{-\mathrm{i}\lambda} - \frac{1+y}{2}\boldsymbol{N}^*e^{\mathrm{i}\lambda},\end{aligned}$$

with $x = \cos a$, $y = \cos b$, and $z = \cos c$. To perform the following calculations, one has to keep in mind fundamental geometrical relations valid in any triangles

$$k = pz + qy, \qquad p = kz + qx, \qquad q = px + ky, \qquad \frac{k}{\sin a} = \frac{p}{\sin b} = \frac{q}{\sin c}. \tag{C.21}$$

Finally, since $\boldsymbol{p}$ and $\boldsymbol{q}$ have symmetric behaviours, one has both

$$\int e^{2\mathrm{i}\lambda} F(\boldsymbol{k},\boldsymbol{p},\boldsymbol{q})\mathrm{d}^3\boldsymbol{p} = \int e^{2\mathrm{i}\lambda} F(\boldsymbol{k},\boldsymbol{q},\boldsymbol{p})\mathrm{d}^3\boldsymbol{p}, \qquad \int f(\boldsymbol{p})\mathrm{d}^3\boldsymbol{p} = \int \frac{1}{2}(f(\boldsymbol{p})+f(\boldsymbol{q}))\mathrm{d}^3\boldsymbol{p}. \tag{C.22}$$

C.2.2 Computation of $\mathfrak{T}^{\mathrm{QN}}_{ijn}$

Starting from (2.39), the main term to compute is $k_l\mathfrak{T}^{\mathrm{QN}}_{ijl}$, divided into two parts

$$\frac{k_l}{2}\mathfrak{T}^{\mathrm{QN}}_{ijl}(\boldsymbol{k},\boldsymbol{p},t) = \underbrace{\hat{R}_{mj}\Big(P'_{imn}\hat{R}''_{nl}k_l + k_l P'_{lmn}\hat{R}''_{ni}\Big)}_{\tau^-_{ij}} + \underbrace{\frac{1}{2}P_{jmn}k_l\Big(\hat{R}''_{ni}\hat{R}'_{ml} + \hat{R}'_{ni}\hat{R}''_{ml}\Big)}_{\tau^+_{ij}}, \tag{C.23}$$

such that

$$\tau^-_{ij} + \tau^+_{ij} = \hat{R}''_{nl}(k_l\delta_{ip} + k_p\delta_{il})\Big(P'_{pmn}\hat{R}_{mj} + \frac{1}{2}P_{jmn}\hat{R}'_{mp}\Big).$$

Computation of τ^-_{ij}: starting from the expression of τ^-_{ij} given in (C.23) and using the fact that $p_m\hat{R}''_{ml} = -k_m\hat{R}''_{ml}$ thanks to the incompressibility condition, and that $k_m\hat{R}_{mj} = 0$, one finds

$$\tau^-_{ij} = \frac{1}{2}k_l\left[k_n\hat{R}''_{ln}\left(2\alpha'_i\alpha'_m\hat{R}_{mj} - \hat{R}_{ij}\right) + 2\alpha'_m qx\hat{R}_{mj}\hat{R}''_{li}\right]. \tag{C.24}$$

Using (2.30), geometrical relations and equalities such as $W_i\beta_i = 1$ and $\beta_i\gamma_i = 0$, one has

$$\begin{aligned}
k_l\hat{R}''_{ln}k_n &= k^2(1-y^2)\Big(\mathcal{E}'' + \Re X''\Big) = kp(xy+z)\Big(\mathcal{E}'' + \Re X''\Big),\\
k_l\hat{R}''_{ln}N_n &= e^{\mathrm{i}\lambda}k\sin b\Big(\mathcal{E}''y + \frac{y+1}{2}X'' - \frac{1-y}{2}X''^*\Big) = e^{\mathrm{i}\lambda}k\sin b\Big(y(\mathcal{E}''+\Re X'') + \mathrm{i}\Im X''\Big),
\end{aligned}$$

where $X = Ze^{2\mathrm{i}\lambda}$, $X' = Z'e^{2\mathrm{i}\lambda'}$ and $X'' = Z''e^{2\mathrm{i}\lambda''}$. Similarly,

$$k_l\hat{R}''_{ln}N^*_n = e^{-\mathrm{i}\lambda}k\sin b\Big(y(\mathcal{E}''+\Re X'') - \mathrm{i}\Im X''\Big).$$

Then, using $p_mN_m = p\alpha'_mN_m = -pe^{\mathrm{i}\lambda}\sin c$,

$$p_m\hat{R}_{mj}N_j = -p\sin c\Big(\mathcal{E}e^{\mathrm{i}\lambda} + Z^*e^{-\mathrm{i}\lambda}\Big), \qquad p_m\hat{R}_{mj}N^*_j = -p\sin c\Big(\mathcal{E}e^{-\mathrm{i}\lambda} + Ze^{\mathrm{i}\lambda}\Big).$$

↪ Now, the contribution of τ^-_{ij} to the polarization transfer is evaluated. Using $q\sin b\sin c = p(1-z^2)$, this yields

$$\begin{aligned}
\frac{1}{2}\tau^-_{ij}N^*_iN^*_j &= \frac{\mathrm{i}}{2}kpx(1-z^2)(\mathcal{E}e^{-2\mathrm{i}\lambda} + Z)\Im X''\\
&\quad + \frac{1}{2}kp\Big(\mathcal{E}'' + \Re X''\Big)\Big(z(1-z^2)\mathcal{E}e^{-2\mathrm{i}\lambda} - Z(xy+z^3)\Big).
\end{aligned} \tag{C.25}$$

↪ Finally, the contribution of τ^-_{ij} to the directional transfer is computed. Using $\hat{R}_{ij}N_iN^*_j = \hat{R}_{ij}N^*_iN_j = R_{ii} = 2\mathcal{E}$ and $2\tau^-_{ii} = (N_iN^*_j + N^*_iN_j)\tau^-_{ij}$, this gives

$$\frac{1}{2}\tau^-_{ii} = \frac{1}{2}kp\Big(\mathcal{E}'' + \Re X''\Big)\Big(z(1-z^2)\Re X - (xy+z^3)\mathcal{E}\Big) + \frac{1}{2}kpx(1-z^2)\Im X\Im X''. \tag{C.26}$$

Computation of τ^+_{ij}: starting from

$$\tau^+_{ij} = k_lP_{jmn}\hat{R}'_{ml}\hat{R}''_{ni} = \frac{1}{2}\alpha_l\alpha_m\hat{R}'_{lm}(k^2\hat{R}''_{ji} - 2k_jk_n\hat{R}''_{ni}) + \frac{1}{2}k_nk_l\hat{R}''_{ni}\hat{R}'_{jl},$$

and using the facts that $\alpha_i\alpha_i' = -z$, $\alpha_i N_i' = e^{\mathrm{i}\lambda'}\sqrt{1-z^2}$ and $\alpha_i N_i'^* = e^{-\mathrm{i}\lambda'}\sqrt{1-z^2}$ one finds

$$\alpha_m\alpha_l\hat{R}'_{ml} = (1-z^2)(\mathcal{E}' + \Re X').$$

Similar calculations, with $\alpha_i'' W_i^* = \sqrt{1-y^2}$ and $W_i W_i = 0$, yield

$$\begin{aligned} N_i^* N_j^* \hat{R}''_{ij} &= e^{-2\mathrm{i}\lambda}\Big((1+y^2)(\mathcal{E}'' + \Re X'') - 2\mathcal{E}'' - 2\mathrm{i}y\Im X''\Big), \\ k_n N_i^* \hat{R}'_{ni} &= -k\sqrt{1-z^2}e^{-\mathrm{i}\lambda}\Big(z(\mathcal{E}' + \Re X') - \mathrm{i}\Im X'\Big). \end{aligned}$$

$\hookrightarrow$ Now, the contribution of τ_{ij}^+ to the polarization transfer is evaluated. Using the previous calculations and a symmetric writing, one finds

$$\begin{aligned} \tau_{ij}^+ N_i^* N_j^* = &\frac{1}{4}k^2 e^{-2\mathrm{i}\lambda}(1-z^2)(\mathcal{E}' + \Re X')\Big((1+y^2)(\mathcal{E}'' + \Re X'') - 2\mathcal{E}'' - 2\mathrm{i}y\Im X''\Big) \\ &+ \frac{1}{4}k^2 e^{-2\mathrm{i}\lambda}(1-y^2)(\mathcal{E}'' + \Re X'')\Big((1+z^2)(\mathcal{E}' + \Re X') - 2\mathcal{E}' - 2\mathrm{i}z\Im X'\Big) \\ &- \frac{1}{2}k^2 e^{-2\mathrm{i}\lambda}(x+yz)(y(\mathcal{E}'' + \Re X'') - \mathrm{i}\Im X'')(z(\mathcal{E}' + \Re X') - \mathrm{i}\Im X'). \end{aligned} \tag{C.27}$$

Let's simplify the geometric factor that affects $(\mathcal{E}'' + \Re X'')(\mathcal{E}' + \Re X')$. Using the following relations

$$(1-z^2) = \frac{q}{p}(x+yz) = \frac{q^2}{p^2}(1-y^2), \qquad k(2yz+x) = qz + py, \qquad 2xyz = 1 - x^2 - y^2 - z^2,$$

one finds

$$k^2(1 - 2y^2z^2 - xyz) = kp(xy + z^3) + kq(xz + y^3). \tag{C.28}$$

Thus, with $p \leftrightarrow q$ symmetry

$$\begin{aligned} &\frac{k^2 e^{-2\mathrm{i}\lambda}}{2}(1 - 2y^2z^2 - xyz)(\mathcal{E}'' + \Re X'')(\mathcal{E}' + \Re X') \\ &= \frac{e^{-2\mathrm{i}\lambda}}{2}\Big(kp(xy+z^3) + kq(xz+y^3)\Big)(\mathcal{E}'' + \Re X'')(\mathcal{E}' + \Re X') \\ &= e^{-2\mathrm{i}\lambda}kp(xy+z^3)(\mathcal{E}'' + \Re X'')(\mathcal{E}' + \Re X'). \end{aligned} \tag{C.29}$$

The term

$$-\frac{k^2 e^{-2\mathrm{i}\lambda}}{4}\Big((1-z^2)(\mathcal{E}' + \Re X')2\mathcal{E}'' + (1-y^2)(\mathcal{E}'' + \Re X'')2\mathcal{E}'\Big)$$

simplifies using $k(1-z^2) = q(xz+y)$ and $k(1-y^2) = p(xy+z)$, into

$$\begin{aligned} &-\frac{k^2 e^{-2\mathrm{i}\lambda}}{4}\Big((1-z^2)(\mathcal{E}' + \Re X')2\mathcal{E}'' + (1-y^2)(\mathcal{E}'' + \Re X'')2\mathcal{E}'\Big) \\ &= -kpe^{-2\mathrm{i}\lambda}(xy+z)(\mathcal{E}'' + \Re X'')\mathcal{E}'. \end{aligned} \tag{C.30}$$

The remaining imaginary term

$$\frac{\mathrm{i}k^2 e^{-2\mathrm{i}\lambda}}{2}\Big[\Im X''(\mathcal{E}' + \Re X')(z(x+yz) - y(1-z^2)) + \Im X'(\mathcal{E}'' + \Re X'')(y(x+yz) - z(1-y^2))\Big]$$

can be simplified using $p \leftrightarrow q$ symmetry and the following relations

$$k(1-z^2) = q(xz+y), \qquad k(1-y^2) = p(xy+z), \qquad k(x+yz) = p(y+xz) = q(z+xy).$$

Therefore

$$\frac{\mathrm{i}k^2 e^{-2\mathrm{i}\lambda}}{2}\Big[\Im X''(\mathcal{E}' + \Re X')(z(x+yz) - y(1-z^2)) + \Im X'(\mathcal{E}'' + \Re X'')(y(x+yz) - z(1-y^2))\Big]$$

$$= ikp(y^2 - z^2)e^{-2\mathrm{i}\lambda}\Im X'(\mathcal{E}'' + \Re X''). \tag{C.31}$$

The last term is

$$\frac{k^2 e^{-2\mathrm{i}\lambda}}{2}(x + yz)\Im X'\Im X'' = kpye^{-2\mathrm{i}\lambda}(1 - z^2)\Im X'\Im X'' \tag{C.32}$$

due to $kpy(1 - z^2) + kqz(1 - y^2) = k^2(x + yz)$. The final contribution of τ_{ij}^+ to T_Z is

$$\tau_{ij}^+ N_i^* N_j^* = kpe^{-2\mathrm{i}\lambda}\Big[y(1 - z^2)\Im X'\Im X'' + (\mathcal{E}'' + \Re X'')\Big((xy + z^3)(\mathcal{E}' + \Re X') - (xy + z)\mathcal{E}' + \mathrm{i}(y^2 - z^2)\Im X'\Big)\Big].$$

↪ Let's now consider the contribution of τ_{ij}^+ to $T_{\mathcal{E}}$. As before, $\tau_{ij}^+(N_i N_j^* + N_i^* N_j) = 2P_{ij}\tau_{ij}^+$ is computed. One has

$$\hat{R}''_{ij}P_{ij} = \mathcal{E}''(1 + y^2) - \Re X''(1 - y^2), \qquad k_n\hat{R}''_{ni}N_i = k\sin be^{\mathrm{i}\lambda}(y(\mathcal{E}'' + \Re X'') + \mathrm{i}\Im X'').$$

All other useful quantities have already been detailed. Thus, under a symmetric form

$$\begin{aligned}2\tau_{ij}^+(N_i N_j^* + N_i^* N_j) &= k^2(\mathcal{E}'' + \Re X'')\Big((\mathcal{E}' + \Re X')(z^2 - 2y^2z^2 - xyz) + (1 - y^2)(\mathcal{E}' - \Re X')\Big)\\ &- k^2(x + yz)\Im X'\Im X'' + k^2(\mathcal{E}' + \Re X')\Big((\mathcal{E}'' + \Re X'')(y^2 - 2y^2z^2 - xyz) + (1 - z^2)(\mathcal{E}'' - \Re X'')\Big).\end{aligned} \tag{C.33}$$

Using previous geometric relations, the total contribution of τ_{ij}^+ to $T_{\mathcal{E}}$ becomes

$$\tau_{ij}^+(N_i N_j^* + N_i^* N_j) = 2kp\Big[(xy + z^3)(\mathcal{E}'' + \Re X'')(\mathcal{E}' + \Re X') - (xy + z)(\mathcal{E}'' + \Re X'')\Re X' - y(1 - z^2)\Im X'\Im X''\Big]. \tag{C.34}$$

Final step: The equation for τ_{ij} is

$$\tau_{ij}(\boldsymbol{k}, t) = k_l \int \theta_{kpq}\mathfrak{T}_{ijl}^{\mathrm{QN}}(\boldsymbol{k}, \boldsymbol{p}, t)\mathrm{d}^3\boldsymbol{p}. \tag{C.35}$$

With the definitions of τ_{ij}^- and τ_{ij}^+ given in (C.23), and using the fact that τ_{ij} is real (because there is no helicity), one finds

$$\tau_{ij}(\boldsymbol{k}, t) = 2\int_{k+p+q=0} \theta_{kpq}(\tau_{ij}^- + \tau_{ij}^+ + \tau_{ij}^{-*} + \tau_{ij}^{+*})\mathrm{d}^3\boldsymbol{p} = 4\int_{k+p+q=0} \theta_{kpq}(\tau_{ij}^- + \tau_{ij}^+)\mathrm{d}^3\boldsymbol{p}. \tag{C.36}$$

Consequently, (2.41) and (2.42) are obtained.

Return to isotropy: some details to obtain $T^{(\mathrm{RTI})}$ in equation (2.69) are given. Using previous relations, one gets

$$\alpha_i\tau_{ij}^- N_j^* = k(1 - y^2)\sqrt{1 - z^2}(zk - qx)e^{-\mathrm{i}\lambda}(\mathcal{E}'' + \Re X'')(\mathcal{E} + X)$$

and, with $p \leftrightarrow q$ symmetry

$$\alpha_i\tau_{ij}^+ N_j^* = -k^2(1 - y^2)\sqrt{1 - z^2}e^{-\mathrm{i}\lambda}(\mathcal{E}'' + \Re X'')(z(\mathcal{E}' + \Re X') - \mathrm{i}\Im X'),$$

so that (2.69) is recovered.

C.3 Spherically-averaged non-linear transfers

C.3.1 λ-integration

In the anisotropic framework, the difficulty is to solve the integral that depends on the orientation of the plane of the triad. Triple integrals simplify using the change of variable

$$\int\int\int f_1(\boldsymbol{k},\boldsymbol{p},t)\mathrm{d}^3\boldsymbol{p} = \int\int_{\Delta_k} \frac{pq}{k}\left(\int_0^{2\pi} f_2(\boldsymbol{k},p,q,\lambda)\mathrm{d}\lambda\right)\mathrm{d}p\mathrm{d}q, \tag{C.37}$$

where λ as been defined in (C.16). Δ_k is the domain where k, p and q are the lengths of the sides of the triangle formed by the triad. In the isotropic case, the λ-integral amounts to a multiplication by 2π which is not true anymore in the anisotropic case. In this part, the main integrals that are useful for the calculations are

$$\int_0^{2\pi} \alpha_i'\alpha_j'\mathrm{d}\lambda = \pi[(1-z^2)\delta_{ij} + (3z^2-1)\alpha_i\alpha_j], \qquad \int_0^{2\pi} e^{-2\mathrm{i}\lambda}\alpha_i'\alpha_j'\mathrm{d}\lambda = \pi\frac{1-z^2}{2}N_i^*N_j^*,$$

$$\int_0^{2\pi} W_i'W_j'\mathrm{d}\lambda = \int_0^{2\pi} W_i'^*W_j'^*\mathrm{d}\lambda = \pi(z^2-1)(\delta_{ij} - 3\alpha_i\alpha_j),$$

$$\int_0^{2\pi} e^{-2\mathrm{i}\lambda}W_i'W_j'\mathrm{d}\lambda = \pi\frac{(z+1)^2}{2}N_i^*N_j^*, \qquad \int_0^{2\pi} e^{-2\mathrm{i}\lambda}W_i'^*W_j'^*\mathrm{d}\lambda = \pi\frac{(1-z)^2}{2}N_i^*N_j^*.$$

Similar results regarding $''$ quantities are obtained by changing z to y. Then, λ-integrations of $\mathcal{E}$ and Z give

$$\int_0^{2\pi} \mathcal{E}^{(\mathrm{dir})'}\mathrm{d}\lambda = 15\pi\mathcal{E}_0'H_{ij}^{(\mathrm{dir})'}(1-3z^2)\alpha_i\alpha_j, \qquad \int_0^{2\pi} \mathcal{E}^{(\mathrm{dir})}\mathrm{d}\lambda = -30\pi\mathcal{E}_0H_{ij}^{(\mathrm{dir})}\alpha_i\alpha_j,$$

$$\int_0^{2\pi} e^{-2\mathrm{i}\lambda}\mathcal{E}^{(\mathrm{dir})'}\mathrm{d}\lambda = \frac{15}{2}\pi\mathcal{E}_0'H_{ij}^{(\mathrm{dir})'}(z^2-1)N_i^*N_j^*, \qquad \int_0^{2\pi} e^{-2\mathrm{i}\lambda}\mathcal{E}^{(\mathrm{dir})}\mathrm{d}\lambda = 0,$$

$$\int_0^{2\pi} \Re X'\mathrm{d}\lambda = \frac{15}{2}\pi\mathcal{E}_0'H_{ij}^{(\mathrm{pol})'}(1-z^2)\alpha_i\alpha_j, \qquad \int_0^{2\pi} \Re X\mathrm{d}\lambda = 0,$$

$$\int_0^{2\pi} e^{-2\mathrm{i}\lambda}\Re X'\mathrm{d}\lambda = \frac{5}{4}\pi\mathcal{E}_0'H_{ij}^{(\mathrm{pol})'}(1+z^2)N_i^*N_j^*, \qquad \int_0^{2\pi} e^{-2\mathrm{i}\lambda}\Re X\mathrm{d}\lambda = \frac{5}{2}\pi\mathcal{E}_0H_{ij}^{(\mathrm{pol})}N_i^*N_j^*,$$

$$\int_0^{2\pi} e^{-2\mathrm{i}\lambda}\Im X'\mathrm{d}\lambda = -\frac{5}{2}\pi\mathcal{E}_0'H_{ij}^{(\mathrm{pol})'}zN_i^*N_j^*, \qquad \int_0^{2\pi} e^{-2\mathrm{i}\lambda}X\mathrm{d}\lambda = 5\pi\mathcal{E}_0H_{ij}^{(\mathrm{pol})}N_i^*N_j^*.$$

C.3.2 Spherical integration

In the context of moderate anisotropy, only the second order of the $\hat{R}_{ij}$ expansion is kept. This means that all quadratic contributions $H_{ij}^{()}H_{mn}^{()}$ can be simplified, because there are negligible with respect to $H_{ij}^{()}$. Remembering that $H_{ii}^{()} = 0$ and $H_{ij}^{()} = H_{ji}^{()}$, and using the following relations

$$\int_{S_k} \alpha_i\alpha_j\mathrm{d}^2\boldsymbol{k} = \frac{4\pi k^2}{3}\delta_{ij}, \qquad \int_{S_k} \alpha_i\alpha_j\alpha_m\alpha_n\mathrm{d}^2\boldsymbol{k} = \frac{4\pi k^2}{15}(\delta_{ij}\delta_{mn} + \delta_{im}\delta_{jn} + \delta_{in}\delta_{jm}),$$

$$\int_{S_k} \alpha_i\mathrm{d}^2\boldsymbol{k} = \int_{S_k} \alpha_i\alpha_j\alpha_n\mathrm{d}^2\boldsymbol{k} = 0,$$

$$\int_{S_k} H_{mn}^{()}\alpha_m\alpha_nP_{ij}\mathrm{d}^2\boldsymbol{k} = -\frac{8}{15}\pi k^2H_{ij}^{()}, \qquad \int_{S_k} H_{mn}^{()}N_m^*N_n^*N_iN_j\mathrm{d}^2\boldsymbol{k} = \frac{16}{5}\pi k^2H_{ij}^{()},$$

it is possible to integrate spherically the directional and polarization transfer terms $T_{\mathcal{E}}$ and T_Z given by (2.41) and (2.42). Let's define $S^{\mathrm{NL(iso)}}$, the non-linear spherically-averaged isotropic transfer is obtained by spherically averaging $T_{\mathcal{E}}$ as defined in (2.56). One can note that

$$\int_{S_k} \alpha_i \alpha_j H_{ij}^{()} \mathrm{d}^2\boldsymbol{k} = 0,$$

and thus the classical isotropic transfer term (2.57) is recovered. For the anisotropic transfer terms, the first thing to do is to discard terms such as $\mathcal{E}^{(\mathrm{dir})'}\mathcal{E}^{(\mathrm{dir})''}$ or $\mathcal{E}^{(\mathrm{dir})'}\Re X''$ and so on, because they are quadratic in $H_{ij}^{()}$. Using the previous relations for λ-integration and spherical averaging, expressions (2.59) and (2.61) are recovered.

C.4 Spherically-averaged linear transfers

Now, the emphasis is put on the linear terms that contribute to the total transfer. It is possible to write the Craya equation (2.13) as

$$\frac{\partial \hat{R}_{ij}}{\partial t} + 2\nu k^2 \hat{R}_{ij} = T_{ij}^{\mathrm{NL}} + T_{ij}^{\mathrm{L}}, \tag{C.38}$$

with the linear transfer being (starting from $\mathcal{E}$-Lin and Z-Lin equations is more complicated)

$$T_{ij}^{\mathrm{L}} = 2A_{ln}\alpha_l(\alpha_i \hat{R}_{nj} + \alpha_j \hat{R}_{ni}) + A_{ln}k_l \frac{\partial \hat{R}_{ij}}{\partial k_n} - (A_{il}\hat{R}_{lj} + A_{jl}\hat{R}_{il}). \tag{C.39}$$

C.4.1 Spherical integration

The previous relations are still verified. The following ones are used as well

$$A_{ln}\int_{S_k} \alpha_i\alpha_j\alpha_l\alpha_n \mathrm{d}^2\boldsymbol{k} = \frac{8\pi k^2}{15} A_{ij}^{+}, \qquad \int_{S_k} A_{ln}k_l \frac{\partial \mathcal{E}_0 \alpha_i\alpha_j}{\partial k_n}\mathrm{d}^2\boldsymbol{k} = \frac{8\pi k^2}{15} A_{ij}^{+}\left(3\mathcal{E}_0 + k\frac{\partial \mathcal{E}_0}{\partial k}\right),$$

$$\int_{S_k} A_{ln}k_l \frac{\partial H_{pq}^{()}\alpha_p\alpha_q}{\partial k_n}\mathrm{d}^2\boldsymbol{k} = \frac{8\pi k^2}{15} A_{ln}^{+}\left(k\frac{\partial H_{ln}^{()}}{\partial k} + 3H_{ln}^{()}\right),$$

$$A_{ln}H_{pq}^{()}\int_{S_k} \alpha_i\alpha_j\alpha_l\alpha_n\alpha_p\alpha_q \mathrm{d}^2\boldsymbol{k} = \frac{8\pi k^2}{105}\left(2A_{il}^{+}H_{jl}^{()} + 2A_{jl}^{+}H_{il}^{()} + A_{ln}^{+}H_{ln}^{()}\delta_{ij}\right),$$

$$\int_{S_k} A_{ln}k_l \frac{\partial H_{pq}^{()}\alpha_p\alpha_q\alpha_i\alpha_j}{\partial k_n}\mathrm{d}^2\boldsymbol{k} = \frac{8\pi k^2}{105}\Big((A_{li} + A_{il})\left(k\frac{\partial H_{lj}^{()}}{\partial k} + 3H_{lj}^{()}\right)$$
$$+ (A_{lj} + A_{jl})\left(k\frac{\partial H_{li}^{()}}{\partial k} + 3H_{li}^{()}\right) + A_{ln}\left(k\frac{\partial H_{ln}^{()}}{\partial k} + 3H_{ln}^{()}\right)\delta_{ij}\Big),$$

$$k\frac{\partial}{\partial k}(\mathcal{E}_0 H_{ij}^{()}) + 3H_{ij}^{()}\mathcal{E}_0 = \frac{1}{4\pi k^2}\frac{\partial}{\partial k}(kEH_{ij}^{()}).$$

C.4.2 Computation of T_{ij}^{L}

The method to compute the linear transfers is the following one: firstly, the linear isotropic term $S^L(k,t)$ is evaluated. Then, the total linear term, defined in (2.77), is computed. The linear directional transfer $S_{ij}^{\mathrm{L(dir)}}(k,t)$, without the isotropic part, is calculated. Finally, both the isotropic and directional parts

are subtracted from the total linear transfer to obtain the polarization one $S_{ij}^{\mathrm{L(pol)}}(k,t)$. This process is easier than computing directly the polarization transfer. Hence, one has

$$S_{ij}^{\mathrm{L(tot)}}(k,t) = \int_{S_k} T_{ij}^{\mathrm{L}}(k,t)\mathrm{d}^2\boldsymbol{k} = 2\Big(\frac{\delta_{ij}}{3}S^{\mathrm{L(iso)}}(k,t) + S_{ij}^{\mathrm{L(dir)}}(k,t) + S_{ij}^{\mathrm{L(pol)}}(k,t)\Big).$$

A convenient expression of $\hat{R}_{ij}$ is used

$$\hat{R}_{ij} = \hat{R}_{ij}^{\mathrm{e}} + \hat{R}_{ij}^{\mathrm{z}} = \mathcal{E}_0 P_{ij}\Big(1 - 15H_{pq}^{(\mathrm{dir})}\alpha_p\alpha_q\Big) + 5\mathcal{E}_0\Big(P_{in}P_{jm}H_{mn}^{(\mathrm{pol})} + \frac{1}{2}P_{ij}H_{pq}^{(\mathrm{pol})}\alpha_p\alpha_q\Big), \tag{C.40}$$

where $\hat{R}_{ij}^{\mathrm{e}}$ accounts for isotropy and directivity, and $\hat{R}_{ij}^{\mathrm{z}}$ for polarization. In the following calculations, the velocity gradient A_{ij} is decomposed into symmetric and antisymmetric matrices

$$A_{ij}^{+} = \frac{A_{ij} + A_{ji}}{2}, \qquad A_{ij}^{-} = \frac{A_{ij} - A_{ji}}{2}.$$

Computation of $S^{\mathrm{L(iso)}}$ and $S_{ij}^{\mathrm{L(tot)}}$: Using $P_{ii} = 2$ and $\hat{R}_{ii}^{\mathrm{z}} = 0$, one recovers easily (2.63) for $S^{\mathrm{L(iso)}}$. To compute the total linear transfer, three contributions of (C.39) have to be calculated for $\hat{R}_{ij}^{\mathrm{e}}$ and $\hat{R}_{ij}^{\mathrm{z}}$, namely

$$\begin{aligned}
&\int_{S_k} 2A_{ln}\alpha_l(\alpha_i\hat{R}_{nj}^{\mathrm{e}} + \alpha_j\hat{R}_{ni}^{\mathrm{e}})\mathrm{d}^2\boldsymbol{k} = \\
&\frac{4}{5}EA_{ij}^{+} - \frac{12}{7}E\Big(A_{lj}^{+}H_{li}^{(\mathrm{dir})} + A_{li}^{+}H_{lj}^{(\mathrm{dir})} - \frac{2}{3}\delta_{ij}A_{lm}^{+}H_{lm}^{(\mathrm{dir})}\Big) + 4E\Big(A_{jl}^{-}H_{il}^{(\mathrm{dir})} + A_{il}^{-}H_{jl}^{(\mathrm{dir})}\Big), \\
&\int_{S_k} 2A_{ln}\alpha_l(\alpha_i\hat{R}_{nj}^{\mathrm{z}} + \alpha_j\hat{R}_{ni}^{\mathrm{z}})\mathrm{d}^2\boldsymbol{k} = \\
&\frac{12}{7}E\Big(A_{lj}^{+}H_{li}^{(\mathrm{pol})} + A_{li}^{+}H_{lj}^{(\mathrm{pol})} - \frac{2}{3}\delta_{ij}A_{lm}^{+}H_{lm}^{(\mathrm{pol})}\Big) + \frac{4}{3}E\Big(A_{jl}^{-}H_{il}^{(\mathrm{pol})} + A_{il}^{-}H_{jl}^{(\mathrm{pol})}\Big) \\
&\int_{S_k} A_{ln}k_l\frac{\partial\hat{R}_{ij}^{\mathrm{e}}}{\partial k_n}\mathrm{d}^2\boldsymbol{k} = -\frac{2}{15}A_{ij}^{+}\frac{\partial kE}{\partial k} \\
&+ \frac{4}{7}\Big(A_{il}^{+}\frac{\partial}{\partial k}(kEH_{lj}^{(\mathrm{dir})}) + A_{jl}^{+}\frac{\partial}{\partial k}(kEH_{li}^{(\mathrm{dir})}) - 3\delta_{ij}A_{lm}^{+}\frac{\partial}{\partial k}(kEH_{lm}^{(\mathrm{dir})})\Big), \\
&\int_{S_k} A_{ln}k_l\frac{\partial\hat{R}_{ij}^{\mathrm{z}}}{\partial k_n}\mathrm{d}^2\boldsymbol{k} = -\frac{4}{7}\Big(A_{il}^{+}\frac{\partial}{\partial k}(kEH_{lj}^{(\mathrm{pol})}) + A_{jl}^{+}\frac{\partial}{\partial k}(kEH_{li}^{(\mathrm{pol})}) - \frac{2}{3}\delta_{ij}A_{lm}^{+}\frac{\partial}{\partial k}(kEH_{lm}^{(\mathrm{pol})})\Big), \\
&\int_{S_k} (A_{il}\hat{R}_{lj}^{\mathrm{e}} + A_{jl}\hat{R}_{il}^{\mathrm{e}})\mathrm{d}^2\boldsymbol{k} = \frac{4}{3}EA_{ij}^{+} + 2E\Big(A_{il}^{+}H_{jl}^{(\mathrm{dir})} + A_{jl}^{+}H_{il}^{(\mathrm{dir})} + A_{il}^{-}H_{jl}^{(\mathrm{dir})} + A_{jl}^{-}H_{il}^{(\mathrm{dir})}\Big), \\
&\int_{S_k} (A_{il}\hat{R}_{lj}^{\mathrm{z}} + A_{jl}\hat{R}_{il}^{\mathrm{z}})\mathrm{d}^2\boldsymbol{k} = 2E\Big(A_{il}^{+}H_{jl}^{(\mathrm{pol})} + A_{jl}^{+}H_{il}^{(\mathrm{pol})} + A_{il}^{-}H_{jl}^{(\mathrm{pol})} + A_{jl}^{-}H_{il}^{(\mathrm{pol})}\Big).
\end{aligned}$$

Computation of $S_{ij}^{\mathrm{L(dir)}}$ and $S_{ij}^{\mathrm{L(pol)}}$: the definition of $S_{ij}^{\mathrm{L(dir)}}$ is given in (2.64). Firstly,

$$\begin{aligned}
\frac{1}{4}A_{ln}\int_{S_k} k_l\frac{\partial\hat{R}_{mm}^{\mathrm{e}}}{\partial k_n}P_{ij}\mathrm{d}^2\boldsymbol{k} = &-\frac{1}{15}A_{ij}^{+}\frac{\partial}{\partial k}(kE) + \frac{1}{5}A_{ij}^{+}E + E\Big(A_{jn}^{-}H_{ni}^{(\mathrm{dir})} + A_{in}^{-}H_{nj}^{(\mathrm{dir})}\Big) \\
&+ \frac{2}{7}\left(A_{il}^{+}\frac{\partial}{\partial k}(kEH_{jl}^{(\mathrm{dir})}) + A_{jl}^{+}\frac{\partial}{\partial k}(kEH_{il}^{(\mathrm{dir})}) - 3A_{lm}^{+}\delta_{ij}\frac{\partial}{\partial k}(kEH_{lm}^{(\mathrm{dir})})\right) \\
&- \frac{3}{7}E\left(A_{jl}^{+}H_{il}^{(\mathrm{dir})} + A_{il}^{+}H_{jl}^{(\mathrm{dir})} - \frac{2}{3}A_{lm}^{+}H_{lm}^{(\mathrm{dir})}\delta_{ij}\right),
\end{aligned}$$

and $\hat{R}_{mm}^{\mathrm{z}} = 0$. Similarly,

$$\frac{1}{2}A_{ln}\int_{S_k} \hat{R}_{ln}^{\mathrm{e}}P_{ij}\mathrm{d}^2\boldsymbol{k} = \frac{1}{15}EA_{ij}^{+} - \frac{2}{7}E\Big(A_{lj}^{+}H_{il}^{(\mathrm{dir})} + A_{li}^{+}H_{jl}^{(\mathrm{dir})} - 3A_{ln}^{+}\delta_{ij}H_{ln}^{(\mathrm{dir})}\Big),$$

$$\frac{1}{2}A_{ln}\int_{S_k}\hat{R}^{\mathrm{z}}_{ln}P_{ij}\mathrm{d}^2\boldsymbol{k}=\frac{2}{7}E\Big(A^+_{lj}H^{(\mathrm{pol})}_{il}+A^+_{li}H^{(\mathrm{pol})}_{jl}+\frac{5}{3}A^+_{ln}\delta_{ij}H^{(\mathrm{pol})}_{ln}\Big).$$

Summing the three previous terms and removing the isotropic part $\delta_{ij}S^{\mathrm{L(iso)}}/3$ gives (2.65). The linear polarization transfer is obtained by removing the directional and isotropic linear transfers from half of the total contribution, according to (2.77). Equation (2.67) is then recovered.

C.4.3 Return to isotropy

The following relations for the λ-integration and spherical integration are needed

$$\int_0^{2\pi}\alpha''_i\alpha''_j e^{-\mathrm{i}\lambda}\mathrm{d}\lambda=-\pi y\sqrt{1-y^2}(\alpha_iN^*_j+\alpha_jN^*_i),$$

$$\int_0^{2\pi}W''_iW''_j e^{-\mathrm{i}\lambda}\mathrm{d}\lambda=\pi(1+y)\sqrt{1-y^2}(\alpha_iN^*_j+\alpha_jN^*_i),$$

$$\int_0^{2\pi}W^{*''}_iW^{*''}_j e^{-\mathrm{i}\lambda}\mathrm{d}\lambda=\pi(y-1)\sqrt{1-y^2}(\alpha_iN^*_j+\alpha_jN^*_i),$$

$$\int_0^{2\pi}\mathcal{E}^{(\mathrm{dir})''}e^{-\mathrm{i}\lambda}\mathrm{d}\lambda=30\pi y\sqrt{1-y^2}\mathcal{E}''_0H^{(\mathrm{dir})''}_{ij}\alpha_iN^*_j,$$

$$\int_0^{2\pi}\Re X''e^{-\mathrm{i}\lambda}\mathrm{d}\lambda=5\pi y\sqrt{1-y^2}\mathcal{E}''_0H^{(\mathrm{pol})''}_{ij}\alpha_iN^*_j,$$

$$\int_0^{2\pi}i\Im X''e^{-\mathrm{i}\lambda}\mathrm{d}\lambda=-5\pi\sqrt{1-y^2}\mathcal{E}''_0H^{(\mathrm{pol})''}_{ij}\alpha_iN^*_j.$$

The p quantities (with $'$) are obtained by multiplying by -1 the rhs term and replacing y by z. Here, the useful relation for spherical integration is

$$\Re\Big(H^{()}_{mn}\alpha_m\alpha_iN^*_nN_j\Big)\mathrm{d}^2\boldsymbol{k}=\frac{4\pi k^2}{5}H^{()}_{ij}.$$

Then, from the definition of $S^{(\mathrm{RTI})}_{ij}$ given in (2.70), it is possible to integrate spherically W_{ij} using the previous relations, and to find equation (2.71).

C.4.4 Rotation

The effect of rotation on the velocity field was detailed in section C.1. It was revealed that the evolution equation of Z only was affected by rotation. Rotation was already taken into account in the Craya equation through the tensor M_{ij}, accordingly modified in (C.4). We call $\tilde{M}_{ij}$ the rotating part of this tensor. One has first to evaluate the corresponding total linear transfer

$$\tilde{S}^{\mathrm{L(tot)}}_{ij}=-\int_{S_k}(\tilde{M}_{in}\hat{R}_{nj}+\tilde{M}_{jn}\hat{R}_{ni})\mathrm{d}^2\boldsymbol{k}.$$

There are no contributions from $\hat{R}^{\mathrm{e}}_{ij}$: all terms like $\epsilon_{lmn}\alpha_l\alpha_n$ are zero which tremendously simplify the calculations. In the end, the polarization transfer is simply half the total contribution, which yields

$$\begin{aligned}\tilde{S}^{\mathrm{L(pol)}}_{ij}&=\frac{1}{2}\tilde{S}^{\mathrm{L(tot)}}_{ij}=-\frac{1}{2}\int_{S_k}(\tilde{M}_{in}\hat{R}_{nj}+\tilde{M}_{jn}\hat{R}_{ni})\mathrm{d}^2\boldsymbol{k}\\&=-\frac{4}{3}E(k,t)\Omega_m\Big(\epsilon_{imp}H^{(\mathrm{pol})}_{jp}+\epsilon_{jmp}H^{(\mathrm{pol})}_{ip}\Big).\end{aligned}\tag{C.41}$$

C.5 Kinetic quadratic anisotropic contributions

In this part, some details are given about the calculations of the second-order spherically-averaged non-linear transfer terms, which take into account quadratic contributions of anisotropy. The convenient notation is used

$$H_{li}^{(\mathrm{dir})''}H_{lj}^{(\mathrm{dir})'}+H_{lj}^{(\mathrm{dir})''}H_{li}^{(\mathrm{dir})'}-\frac{2}{3}H_{ln}^{(\mathrm{dir})''}H_{ln}^{(\mathrm{dir})'}\delta_{ij}=\left\{H^{(\mathrm{dir})''},H^{(\mathrm{dir})'}\right\}_{ij}.$$

Here are some useful relations

$$\sqrt{1-y^2}\sqrt{1-z^2}=(x+yz),\qquad 2xyz=1-x^2-y^2-z^2,$$
$$\int_{S_k}H''_{ln}H'_{pq}\alpha_l\alpha_n\alpha_p\alpha_q P_{ij}\mathrm{d}^2\boldsymbol{k}=-\frac{16\pi k^2}{105}\Big(H''_{li}H'_{lj}+H''_{lj}H'_{li}-3H''_{ln}H'_{ln}\delta_{ij}\Big),$$
$$\int_{S_k}H''_{ln}H'_{pq}\Big(\alpha_n\alpha_p\delta_{lq}+\alpha_n\alpha_q\delta_{lp}+\alpha_l\alpha_p\delta_{nq}+\alpha_l\alpha_q\delta_{np}\Big)P_{ij}\mathrm{d}^2\boldsymbol{k}$$
$$=-\frac{16\pi k^2}{15}\Big(H''_{li}H'_{lj}+H''_{lj}H'_{li}-4H''_{ln}H'_{ln}\delta_{ij}\Big),$$
$$\int_{S_k}H''_{ln}H'_{pq}\Big(\delta_{ip}\delta_{jq}+\delta_{iq}\delta_{jp}-\alpha_n\alpha_p\delta_{lq}-\alpha_n\alpha_q\delta_{lp}-\alpha_l\alpha_p\delta_{nq}-\alpha_l\alpha_q\delta_{np}\Big)P_{ij}\mathrm{d}^2\boldsymbol{k},$$
$$=\frac{16\pi k^2}{15}\Big(H''_{li}H'_{lj}+H''_{lj}H'_{li}+H''_{ln}H'_{ln}\delta_{ij}\Big),$$
$$\int_{S_k}H''_{ln}H'_{pq}\alpha_l\alpha_n N_p^*N_q^*N_iN_j\mathrm{d}^2\boldsymbol{k}=-\frac{32\pi k^2}{35}\Big(H''_{li}H'_{lj}+H''_{lj}H'_{li}-\frac{2}{3}H''_{ln}H'_{ln}\delta_{ij}\Big),$$
$$\int_{S_k}H''_{ln}H'_{pq}(\alpha_nN_l^*+\alpha_lN_n^*)(\alpha_pN_q^*+\alpha_qN_p^*)N_iN_j\mathrm{d}^2\boldsymbol{k}=\frac{96\pi k^2}{35}\Big(H''_{li}H'_{lj}+H''_{lj}H'_{li}-\frac{2}{3}H''_{ln}H'_{ln}\delta_{ij}\Big),$$
$$-\Re\Big(\int_{S_k}H''_{ln}H'_{pq}N_l^*N_n^*(\alpha_pN_q+\alpha_qN_p)(\alpha_jN_i+\alpha_iN_j)\mathrm{d}^2\boldsymbol{k}\Big)=-\frac{96\pi k^2}{35}\Big(H''_{li}H'_{lj}+H''_{lj}H'_{li}-\frac{2}{3}H''_{ln}H'_{ln}\delta_{ij}\Big),$$
$$-\Re\Big(\int_{S_k}H''_{ln}H'_{pq}\alpha_l\alpha_n(\alpha_pN_q^*+\alpha_qN_p^*)(\alpha_jN_i+\alpha_iN_j)\mathrm{d}^2\boldsymbol{k}\Big)=-\frac{16\pi k^2}{35}\Big(H''_{li}H'_{lj}+H''_{lj}H'_{li}-\frac{2}{3}H''_{ln}H'_{ln}\delta_{ij}\Big).$$

Since $H_{ln}^{()}$ and $H_{pq}^{()}$ are deviatoric tensors, terms in δ_{ln} and δ_{pq} do not bring any contributions.

Non-linear directional and isotropic transfers: the three main parts to compute of the directional transfer (2.41) are

$$T_{\mathcal{E}}^1=\mathcal{E}_0''\Big(H_{ij}^{(\mathrm{dir})''}\alpha_i''\alpha_j''+\Re(H_{ij}^{(\mathrm{pol})''}W_i^{*''}W_j^{*''})\Big)\Big(\mathcal{E}_0'H_{pq}^{(\mathrm{dir})'}\alpha_p'\alpha_q'-\mathcal{E}_0H_{pq}^{(\mathrm{dir})}\alpha_p\alpha_q\Big),$$
$$T_{\mathcal{E}}^2=\mathcal{E}_0''\Big(H_{ij}^{(\mathrm{dir})''}\alpha_i''\alpha_j''+\Re(H_{ij}^{(\mathrm{pol})''}W_i^{*''}W_j^{*''})\Big)\Re\Big(\mathcal{E}_0'H_{pq}^{(\mathrm{pol})'}W_p^{*'}W_q^{*'}-\mathcal{E}_0H_{pq}^{(\mathrm{pol})}W_p^*W_q^*\Big),$$
$$T_{\mathcal{E}}^3=\mathcal{E}_0''\Im(H_{ij}^{(\mathrm{pol})''}W_i^{*''}W_j^{*''})\Im\Big(x\mathcal{E}_0H_{pq}^{(\mathrm{pol})}W_p^*W_q^*-y\mathcal{E}_0'H_{pq}^{(\mathrm{pol})'}W_p^{*'}W_q^{*'}\Big).$$

For the λ-integration and spherical integration, here are some useful expressions

$$\int_0^{2\pi}\alpha_i''\alpha_j''\alpha_p'\alpha_q'\mathrm{d}\lambda=-yz\pi(x+yz)(\alpha_i\alpha_p\delta_{jq}+\alpha_i\alpha_q\delta_{jp}+\alpha_j\alpha_p\delta_{iq}+\alpha_j\alpha_q\delta_{ip})$$
$$+\alpha_i\alpha_j\alpha_p\alpha_q\pi\Big[2y^2z^2+\frac{3}{4}(1-y^2)(1-z^2)-y^2(1-z^2)-z^2(1-y^2)+4yz(x+yz)\Big]$$
$$+\frac{\pi}{4}(1-y^2)(1-z^2)\Big[\delta_{ip}\delta_{jq}+\delta_{iq}\delta_{jp}-\alpha_i\alpha_p\delta_{jq}-\alpha_i\alpha_q\delta_{jp}-\alpha_j\alpha_p\delta_{iq}-\alpha_j\alpha_q\delta_{ip}\Big],$$
$$\int_0^{2\pi}\alpha_i''\alpha_j''\alpha_p\alpha_q\mathrm{d}\lambda=\pi(3y^2-1)\alpha_i\alpha_j\alpha_p\alpha_q,$$
$$\int_0^{2\pi}\Re(W_i^{*''}W_j^{*''})\alpha_p'\alpha_q'\mathrm{d}\lambda=yz\pi(x+yz)(\alpha_i\alpha_p\delta_{jq}+\alpha_i\alpha_q\delta_{jp}+\alpha_j\alpha_p\delta_{iq}+\alpha_j\alpha_q\delta_{ip})$$

$$+ \alpha_i\alpha_j\alpha_p\alpha_q\pi\Big[3z^2(1-y^2)+\frac{1}{4}(1+y^2)(1-z^2)-\frac{3}{2}(1-y^2)(1-z^2)-4yz(x+yz)\Big]$$
$$+\frac{\pi}{4}(1+y^2)(1-z^2)\Big[\delta_{ip}\delta_{jq}+\delta_{iq}\delta_{jp}-\alpha_i\alpha_p\delta_{jq}-\alpha_i\alpha_q\delta_{jp}-\alpha_j\alpha_p\delta_{iq}-\alpha_j\alpha_q\delta_{ip}\Big],$$
$$\int_0^{2\pi}\Re(W_i^{*''}W_j^{*''})\alpha_p\alpha_q\mathrm{d}\lambda=3\pi(1-y^2)\alpha_i\alpha_j\alpha_p\alpha_q,$$
$$\int_{S_k}\Big(\int_0^{2\pi}T^1_{\mathcal{E}}\mathrm{d}\lambda\Big)\Big(P_{ij}-\frac{\delta_{ij}}{3}\Big)\mathrm{d}^2\boldsymbol{k}=\frac{16\pi^2k^2}{105}\mathcal{E}_0''\Bigg[$$
$$\mathcal{E}_0'(1+3xyz)\Big(H_{li}^{(\mathrm{dir})''}H_{lj}^{(\mathrm{dir})'}+H_{lj}^{(\mathrm{dir})''}H_{li}^{(\mathrm{dir})'}-\frac{2}{3}H_{ln}^{(\mathrm{dir})''}H_{ln}^{(\mathrm{dir})'}\delta_{ij}\Big)$$
$$+\mathcal{E}_0(3y^2-1)\Big(H_{li}^{(\mathrm{dir})''}H_{lj}^{(\mathrm{dir})}+H_{lj}^{(\mathrm{dir})''}H_{li}^{(\mathrm{dir})}-\frac{2}{3}H_{ln}^{(\mathrm{dir})''}H_{ln}^{(\mathrm{dir})}\delta_{ij}\Big)$$
$$+\mathcal{E}_0'(3-6z^2-3xyz)\Big(H_{li}^{(\mathrm{pol})''}H_{lj}^{(\mathrm{dir})'}+H_{lj}^{(\mathrm{pol})''}H_{li}^{(\mathrm{dir})'}-\frac{2}{3}H_{ln}^{(\mathrm{pol})''}H_{ln}^{(\mathrm{dir})'}\delta_{ij}\Big)$$
$$+3\mathcal{E}_0(1-y^2)\Big(H_{li}^{(\mathrm{pol})''}H_{lj}^{(\mathrm{dir})}+H_{lj}^{(\mathrm{pol})''}H_{li}^{(\mathrm{dir})}-\frac{2}{3}H_{ln}^{(\mathrm{pol})''}H_{ln}^{(\mathrm{dir})}\delta_{ij}\Big)\Bigg],$$
$$\int_{S_k}\Bigg(\int_0^{2\pi}T^1_{\mathcal{E}}\mathrm{d}\lambda\Big)\mathrm{d}^2\boldsymbol{k}=\frac{16\pi^2k^2}{15}\mathcal{E}_0''\Big[(3x^2-1)\mathcal{E}_0'H_{ln}^{(\mathrm{dir})''}H_{ln}^{(\mathrm{dir})'}+(3-3x^2)\mathcal{E}_0'H_{ln}^{(\mathrm{pol})''}H_{ln}^{(\mathrm{dir})'}$$
$$-(3y^2-1)\mathcal{E}_0H_{ln}^{(\mathrm{dir})''}H_{ln}^{(\mathrm{dir})}-3(1-y^2)\mathcal{E}_0H_{ln}^{(\mathrm{pol})''}H_{ln}^{(\mathrm{dir})}\Bigg],$$
$$\int_0^{2\pi}\alpha_p''\alpha_q''\Re(W_i^*W_j^*)\mathrm{d}\lambda=2\pi(1-y^2)$$
$$\Big(\alpha_i\alpha_j\alpha_p\alpha_q+\delta_{ip}\delta_{jq}+\delta_{iq}\delta_{jp}-\alpha_i\alpha_p\delta_{jq}-\alpha_i\alpha_q\delta_{jp}-\alpha_j\alpha_p\delta_{iq}-\alpha_j\alpha_q\delta_{ip}\Big),$$
$$\int_0^{2\pi}\Re(W_i^{*''}W_j^{*''})\Re(W_p^{'*}W_q^{'*})\mathrm{d}\lambda=-\pi yz(x+yz)(\alpha_i\alpha_p\delta_{jq}+\alpha_i\alpha_q\delta_{jp}+\alpha_j\alpha_p\delta_{iq}+\alpha_j\alpha_q\delta_{ip})$$
$$+2\pi\alpha_i\alpha_j\alpha_p\alpha_q\Big[\frac{9}{4}(1-y^2)(1-z^2)+2yz(x+yz)+\frac{1}{8}(1+y^2)(1+z^2)\Big]$$
$$+\frac{\pi}{4}(1+y^2)(1+z^2)\Big[\delta_{ip}\delta_{jq}+\delta_{iq}\delta_{jp}-\alpha_i\alpha_p\delta_{jq}-\alpha_i\alpha_q\delta_{jp}-\alpha_j\alpha_p\delta_{iq}-\alpha_j\alpha_q\delta_{ip}\Big],$$
$$\int_0^{2\pi}\Re(W_i^{*''}W_j^{*''})\Re(W_p^*W_q^*)\mathrm{d}\lambda=\frac{\pi}{2}(1+y^2)$$
$$\Big(\alpha_i\alpha_j\alpha_p\alpha_q+\delta_{ip}\delta_{jq}+\delta_{iq}\delta_{jp}-\alpha_i\alpha_p\delta_{jq}-\alpha_i\alpha_q\delta_{jp}-\alpha_j\alpha_p\delta_{iq}-\alpha_j\alpha_q\delta_{ip}\Big),$$
$$\int_{S_k}\Big(\int_0^{2\pi}T^2_{\mathcal{E}}\mathrm{d}\lambda\Big)\Big(P_{ij}-\frac{\delta_{ij}}{3}\Big)\mathrm{d}^2\boldsymbol{k}=\frac{16\pi^2k^2}{105}\mathcal{E}_0''\Bigg[$$
$$+\mathcal{E}_0'(3-6y^2-3xyz)\Big(H_{li}^{(\mathrm{dir})''}H_{lj}^{(\mathrm{pol})'}+H_{lj}^{(\mathrm{dir})''}H_{li}^{(\mathrm{pol})'}-\frac{2}{3}H_{ln}^{(\mathrm{dir})''}H_{ln}^{(\mathrm{pol})'}\delta_{ij}\Big)$$
$$-3\mathcal{E}_0(1-y^2)\Big(H_{li}^{(\mathrm{dir})''}H_{lj}^{(\mathrm{pol})}+H_{lj}^{(\mathrm{dir})''}H_{li}^{(\mathrm{pol})}-\frac{2}{3}H_{ln}^{(\mathrm{dir})''}H_{ln}^{(\mathrm{pol})}\delta_{ij}\Big)$$
$$+\mathcal{E}_0'(3-6x^2-9xyz)\Big(H_{li}^{(\mathrm{pol})''}H_{lj}^{(\mathrm{pol})'}+H_{lj}^{(\mathrm{pol})''}H_{li}^{(\mathrm{pol})'}-\frac{2}{3}H_{ln}^{(\mathrm{pol})''}H_{ln}^{(\mathrm{pol})'}\delta_{ij}\Big)$$
$$-3\mathcal{E}_0(1+y^2)\Big(H_{li}^{(\mathrm{pol})''}H_{lj}^{(\mathrm{pol})}+H_{lj}^{(\mathrm{pol})''}H_{li}^{(\mathrm{pol})}-\frac{2}{3}H_{ln}^{(\mathrm{pol})''}H_{ln}^{(\mathrm{pol})}\delta_{ij}\Big)\Bigg],$$
$$\int_{S_k}\Big(\int_0^{2\pi}T^2_{\mathcal{E}}\mathrm{d}\lambda\Big)\mathrm{d}^2\boldsymbol{k}=\frac{16\pi^2k^2}{15}\mathcal{E}_0''\Bigg[\mathcal{E}_0'(3x^2+3)H_{ln}^{(\mathrm{pol})''}H_{ln}^{(\mathrm{pol})'}+(3-3x^2)\mathcal{E}_0'H_{ln}^{(\mathrm{dir})''}H_{ln}^{(\mathrm{pol})'}$$
$$-3(1-y^2)\mathcal{E}_0H_{ln}^{(\mathrm{dir})''}H_{ln}^{(\mathrm{pol})}-3\mathcal{E}_0(1+y^2)H_{ln}^{(\mathrm{pol})''}H_{ln}^{(\mathrm{pol})}\Bigg],$$
$$\int_0^{2\pi}\Im(W_i^{*''}W_j^{*''})\Im(W_p^{*'}W_q^{*'})\mathrm{d}\lambda=-\pi(x+yz)(\alpha_i\alpha_p\delta_{jq}+\alpha_i\alpha_q\delta_{jp}+\alpha_j\alpha_p\delta_{iq}+\alpha_j\alpha_q\delta_{ip})$$

$$+\pi\alpha_i\alpha_j\alpha_p\alpha_q\Big[4(x+yz)+yz\Big]+\pi yz\Big[\delta_{ip}\delta_{jq}+\delta_{iq}\delta_{jp}-\alpha_i\alpha_p\delta_{jq}-\alpha_i\alpha_q\delta_{jp}-\alpha_j\alpha_p\delta_{iq}-\alpha_j\alpha_q\delta_{ip}\Big],$$

$$\int_0^{2\pi}\Im(W_i^{*''}W_j^{*''})\Im(W_p^*W_q^*)\mathrm{d}\lambda=$$

$$-\pi y(\alpha_i\alpha_j\alpha_p\alpha_q+\delta_{ip}\delta_{jq}+\delta_{iq}\delta_{jp}-\alpha_i\alpha_p\delta_{jq}-\alpha_i\alpha_q\delta_{jp}-\alpha_j\alpha_p\delta_{iq}-\alpha_j\alpha_q\delta_{ip}),$$

$$\int_{S_k}\Big(\int_0^{2\pi}T_{\mathcal{E}}^3\mathrm{d}\lambda\Big)\Big(P_{ij}-\frac{\delta_{ij}}{3}\Big)\mathrm{d}^2\boldsymbol{k}=$$

$$\frac{16\pi^2k^2}{105}\mathcal{E}_0''\Bigg[-6xy\mathcal{E}_0\Big(H_{li}^{(\mathrm{pol})''}H_{lj}^{(\mathrm{pol})}+H_{lj}^{(\mathrm{pol})''}H_{li}^{(\mathrm{pol})}-\frac{2}{3}H_{ln}^{(\mathrm{pol})''}H_{ln}^{(\mathrm{pol})}\delta_{ij}\Big)$$

$$-y\mathcal{E}_0'(3x+9yz)\Big(H_{li}^{(\mathrm{pol})''}H_{lj}^{(\mathrm{pol})'}+H_{lj}^{(\mathrm{pol})''}H_{li}^{(\mathrm{pol})'}-\frac{2}{3}H_{ln}^{(\mathrm{pol})''}H_{ln}^{(\mathrm{pol})'}\delta_{ij}\Big)\Bigg],$$

$$\int_{S_k}\Big(\int_0^{2\pi}T_{\mathcal{E}}^3\mathrm{d}\lambda\Big)\mathrm{d}^2\boldsymbol{k}=\frac{16\pi^2k^2}{15}\mathcal{E}_0''\Bigg[-6xy\mathcal{E}_0H_{ln}^{(\mathrm{pol})''}H_{ln}^{(\mathrm{pol})}-y\mathcal{E}_0'(-6x)H_{ln}^{(\mathrm{pol})''}H_{ln}^{(\mathrm{pol})'}\Bigg].$$

Non-linear polarization transfer: the three main parts to compute of the polarization transfer (2.42) are

$$T_Z^1=\mathcal{E}_0''\Big(H_{ij}^{(\mathrm{dir})''}\alpha_i''\alpha_j''+\Re(H_{ij}^{(\mathrm{pol})''}W_i^{*''}W_j^{*''})\Big)\Big(\Re(\mathcal{E}_0'H_{pq}^{(\mathrm{pol})'}W_p^{*'}W_q^{*'})-\mathcal{E}_0H_{pq}^{(\mathrm{pol})}W_p^*W_q^*\Big),$$

$$T_Z^2=\mathcal{E}_0''\Big(H_{ij}^{(\mathrm{dir})''}\alpha_i''\alpha_j''+\Re(H_{ij}^{(\mathrm{pol})''}W_i^{*''}W_j^{*''})\Big)\Big(\mathcal{E}_0'H_{pq}^{(\mathrm{dir})'}\alpha_p'\alpha_q'-\mathcal{E}_0H_{pq}^{(\mathrm{dir})}\alpha_p\alpha_q\Big),$$

$$T_Z^3=\mathrm{i}\mathcal{E}_0''\Big(H_{ij}^{(\mathrm{dir})''}\alpha_i''\alpha_j''+\Re(H_{ij}^{(\mathrm{pol})''}W_i^{*''}W_j^{*''})\Big)\Im(H_{pq}^{(\mathrm{pol})'}W_p^{*'}W_q^{*'}),$$

$$T_Z^4=\mathrm{i}\mathcal{E}_0''\Im(H_{ij}^{(\mathrm{pol})''}W_i^{*''}W_j^{*''})\Big(x\mathcal{E}_0(H_{pq}^{(\mathrm{dir})}\alpha_p\alpha_q+H_{pq}^{(\mathrm{pol})}W_p^*W_q^*)-\mathrm{i}y\mathcal{E}_0'\Im(H_{pq}^{(\mathrm{pol})'}W_p^{*'}W_q^{*'})\Big).$$

For the λ-integration and spherical integration, here are some useful expressions

$$\int_0^{2\pi}e^{-2\mathrm{i}\lambda}\alpha_i''\alpha_j''\Re(W_p^{*'}W_q^{*'})\mathrm{d}\lambda=\frac{\pi}{2}yz(x+yz)(\alpha_iN_j^*+\alpha_jN_i^*)(\alpha_pN_q^*+\alpha_qN_p^*)$$

$$+\pi\alpha_i\alpha_jN_p^*N_q^*\Big(-\frac{1}{4}(1-y^2)(1+z^2)+\frac{1}{2}y^2(1+z^2)\Big)+\frac{3\pi}{4}(1-y^2)(1-z^2)\alpha_p\alpha_qN_i^*N_j^*,$$

$$\int_0^{2\pi}e^{-2\mathrm{i}\lambda}\Re(W_i^{*''}W_j^{*''})\Re(W_p^{*'}W_q^{*'})\mathrm{d}\lambda=-\frac{\pi}{2}yz(x+yz)(\alpha_iN_j^*+\alpha_jN_i^*)(\alpha_pN_q^*+\alpha_qN_p^*)$$

$$+\frac{3\pi}{4}(1-y^2)(1+z^2)\alpha_i\alpha_jN_p^*N_q^*+\frac{3\pi}{4}(1+y^2)(1-z^2)\alpha_p\alpha_qN_i^*N_j^*,$$

$$\int_0^{2\pi}e^{-2\mathrm{i}\lambda}\alpha_i''\alpha_j''N_p^*N_q^*\mathrm{d}\lambda=\pi(3y^2-1)\alpha_i\alpha_jN_p^*N_q^*,$$

$$\int_0^{2\pi}e^{-2\mathrm{i}\lambda}\Re(W_i^{*''}W_j^{*''})W_p^*W_q^*\mathrm{d}\lambda=3\pi(1-y^2)\alpha_i\alpha_jN_p^*N_q^*,$$

$$\int_{S_k}\Big(\int_0^{2\pi}T_Z^1\mathrm{d}\lambda\Big)N_i^*N_j^*\mathrm{d}^2\boldsymbol{k}=\frac{16\pi^2k^2}{35}\mathcal{E}_0''\Bigg[$$

$$\mathcal{E}_0'(3xyz+2z^2-1)\Big\{H^{(\mathrm{dir})''},H^{(\mathrm{pol})'}\Big\}_{ij}-3(xyz+1)\mathcal{E}_0'\Big\{H^{(\mathrm{pol})''},H^{(\mathrm{pol})'}\Big\}_{ij}$$

$$+2(3y^2-1)\mathcal{E}_0\Big\{H^{(\mathrm{dir})''},H^{(\mathrm{pol})}\Big\}_{ij}+6(1-y^2)\mathcal{E}_0\Big\{H^{(\mathrm{pol})''},H^{(\mathrm{pol})}\Big\}_{ij}\Bigg],$$

$$\int_0^{2\pi}e^{-2\mathrm{i}\lambda}\alpha_i''\alpha_j''\alpha_p'\alpha_q'\mathrm{d}\lambda=-\frac{\pi}{2}yz(x+yz)(\alpha_iN_j^*+\alpha_jN_i^*)(\alpha_pN_q^*+\alpha_qN_p^*)$$

$$+\pi\alpha_i\alpha_jN_p^*N_q^*\Big(-\frac{1}{4}(1-y^2)(1-z^2)+\frac{1}{2}y^2(1-z^2)\Big)$$

$$+\pi\alpha_p\alpha_qN_i^*N_j^*\Big(-\frac{1}{4}(1-y^2)(1-z^2)+\frac{1}{2}z^2(1-y^2)\Big),$$

$$\int_0^{2\pi} e^{-2\mathrm{i}\lambda}\alpha_i''\alpha_j''\alpha_p\alpha_q\mathrm{d}\lambda = \frac{\pi}{2}(1-y^2)\alpha_p\alpha_q N_i^* N_j^*,$$

$$\int_0^{2\pi} e^{-2\mathrm{i}\lambda}\Re(W_i^{*''}W_j^{*''})\alpha_p\alpha_q\mathrm{d}\lambda = \frac{\pi}{2}(1+y^2)\alpha_p\alpha_q N_i^* N_j^*,$$

$$\int_{S_k}\Big(\int_0^{2\pi} T_Z^2\mathrm{d}\lambda\Big)N_i^*N_j^*\mathrm{d}^2\boldsymbol{k} = \frac{16\pi^2k^2}{35}\mathcal{E}_0''\Bigg[\mathcal{E}_0'(xyz+2x^2-1)\Big\{H^{(\mathrm{dir})''},H^{(\mathrm{dir})'}\Big\}_{ij}$$

$$+(1+y^2)\mathcal{E}_0\Big\{H^{(\mathrm{pol})''},H^{(\mathrm{dir})}\Big\}_{ij}+\mathcal{E}_0'(3xyz+2y^2-1)\Big\{H^{(\mathrm{pol})''},H^{(\mathrm{dir})'}\Big\}_{ij}+(1-y^2)\mathcal{E}_0\Big\{H^{(\mathrm{dir})''},H^{(\mathrm{dir})}\Big\}_{ij}\Bigg],$$

$$\int_0^{2\pi}\mathrm{i}e^{-2\mathrm{i}\lambda}\alpha_i''\alpha_j''\Im(W_p^{*'}W_q^{*'})\mathrm{d}\lambda = -\frac{\pi}{2}y(x+yz)(\alpha_iN_j^*+\alpha_jN_i^*)(\alpha_pN_q^*+\alpha_qN_p^*)$$

$$+\frac{\pi}{2}z(1-3y^2)\alpha_i\alpha_jN_p^*N_q^*,$$

$$\int_0^{2\pi}\mathrm{i}e^{-2\mathrm{i}\lambda}\Re(W_i^{*''}W_j^{*''})\Im(W_p^{*'}W_q^{*'})\mathrm{d}\lambda = \frac{\pi}{2}y(x+yz)(\alpha_iN_j^*+\alpha_jN_i^*)(\alpha_pN_q^*+\alpha_qN_p^*)$$

$$-\frac{3\pi}{2}z(1-y^2)\alpha_i\alpha_jN_p^*N_q^*,$$

$$\int_{S_k}\Big(\int_0^{2\pi} T_Z^3\mathrm{d}\lambda\Big)N_i^*N_j^*\mathrm{d}^2\boldsymbol{k} = \frac{16\pi^2k^2}{35}\mathcal{E}_0''\Bigg[3(xy+z)\mathcal{E}_0'\Big\{H^{(\mathrm{pol})''},H^{(\mathrm{pol})'}\Big\}_{ij}$$

$$-(3xy+z)\mathcal{E}_0'\Big\{H^{(\mathrm{dir})''},H^{(\mathrm{pol})'}\Big\}_{ij}\Bigg],$$

$$\int_0^{2\pi}\mathrm{i}e^{-2\mathrm{i}\lambda}\Im(W_i^{*''}W_j^{*''})\alpha_p\alpha_q\mathrm{d}\lambda = -\pi y\alpha_p\alpha_qN_i^*N_j^*, \qquad \int_0^{2\pi} ie^{-2\mathrm{i}\lambda}\Im(W_i^{*''}W_j^{*''})N_p^*N_q^*\mathrm{d}\lambda = 0,$$

$$\int_0^{2\pi} e^{-2\mathrm{i}\lambda}\Im(W_i^{*''}W_j^{*''})\Im(W_p^{*'}W_q^{*'})\mathrm{d}\lambda = \frac{\pi}{2}(x+yz)(\alpha_iN_j^*+\alpha_jN_i^*)(\alpha_pN_q^*+\alpha_qN_p^*),$$

$$\int_{S_k}\Big(\int_0^{2\pi} T_Z^4\mathrm{d}\lambda\Big)N_i^*N_j^*\mathrm{d}^2\boldsymbol{k} = \frac{16\pi^2k^2}{35}\mathcal{E}_0''\Bigg[2xy\mathcal{E}_0\Big\{H^{(\mathrm{pol})''},H^{(\mathrm{dir})}\Big\}_{ij}+3y(x+yz)\mathcal{E}_0'\Big\{H^{(\mathrm{pol})''},H^{(\mathrm{pol})'}\Big\}_{ij}\Bigg].$$

Non-linear return to isotropy transfer: the three main parts to compute of the non-linear return to isotropy transfer (2.69) are

$$T_{\mathrm{RTI}}^1 = \mathcal{E}_0''\mathcal{E}_0\Big(H_{ij}^{(\mathrm{dir})''}\alpha_i''\alpha_j''+\Re(H_{ij}^{(\mathrm{pol})''}W_i^{*''}W_j^{*''})\Big)\Big(H_{pq}^{(\mathrm{dir})}\alpha_p\alpha_q+H_{pq}^{(\mathrm{pol})}W_p^*W_q^*\Big),$$

$$T_{\mathrm{RTI}}^2 = \mathcal{E}_0''\mathcal{E}_0'\Big(H_{ij}^{(\mathrm{dir})''}\alpha_i''\alpha_j''+\Re(H_{ij}^{(\mathrm{pol})''}W_i^{*''}W_j^{*''})\Big)\Big(H_{pq}^{(\mathrm{dir})'}\alpha_p'\alpha_q'+\Re(H_{pq}^{(\mathrm{pol})'}W_p^{*'}W_q^{*'})\Big),$$

$$T_{\mathrm{RTI}}^3 = i\mathcal{E}_0''\mathcal{E}_0'\Big(H_{ij}^{(\mathrm{dir})''}\alpha_i''\alpha_j''+\Re(H_{ij}^{(\mathrm{pol})''}W_i^{*''}W_j^{*''})\Big)\Im(H_{pq}^{(\mathrm{pol})'}W_p^{*'}W_q^{*'}).$$

For the λ-integration and spherical integration, here are some useful expressions

$$\int_0^{2\pi} e^{-\mathrm{i}\lambda}\alpha_i''\alpha_j''\alpha_p\alpha_q\mathrm{d}\lambda = -\pi y\sqrt{1-y^2}\alpha_p\alpha_q(\alpha_iN_j^*+\alpha_jN_i^*),$$

$$\int_0^{2\pi} e^{-\mathrm{i}\lambda}\alpha_i''\alpha_j''W_p^*W_q^*\mathrm{d}\lambda = -\pi y\sqrt{1-y^2}N_p^*N_q^*(\alpha_iN_j+\alpha_jN_i),$$

$$\int_0^{2\pi} e^{-\mathrm{i}\lambda}\Re(W_i''^*W_j''^*)\alpha_p\alpha_q\mathrm{d}\lambda = \pi y\sqrt{1-y^2}\alpha_p\alpha_q(\alpha_iN_j^*+\alpha_jN_i^*),$$

$$\int_0^{2\pi} e^{-\mathrm{i}\lambda}\Re(W_i''^*W_j''^*)W_p^*W_q^*\mathrm{d}\lambda = \pi y\sqrt{1-y^2}N_p^*N_q^*(\alpha_iN_j+\alpha_jN_i),$$

$$-\Re\int_{S_k}\Big(\int_0^{2\pi} T_{\mathrm{RTI}}^1\mathrm{d}\lambda\Big)(\alpha_iN_j+\alpha_jN_i)\mathrm{d}^2\boldsymbol{k} = \frac{16\pi^2k^2}{35}\mathcal{E}_0''\mathcal{E}_0y\sqrt{1-y^2}\Bigg[$$

$$\left\{H^{(\mathrm{dir})''}, H^{(\mathrm{dir})}\right\}_{ij} + 6\left\{H^{(\mathrm{dir})''}, H^{(\mathrm{pol})}\right\}_{ij} - \left\{H^{(\mathrm{pol})''}, H^{(\mathrm{dir})}\right\}_{ij} - 6\left\{H^{(\mathrm{pol})''}, H^{(\mathrm{pol})}\right\}_{ij}\Bigg],$$

$$\int_0^{2\pi} e^{-\mathrm{i}\lambda}\alpha_i''\alpha_j''\alpha_p'\alpha_q'\mathrm{d}\lambda = 2\pi$$

$$\Bigg[\frac{3y^2-1}{4}z\sqrt{1-z^2}\alpha_i\alpha_j(\alpha_p N_q^* + \alpha_q N_p^*) + \frac{1-3z^2}{4}y\sqrt{1-y^2}\alpha_p\alpha_q(\alpha_i N_j^* + \alpha_j N_i^*)$$

$$+ \frac{1-y^2}{8}z\sqrt{1-z^2}N_i^* N_j^*(\alpha_p N_q + \alpha_q N_p) - \frac{1-z^2}{8}y\sqrt{1-y^2}N_p^* N_q^*(\alpha_i N_j + \alpha_j N_i)\Bigg],$$

$$\int_0^{2\pi} e^{-\mathrm{i}\lambda}\alpha_i''\alpha_j''\Re(W_p'^* W_q'^*)\mathrm{d}\lambda = 2\pi$$

$$\Bigg[\frac{1-3y^2}{4}z\sqrt{1-z^2}\alpha_i\alpha_j(\alpha_p N_q^* + \alpha_q N_p^*) - \frac{3}{4}y\sqrt{1-y^2}(1-z^2)\alpha_p\alpha_q(\alpha_i N_j^* + \alpha_j N_i^*)$$

$$- \frac{1-y^2}{8}z\sqrt{1-z^2}N_i^* N_j^*(\alpha_p N_q + \alpha_q N_p) - \frac{1+z^2}{8}y\sqrt{1-y^2}N_p^* N_q^*(\alpha_i N_j + \alpha_j N_i)\Bigg],$$

$$\int_0^{2\pi} e^{-\mathrm{i}\lambda}\Re(W_i''^* W_j''^*)\Re(W_p'^* W_q'^*)\mathrm{d}\lambda = 2\pi$$

$$\Bigg[\frac{1+z^2}{8}y\sqrt{1-y^2}N_p^* N_q^*(\alpha_i N_j + \alpha_j N_i) + \frac{3}{4}y\sqrt{1-y^2}(1-z^2)\alpha_p\alpha_q(\alpha_i N_j^* + \alpha_j N_i^*)$$

$$- \frac{1}{8}z\sqrt{1-z^2}\Big(6(1-y^2)\alpha_i\alpha_j(\alpha_p N_q^* + \alpha_q N_p^*) + (1+y^2)N_i^* N_j^*(\alpha_p N_q + \alpha_q N_p)\Big)\Bigg],$$

$$-\Re\int_{S_k}\Big(\int_0^{2\pi} T_{\mathrm{RTI}}^2\mathrm{d}\lambda\Big)(\alpha_i N_j + \alpha_j N_i)\mathrm{d}^2\boldsymbol{k} = \frac{16\pi^2 k^2}{35}\mathcal{E}_0''\mathcal{E}_0'$$

$$\Bigg[(y\sqrt{1-y^2} - z\sqrt{1-z^2})\left\{H^{(\mathrm{dir})''}, H^{(\mathrm{dir})'}\right\}_{ij} + (3y\sqrt{1-y^2} + z\sqrt{1-z^2})\left\{H^{(\mathrm{dir})''}, H^{(\mathrm{pol})'}\right\}_{ij}$$

$$- (y\sqrt{1-y^2} + 3z\sqrt{1-z^2})\left\{H^{(\mathrm{pol})''}, H^{(\mathrm{dir})'}\right\}_{ij} + 3(z\sqrt{1-z^2} - y\sqrt{1-y^2})\left\{H^{(\mathrm{pol})''}, H^{(\mathrm{pol})'}\right\}_{ij}\Bigg],$$

$$\int_0^{2\pi} \mathrm{i}e^{-\mathrm{i}\lambda}\alpha_i''\alpha_j''\Im(W_p'^* W_q'^*)\mathrm{d}\lambda = 2\pi\Bigg[\frac{y^2-1}{8}\sqrt{1-z^2}N_i^* N_j^*(\alpha_p N_q + \alpha_q N_p)$$

$$\frac{3y^2-1}{4}\sqrt{1-z^2}\alpha_i\alpha_j(\alpha_p N_q^* + \alpha_q N_p^*) + \frac{1}{4}yz\sqrt{1-y^2}N_p^* N_q^*(\alpha_i N_j + \alpha_j N_i)\Bigg],$$

$$\int_0^{2\pi} \mathrm{i}e^{-\mathrm{i}\lambda}\Re(W_i''^* W_j''^*)\Im(W_p'^* W_q'^*)\mathrm{d}\lambda = 2\pi\Bigg[-\frac{1+y^2}{8}\sqrt{1-z^2}N_i^* N_j^*(\alpha_p N_q + \alpha_q N_p)$$

$$\frac{3}{4}(1-y^2)\sqrt{1-z^2}\alpha_i\alpha_j(\alpha_p N_q^* + \alpha_q N_p^*) - \frac{1}{4}yz\sqrt{1-y^2}N_p^* N_q^*(\alpha_i N_j + \alpha_j N_i)\Bigg],$$

$$-\Re\int_{S_k}\Big(\int_0^{2\pi} T_{\mathrm{RTI}}^3\mathrm{d}\lambda\Big)(\alpha_i N_j + \alpha_j N_i)\mathrm{d}^2\boldsymbol{k} = \frac{16\pi^2 k^2}{35}\mathcal{E}_0''\mathcal{E}_0'$$

$$\Bigg[((2-3y^2)\sqrt{1-z^2} - 3yz\sqrt{1-y^2})\left\{H^{(\mathrm{dir})''}, H^{(\mathrm{pol})'}\right\}_{ij}$$

$$+ 3(y^2\sqrt{1-z^2} + yz\sqrt{1-y^2})\left\{H^{(\mathrm{pol})''}, H^{(\mathrm{pol})'}\right\}_{ij}\Bigg],$$

Final quadratic anisotropic non-linear transfers: the quadratic anisotropic isotropic transfer term is conservative and reads

$$
\begin{aligned}
Q^{\mathrm{NL(iso)}}(k,t) = 20 \int_{\Delta_k} \theta_{kpq} \pi^2 k^2 p^2 q \mathcal{E}_0'' \Bigg[& 2xy(1-z^2) H_{ln}^{(\mathrm{pol})''} \Big(\mathcal{E}_0' H_{ln}^{(\mathrm{pol})'} - \mathcal{E}_0 H_{ln}^{(\mathrm{pol})} \Big) \\
& + 6(xy+z^3) \Bigg(2H_{ln}^{(\mathrm{dir})''} \Big((3x^2-1)\mathcal{E}_0' H_{ln}^{(\mathrm{dir})'} - (3y^2-1)\mathcal{E}_0 H_{ln}^{(\mathrm{dir})} \Big) \\
& - H_{ln}^{(\mathrm{pol})''} \Big((1-x^2)\mathcal{E}_0' H_{ln}^{(\mathrm{dir})'} - (1-y^2)\mathcal{E}_0 H_{ln}^{(\mathrm{dir})} \Big) \Bigg) \\
& + z(z^2-1) \Bigg(H_{ln}^{(\mathrm{pol})''} \Big((1+x^2)\mathcal{E}_0' H_{ln}^{(\mathrm{pol})'} - (1+y^2)\mathcal{E}_0 H_{ln}^{(\mathrm{pol})} \Big) \\
& - 6H_{ln}^{(\mathrm{dir})''} \Big((1-x^2)\mathcal{E}_0' H_{ln}^{(\mathrm{pol})'} - (1-y^2)\mathcal{E}_0 H_{ln}^{(\mathrm{pol})} \Big) \Bigg) \Bigg] \mathrm{d}p\mathrm{d}q. \qquad \text{(C.42)}
\end{aligned}
$$

The quadratic anisotropic directional transfer term is

$$
\begin{aligned}
Q_{ij}^{\mathrm{NL(dir)}}(k,t) = \frac{20}{7} \int_{\Delta_k} \theta_{kpq} \pi^2 k^2 p^2 q \mathcal{E}_0'' \Bigg[& \\
& 12(xy+z^3) \Big[(1+3xyz)\mathcal{E}_0' \Big\{ H^{(\mathrm{dir})''}, H^{(\mathrm{dir})'} \Big\}_{ij} + (3y^2-1)\mathcal{E}_0 \Big\{ H^{(\mathrm{dir})''}, H^{(\mathrm{dir})} \Big\}_{ij} \Big] \\
& - 6(xy+z^3) \Big[(1-2z^2-xyz)\mathcal{E}_0' \Big\{ H^{(\mathrm{pol})''}, H^{(\mathrm{dir})'} \Big\}_{ij} + (1-y^2)\mathcal{E}_0 \Big\{ H^{(\mathrm{pol})''}, H^{(\mathrm{dir})} \Big\}_{ij} \Big] \\
& + 6z(1-z^2) \Big[(1-2y^2-xyz)\mathcal{E}_0' \Big\{ H^{(\mathrm{dir})''}, H^{(\mathrm{pol})'} \Big\}_{ij} - (1-y^2)\mathcal{E}_0 \Big\{ H^{(\mathrm{dir})''}, H^{(\mathrm{pol})} \Big\}_{ij} \Big] \\
& + z(z^2-1) \Big[(1-2x^2-3xyz)\mathcal{E}_0' \Big\{ H^{(\mathrm{pol})''}, H^{(\mathrm{pol})'} \Big\}_{ij} - (1+y^2)\mathcal{E}_0 \Big\{ H^{(\mathrm{pol})''}, H^{(\mathrm{pol})} \Big\}_{ij} \Big] \\
& - y(1-z^2) \Big[(x+3yz)\mathcal{E}_0' \Big\{ H^{(\mathrm{pol})''}, H^{(\mathrm{pol})'} \Big\}_{ij} + 2x\mathcal{E}_0 \Big\{ H^{(\mathrm{pol})''}, H^{(\mathrm{pol})} \Big\}_{ij} \Big] \Bigg] \mathrm{d}p\mathrm{d}q. \qquad \text{(C.43)}
\end{aligned}
$$

The quadratic anisotropic polarization transfer term is

$$
\begin{aligned}
Q_{ij}^{\mathrm{NL(pol)}}(k,t) = \frac{60}{7} \int_{\Delta_k} \theta_{kpq} \pi^2 k^2 p^2 q \mathcal{E}_0'' \Bigg[& \\
& - (xy+z^3) \Big[2(3xyz+2z^2-1)\mathcal{E}_0' \Big\{ H^{(\mathrm{dir})''}, H^{(\mathrm{pol})'} \Big\}_{ij} + (1+xyz)\mathcal{E}_0' \Big\{ H^{(\mathrm{pol})''}, H^{(\mathrm{pol})'} \Big\}_{ij} \Big] \\
& + 2(xy+z^3) \Big[2(1-3y^2)\mathcal{E}_0 \Big\{ H^{(\mathrm{dir})''}, H^{(\mathrm{pol})} \Big\}_{ij} + (1-y^2)\mathcal{E}_0 \Big\{ H^{(\mathrm{pol})''}, H^{(\mathrm{pol})} \Big\}_{ij} \Big] \\
& - 2z(1-z^2) \Big[6(xyz+2x^2-1)\mathcal{E}_0' \Big\{ H^{(\mathrm{dir})''}, H^{(\mathrm{dir})'} \Big\}_{ij} - (3xyz+2y^2-1)\mathcal{E}_0' \Big\{ H^{(\mathrm{pol})''}, H^{(\mathrm{dir})'} \Big\}_{ij} \\
& + 6(1-y^2)\mathcal{E}_0 \Big\{ H^{(\mathrm{dir})''}, H^{(\mathrm{dir})} \Big\}_{ij} - (1+y^2)\mathcal{E}_0 \Big\{ H^{(\mathrm{pol})''}, H^{(\mathrm{dir})} \Big\}_{ij} \Big] \\
& + (y^2-z^2) \Big[(xy+z)\mathcal{E}_0' \Big\{ H^{(\mathrm{pol})''}, H^{(\mathrm{pol})'} \Big\}_{ij} + 2(3xy+z)\mathcal{E}_0' \Big\{ H^{(\mathrm{dir})''}, H^{(\mathrm{pol})'} \Big\}_{ij} \Big] \\
& - y(1-z^2) \Big[4x\mathcal{E}_0 \Big\{ H^{(\mathrm{pol})''}, H^{(\mathrm{dir})} \Big\}_{ij} - (x+yz)\mathcal{E}_0' \Big\{ H^{(\mathrm{pol})''}, H^{(\mathrm{pol})'} \Big\}_{ij} \Big] \Bigg] \mathrm{d}p\mathrm{d}q. \qquad \text{(C.44)}
\end{aligned}
$$

The quadratic anisotropic RTI transfer term is

$$
\begin{aligned}
Q_{ij}^{\mathrm{NL(RTI)}}(k,t) = \frac{120}{7}\int_{\Delta_k} \theta_{kpq}\pi^2 kp^2 q\mathcal{E}_0''\Bigg[&2y(x+yz)(xy+z)(zk-qx)\mathcal{E}_0 \\
&\left(6\left\{H^{(\mathrm{dir})''},H^{(\mathrm{dir})}\right\}_{ij} - 6\left\{H^{(\mathrm{dir})''},H^{(\mathrm{pol})}\right\}_{ij} + \left\{H^{(\mathrm{pol})''},H^{(\mathrm{dir})}\right\}_{ij} - \left\{H^{(\mathrm{pol})''},H^{(\mathrm{pol})}\right\}_{ij}\right) \\
&- kz(xy+z)\mathcal{E}_0'\Bigg(12(y(x+yz)-z(1-z^2))\left\{H^{(\mathrm{dir})''},H^{(\mathrm{dir})'}\right\}_{ij} \\
&- (6y(x+yz)+2z(1-z^2))\left\{H^{(\mathrm{dir})''},H^{(\mathrm{pol})'}\right\}_{ij} + (2y(x+yz)+6z(1-z^2))\left\{H^{(\mathrm{pol})''},H^{(\mathrm{dir})'}\right\}_{ij} \\
&+ (z(1-z^2)-y(x+yz))\left\{H^{(\mathrm{pol})''},H^{(\mathrm{pol})'}\right\}_{ij}\Bigg) + k(xy+z)\mathcal{E}_0' \\
&\left((6y(y+xz)-4(1-z^2))\left\{H^{(\mathrm{dir})''},H^{(\mathrm{pol})'}\right\}_{ij} + y(y+xz)\left\{H^{(\mathrm{pol})''},H^{(\mathrm{pol})'}\right\}_{ij}\right)\Bigg]\mathrm{d}p\mathrm{d}q. \qquad \text{(C.45)}
\end{aligned}
$$

The impact of quadratic anisotropic contributions on the non-linear transfers is revealed in Fig. C.1a. One can note that the global shape of the transfers is preserved and that there is a rather small change in intensity, mainly at large scales which is expected since this is where anisotropy is dominant. The isotropic and polarization parts of the transverse component $()_{33}$ are more affected by the quadratic contributions than the directional part. This might also be the consequence of the Re_λ which is slightly higher, at $St = 50$, for the simulation with the quadratic anisotropic contributions than the one without. Regarding the b_{ij} in Fig. C.1b: the asymptotic values are almost the same with and without the quadratic anisotropic contributions. One can observe a slight increase of the streamwise anisotropy and decrease of the transverse one. Moreover, the kinetic spectra scalings and the exponential growth rate of the kinetic energy are not displayed since the difference when adding the second-order contributions is not distinguishable. In conclusion, the quite heavy analytical calculations, which led to the second-order anisotropic contributions in the non-linear transfers, do not provide significant changes with regard to the first order developed in Chapter 3: this is why they are not used.

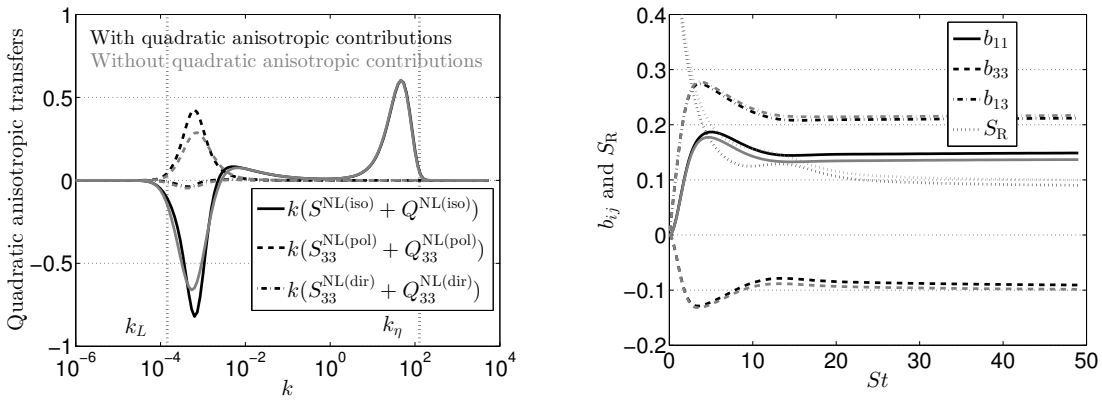

(a) (b)

Figure C.1: Quadratic anisotropic contributions in the non-linear transfers at $St = 50$, with $\sigma = 2$. (a) Budget terms along with the integral and Kolmogorov wavenumbers k_L and k_η: grey curves represent the classical transfers without the quadratic anisotropic contributions. (b) b_{ij} and shear rapidity ϵ/KS, where grey curves are without the quadratic anisotropic contributions.

C.6 Fourth-order expansion for $\mathcal{E}$ and Z

Here, some details are given about the method to obtain the fourth order expansions of $\mathcal{E}$ and Z (2.44) and (2.45). Starting from

$$\mathcal{E}(\boldsymbol{k},t) = \mathcal{E}_0\Big(1 - 15H_{ij}^{(\mathrm{dir})}(k,t)\alpha_i\alpha_j + U_{ijpq}^{(\mathrm{dir})4}(k,t)\alpha_i\alpha_j\alpha_p\alpha_q + \dots\Big), \tag{C.46}$$

$$Z(\boldsymbol{k},t) = \frac{1}{2}\mathcal{E}_0\Big(5H_{ij}^{(\mathrm{pol})}(k,t) + U_{ijpq}^{(\mathrm{pol})4}(k,t)\alpha_p\alpha_q + \dots\Big)N_i^*(\boldsymbol{k})N_j^*(\boldsymbol{k}), \tag{C.47}$$

and using the definitions of the generalized operators P_{ijpq} and N_{ijpq} given in (2.49) and (2.50), one gets

$$\int_{S_k} \mathcal{E}(\boldsymbol{k})\, P_{ijpq}(\boldsymbol{k})\, \mathrm{d}^2\boldsymbol{k} = \frac{24}{945}E(k)U_{ijpq}^{(\mathrm{dir})}(k), \qquad \int_{S_k} \Re\Big(Z(\boldsymbol{k})N_{ijpq}(\boldsymbol{k})\Big)\, \mathrm{d}^2\boldsymbol{k} = \frac{4}{21}E(k)U_{ijpq}^{(\mathrm{pol})}(k).$$

The tensors $U_{ijpq}^{()4}$ have the same properties as $H_{ijpq}^{()}$. Combining these two equations with the definitions of $H_{ijpq}^{(\mathrm{dir})}$ and $H_{ijpq}^{(\mathrm{pol})}$ given in (2.47) and (2.48) yields the fourth order-expansions (2.44) and (2.45). Finally, the expansion of the spectral Reynolds tensor in terms of the deviatoric tensors $H_{ij}^{(\mathrm{dir})}$, $H_{ij}^{(\mathrm{pol})}$, $H_{ijpq}^{(\mathrm{dir})}$ and $H_{ijpq}^{(\mathrm{pol})}$ reads

$$\begin{aligned}\hat{R}_{ij} = &\underbrace{\mathcal{E}_0 P_{ij}\Big(1 - 15H_{pq}^{(\mathrm{dir})}\alpha_p\alpha_q + \frac{945}{12}H_{rspq}^{(\mathrm{dir})}\alpha_r\alpha_s\alpha_p\alpha_q\Big)}_{\hat{R}_{ij}^{\mathrm{e}2}+\hat{R}_{ij}^{\mathrm{e}4}} \\ &+ \underbrace{\frac{1}{2}\mathcal{E}_0\Big(5H_{pq}^{(\mathrm{pol})} + \frac{21}{2}H_{pqrs}^{(\mathrm{pol})}\alpha_r\alpha_s\Big)\Big(2P_{ip}P_{jq} + P_{ij}\alpha_p\alpha_q\Big)}_{\hat{R}_{ij}^{\mathrm{z}2}+\hat{R}_{ij}^{\mathrm{z}4}}.\end{aligned} \tag{C.48}$$

C.6.1 Fourth order linear transfers

In this part, we aim at computing the linear directional and polarization transfers $T_{\mathcal{E}}^{\mathrm{L}}$ and T_Z^{L} associated with the evolution equations of $\mathcal{E}$ and Z. The linear spherically-averaged directional and polarization transfers at the fourth-order are defined by

$$S_{ijpq}^{\mathrm{L(dir)}}(k) = \frac{1}{2}\int_{S_k} T_{\mathcal{E}}^{\mathrm{L}}(\boldsymbol{k})P_{ijpq}(\boldsymbol{k})\, \mathrm{d}^2\boldsymbol{k}, \qquad S_{ijpq}^{\mathrm{L(pol)}}(k) = \frac{1}{2}\int_{S_k} \Re\Big(T_Z^{\mathrm{L}}(\boldsymbol{k})N_{ijpq}(\boldsymbol{k})\Big)\, \mathrm{d}^2\boldsymbol{k}. \tag{C.49}$$

Contributions of $H_{ijpq}^{(\mathrm{dir})}$ and $H_{ijpq}^{(\mathrm{pol})}$ in $S_{ij}^{\mathrm{L(dir)}}$ and $S_{ij}^{\mathrm{L(pol)}}$: here are some useful formula for the spherical integration:

$$\int_{S_k} \alpha_l\alpha_p\alpha_r\alpha_s A_{ln}H_{rspn}^{()}\mathrm{d}^2\boldsymbol{k} = 0, \qquad \int_{S_k} \alpha_i\alpha_j\alpha_p\alpha_q\alpha_m\alpha_n\alpha_r\alpha_s H_{mnrs}^{()}\mathrm{d}^2\boldsymbol{k} = \frac{24}{945}4\pi k^2 H_{ijpq}^{()},$$

$$\int_{S_k} \alpha_i\alpha_j\alpha_p\alpha_l\alpha_r\alpha_s A_{ln}H_{rspn}^{()}\mathrm{d}^2\boldsymbol{k} = \frac{6}{105}4\pi k^2 H_{ijln}^{()}A_{ln}^{+}, \qquad \int_{S_k} \alpha_i\alpha_j\alpha_p\alpha_q\alpha_l\alpha_n A_{ln}H_{ijpq}^{()}\mathrm{d}^2\boldsymbol{k} = 0.$$

$$\int_{S_k} \alpha_i\alpha_j\alpha_p\alpha_q\alpha_l\alpha_n\alpha_r\alpha_s H_{pqrs}^{()}A_{ln}\mathrm{d}^2\boldsymbol{k} = \frac{24}{945}4\pi k^2 H_{ijln}^{()}A_{ln}^{+}, \qquad \int_{S_k} A_{lj}\alpha_r\alpha_s\alpha_p\alpha_q\alpha_i\alpha_l H_{rspq}^{()}\mathrm{d}^2\boldsymbol{k} = 0.$$

Consequently, one has for the directional transfer

$$A_{ln}\int_{S_k} \hat{R}_{ln}^{\mathrm{e}4}P_{ij}\mathrm{d}^2\boldsymbol{k} = 2A_{ln}^{+}EH_{ijln}^{(\mathrm{dir})}, \qquad A_{ln}\int_{S_k} k_l\frac{\partial\hat{R}_{mm}^{\mathrm{e}4}}{\partial k_n}P_{ij}\mathrm{d}^2\boldsymbol{k} = -4A_{ln}^{+}\Big(2EH_{lnij}^{(\mathrm{dir})} + \frac{\partial(kEH_{ijln}^{(\mathrm{dir})})}{\partial k}\Big),$$

$$A_{ln}\int_{S_k} \hat{R}_{ln}^{\mathrm{z}4}P_{ij}\mathrm{d}^2\boldsymbol{k} = -\frac{1}{3}A_{ln}^{+}EH_{ijln}^{(\mathrm{pol})}, \qquad A_{ln}\int_{S_k} k_l\frac{\partial\hat{R}_{mm}^{\mathrm{z}4}}{\partial k_n}P_{ij}\mathrm{d}^2\boldsymbol{k} = 0.$$

For the total transfer, one gets

$$2A_{ln}\int_{S_k}\alpha_i\alpha_l(\hat{R}^{\mathrm{e}4}_{nj}+\hat{R}^{\mathrm{z}4}_{nj})\mathrm{d}^2\boldsymbol{k}=-4A^+_{ln}EH^{(\mathrm{dir})}_{ijln}+\frac{2}{3}A^+_{ln}EH^{(\mathrm{pol})}_{ijln},$$

$$A_{ln}\int_{S_k}k_l\frac{\partial(\hat{R}^{\mathrm{e}4}_{ij}+\hat{R}^{\mathrm{z}4}_{ij})}{\partial k_n}\mathrm{d}^2\boldsymbol{k}=-2A^+_{ln}\frac{\partial(kEH^{(\mathrm{dir})}_{ijln})}{\partial k}+\frac{1}{3}A^+_{ln}\frac{\partial(kEH^{(\mathrm{pol})}_{ijln})}{\partial k}.$$

One can then compute $S^{\mathrm{L(pol4)}}_{ij}=S^{\mathrm{L(tot4)}}_{ij}/2-S^{\mathrm{L(dir4)}}_{ij}$. Finally, the additional contributions to $S^{\mathrm{L(dir)}}_{ij}$ and $S^{\mathrm{L(pol)}}_{ij}$ resulting from the expansions of $\mathcal{E}$ and Z at the fourth order are

$$S^{\mathrm{L(dir4)}}_{ij}(k,t)=-3A^+_{ln}EH^{(\mathrm{dir})}_{ijln}-A^+_{ln}\frac{\partial(kEH^{(\mathrm{dir})}_{ijln})}{\partial k}+\frac{1}{6}A^+_{ln}EH^{(\mathrm{pol})}_{ijln}, \tag{C.50}$$

$$S^{\mathrm{L(pol4)}}_{ij}(k,t)=-A^+_{ln}EH^{(\mathrm{dir})}_{ijln}+\frac{1}{2}A^+_{ln}EH^{(\mathrm{pol})}_{ijln}+\frac{1}{6}A^+_{ln}\frac{\partial(kEH^{(\mathrm{pol})}_{ijln})}{\partial k}. \tag{C.51}$$

Contributions of $H^{(\mathrm{dir})}_{ij}$ and $H^{(\mathrm{pol})}_{ij}$ in $S^{\mathrm{L(dir)}}_{ijpq}$: here are some useful formula for the spherical integration:

$$\int_{S_k}P_{ijpq}\mathrm{d}^2\boldsymbol{k}=0,\qquad \int_{S_k}H^{()}_{rs}\alpha_r\alpha_sP_{ijpq}\mathrm{d}^2\boldsymbol{k}=0,$$

$$\int_{S_k}A_{ln}\alpha_l\alpha_nP_{ijpq}\mathrm{d}^2\boldsymbol{k}=0,\qquad \int_{S_k}A_{ln}H^{()}_{ls}\alpha_s\alpha_nP_{ijpq}\mathrm{d}^2\boldsymbol{k}=0.$$

Furthermore, a complex and lengthy calculation yields

$$\begin{aligned}\int_{S_k}\mathcal{E}_0A_{ln}H^{()}_{rs}\alpha_l\alpha_n\alpha_r\alpha_sP_{ijpq}\mathrm{d}^2\boldsymbol{k}&=\frac{2}{6615}E\Bigg[\frac{8}{5}A^+_{ln}H^{()}_{ln}\Big(\delta_{ij}\delta_{pq}+\delta_{ip}\delta_{jq}+\delta_{iq}\delta_{jp}\Big)\\&-4\Big[\delta_{ij}(A^+_{lp}H^{()}_{lq}+A^+_{lq}H^{()}_{lp})+\delta_{pq}(A^+_{li}H^{()}_{lj}+A^+_{lj}H^{()}_{li})+A^+_{lp}(H^{()}_{lj}\delta_{iq}+H^{()}_{li}\delta_{jq})+A^+_{lq}(H^{()}_{lj}\delta_{ip}+H^{()}_{li}\delta_{jp})\\&+H^{()}_{lp}(A^+_{jl}\delta_{iq}+A^+_{il}\delta_{jq})+H^{()}_{lq}(A^+_{jl}\delta_{ip}+A^+_{il}\delta_{jp})\Big]+14\Big(A^+_{ij}H^{()}_{pq}+A^+_{pq}H^{()}_{ij}+A^+_{ip}H^{()}_{jq}+A^+_{iq}H^{()}_{jp}\\&+A^+_{jp}H^{()}_{iq}+A^+_{jq}H^{()}_{ip}\Big)\Bigg]=\frac{2}{6615}\mathcal{H}^{(2,\mathrm{e})}_{ijpq}[EH^{()}].\end{aligned}$$

Then, one obtains

$$A_{ln}\int_{S_k}\hat{R}^{\mathrm{e}2}_{ln}P_{ijpq}\mathrm{d}^2\boldsymbol{k}=\frac{30}{6615}\mathcal{H}^{(2,\mathrm{e})}_{ijpq}[EH^{(\mathrm{dir})}],\qquad A_{ln}\int_{S_k}\hat{R}^{\mathrm{z}2}_{ln}P_{ijpq}\mathrm{d}^2\boldsymbol{k}=\frac{5}{6615}\mathcal{H}^{(2,\mathrm{e})}_{ijpq}[EH^{(\mathrm{pol})}],$$

$$A_{ln}\int_{S_k}k_l\frac{\partial\hat{R}^{\mathrm{e}2}_{mm}}{\partial k_n}P_{ijpq}\mathrm{d}^2\boldsymbol{k}=\frac{60}{6615}\Big(5\mathcal{H}^{(2,\mathrm{e})}_{ijpq}[EH^{(\mathrm{dir})}]-\mathcal{H}^{(2,\mathrm{e})}_{ijpq}[\partial_k(kEH^{(\mathrm{dir})})]\Big).$$

Hence, the contribution of $H^{(\mathrm{dir})}_{ij}$ and $H^{(\mathrm{pol})}_{ij}$ to $S^{\mathrm{L(dir)}}_{ijpq}$ is

$$S^{\mathrm{L(dir2)}}_{ijpq}(k,t)=\frac{1}{441}\Big(-\frac{1}{6}\mathcal{H}^{(2,\mathrm{e})}_{ijpq}[EH^{(\mathrm{pol})}]+4\mathcal{H}^{(2,\mathrm{e})}_{ijpq}[EH^{(\mathrm{dir})}]-\mathcal{H}^{(2,\mathrm{e})}_{ijpq}[\partial_k(kEH^{(\mathrm{dir})})]\Big). \tag{C.52}$$

Contributions of $H^{(\mathrm{dir})}_{ij}$ and $H^{(\mathrm{pol})}_{ij}$ in $S^{\mathrm{L(pol)}}_{ijpq}$: here are some useful formula for the spherical integration:

$$\int_{S_k}H^{()}_{rs}N^*_rN^*_sN_{ijpq}\mathrm{d}^2\boldsymbol{k}=0,\qquad \int_{S_k}A_{nl}H^{()}_{ls}N^*_nN^*_sN_{ijpq}\mathrm{d}^2\boldsymbol{k}=0,\qquad \int_{S_k}A^+_{ln}N^*_lN^*_nN_{ijpq}\mathrm{d}^2\boldsymbol{k}=0,$$

and moreover, lengthy calculations yield

$$\int_{S_k}\mathcal{E}_0A^+_{ln}H^{()}_{rs}\alpha_l\alpha_nN^*_rN^*_sN_{ijpq}\mathrm{d}^2\boldsymbol{k}=\int_{S_k}\mathcal{E}_0A_{ln}H^{()}_{rs}\alpha_l\alpha_sN^*_rN^*_nN_{ijpq}\mathrm{d}^2\boldsymbol{k}$$

$$= \frac{4}{2205} E\Bigg[4A^{+}_{ln} H^{()}_{ln} \Big(\delta_{ij}\delta_{pq} + \delta_{ip}\delta_{jq} + \delta_{iq}\delta_{jp} \Big) - 10 \Big[\delta_{ij}(A^{+}_{lp} H^{()}_{lq} + A^{+}_{lq} H^{()}_{lp}) + \delta_{pq}(A^{+}_{li} H^{()}_{lj} + A^{+}_{lj} H^{()}_{li})$$
$$+ A^{+}_{lp}(H^{()}_{lj}\delta_{iq} + H^{()}_{li}\delta_{jq}) + A^{+}_{lq}(H^{()}_{lj}\delta_{ip} + H^{()}_{li}\delta_{jp}) + H^{()}_{lp}(A^{+}_{jl}\delta_{iq} + A^{+}_{il}\delta_{jq}) + H^{()}_{lq}(A^{+}_{jl}\delta_{ip} + A^{+}_{il}\delta_{jp}) \Big]$$
$$+ 35 \Big(A^{+}_{ij} H^{()}_{pq} + A^{+}_{pq} H^{()}_{ij} + A^{+}_{ip} H^{()}_{jq} + A^{+}_{iq} H^{()}_{jp} + A^{+}_{jp} H^{()}_{iq} + A^{+}_{jq} H^{()}_{ip} \Big) \Bigg] = \frac{4}{2205} \mathcal{H}^{(2,\mathrm{z})}_{ijpq}[EH^{()}].$$

Then, one obtains

$$A_{rl} \int_{S_k} \hat{R}^{\mathrm{z}2}_{ls} N^{*}_{r} N^{*}_{s} N_{ijpq} \mathrm{d}^2\boldsymbol{k} = -\frac{2}{441} \mathcal{H}^{(2,\mathrm{z})}_{ijpq}[EH^{(\mathrm{pol})}],$$
$$A_{ln} \int_{S_k} k_l \frac{\partial \hat{R}^{\mathrm{z}2}_{rs}}{\partial k_n} N^{*}_{r} N^{*}_{s} N_{ijpq} \mathrm{d}^2\boldsymbol{k} = 5 \int_{S_k} \Big[A^{+}_{ln} N^{*}_{r} N^{*}_{s} \alpha_l \alpha_n k \frac{\partial \mathcal{E}_0 H^{(\mathrm{pol})}_{rs}}{\partial k} - 2A_{ln}\alpha_l\alpha_s \mathcal{E}_0 H_{rs} N^{*}_{r} N^{*}_{n} \Big] N_{ijpq} \mathrm{d}^2\boldsymbol{k}$$
$$= \frac{4}{441} \Big(-5\mathcal{H}^{(2,\mathrm{z})}_{ijpq}[EH^{(\mathrm{pol})}] + \mathcal{H}^{(2,\mathrm{z})}_{ijpq}[\partial_k(kEH^{(\mathrm{pol})})] \Big),$$

$$A_{ln} \int_{S_k} k_l \frac{\partial \hat{R}^{\mathrm{e}2}_{rs}}{\partial k_n} N^{*}_{r} N^{*}_{s} N_{ijpq} \mathrm{d}^2\boldsymbol{k} = 0, \qquad A_{rl} \int_{S_k} \hat{R}^{\mathrm{e}2}_{ls} N^{*}_{r} N^{*}_{s} N_{ijpq} \mathrm{d}^2\boldsymbol{k} = -\frac{12}{441} \mathcal{H}^{(2,\mathrm{z})}_{ijpq}[EH^{(\mathrm{dir})}].$$

Hence, the contribution of $H^{(\mathrm{dir})}_{ij}$ and $H^{(\mathrm{pol})}_{ij}$ to $S^{\mathrm{L(pol)}}_{ijpq}$ is

$$S^{\mathrm{L(pol2)}}_{ijpq}(k,t) = \frac{1}{441} \Big(6\mathcal{H}^{(2,\mathrm{z})}_{ijpq}[EH^{(\mathrm{dir})}] - 4\mathcal{H}^{(2,\mathrm{z})}_{ijpq}[EH^{(\mathrm{pol})}] + \mathcal{H}^{(2,\mathrm{z})}_{ijpq}[\partial_k(kEH^{(\mathrm{pol})})] \Big). \tag{C.53}$$

Contributions of $H^{(\mathrm{dir})}_{ijpq}$ and $H^{(\mathrm{pol})}_{ijpq}$ in $S^{\mathrm{L(dir)}}_{ijpq}$ and $S^{\mathrm{L(pol)}}_{ijpq}$: lengthy calculations provide the following compact formula

$$\int_{S_k} \mathcal{E}_0 A^{+}_{ln} H^{()}_{abrs} \alpha_a\alpha_b\alpha_l\alpha_n\alpha_r\alpha_s P_{ijpq} \mathrm{d}^2\boldsymbol{k} = \frac{16}{3465} E\Bigg[A^{+}_{li} H^{()}_{jlpq} + A^{+}_{lj} H^{()}_{ilpq} + A^{+}_{lp} H^{()}_{ijlq} + A^{+}_{lq} H^{()}_{ijlp}$$
$$- \frac{2}{7} A^{+}_{ln} \Big(\delta_{ij} H^{()}_{lnpq} + \delta_{pq} H^{()}_{lnij} + \delta_{ip} H^{()}_{lnjq} + \delta_{iq} H^{()}_{lnjp} + \delta_{jp} H^{()}_{lniq} + \delta_{jq} H^{()}_{lnip} \Big) \Bigg] = \frac{16}{3465} \mathcal{H}^{(4)}_{ijpq}[EH^{()}],$$
$$\int_{S_k} \mathcal{E}_0 A^{+}_{ln} H^{()}_{abrs} N^{*}_{l} N^{*}_{n} \alpha_a\alpha_b\alpha_r\alpha_s N_{ijpq} \mathrm{d}^2\boldsymbol{k} = -\frac{48}{385} \mathcal{H}^{(4)}_{ijpq}[EH^{()}],$$
$$\int_{S_k} \mathcal{E}_0 A^{+}_{ln} H^{()}_{abrs} N^{*}_{r} N^{*}_{s} \alpha_a\alpha_b\alpha_l\alpha_n N_{ijpq} \mathrm{d}^2\boldsymbol{k} = \frac{32}{1155} \mathcal{H}^{(4)}_{ijpq}[EH^{()}].$$

Antisymmetric contributions arise from

$$\int_{S_k} \mathcal{E}_0 A_{ln} \alpha_l\alpha_b\alpha_r\alpha_s H^{()}_{nbrs} P_{ijpq} \mathrm{d}^2\boldsymbol{k} =$$
$$\frac{42}{6615} \Big(\mathcal{H}^{(4)}_{ijpq}[EH^{()}] + E\Big[A^{-}_{il} H^{()}_{jpql} + A^{-}_{jl} H^{()}_{ipql} + A^{-}_{pl} H^{()}_{ijlq} + A^{-}_{ql} H^{()}_{ijlp} \Big] \Big),$$
$$\int_{S_k} \mathcal{E}_0 A_{ln} \alpha_a\alpha_b N^{*}_{l} N^{*}_{s} H^{()}_{abns} N_{ijpq} \mathrm{d}^2\boldsymbol{k} =$$
$$\frac{2}{21} \Big(\mathcal{H}^{(4)}_{ijpq}[EH^{()}] + E\Big[A^{-}_{il} H^{()}_{jpql} + A^{-}_{jl} H^{()}_{ipql} + A^{-}_{pl} H^{()}_{ijlq} + A^{-}_{ql} H^{()}_{ijlp} \Big] \Big),$$
$$\int_{S_k} \mathcal{E}_0 A_{ln} \alpha_n\alpha_s\alpha_a\alpha_b N^{*}_{l} N^{*}_{r} H^{()}_{abrs} N_{ijpq} \mathrm{d}^2\boldsymbol{k} =$$
$$\frac{2}{35} \Big(\frac{9}{11} \mathcal{H}^{(4)}_{ijpq}[EH^{()}] + E\Big[A^{-}_{il} H^{()}_{jpql} + A^{-}_{jl} H^{()}_{ipql} + A^{-}_{pl} H^{()}_{ijlq} + A^{-}_{ql} H^{()}_{ijlp} \Big] \Big).$$

Then, one gets

$$A^{+}_{ln} \int_{S_k} \hat{R}^{\mathrm{e}4}_{ln} P_{ijpq} \mathrm{d}^2\boldsymbol{k} = -\frac{4}{11} \mathcal{H}^{(4)}_{ijpq}[EH^{(\mathrm{dir})}], \qquad A^{+}_{ln} \int_{S_k} \hat{R}^{\mathrm{z}4}_{ln} P_{ijpq} \mathrm{d}^2\boldsymbol{k} = -\frac{6}{55} \mathcal{H}^{(4)}_{ijpq}[EH^{(\mathrm{pol})}],$$

$$A_{rl}\int_{S_k}\hat{R}^{\mathrm{e4}}_{ls}N^*_rN^*_sN_{ijpq}\mathrm{d}^2\boldsymbol{k}=-\frac{108}{11}\mathcal{H}^{(4)}_{ijpq}[EH^{(\mathrm{dir})}],$$

$$A_{rl}\int_{S_k}\hat{R}^{\mathrm{z4}}_{ls}N^*_rN^*_sN_{ijpq}\mathrm{d}^2\boldsymbol{k}=-\frac{8}{55}\mathcal{H}^{(4)}_{ijpq}[EH^{(\mathrm{pol})}]+\frac{2}{5}E\Big[A^-_{il}H^{(\mathrm{pol})}_{jpql}+A^-_{jl}H^{(\mathrm{pol})}_{ipql}+A^-_{pl}H^{(\mathrm{pol})}_{ijlq}+A^-_{ql}H^{(\mathrm{pol})}_{ijlp}\Big],$$

$$A_{ln}\int_{S_k}k_l\frac{\partial\hat{R}^{\mathrm{e4}}_{mm}}{\partial k_n}P_{ijpq}\mathrm{d}^2\boldsymbol{k}=\frac{8}{11}\mathcal{H}^{(4)}_{ijpq}[\partial_k(kEH^{(\mathrm{dir})})]-\frac{12}{11}\mathcal{H}^{(4)}_{ijpq}[EH^{(\mathrm{dir})}]$$
$$+4E\Big(A^-_{il}H^{(\mathrm{dir})}_{jpql}+A^-_{jl}H^{(\mathrm{dir})}_{ipql}+A^-_{pl}H^{(\mathrm{dir})}_{ijlq}+A^-_{ql}H^{(\mathrm{dir})}_{ijlp}\Big),$$

$$A_{ln}\int_{S_k}k_l\frac{\partial\hat{R}^{\mathrm{z4}}_{rs}}{\partial k_n}N^*_rN^*_sN_{ijpq}\mathrm{d}^2\boldsymbol{k}=\frac{8}{5}\Bigg[\frac{2}{11}\mathcal{H}^{(4)}_{ijpq}[\partial_k(kEH^{(\mathrm{pol})})]-\frac{3}{11}\mathcal{H}^{(4)}_{ijpq}[EH^{(\mathrm{pol})}]$$
$$+2E\Big(A^-_{il}H^{(\mathrm{pol})}_{jpql}+A^-_{jl}H^{(\mathrm{pol})}_{ipql}+A^-_{pl}H^{(\mathrm{pol})}_{ijlq}+A^-_{ql}H^{(\mathrm{pol})}_{ijlp}\Big)\Bigg],$$

so that the contributions of $H^{(\mathrm{dir})}_{ijpq}$ and $H^{(\mathrm{pol})}_{ijpq}$ to $S^{\mathrm{L(dir)}}_{ijpq}$ and $S^{\mathrm{L(pol)}}_{ijpq}$ are

$$S^{\mathrm{L(dir4)}}_{ijpq}(k,t)=\frac{1}{11}\Big(2\mathcal{H}^{(4)}_{ijpq}[\partial_k(kEH^{(\mathrm{dir})})]-\mathcal{H}^{(4)}_{ijpq}[EH^{(\mathrm{dir})}]+\frac{3}{5}\mathcal{H}^{(4)}_{ijpq}[EH^{(\mathrm{pol})}]\Big)$$
$$+E\Big(A^-_{il}H^{(\mathrm{dir})}_{jpql}+A^-_{jl}H^{(\mathrm{dir})}_{ipql}+A^-_{pl}H^{(\mathrm{dir})}_{ijlq}+A^-_{ql}H^{(\mathrm{dir})}_{ijlp}\Big),\tag{C.54}$$

$$S^{\mathrm{L(pol4)}}_{ijpq}(k,t)=\frac{1}{11}\Big(\frac{4}{5}\mathcal{H}^{(4)}_{ijpq}[\partial_k(kEH^{(\mathrm{pol})})]-\frac{2}{5}\mathcal{H}^{(4)}_{ijpq}[EH^{(\mathrm{pol})}]+54\mathcal{H}^{(4)}_{ijpq}[EH^{(\mathrm{dir})}]\Big)$$
$$+\frac{3}{5}E\Big(A^-_{il}H^{(\mathrm{pol})}_{jpql}+A^-_{jl}H^{(\mathrm{pol})}_{ipql}+A^-_{pl}H^{(\mathrm{pol})}_{ijlq}+A^-_{ql}H^{(\mathrm{pol})}_{ijlp}\Big).\tag{C.55}$$

C.6.2 Fourth order non-linear transfers

The non-linear spherically-averaged directional and polarization transfers at the fourth-order are defined by

$$S^{\mathrm{NL(dir)}}_{ijpq}(k)=\frac{1}{2}\int_{S_k}T_{\mathcal{E}}(\boldsymbol{k})P_{ijpq}(\boldsymbol{k})\,\mathrm{d}^2\boldsymbol{k},\qquad S^{\mathrm{NL(pol)}}_{ijpq}(k)=\frac{1}{2}\int_{S_k}\Re\Big(T_Z(\boldsymbol{k})N_{ijpq}(\boldsymbol{k})\Big)\,\mathrm{d}^2\boldsymbol{k}.\tag{C.56}$$

There are no contributions from the fourth order tensors $H^{(\mathrm{dir})}_{ijpq}$ and $H^{(\mathrm{pol})}_{ijpq}$ in the isotropic, directional and polarization non-linear transfers $S^{\mathrm{NL(iso)}}_{ij}$, $S^{\mathrm{NL(dir)}}_{ij}$ and $S^{\mathrm{NL(pol)}}_{ij}$, and similarly there are no contributions from $H^{(\mathrm{dir})}_{ij}$ and $H^{(\mathrm{pol})}_{ij}$ in $S^{\mathrm{NL(dir)}}_{ijpq}$ and $S^{\mathrm{NL(pol)}}_{ijpq}$, because

$$\int_{S_k}P_{rs}\alpha_i\alpha_j\alpha_p\alpha_qH^{()}_{ijpq}\mathrm{d}^2\boldsymbol{k}=0,\qquad\int_{S_k}\alpha_i\alpha_jN^*_pN^*_qN_rN_sH^{()}_{ijpq}\mathrm{d}^2\boldsymbol{k}=0.$$

For the λ-integration to compute $S^{\mathrm{NL(dir)}}_{ijpq}$, one needs

$$\int_0^{2\pi}\alpha'_i\alpha'_j\alpha'_p\alpha'_qH^{()'}_{ijpq}\mathrm{d}\lambda=\frac{\pi}{4}\alpha_i\alpha_j\alpha_p\alpha_qH^{()'}_{ijpq}(35z^4-30z^2+3),$$

$$\int_0^{2\pi}\alpha''_i\alpha''_j\,\Re(W''^*_pW''^*_q)H^{()''}_{ijpq}\mathrm{d}\lambda=\frac{5\pi}{4}(1-y^2)(7y^2-1)\alpha_i\alpha_j\alpha_p\alpha_qH^{()''}_{ijpq}.$$

This yields, after spherical-integration,

$$S^{\mathrm{NL(dir)}}_{ijpq}(k,t)=2\int_{\Delta_k}\theta_{kpq}\pi^2k^2p^2q(xy+z^3)\mathcal{E}''_0\Bigg[\mathcal{E}'_0\Big(H^{(\mathrm{dir})'}_{ijpq}(35z^4-30z^2+3)$$
$$+H^{(\mathrm{dir})''}_{ijpq}(35y^4-30y^2+3)\Big)-\mathcal{E}_0\Big(8H^{(\mathrm{dir})}_{ijpq}+H^{(\mathrm{dir})''}_{ijpq}(35y^4-30y^2+3)\Big)\Bigg]\mathrm{d}p\mathrm{d}q$$

$$+\frac{2}{3}\int_{\Delta_k}\theta_{kpq}\pi^2k^2p^2q\mathcal{E}_0''\left[(xy+z^3)(1-y^2)(7y^2-1)(\mathcal{E}_0'-\mathcal{E}_0)H_{ijpq}^{(\mathrm{pol})''}+z(1-z^2)^2(1-7z^2)\mathcal{E}_0'H_{ijpq}^{(\mathrm{pol})'}\right]\mathrm{d}p\mathrm{d}q. \tag{C.57}$$

For the λ-integration to compute $S_{ijpq}^{\mathrm{NL(pol)}}$, one needs

$$\int_0^{2\pi}e^{-2\mathrm{i}\lambda}\alpha_r''\alpha_s''\Re(W_p^{''*}W_q^{''*})H_{rspq}^{()''}\mathrm{d}\lambda=\frac{\pi}{2}\alpha_r\alpha_sN_p^*N_q^*H_{rspq}^{()''}(1-6y^2+7y^4),$$
$$\int_0^{2\pi}ie^{-2\mathrm{i}\lambda}\alpha_r'\alpha_s'\Im(W_p^{'*}W_q^{'*})H_{rspq}^{()'}\mathrm{d}\lambda=\frac{\pi}{2}\alpha_r\alpha_sN_p^*N_q^*H_{rspq}^{()'}z(5-7z^2),$$
$$\int_0^{2\pi}e^{-2\mathrm{i}\lambda}\alpha_r''\alpha_s''\alpha_p''\alpha_q''H_{rspq}^{()''}\mathrm{d}\lambda=-\frac{\pi}{2}\alpha_r\alpha_sN_p^*N_q^*H_{rspq}^{()''}(1-8y^2+7y^4),$$

and for the spherical integration

$$\int_{S_k}\alpha_r\alpha_s\alpha_p\alpha_qN_l^*N_n^*N_iN_jH_{rsln}^{()}\mathrm{d}^2\boldsymbol{k}=\frac{4}{63}4\pi k^2H_{ijpq}^{()},\qquad\int_{S_k}\alpha_r\alpha_sN_l^*N_n^*N_{ijpq}H_{rsln}^{()}\mathrm{d}^2\boldsymbol{k}=\frac{8}{21}4\pi k^2H_{ijpq}^{()}.$$

This gives

$$\begin{aligned}S_{ijpq}^{\mathrm{NL(pol)}}(k,t)=4\int_{\Delta_k}\theta_{kpq}\pi^2k^2p^2q\mathcal{E}_0''\Bigg[&z(5-7z^2)(y^2-z^2)\mathcal{E}_0'H_{ijpq}^{(\mathrm{pol})'}+xy(5-7y^2)(1-z^2)\mathcal{E}_0H_{ijpq}^{(\mathrm{pol})''}\\&+(\mathcal{E}_0'-\mathcal{E}_0)H_{ijpq}^{(\mathrm{pol})''}z(z^2-1)(1-6y^2+7y^4)+(xy+z^3)\Big(\mathcal{E}_0'H_{ijpq}^{(\mathrm{pol})'}(1-6z^2+7z^4)-4\mathcal{E}_0H_{ijpq}^{(\mathrm{pol})}\Big)\Bigg]\mathrm{d}p\mathrm{d}q\\&+60\int_{\Delta_k}\theta_{kpq}\pi^2k^2p^2q\mathcal{E}_0''z(1-z^2)\left[(1-8y^2+7y^4)(\mathcal{E}_0'-\mathcal{E}_0)H_{ijpq}^{(\mathrm{dir})''}+(1-8z^2+7z^4)\mathcal{E}_0'H_{ijpq}^{(\mathrm{dir})'}\right]\mathrm{d}p\mathrm{d}q.\end{aligned} \tag{C.58}$$

C.6.3 Fourth-order final spherically-averaged equations

The evolution equations of the fourth-order anisotropic descriptors $H_{ijpq}^{(\mathrm{dir})}$ and $H_{ijpq}^{(\mathrm{pol})}$ are then simply

$$\left(\frac{\partial}{\partial t}+2\nu k^2\right)E(k,t)H_{ijpq}^{(\mathrm{dir})}(k,t)=S_{ijpq}^{\mathrm{L(dir)}}(k,t)+S_{ijpq}^{\mathrm{NL(dir)}}(k,t), \tag{C.59}$$
$$\left(\frac{\partial}{\partial t}+2\nu k^2\right)E(k,t)H_{ijpq}^{(\mathrm{pol})}(k,t)=S_{ijpq}^{\mathrm{L(pol)}}(k,t)+S_{ijpq}^{\mathrm{NL(pol)}}(k,t), \tag{C.60}$$

where $S_{ijpq}^{\mathrm{L(dir)}}=S_{ijpq}^{\mathrm{L(dir2)}}+S_{ijpq}^{\mathrm{L(dir4)}}$, and similarly for the polarization. The direct retro-action of the fourth-order terms on the second-order ones is done through the additional linear transfers $S_{ij}^{\mathrm{L(dir4)}}$ and $S_{ij}^{\mathrm{L(pol4)}}$ so that

$$\left(\frac{\partial}{\partial t}+2\nu k^2\right)E(k,t)H_{ij}^{(\mathrm{dir})}(k,t)=\underbrace{S_{ij}^{\mathrm{L(dir2)}}(k,t)+S_{ij}^{\mathrm{L(dir4)}}(k,t)}_{S_{ij}^{\mathrm{L(dir)}}(k,t)}+S_{ij}^{\mathrm{NL(dir)}}(k,t), \tag{C.61}$$
$$\left(\frac{\partial}{\partial t}+2\nu k^2\right)E(k,t)H_{ij}^{(\mathrm{pol})}(k,t)=\underbrace{S_{ij}^{\mathrm{L(pol2)}}(k,t)+S_{ij}^{\mathrm{L(pol4)}}(k,t)}_{S_{ij}^{\mathrm{L(pol)}}(k,t)}+S_{ij}^{\mathrm{NL(pol)}}(k,t), \tag{C.62}$$

where $S_{ij}^{\mathrm{L(dir2)}}$ and $S_{ij}^{\mathrm{L(pol2)}}$ are the linear transfers computed with the second-order expansions.

Appendix D

Additional Results for the Velocity Field in Homogeneous Turbulence

In this appendix, additional results, with respect to the ones presented in Chapter 3 which focused on shear flows, are proposed. Notably, (i) rapid distortion theory (RDT) is briefly addressed; (ii) some calculations about axisymmetric turbulence and plane distortion are presented; (iii) the pressure fluctuations are investigated to derive the equation for the pressure spectrum; and finally, (iv) some details about the helical field in skew-isotropic turbulence are given.

D.1 Rapid Distortion Theory

In this part, some details about the **Rapid Distortion Theory** (RDT) are given, in order to derive initial conditions for anisotropic flows and a solution for short times as well. This section is inspired by Townsend (1976). Firstly, the non-linear terms from Navier-Stokes equation (2.1) in physical space are discarded

$$\frac{\partial}{\partial t} + A_{jl}x_l\frac{\partial u_i}{\partial x_j} + A_{ij}u_l = -\frac{\partial p}{\partial x_i} + \nu\Delta u_i. \tag{D.1}$$

In RDT, solutions valid for short times only are derived: indeed, non-linear terms are negligible only at the beginning of the simulation, when anisotropy grows thanks to production terms. In the early times of the flow, the Reynolds number is important, and thus viscous effects are small with respect to inertial ones. For this reason, $\nu\Delta u_i$ is neglected as well. Then, the following Fourier decomposition for the fluctuating velocity and pressure fields is used

$$u_i(\boldsymbol{x},t) = a_i(t)\exp(\mathrm{i}\boldsymbol{k}.\boldsymbol{x}) \qquad p(\boldsymbol{x},t) = b(t)\exp(\mathrm{i}\boldsymbol{k}.\boldsymbol{x}). \tag{D.2}$$

Then, with $\mathrm{d}k_i/\mathrm{d}t = -A_{ji}k_j$, equation (D.1) becomes, after projecting on the plane perpendicular to k_ip,

$$\frac{\mathrm{d}a_i}{\mathrm{d}t} + (\delta_{in} - 2\alpha_i\alpha_n)A_{nj}a_j = 0. \tag{D.3}$$

Thanks to the previous linearity assumption, it is possible to compute at each time the fluctuating velocity

$$a_i(t) = G_{ij}(t,t_0)a_j(t_0), \tag{D.4}$$

where G_{ij} is the Green's function and t_0 the initial time (chosen to be 0 in the simulations). The wavenumber at each time is given by

$$k_i(t) = F^{-1}_{ji}(t,t_0)k_j(t_0), \tag{D.5}$$

where F_{ij} is the **Cauchy matrix**, or the displacement matrix, which depends on the kind of anisotropy. The initial Green's function is

$$G_{ij}(t_0, t_0) = \delta_{ij} - \alpha_i \alpha_j = P_{ij}(t_0),$$

so that at each time $k_i G_{ij} = 0$. Finally, the second order spectral tensor is given by

$$\phi_{ij}(\boldsymbol{k}, t) = G_{in}(\boldsymbol{k}, t, t_0) G_{jm}(\boldsymbol{k}, t, t_0) \phi_{nm}(\boldsymbol{k}(t_0), t_0). \tag{D.6}$$

For the sake of clarity, the following notations are used

$$K_i = k_i(t_0), \qquad K_0^2 = K_1^2 + K_2^2 + K_3^2, \qquad K_\perp^2 = K_1^2 + K_2^2.$$

Turbulent shear flows: For a pure shear flow with gradient matrix A_{ij}, the associated Cauchy matrix F_{ij} is

$$A_{ij} = \begin{bmatrix} 0 & 0 & S \\ 0 & 0 & 0 \\ 0 & 0 & 0 \end{bmatrix}, \qquad F_{ij} = \begin{bmatrix} 1 & 0 & -St \\ 0 & 1 & 0 \\ 0 & 0 & 1 \end{bmatrix}$$

where S is the shear rate. The wavenumbers are $k_1(t) = K_1$, $k_2(t) = K_2$, and $k_3(t) = K_3 - StK_1$, with $k^2 = k_1^2 + k_2^2 + k_3^2$. The three coupled equations to solve are consequently

$$\frac{\mathrm{d}a_1}{\mathrm{d}t} = S(2\alpha_1\alpha_1 - 1)a_3(t) \qquad \frac{\mathrm{d}a_2}{\mathrm{d}t} = 2S\alpha_1\alpha_2 a_3(t) \qquad \frac{\mathrm{d}a_3}{\mathrm{d}t} = 2S\alpha_1\alpha_3 a_3(t). \tag{D.7}$$

After some algebra, one gets

$$a_3(t) = \frac{K_0^2}{K_\perp^2 + (K_3 - K_1 St)^2} a_3(t_0). \tag{D.8}$$

Then, using the change of variable $T = (K_3 - StK_1)/K_\perp$ and $\arctan a - \arctan b = \arctan\left((a-b)/(1+ab)\right)$, one finds

$$a_1(t) = \frac{K_0^2}{K_\perp^2} Q_1(t) a_3(t_0) + a_1(t_0), \tag{D.9}$$

$$a_2(t) = \frac{K_1 K_2}{K_\perp^2} Q_2(t) a_3(t_0) + a_2(t_0), \tag{D.10}$$

with

$$Q_1(t) = -\frac{K_2^2}{K_1 K_\perp} \arctan\left(\frac{StK_\perp}{K_0^2 - StK_1K_3}\right) + \frac{StK_1^2(K_0^2 - 2K_3^2 + StK_1K_3)}{K_0^2 k^2(t)}, \tag{D.11}$$

$$Q_2(t) = \frac{K_0^2}{K_1 K_\perp} \arctan\left(\frac{StK_\perp}{K_0^2 - StK_1K_3}\right) + \frac{St(K_0^2 - 2K_3^2 + StK_1K_3)}{k^2(t)}. \tag{D.12}$$

Then, ϕ_{ij} is computed thanks to (D.6) with the Green's function

$$\boldsymbol{G} = \begin{bmatrix} 1 & 0 & Q_1 K_0^2/K_\perp^2 \\ 0 & 1 & Q_2 K_1 K_2/K_\perp^2 \\ 0 & 0 & K_0^2/k^2 \end{bmatrix} \tag{D.13}$$

and with the initial value

$$\phi_{ij}(\boldsymbol{k}(t_0), t_0) = \frac{E(k, t_0)}{4\pi k^2} P_{ij}.$$

D.2 Homogeneous Axisymmetric Turbulence

In this part, homogeneous axisymmetric turbulence (HAxT) is briefly addressed. Axisymmetric expansions (or contraction) are quite representative of grid turbulence: this is why this configuration has

received some interest. Furthermore, the axisymmetric case is less restrictive than the isotropic one, but still presents some interesting symmetries for tensorial developments: see for instant the local axisymmetry theory of George & Hussein (1991). The case of a maintained axisymmetric turbulence is nevertheless not addressed: indeed, as discussed in Sagaut & Cambon (2008), when this kind of anisotropy is forced, the turbulence becomes 1D or 2D (depending on the compression or dilatation case), and the present 3D modelling cannot handle such singular flows. In general, the flow experiences a contraction (or expansion) and then freely decays, thus progressively returning to isotropy. In the expansion case, the mean velocity gradient matrix is

$$A_{ij}^{\text{exp}} = \begin{bmatrix} S & 0 & 0 \\ 0 & S & 0 \\ 0 & 0 & -2S \end{bmatrix}.$$

For the contraction, $A_{ij}^{\text{con}} = -A_{ij}^{\text{exp}}$. The kinetic energy $K(t)$ follows the evolution equation

$$\frac{\mathrm{d}K}{\mathrm{d}t} = -2S(R_{11} + R_{22} - 2R_{33}) - \epsilon. \tag{D.14}$$

Firstly, the anisotropy tensors b_{ij} are investigated in Fig. D.1, in the cases of Saffman and Batchelor turbulence. In both cases, one has $b_{11} = b_{22} = -b_{33}/2$. For $\sigma = 2$, the b_{ij} reach an asymptotic anisotropic state, as in HSRT, whereas it continuously decreases for $\sigma = 4$. Thus, as in HSRT, there is only a RTI of small scales, consequently leading to a global partial return to isotropy.

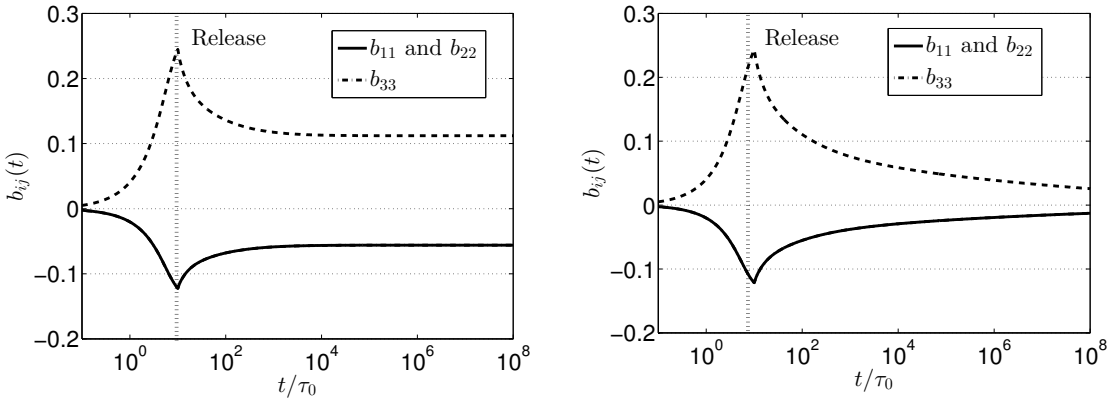

(a) (b)

Figure D.1: Anisotropy tensor b_{ij} with $St = 0.1$: (a) $\sigma = 2$; (b) $\sigma = 4$.

Since A_{ij} is diagonal, the only way to observe a $k^{-7/3}$ slope for the kinetic spectrum is to look at ϕ_{ii} (no summation) without the isotropic part, *i.e.* $E(k,t)H_{ii}(k,t)^{()}$, as shown in Fig. D.2. Furthermore, it is recovered that the decay exponent of kinetic energy is still valid in HAxT.

Since axisymmetric turbulence is rather a classical configuration, it is proposed in Fig. D.3 to compare the results of the present anisotropic EDQNM modelling to the DNS of Davidson *et al.* (2012) in Saffman HAxT (this comparison was included in the first publication in *Journal of Turbulence*). The initial conditions are detailed in the appendix of Davidson *et al.* (2012): runs 11 and 12 and considered here (initial isotropic turbulence submitted to a contraction and expansion respectively). The streamwise direction is $()_{33}$: R_{33} is noted $u_\parallel^2$ and $R_{11} = R_{22} = u_\perp^2$. The initial Reynolds number $Re_\perp(0)$ is based on the integral scale $l_\perp$, and the corresponding Taylor Reynolds number is computed with $Re_\lambda = \sqrt{20Re_\perp/3}$: simulations show that a slightly higher or lower $Re_\lambda(0)$ has no significant influence on the results. The characteristic time is defined as $T = 1/(\sqrt{q^2}k_L(0))$. Firstly, the ratio $u_\parallel^2/u_\perp^2$ is presented in both cases of expansion and contraction. A good agreement is obtained in the transition zone $t < 50T$, and for the asymptotic values as well, where the relative error is $\simeq 3.5\%$. Then, the decay of the streamwise and

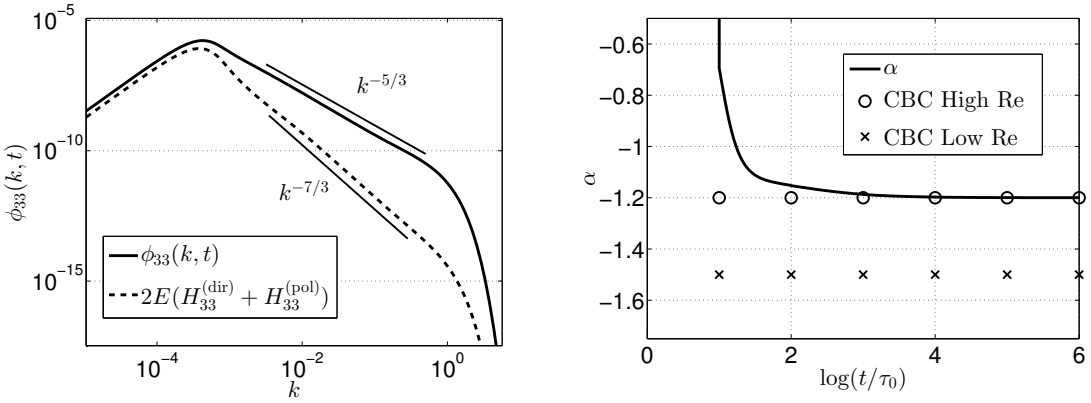

(a) (b)

Figure D.2: (a) Spectral tensor ϕ_{33}. (b) Decay exponent α. Both for $St = 0.1$ and $\sigma = 2$ in HAxT.

spanwise energies $u_\parallel^2$ and $u_\perp^2$ is investigated for the expansion: despite a slight discrepancy at small t/T, the $t^{-6/5}$ decay of Saffman turbulence is well-recovered.

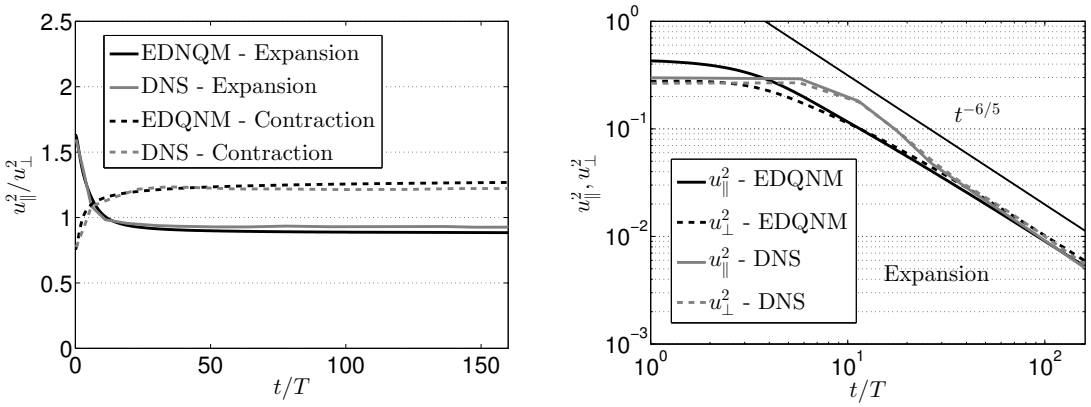

(a) (b)

Figure D.3: Comparison with Davidson *et al.* (2012): grey lines correspond to the DNS and black ones to EDQNM. For the expansion, $Re_\lambda(0) = 36$ and for the contraction $Re_\lambda(0) = 25$. (a) Ratio $u_\parallel^2/u_\perp^2$ in axisymmetric expansion (plain line) and contraction (dashed line). (b) $u_\parallel^2$ (plain line) and $u_\perp^2$ (dashed line) decay in axisymmetric expansion only.

D.3 Homogeneous Plane Distortion

Here, the case homogeneous distortion-released turbulence (HDRT) is highlighted. In this framework, the mean-velocity gradient matrix reads

$$\boldsymbol{A} = \begin{bmatrix} 0 & 0 & -S \\ 0 & 0 & 0 \\ -S & 0 & 0 \end{bmatrix}$$

and the kinetic energy $K(t)$ follows the evolution equation

$$\frac{\mathrm{d}K}{\mathrm{d}t} = 2SR_{13} - \epsilon, \tag{D.15}$$

which is formally equivalent to the one in shear flows. The evolution equation of the non-diagonal component is

$$\frac{\mathrm{d}R_{13}}{\mathrm{d}t} = S(R_{11} + R_{33}) + \Pi_{13} - \epsilon_{13}. \tag{D.16}$$

In such a configuration, one has $b_{22} = -2b_{11} = -2b_{33}$. The anisotropy tensor b_{ij}, displayed in Fig. D.4a for Saffman turbulence, reaches an asymptotic anisotropic after the release of the mean velocity gradients. The decay exponents α and α_{13} of $K(t)$ and $R_{13}(t)$ respectively are presented in Fig. D.4b: classical CBC theoretical decay exponents are recovered.

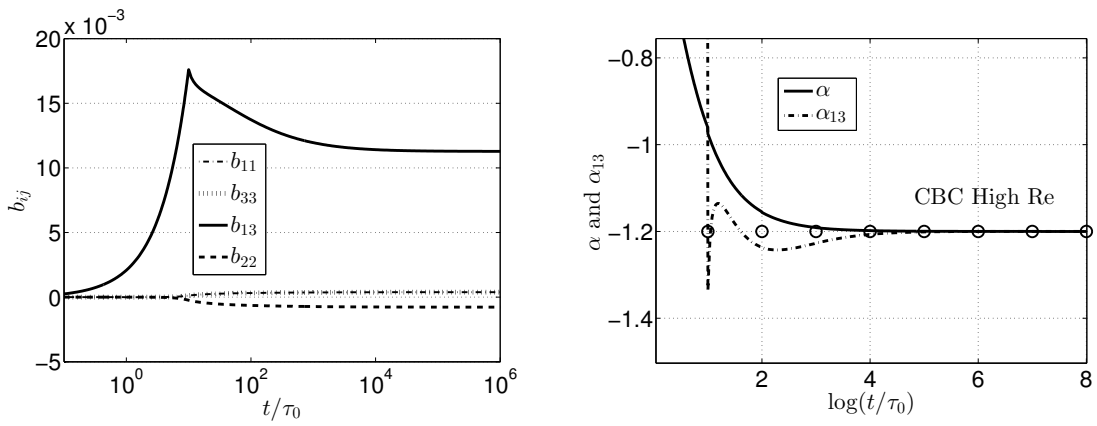

Figure D.4: (a) Anisotropy tensor b_{ij} with $St = 10$. (b) Decay exponents of $K(t)$ and $R_{13}(t)$. Both for $\sigma = 2$.

Finally, in Fig. D.5, α and α_{13} are presented in Batchelor HDRT. The strong result is that the extended coefficient p_S introduced in Chapter 3 for HSRT is still valid here for an initial plane distortion. Hence, p_S does not depend on the shear rate S, nor on the kind of anisotropy.

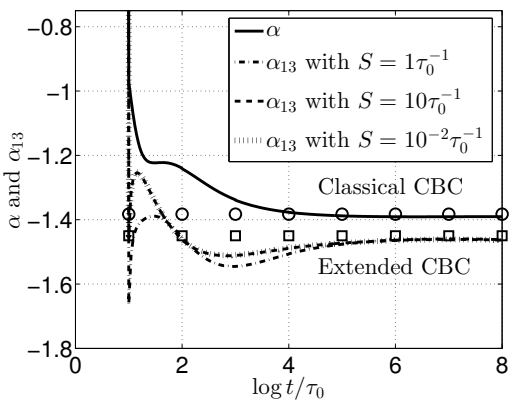

Figure D.5: Decay exponents of $K(t)$ and $R_{13}(t)$ for $\sigma = 4$ and various S in HDRT.

D.4 Pressure fluctuations in HAT

In this section, the pressure field is investigated. The main equations are derived in spectral space, and then applied in both HIT and HST. The contents of this part were included in the publication in *Physical Review Fluids*.

D.4.1 Evolution equation of the pressure correlation $\mathcal{E}_P$

The pressure fluctuations satisfy the **Poisson equation** obtained by taking the divergence of the Navier-Stokes equation (2.1)

$$\boxed{-\Delta p = \frac{\partial^2 u_i u_j}{\partial x_i \partial x_j} + 2A_{ij}\frac{\partial u_j}{\partial x_i}.} \tag{D.17}$$

The Fourier transform yields

$$\hat{p}(\boldsymbol{k},t) = -\alpha_i\alpha_j\widehat{u_iu_j}(\boldsymbol{k},t) + \frac{2\mathrm{i}}{k}A_{ij}\alpha_i\hat{u}_j(\boldsymbol{k},t). \tag{D.18}$$

The spectral two-point second-order pressure correlation is defined as

$$\mathcal{E}_P(\boldsymbol{k},t)\delta(\boldsymbol{k}-\boldsymbol{p}) =< \hat{p}(\boldsymbol{k},t)\hat{p}^*(\boldsymbol{p},t) > \tag{D.19}$$

so that the **pressure spectrum** reads

$$E_P(k,t) = \int_{S_k}\mathcal{E}_P(\boldsymbol{k},t)\mathrm{d}^2\boldsymbol{k}. \tag{D.20}$$

The spectral pressure correlation is computed according to

$$\begin{aligned}\hat{p}\hat{p}'^* &= \alpha_i\alpha_j\alpha'_p\alpha'_q\widehat{u_iu_j}\widehat{u_pu_q}'^* + 4\frac{\alpha_i\alpha'_p}{kp}A_{ij}A_{pq}\hat{u}_j\hat{u}'^*_q \\ &+ 2\mathrm{i}\left(\frac{\alpha'_p}{p}A_{pq}\hat{u}'^*_q\alpha_i\alpha_j\widehat{u_iu_j} - \frac{\alpha_i}{k}A_{ij}\hat{u}_j\alpha'_p\alpha'_q\widehat{u_pu_q}'^*\right).\end{aligned}$$

The latter term will bring no contribution during the spherical integration and is thus discarded from here. Ensemble average gives

$$\begin{aligned}&\mathcal{E}_P(\boldsymbol{k})\delta(\boldsymbol{k}-\boldsymbol{p}) = 4\frac{\alpha_i\alpha'_p}{kp}A_{ij}A_{pq}\hat{R}_{jq}\delta(\boldsymbol{k}-\boldsymbol{p}) \\ &+\alpha_i\alpha_j\alpha'_p\alpha'_q\int\int\int\int < \hat{u}_i(\boldsymbol{r})\hat{u}_j(\boldsymbol{s})\hat{u}^*_p(\boldsymbol{v})\hat{u}^*_q(\boldsymbol{w}) > \delta(\boldsymbol{k}-\boldsymbol{r}-\boldsymbol{s})\delta(\boldsymbol{p}-\boldsymbol{v}-\boldsymbol{w})\mathrm{d}^3\boldsymbol{r}\mathrm{d}^3\boldsymbol{v}\mathrm{d}^3\boldsymbol{s}\mathrm{d}^3\boldsymbol{w}.\end{aligned}$$

The quasi-normal procedure is then used: the integral gives three terms that are products of two spectral Reynolds tensors. After integration over $\boldsymbol{r}$ and $\boldsymbol{p}$ (the latter erases the Dirac functions) only two terms remain that are equal, so that

$$\boxed{\mathcal{E}_P(\boldsymbol{k},t) = 2\alpha_i\alpha_j\alpha_p\alpha_q\int_{\boldsymbol{k}=\boldsymbol{p}+\boldsymbol{q}}\hat{R}_{iq}(\boldsymbol{p},t)\hat{R}_{jp}(\boldsymbol{q},t)\mathrm{d}^3\boldsymbol{p} + 4\frac{\alpha_i\alpha_p}{k^2}A_{ij}A_{pq}\hat{R}_{jq}(\boldsymbol{k},t).} \tag{D.21}$$

For the λ-integration, relations of Appendix C are used. At first order in anisotropy, five terms remain from the integration. Four of them are like $\alpha_i\alpha_jH^{()}_{ij}$ and thus bring no contribution to the spherical average. The explicit expression of the pressure spectrum is then

$$E_P(k,t) = 16\pi^2\int_{\Delta_k}kpq(1-y^2)(1-z^2)\mathcal{E}'_0\mathcal{E}''_0\mathrm{d}p\mathrm{d}q$$

$$+4\frac{E}{k^2}\left(\frac{1}{5}A^+_{ij}A^+_{ij}+\frac{1}{3}A^-_{ij}A^-_{ij}-H^{(\mathrm{dir})}_{il}\left[\frac{6}{7}A^+_{ij}A^+_{jl}+2A^-_{ij}(A^-_{lj}+2A^+_{lj})\right]\right)$$
$$+8\frac{E}{k^2}H^{(\mathrm{pol})}_{il}\left[\frac{3}{7}A^+_{ij}A^+_{lj}+A^-_{ij}\left(A^-_{lj}-\frac{2}{3}A^+_{lj}\right)\right]. \tag{D.22}$$

The first contribution is purely isotropic and is therefore referred to as $E_P^{(\mathrm{iso})}$ (also called the turbulence-turbulence interaction). Whereas the second contribution $E_P^{(\mathrm{S})}$ arises from velocity gradients and is quadratic in A_{ij} (also called turbulence-mean-shear interaction). $E_P^{(\mathrm{iso})}$ is in agreement with the one derived by George *et al.* (1984). There may be a factor 2 missing in the more recent work of Meldi & Sagaut (2013*b*) regarding $E_P^{(\mathrm{iso})}$.

D.4.2 Spectrum and pressure variance

First, the case of HIT is addressed. From the expression of $E_P^{(\mathrm{iso})}$, or dimensional analysis, it directly follows that

$$E_P^{(\mathrm{iso})}(k,t)=C_P\epsilon^{4/3}k^{-7/3}, \tag{D.23}$$

and the $k^{-7/3}$ scaling is recovered numerically in Fig. D.6a. The value of C_P is discussed hereafter for shear flows and USHT. Then, from the Poisson equation (D.17), it is clear that the fluctuating pressure evolves as $p\sim u^2$. This directly means that the decay exponent of the pressure variance is

$$K_P(t)\sim t^{\alpha_P},\qquad \alpha_P=2\alpha. \tag{D.24}$$

This is verified in Fig. D.6b for both high and low Reynolds numbers regimes and for Saffman and Batchelor turbulence. Regarding the pressure spectrum infrared slope, it is obtained in Fig. D.6c that it does not depend on σ and always results in k^2, as predicted by Batchelor (1951); Lesieur *et al.* (1999). Indeed, for an initial k^4 infrared range, the pressure spectrum $E_P(k,t)$ changes very rapidly into k^2.

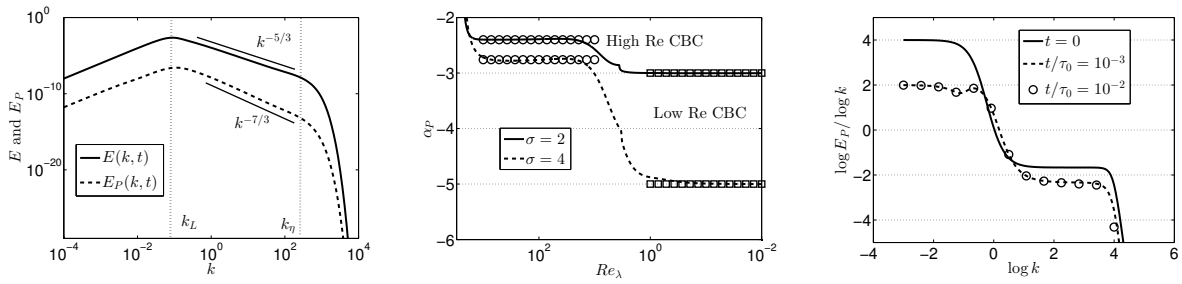

(a) (b) (c)

Figure D.6: (a) Pressure spectrum $E_P(k,t)$ in isotropic Saffman turbulence. (b) Decay of the pressure variance K_P in Saffman and Batchelor turbulence: ∘ high Reynolds predictions, □ low Reynolds predictions. (c) Infrared slope of the pressure spectrum E_P with initial $\sigma=4$.

The framework of a turbulent shear flow is now investigated; pressure spectra in unstably stratified homogeneous turbulence are studied in Chapter 7. The scaling of the turbulence-turbulence interaction spectrum $E_P^{(\mathrm{iso})}$ remains unchanged compared to HIT, whereas the turbulence-mean-shear interaction spectrum $E_P^{(\mathrm{S})}$ arises with non-zero mean velocity gradients. Given its expression (D.22), it is straightforward that it evolves in $k^{-11/3}$ in the inertial range. Dimensional analysis yields

$$E_P^{(\mathrm{S})}(k,t)=C_P^{(\mathrm{S})}S^2\epsilon^{2/3}k^{-11/3}, \tag{D.25}$$

as given in George *et al.* (1984). The $k^{-11/3}$ scaling is recovered in Fig. D.7a. The total pressure spectrum $E_P(k,t)$ evolves in $k^{-7/3}$ in the inertial range, and is not presented since it cannot be distinguished

from $E_P^{(\mathrm{iso})}$. In Fig. D.7b, the compensated $E_P^{(\mathrm{S})}$ indicates that $C_P^{(\mathrm{S})} \simeq 1.44$, which is close to the Kolmogorov constant, and this is expected since $E_P^{(\mathrm{S})}$ scales in E/k^2 in (D.22). Furthermore, the value $C_P^{(\mathrm{S})} \simeq 1.44$ is in good agreement with the prediction (George *et al.*, 1984), where the constant would be $C_P^{(\mathrm{S})} = 16K_0/15 = 1.40$.

The compensated isotropic pressure spectra $E_P^{(\mathrm{iso})} k^{7/3} \epsilon^{-4/3}$ for shear flows and USHT are presented in Fig. D.7b and 7.13b: the plateau settles around 2.5 for shear and 2.3 for USHT, which is quite close and proves some universality of the isotropic pressure spectrum between two completely different flows. Furthermore, these values are in good agreement with the prediction of George *et al.* (1984), where the constant would be $C_P = 1.32K_0^2 = 2.27$, close to our result.

Finally, the pressure variance

$$K_P(t) = \int_0^\infty E_P(k,t)\mathrm{d}k = K_P^{(\mathrm{iso})}(t) + K_P^{(\mathrm{S})}(t), \tag{D.26}$$

can be divided into isotropic and anisotropic parts. Both the isotropic $K_P^{(\mathrm{iso})}$ and shear $K_P^{(\mathrm{S})}$ parts of the total pressure variance K_P grow exponentially at a rate $\gamma_P = 2\gamma$ as revealed in Fig. D.7c, and in agreement with theoretical predictions by George *et al.* (1984) (K_P and $K_P^{(\mathrm{S})}$ cannot be distinguished).

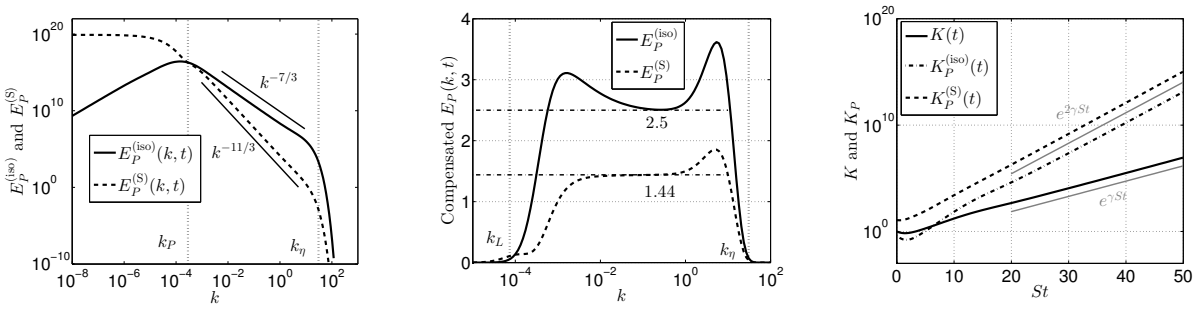

(a) (b) (c)

Figure D.7: Pressure spectra in shear flows for $\sigma = 2$ at $Re_\lambda = 2.10^4$. (a) Isotropic and anisotropic pressure spectra $E_P^{(\mathrm{iso})}$ and $E_P^{(\mathrm{S})}$, along with the integral and Kolmogorov wavenumbers $k_L \sim k_P$ and k_η, at $Re_\lambda \simeq 10^4$. (b) Compensated pressure spectra $E_P^{(\mathrm{iso})} k^{7/3}\epsilon^{-4/3}$ and $E_P^{(\mathrm{S})} k^{11/3}\epsilon^{-2/3}/S^2$. (c) Isotropic and anisotropic parts $K_P^{(\mathrm{iso})}$ and $K_P^{(\mathrm{S})}$ of the pressure variance K_P, along with the kinetic energy K for comparison: grey lines indicate the curves $\exp(\gamma St)$ and $\exp(2\gamma St)$.

D.5 Details on helical turbulence

In this section, details are provided regarding (i) the computation of the non-linear transfers involving the helical spectrum, (ii) the simplification of the evolution equation of the helical dissipation rate ϵ_H, and (iii) the wavenumber k_η^H defined in (8.22). Before that, the equation of the physical and spectral fluctuating vorticity are given explicitly. One has

$$\frac{\partial \omega_i}{\partial t} + u_l \frac{\partial \omega_i}{\partial x_l} + U_l \frac{\partial \omega_i}{\partial x_l} = \omega_l \frac{\partial u_i}{\partial x_l} + A_{il}\omega_l + \nu \frac{\partial^2 \omega_i}{\partial x_l \partial x_l}, \tag{D.27}$$

and the spectral counterpart is thus

$$\left(\frac{\partial}{\partial t} - A_{lj}k_l \frac{\partial}{\partial k_j} + \nu k^2\right)\hat{\omega}_i(\boldsymbol{k}) = A_{il}\hat{\omega}_l(\boldsymbol{k}) + \mathrm{i}k_l\left(\widehat{u_i\omega_l - u_l\omega_i}\right)(\boldsymbol{k}). \tag{D.28}$$

From this equation and (C.3), the helical Craya equation (8.5) is obtained (without mean velocity gradients). Regarding the evolution equation of $K_H =< u_i\omega_i > /2$ in physical space, the solenoidal property of ω_i provides $< \omega_i \partial_i p >= 0$ in the homogeneous framework.

D.5.1 Non-linear helical transfer T_H

The non-linear helical transfer is computed using (8.6). This expression can be simplified considering the real and imaginary contributions of τ_{ij} into

$$T_H(\boldsymbol{k}, t) = -\mathrm{i}\epsilon_{ijl} k_l \tau_{ij}(\boldsymbol{k}, t). \tag{D.29}$$

Using the quasi-normal closure already detailed in Chapter 2 and Appendix C, there are three terms to compute

$$\epsilon_{ijl} k_l \tau_{ij} = 2k_l k_n \epsilon_{ijl} \Big(P''_{ipq} R_{pj} R'_{qn} + P_{jpq} R'_{pn} R''_{qi} + P'_{npq} R''_{pi} R_{qj} \Big). \tag{D.30}$$

A careful attention has to be given to the order of the index for the spectral Reynolds tensor which is not symmetric anymore. Then, the products of Reynolds tensors generate imaginary and real parts. Only the imaginary part is computed here since the other terms bring no contributions to the spherical integration. The different contributions are

$$\begin{aligned}
2k_l k_n \epsilon_{ijl} P''_{ipq} R_{pj} R'_{qn} &= \mathrm{i}k^2 p \Big(\mathcal{E}''_0 \frac{\mathcal{H}}{k} (z(x^2-1) - (xy+z^3)) + \mathcal{E}_0 \frac{\mathcal{H}''}{q} (x+yz) \Big), \\
2k_l k_n \epsilon_{ijl} P_{jpq} R'_{pn} R''_{qi} &= 2\mathrm{i}k^3 \mathcal{E}''_0 \frac{\mathcal{H}'}{p} \Big(z(1-2y^2) - xy \Big), \\
2k_l k_n \epsilon_{ijl} P'_{npq} R''_{pi} R_{qj} &= \mathrm{i}k^2 p \Big(\mathcal{E}''_0 \frac{\mathcal{H}}{k} (z(1-x^2) - (xy+z^3)) + \mathcal{E}_0 \frac{\mathcal{H}''}{q} (x(2z^2-1) + yz) \Big).
\end{aligned}$$

The different relations used intensively to obtain these compact forms, in addition to the ones presented in Appendix C, are

$$\alpha_j P_{jp} = 0, \qquad \epsilon_{ijl} P_{ij} = 0, \qquad \alpha_i \alpha_n P'_{in} = 1 - z^2, \qquad \alpha'_i \alpha'_p P''_{in} = 1 - x^2, \qquad \alpha''_i \alpha''_n P_{in} = 1 - y^2,$$

$$\alpha_n \alpha''_i P'_{in} = -(y + xz), \qquad \alpha_j \alpha''_p P_{jp} = -(x + yz), \qquad \alpha_i \alpha_q P''_{iq} = -(z + xy), \qquad 2xyz = 1 - x^2 - y^2 - z^2.$$

Finally, the key relation to use in order to obtain helical transfers similar to the classical isotropic kinetic ones, is for the $\mathcal{E}''_0 \mathcal{H}'/p$ term. One can show that

$$k^2(y - xz - 2yz^2) = q^2(xz + y^3) - p^2 z(x + yz). \tag{D.31}$$

This allows, combined with $p \leftrightarrow q$ symmetrization, to gather the three contributions. For a skew-isotropic flow, the λ and spherical integrations reduce to

$$\int_{S_k} \int_0^{2\pi} (...) \, \mathrm{d}\lambda \, \mathrm{d}^2\boldsymbol{k} \to (...) 2\pi \frac{pq}{k} 4\pi k^2,$$

which immediately yields the expression (8.12).

D.5.2 Non-linear purely helical transfer

Helicity creates a purely helical transfer in the evolution equation of $E(k, t)$, coming exclusively from products of $\hat{R}^{(\mathrm{hel})}_{ij}$ (products of $\hat{R}^{(\mathrm{iso})}_{ij}$ and $\hat{R}^{(\mathrm{hel})}_{ij}$ have zero contribution to the spherical integration). Then, transfers are computed with the spherical-integration of $2T_{\mathcal{E}} = \tau_{ii} + \tau^*_{ii}$. Considering only the

products of imaginary parts, one has $\tau_{ii} = \tau_{ii}^*$. The three terms to compute are then

$$k_l \tau_{ii} = 2k_l \Big(P''_{imn} R_{mi} R'_{nl} + P_{imn} R'_{ml} R''_{ni} + P'_{lmn} R''_{mi} R_{ni} \Big).$$

This gives

$$2k_l P''_{imn} R_{mi} R'_{nl} = \frac{q}{p} \mathcal{H}\mathcal{H}'(x+yz) = \frac{p}{q} \mathcal{H}\mathcal{H}''(x+yz),$$

$$2k_l P_{imn} R'_{ml} R''_{ni} = -k^2 \frac{\mathcal{H}'\mathcal{H}''}{pq}(x+yz), \qquad 2k_l P'_{lmn} R''_{mi} R_{ni} = -\frac{p}{q} \mathcal{H}\mathcal{H}''(x - yz - 2xz^2).$$

The key relations to use are

$$y + xz = \frac{k}{p}(x+yz), \qquad k^2 \frac{\mathcal{H}'\mathcal{H}''}{pq}(x+yz) = 2\mathcal{H}'\mathcal{H}'' \frac{k}{q} z(x+yz) \qquad \text{(using } p \leftrightarrow q \text{ symmetry)}.$$

This results into (8.14).

D.5.3 Details on the evolution equation of ϵ_H

In this part, details about the calculations and algebra used in section 8.3.2 are gathered. The evolution equation of ϵ_H is obtained starting from the equations of u_i and ω_i (2.1) and (D.27) in HHT, so that

$$\frac{\partial}{\partial t} < \frac{\partial u_i}{\partial x_j} \frac{\partial \omega_i}{\partial x_j} > + \underbrace{< \frac{\partial^2 u_l \omega_i}{\partial x_j \partial x_l} \frac{\partial u_i}{\partial x_j} > + < \frac{\partial^2 u_l u_i}{\partial x_j \partial x_l} \frac{\partial \omega_i}{\partial x_j} > - < \frac{\partial^2 u_i \omega_l}{\partial x_j \partial x_l} \frac{\partial u_i}{\partial x_j} >}_{D[u,\omega]}$$
$$= - < \frac{\partial^2 p}{\partial x_i \partial x_j} \frac{\partial \omega_i}{\partial x_j} > + \nu \left(< \frac{\partial^3 \omega_i}{\partial x_j \partial x_l \partial x_l} \frac{\partial u_i}{\partial x_j} > + < \frac{\partial^3 u_i}{\partial x_j \partial x_l \partial x_l} \frac{\partial \omega_i}{\partial x_j} > \right).$$

To simplify the dissipative term, one uses $< \partial^2_{ll}(\partial_j u_i \, \partial_j \omega_i) >= 0$. The pressure term is zero since ω_i is solenoidal and $< \partial_i(\partial_j \omega_i \, \partial_j p) >= 0$. The term $D[u,\omega]$, arising from the non-linearity, is the production term of ϵ_H. One needs to expand $< \partial_l(u_l \, \partial_j u_i \partial_j \omega_i) >= 0$ and $< \partial_l(\omega_l \, \partial_j u_i \partial_j u_i) >= 0$, which gives

$$< u_l \frac{\partial u_i}{\partial x_j} \frac{\partial^2 \omega_i}{\partial x_j \partial x_l} > + < u_l \frac{\partial \omega_i}{\partial x_j} \frac{\partial^2 u_i}{\partial x_j \partial x_l} >= 0, \qquad < \omega_l \frac{\partial u_i}{\partial x_j} \frac{\partial^2 u_i}{\partial x_j \partial x_l} >= 0, \tag{D.32}$$

and yields (8.55).

Simplification of ϵ_H: the explicit derivation of R^H_{ij} gives

$$\begin{aligned}
\frac{\partial^2 R^H_{ij}}{\partial r_p \partial r_q} &= (\delta_{ip}\delta_{jq} + \delta_{iq}\delta_{jp}) \left(\frac{h'}{r^2} - \frac{h}{r^3} \right) - \delta_{ij}\delta_{pq} \left(\frac{h''}{r} + \frac{h'}{r^2} - \frac{h}{r^3} \right) + \\
&+ \frac{r_i r_j \delta_{pq} + r_i r_p \delta_{jq} + r_i r_q \delta_{jp} + r_j r_p \delta_{iq} + r_j r_q \delta_{ip}}{r^2} \left(\frac{h''}{r} - 3\frac{h'}{r^2} + 3\frac{h}{r^3} \right) \\
&- \frac{r_p r_q \delta_{ij}}{r^2} \left(h''' - 3\frac{h'}{r^2} + 3\frac{h}{r^3} \right) + \frac{r_i r_j r_p r_q}{r^4} \left(h''' - 6\frac{h''}{r} + 15\frac{h'}{r} - 15\frac{h}{r} \right) \\
&+ \epsilon_{ijl} \Big[\frac{r_l \delta_{pq} + r_p \delta_{lq} + r_q \delta_{lp}}{r} \left(\frac{f'''}{2} + \frac{f''}{r} - \frac{f'}{r^2} \right) + \frac{r_l r_p r_q}{2r^3} \left(r f^{(iv)} + f''' - 6\frac{f''}{r} + 6\frac{f'}{r^2} \right) \Big],
\end{aligned} \tag{D.33}$$

where the prime $'$ denotes the spatial derivative $\partial/\partial r$. From this general equation, one notably obtains the quantity of interest here

$$< \frac{\partial u_i}{\partial x_j} \frac{\partial \omega'_i}{\partial x'_j} >= 2 \left(h''' + 4\frac{h''}{r} \right), \tag{D.34}$$

where h'' and h''' can be expressed as specific components of the velocity and vorticity fields thanks to various relations coming from (D.33): one gets

$$h'''(0) =< \frac{\partial u_2}{\partial x_1}\frac{\partial \omega_2}{\partial x_1} > -\frac{1}{2} < \frac{\partial u_1}{\partial x_1}\frac{\partial \omega_1}{\partial x_1} >, \tag{D.35}$$

$$h'''(0) = \lim_{r\to 0}\frac{\partial^3}{\partial r^3} < u_2 u_3' >=< u_2 \frac{\partial^3 u_3}{\partial x_1^3} >, \tag{D.36}$$

where the two expressions are linked using homogeneity and the definition of ω_i. Then, a Taylor expansion of $h(r)$ for $r \to 0$ in (D.34) gives $\epsilon_H = 10\nu h'''(0)$, with $h''(0) = 0$ since ϵ_H is finite. Finally, Taylor expansions in (D.35) give, using only $h(0) = 0$ since the $h'(0)$ and $h''(0)$ terms vanish,

$$< \frac{\partial u_2}{\partial x_1}\frac{\partial \omega_2}{\partial x_1} >= \frac{4}{3}h'''(0) = 2 < \frac{\partial u_1}{\partial x_1}\frac{\partial \omega_1}{\partial x_1} >, \tag{D.37}$$

which eventually yields (8.58).

Simplification of $D[u,\omega]$: Classical algebra yields

$$\begin{aligned}\phi_{ijl}^{(uu\omega)} &= \frac{\epsilon_{lpq}}{2r^3}(k - rk')(\delta_{ip}r_jr_q + \delta_{jp}r_ir_q) + \frac{\epsilon_{lpq}}{4r}\Big[(2k + rk')(\delta_{iq}\delta_{jp} + \delta_{jq}\delta_{ip}) \\ &+ \frac{-2k + 2rk' + r^2k''}{r^2}(\delta_{iq}r_jr_p + \delta_{jq}r_ir_p)\Big] + S'\Big[2\frac{r_ir_jr_l}{r^3} - \delta_{il}\frac{r_j}{r} - \delta_{jl}\frac{r_i}{r}\Big] \\ &- \frac{S}{r}\Big[4\frac{r_ir_jr_l}{r^3} - 2\delta_{ij}\frac{r_l}{r} + \delta_{il}\frac{r_j}{r} + \delta_{jl}\frac{r_i}{r}\Big].\end{aligned} \tag{D.38}$$

From this expression, one notably obtains

$$\phi_{\mathrm{LNN}}^{(uu\omega)} = -S' - \frac{S}{r}, \qquad \phi_{\mathrm{LLL}}^{(uu\omega)} = -4\frac{S}{r}, \qquad \phi_{\mathrm{LLN}}^{(uu\omega)} = 2\frac{S}{r}, \qquad \phi_{\mathrm{LNL}}^{(uu\omega)} = 0, \tag{D.39}$$

where L is the longitudinal component, *i.e.* $r_1 = r$, and N is either the second or third component, with $r_2 = r_3 = 0$ as usual. The second tensor used in Gomez *et al.* (2000) reads

$$\phi_{ijl}^{(\omega uu)} = A\frac{r_ir_jr_l}{r^3} + B\delta_{jl}\frac{r_i}{r} + C\delta_{il}\frac{r_j}{r} + D\delta_{ij}\frac{r_l}{r} + E\epsilon_{ilm}\frac{r_jr_m}{r^2} + F\epsilon_{jlm}\frac{r_ir_m}{r^2} + G\epsilon_{ijm}\frac{r_lr_m}{r^2}, \tag{D.40}$$

where A, B, C, D, E, F and G are functions of r only. Unlike $\phi_{ijl}^{(uu\omega)}$ which is expressed as a function of $k(r)$ and $S(r)$, $\phi_{ijl}^{(\omega uu)}$ depends on unknown functions, and is not symmetric in is two first indices. Nevertheless, some words can be said about $\phi_{ijl}^{(\omega uu)}$: using incompressibility $\partial_{r_l}\phi_{iil}^{(\omega uu)} = 0$ and some algebra given in von Karman & Howarth (1938), one obtains $A+B+C+3D = 0$, which notably implies that

$$\phi_{ii\mathrm{L}}^{(\omega uu)} = 0, \qquad \phi_{\mathrm{NNL}}^{(\omega uu)} = -\frac{1}{2}\phi_{\mathrm{LLL}}^{(\omega uu)}. \tag{D.41}$$

Combining this with relations such as $< u_{\mathrm{L}}u_{\mathrm{L}}'\omega_{\mathrm{L}}' >= - < u_{\mathrm{L}}\omega_{\mathrm{L}}u_{\mathrm{L}}' >$, one obtains an expression already given in Gomez *et al.* (2000),

$$D^{(uu\omega)} = 4\phi_{\mathrm{LNN}}^{(uu\omega)} + 2\phi_{\mathrm{LLL}}^{(uu\omega)} + 4\phi_{\mathrm{NLN}}^{(\omega uu)} - 4\phi_{\mathrm{LNN}}^{(\omega uu)}. \tag{D.42}$$

Using the results (8.50) and (D.39), one gets

$$\Delta\phi = \phi_{\mathrm{NLN}}^{(\omega uu)} - \phi_{\mathrm{LNN}}^{(\omega uu)} = -S' - 3\frac{S}{r}. \tag{D.43}$$

This expression of $\Delta\phi$ is essential since it links $\phi_{ijl}^{(\omega uu)}$ to $S(r)$. Now, let's express $D[u,\omega]$ as a function of the derivatives of $\phi_{ijl}^{(uu\omega)}$ and $\phi_{ijl}^{(\omega uu)}$. One has

$$\begin{aligned}\frac{\partial^3\phi_{ijl}^{(uu\omega)}}{\partial r_n\partial r_p\partial r_q} =&< \frac{\partial u_i}{\partial x_q}\frac{\partial u_j}{\partial x_p}\frac{\partial \omega_l'}{\partial x_n'} > + < \frac{\partial u_i}{\partial x_p}\frac{\partial u_j}{\partial x_q}\frac{\partial \omega_l'}{\partial x_n'} > \\ &+ < u_i\frac{\partial \omega_l'}{\partial x_n'}\frac{\partial^2 u_j}{\partial x_p\partial x_q} > + < u_j\frac{\partial \omega_l'}{\partial x_n'}\frac{\partial^2 u_i}{\partial x_p\partial x_q} >, \end{aligned} \tag{D.44}$$

$$\begin{aligned}\frac{\partial^3\phi_{ijl}^{(\omega uu)}}{\partial r_n\partial r_p\partial r_q} =&< \frac{\partial u_l'}{\partial x_n'}\frac{\partial u_j}{\partial x_q}\frac{\partial \omega_i}{\partial x_p} > + < \frac{\partial u_l'}{\partial x_n'}\frac{\partial u_j}{\partial x_p}\frac{\partial \omega_i}{\partial x_q} > \\ &+ < u_j\frac{\partial u_l'}{\partial x_n'}\frac{\partial^2 \omega_i}{\partial x_p\partial x_q} > + < \omega_i\frac{\partial \omega_l'}{\partial x_n'}\frac{\partial^2 u_j}{\partial x_p\partial x_q} > . \end{aligned} \tag{D.45}$$

Using (D.32), one obtains (8.64), with $\phi_{ili}^{(\omega uu)} - \phi_{lii}^{(\omega uu)} = 2r_l\Delta\phi/r$. The explicit calculation of the above expression yields

$$\begin{aligned}&\frac{\partial^3}{\partial r_j\partial r_j\partial r_l}\left[\phi_{ili}^{(uu\omega)} + \phi_{ili}^{(\omega uu)} - \phi_{lii}^{(\omega uu)}\right] \\ &= \frac{1}{r^2}\frac{\partial}{\partial r}\left(r^2\frac{\partial}{\partial r}\Big[\underbrace{-2\left(S'' + 5\frac{S'}{r} + 3\frac{S}{r^2}\right)}_{\partial_{r_l}\phi_{ili}^{(uu\omega)}} + 2\underbrace{\left(\Delta\phi' + \frac{2}{r}\Delta\phi\right)}_{\partial_{r_l}(\Delta\phi\, r_l/r)}\Big]\right) \\ &= -\frac{4}{r^4}\left[r^4S^{(iv)} + 7r^3S''' + 3r^2S'' - 6rS' + 6S\right] = 2\frac{\partial^3\phi_{ili}^{(uu\omega)}}{\partial r_j\partial r_j\partial r_l}. \end{aligned} \tag{D.46}$$

It is worth noting, afterwards, that only derivatives of $\phi_{ijl}^{(uu\omega)}$ are necessary to compute $D[u,\omega]$. To conclude the first step, *i.e.* expressing $D[u,\omega]$ as a function of the derivatives of $S(r)$, one uses a Taylor expansion for $S(r)$ when $r\to 0$, remembering that $S(0)=0$,

$$D[u,\omega] = -\frac{32}{r}S'''(0) - 35S^{(iv)}(0) + \mathcal{O}(r). \tag{D.47}$$

Since $D[u,\omega]$ is finite, because ϵ_H is, one has $S'''(0)=0$. In the end, one recovers (8.65), where only $S(0)=S'''(0)=0$ was used.

The general expression of $\partial^3_{npq}\phi_{ijl}^{(uu\omega)}$ is now derived to obtain the explicit expression of $S^{(iv)}(0)$: this is a lengthy calculation. Nevertheless, since we search for derivatives of $S(r)$, only the corresponding part is considered in (D.38): the part with derivatives of $k(r)$ vanishes with the appropriate indices contractions. This yields

$$\begin{aligned}&\frac{\partial^3\phi_{ijl}^{(uu\omega)}}{\partial r_n\partial r_p\partial r_q} = \left(2S^{(iv)} - 28\frac{S'''}{r} + 174\frac{S''}{r^2} - 558\frac{S'}{r^3} + 768\frac{S}{r^4}\right)\frac{r_ir_jr_lr_nr_pr_q}{r^6} \\ &+ \frac{1}{r^4}\left(2\frac{S'''}{r} - 18\frac{S''}{r^2} + 66\frac{S'}{r^3} - 96\frac{S}{r^4}\right)\Big[\delta_{in}r_jr_lr_pr_q + \delta_{jn}\ldots + \delta_{ln}\ldots + \delta_{pn}\ldots + \delta_{qn}\ldots + \\ &\delta_{ip}\ldots + \delta_{iq}\ldots + \delta_{jp}\ldots + \delta_{jq}\ldots + \delta_{ij}\ldots + \delta_{pl}\ldots + \delta_{ql}\ldots + \delta_{pq}\ldots\Big] \\ &- \frac{1}{r^4}\left(S^{(iv)} - 5\frac{S'''}{r} + 6\frac{S''}{r^2} + 18\frac{S'}{r^3} - 48\frac{S}{r^4}\right)\Big[\delta_{il}r_jr_nr_pr_q + \delta_{jl}r_ir_nr_pr_q\Big] \\ &+ \frac{1}{r^2}\left(2\frac{S''}{r^2} - 10\frac{S'}{r^3} + 16\frac{S}{r^4}\right)\Big[r_ir_jP^{(3)}_{lnpq} + r_ir_lP^{(3)}_{jnpq} + r_jr_lP^{(3)}_{inpq} + r_lr_pP^{(3)}_{ijnq} + r_lr_qP^{(3)}_{ijnp} + \\ &r_lr_nP^{(3)}_{ijpq} + r_ir_p(\delta_{jn}\delta_{lq} + \delta_{ln}\delta_{jq}) + r_ir_q(\delta_{jn}\delta_{lp} + \delta_{ln}\delta_{jp}) + r_jr_p(\delta_{in}\delta_{lq} + \delta_{ln}\delta_{iq}) + \\ &r_jr_q(\delta_{in}\delta_{lp} + \delta_{ln}\delta_{ip}) + r_ir_n(\delta_{jp}\delta_{lq} + \delta_{lp}\delta_{jq}) + r_jr_n(\delta_{ip}\delta_{lq} + \delta_{lp}\delta_{iq}) + \\ &\delta_{ij}(r_pr_n\delta_{lq} + r_qr_n\delta_{lp} + r_pr_q\delta_{ln})\Big]\end{aligned}$$

$$
\begin{aligned}
&-\frac{1}{r^2}\left(\frac{S'''}{r}-2\frac{S''}{r^2}-2\frac{S'}{r^3}+8\frac{S}{r^4}\right)\Big[r_n r_p(\delta_{il}\delta_{jq}+\delta_{jl}\delta_{iq})+r_n r_q(\delta_{il}\delta_{jp}+\delta_{jl}\delta_{ip})+\\
&r_p r_q(\delta_{il}\delta_{jn}+\delta_{jl}\delta_{in})+r_j\delta_{il}(r_n\delta_{pq}+r_p\delta_{qn}+r_q\delta_{pn})+r_i\delta_{jl}(r_n\delta_{pq}+r_p\delta_{qn}+r_q\delta_{pn})\Big]\\
&+\left(2\frac{S'}{r^3}-4\frac{S}{r^4}\right)\Big[\delta_{in}(\delta_{jq}\delta_{lp}+\delta_{jp}\delta_{lq})+\delta_{jn}(\delta_{iq}\delta_{lp}+\delta_{ip}\delta_{lq})+\delta_{ij}(\delta_{lq}\delta_{pn}+\delta_{lp}\delta_{qn})+\delta_{ln}P^{(3)}_{ijpq}\Big]\\
&-\left(\frac{S''}{r^2}-2\frac{S}{r^4}\right)\Big[\delta_{il}P^{(3)}_{jnpq}+\delta_{jl}P^{(3)}_{inpq}\Big],
\end{aligned}
\tag{D.48}
$$

where $P^{(3)}_{ijpq}=\delta_{ij}\delta_{pq}+\delta_{ip}\delta_{jq}+\delta_{iq}\delta_{jp}$. With this equation, one can obviously recover (D.46). Even though this would be tedious, this equation (D.48), combined with (D.44), can determine each non-zero component of $\partial^3_{npq}\phi^{(uu\omega)}_{ijl}$ as a function of derivatives of $S(r)$. This expression is of course an important result and could be used for further theoretical developments. One gets in particular

$$
\frac{\partial^3\phi^{(uu\omega)}_{111}}{\partial r_1^3}=-4\frac{S'''}{r}+12\frac{S''}{r^2}-24\frac{S'}{r^3}+24\frac{S}{r^4}. \tag{D.49}
$$

Using as before a Taylor expansion of $S(r)$ when $r\to 0$, the $S'(0)$, $S''(0)$ and $S'''(0)$ terms vanish, and with $S(0)=0$, this yields (8.66). Furthermore, using (D.44), one obtains

$$
\left(\frac{\partial^3\phi^{(uu\omega)}_{111}}{\partial r_1^3}\right)_{r=0}=2<\left(\frac{\partial u_1}{\partial x_1}\right)^2\frac{\partial\omega_1}{\partial x_1}>+2<u_1\frac{\partial^2 u_1}{\partial x_1^2}\frac{\partial\omega_1}{\partial x_1}>=<\frac{\partial^2 u_1^2}{\partial x_1^2}\frac{\partial\omega_1}{\partial x_1}>. \tag{D.50}
$$

The two previous equations give (8.67).

D.5.4 Re-interpretation of the helical viscous cutoff k_η^H

In this section, another interpretation of the wavenumber k_η^H, defined in (8.22), is proposed. This wavenumber was originally derived by Ditlevsen & Giuliani (2001) as a helical viscous cutoff. However, it was revealed in Fig. 8.1b that k_η^H is not a wavenumber equivalent to k_η for the helical spectrum, since both E and H have a $k^{-5/3}$ inertial range which extends up to k_η.

Here are some elements, based on the demonstration of Ditlevsen & Giuliani (2001), to explain why k_η^H cannot be a helical viscous cutoff. First, it is assumed in the latter reference that $H(k,t)$ scales as $kE(k,t)$ in the spectral definition of ϵ_H, and that the dominant contribution of the integral comes from the largest wavenumber, which gives

$$
\epsilon_H=2\nu\int_0^\infty k^2H(k,t)\mathrm{d}k\sim\nu {k_\eta^H}^4E(k_\eta^H,t)=\nu {k_\eta^H}^{7/3}\epsilon^{2/3}, \tag{D.51}
$$

and thus recovers (8.22). However, a scaling like $H\sim kE$ would imply that $H\sim k^{-2/3}$ in the inertial range, which is not the case as illustrated in Fig. 8.1b. Hence, the assumption $H\sim kE$ in the inertial range is wrong, and moreover, it is worth noting that if the scaling (8.20) is used in the previous integral, one recovers $k_\eta^H=k_\eta$, as shown by Chen *et al.* (2003).

Instead, it is shown hereafter analytically that k_η^H can be seen as the wavenumber at which viscous dissipation of helicity balances non-linear helical transfers. In the kinetic and helical Lin evolution equations (8.15) and (8.16), writing that at $k=k_\eta^H$ there is a balance between convection and viscous dissipation yields $\nu {k_\eta^H}^2E(k_\eta^H)\sim\theta k_\eta^H H(k_\eta^H)^2$, where $\theta=\theta_{kkk}$. With the relation (8.21), one further has $E/H\sim\epsilon/\epsilon_H$. Then, for the characteristic time, $\theta\sim 1/(\nu {k_\eta^H}^2)$ is chosen, in agreement with dissipation being dynamically important at large wavenumbers in the definition (2.40) of θ_{kpq}. Finally, the classical

inertial scaling (8.20) is used for H, so that

$$\nu {k_\eta^H}^2 \frac{E(k_\eta^H)}{H(k_\eta^H)} \sim \frac{1}{\nu {k_\eta^H}^2} k_\eta^H \left(\epsilon_H \epsilon^{-1/3} {k_\eta^H}^{-5/3}\right) \qquad \Leftrightarrow \qquad {k_\eta^H}^{14/3} \sim \epsilon_H^2 \epsilon^{-4/3} \nu^{-2}, \tag{D.52}$$

from which one recovers (8.22). Here, the evolution equation of E has been used: the final result can also be obtained starting from the evolution equation of $H(k)$, and writing $\nu {k_\eta^H}^2 H(k_\eta^H) \sim \theta {k_\eta^H}^3 E(k_\eta^H) H(k_\eta^H)$. The wavenumber k_η^H is shown to be quite relevant in Fig. 8.9 at large Reynolds numbers: indeed, from k_η^H, there is a balance between $-2\nu k^3 H$ and $k S_H^{\mathrm{NL}}$. However, this is much less relevant at moderate Reynolds numbers: this is expected since in the previous demonstration, inertial scalings were used, which are valid only at large Reynolds numbers.

As a conclusion, the original helical viscous cutoff k_η^H proposed by Ditlevsen & Giuliani (2001) was re-interpreted in terms of high Reynolds numbers balance between the viscous dissipation of helicity and non-linear helical transfers.

Appendix E

Details on Spherically-Averaged Scalar Lin Equations

In this appendix, all the calculations yielding to the scalar spherically-averaged Lin equations of the passive scalar field and scalar flux are fully detailed. Additional theoretical results are presented as well, such as the quadratic anisotropic contributions in the non-linear transfers with illustrations in USHT, and an alternative modelling for the scalar flux.

E.1 Scalar-scalar correlation

In this section, the spectral scalar-scalar correlation is first addressed: the quasi-normal procedure along with the calculations of the linear and non-linear transfers are detailed.

E.1.1 Scalar Craya equation

The scalar-scalar correlation $\mathcal{E}^T$ is defined in (4.5). Its evolution equation is obtained by multiplying (4.3) by $\hat{\theta}^*(\boldsymbol{p})$ and summing it to the evolution equation of $\hat{\theta}^*(\boldsymbol{p})$ multiplied by $\hat{\theta}(\boldsymbol{k})$. Ensemble average and integration over the whole domain gives the scalar Craya equation (4.6). The calculation of the scalar non-linear transfer $T^{\mathrm{T,NL}}$ deserves some additional details. Firstly, one has to use Hermitian symmetry for the scalar fluctuation $\theta(\boldsymbol{k})^* = \theta(-\boldsymbol{k})$ so that the scalar potential satisfies $\mathcal{E}^T(\boldsymbol{k})^* = \mathcal{E}^T(-\boldsymbol{k})$.

Before using ensemble average, (4.6) reads, with the use of Hermitian symmetry

$$\begin{aligned}\frac{\partial \hat{\theta}(\boldsymbol{k})\hat{\theta}^*(\boldsymbol{p})}{\partial t} + ... &= -\mathrm{i}k_j \int_{\boldsymbol{k}=\boldsymbol{r}+\boldsymbol{s}} \hat{\theta}^*(\boldsymbol{p})\hat{\theta}(\boldsymbol{r})\hat{u}_j(\boldsymbol{s})\mathrm{d}\boldsymbol{r} + \mathrm{i}p_j \int_{\boldsymbol{p}=\boldsymbol{r}+\boldsymbol{s}} \hat{\theta}(\boldsymbol{k})\hat{\theta}^*(\boldsymbol{r})\hat{u}_j^*(\boldsymbol{s})\mathrm{d}\boldsymbol{r}, \\ &= -\mathrm{i}k_j \int_{\boldsymbol{k}=\boldsymbol{r}+\boldsymbol{s}} \hat{\theta}(-\boldsymbol{p})\hat{\theta}(\boldsymbol{r})\hat{u}_j(\boldsymbol{s})\mathrm{d}\boldsymbol{r} + \mathrm{i}p_j \int_{\boldsymbol{p}=\boldsymbol{r}+\boldsymbol{s}} \hat{\theta}^*(-\boldsymbol{k})\hat{\theta}^*(\boldsymbol{r})\hat{u}_j^*(\boldsymbol{s})\mathrm{d}\boldsymbol{r}.\end{aligned}$$

Then, ensemble average gives

$$\frac{\partial \mathcal{E}^T\delta(\boldsymbol{k}-\boldsymbol{p})}{\partial t} + ... = -k_j \int_{\boldsymbol{k}=\boldsymbol{r}+\boldsymbol{s}} S_j^T(-\boldsymbol{p},\boldsymbol{r})\delta(\boldsymbol{r}+\boldsymbol{s}-\boldsymbol{p})\mathrm{d}\boldsymbol{r} - p_j \int_{\boldsymbol{p}=\boldsymbol{r}+\boldsymbol{s}} S_j^{T*}(-\boldsymbol{k},\boldsymbol{r})\delta(\boldsymbol{r}+\boldsymbol{s}-\boldsymbol{k})\mathrm{d}\boldsymbol{r}.$$

One has to integrate over $\boldsymbol{p}$

$$\frac{\partial \mathcal{E}^T(\boldsymbol{k})}{\partial t} + ... = -\int \Big(k_j \int_{\boldsymbol{k}=\boldsymbol{r}+\boldsymbol{s}} S_j^T(-\boldsymbol{p},\boldsymbol{r})\delta(\boldsymbol{k}-\boldsymbol{p})\mathrm{d}\boldsymbol{r}\Big)\mathrm{d}\boldsymbol{p}$$
$$-\int \Big(p_j \int_{\boldsymbol{p}=\boldsymbol{r}+\boldsymbol{s}} S_j^{T*}(-\boldsymbol{k},\boldsymbol{r})\delta(\boldsymbol{p}-\boldsymbol{k})\mathrm{d}\boldsymbol{r}\Big)\mathrm{d}\boldsymbol{p}.$$

Using the fact that the Dirac function is even, one obtains

$$\frac{\partial \mathcal{E}^T(\boldsymbol{k})}{\partial t} + ... = -k_j \int S_j^T(-\boldsymbol{k},\boldsymbol{p})\mathrm{d}\boldsymbol{p} - k_j \int S_j^{T*}(-\boldsymbol{k},\boldsymbol{p})\mathrm{d}\boldsymbol{p} = -2k_j \Re\Big(\int S_j^T(-\boldsymbol{k},\boldsymbol{p})\mathrm{d}\boldsymbol{p}\Big).$$

This equation implies that the scalar correlation $\mathcal{E}^T$ is real, as the Reynolds stress tensor (without helicity), and thus follows the property $\mathcal{E}^T(\boldsymbol{k}) = \mathcal{E}^T(-\boldsymbol{k})$, which leads to

$$\frac{\partial \mathcal{E}^T(\boldsymbol{k})}{\partial t} + ... = 2k_j \Re\Big(\int S_j^T(\boldsymbol{k},\boldsymbol{p})\mathrm{d}\boldsymbol{p}\Big).$$

E.1.2 EDQNM closure for $\mathcal{E}^T$

Some details about how to obtain the closure (4.24) for $\mathfrak{T}_i^{\mathrm{T,QN}}(\boldsymbol{k},\boldsymbol{p})$ are given. Firstly, the fourth-order correlation is defined

$$T_{jl}^T(\boldsymbol{k},\boldsymbol{p},t)\delta(\boldsymbol{k}+\boldsymbol{p}+\boldsymbol{q}+\boldsymbol{v}) = -\mathrm{i} < \hat{u}_j(\boldsymbol{q})\hat{\theta}(\boldsymbol{k})\hat{\theta}(\boldsymbol{p})\hat{u}_l(\boldsymbol{v}) > . \tag{E.1}$$

The process is slightly different from the purely kinetic one since the relation is not symmetric. The third-order scalar correlation $S_j^T(\boldsymbol{k},\boldsymbol{p})$ evolution equation can be written as

$$\Big(\frac{\partial}{\partial t} + a(k^2+p^2) + \nu q^2\Big)\hat{\theta}(\boldsymbol{k})\hat{\theta}(\boldsymbol{p})\hat{u}_j(\boldsymbol{q}) + ... = -\mathrm{i}$$
$$\Big(k_l \int_{\boldsymbol{k}=\boldsymbol{r}+\boldsymbol{s}} \hat{\theta}(\boldsymbol{r})\hat{\theta}(\boldsymbol{p})\hat{u}_l(\boldsymbol{s})\hat{u}_j(\boldsymbol{q})\mathrm{d}^3\boldsymbol{r} + p_l \int_{\boldsymbol{p}=\boldsymbol{r}+\boldsymbol{s}} \hat{\theta}(\boldsymbol{r})\hat{\theta}(\boldsymbol{k})\hat{u}_l(\boldsymbol{s})\hat{u}_j(\boldsymbol{q})\mathrm{d}^3\boldsymbol{r}$$
$$+ P_{jmn}(\boldsymbol{q})\int_{\boldsymbol{q}=\boldsymbol{r}+\boldsymbol{s}} \hat{\theta}(\boldsymbol{k})\hat{\theta}(\boldsymbol{p})\hat{u}_m(\boldsymbol{r})\hat{u}_n(\boldsymbol{s})\mathrm{d}^3\boldsymbol{r}\Big),$$

which becomes, after ensemble average and convolution rules

$$\Big(\frac{\partial}{\partial t} + a(k^2+p^2) + \nu q^2\Big) S_j^T(\boldsymbol{k},\boldsymbol{p},t)\delta(\boldsymbol{k}+\boldsymbol{p}+\boldsymbol{q}) + ... =$$
$$k_l \int_{\boldsymbol{k}=\boldsymbol{r}+\boldsymbol{s}} T_{jl}^T(\boldsymbol{r},\boldsymbol{p})\delta(\boldsymbol{k}+\boldsymbol{p}+\boldsymbol{q})\mathrm{d}^3\boldsymbol{r} + p_l \int_{\boldsymbol{p}=\boldsymbol{r}+\boldsymbol{s}} T_{jl}^T(\boldsymbol{k},\boldsymbol{r})\delta(\boldsymbol{k}+\boldsymbol{p}+\boldsymbol{q})\mathrm{d}^3\boldsymbol{r} +$$
$$+ P_{jmn}(\boldsymbol{q})\int_{\boldsymbol{q}=\boldsymbol{r}+\boldsymbol{s}} T_{mn}^T(\boldsymbol{k},\boldsymbol{p})\delta(\boldsymbol{k}+\boldsymbol{p}+\boldsymbol{q})\mathrm{d}^3\boldsymbol{r}.$$

There is no need to go further for the evolution equation. Then, the quasi-normal approximation is used, consisting into neglecting the fourth order cumulants. The first rhs term gives

$$\int_{\boldsymbol{k}=\boldsymbol{r}+\boldsymbol{s}} F_l(\boldsymbol{r})F_j(\boldsymbol{p})\delta(\boldsymbol{r}+\boldsymbol{s})\delta(\boldsymbol{p}+\boldsymbol{q})\mathrm{d}^3\boldsymbol{r} + \int_{\boldsymbol{k}=\boldsymbol{r}+\boldsymbol{s}} \mathcal{E}^T(\boldsymbol{p})\hat{R}_{jl}(\boldsymbol{q})\delta(\boldsymbol{r}+\boldsymbol{p})\delta(\boldsymbol{s}+\boldsymbol{q})\mathrm{d}^3\boldsymbol{r}$$
$$+ \int_{\boldsymbol{k}=\boldsymbol{r}+\boldsymbol{s}} F_j(\boldsymbol{r})F_l(\boldsymbol{p})\delta(\boldsymbol{r}+\boldsymbol{q})\delta(\boldsymbol{p}+\boldsymbol{s})\mathrm{d}^3\boldsymbol{r} = k_l\delta(\boldsymbol{k}+\boldsymbol{p}+\boldsymbol{q})\Big(\mathcal{E}^T(\boldsymbol{p})\hat{R}_{jl}(\boldsymbol{q}) + F_j^*(\boldsymbol{q})F_l(\boldsymbol{p})\Big).$$

The second term yields

$$\int_{\boldsymbol{p}=\boldsymbol{r}+\boldsymbol{s}} F_l(\boldsymbol{r})F_j(\boldsymbol{k})\delta(\boldsymbol{r}+\boldsymbol{s})\delta(\boldsymbol{k}+\boldsymbol{q})\mathrm{d}^3\boldsymbol{r} + \int_{\boldsymbol{p}=\boldsymbol{r}+\boldsymbol{s}} \mathcal{E}^T(\boldsymbol{k})\hat{R}_{jl}(\boldsymbol{q})\delta(\boldsymbol{r}+\boldsymbol{k})\delta(\boldsymbol{s}+\boldsymbol{q})\mathrm{d}^3\boldsymbol{r}$$
$$+ \int_{\boldsymbol{p}=\boldsymbol{r}+\boldsymbol{s}} F_j(\boldsymbol{r})F_l(\boldsymbol{k})\delta(\boldsymbol{r}+\boldsymbol{q})\delta(\boldsymbol{k}+\boldsymbol{s})\mathrm{d}^3\boldsymbol{r} = p_l\delta(\boldsymbol{k}+\boldsymbol{p}+\boldsymbol{q})\Big(\mathcal{E}^T(\boldsymbol{k})\hat{R}_{jl}(\boldsymbol{q}) + F_j^*(\boldsymbol{q})F_l(\boldsymbol{k})\Big).$$

The last term gives

$$\int_{\boldsymbol{q}=\boldsymbol{r}+\boldsymbol{s}} F_m(\boldsymbol{k})F_n(\boldsymbol{p})\delta(\boldsymbol{r}+\boldsymbol{k})\delta(\boldsymbol{s}+\boldsymbol{p})\mathrm{d}^3\boldsymbol{r} + \int_{\boldsymbol{q}=\boldsymbol{r}+\boldsymbol{s}} \mathcal{E}^T(\boldsymbol{k})\hat{R}_{mn}(\boldsymbol{r})\delta(\boldsymbol{r}+\boldsymbol{s})\delta(\boldsymbol{k}+\boldsymbol{p})\mathrm{d}^3\boldsymbol{r}$$
$$+ \int_{\boldsymbol{q}=\boldsymbol{r}+\boldsymbol{s}} F_m(\boldsymbol{p})F_n(\boldsymbol{k})\delta(\boldsymbol{r}+\boldsymbol{p})\delta(\boldsymbol{k}+\boldsymbol{s})\mathrm{d}^3\boldsymbol{r} = 2P_{jmn}(\boldsymbol{q})\delta(\boldsymbol{k}+\boldsymbol{p}+\boldsymbol{q})F_m(\boldsymbol{p})F_n(\boldsymbol{k}).$$

Finally, using relations such as $p_l\hat{R}''_{jl} = -k_l\hat{R}''_{jl}$, one recovers the previous expression of $\mathfrak{T}_i^{\mathrm{T,QN}}(\boldsymbol{k},\boldsymbol{p})$. The main term to compute is then $k_i\mathfrak{T}_i^{\mathrm{T,QN}}$. To do so, the same method as in the purely kinetic case is applied: using

$$k_l\hat{R}''_{ln}k_n = kp(xy+z)\Big(\mathcal{E}'' + \Re X''\Big),$$

and relations such as $k_i\alpha''_i = -ky$, $q_nF_n = -p_nF_n$ and $q_nF'_n = -k_nF'_n$, one gets

$$k_i\mathfrak{T}_i^{\mathrm{T,QN}} = 2kp(xy+z)(\mathcal{E}'' + \Re X'')(\mathcal{E}'^T - \mathcal{E}^T)$$
$$+ k_nF''^*_n(p_mF_m + k_mF'_m) + p_mF_mk_nF'_n\frac{ky-px}{q}.$$

The non-linear scalar transfer $T^{\mathrm{T,NL}}(\boldsymbol{k},t)$ of (4.26) is thus recovered.

E.1.3 Spherically-averaged scalar Lin equations

Now, as in the kinetic case, spherical integrations are performed on this non-linear scalar transfer term to transform the $(\boldsymbol{k},t)$ dependence into a (k,t) one. All quadratic contributions such as $\mathcal{E}''\mathcal{E}_T$, $\Re X''\mathcal{E}_T$, ... are discarded in the moderate anisotropy framework. Finally, products of the cospectrum flux in (4.26) like $F''^*_iF_j$ and F'_iF_j are neglected as well: indeed, since F_i is zero in the isotropic case, it is a purely anisotropic quantity and thus quadratic contributions can be neglected.

The definition of the non-linear isotropic scalar transfer is given by (4.39). From (4.26), only six terms remain after the λ-integration. The two relations of use are

$$\int_{S_k} \alpha_i\alpha_jH^{()}_{ij}\mathrm{d}^2\boldsymbol{k} = 0, \qquad \int_{S_k} H^{()}_{mn}\alpha_m\alpha_nP_{ij}\mathrm{d}^2\boldsymbol{k} = -\frac{8}{15}\pi k^2H^{()}_{ij}.$$

There is only one term left from the λ-integration. The non-linear isotropic scalar transfer (4.40) is recovered with the first of this formula. The non-linear directional scalar transfer is defined by (4.41). The λ-integration also gives six terms: one of them is simplified when the isotropic part is subtracted. One has to use the second formula of spherical average to obtain (4.42).

The linear isotropic scalar transfer $S^{\mathrm{T,L(iso)}}$ defined in (4.43) is computed using previous relations of Appendix C such as

$$\int_{S_k} A_{ln}k_l\frac{\partial\mathcal{E}^TH^{(T)}_{pq}\alpha_p\alpha_q}{\partial k_n}\mathrm{d}^2\boldsymbol{k} = \frac{8\pi k^2}{15}A_{ln}\left(k\frac{\partial H^{(T)}_{ln}\mathcal{E}^T_0}{\partial k} + 3H^{(T)}_{ln}\mathcal{E}^T_0\right),$$

which yields (4.44). The linear spherically-averaged directional scalar transfer is defined by (4.45). Equation (4.46) is recovered using

$$A_{ln}H_{pq}^{(T)}\int_{S_k}\alpha_i\alpha_j\alpha_l\alpha_n\alpha_p\alpha_q\mathrm{d}^2\boldsymbol{k}=\frac{8\pi k^2}{105}\Big(2A_{li}^{+}H_{jl}^{(T)}+2A_{lj}^{+}H_{il}^{(T)}+A_{ln}H_{ln}^{(T)}\delta_{ij}\Big),$$
$$\int_{S_k}A_{ln}k_l\frac{\partial H_{pq}^{(T)}\alpha_p\alpha_q\alpha_i\alpha_j}{\partial k_n}\mathrm{d}^2\boldsymbol{k}=\frac{8\pi k^2}{105}\Big(2A_{li}^{+}\left(k\frac{\partial H_{lj}^{(T)}}{\partial k}+3H_{lj}^{(T)}\right)$$
$$+2A_{lj}^{+}\left(k\frac{\partial H_{li}^{(T)}}{\partial k}+3H_{li}^{(T)}\right)+A_{ln}\left(k\frac{\partial H_{ln}^{(T)}}{\partial k}+3H_{ln}^{(T)}\right)\delta_{ij}\Big).$$

E.1.4 Scalar quadratic anisotropic contributions

The quadratic anisotropic contributions in the non linear scalar transfer (4.26) are computed analytically. The calculations involve expressions given in Appendix C for the kinetic case. After some algebra, one gets the scalar second-order isotropic term

$$Q^{\mathrm{T,NL(iso)}}(k,t)=12\int_{\Delta_k}\theta_{kpq}^{T}\pi^2k^2pq(x+yz)\Big[\mathcal{E}_i^{F''}(kx\mathcal{E}_i^{F'}-py\mathcal{E}_i^{F})+z\mathcal{E}_i^{F'}\mathcal{E}_i^{F}(ky-px)\Big]\mathrm{d}p\mathrm{d}q$$
$$+120\int_{\Delta_k}\theta_{kpq}^{T}\pi^2k^2p^2q(xy+z)\mathcal{E}_0''\Bigg[2H_{ij}^{(\mathrm{dir})''}\Big(\mathcal{E}_0^{T'}H_{ij}^{(T)'}(3x^2-1)-\mathcal{E}_0^{T}H_{ij}^{(T)}(3y^2-1)\Big)$$
$$-H_{ij}^{(\mathrm{pol})''}\Big(\mathcal{E}_0^{T'}H_{ij}^{(T)'}(1-x^2)-\mathcal{E}_0^{T}H_{ij}^{(T)}(1-y^2)\Big)\Bigg]\mathrm{d}p\mathrm{d}q, \tag{E.2}$$

and the scalar second-order directional term

$$Q_{ij}^{\mathrm{T,NL(dir)}}(k,t)=\frac{3}{5}\int_{\Delta_k}\theta_{kpq}^{T}\pi^2k^2pq(x+yz)\Big[z(ky-px)\Big\{\mathcal{E}^{F},\mathcal{E}^{F'}\Big\}_{ij}-py\Big\{\mathcal{E}^{F},\mathcal{E}^{F''}\Big\}_{ij}$$
$$-k(2x+3yz)\Big\{\mathcal{E}^{F'},\mathcal{E}^{F''}\Big\}_{ij}\Big]\mathrm{d}p\mathrm{d}q$$
$$+\frac{120}{7}\int_{\Delta_k}\theta_{kpq}^{T}\pi^2k^2p^2q(xy+z)\mathcal{E}_0''\Bigg[2(1+3xyz)\mathcal{E}_0^{T'}\Big\{H^{(\mathrm{dir})''},H^{(T)'}\Big\}_{ij}+2(3y^2-1)\mathcal{E}_0^{T}\Big\{H^{(\mathrm{dir})''},H^{(T)}\Big\}_{ij}$$
$$-(1-xyz-2z^2)\mathcal{E}_0^{T'}\Big\{H^{(\mathrm{pol})''},H^{(T)'}\Big\}_{ij}-(1-y^2)\mathcal{E}_0^{T}\Big\{H^{(\mathrm{pol})''},H^{(T)}\Big\}_{ij}\Bigg]\mathrm{d}p\mathrm{d}q, \tag{E.3}$$

where

$$\Big\{\mathcal{E}^{F},\mathcal{E}^{F'}\Big\}_{ij}=\mathcal{E}_i^{F}\mathcal{E}_j^{F'}+\mathcal{E}_j^{F}\mathcal{E}_i^{F'}-\frac{2}{3}\mathcal{E}_l^{F}\mathcal{E}_l^{F'}\delta_{ij}.$$

E.2 Scalar-velocity correlation $\boldsymbol{F}$

In this section, the spectral velocity-scalar correlation is addressed: the quasi-normal procedure along with the calculations of the linear and non-linear transfers are detailed. An alternative modelling for the scalar flux is proposed as well, and details are provided for the additional contributions linked to helicity in HHTSG.

E.2.1 Craya equation for the cospectrum flux

The scalar-velocity correlation is defined in (4.9). Its evolution equation is obtained by multiplying (4.3) by $\hat{u}_i^*(\boldsymbol{p})$ and summing it to the evolution equation of $\hat{u}_i^*(\boldsymbol{p})$ multiplied by $\hat{\theta}(\boldsymbol{k})$. After ensemble average and integration over the whole domain to simplify $\delta(\boldsymbol{k}-\boldsymbol{p})$, one has

$$\left(\frac{\partial}{\partial t} - A_{jl}k_j\frac{\partial}{\partial k_l} + (\nu+a)k^2\right)F_i + M_{ij}F_j - k_j\lambda_l\frac{\partial \hat{R}_{ij}}{\partial k_l} = T_i^{\mathrm{F,NL}}.$$

Moreover, since $k_j\hat{R}_{ij} = 0$, one recovers the scalar flux Craya equation (4.10). Additional details on how $T_i^{\mathrm{F,NL}}$ is obtained are now provided. Before spherical-averaging, one has

$$\begin{aligned}
\frac{\partial \hat{u}_i^*(\boldsymbol{p})\hat{\theta}(\boldsymbol{k})}{\partial t} + ... &= -\mathrm{i}k_j\int_{\boldsymbol{k}=\boldsymbol{r}+\boldsymbol{s}}\hat{\theta}(\boldsymbol{r})\hat{u}_j(\boldsymbol{s})\hat{u}_i^*(\boldsymbol{p})\mathrm{d}^3\boldsymbol{r} + \mathrm{i}P_{imn}(\boldsymbol{p})\int_{\boldsymbol{p}=\boldsymbol{r}+\boldsymbol{s}}\hat{\theta}(\boldsymbol{k})\hat{u}_m^*(\boldsymbol{r})\hat{u}_n^*(\boldsymbol{s})\mathrm{d}^3\boldsymbol{r},\\
&= -\mathrm{i}k_j\int\int\hat{\theta}(\boldsymbol{r})\hat{u}_j(\boldsymbol{s})\hat{u}_i^*(\boldsymbol{p})\delta(\boldsymbol{k}-\boldsymbol{r}-\boldsymbol{s})\mathrm{d}^3\boldsymbol{r}\mathrm{d}^3\boldsymbol{s}\\
&+ \mathrm{i}P_{imn}(\boldsymbol{p})\int\int\hat{\theta}(\boldsymbol{k})\hat{u}_m^*(\boldsymbol{r})\hat{u}_n^*(\boldsymbol{s})\delta(\boldsymbol{p}-\boldsymbol{r}-\boldsymbol{s})\mathrm{d}^3\boldsymbol{r}\mathrm{d}^3\boldsymbol{s},\\
&= -\mathrm{i}k_j\int\int\hat{\theta}^*(\boldsymbol{r})\hat{u}_j^*(\boldsymbol{s})\hat{u}_i^*(\boldsymbol{p})\delta(\boldsymbol{k}+\boldsymbol{r}+\boldsymbol{s})\mathrm{d}^3\boldsymbol{r}\mathrm{d}^3\boldsymbol{s}\\
&+ \mathrm{i}P_{imn}(\boldsymbol{p})\int\int\hat{\theta}(\boldsymbol{k})\hat{u}_m(\boldsymbol{r})\hat{u}_n(\boldsymbol{s})\delta(\boldsymbol{p}+\boldsymbol{r}+\boldsymbol{s})\mathrm{d}^3\boldsymbol{r}\mathrm{d}^3\boldsymbol{s}.
\end{aligned}$$

Ensemble average further gives

$$\begin{aligned}
\frac{\partial F_i(\boldsymbol{k},t)\delta(\boldsymbol{k}-\boldsymbol{p})}{\partial t} + ... &= k_j\int\int S_{ji}^{F*}(\boldsymbol{r},\boldsymbol{p})\delta(\boldsymbol{p}+\boldsymbol{r}+\boldsymbol{s})\delta(\boldsymbol{k}+\boldsymbol{r}+\boldsymbol{s})\mathrm{d}^3\boldsymbol{r}\mathrm{d}^3\boldsymbol{s}\\
&+ P_{imn}(\boldsymbol{p})\int\int S_{nm}^{F}(\boldsymbol{k},\boldsymbol{r})\delta(\boldsymbol{p}+\boldsymbol{r}+\boldsymbol{s})\delta(\boldsymbol{k}+\boldsymbol{r}+\boldsymbol{s})\mathrm{d}^3\boldsymbol{r}\mathrm{d}^3\boldsymbol{s}.
\end{aligned}$$

Integration over $\boldsymbol{p}$ simplify the first Dirac function, and integration over $\boldsymbol{s}$ in the rhs term of the equation erase the second one

$$\begin{aligned}
\frac{\partial F_i(\boldsymbol{k},t)}{\partial t} + ... &= k_j\int\int S_{ji}^{F*}(\boldsymbol{r},-\boldsymbol{r}-\boldsymbol{s})\delta(\boldsymbol{k}+\boldsymbol{r}+\boldsymbol{s})\mathrm{d}^3\boldsymbol{r}\mathrm{d}^3\boldsymbol{s}\\
&+ P_{imn}(-\boldsymbol{r}-\boldsymbol{s})\int\int S_{nm}^{F}(\boldsymbol{k},\boldsymbol{r})\delta(\boldsymbol{k}+\boldsymbol{r}+\boldsymbol{s})\mathrm{d}^3\boldsymbol{r}\mathrm{d}^3\boldsymbol{s},
\end{aligned}$$

$$\frac{\partial F_i(\boldsymbol{k},t)}{\partial t} + ... = k_j\int S_{ji}^{F*}(\boldsymbol{r},\boldsymbol{k})\mathrm{d}^3\boldsymbol{r} + P_{imn}(\boldsymbol{k})\int S_{nm}^{F}(\boldsymbol{k},\boldsymbol{r})\mathrm{d}^3\boldsymbol{r}.$$

E.2.2 Quasi-normal approximation for F_i

Some details on how the closure (4.25) is obtained are given. Firstly, the fourth-order correlation is defined as

$$T_{ijl}^F(\boldsymbol{k},\boldsymbol{p},t)\delta(\boldsymbol{k}+\boldsymbol{p}+\boldsymbol{q}+\boldsymbol{v}) = -\mathrm{i} < \hat{u}_i(\boldsymbol{q})\hat{\theta}(\boldsymbol{k})\hat{u}_j(\boldsymbol{p})\hat{u}_l(\boldsymbol{v}) > . \tag{E.4}$$

The process is similar to the scalar one. The third-order scalar flux correlation $S_{ij}^F(\boldsymbol{k},\boldsymbol{p})$ evolution equation can be written as

$$\begin{aligned}
&\left(\frac{\partial}{\partial t} + ak^2 + \nu(p^2+q^2)\right)\hat{\theta}(\boldsymbol{k})\hat{u}_j(\boldsymbol{p})\hat{u}_i(\boldsymbol{q}) + ... = -\mathrm{i}\\
&\Big(k_l\int_{\boldsymbol{k}=\boldsymbol{r}+\boldsymbol{s}}\hat{\theta}(\boldsymbol{r})\hat{u}_j(\boldsymbol{p})\hat{u}_l(\boldsymbol{s})\hat{u}_i(\boldsymbol{q})\mathrm{d}^3\boldsymbol{r} + P_{jmn}(\boldsymbol{p})\int_{\boldsymbol{p}=\boldsymbol{r}+\boldsymbol{s}}\hat{\theta}(\boldsymbol{k})\hat{u}_n(\boldsymbol{s})\hat{u}_m(\boldsymbol{r})\hat{u}_i(\boldsymbol{q})\mathrm{d}^3\boldsymbol{r}
\end{aligned}$$

$$+ P_{imn}(\boldsymbol{q}) \int_{\boldsymbol{q}=\boldsymbol{r}+\boldsymbol{s}} \hat{\theta}(\boldsymbol{k})\hat{u}_m(\boldsymbol{r})\hat{u}_n(\boldsymbol{s})\hat{u}_j(\boldsymbol{p})\mathrm{d}^3\boldsymbol{r}\Big),$$

which becomes, after ensemble average and convolution rules

$$\left(\frac{\partial}{\partial t} + ak^2 + \nu(p^2+q^2)\right) S^F_{ij}(\boldsymbol{k},\boldsymbol{p},t)\delta(\boldsymbol{k}+\boldsymbol{p}+\boldsymbol{q}) + ... =$$
$$k_l \int_{\boldsymbol{k}=\boldsymbol{r}+\boldsymbol{s}} T^F_{ijl}(\boldsymbol{r},\boldsymbol{p})\delta(\boldsymbol{k}+\boldsymbol{p}+\boldsymbol{q})\mathrm{d}^3\boldsymbol{r} + P_{jmn}(\boldsymbol{p}) \int_{\boldsymbol{p}=\boldsymbol{r}+\boldsymbol{s}} T^F_{imn}(\boldsymbol{k},\boldsymbol{r})\delta(\boldsymbol{k}+\boldsymbol{p}+\boldsymbol{q})\mathrm{d}^3\boldsymbol{r} +$$
$$+ P_{imn}(\boldsymbol{q}) \int_{\boldsymbol{q}=\boldsymbol{r}+\boldsymbol{s}} T^T_{mjn}(\boldsymbol{k},\boldsymbol{p})\delta(\boldsymbol{k}+\boldsymbol{p}+\boldsymbol{q})\mathrm{d}^3\boldsymbol{r}.$$

The quasi-normal approximation yields calculations very similar to the scalar case. The three terms are respectively

$$\delta(\boldsymbol{k}+\boldsymbol{p}+\boldsymbol{q})\left[k_l\Big(F^*_j(\boldsymbol{p})\hat{R}_{il}(\boldsymbol{q}) + F^*_i(\boldsymbol{q})\hat{R}_{jl}(\boldsymbol{p})\Big) + 2P_{jmn}(\boldsymbol{p})\hat{R}_{in}(\boldsymbol{q})F_m(\boldsymbol{k}) + 2P_{imn}(\boldsymbol{q})\hat{R}_{jn}(\boldsymbol{p})F_m(\boldsymbol{k})\right].$$

E.2.3 Computation of the non-linear transfers of F_i

The non-linear scalar flux transfer is defined by (4.14). The following calculations allow to recover (4.47).

Computation of $\tau^F_i(\boldsymbol{k},\boldsymbol{p})$: the starting point is

$$\tau^F_i(\boldsymbol{k},\boldsymbol{p}) = k_n k_j\Big(\hat{R}''_{nj}F'^*_i + \hat{R}'_{ni}F''^*_j\Big) + 2F_m k_j\Big(P''_{jmn}\hat{R}'_{ni} + P'_{imn}\hat{R}''_{nj}\Big). \tag{E.5}$$

Symmetry for the second rhs term can be used thanks to $\theta^F_{kpq} = \theta^F_{kqp}$. Useful relations are

$$k_l\hat{R}''_{ln}k_n = kp(xy+z)\Big(\mathcal{E}'' + \Re X''\Big), \qquad k_n\hat{R}'_{ni} = k\mathcal{E}'_0(\alpha_i + z\alpha'_i), \qquad q - ky = px,$$
$$k\sqrt{1-y^2}\sqrt{1-z^2} = \frac{kq}{p}(1-y^2) = k(x+yz) = q(xy+z), \qquad \alpha_l\alpha_n\hat{R}'_{ln} = (1-z^2)(\mathcal{E}' + \Re X').$$

The terms to compute are, at first order in anisotropy

$$k_n k_j\hat{R}''_{nj}F'^*_i = \frac{3}{2}kp(xy+z)\mathcal{E}''_0\mathcal{E}^{F'}_j P'_{ij}, \qquad k_n k_j\hat{R}'_{ni}F''^*_j = \frac{3}{2}k^2\mathcal{E}'_0(\alpha_i + z\alpha'_i)\mathcal{E}^{F''}_j(\alpha_j + y\alpha''_j),$$
$$k_j F_m P''_{jmn}\hat{R}'_{ni} = \frac{3}{4}k\mathcal{E}'_0(\alpha_i + z\alpha'_i)\mathcal{E}^F_j(\alpha''_j + y\alpha_j)(q-2ky),$$
$$k_j F_m P''_{imn}\hat{R}'_{nj} = \frac{3}{4}kq\mathcal{E}'_0\mathcal{E}^F_j\left((\alpha_i + z\alpha'_i)(\alpha''_j + y\alpha_j) + (y+xz)\Big(2\alpha''_i(\alpha''_j + y\alpha_j) - P_{ij}\Big)\right).$$

Computation of $\tau^{F*}_i(\boldsymbol{p},\boldsymbol{k})$: the starting point is

$$\tau^{F*}_i(\boldsymbol{p},\boldsymbol{k}) = p_n k_j\Big(\hat{R}''_{nj}F_i + \hat{R}_{ni}F''_j\Big) + 2k_j F'^*_m\Big(P''_{jmn}\hat{R}_{ni} + P_{imn}\hat{R}''_{nj}\Big).$$

Useful relations are

$$p_n\hat{R}''_{nj}k_j = -kp(xy+z)\Big(\mathcal{E}'' + \Re X''\Big), \qquad p_n\hat{R}'_{ni} = p\mathcal{E}_0(\alpha'_i + z\alpha_i), \qquad \alpha'_n\alpha''_n = -x.$$

The terms to compute are

$$p_n k_j\hat{R}''_{nj}F_i = -\frac{3}{2}kp(xy+z)\mathcal{E}''_0\mathcal{E}^F_j P_{ij}, \qquad p_n k_j\hat{R}_{ni}F''_j = \frac{3}{2}kp\mathcal{E}_0(\alpha'_i + z\alpha_i)\mathcal{E}^{F''}_j(\alpha''_j + y\alpha''_j),$$

$$2k_jF_m'^*P_{jmn}''\hat{R}_{ni} = \frac{3}{2}kq\mathcal{E}_0(\alpha_i'' + y\alpha_i)\mathcal{E}_j^{F'}\Big(\alpha_j + z\alpha_j' + 2y(\alpha_j'' + x\alpha_j')\Big),$$
$$2k_jF_m'^*P_{imn}\hat{R}_{nj}'' = \frac{3}{2}k^2\mathcal{E}_0''\mathcal{E}_j^{F'}\Bigg((\alpha_i + y\alpha_i'')(\alpha_j + z\alpha_j') + (1-y^2)\Big(P_{ij}' - 2\alpha_i(\alpha_j + z\alpha_j')\Big)\Bigg).$$

Computation of $W_i^F(\boldsymbol{k},\boldsymbol{p})$: one has $W_i^F = -\alpha_i\alpha_j\tau_j^F$. The two first terms can be grouped together

$$\alpha_i\alpha_jk_nk_l(\hat{R}_{nl}''F_j'^* + \hat{R}_{nj}'F_l''^*) = 3k^2(1-y^2)\mathcal{E}_0''\mathcal{E}_j^{F'}\alpha_i(\alpha_j + z\alpha_j').$$

With symmetrization, there is only one term left to compute

$$2\alpha_i\alpha_jF_mk_lP_{jmn}''\hat{R}_{nl}' = \frac{3}{2}kq\mathcal{E}_0'\mathcal{E}_j^F\alpha_i\Big(1 - z^2 - 2y(y + xz)\Big)(\alpha_j'' + y\alpha_j).$$

E.2.4 Spherically-averaged cospectrum Lin equations

The useful parts of the λ-integration are the following ones

$$\int_0^{2\pi}\alpha_i\alpha_j'\mathrm{d}\lambda = -2\pi z\alpha_i\alpha_j, \qquad \int_0^{2\pi}\alpha_i\alpha_j''\mathrm{d}\lambda = -2\pi y\alpha_i\alpha_j,$$

$$\int_0^{2\pi}\alpha_i'\alpha_j''\mathrm{d}\lambda = \pi[\alpha_i\alpha_j(x + 3yz) - \delta_{ij}(x + yz)], \qquad \int_0^{2\pi}P_{ij}'\mathrm{d}\lambda = \pi(1 + z^2)\delta_{ij} - \pi\alpha_i\alpha_j(3z^2 - 1).$$

The term in $\mathcal{E}_0'\mathcal{E}_j^F$ of W_i^F brings no contribution to the λ-integration. For the spherical integration, the different terms are the following ones

$$\int_{S_k}M_{ij}F_j\mathrm{d}^2\boldsymbol{k} = \frac{2}{5}A_{ij}^+E_j^F, \qquad \int_{S_k}A_{jl}k_j\frac{\partial F_i}{\partial k_l}\mathrm{d}^2\boldsymbol{k} = -\frac{1}{5}A_{ij}^+\frac{\partial}{\partial k}(kE_j^F), \qquad \int_{S_k}P_{ij}\mathcal{E}_j^F\mathrm{d}^2\boldsymbol{k} = \frac{8\pi k^2}{3}\mathcal{E}_i^F.$$

The "rapid-pressure" part is given by

$$\int_{S_k}2\alpha_i\alpha_nA_{nj}F_j\mathrm{d}^2\boldsymbol{k} = \frac{3}{5}A_{ij}^+E_j^F + A_{ij}^-E_j^F.$$

E.2.5 Alternative modelling for $\boldsymbol{F}$

The modelling for the scalar flux is now based on a helical decomposition and reads

$$F_i(\boldsymbol{k},t) = \mathcal{E}_j^F(k,t)P_{ij}(\boldsymbol{k},t) = \phi_+(k,t)N_i(\boldsymbol{k},t) + \phi_-(k,t)N_i^*(\boldsymbol{k},t). \tag{E.6}$$

The scalar flux is solenoidal so that the $\phi_\pm$ functions read

$$\phi_+(k,t) = \frac{1}{2}\mathcal{E}_j^F(k,t)N_j^*(\boldsymbol{k},t), \qquad \phi_-(k,t) = \frac{1}{2}\mathcal{E}_j^F(k,t)N_j(\boldsymbol{k},t). \tag{E.7}$$

Convenient notations are used for computation

$$Y_+(k,t) = \phi_+(k,t)e^{\mathrm{i}\lambda} + \phi_-(k,t)e^{-\mathrm{i}\lambda}, \qquad Y_-(k,t) = \phi_+(k,t)e^{\mathrm{i}\lambda} - \phi_-(k,t)e^{-\mathrm{i}\lambda}. \tag{E.8}$$

The pressure part of the non-linear transfer has no contribution with the present helical decomposition (E.6) because $\alpha_iN_i = 0$. The non-linear transfers associated with ϕ_+ and ϕ_- are consequently

$$T_+^F(\boldsymbol{k},t) = \frac{1}{2}T_i^{\mathrm{F,NL}}(\boldsymbol{k},t)N_i^*(\boldsymbol{k},t), \qquad T_-^F(\boldsymbol{k},t) = \frac{1}{2}T_i^{\mathrm{F,NL}}(\boldsymbol{k},t)N_i(\boldsymbol{k},t), \tag{E.9}$$

so that

$$T_i^{\mathrm{F,NL}}(\boldsymbol{k},t) = P_{ij}(\boldsymbol{k},t)T_j^{\mathrm{F,NL}}(\boldsymbol{k},t) = T_+^F(\boldsymbol{k},t)N_i(\boldsymbol{k},t) + T_-^F(\boldsymbol{k},t)N_i^*(\boldsymbol{k},t). \tag{E.10}$$

Computation of $\tau_i(\boldsymbol{k},\boldsymbol{p})$: in this case, a symmetric expression of the closure (2.36) is used, more convenient for calculations

$$\mathfrak{T}_{ij}^{\mathrm{F,QN}}(\boldsymbol{k},\boldsymbol{p}) = k_n\Big(\hat{R}_{ni}(\boldsymbol{q})F_j^*(\boldsymbol{p}) + \hat{R}_{nj}(\boldsymbol{p})F_i^*(\boldsymbol{q})\Big) + 2F_m(\boldsymbol{k})\Big(P_{imn}(\boldsymbol{q})\hat{R}_{nj}(\boldsymbol{p}) + P_{jmn}(\boldsymbol{q})\hat{R}_{ni}(\boldsymbol{p})\Big).$$

Additional useful results are

$$\sqrt{1-y^2}\sqrt{1-z^2} = (x+yz), \qquad kx - qz = y(qx-kz), \qquad 4kyz + 2kx - 2qz = 2py,$$

The different parts of the computation are the following ones

$$k_nk_j\hat{R}''_{nj}F_i'^*N_i^* = -k^2(1-y^2)\mathcal{E}_0''e^{-\mathrm{i}\lambda}(Y_-'^* + zY_+'^*), \qquad k_nk_j\hat{R}''_{nj}F_i'^*N_i = k^2(1-y^2)\mathcal{E}_0''e^{\mathrm{i}\lambda}(Y_-'^* - zY_+'^*),$$

$$k_nk_j\hat{R}'_{ni}F_j''^*N_i^* = k^2z(x+yz)\mathcal{E}_0'e^{-\mathrm{i}\lambda}Y_+''^*, \qquad k_nk_j\hat{R}'_{ni}F_j''^*N_i = k^2z(x+yz)\mathcal{E}_0'e^{\mathrm{i}\lambda}Y_+''^*,$$

$$2F_mk_j\hat{R}'_{ni}P''_{jmn}N_i^* = k(2ky-q)z(x+yz)\mathcal{E}_0'e^{-\mathrm{i}\lambda}Y_+,$$

$$2F_mk_j\hat{R}'_{ni}P''_{jmn}N_i = k(2ky-q)z(x+yz)\mathcal{E}_0'e^{\mathrm{i}\lambda}Y_+,$$

$$2F_mk_j\hat{R}'_{nj}P''_{imn}N_i^* = -k^2(1-z^2)\mathcal{E}_0'e^{-\mathrm{i}\lambda}(Y_+ + Y_-) + k\Big(2k(x+yz) - qz\Big)(x+yz)\mathcal{E}_0'e^{-\mathrm{i}\lambda}Y_+,$$

$$2F_mk_j\hat{R}'_{nj}P''_{imn}N_i = -k^2(1-z^2)\mathcal{E}_0'e^{\mathrm{i}\lambda}(Y_+ - Y_-) + k\Big(2k(x+yz) - qz\Big)(x+yz)\mathcal{E}_0'e^{\mathrm{i}\lambda}Y_+.$$

Hence, the $p \leftrightarrow q$ symmetry for the $\mathcal{E}_0''$ part - valid thanks to $\theta^F_{kpq} = \theta^F_{kqp}$ - gives

$$\tau_iN_i^* = k\mathcal{E}_0'e^{-\mathrm{i}\lambda}\left[k\left(-(1-z^2)(Y_+ + Y_-) + Y_+''^*(xz + 2yz^2 - y) - (1-z^2)Y_-''^*\right) + 2py(x+yz)Y_+\right],$$

$$\tau_iN_i = k\mathcal{E}_0'e^{\mathrm{i}\lambda}\left[k\left(-(1-z^2)(Y_+ - Y_-) + Y_+''^*(xz + 2yz^2 - y) + (1-z^2)Y_-''^*\right) + 2py(x+yz)Y_+\right].$$

Computation of $\tau_i^*(\boldsymbol{p},\boldsymbol{k})$: here, no symmetry can be performed because of the θ^F_{pkq}. The different parts of the computation are the following ones

$$p_nk_j\hat{R}''_{nj}F_iN_i^* = -k^2(1-y^2)\mathcal{E}_0''e^{-\mathrm{i}\lambda}(Y_+ + Y_-), \qquad p_nk_j\hat{R}''_{nj}F_iN_i = -k^2(1-y^2)\mathcal{E}_0''e^{\mathrm{i}\lambda}(Y_+ - Y_-),$$

$$p_nk_j\hat{R}_{ni}F_j''N_i^* = kp(x+yz)\mathcal{E}_0e^{-\mathrm{i}\lambda}Y_+'', \qquad p_nk_j\hat{R}_{ni}F_j''N_i = kp(x+yz)\mathcal{E}_0e^{\mathrm{i}\lambda}Y_+'',$$

$$2F_m'^*k_j\hat{R}_{ni}P''_{jmn}N_i^* = kp\mathcal{E}_0e^{-\mathrm{i}\lambda}Y_+'^*(x^2-y^2), \qquad 2F_m'^*k_j\hat{R}_{ni}P''_{jmn}N_i = kp\mathcal{E}_0e^{\mathrm{i}\lambda}Y_+'^*(x^2-y^2),$$

$$2F_m'^*k_j\hat{R}''_{nj}P_{imn}N_i^* = k^2\mathcal{E}_0''e^{-\mathrm{i}\lambda}\Big((xy - z + 2y^2z)Y_+'^* + (y^2-1)Y_-'^*\Big),$$

$$2F_m'^*k_j\hat{R}''_{nj}P_{imn}N_i = k^2\mathcal{E}_0''e^{\mathrm{i}\lambda}\Big((xy - z + 2y^2z)Y_+'^* + (1-y^2)Y_-'^*\Big).$$

Hence

$$\begin{aligned}\tau_i'^*N_i^* &= k^2\mathcal{E}_0''e^{-\mathrm{i}\lambda}\Big[(xy + 2zy^2 - z)Y_+'^* - (1-y^2)(Y_-'^* + Y_+ + Y_-)\Big] \\ &\quad + kp\mathcal{E}_0e^{-\mathrm{i}\lambda}\Big[(x+yz)Y_+'' + (x^2-y^2)Y_+'^*\Big],\end{aligned} \tag{E.11}$$

$$\begin{aligned}\tau_i'^*N_i &= k^2\mathcal{E}_0''e^{\mathrm{i}\lambda}\Big[(xy + 2zy^2 - z)Y_+'^* + (1-y^2)(Y_-'^* - Y_+ + Y_-)\Big] \\ &\quad + kp\mathcal{E}_0e^{\mathrm{i}\lambda}\Big[(x+yz)Y_+'' + (x^2-y^2)Y_+'^*\Big].\end{aligned} \tag{E.12}$$

λ-integration: useful results are the following ones

$$\int_0^{2\pi} e^{-\mathrm{i}\lambda}(Y_+ + Y_-)\mathrm{d}\lambda = 2\pi\mathcal{E}_i^F N_i^*, \qquad \int_0^{2\pi} e^{\mathrm{i}\lambda}(Y_+ + Y_-)\mathrm{d}\lambda = 2\pi\mathcal{E}_i^F N_i,$$
$$\int_0^{2\pi} e^{-\mathrm{i}\lambda}Y_-'^*\mathrm{d}\lambda = -\pi\mathcal{E}_i^{F'} N_i^*, \qquad \int_0^{2\pi} e^{\mathrm{i}\lambda}Y_-'^*\mathrm{d}\lambda = \pi\mathcal{E}_i^{F'} N_i, \qquad \int_0^{2\pi} e^{\pm\mathrm{i}\lambda}Y_+'^*\mathrm{d}\lambda = -z\pi\mathcal{E}_i^{F'} N_i,$$
$$\int_0^{2\pi} e^{\mathrm{i}\lambda}Y_+''^*\mathrm{d}\lambda = \int_0^{2\pi} e^{-\mathrm{i}\lambda}Y_+''\mathrm{d}\lambda = -y\pi\mathcal{E}_i^{F''} N_i^*, \qquad \int_0^{2\pi} e^{-\mathrm{i}\lambda}Y_-''^*\mathrm{d}\lambda = -\pi\mathcal{E}_i^{F''} N_i^*,$$
$$\int_0^{2\pi} e^{\mathrm{i}\lambda}Y_+''^*\mathrm{d}\lambda = \int_0^{2\pi} e^{\mathrm{i}\lambda}Y_+''\mathrm{d}\lambda = -y\pi\mathcal{E}_i^{F''} N_i, \qquad \int_0^{2\pi} e^{\mathrm{i}\lambda}Y_-''^*\mathrm{d}\lambda = \pi\mathcal{E}_i^{F''} N_i.$$

This yields the following equations which have to be multiplied by pq/k:

$$\begin{aligned}\int_0^{2\pi}(\tau_j + \tau_j'^*)N_j^*\mathrm{d}\lambda = {}& \pi k\mathcal{E}_0' N_j^*\Big[k\Big(2(1-z^2)\mathcal{E}_j^F + (1+y^2-z^2-xyz-2y^2z^2)\mathcal{E}_j^{F''}\Big) + 2py(x+yz)\mathcal{E}_j^F\Big]\\ &- \pi k N_j^*\Big[k\mathcal{E}_0''\Big((xyz+2y^2z^2-z^2)\mathcal{E}_j^{F'} + (1-y^2)(2\mathcal{E}_j^F - \mathcal{E}_j^{F'})\Big)\\ &+ p\mathcal{E}_0\Big(y(x+yz)\mathcal{E}_j^{F''} + (z-z^3+2xyz+2y^2z^2)\mathcal{E}_j^{F'}\Big)\Big] = 2\int_0^{2\pi} T_+^F\mathrm{d}\lambda,\end{aligned} \tag{E.13}$$

$$\begin{aligned}\int_0^{2\pi}(\tau_j + \tau_j'^*)N_j\mathrm{d}\lambda = {}& \pi k\mathcal{E}_0' N_j\Big[k\Big(2(1-z^2)\mathcal{E}_j^F + (1+y^2-z^2-xyz-2y^2z^2)\mathcal{E}_j^{F''}\Big) + 2py(x+yz)\mathcal{E}_j^F\Big]\\ &- \pi k N_j\Big[k\mathcal{E}_0''\Big((xyz+2y^2z^2-z^2)\mathcal{E}_j^{F'} + (1-y^2)(2\mathcal{E}_j^F - \mathcal{E}_j^{F'})\Big)\\ &+ p\mathcal{E}_0\Big(y(x+yz)\mathcal{E}_j^{F''} + (z-z^3+2xyz+2y^2z^2)\mathcal{E}_j^{F'}\Big)\Big] = 2\int_0^{2\pi} T_-^F\mathrm{d}\lambda.\end{aligned} \tag{E.14}$$

Spherical integration: the useful relation is

$$\int_{S_k} N_i^* N_j \mathcal{E}_j^F \mathrm{d}^2\boldsymbol{k} = \frac{8\pi k^2}{3}\mathcal{E}_i^F. \tag{E.15}$$

Then, (E.13) is contracted with N_i and (E.14) with N_i^*. This yields the spherically averaged non-linear transfer of the scalar flux, and one can note that the $()_+$ and $()_-$ components are equal

$$\begin{aligned}S_i^{\mathrm{F,NL}} &= \int_{S_k}\int_0^{2\pi}\Big(T_+^F(\boldsymbol{k},t)N_i(\boldsymbol{k},t) + T_-^F(\boldsymbol{k},t)N_i^*(\boldsymbol{k},t)\Big)\mathrm{d}\lambda\mathrm{d}^2\boldsymbol{k}\\ &= \int_{\Delta_k}\frac{8}{3}\pi^2\theta_{kpq}^F k^2 pq\mathcal{E}_0'\Big[k\Big(-2(1-z^2)\mathcal{E}_i^F + (1+y^2-z^2-xyz-2y^2z^2)\mathcal{E}_i^{F''}\Big) + 2py(x+yz)\mathcal{E}_i^F\Big]\mathrm{d}p\mathrm{d}q\\ &+ \int_{\Delta_k}\frac{8}{3}\pi^2\theta_{pkq}^F k^2 pq\Big[k\mathcal{E}_0''\Big((1-y^2+z^2-xyz-2y^2z^2)\mathcal{E}_i^{F'} - 2(1-y^2)\mathcal{E}_i^F\Big)\\ &- p\mathcal{E}_0\Big(y(x+yz)\mathcal{E}_i^{F''} + z(x^2-y^2)\mathcal{E}_i^{F'}\Big)\Big]\mathrm{d}p\mathrm{d}q.\end{aligned} \tag{E.16}$$

Moreover, $k(1-z^2) = q(y+xz)$ and $p(x+yz) = q(1-y^2)$ so that $-2k(1-z^2)\mathcal{E}_i^F + 2py(x+yz)\mathcal{E}_i^F = -2q(xz+y^3)\mathcal{E}_i^F$. In addition, $p(x^2-y^2)$ comes from $p(1-z^2-2(y^2(1-z^2)+yz(x+yz)))$ which can be written $q(x-yz-2xy^2)$. Consequently, the non-linear transfer (4.49) computed directly with $F_i \sim P_{ij}\mathcal{E}_j^F$ is recovered. Here are some remarks on this modelling:

- The helical decomposition is not sufficient to completely compute the scalar flux non-linear transfer: indeed, a model is required for ϕ_+ and ϕ_-.
- The calculations are more complicated since they involve helical modes instead of projectors.

- All calculations are made twice (once for T_+^F and once for T_-^F which are eventually equal) whereas only a single process is needed when directly injecting $F_i = P_{ij}\mathcal{E}_j^F$ in the closure.
- The helical decomposition does not permit to compute easily the pressure part of the non-linear transfers.
- It brings information on the toroidal-poloidal structure of the scalar flux: any solenoidal field, such as the scalar flux, can be decomposed, in the Craya-Herring frame (e_i^1, e_i^2), into toroidal and poloidal parts
$$F_i(\boldsymbol{k},t) = F_{\text{tor}}(k,t)e_i^1(\boldsymbol{k},t) + F_{\text{pol}}(k,t)e_i^2(\boldsymbol{k},t). \tag{E.17}$$
Thus, using (E.6) and the definition (2.27) of the helical modes, the scalar flux helical decomposition reads
$$F_i(\boldsymbol{k},t) = \underbrace{\mathrm{i}\Big(\phi_-(k,t) - \phi_+(k,t)\Big)}_{F_{\text{tor}}(k,t)} e_i^1(\boldsymbol{k},t) + \underbrace{\Big(\phi_+(k,t) + \phi_-(k,t)\Big)}_{F_{\text{pol}}(k,t)} e_i^2(\boldsymbol{k},t). \tag{E.18}$$
The previous calculations showed that ϕ_+ and ϕ_- led the same contribution to the non-linear transfer ($T_+^F N_i + T_-^F N_i^* = 2T_+^F N_i$). Consequently, one can conclude that the scalar flux has a poloidal structure only. Finally, since $\mathcal{E} \sim$ (toroidal) + (poloidal) and $Z \sim$ (poloidal) − (toroidal), a single quantity only is needed to describe anisotropy at the scalar flux level.

E.2.6 Scalar flux quadratic anisotropic contributions

Here, the second-order contributions in anisotropy of the non linear scalar flux transfer are computed analytically. The calculations are quite lengthy and involve some expressions gathered in Appendix C for the kinetic case. Afterwards, some illustrations for USHT are proposed. Here are some additional useful formula for the λ-integration:

$$\begin{aligned}
\int_0^{2\pi} \alpha_l\alpha_p'\alpha_q'\alpha_i' H_{pq}^{()}\mathrm{d}\lambda &= \alpha_i\alpha_l\alpha_p\alpha_q H_{pq}^{()} z\Big(3-5z^2\Big) + 2z(z^2-1)\alpha_i\alpha_p H_{pl}^{()},\\
\int_0^{2\pi} \alpha_l\alpha_p'\alpha_q'\alpha_i'' H_{pq}^{()}\mathrm{d}\lambda &= \alpha_i\alpha_l\alpha_p\alpha_q H_{pq}^{()}\Big(-5yz^2+y-2xz\Big) + 2z(x+yz)\alpha_i\alpha_p H_{pl}^{()},\\
\int_0^{2\pi} \alpha_i'\alpha_p'\alpha_q'\alpha_l'' H_{pq}^{()}\mathrm{d}\lambda &= \alpha_i\alpha_l\alpha_p\alpha_q H_{pq}^{()}\Big(\frac{35}{4}yz^3 - \frac{15}{4}yz + \frac{15}{4}xz^2 - \frac{3}{4}x\Big)\\
&\quad + \alpha_i\alpha_p H_{pl}^{()}\Big(-5yz^3+3yz-3xz^2+x\Big) + \frac{1}{2}H_{il}^{()}\Big(xz^2+yz^3-x-yz\Big),\\
\int_0^{2\pi} \alpha_n\alpha_i'\alpha_p'\alpha_l'' H_{np}^{()}\mathrm{d}\lambda &= \alpha_i\alpha_l\alpha_p\alpha_q H_{pq}^{()}\Big(-5yz^2+y-2xz\Big) + \alpha_i\alpha_p H_{pl}^{()}\Big(-y+xz+2yz^2\Big),\\
\int_0^{2\pi} \Re(W_p''W_q'')\alpha_l\alpha_i' H_{np}^{()}\mathrm{d}\lambda &= \alpha_i\alpha_l\alpha_p\alpha_q H_{pq}^{()}\Big(5yz^2-3z+2xy\Big) - 2y\alpha_i\alpha_p H_{pl}^{()}\Big(x+yz\Big).
\end{aligned}$$

The total second-order transfer for the scalar flux can be divided into two parts according to
$$Q_i^{\text{F,NL}}(k,t) = Q_i^{\text{F,cons}}(k,t) + Q_i^{\text{F,RTI}}(k,t), \tag{E.19}$$
with the conservative part,
$$\begin{aligned}
Q_i^{\text{F,cons}}(k,t) = 6\int_{\Delta_k} \theta_{kpq}^F \pi^2 k^2 p^2 q \mathcal{E}_0'' \Bigg[&(xy+z)\mathcal{E}_l^{F'}\Big[2(3x^2-1)H_{il}^{(\text{dir})''} + (x^2-1)H_{il}^{(\text{pol})''}\Big]\\
&+ \mathcal{E}_l^F H_{il}^{(\text{pol})''}\Big[xy(z^2-x^2)+z(1-y^2)\Big] - 2\mathcal{E}_l^F H_{il}^{(\text{dir})''}\Big[(xy+z)+(x^2-z^2)(3xy+2z)\Big]\Bigg]\mathrm{d}p\mathrm{d}q
\end{aligned}$$

$$+12\int_{\Delta_k}\theta^F_{kpq}\pi^2k^2pq\mathcal{E}_0'(H_{il}^{(\mathrm{dir})'}+H_{il}^{(\mathrm{pol})'})\Big[kx(x+yz)\mathcal{E}_l^{F''}-q\Big[x(xy+z)+y(y^2-1)\Big]\mathcal{E}_l^F\Big]\mathrm{d}p\mathrm{d}q,$$
$$+6\int_{\Delta_k}\theta^F_{pkq}\pi^2k^2pq\Big[p(xy+z)\mathcal{E}_0''\mathcal{E}_l^F\Big[-2(3y^2-1)H_{il}^{(\mathrm{dir})''}+(1-y^2)H_{il}^{(\mathrm{pol})''}\Big]$$
$$-2\mathcal{E}_0(H_{il}^{(\mathrm{dir})}+H_{il}^{(\mathrm{pol})})\Big(py(x+yz)\mathcal{E}_l^{F''}+q\mathcal{E}_l^{F'}\Big[x(xy+z)+y(y^2-1)\Big]\Big)$$
$$+k\mathcal{E}_0''\mathcal{E}_l^{F'}\Big(2H_{il}^{(\mathrm{dir})''}\Big[x(x+yz)+(1-y^2)(3y^2-z^2)\Big]+H_{il}^{(\mathrm{pol})''}\Big[2x(x+yz)-(1-y^2)(2-y^2-z^2)\Big]\Big)\Big]\mathrm{d}p\mathrm{d}q, \tag{E.20}$$

and the return to isotropy part

$$Q_i^{\mathrm{F,RTI}}(k,t)=12\int_{\Delta_k}\theta^F_{kpq}\pi^2k^2pq\mathcal{E}_0''\Big[p(xy+z)\mathcal{E}_l^{F'}\Big(2\Big[3y(y+xz)+(z^2-1)\Big]H_{il}^{(\mathrm{dir})''}-x(x+yz)H_{il}^{(\mathrm{pol})''}\Big)$$
$$+(p-2kz)y(1-y^2)(x+yz)\mathcal{E}_l^F(6H_{il}^{(\mathrm{dir})''}+H_{il}^{(\mathrm{pol})''})\Big]\mathrm{d}p\mathrm{d}q. \tag{E.21}$$

The influence of the quadratic contributions of anisotropy in the non-linear transfers is illustrated for USHT. Their impact is comparable to the case of sustained shear flows, illustrated in Appendix C. The scalar quadratic contributions are numerically the most intense ones in USHT, compared to the scalar flux and kinetic ones.

First, the fluxes $\Pi_Q^{(\mathrm{iso})}$ and $\Pi_Q^{\mathrm{T(iso)}}$ of the isotropic part of the quadratic kinetic and scalar transfers $Q^{\mathrm{NL(iso)}}$ and $Q^{\mathrm{NL,T(iso)}}$ are shown to be conservative in Fig. E.1a. The flux $\Pi_Q^{\mathrm{F(cons)}}$ of the conservative part of the cospectrum quadratic transfer $Q_3^{\mathrm{F(cons)}}$ is presented as well, along with the flux $\Pi_Q^{\mathrm{F(tot)}}$ of the total cospectrum quadratic transfer $Q_3^{\mathrm{F,NL}}$. One can remark that these anisotropic contributions mainly act at large scales. It is worth noting that the flux of the (first-order in anisotropy) isotropic scalar transfer $S^{\mathrm{T,NL(iso)}}$ is more than ten times higher than $\Pi_Q^{\mathrm{T(iso)}}$. Secondly, the impact of the quadratic contributions on the one-point statistics is revealed in Fig. E.1b: they slightly increase the global level of anisotropy of the flow. The main difference with the case without these quadratic contributions (in grey) is observed for the Froude number. Nevertheless, this is has less impact than changing the eddy-damping constants, as seen before in section 7.3.7. Finally, the inclusion in the simulations of these quadratic contributions does not change at all the growth rate β of the kinetic energy, nor the scalings of the spectra.

E.2.7 Scalar flux in HHTSG

In this section, the framework of homogeneous helical turbulence with a mean scalar gradient (HHTSG) is considered, and some details about how to obtain $S_i^{\mathrm{F,NL(hel)}}$ and $S_i^{\mathrm{Q,NL}}$, given in (8.75) and (8.77), are provided.

Computation of $\tau_i^F(\boldsymbol{k},\boldsymbol{p})$: one can use $p\leftrightarrow q$ symmetry here, and $k(x+yz)=p(y+xz)=q(z+xy)$ as well, so that

$$k_nk_j\hat{R}''_{nj}F_i^{'*}=0,$$
$$k_nk_j\hat{R}'_{ni}F_j^{''*}=\frac{3}{2}\frac{k^2}{pq}\mathcal{H}'\Big[-\mathcal{E}_i^{Q''}(x+yz)+\alpha_i\mathcal{E}_l^{Q''}(x\alpha_l-y\alpha_l')-\alpha_i''\mathcal{E}_l^{Q''}(z\alpha_l+\alpha_l')\Big],$$
$$2F_mk_jP''_{jmn}\hat{R}'_{ni}=-\frac{3}{2}\frac{p}{q}\mathcal{H}''\Big[\mathcal{E}_i^Q(x-yz-2xz^2)-\alpha_i\mathcal{E}_l^Q(x\alpha_l+2xz\alpha_l'+z\alpha_l'')$$
$$+\alpha_i'\mathcal{E}_l^Q(y\alpha_l+2yz\alpha_l'+(1-2z^2)\alpha_l'')\Big],$$

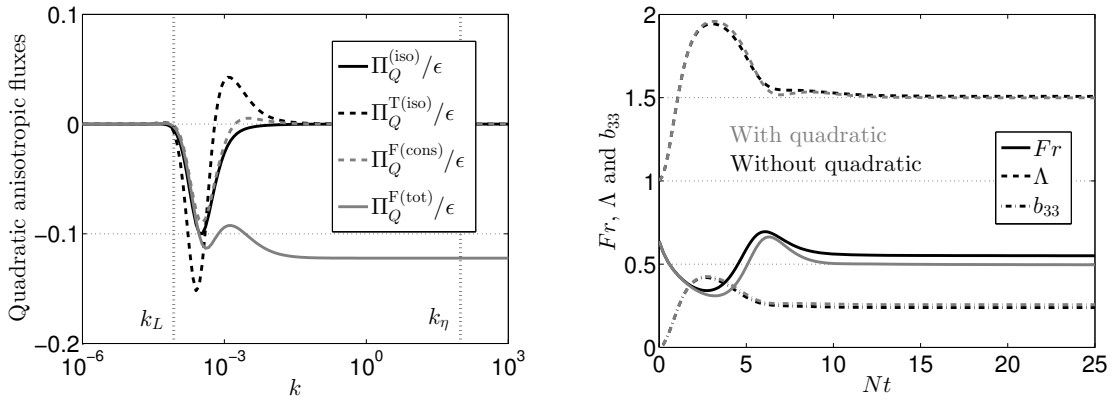

(a) (b)

Figure E.1: Effects of quadratic contributions of anisotropy in the non-linear transfers. (a) Quadratic anisotropic fluxes along with the integral and Kolmogorov wavenumbers k_L and k_η. Grey curves correspond to the cospectrum. (b) Time evolution of Fr, Λ and b_{33} without (black) and with (grey) the quadratic anisotropic contributions.

$$2F_m k_j P'_{imn}\hat{R}''_{nj} = -\frac{3}{2}\frac{p}{q}\mathcal{H}''\Big[-\mathcal{E}_i^Q(x+yz)+\alpha_i\mathcal{E}_l^Q(x\alpha_l+y\alpha'_l-2z\alpha''_l)$$
$$+2\alpha'_i\mathcal{E}_l^Q(xz\alpha_l+(x+yz)\alpha'_l-z^2\alpha''_l)+\alpha''_i\mathcal{E}_l^Q(z\alpha_l+\alpha'_l)\Big].$$

Computation of $\tau_i^{F*}(\boldsymbol{p},\boldsymbol{k})$: no $p\leftrightarrow q$ symmetry is used here

$$p_n k_j \hat{R}^{*''}_{nj}F_i = \frac{3}{2}\frac{kp}{q}\mathcal{H}''\Big[\alpha_i\mathcal{E}_l^F(y\alpha'_l-z\alpha''_l)-\alpha'_i\mathcal{E}_l^F(y\alpha_l+\alpha''_l)+\alpha''_i\mathcal{E}_l^F(z\alpha_l+\alpha'_l)\Big],$$
$$p_n k_j \hat{R}^{*}_{ni}F''_j = \frac{3}{2}p\mathcal{H}\Big[\mathcal{E}_i^{F''}(x+yz)+\alpha_i\mathcal{E}_l^{F''}(-x\alpha_l+y\alpha'_l)+\alpha''_i\mathcal{E}_l^{F''}(z\alpha_l+\alpha'_l)\Big],$$
$$2F'^{*}_m k_j P''_{jmn}\hat{R}^{*}_{ni} = -\frac{3}{2}q\mathcal{H}\Big[\mathcal{E}_i^{F'}(x-yz-2xy^2)+\alpha_i\mathcal{E}_l^{F'}(-x\alpha_l+z\alpha''_l)$$
$$+\alpha'_i\mathcal{E}_l^{F'}(-y\alpha_l+(1-2y^2)\alpha''_l)+2y\alpha''_i\mathcal{E}_l^{F'}(-x\alpha_l+z\alpha''_l)\Big],$$
$$2F'^{*}_m k_j P_{imn}\hat{R}''^{*}_{nj} = -\frac{3}{2}\frac{k^2}{q}\mathcal{H}''\Big[\mathcal{E}_i^{F'}(x+yz)+\alpha_i\mathcal{E}_l^{F'}(-x\alpha_l+z\alpha''_l)+\alpha'_i\mathcal{E}_l^{F'}(y\alpha_l+\alpha''_l)\Big].$$

Computation of $\mathrm{i}\epsilon_{ijl}k_l\tau_j^F(\boldsymbol{k},\boldsymbol{p})$

$$\mathrm{i}\epsilon_{ijl}k_l k_n k_p \hat{R}''_{np}F'^{*}_j = \frac{3}{2}\frac{k^3}{p}(1-y^2)\mathcal{E}''_0(\alpha'_i\alpha_l\mathcal{E}_l^{Q'}+z\mathcal{E}_i^{Q'}),$$
$$\mathrm{i}\epsilon_{ijl}k_l k_n k_p \hat{R}'_{nj}F''^{*}_p = \frac{3}{2}\frac{k^3}{q}z\mathcal{E}'_0\Big(\alpha_i\mathcal{E}_l^{Q''}(-y\alpha'_l+x\alpha_l)-\mathcal{E}_i^{Q''}(x+yz)-\alpha''_i\mathcal{E}_l^{Q''}(z\alpha_l+\alpha'_l)\Big)$$
$$+\frac{3}{2}\frac{k^3}{p}\mathcal{H}'\mathcal{E}_l^{F''}(\alpha_l+y\alpha''_l)(z\alpha_i+\alpha'_i),$$
$$2\mathrm{i}\epsilon_{ijl}k_l k_r F_m \hat{R}'_{nj}P''_{rmn} = -\frac{3}{2}kq\mathcal{E}'_0\Big(\mathcal{E}_i^Q(xz-y+yx^2+y^3)+\alpha_i\mathcal{E}_l^Q(\alpha_l(2y-xz-2x^2y)$$
$$+\alpha'_l(yz+2xy^2)+2y^2\alpha''_l)+\alpha''_i\mathcal{E}_l^Q(\alpha_l(1-x^2+y^2)+\alpha'_l(2xy+z)+2y\alpha''_l)\Big)$$
$$+\frac{3}{2}\frac{k^2q}{p}\mathcal{H}'\mathcal{E}_l^F\Big(z\alpha_i(y\alpha_l+\alpha''_l)+2yz\alpha''_i(y\alpha_l+\alpha''_l)+\alpha'_i(y\alpha_l+\alpha''_l)(1-2y^2)\Big),$$
$$2\mathrm{i}\epsilon_{ijl}k_l k_r F_m \hat{R}''_{nr}P'_{jmn} = -\frac{3}{2}kp\mathcal{E}''_0\Big(\mathcal{E}_i^Q(-xy-z-zx^2+z^3)+\alpha_i\mathcal{E}_l^Q(\alpha_l(xy+2z)$$

$$
\begin{aligned}
&+ \alpha_l' 2z(xy+z) + yz\alpha_l'') + \alpha_i' \mathcal{E}_l^Q (\alpha_l(1-x^2+z^2) + \alpha_l' 2(xy+z) + y\alpha_l'')\Big) \\
&+ \frac{3}{2}\frac{k^2 p}{q}\mathcal{H}''\mathcal{E}_l^F \Big(\alpha_i(-2z\alpha_l(y+xz) + \alpha_l'(y+2xz) + z\alpha_l'') - (y\alpha_i + \alpha_i'')(\alpha_l' + z\alpha_l) \\
&+ \alpha_i'(\alpha_l(y-2xz-2yz^2) + \alpha_l' 2(x+yz) + \alpha_l'') + \alpha_i''(\alpha_l z(2z^2-3) + \alpha_l'(1-2z^2))\Big)
\end{aligned}
$$

Computation of $\mathrm{i}\epsilon_{ijl}k_l\tau_j^{F*}(\boldsymbol{p},\boldsymbol{k})$

$$
\begin{aligned}
\mathrm{i}\epsilon_{ijl}k_l p_n k_p \hat{R}_{np}^{*''} F_j &= \frac{3}{2}kp(xy+z)\mathcal{E}_0''(\alpha_i\alpha_l\mathcal{E}_l^Q - \mathcal{E}_i^Q) \\
&+ \frac{3}{2}\frac{k^2 p}{q}\mathcal{H}''\mathcal{E}_l^F\Big(\alpha_i(y\alpha_l' - z\alpha_l'') - \alpha_i'(y\alpha_l + \alpha_l'') + \alpha_i''(z\alpha_l + \alpha_l')\Big), \\
\mathrm{i}\epsilon_{ijl}k_l p_n k_p \hat{R}_{nj}^{*} F_p^{''} &= \frac{3}{2}kp\mathcal{H}\mathcal{E}_l^{F''}(\alpha_i + z\alpha_i')(\alpha_l + y\alpha_l'') \\
&- \frac{3}{2}\frac{k^2 p}{q}\mathcal{E}_0\Big(\alpha_i\mathcal{E}_l^{Q''}(x\alpha_l - y\alpha_l') - \alpha_i''\mathcal{E}_l^{Q''}(z\alpha_l + \alpha_l') - \mathcal{E}_i^{Q''}(x+yz)\Big), \\
2\mathrm{i}\epsilon_{ijl}k_l k_p F_m^{*'}\hat{R}_{nj}^{*}P_{pmn}'' &= \frac{3}{2}kq\mathcal{H}\mathcal{E}_l^{F'}(y\alpha_i + \alpha_i'')(\alpha_l + (2xy+z)\alpha_l' + 2y\alpha_l'') \\
&+ \frac{3}{2}\frac{k^2 q}{p}\mathcal{E}_0\Big(\alpha_i\mathcal{E}_l^{Q'}(x\alpha_l - z\alpha_l'') + \alpha_i'\mathcal{E}_l^{Q'}(y\alpha_l + (2y^2-1)\alpha_l'') \\
&+ \alpha_i''(2xy\alpha_l - 2yz\alpha_l'') + \mathcal{E}_i^{Q'}(-x+yz+2xy^2)\Big), \\
2\mathrm{i}\epsilon_{ijl}k_l k_p F_m^{*'}\hat{R}_{np}^{*''}P_{jmn} &= \frac{3}{2}\frac{k^3}{q}\mathcal{H}''\mathcal{E}_l^{F'}(y\alpha_i + \alpha_i'')(\alpha_l + z\alpha_l') + \frac{3}{2}\frac{k^3}{p}\mathcal{E}_0''\Big((1-y^2)(z\mathcal{E}_i^{Q'} + \alpha_i'\alpha_l\mathcal{E}_l^{Q'}) \\
&+ y(\alpha_i\mathcal{E}_l^{Q'}(x\alpha_l - z\alpha_l'') - \alpha_i'\mathcal{E}_l^{Q'}(y\alpha_l + \alpha_l'') - \mathcal{E}_i^{Q'}(x+yz)\Big).
\end{aligned}
$$

For $W_i^F(\boldsymbol{k},\boldsymbol{p})$: there is no contribution after the λ-integration for $S_i^{\mathrm{F,NL(hel)}}$, and the RTI transfer vanishes for $S_i^{\mathrm{Q,NL}}$. Finally, all the formula for the λ and spherical integrations have been previously given so that the final steps are straightforward. One useful relation is $kpq^2(x - yz - 2xy^2) = kpq(x+yz)(q-2yk)$.

Bibliography

Alexakis, A. 2017 Helically decomposed turbulence. *Journal of Fluid Mechanics* **812**, 752–770.

André, J. C. & Lesieur, M. 1977 Influence of helicity on the evolution of isotropic turbulence at high reynolds number. *Journal of Fluid Mechanics* **81**, 187–207.

Antonia, R. A., Lee, S. K., Djenidi, L. & Danaila, L. 2013 Invariants for slightly heated decaying grid turbulence. *Journal of Fluid Mechanics* **727**, 379–406.

Antonia, R. A. & Orlandi, P. 2004 Similarity of decaying isotropic turbulence with a passive scalar. *Journal of Fluid Mechanics* **505**, 123–151.

Antonia, R. A., Ould-Rouis, M., Anselmet, F. & Zhu, Y. 1997 Analogy between predictions of kolmogorov and yaglom. *Journal of Fluid Mechanics* **332**, 395–409.

Antonia, R. A., Tang, S. L., Djenidi, L. & Danaila, L. 2015 Boundedness of the velocity derivative skewness in various turbulent flows. *Journal of Fluid Mechanics* **781**, 727–744.

Antonia, R. A. & Zhu, Y. 1994 Inertial range behavior of the longitudinal heat flux cospectrum. *Boundary-Layer Meteorology* **70**, 429–434.

Baerenzung, J., Politano, H., Ponty, Y. & Pouquet, A. 2008*a* Spectral modeling of magnetohydrodynamic turbulent flows. *Physical Review E* **78** (5), 026310.

Baerenzung, J., Politano, H., Ponty, Y. & Pouquet, A. 2008*b* Spectral modeling of turbulent flows and the role of helicity. *Physical Review E* **77** (5), 046303.

Batchelor, G. K. 1951 Pressure fluctuations in isotropic turbulence. *Mathematical Proceedings of the Cambridge Philosophical Society* **47** (2), 165–182.

Batchelor, G. K. 1959 Small-scale variation of convected quantities like temperature in turbulent fluid part 1. general discussion and the case of small conductivity. *Journal of Fluid Mechanics* **5** (1), 113–133.

Bertoglio, J.-P., Bataille, F. & Marion, J.-D. 2001 Two-point closures for weakly compressible turbulence. *Physics of Fluids* **13** (1), 290–310.

Biferale, L., Musacchio, S. & Toschi, F. 2012 Inverse energy cascade in three-dimensional isotropic turbulence. *Physical Review Letters* **108**, 164501.

Biferale, L., Musacchio, S. & Toschi, F. 2013 Split energy–helicity cascades in three-dimensional homogeneous and isotropic turbulence. *Journal of Fluid Mechanics* **730**, 309–327.

Boldyrev, S., Perez, J. C., Borovsky, J. E. & Podesta, J. J. 2011 Spectral scaling laws in magnetohydrodynamics turbulence simulations and in the solar wind. *The Astrophysical Journal Letters* **741** (1), L19.

Borgas, M. S., Sawford, B. L., Xu, S., Donzis, D.A. & Yeung, P.K. 2004 High schmidt number scalars in turbulence: Structure functions and lagrangian theory. *Physics of Fluids* **16** (11), 3888–3899.

Borue, V. & Orszag, A. 1997 Spectra in helical three-dimensional homogeneous isotropic turbulence. *Physical Review E* **55** (6), 7005–7009.

Bos, W. J. T. 2005 Passive scalar mixing in turbulent flow. PhD thesis, Ecole Centrale Lyon.

Bos, W. J. T. 2014 On the anisotropy of the turbulent passive scalar in the presence of a mean scalar gradient. *Journal of Fluid Mechanics* **744**, 38–64.

Bos, W. J. T. & Bertoglio, J.-P. 2006 A single-time two-point closure based on fluid particle displacements. *Physics of Fluids* **18** (3), 031706.

Bos, W. J. T. & Bertoglio, J.-P. 2007 Inertial range scaling of scalar flux spectra in uniformly sheared turbulence. *Physics of Fluids* **19**, 025104.

Bos, W. J. T., Chevillard, L., Scott, J. F. & Rubinstein, R. 2012 Reynolds number effect on the velocity increment skewness in isotropic turbulence. *Physics of Fluids* **24**, 015108.

Bos, W. J. T., Kadoch, B., Schneider, K. & Bertoglio, J. P. 2009 Inertial range scaling of the scalar flux spectrum in two-dimensional turbulence. *Physics of Fluids* **21**, 115105, 1–8.

Bos, W. J. T., Touil, H. & Bertoglio, J.-P. 2005 Reynolds number dependency of the scalar flux spectrum in isotropic turbulence with a uniform scalar gradient. *Physics of Fluids* **17**, 125108.

Bos, W. J. T., Touil, H., Shao, L. & Bertoglio, J.-P. 2004 On the behavior of the velocity-scalar cross correlation spectrum in the inertial range. *Physics of Fluids* **16** (10), 3818–3823.

Brethouwer, G. 2005 The effect of rotation on rapidly sheared homogeneous turbulence and passive scalar transport. linear theory and direct numerical simulation. *Journal of Fluid Mechanics* **542**, 305–342.

Brissaud, A., Frisch, U., Leorat, J., Lesieur, M. & Mazure, A. 1973 Helicity cascades in fully developed isotropic turbulence. *The Physics of Fluids* **16** (8), 1366–1367.

Buch, K. A. & Dahm, W. J. A. 1996 Experimental study of the fine-scale structure of conserved scalar mixing in turbulent shear flows. part 1. $sc \geq 1$. *Journal of Fluid Mechanics* **317**, 21–71.

Burlot, A., Gréa, B.-J., Godeferd, F. S., Cambon, C. & Griffond, J. 2015*a* Spectral modelling of high reynolds number unstably stratified homogeneous turbulence. *Journal of Fluid Mechanics* **765**, 17– 44.

Burlot, A., Gréa, B.-J., Godeferd, F. S., Cambon, C. & Soulard, O. 2015*b* Large reynolds number self-similar states of unstably stratified homogeneous turbulence. *Physics of Fluids* **27**, 065114.

Cambon, C., Danaila, L., Godeferd, F. S. & Scott, J. F. 2013 Third-order statistics and the dynamics of strongly anisotropic turbulent flows. *Journal of Turbulence* **14** (3), 121–160.

Cambon, C. & Jacquin, L. 1989 Spectral approach to non-isotropic turbulence subjected to rotation. *Journal of Fluid Mechanics* **202**, 295–317.

Cambon, C., Jeandel, J. & Mathieu, J. 1981 Spectral modelling of homogeneous non-isotropic turbulence. *Journal of Fluid Mechanics* **104**, 247–262.

Cambon, C., Mansour, N. N. & Godeferd, F. S. 1997 Energy transfer in rotating turbulence. *Journal of Fluid Mechanics* **337**, 303–332.

Cambon, C., Mons, V., Gréa, B.-J. & Rubinstein, R. 2017 Anisotropic triadic closures for shear-driven and buoyancy-driven turbulent flows. *Computers and Fluids* **151**, 73–84.

Cambon, C. & Rubinstein, R. 2006 Anisotropic developments for homogeneous shear flows. *Physics of Fluids* **18**, 085106.

Cambon, C., Rubinstein, R. & Godeferd, F. S. 2004 Advances in wave turbulence: rapidly rotating flows. *New Journal of Physics* **6** (1), 73.

Cambon, C. & Scott, J. F. 1999 Linear and nonlinear models of anisotropic turbulence. *Annual Review of Fluid Mechanics* **31**, 1–53.

Chasnov, J., Canuto, V. M. & Rogallo, R. S. 1989 Turbulence spectrum of strongly conductive temperature field in a rapidly stirred fluid. *Physics of Fluids A* **1** (10), 1698–1700.

Chasnov, J. R. 1991 Simulation of the inertial-conductive subrange. *Physics of Fluids A* **3** (5), 1164–1168.

Chasnov, J. R. 1995 Similarity states of passive scalar transport in buoyancy-generated turbulence. *Physics of Fluids* **7** (6), 1498–1506.

Chen, Q., Chen, S. & Eyink, G. L. 2003 The joint cascade of energy and helicity in three-dimensional turbulence. *Physics of Fluids* **15** (2), 361–374.

Chkhetiani, O. G. 1996 On the third moments in helical turbulence. *Journal of Experimental and Theoretical Physics Letters* **63**, 808–812.

Chollet, C.E. & Lesieur, M. 1981 Parametrization of small scales of three-dimensional isotropic turbulence utilizing spectral closures. *Journal of the Atmospheric Sciences* **38**, 2747.

Chung, D. & Pullin, D. I. 2010 Direct numerical simulation and large-eddy simulation of stationary buoyancy-driventurbulence. *Journal of Fluid Mechanics* **643**, 279–308.

Clark, T. T. & Zemach, C. 1995 A spectral model applied to homogeneous turbulence. *Physics of Fluids* **7** (7), 1674–1694.

Comte-Bellot, G. & Corrsin, S. 1966 The use of a contraction to improve the isotropy of a grid generated turbulence. *Journal of Fluid Mechanics* **25**, 657–682.

Corrsin, S. 1951*a* The decay of isotropic temperature fluctuations in an isotropic turbulence. *Journal of the Aeronautical Sciences* **18**, 417–423.

Corrsin, S. 1951*b* On the spectrum of isotropic temperature fluctuations in an isotropic turbulence. *Journal of Applied Physics* **22**, 469–473.

Danaila, L., Anselmet, F., Zhou, T. & Antonia, R. A. 1999*a* A generalization of yaglom's equation which accounts for the large-scale forcing in heated decaying turbulence. *Journal of Fluid Mechanics* **391**, 359–372.

Danaila, L., Le Gal, P., Anselmet, F., Plaza, F. & Pinton, J. F. 1999*b* Some new features of the passive scalar mixing in a turbulent flow. *Physics of Fluids* **11** (3), 636–646.

Danaila, L., Zhou, T., Anselmet, F. & Antonia, R. A. 2000 Calibration of a temperature dissipation probe in decaying grid turbulence. *Experiments in Fluids* **28**, 45–50.

Davidson, P. A. 2010 On the decay of saffman turbulence subject to rotation, stratification or an imposed magnetic field. *Journal of Fluid Mechanics* **663**, 268–292.

Davidson, P. A., Okamoto, N. & Kaneda, Y. 2012 On freely decaying, anisotropic, axisymmetric saffman turbulence. *Journal of Fluid Mechanics* **706**, 150–172.

De Marinis, D., Chibbaro, S., Meldi, M. & Sagaut, P. 2013 Temperature dynamics in decaying isotropic turbulence with joule heat production. *Journal of Fluid Mechanics* **724**, 425–449.

De Souza, F. A., Nguyen, V. D. & Tavoularis, S. 1995 The structure of highly sheared turbulence. *Journal of Fluid Mechanics* **303**, 155–167.

Dimotakis, P. E. 1991 Turbulent free shear layer mixing and combustion. In *Progress in Astronautics and Aeronautics, High-Speed Flight Propulsion Systems* (ed. E. T. Curran & S. N. B. Murthy), chap. 5, pp. 265–340. The American Institute of Aeronautics and Astronautics.

Ditlevsen, P. D. & Giuliani, P. 2001 Dissipation in helical turbulence. *Physics of Fluids* **13** (11), 3508–3509.

Donzis, D. A. & Yeung, P. K. 2010 Resolution effects and scaling in numerical simulations of passive scalar mixing in turbulence. *Physica D* **239**, 1278–1287.

Eyink, G. L. & Thomson, D. J. 2000 Free decay of turbulence and breakdown of self-similarity. *Physics of Fluids* **12** (3), 477–479.

Ferchihi, M. & Tavoularis, S. 2002 Scalar probability density function and fine structure in uniformly sheared turbulence. *Journal of Fluid Mechanics* **461**, 155–182.

Galmiche, M. & Hunt, J. C. R. 2002 The formation of shear and density layers in stably stratified turbulent flows: linear processes. *Journal of Fluid Mechanics* **455**, 243–262.

Garg, S. & Warhaft, Z. 1998 On the small scale structure of simple shear flow. *Physics of Fluids* **10** (3), 662–673.

George, W. K. 1992*a* The decay of homogeneous isotropic turbulence. *Physics of Fluids A* **7**, 1492–1509.

George, W. K. 1992*b* *Self-Preservation of Temperature Fluctuations in Isotropic Turbulence*, pp. 514–528. New York, NY: Springer New York.

George, W. K., Beuther, P. D. & Arndt, R.E.A 1984 Pressure spectra in turbulent free shear flows. *Journal of Fluid Mechanics* **148**, 155–191.

George, W. K. & Hussein, H. J. 1991 Locally axisymmetric turbulence. *Journal of Fluid Mechanics* **233**, 1–23.

Germano, M., Piomelli, U., Moin, P. & Cabot, W. H. 1991 A dynamic subgrid-scale eddy viscosity model. *Physics of Fluids A* **3** (7), 1760–1765.

Gibson, C. H. 1968 Fine structure of scalar fields mixed by turbulence. ii. spectral theory. *The Physics of Fluids* **11** (11), 2316–2327.

Gomez, T., Politano, H. & Pouquet, A. 2000 Exact relationship for third-order structure functions in helical flows. *Physical Review E* **61** (5), 5321–5325.

Gonzalez, M. 2000 Asymptotic evolution of a passive scalar advected by homogeneous turbulent shear flow. *International Journal of Heat and Mass Transfer* **43**, 387–397.

Gotoh, T., Fukayama, D. & Nakano, T. 2002 Velocity field statistics in homogeneous steady turbulence obtained using a high-resolution direct numerical simulation. *Physics of Fluids* **14** (3), 1065–1081.

Gotoh, T. & Watanabe, T. 2012 Scalar flux in a uniform mean scalar gradient in homogeneous isotropic steady turbulence. *Physica D* **241**, 141–148.

Gotoh, T. & Watanabe, T. 2015 Power and nonpower laws of passive scalar moments convected by isotropic turbulence. *Physical Review Letter* **115**, 114502.

Granatstein, V. L. & Buchsbaum, S. J. 1966 Fluctuation spectrum of a plasma additive in a turbulence gas. *Physical Review Letters* **16**, 504–507.

Grappin, R., Frisch, U., Léorat, J. & Pouquet, A. 1982 Alfvenic fluctuations as asymptotic states of mhd turbulence. *Astronomy and Astrophysics* **105**, 6–14.

Gréa, B.-J. 2013 The rapid acceleration model and the growth rate of a turbulent mixing zone induced by rayleigh-taylor instability. *Physics of Fluids* **25**, 015118.

Gréa, B.-J., Burlot, A., Godeferd, F., Griffond, J., Soulard, O. & Cambon, C. 2016*a* Dynamics and structure of unstably stratified homogeneous turbulence. *Journal of Turbulence* **17** (7), 651–663.

Gréa, B.-J., Burlot, A., Griffond, J. & Llor, A. 2016*b* Challenging mix models on transients to self-similarity of unstably stratified homogeneous turbulence. *Journal of Fluids Engineering* **138**, 070904.

Griffond, J., Gréa, B.-J. & Soulard, O. 2015 Numerical investigation of self-similar unstably stratified homogeneous turbulence. *Journal of Turbulence* **16** (2), 167–183.

Gualtieri, P., Casciola, C. M., Benzi, R., Amati, G. & Piva, R. 2002 Scaling laws and intermittency in homogeneous shear flow. *Physics of Fluids* **14** (2), 583–596.

Gylfason, A. & Warhaft, Z. 2009 Effects of axisymmetric strain on a passive scalar field: modelling and experiment. *Journal of Fluid Mechanics* **628**, 339–356.

Herr, S., Wang, L.-P. & Collins, L. R. 1996 Edqnm model of a passive scalar with a uniform mean gradient. *Physics of Fluids* **8** (6), 1588–1608.

Herring, J. R., Schertzer, D., Lesieur, M., Newman, G. R., Chollet, J. P. & Larcheveque, M. 1982 A comparative assessment of spectral closures as applied to passive scalar diffusion. *Journal of Fluid Mechanics* **124**, 411–437.

Holzer, M. & Siggia, E. D. 1994 Turbulent mixing of a passive scalar. *Physics of Fluids* **6** (5), 1820–1837.

Isaza, J. C. & Collins, L. R. 2009 On the asymptotic behaviour of large-scale turbulence in homogeneous shear flow. *Journal of Fluid Mechanics* **637**, 213–239.

Ishihara, T., Morishita, K., Yokokawa, M., Uno, A. & Kaneda, Y. 2016 Energy spectrum in high-resolution direct numerical simulations of turbulence. *Physical Review Fluids* **1** (8), 082403.

Ishihara, T., Yoshida, K. & Kaneda, Y. 2002 Anisotropic velocity correlation spectrum at small scales in a homogeneous turbulent shear flow. *Physical Review Letter* **88** (15), 154501.

von Karman, T. & Howarth, L. 1938 On the statistical theory of isotropic turbulence. *Proceedings of the Royal Society of London A: Mathematical, Physical and Engineering Sciences* **164** (917), 192–215.

Karnik, U. & Tavoularis, S. 1987 Generation and manipulation of uniform shear with the use of screens. *Experiments in Fluids* **5**, 247–254.

Karnik, U. & Tavoularis, S. 1989 Measurements of heat diffusion from a continuous line source in a uniformly sheared turbulent flow. *Journal of Fluid Mechanics* **202**, 233– 261.

Kassinos, S. C., Knaepen, B. & Carati, D. 2007 The transport of a passive scalar in magnetohydrodynamic turbulence subjected to mean shear and frame rotation. *Physics of Fluids* **19**, 015105.

Kassinos, S. C., Reynolds, W. C. & Rogers, M. M. 2001 One-point turbulence structure tensors. *Journal of Fluid Mechanics* **428**, 213–248.

Kerr, R. M. 1985 Higher-order derivative correlations and the alignment of small-scale structures in isotropic numerical turbulence. *Journal of Fluid Mechanics* **153**, 31–58.

Knaus, R. & Pantano, C. 2009 On the effect of heat release in turbulence spectra of non-premixed reacting shear layers. *Journal of Fluid Mechanics* **626**, 67–109.

Kolmogorov, A. N. 1941*a* Dissipation of energy in locally isotropic turbulence. *Dokl. Akad. Nauk SSSR* **32**, 16.

Kolmogorov, A. N. 1941*b* The local structure of turbulence in incompressible viscous fluid for very large reynolds numbers. *Dokl. Akad. Nauk SSSR* **30**, 301–305.

Kraichnan, R. H. 1959 The structure of isotropic turbulence at very high reynolds numbers. *Journal of Fluid Mechanics* **5**, 497.

Kraichnan, R. H. 1965 Lagrangian history closure approximation for turbulence. *The Physics of Fluids* **8** (4), 575–598.

Kraichnan, R. H. 1967 Inertial ranges in two-dimensional turbulence. *The Physics of Fluids* **10** (7), 1417–1423.

Kraichnan, R. H. 1971 An almost-markovian galilean-invariant turbulence model. *Journal of Fluid Mechanics* **47**, 513–524.

Kraichnan, R. H. 1973 Helical turbulence and absolute equilibrium. *Journal of Fluid Mechanics* **59**, 745–752.

Kurien, S., Taylor, M. A. & Matsumoto, T. 2004 Isotropic third-order statistics in turbulence with helicity: the 2/15-law. *Journal of Fluid Mechanics* **515**, 87–97.

Launder, B. E., Reece, G. J. & Rodi, W. 1975 Progress in the development of a reynolds-stress turbulence closure. *Journal of Fluid Mechanics* **68**, 537–566.

Lavertu, T. M., Mydlarski, L. & Gaskin, S. J. 2008 Differential diffusion of high-schmidt-number passive scalars in a turbulent jet. *Journal of Fluid mechanics* **612**, 439–475.

Lavoie, P., Djenidi, L. & Antonia, R. A. 2007 Effects of initial conditions in decaying turbulence generated by passive grids. *Journal of Fluid Mechanics* **585**, 395–420.

Lee, M. J., Kim, J. & Moin, P. 1990 Structure of turbulence at high shear rate. *Journal of Fluid Mechanics* **216**, 561–583.

Lee, S. K., Benaissa, A., Djenidi, L., Lavoie, P. & Antonia, R. A. 2012 Scaling range of velocity and passive scalar spectra in grid turbulence. *Physics of Fluids* **24**, 075101.

Leith, C.E. 1971 Atmospheric predictability and two-dimensional turbulence. *Journal of the Atmospheric Sciences* **28**, 145.

Lesieur, M. 2008 *Turbulence in fluids*. Dordrecht: Springer, 4th Edition.

Lesieur, M., Montmory, C. & Chollet, J.P. 1987 The decay of kinetic energy and temperature variance in threedimensional isotropic turbulence. *Physics of Fluids* **30** (4), 1278–1286.

Lesieur, M. & Ossia, S. 2000 3d isotropic turbulence at very high reynolds numbers: Edqnm study. *Journal of Turbulence* **1** (7).

Lesieur, M., Ossia, S. & Metais, O. 1999 Infrared pressure spectra in two- and three-dimensional isotropic incompressible turbulence. *Physics of Fluids* **11** (6), 1535–1543.

Lesieur, M. & Schertzer, D. 1978 Amortissement autosimilaire d'une turbulence á grand nombre de reynolds. *Journal de Mécanique* **17** (4), 609–644.

Levshin, A. O. & Chkhetiani, O. G. 2013 Decay of helicity in homogeneous turbulence. *Letters to Journal of Experimental and Theoretical Physics* **90** (10), 598–602.

Lin, S. C. & Lin, S. C. 1973 Turbulence spectrum of a passive temperature field: results of a numerical simulation. *Physics of Fluids* **16** (10), 1587–1598.

Livescu, D. & Ristorcelli, J. R. 2007 Buoyancy-driven variable-density turbulence. *Joural of Fluid Mechanics* **591**, 43–71.

Llor, A. & Soulard, O. 2013 Comment on "energy spectra at low wavenumbers in homogeneous incompressible turbulence" [phys. lett. a 375 (2011) 2850]. *Physics Letters A* **377**, 1157–1159.

Lumley, J. L. 1967 Similarity and the turbulent energy spectrum. *Physics of Fluids* **10** (4), 855–858.

Lumley, J. L. 1970 *Stochastic Tools in Turbulence*. New York: Reprint of the Academic Press.

Meldi, M. & Sagaut, P. 2012 On non-self-similar regimes in homogeneous isotropic turbulence decay. *Journal of Fluid Mechanics* **711**, 364–393.

Meldi, M. & Sagaut, P. 2013*a* Further insights into self-similarity and self-preservation in freely decaying isotropic turbulence. *Journal of Turbulence* **14** (8), 24–53.

Meldi, M. & Sagaut, P. 2013*b* Pressure statistics in self-similar freely decaying isotropic turbulence. *Journal of Fluid Mechanics* **717, R2**, 1–12.

Métais, O. & Lesieur, M. 1986 Statistical predictability of decaying turbulence. *Journal of the atmospheric sciences* **43** (9), 857–870.

Meyers, J. & Meneveau, C. 2008 A functional form of the energy spectrum parametrizing bottleneck and intermittency effects. *Physics of Fluids* **20**, 065109.

Miller, P. L. & Dimotakis, P. E. 1996 Measurements of scalar power spectra in high schmidt number turbulent jets. *Journal of Fluid Mechanics* **308**, 129–146.

Moffatt, H. K. 1969 The degree of knottedness of tangled vortex lines. *Journal of Fluid Mechanics* **35**, 117–129.

Moffatt, H. K. 1983 Transport effects associated with turbulence with particular attention to the influence of helicity. *Reports on Progress in Physics* **46**, 621–664.

Moffatt, H. K. & Tsinober, A. 1992 Helicity in laminar and turbulent flow. *Annual Review of Fluid Mechanics* **24**, 281–312.

Monin, A.S. & Yaglom, A.M. 1971 *Statistical Fluid Mechanics: Mechanics of Turbulence*. *Dover books on physics* 2. MIT Press.

Mons, V., Cambon, C. & Sagaut, P. 2016 A spectral model for homogeneous shear-driven anisotropic turbulence in terms of spherically-averaged descriptors. *Journal of Fluid Mechanics* **788**, 147–182.

Mons, V., Chassaing, J. C., Gomez, T. & Sagaut, P. 2014*a* Is isotropic turbulence decay governed by asymptotic behavior of large scales? an eddy-damped quasi-normal markovian-based data assimilation study. *Physics of Fluids* **26**, 115105.

Mons, V., Meldi, M. & Sagaut, P. 2014*b* Numerical investigation on the partial return to isotropy of freely decaying homogeneous axisymmetric turbulence. *Physics of Fluids* **26**, 025110.

Mydlarski, L. 2003 Mixed velocity–passive scalar statistics in high-reynolds-number turbulence. *Journal of Fluid Mechanics* **475**, 173–203.

Mydlarski, L. & Warhaft, Z. 1998 Passive scalar statistics in high-péclet-number grid turbulence. *Journal of Fluid Mechanics* **358**, 135–175.

Obukhov, A. M. 1949 Structure of the temperature field in turbulent flow. *Izvestiia Akademii Nauk S.S.S.R., Ser. Geogr. Goofiz.* **13**, 58–69.

O'Gorman, P. A. & Pullin, D. I. 2005 Effect of schmidt number on the velocity–scalar cospectrum in isotropic turbulence with a mean scalar gradient. *Journal of Fluid Mechanics* **532**, 111–140.

Orszag, S.A. 1977 The statistical theory of turbulence. In *Fluid Dynamics* (ed. A. Balian & J.L. Peube), pp. 237–374. Gordon and Breach, New York.

Orszag, S. A. 1970 Analytical theories of turbulence. *Journal of Fluid Mechanics* **41**, 363–386.

Overholt, M. R. & Pope, S. B. 1996 Direct numerical simulation of a passive scalar with imposed mean gradient in isotropic turbulence. *Physics of Fluids* **8** (11), 3128–3148.

Pierrehumbert, R. T. 1994 Tracer microstructure in the large-eddy dominated regime. *Chaos, Solitons & Fractals* **4** (6), 1091–1110.

Piquet, J. 2001 *Turbulent Flows: Models and Physics*, 2nd edn. New York: Springer-Verlag Berlin Heidelberg.

Polifke, W. 1991 Statistics of helicity fluctuations in homogeneous turbulence. *Physics of Fluids A* **3** (1), 115–129.

Polifke, W. & Shtilman, L. 1989 The dynamics of helical decaying turbulence. *Physics of Fluids A* **1** (12), 2025–2033.

Pope, S. B. 2000 *Turbulent Flows*. Cambridge University Press.

Poujade, O. 2006 Rayleigh-taylor turbulence is nothing like kolmogorov turbulence in the self-similar regime. *Physical Review Letters* **97**, 185002.

Poujade, O. & Peybernes, M. 2010 Growth rate of rayleigh-taylor turbulent mixing layers with the foliation approach. *Physical Review E* **81**, 016316.

Pouquet, A., Frisch, U. & Léorat, J.-L. 1976 Strong mhd helical turbulence and the nonlinear dynamo effect. *Journal of Fluid Mechanics* **77**, 321–354.

Pouquet, A., Lesieur, M., André, J. C. & Basdevant, C. 1975 Evolution of high reynolds number two-dimensional turbulence. *Journal of Fluid Mechanics* **72**, 305–319.

Pumir, A. 1994 A numerical study of the mixing of a passive scalar in three dimensions in the presence of a mean gradient. *Physics of Fluids* **6** (6), 2118–2132.

Pumir, A. 1996 Turbulence in homogeneous shear flows. *Physics of Fluids* **8** (11), 3112–3127.

Pumir, A. & Shraiman, B. I. 1995 Persistent small scale anisotropy in homogeneous shear flows. *Physical Review Letters* **75** (17), 3114–3117.

Qian, J. 1995 Viscous range of turbulent scalar of large prandtl number. *Fluid Dynamics Research* **15**, 103–112.

Ristorcelli, J. R. 2006 Passive scalar mixing: Analytic study of time scale ratio, variance, and mix rate. *Physics of Fluids* **18**, 075101.

Rogers, M. M. 1991 The structure of a passive scalar field with a uniform mean gradient in rapidly sheared homogeneous turbulent flow. *Physics of Fluids A* **3** (1), 144–154.

Rogers, M. M., Mansour, N. N. & Reynolds, W. C. 1989 An algebraic model for the turbulent flux of a passive scalar. *Journal of Fluid Mechanics* **203**, 77–101.

Rogers, M. M. & Moin, P. 1987 The structure of the vorticity field in homogeneous turbulent flows. *Journal of Fluid Mechanics* **176**, 33–66.

Rubinstein, R., Kurien, S. & Cambon, C. 2015 Scalar and tensor spherical harmonics expansion of the velocity correlation in homogeneous anisotropic turbulence. *Journal of Turbulence* **16** (11), 1058–1075.

Rust, J. H. & Sesonske, A. 1966 Turbulent temperature fluctuations in mercury and ethylene glycol in pipe flow. *International Journal of Heat and Mass Tranfer* **9**, 215–227.

Saffman, P. G. 1967 The large-scale structure of homogeneous turbulence. *Journal of Fluid Mechanics* **27** (3), 551–593.

Saffman, P. G. & Pullin, D. I. 1996 Calculation of velocity structure functions for vortex models of isotropic turbulence. *Physics of Fluids* **8** (11), 3072–3084.

Sagaut, P. & Cambon, C. 2008 *Homogeneous Turbulence Dynamics*. Cambridge University Press.

Sarkar, S. & Speziale, C. G. 1990 A simple nonlinear model for the return to isotropy in turbulence. *Physics of Fluids A* **2** (1), 84–93.

Scalo, C., Piomelli, U. & Boegman, L. 2012 High-schmidt-number mass transport mechanisms from a turbulent flow to absorbing sediments. *Physics of Fluids* **24**, 085103.

Schumacher, J. 2004 Relation between shear parameter and reynolds number in statistically stationary turbulent shear flows. *Physics of Fluids* **16** (8), 3094–3102.

Schumacher, J., Sreenivasan, K. R. & Yeung, P. K. 2003*a* Derivative moments in turbulent shear flows. *Physics of Fluids* **15** (1), 84–90.

Schumacher, J., Sreenivasan, K. R. & Yeung, P. K. 2003*b* Schmidt number dependence of derivative moments for quasi-static straining motion. *Journal of Fluid Mechanics* **479**, 221–230.

Shen, X. & Warhaft, Z. 2000 The anisotropy of the small scale structure in high reynolds number ($r_\lambda \sim 1000$) turbulent shear flow. *Physics of Fluids* **12** (11), 2976–2989.

Shih, T.H. & Lumley, J.L. 1985 *Modeling of Pressure Correlation Terms in Reynolds Stress and Scalar Flux Equations*. Sibley School of Mechanical and Equations Aerospace Engineering, Cornell University.

Shirani, E., Ferziger, J. H. & Reynolds, W. C. 1981 Mixing of a passive scalar in isotropic and sheared homogeneous turbulence. *Tech. Rep.* Tf15 CR164938. NASA.

Sigman, D. M., Jaccard, S. L. & Haug, G. H. 2004 Polar ocean stratification in a cold climate. *Nature* **428**, 59–63.

Simonsen, A. J. & Krogstad, P.-A. 2005 Turbulent stress invariant analysis: Clarification of existing terminology. *Physics of Fluids* **17**, 088103.

Sirivat, A. & Warhaft, Z. 1983 The effect of a passive cross-stream temperature gradient on the evolution of temperature variance and heat flux in grid turbulence. *Journal of Fluid Mechanics* **128**, 323–346.

Soulard, O. & Griffond, J. 2012 Inertial-range anisotropy in rayleigh-taylor turbulence. *Physics of Fluids* **24**, 025101.

Soulard, O., Griffond, J. & Gréa, B-J. 2014 Large-scale analysis of self-similar unstably stratified homogeneous turbulence. *Physics of Fluids* **26**, 015110.

Soulard, O., Griffond, J. & Gréa, B-J. 2016 Influence of the mixing parameter on the second order moments of velocity and concentration in rayleigh–taylor turbulence. *Physics of Fluids* **28**, 065107.

Sreenivasan, K. R. 1991 On local isotropy of passive scalars in turbulent shear flows. *Proceedings: Mathematical and Physical Sciences* **434**, 165–182.

Sreenivasan, K. R., Antonia, R. A. & Britz, D. 1979 Local isotropy and large structures in a heated turbulent jet. *Journal of Fluid Mechanics* **94**, 745–775.

Sreenivasan, K. R. & Tavoularis, S. 1980 On the skewness of the temperature derivative in turbulent flows. *Journal of Fluid Mechanics* **101**, 783–795.

Sukheswalla, P., Vaithianathan, T. & Collins, L. R. 2013 Simulation of homogeneous turbulent shear flows at higher reynolds numbers: numerical challenges and a remedy. *Journal of Turbulence* **14** (5), 60–97.

Tavoularis, S. 1985 Asymptotic laws for transversely homogeneous turbulent shear flows. *Physics of Fluids* **28** (3), 999–1001.

Tavoularis, S. & Corrsin, S. 1981 Experiments in nearly homogenous turbulent shear flow with a uniform mean temperature gradient. part 1. *Journal of Fluid Mechanics* **104**, 311–347.

Tavoularis, S. & Karnik, U. 1989 Further experiments on the evolution of turbulent stresses and scales in uniformly sheared turbulence. *Journal of Fluid Mechanics* **204**, 457–478.

Tchoufag, J., Sagaut, P. & Cambon, C. 2012 Spectral approach to finite reynolds number effects on kolmogorov's 4/5 law in isotropic turbulence. *Physics of Fluids* **24**, 015107.

Tennekes, H. & Lumley, J.L. 1972 *A first course in Turbulence*. Cambridge: MIT Press.

Tong, C. & Warhaft, Z. 1994 On passive scalar derivative statistics in grid turbulence. *Physics of Fluids* **6** (6), 2165–2176.

Townsend, A. A. 1976 *The structure of turbulent shear flow*, 2nd edn. New York: Cambridge University Press Cambridge.

Venkataramani, K. S. & Chevray, R. 1978 Statistical features of heat transfer in grid-generated turbulence: constant-gradient case. *Journal of Fluid Mechanics* **86**, 513–543.

Vreman, A. W. & Kuerten, J. G. M. 2014 Statistics of spatial derivatives of velocity and pressure in turbulent channel flow. *Physics of Fluids* **26**, 085103.

Waleffe, F. 1992 The nature of triad interactions in homogeneous turbulence. *Physics of Fluids* **4** (2), 350–363.

Warhaft, Z. 1980 An experimental study of the effect of uniform strain on thermal fluctuations in grid-generated turbulence. *Journal of Fluid Mechanics* **99**, 545–573.

Warhaft, Z. 2000 Passive scalars in turbulent flows. *Annual Review of Fluid Mechanics* **32** (3), 203–240.

Warhaft, Z. & Lumley, J. L. 1978 An experimental study of the decay of temperature fluctuations in grid generated turbulence. *Journal of Fluid Mechanics* **88**, 659–684.

Warrior, H., Mathews, S., Maity, S. & Sasmal, K. 2014 An improved model for the return to isotropy of homogeneous turbulence. *Journal of Fluids Engineering* **136**, 034501.

Watanabe, T. & Gotoh, T. 2004 Statistics of a passive scalar in homogeneous turbulence. *New Journal of Physics* **6** (1), 40.

Watanabe, T. & Gotoh, T. 2007 Scalar flux spectrum in isotropic steady turbulence with a uniform mean gradient. *Physics of Fluids* **19**, 121701.

Wikström, P. M., Wallin, S. & Johansson, A. V. 2000 Derivation and investigation of a new explicit algebraic model for the passive scalar flux. *Physics of Fluids* **12** (3), 688–702.

Wyngaard, J. C. 1971 The effect of velocity sensitivity on temperature derivative statistics in isotropic turbulence. *Journal of Fluid Mechanics* **48**, 763–769.

Wyngaard, J. C. & Coté, O. R. 1972 Cospectral similarity in the atmospheric surface layer. *Quarterly Journal of the Royal Meteorological Society* **98**, 590–603.

Yaglom, A. M. 1949 On the local structure of a temperature field in a turbulent flow. *Dokl. Akad. Nauk SSSR* **69**, 743–746.

Yeung, P. K., Donzis, D. A. & Sreenivasan, K. R. 2005 High-reynolds-number simulation of turbulent mixing. *Physics of Fluids* **17**, 081703.

Yeung, P. K. & Sreenivasan, K. R. 2014 Direct numerical simulation of turbulent mixing at very low schmidt number with a uniform mean gradient. *Physics of Fluids* **26**, 015107.

Yeung, P. K., Xu, S., Donzis, D. A. & Sreenivasan, K. R. 2004 Simulations of three-dimensional turbulent mixing for schmidt numbers of the order 1000. *Flow, Turbulence and Combustion* **72**, 333–347.

Yeung, P. K., Xu, S. & Sreenivasan, K. R. 2002 Schmidt number effects on turbulent transport with uniform mean scalar gradient. *Physics of Fluids* **14** (12), 4178–4191.

Zhou, T., Antonia, R. A. & Chua, L. P. 2002 Performance of a probe for measuring turbulent energy and temperature dissipation rates. *Experiments in Fluids* **33**, 334–345.

Zhou, T., Antonia, R. A., Danaila, L. & Anselmet, F. 2000 Transport equations for the mean energy and temperature dissipation rates grid turbulence. *Experiments in Fluids* **28**, 143–151.